ASME
SETTING THE STANDARD

Transactions of the ASME, Journal of Heat Transfer (ISSN 0022-1481) is published monthly by The American Society of Mechanical Engineers, Three Park Avenue, New York, NY 10016. Periodicals postage paid at New York, NY and additional mailing offices. POSTMASTER: Send address changes to Transactions of the ASME, Journal of Heat Transfer, c/o THE AMERICAN SOCIETY OF MECHANICAL ENGINEERS, 22 Law Drive, Box 2300, Fairfield, NJ 07007-2300. **CHANGES OF ADDRESS** must be received at Society headquarters seven weeks before they are to be effective. Please send old label and new address.

Journal of Heat Transfer

Published Monthly by ASME

VOLUME 132 • NUMBER 5 • MAY 2010

RESEARCH PAPERS

(**Contents continued on inside back cover**)

This journal is printed on acid-free paper, which exceeds the ANSI Z39.48-1992 specification for permanence of paper and library materials. ♾™
♻ 85% recycled content, including 10% post-consumer fibers.

Journal of Heat Transfer Volume 132, Number 5 MAY 2010

The ASME Journal of Heat Transfer is abstracted and indexed in the following:

Applied Science and Technology Index, Chemical Abstracts, Chemical Engineering and Biotechnology Abstracts (Electronic equivalent of Process and Chemical Engineering), Civil Engineering Abstracts, Compendex (The electronic equivalent of Engineering Index), Corrosion Abstracts, Current Contents, E & P Health, Safety, and Environment, Ei EncompassLit, Engineered Materials Abstracts, Engineering Index, Enviroline (The electronic equivalent of Environment Abstracts), Environment Abstracts, Environmental Engineering Abstracts, Environmental Science and Pollution Management, Fluidex, Fuel and Energy Abstracts, Index to Scientific Reviews, INSPEC, International Building Services Abstracts, Mechanical & Transportation Engineering Abstracts, Mechanical Engineering Abstracts, METADEX (The electronic equivalent of Metals Abstracts and Alloys Index), Petroleum Abstracts, Process and Chemical Engineering, Referativnyi Zhurnal, Science Citation Index, SciSearch (The electronic equivalent of Science Citation Index), Theoretical Chemical Engineering

The Effect of Spatially Correlated Roughness and Boundary Conditions on the Conduction of Heat Through a Slab

A. F. Emery
e-mail: emery@u.washington.edu

H. Dillon

A. M. Mescher

Department of Mechanical Engineering,
University of Washington,
Seattle, WA 98195-2600

The nominally one-dimensional conduction of heat through a slab becomes two dimensional when one of the surfaces is rough or when the boundary conditions are spatially nonuniform. This paper develops the stochastic equations for a slab whose surface roughness or convective boundary condition is spatially correlated with correlation lengths ranging from 0 (white noise) to a length long in comparison to the slab thickness. The effect is described in terms of the standard deviation and the resulting spatial correlation of the heat flux as a function of depth into the slab. In contrast to the expectation that the effect is monotonic with respect to the correlation length, it is shown that the effect is maximized at an intermediate correlation length. It is also shown that roughness or a random convective heat transfer coefficient have essentially the same effects on the conducted heat, but that the combination results in a much deeper penetration than does each effect individually. In contrast to the usual methods of solving stochastic problems, both the case of a rough edge and a smooth edge with stochastic convective heat transfer coefficients can only be treated with reasonable computational expense by using direct Monte Carlo simulations. [DOI: 10.1115/1.4000445]

Keywords: surface roughness, correlated boundary conditions, stochastic conduction, uncertainty

1 Introduction

In drawing polymer optical fibers, heating is done by radiation from the furnace walls and convection from the air contained in the furnace. In contrast to drawing glass fibers where the dominant heat transfer is by radiation from the very high temperature furnace walls, the heating of polymer fibers is done at a much lower temperature, on the order of 200°C, and the free convection of the air enclosed in the furnace provides as much as 50% of the heating. We observed that the fiber diameter was strongly affected by the nature of the free convective flow [1], as illustrated in Fig. 1 that shows the variations with respect to the long term mean response.

Looking at Fig. 1(*b*) it appears that the regular variation in the convective heat transfer when the flow is oscillating creates a temperature variation along the length of the fiber that leads to relatively regular changes in diameter. When the flow is chaotic, as detected by the history of the air temperature, the changes in the diameter also become chaotic. Note that the amplitude of the diameter changes is also significantly greater. Since the history of drawing of the fiber from the preform is dependent on the elevated temperature in the preform, it appears that the chaotic heat transfer induces a deeper effect than does the more regularly varying heat transfer. The question is whether the diameter changes interact with the heat transfer variations. Observations of the flow field using particle image velocimetry (PIV) suggested that the convective heat transfer was also stochastic. In an attempt to understand how the diameter and the heat transfer might interact, we embarked on the study reported here. Admittedly, although a steady state problem is not equivalent to the transient fiber drawing case, we felt that it was important to understand the effect of the stochastic boundary conditions before attempting to simulate the entire drawing process, which involves solving for both the free convective flow and the structural changes in the fiber.

2 Steady State Conduction

Consider the conduction of heat through a slab of thickness W and unit depth whose rough surface at $x=0$ is presumed to be locally random with a correlation length $\mathcal{L}$, Fig. 2. Because of the two-dimensional nature of the surface, both x and y components of heat will exist. A similar situation will exist if the surface temperature, the convective heat transfer coefficient, or both vary in the y direction. For a value of $\mathcal{L}$ that is small in relation to the slab width W, i.e., approaching white noise, the effects are expected to attenuate quickly with increasing distance into the slab. For larger values of $\mathcal{L}$, implying smoother variations with respect to y, the effects are expected to propagate with little change through the thickness.

Let both the deviation of the edge from the nominal value of $x=0$, defined as $r(y)$, and the variation of the convective heat transfer coefficient be characterized by the random field, $\xi(y)$, such that

$$r(y) = \sigma\xi(y) \tag{1a}$$

and

$$h(y) = \bar{h} + \sigma\xi(y) \tag{1b}$$

where $\xi(y)$ is a random field whose mean at any specific value of y is zero with a standard deviation of unity and σ is the standard deviation of the field. $\xi(y)$ has a spatial correlation length of $\mathcal{L}$. If $\mathcal{L}=0$, i.e., $\xi(y)$ is characterized by white noise, we expect that the region in which the conductive flux is two dimensional will be very thin and approach zero in extent, while if $\mathcal{L}$ is large in comparison to H, $\xi(y)$ will be nearly constant with respect to y, i.e., be a random variable with $\xi(y)=\bar{\xi}$ and the heat transfer will approach

Contributed by the Heat Transfer Division of ASME for publication in the JOURNAL OF HEAT TRANSFER. Manuscript received February 2, 2009; final manuscript received October 1, 2009; published online March 8, 2010. Assoc. Editor: O. A. Ezekoye.

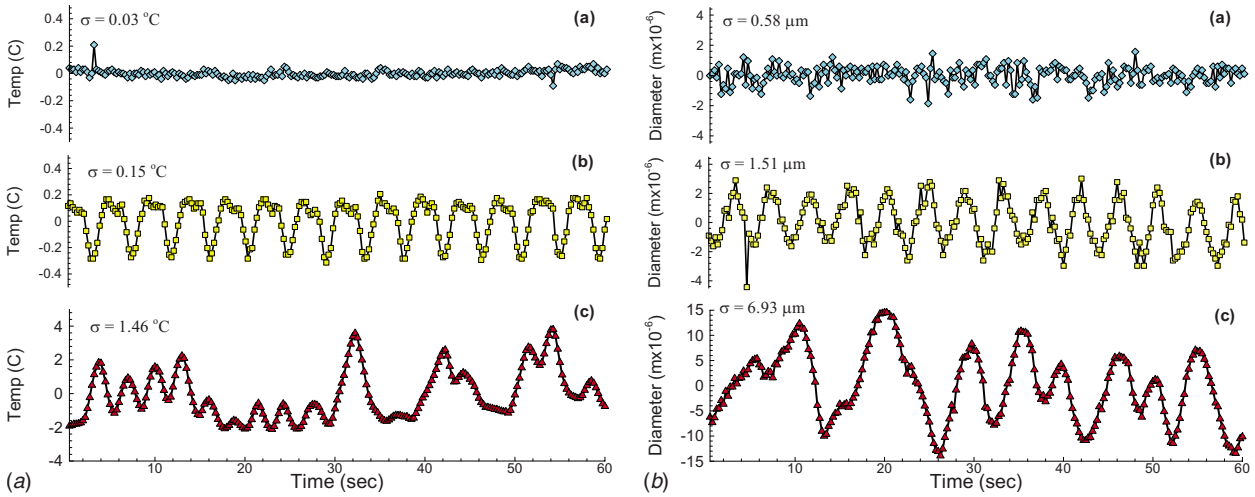

Fig. 1 Characteristic air and fiber diameter histories: (*a*) laminar, (*b*) oscillatory, and (*c*) chaotic flow regimes (note the different scales)

that of one-dimensional conduction with values per unit depth of

$$\overline{q}_x = \frac{k\Delta T}{\overline{W}} \quad \text{with} \quad \sigma(q_x) \approx \overline{q}_x \frac{\sigma(\xi)}{\overline{W}} \tag{2a}$$

and

$$q_x = \frac{k\Delta T}{(\overline{W} + k/\overline{h})} \quad \text{with} \quad \sigma(q_x) \approx \overline{q}_x \frac{\overline{k}}{\overline{h}} \frac{\sigma(\xi)}{\overline{h}} \tag{2b}$$

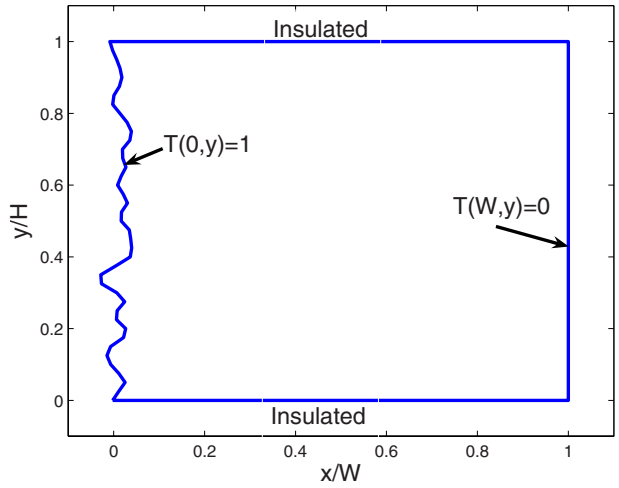

Fig. 2 Schematic of a slab with a rough surface

where the overbars represent averages. Consider a square, with $W=1$, $\Delta T=100$, and $k=1$. For zero roughness, the nondimensional heat flux $q_x=100$ is independent of x and y. Figures 3(*a*) and 3(*b*) illustrate the effect of a triangular roughness on the x component of heat flux. While keeping the magnitude of the surface deviation constant, as the number of triangular surface elements increases, the region affected by their presence diminishes. Without detailed analysis, it might then be reasonable to assume that the region in which two-dimensional conduction is important will gradually diminish in size as $\mathcal{L}$ decreases. As shown in Sec. 8 this is not the case and there is actually an amplification of the uncertainty in a region near the rough edge.

Because of the random nature of the surface, this system is stochastic in nature and the evaluation of the net heat transfer will involve the solution of a partial differential equation over a random region or if the boundary condition is stochastic, solving the partial differential equation (pde) with a stochastic boundary condition. In most of the reported literature, the stochasticity is associated with a property such as the thermal conductivity or a boundary condition, usually the temperature. The two problems,

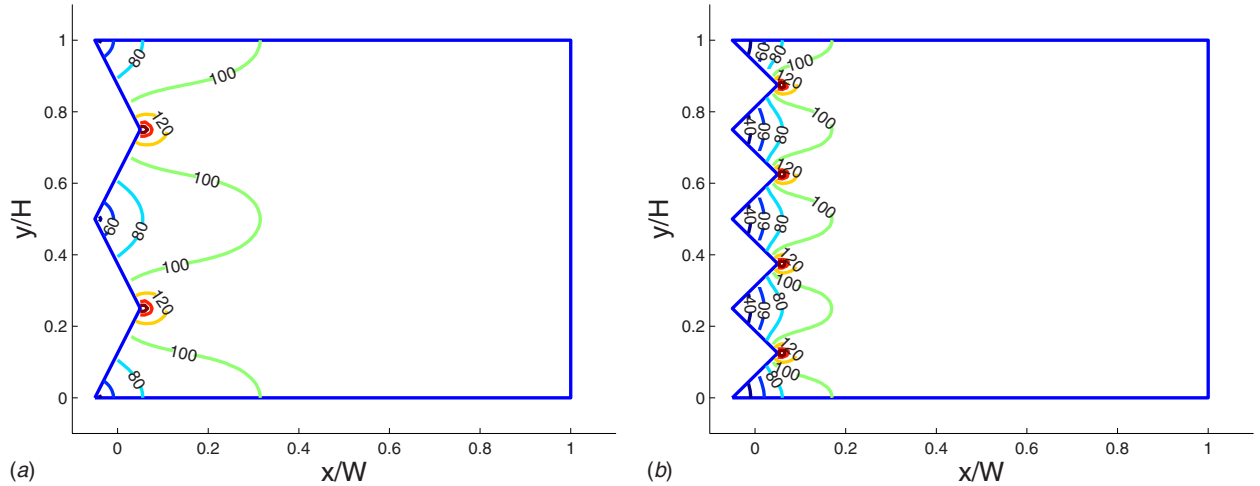

Fig. 3 Contours of $q_x(x,y)$ for $W=1$, $\Delta T=100$, and $k=1$

that of a random roughness and that of a random boundary condition, are fundamentally different and require different approaches.

There are very few reported results for random regions [2–5]. Lin et al. [3] solved the problem of a rough leading edge on a wedge in supersonic flow using polynomial chaos coupled with a perturbation analysis of the flow equations and a mapping of the region. However, the mapping technique is valid only for Neumann boundary conditions. References [4,5] suggest a method in which a coordinate system is embedded in an elastic domain whose shape is that of the mean region being studied. The embedded coordinate system is similar to that used for deterministic irregular surfaces [6]. Forces are applied to the domain and using the distorted coordinate system the field equations are solved for the desired quantity, temperature in our case. These forces are determined by solving the inverse elasticity problem, with the distorted grid being a natural consequence of the solution of the coupled equations of elasticity. For each simulation, solving for the temperature requires the evaluation of the conductance matrix based on the movement of the embedded nodal points. This approach is both complex and computationally expensive and it is not clear that it is less expensive than using the highly efficient mesh generators available in commercial software.

3 Solving the Stochastic Equations for a Stochastic Region

When the region is stochastic, e.g., the rough edge, the usual finite element approach is not appropriate because the limits of integration for the necessary matrices are not fixed, but random. A possible approach is to convert the problem of a stochastic region to one in which the conductivity is stochastic. This is done by redefining the coordinate system from x,y to s,t. Let the problem be changed slightly such that the rough edge is at $x=W$ and let

$$s(y) = x/W(y) \quad 0 \le s(y) \le 1 \tag{3a}$$

$$t = y/H \quad 0 \le t \le 1 \tag{3b}$$

In terms of s,t the problem is one of a constant region and the two-dimensional conduction equation with unit conductivity becomes

$$\frac{\partial T^2}{\partial x^2} + \frac{\partial T^2}{\partial y^2} = s\left(2\left(\frac{W'}{W}\right)^2 - \frac{W''}{W}\right)\frac{\partial T}{\partial s} + \left(\frac{sW'}{W}\right)^2\frac{\partial^2 T}{\partial s^2} - 2\frac{sW'}{W}\frac{\partial^2 T}{\partial s\,\partial t} + \frac{\partial^2 T}{\partial t^2} \tag{3c}$$

where W' and W'' represent derivatives with respect to y. The equation can be solved by (a) Monte Carlo simulation, (b) the Neumann expansion of the conductance matrix, and (c) polynomial chaos. Regardless of the method used, the solution of Eq. (3*c*) is difficult because of the following reasons.

(1) The terms $\partial T/\partial s$ and $\partial^2 T/\partial s\,\partial t$ introduce a pseudo-advection effect coupled with an equivalent pseudo-anisotropic conductivity, both of which are stochastic. In addition, the anisotropic conductivities k_{st} and k_{ts} are of the form $-sW'/W$ and when negative can cause significant numerical problems.
(2) The term $sW''/W\,\partial T/\partial s$ imputes a behavior similar to the advection term in computational fluid dynamics (CFD). Given that it required several generations of effort to understand how to correctly evaluate the advection term, the authors are not eager to invest a comparable effort in solving Eq. (3*c*).
(3) Irrespective of how Eq. (3*c*) is solved, since W and its derivatives will need to be expressed as a sum of eigenfunctions (see Sec. 4) this will lead to an excessive number of coupled equations to solve.

One obvious choice is to use the Monte Carlo simulation approach with a mesh generated for each realization of the rough surface. This of course is computationally ultra-expensive, involving both the generation of the mesh, the formation of the conductance matrix, its inversion, and the solution.

4 Meshing and Representation of a Random Field

To solve the problem using finite elements/volumes requires resolving the questions of the mesh size and how to represent the random field within the element. Unfortunately there are no definitive answers to either question. Several common approaches are (a) integrating $\xi(x,y)$ over the element, (b) using a centroidal value, and (c) evaluating $\xi(x,y)$ at the nodal points and interpolating. In general, centroidal values tend to overpredict and spatial averaging underpredicts the variability of $\xi(x,y)$ over the element. The approach depends on the scale of fluctuations [7] and Li and Der Kiureghian [8] summarized several approaches.

The question of the appropriate mesh size is more difficult to resolve. One suggestion is that the correlation length $\mathcal{L}$ should span two to three elements [7]. If $\xi(y)$ is a zero mean, wide sense stationary, random field, some guidance can be found by considering how $\xi(y)$ is represented through the Karhunen–Loeve (KL) expansion in eigenfunctions given by [9]

$$\xi(y) = \sum_{i=1}^{\infty} \sqrt{\lambda_i} f_i(y) u_i \tag{4a}$$

where u_i are uncorrelated random variables and λ_i and $f_i(y)$ are the eigenvalues and orthogonal eigenfunctions that satisfy

$$f_i(y) = \frac{1}{\lambda_i}\int C(y,y')f_i(y')dy' \tag{4b}$$

$$\int f_i(y)f_j(y)dy = \delta_{ij} \tag{4c}$$

where $C(y,y')$ is the covariance function and δ_{ij} is the Kronecker delta. Equation (4*a*) defines a realization of $\xi(y)$ as the sum of the deterministic functions $f_i(y)$, which are ordered in terms of their eigenvalues, multiplied by multiple random variables u_i that satisfy

$$E[u_i] = 0, \quad E[u_i u_j] = \delta_{ij} \tag{4d}$$

While u_i are uncorrelated, they are not independent, and the typical procedure involves the following:

(1) representing a random field in terms of uncorrelated random variables, u_i, Eq. (4*a*)
(2) converting all random variables into Gaussian variables [10]

Inasmuch as a lack of correlation does not imply independence, the second step is necessary for both practical and theoretical reasons since uncorrelated Gaussian random variables are independent. Li and Der Kiureghian [8] and Phoon et al. [11] described the techniques for converting the random variables to Gaussian variables, usually in the form of multidimensional Hermite polynomials involving several Gaussian random variables, η_i, $i=1,\ldots,G$. If G is large, the dimensionality of the problem can grow to an unacceptable size.

The series, Eq. (4*a*), is usually terminated at N terms and the combined variance of the first N vectors is given by

$$\sigma^2(\xi) = \sum_{i=1}^{N} \lambda_i^2 \tag{5}$$

The number of such random variables, u_i, needed will depend on the desired accuracy. For a mesh with $\Delta y = 1/140$ over $0 \le y \le 1$, the number of vectors needed to achieve 99.9% of the total vari-

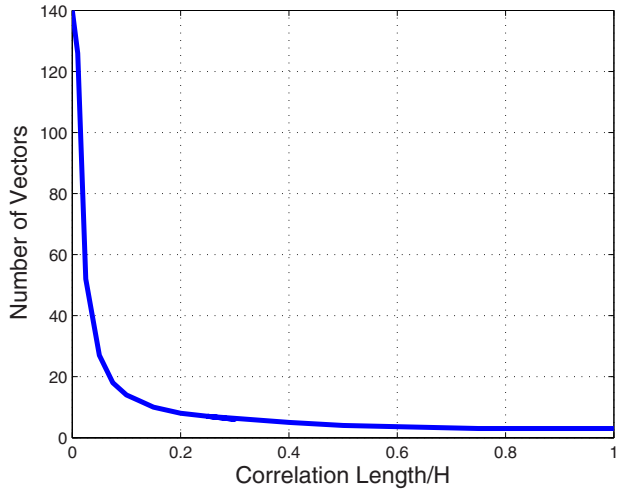

Fig. 4 Number of vectors *N* using Eq. (4*a*) needed to achieve 99.9% of the true variance as a function of the correlation length $\mathcal{L}/H$ (the number approaches infinity as $\mathcal{L}\to 0$ (white noise))

ance is shown in Fig. 4. (Our computed results, see Sec. 8, did not show adequate convergence unless more than 99.9% of the variance of the rough edge was accounted for.) Similar effects were noted by Lin et al. [3] who considered a special covariance kernel to produce a correlated roughness over a finite length and observed that for $\mathcal{L}/H=0.01$ 60 terms were needed.

About the only analytical solution is for the covariance $C(y,y')=\exp(|y-y'|/\mathcal{L})$. Unfortunately this possesses some undesirable characteristics, e.g., a discontinuous slope at $y=y'$, and is not a convenient covariance [12]. For other covariances Eq. (4*a*) must be solved numerically and the eigenfunctions replaced with eigenvectors. In this case, the KL expansion is usually referred to as principal components [13]. Figure 5(*a*) depicts the eigenvectors for the covariance $C(y,y')=\exp((y-y')^2/\mathcal{L}^2)$. Each succeeding vector contributes less to the total variance as shown in Fig. 5(*b*). To achieve 99.9% of the total variance requires nine terms in the expansion, Eq. (4*a*). The ninth vector, indicated by the heavy dashed vector, has a wavelength of approximately $1.5\mathcal{L}$. This proved to be the case for all values of $\mathcal{L}$ examined from $0.01H$ to $3H$. Since boundary conditions usually require of the order of three elements per wavelength for satisfactory results, this suggests that an adequate mesh would be one in which $\Delta y \approx 0.5\mathcal{L}$.

5 Solving the Stochastic Equations for Stochastic Properties

Let us represent the discretized form for the steady state solution of the energy equation as it is commonly expressed in the finite element or finite volume methods

$$T(x,y)=[\mathcal{K}+\mathcal{H}]^{-1}(\mathcal{S}+\mathcal{B}) \tag{6}$$

where $\mathcal{K}$ is the conductance matrix, $\mathcal{H}$ represents the contribution of the boundary conditions, $\mathcal{S}$ represents sources, and $\mathcal{B}$ represents the known components of the boundary conditions, and the effect of the prescribed boundary temperatures is incorporated into the matrix $\mathcal{K}+\mathcal{H}$ and the vector $\mathcal{B}$. The solution of Eq. (6) depends on the nature of the randomness of the problem.

6 Stochastic Properties

Consider the case where either the conductivity or the boundary conditions are stochastic. Let such stochastic properties, p, be represented as $\overline{p}+\sigma\xi$ and the matrices $\mathcal{K}$ and $\mathcal{H}$ and the vectors $\mathcal{S}$ and $\mathcal{B}$ be expressed in the form $\mathcal{K}=\overline{\mathcal{K}}+\mathcal{K}_p$ where $\mathcal{K}_p$ represents the contribution due to the deviation of p from $\overline{p}$. For a deterministic region, $\mathcal{K}_p$ will be of the form $\mathcal{K}_p=\sigma\xi\mathcal{K}'$ where $\mathcal{K}'$ is a function of the geometry. For example, if the conductivity is random, but constant with respect to space, time, and temperature, $\overline{\mathcal{K}}=k\mathcal{G}$ and $\mathcal{K}'=\mathcal{G}$ where $\mathcal{G}$ is found from the usual integration of the weak form

$$\mathcal{G}=\int_x\int_y\begin{pmatrix}\mathcal{N}_x\mathcal{N}_x & \mathcal{N}_x\mathcal{N}_y\\ \mathcal{N}_x\mathcal{N}_y & \mathcal{N}_y\mathcal{N}_y\end{pmatrix}dxdy \tag{7}$$

where $\mathcal{N}$ are the basis functions. For several random properties, $p_1,p_2,\ldots,p_P$, Eq. (6) will be in the form

$$T(x,y)=[\overline{\mathcal{K}}+\mathcal{K}_1+\cdots+\mathcal{K}_P+\overline{\mathcal{H}}+\mathcal{H}_1+\cdots+\mathcal{H}_P]^{-1}$$
$$(\overline{\mathcal{S}}+\mathcal{S}_1+\cdots+\mathcal{S}_P+\overline{\mathcal{B}}+\mathcal{B}_1+\cdots+\mathcal{B}_P) \tag{8}$$

The deviation ξ is taken to have some specific form, most commonly a Gaussian random, or truncated Gaussian, distribution; but other distributions, e.g., log normal, beta, and gamma, may be more appropriate.

There are three common methods of solving Eq. (8): Monte Carlo simulation, Neumann series expansion, and polynomial chaos. Of these, only direct Monte Carlo simulation approach was found to be successful for the rough edge and the Neumann series approach succeeded only for a limited range of correlation lengths. In principal polynomial chaos could be applied, but the dimensionality of this method was too large.

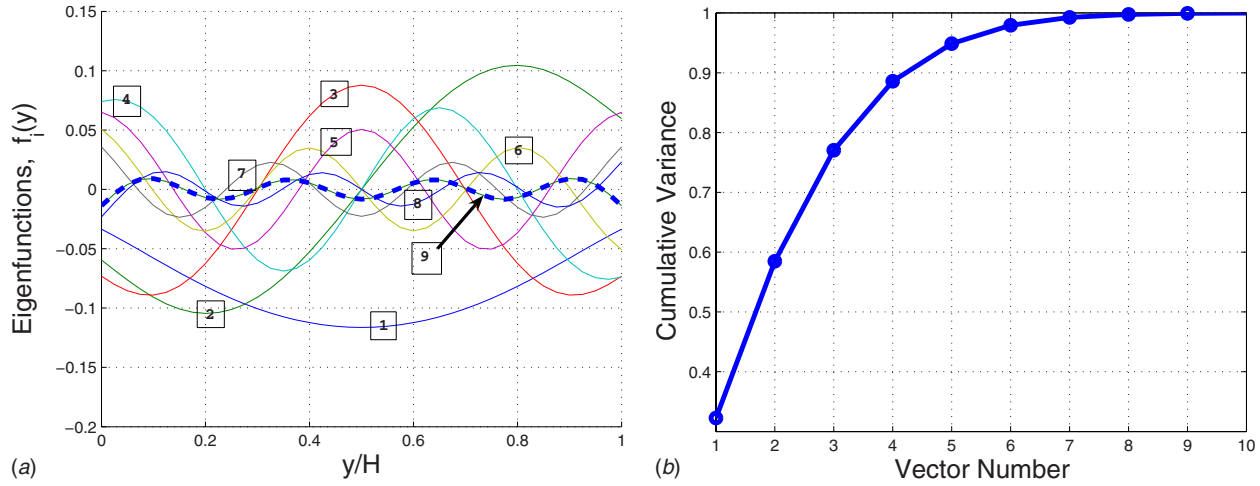

Fig. 5 Principal component analysis for $\mathcal{L}/H=0.2$

6.1 Monte Carlo Simulation. This approach involves sampling the stochastic parameter ξ a large number of times, M, and forming the matrix $\mathcal{K}+\mathcal{H}$ and the right hand side, $\mathcal{S}+\mathcal{B}$, inverting $\mathcal{K}+\mathcal{H}$ and solving for $T(x,y)$ for each sample. The statistics of the resulting solutions, e.g., the mean and the standard deviation, are then easily obtained. While simple, the computational expense is often unacceptably high and the method is usually used only for simple problems or as a check on other approaches.

6.2 Neumann Series Approach. Here denote $\mathcal{K}+\mathcal{H}$ as $\overline{\mathcal{K}\mathcal{H}}(\mathcal{I}+\Delta\mathcal{K}\mathcal{H})$. The inverse of $\mathcal{K}\mathcal{H}$ is then given as

$$[\mathcal{K}\mathcal{H}]^{-1} = (\mathcal{I}+\Delta\mathcal{K}\mathcal{H})^{-1}(\overline{\mathcal{K}\mathcal{H}})^{-1} \tag{9a}$$

and

$$(I+\Delta\mathcal{K}\mathcal{H})^{-1} = \mathcal{I} - \Delta\mathcal{K}\mathcal{H} + (\Delta\mathcal{K}\mathcal{H})^2 - (\Delta\mathcal{K}\mathcal{H})^3\cdots \tag{9b}$$

where $\mathcal{I}$ is the identity matrix. This method succeeds only if the norm of $\Delta\mathcal{K}\mathcal{H}$ is less than 1. One needs to perform only one inversion, that of $\overline{\mathcal{K}\mathcal{H}}$, and then a number of multiplications. For most problems the cost of the inversion is orders of magnitude more than that of the multiplications; so the method, if successful, is usually cheap, particularly compared with the Monte Carlo method.

6.3 Polynomial Chaos. This very popular and extensively used method originally popularized by Ghanem and Spanos [9] differs substantially from the preceding two. It consists of representing the random variable in an infinite series of orthogonal functions, Hermite polynomials for Gaussian random variables, and the solution also in an infinite series, usually of the same functions. Excellent summaries of the method are available in Refs. [14,15]. For example, for the conductivity being a random variable, not a field, i.e., needing only one ξ_i, we use

$$k(\xi) = \sum_{i=1}^{K} k_i h_i(\xi) \tag{10a}$$

and

$$T(x,y,\xi) = \sum_{i=1}^{J} T_i h_i(\xi) \tag{10b}$$

where $h_i(\xi)$ are one-dimensional Hermite polynomials. Since $h_0(\xi)=1$ and $h_1(\xi)=\xi$, if k is a Gaussian random variable, only two terms are needed in Eq. (10*a*). The number of terms used to represent $T(x,y,\xi)$, J, is dependent on the statistical nature of $k(\xi)$ and on the magnitude of σ.

The expressions for $k(\xi)$ and $T(\xi)$ are substituted into the energy equation; the equation is multiplied by $h_m(\xi)$ and integrated over the range of ξ (i.e., projected onto $h_m(\xi)$). Because $h_i(\xi)$ are orthogonal functions, this yields a series of coupled linear differential equations to solve.

For the problem in which the convective heat transfer coefficient is a random field on the boundary, $x=0$, which is represented by N terms in Eq. (4*a*), the orthogonal function representing $h(y)$ becomes a multidimensional function of the N values of u_i. In addition, if u_i is not Gaussian, then each u_i must be represented by an additional multidimensional function, considerably increasing the complexity of the solution.

Even if the field is Gaussian, i.e., only $h_i(\xi)$ is needed to represent the deviation $h(\xi)-\overline{h}$, the total number of terms in the differential equation is large and equal to $(J+N)!/J!N!$, and this becomes computationally infeasible even for small values of J and N. For random fields that are better represented by other multidimensional orthogonal polynomials, the value of K is larger than N. Thus even when the expansion, Eq. (10*a*), is limited to a relatively low order polynomial this number increases at an exceptional speed. For example, using a third order polynomial for $T(x,y)$ with two random variables leads to solving ten coupled equations.

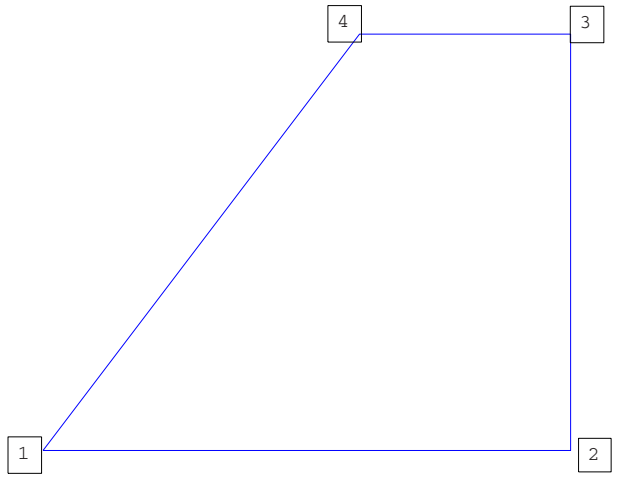

Fig. 6 An element to represent a rough edge

The use of the appropriate polynomials is optimal, in the sense of requiring the smallest number of terms in the expansion, and using Hermite polynomials to represent non-Gaussian processes often requires one or two more terms than the optimal expansion. The problem comes with mixing the representation [15]. For example, if ξ is truly Gaussian, then it should be expanded in Hermite polynomials, but the resulting $T(x,y,\xi)$ may be better approximated with other polynomials. However, the approach described above, Eq. (10*a*), which is based on orthogonality, requires that the same polynomial be used for all expansions and since one does not know in advance what polynomial would be optimal for representing $T(x,y,\xi)$, it is common to express everything in terms of Hermite polynomials. Xiu and Karniadakis [15] gave the details of how to best represent random variables with differing distributions in terms of Hermite polynomials.

LeMaitre et al. [14] solved the problem of free convection in a square region, $W\times H$, with isothermal vertical walls and insulated horizontal walls. The hot wall temperature was fixed at 1 and the cold wall temperature had a stochastic distribution with correlation lengths of 0.5, 1, and 2H. A rectangular mesh of 140×100 elements with ten eigenfunctions to express the stochastic variable cold wall temperature was found to be sufficient when the polynomial chaos representation of the temperature and velocity was linear in the stochastic variable u_i. For our case where we wish to investigate the stochastic nature of the heat flux near the rough wall preliminary calculations suggest that we need the order of $J=3$ and to represent the short correlation lengths, Fig. 4, $K>100$, thus the number of coupled equations needed to be solved is in excess of 10^6 (the equations are strongly coupled because of the terms W' and W' in Eq. (3)). For longer correlation lengths, $\mathcal{L}/H\approx0.2$, we anticipate solving 5000 coupled equations.

7 Nature of Statistical Characteristic of $\mathcal{K}$

It is not easy or intuitive to understand how the conductance matrix $\mathcal{K}$ or the matrix $\mathcal{H}$ behave as functions of the random field ξ. One approach is to examine the behavior of a quadrilateral element whose nodes, nodes 1 and 4 of Fig. 6, can be used to represent the rough edge.

Using isoparametric basis functions, $\mathcal{N}$, the components of the element conductance matrix are

$$\int_A \left\{\frac{d\mathcal{N}}{dx}\right\}\left\langle\frac{d\mathcal{N}}{dx}\right\rangle dxdy = \frac{h}{16}\frac{1}{b}\begin{pmatrix} A & -A & -C & C \\ -A & A & C & -C \\ -C & C & B & -B \\ C & -C & -B & B \end{pmatrix} \tag{11a}$$

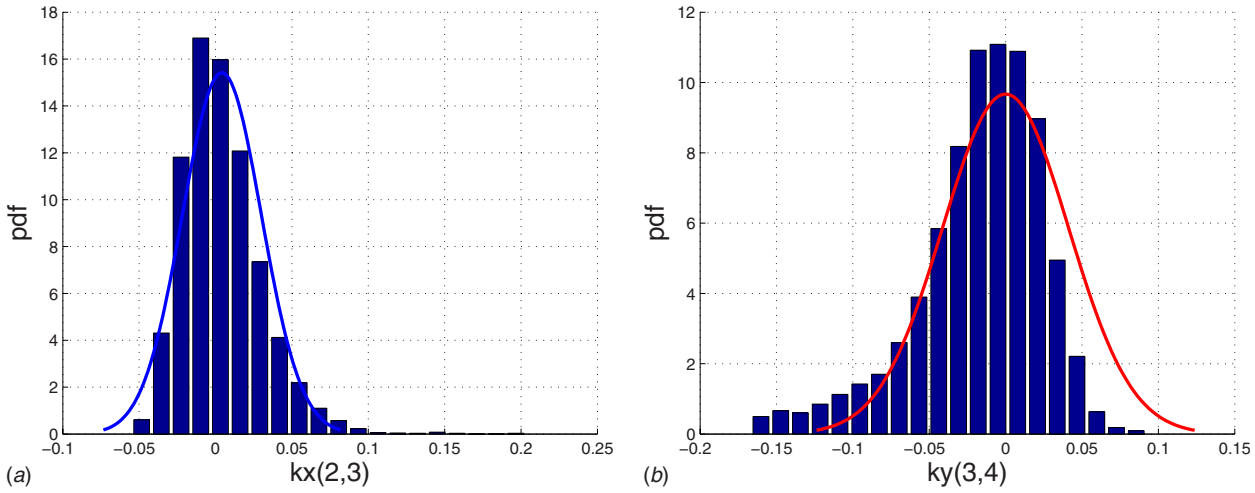

Fig. 7 Variation of terms in the conductance matrix, Eq. (7): (*a*) $k_x(2,3)$ and (*b*) $k_y(3,4)$

$$\int_A \left\{\frac{d\mathcal{N}}{dy}\right\}\left\langle\frac{d\mathcal{N}}{dy}\right\rangle dxdy = \frac{1}{3h}\begin{pmatrix} d1 & D & E & F \\ D & d2 & F & G \\ E & F & d3 & H \\ F & G & H & d4 \end{pmatrix} \tag{11b}$$

where

$$a = x_2 + x_3 - x_1 - x_4 \quad b = x_1 - x_4$$

$$h = y_4 - y_1 = y_3 - y_2$$

$$A = \left(1 + \frac{a}{b}\right)^2 \ln\left(\frac{1 + b/a}{1 - b/a}\right) - 4 - 2\frac{a}{b}$$

$$B = \left(1 - \frac{a}{b}\right)^2 \ln\left(\frac{1 + b/a}{1 - b/a}\right) + 4 - 2\frac{a}{b}$$

$$C = \left(1 - \frac{a^2}{b^2}\right)\ln\left(\frac{1 + b/a}{1 - b/a}\right) + 2\frac{a}{b}$$

$$d1 = 2bA + 4b + 2a \quad d2 = 2bA - 2b + 2a$$

$$d3 = 2bB + 2b + 2a \quad d4 = 2bB - 4b + 2a \tag{11c}$$

$$D = -2bA - b + a$$

$$E = -2bC - 3b - a$$

$$F = 2bC - 2a$$

$$G = -2bC + 3b - 1$$

$$H = -2bB + b + a$$

and the coordinates x_1 and x_4 are the components of the random field $\xi(y)$ at each y mesh line. It appears because of the logarithmic terms in Eq. (11) that a Gaussian distribution of the edge does not introduce a Gaussian distribution of conductance. Figure 7 shows how two of the terms in the element conductance matrices for the x and y conductance, Eq. (8), vary.

It is clear that the conductance matrices will lead to temperature and flux fields that exhibit a non-Gaussian behavior and will lead to suboptimal solutions when using Hermite polynomials, necessitating more terms in Eq. (4*a*) than desired. The Neumann series solution cannot be used because each realization of the random field gives a different form to $\mathcal{K}_p$, meaning that one cannot express the conductance matrix as $\mathcal{K} = \overline{\mathcal{K}} + \sigma\Delta\mathcal{K}_p$ where $\overline{\mathcal{K}}$ and $\Delta\mathcal{K}_p$ are independent of $\xi(y)$.

8 Convergence Studies

The problem was solved for a unit thermal conductivity (all results presented are nondimensional, being normalized by the value of q_x for a smooth edge) and a roughness of 2% of the slab width $\overline{W}$. The value of 2% was chosen as representing a reasonable degree of roughness. Using a Gaussian distribution truncated at $\pm 4\sigma$, the maximum deviation is 0.08% of W, giving a range of thermal resistance from 0.92 to 1.08. One question that must be resolved is what should the value of H be. Because the boundaries at $y=0$ and $y=H$ are insulated, $q_y=0$, the x flux field will be affected. Computations were made with $H=W$, $3W$, and $5W$. Little effect was found on the behavior of $q_x(x)$ in the vicinity of $y=H/2$ and only the case of $H=W$ is reported. The number of simulations to achieve a converged result was a weak function of the correlation length $\mathcal{L}$, usually in the order of 3500. This number is a function of the number of random variables, u_i, $i=1,\ldots,K$. The values of u_i were found using the Latin hypercube approach [16]. The computations were made using the multiphysics program COMSOL [17].

8.1 Convergence of Computations: Monte Carlo Versus Tensor/Sparse Grids. The solution involves determining the expected values of the standard deviations of q_x and q_y in the domain. These expected values can be found in two ways: (a) sampling and quadrature, and (b) Monte Carlo sampling. In previous work [18] we have found that expected values for multinormal distributions require in the order of five to seven Gaussian quadrature points per random variable. For a correlation length of $\mathcal{L}/H=0.075$ for which $K\approx 20$ this would lead to sampling a tensor grid of $5^{20}=3{,}200{,}000$ points. Using a nested sparse grid [19,20] based on the Smolyak algorithm is one way of reducing the number of points. Preliminary calculations indicated that accurate estimates of the heat fluxes required a sparse grid of level 2 and their standard deviations a level 3, which contains 11,561 sparse grid points.

For shorter correlation lengths, K increases rapidly and the number of samples becomes impossibly large. Consequently we turned to traditional Monte Carlo sampling. Values of u_i were chosen using a Latin hypercube based on dividing the cumulative probability distribution (cdf) into 50 equal probability increments. Figure 8(*a*) shows the convergence of the numerical computations

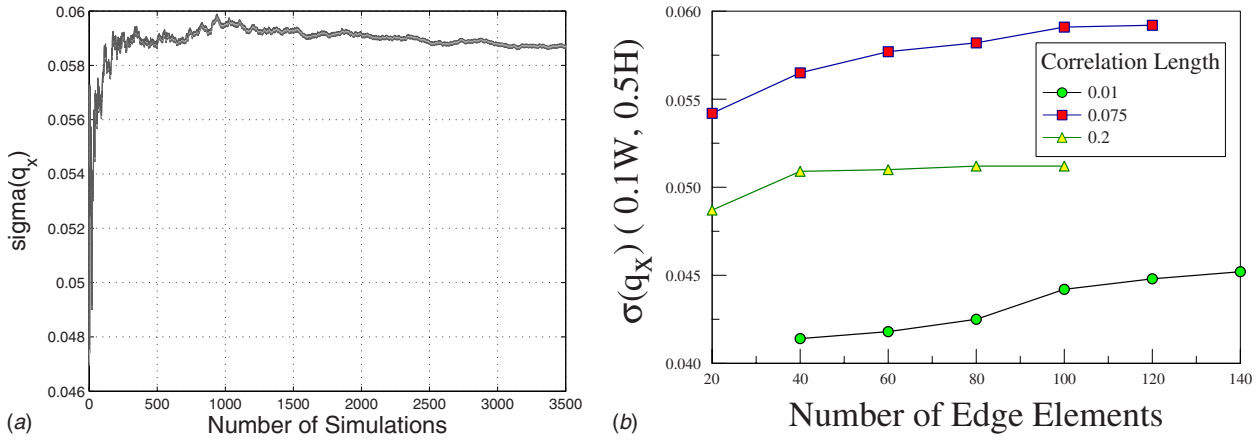

Fig. 8 (*a*) **Convergence for $\mathcal{L}=0.075$. For meshes with degrees of freedom ranging from 1000 to 68,000.** (*b*) **Effect of the number of edge elements on the value of $\sigma(q_x)$ at $x=0.1W$ and $y=0.5H$.**

for $\sigma(q_x)$ at $x=0.1W$ and $y=0.5H$ (similar results were found for other quantities of interest) for $\mathcal{L}/H=0.075$ as a function of the number of simulations for meshes using quadratic Lagrangian triangles and whose number of nodes ranged from 1000 to 68,000 with maximum element areas ranging from 10^{-2} to 10^{-4} and element areas near the rough surface ranging from 10^{-4} to 2.5×10^{-6}, respectively.

The results are seen to converge to a steady value after ~3500 and to be insensitive to the mesh used. The mean value of $\sigma(q_x)$ over the range MC=3500–5000 changed by less than 0.001 with a variation of ±0.0002 over the different meshes.

The effect of the number of elements on the edge $x=0$, $0\le y\le H$ is shown in Fig. 8(*b*). As suggested by the figure, all computations for $\mathcal{L}/H>0.05$ were performed with 120 elements on the edge except for $\mathcal{L}/H=0.01$ for which 140 were used. Convergence was checked by monitoring the value of $\sigma(q_x)$ at $x=0.1W$ and $y=0.5H$. Computations were carried out for 1300 iterations and thereafter at every 100 simulations the mean value of $\sigma(q_x)$ and its standard deviation over the preceeding 100 simulations were examined. Convergence was achieved when the mean changed by less than 0.001 and the standard deviation was less than 0.05%.

9 Results

Computations made using meshes that had 4000 DOFs and 2000 elements and ones that had 68,000 DOFs and 25,000 elements with minimum element areas of 3×10^{-5} to 2.5×10^{-6}, respectively, gave results that differed by less than 1%. The results presented in the following figures were obtained using the next to finest mesh (of the order of 14,000 degrees of freedom and 7000 quadratic triangular elements with a minimum area of approximately 8×10^{-5}) and between 3200 and 3500 Monte Carlo simulations. Figure 9 shows the contours for q_x and q_y for an edge roughness of 2%. Near the right edge, the conduction is essentially one dimensional since the flux in the y direction at all values of y has approached zero and as a consequence the standard deviation of the x flux approaches from below the value obtained from Eq. (2). Near the rough edge, there is a substantial disruption of the heat flow with large values of q_y that are of the order of q_x. Consequently, the standard deviations of both fluxes are significantly larger than that of the edge roughness. In the central portion, $0.2H\le y\le0.8H$ the y flux is unconstrained, but near the insulated edges flow lines of the flux are forced to become aligned with the edge and the result is that q_x must vary more than it does

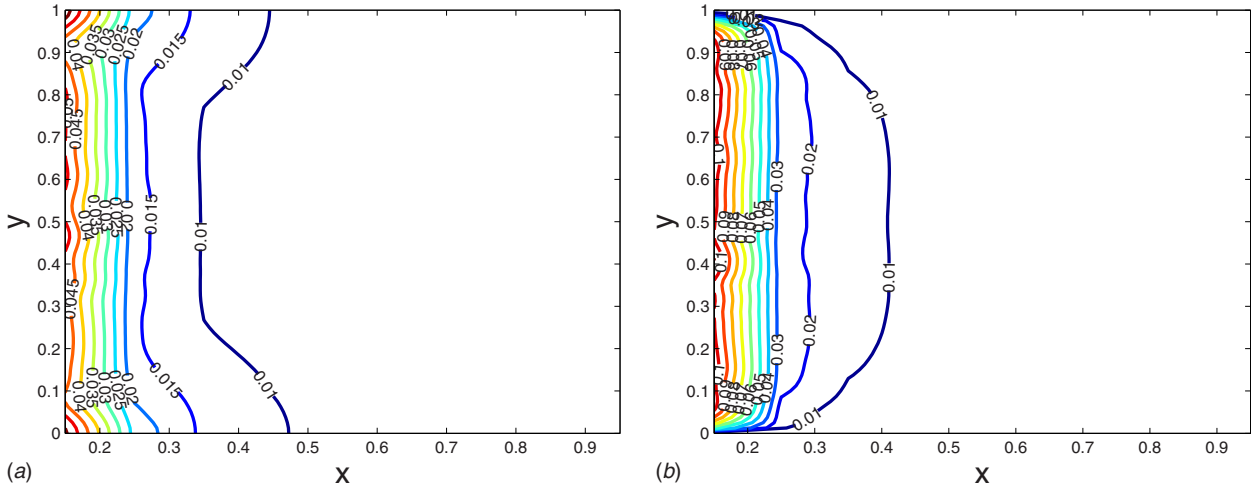

Fig. 9 Contours of the standard deviations of the heat fluxes for an edge roughness of 2% and $\mathcal{L}=0.05W$: (*a*) $\sigma(q_x)$ and (*b*) $\sigma(q_y)$

Table 1 Execution times on a 2.8 GHz CPU with 1 Gbyte of RAM for 1000 simulations: forming mesh 970 s; solving 3900 s; extracting T, q_x, and q_y; 2100 s

$\mathcal{L}/W$	Average No. of DOFs	Average No. of elements	Mesh quality	
			Minimum	Average
0.01	13,474	6614	0.443	0.988
0.10	13,784	6777	0.786	0.989
1.0	14,209	6990	0.813	0.986

Table 2 Performance of the Neumann Series Approach

$\mathcal{L}/W$	% bad	Maximum norm of acceptable $(\overline{\mathcal{KH}}^{-1}\Delta\mathcal{KH})$	Maximum norm $(\overline{\mathcal{KH}}^{-1}\Delta\mathcal{KH})$
0.01	100		13.65
0.025	100		6.49
0.05	100		4.87
0.10	30	0.47	2.56
0.20	9	0.22	1.73
0.25	9	0.10	1.65
0.50	8	0.10	2.76
0.75	8	0.05	2.17
1.00	7	0.09	2.34
2.00	5	0.04	1.59

in the central region. Consequently, the standard deviation near the insulated boundaries is of the order of 1.5 times that in the central core.

Because of the lengthy computational times of COMSOL, we explored the use of a very simple grid, Fig. 10(*b*) with isometric linear quadrilateral elements using the conductances of Eq. 11 for the edge elements. The conductance matrix for the region $0.1 \leq x \leq 1$ was formed once and saved. That for $0 \leq x \leq 0.1$ was formed for each simulation. As shown, this is a relatively coarse mesh and the quality of the elements near the surface varies considerably. These results are denoted by the curve labeled "quad" in Fig. 10(*a*). Considering that only 451 nodes and 400 elements were used, the results are in surprisingly good agreement with those obtained using COMSOL (see Table 1) and indicate that relatively inexpensive computations can be used to get a realistic idea of how the uncertainties affected the heat flux.

Figure 11(*a*) compares the standard deviations for q_x and q_y. As expected, near the rough edge, the fluxes behave similarly. However, $\sigma(q_y) \to 0$ as the isothermal right edge is approached and the flux becomes one dimensional. As expected, when $\mathcal{L} \to 0$, the variation goes to zero and as $\mathcal{L} \to \infty$ it approaches 2%, the value expected from Eq. (2). What is surprising is how the interaction

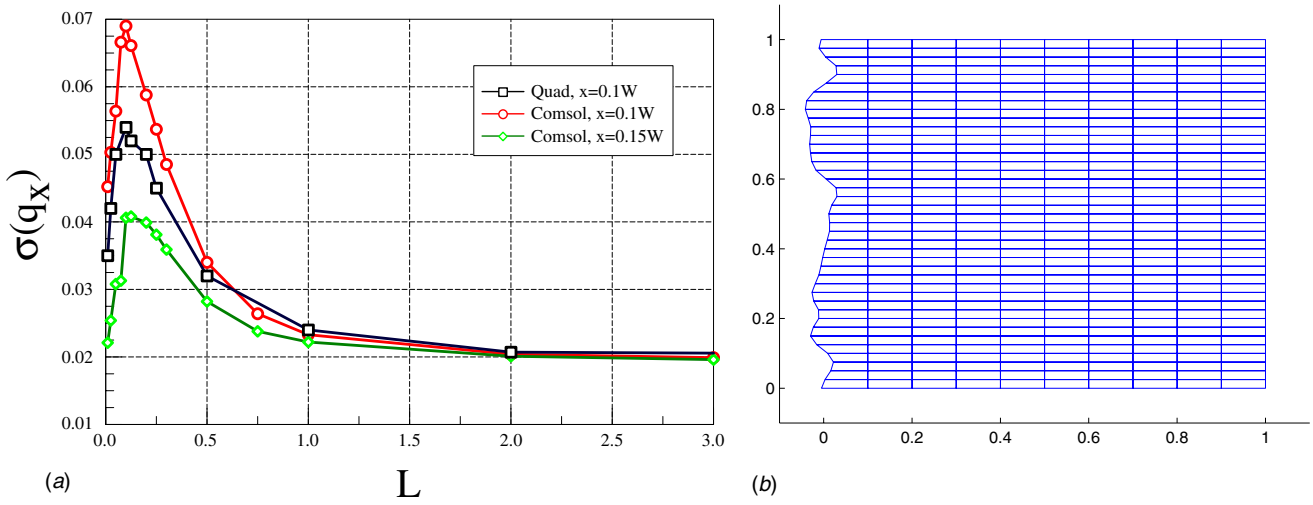

Fig. 10 (*a*) Effect of $\mathcal{L}$ on the behavior of q_x for an edge roughness of 2%. (*b*) Simplified grid for quadrilateral elements for the rough edge.

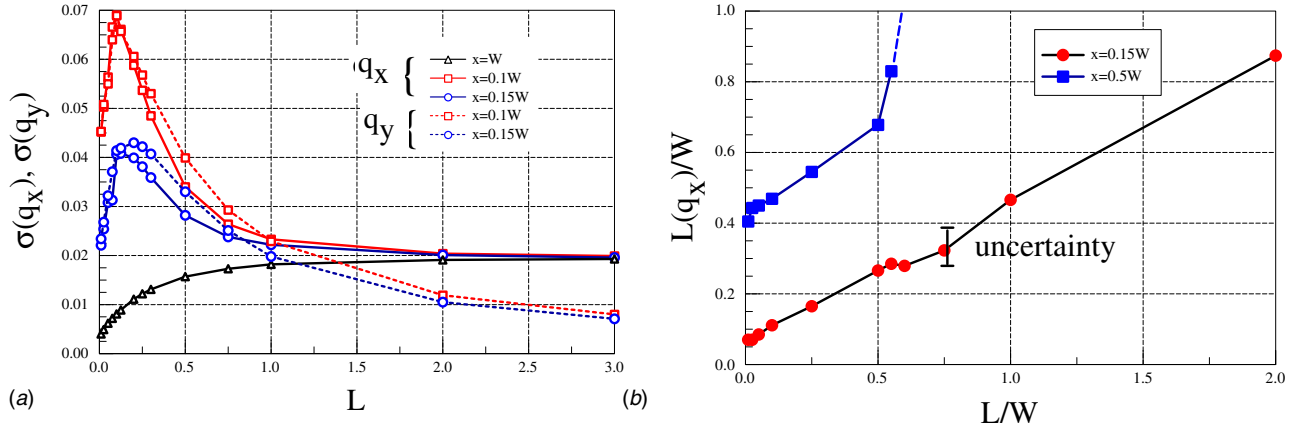

Fig. 11 (*a*) behavior of q_x and q_y and (*b*) correlation length

between q_x and q_y results in a standard deviation at modest values of $\mathcal{L}$ of the order of 7%, or about three times the value expected for large $\mathcal{L}$.

10 Correlation of the Heat Flux

The roughness of the contours of Fig. 9 is most apparent near the rough surface and diminishes as x approaches the right edge, $x=W$. Both this roughness and the standard deviation, shown in Fig. 10, are measures of the effect of the correlation length $\mathcal{L}$. As expected for small values of $\mathcal{L}$ the roughness of the contours diminishes quickly and the flux q_x measured at the right edge is insensitive to the correlation length. Figure 11(b) shows correlation length of q_x (see Sec. 13 for the definition of $\mathcal{L}$). In contrast to the effect of $\mathcal{L}$ on the standard deviation of q_x, the autocorrelation length monotonically increases and becomes greater than W when $\mathcal{L}>0.5W$. The curve is only approximate because of the use of Monte Carlo simulation. Repeated computations suggest a range of uncertainty as indicated.

11 Stochastic Convective Coefficient

Since the computation for the rough edge is so expensive, it is interesting to consider a smooth edge with a random convective heat transfer coefficient field. Taking a Biot number of 10 and a conductivity of 1/0.9 gives the same average resistance as for the rough edge. The standard deviation of h was chosen at 20% since this gives a variation in the total one-dimensional resistance equal to that of the rough edge. However, in this case, $\sigma(q_x)=0.023$ for infinite $\mathcal{L}$ because of the highly nonlinear relationship between q_x and h, Eq. (1b). In this case, it is possible to express the random heat transfer coefficient as $h(\xi)=\overline{h}(1+\sigma\xi(y))$ and to use the Neumann approach, thus, potentially, saving significant amounts of computer time. Figure 12 compares the results of the rough edge and the stochastic convective coefficient at the locations $x=0.15W$, $y=H/2$ and $x=0.5W$, $y=H/2$. These two locations are roughly equivalent since both are $0.05W$ deeper than the region affected. The effects of both stochasticities are very similar in magnitude and relationship to $\mathcal{L}$.

Both the COMSOL and the quad computations were made by direct formulation and inversion of $\mathcal{K}+\mathcal{H}$. We also tried using the Neumann series approach for the stochastic heat transfer coefficient. This method requires that the norm of $\overline{\mathcal{K}}\overline{\mathcal{H}}^{-1}\Delta\mathcal{K}\mathcal{H}$ be less than 1. Table 2 lists the success of this approach. The entries for the norm represent the maximum norm of any $\overline{\mathcal{K}}^{-1}\Delta\mathcal{K}$ that was less than 1 and the maximum of unacceptable values.

The Neumann series approach was successful only for $\mathcal{L}>0.2W$, values for which the effects are beginning to diminish with respect to $\mathcal{L}$. Unfortunately, the most interesting cases, those with small values of $\mathcal{L}$, cannot be treated by this method.

For the rough edge and the convective heat transfer coefficient cases, the temperature at $x=W$ was maintained at $T=0$, i.e., constant with respect to y. This raises the question of how this constancy affects the behavior of q_x. Calculations were also made with Biot numbers on the left and right edges of 12.5, $k=0.8$ which gives the same overall one-dimensional thermal resistance as before. The two cases are compared in Fig. 13, and it appears that there is little effect.

12 Interaction of Roughness and the Convective Boundary Condition

When both the convective coefficient h and the width W are random variables, i.e., $\mathcal{L}$ is large compared with W, the standard deviation of q_x increased to 0.028%. We are particularly interested in determining if these two effects interact. Figure 14 compares the depth of penetration, defined to be that distance into the slab at which $\sigma(q_x)$ equals the standard deviation resulting when $\mathcal{L}\to\infty$. The combined problem shows that the depth is much greater than that for the single effects and occurs at much smaller correlation lengths. While not totally unexpected, this finding is disheartening since it suggests that we will not be able to model the fiber history by treating the fluid convection independently of the history of the fiber.

It is to be expected that the two effects will interact and increase the variation in the heat fluxes. This turns out to be true when the correlation length is long and the usual equation for the propagation of variances applied to Eq. (2b) gives a reasonably correct result of 2.8%. As shown in Fig. 15, this is a slight underestimate because of the relatively strong nonlinear relationship between q_x and h and W of Eq. (2b). The surprising result is that for shorter correlation lengths that $\sigma(q_x)$ for the combined effects is noticeably less than that for the rough edge or the stochastic heat transfer coefficient alone. We have no explanation for this results. But we note from Fig. 14 that the extent of the region affected is larger for the combined effects than for roughness alone, so that the weighted mean of the effect is similar.

13 Interpretation of Results

For the optical fiber with random heat transfer coefficients, the results are easy to interpret. Consider taking N snapshots of the fiber over a given time interval as it is drawn, with each snapshot quantifying the spatial distribution along the fiber, $h(y)$ (such snapshots are usually referred to as *realizations*, each mimicked by a single Monte Carlo simulation). At each position, y_i the variation of $h(y_i)$ with respect to time will be such that the mean is $\overline{h}$ and with a standard deviation of $\sigma(h(y_i))$. A knowledge of how $h(y_j)$ varies with time depends on the correlation of h_i and h_j. If they are uncorrelated, knowledge of h_i will tell us nothing about the variation of h_j. If the correlation is unity, then the two values, h_i and h_j, will move in lock-step. The grid in the fiber and the fluid will be dependent on the degree of correlation, with low levels of correlation requiring significantly greater density of nodal points in the y direction. The correlation length $\mathcal{L}$ is a measure of how far apart y_i and y_j will be for a given degree of correlation. $\mathcal{L}$ is not a physically measurable quantity. Rather it is derived from a model of the covariance. That is, the correlation is expressed by an arbitrary function $C(y_i,y_j)$ that one feels fits the measured response. Several functions are commonly used, $\exp(-|d|/\mathcal{L}$, $\exp(-d^2/\mathcal{L}^2))$, $1-|d|/\mathcal{L}$, where $d=y_i-y_j$. Clearly the value of $\mathcal{L}$ is dependent on the model used and suffers from considerable ambiguity in its interpretation. For these calculations, we used $C(y_i,y_j)=\exp(-d^2/\mathcal{L}^2)$ to describe the random field $\xi(y)$. As expected for this linear problem, the computed covariances at different values of x were found to be well fitted by this model. Figure 16 shows how the correlation length for q_x and q_y varied with distance from the edge, $x=0$ for the rough edge with $\mathcal{L}=0.125W$. The correlation lengths for q_x and q_y were indistinguishable and quickly increased to a value exceeding W, indicating that $q_x(y)$ varied little over the surface, $x=W$.

Application of the results to the case of a slab with a rough edge requires a different point of view. A given slab has a unique roughness that is not likely to change during an experiment. However, one can imagine that the given slab was chosen out of a large set of available slabs. In this case, the statistical results are then to be interpreted in the sense of representing one degree of uncertainty about the variation of the heat flux to be observed. The growth of $\mathcal{L}$ with depth into the slab is essentially the same as that for the stochastic convective heat transfer coefficient, Fig. 16. However, the probability density distributions of the two cases are significantly different as seen in Fig. 17 with the tails of the distributions beginning on opposite sides.

14 Conclusions

From these results it appears that it will not be useful to treat problems of these types by using the Neumann and the polyno-

mial chaos methods. The most interesting situations are those for which the correlated nature of the random field causes unexpected results; i.e., $\mathcal{L} \leq 0.5W$.

For the Neumann approach, the distortion of the conductance matrix is so great that the expansion $(\overline{\mathcal{K}}+\delta\mathcal{K})^{-1}$ in the form $(\mathcal{I}+\overline{\mathcal{K}}^{-1}\delta\mathcal{K})^{-1}=1-\epsilon-\epsilon^2\cdots$ does not converge. Polynomial chaos requires a representation of the random field by K random variables, u_k, $k=1,\ldots,K$, making the problem computationally infeasible.

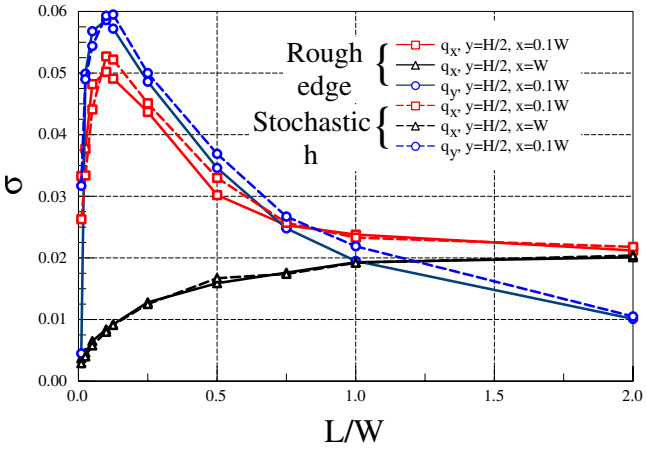

Fig. 12 Comparing the effects of a rough edge and a stochastic convective heat transfer coefficient

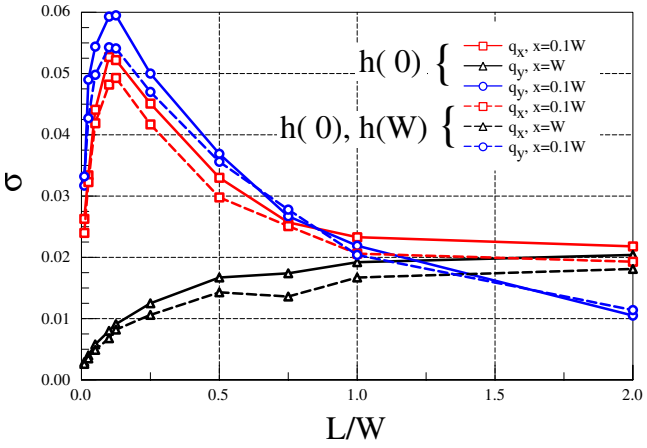

Fig. 13 Comparing the case of $h(0)=10$ and $h(0)=h(W)=10$

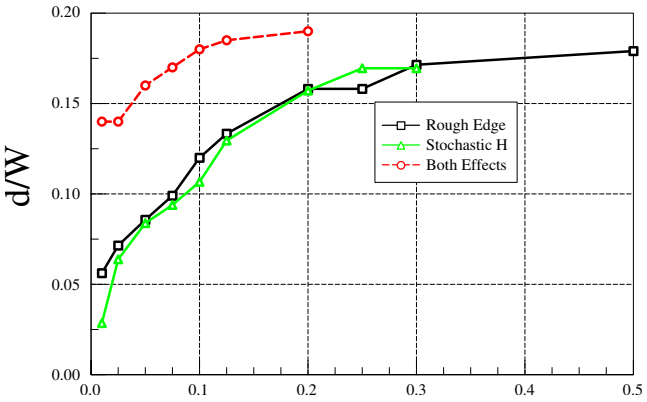

Fig. 14 Depth of penetration at which $\sigma(q_x)=\sigma(q_x(\text{for } \mathcal{L}=\infty))$

From a practical point of view, it is not likely that problems more complicated than one-dimensional ones can be treated at a reasonable cost.

Defining a characteristic depth of the region directly affected by the rough edge to be the maximum roughness, $\approx 4\sigma(\xi)$, and that for the stochastic surface heat transfer coefficient to be the thickness of an equivalent layer of slab, both are $\approx 0.1W$. The results suggest that the region in which the effects are significantly greater than for $\mathcal{L}=\infty$, as measured by the standard deviation of both q_x and q_y, does not exceed twice this characteristic depth.

While the effect on q_x at $x=W$ can be estimated to range from 0 to $\sigma(W)$ as the correlation length varies from 0 to $\approx 0.5W$, the effects internal to the slab are not easily anticipated. One can think of situations other than optical fiber drawing in which the results might be revealing. One case would be in computer boards where the substrate is reasonably homogeneous, but the surface exposed to the cooling air flow can be considered as having a random roughness. In this case, cooling of different parts of the board may differ enough from the average to need consideration.

For the optical fiber drawing problem that initiated our study, the results suggest that one must solve for the mechanical behavior of the fiber, as evidenced by variations in the surface smoothness and diameter, simultaneously with the effect on the free convection of air in the drawing furnace. Fortunately, the interaction is likely to be pronounced only in the early stages of the drawing where the size of the preform is substantial enough to affect the

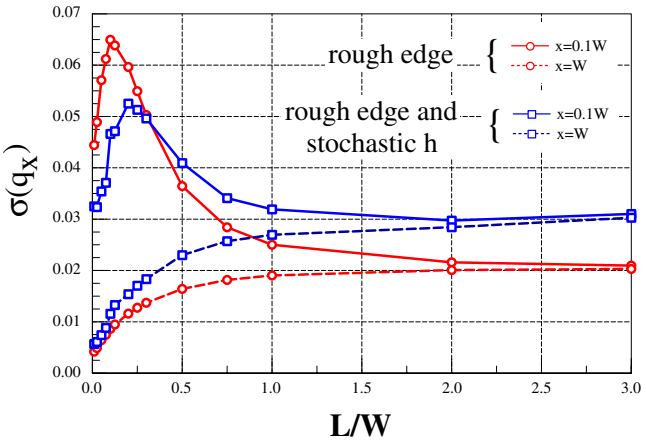

Fig. 15 Effect of $\mathcal{L}/W$ on $\sigma(q_x)$ for a rough edge alone and combined with a stochastic heat transfer coefficient

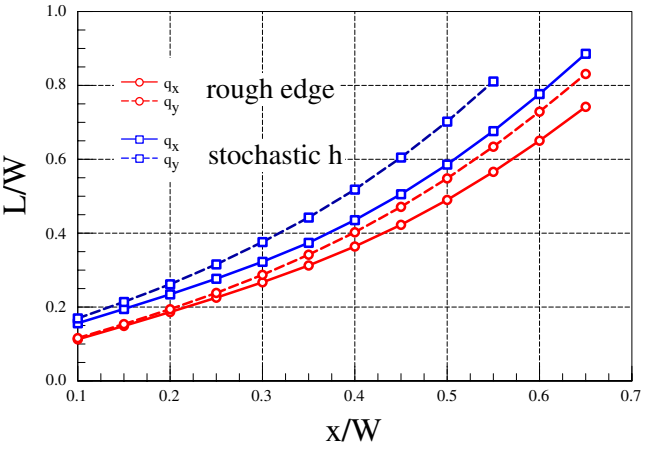

Fig. 16 Correlation depth $\mathcal{L}$ for a rough edge and for a stochastic heat transfer coefficient when $\mathcal{L}/W=0.125$ at $x=0$

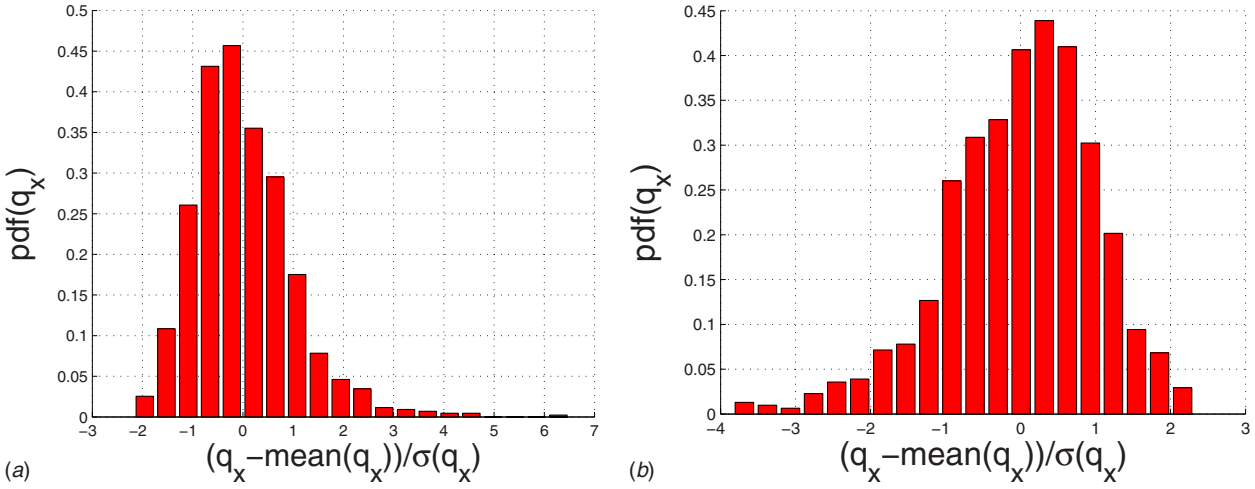

Fig. 17 Probability density distributions at $x=0.1W$ for a rough edge (*a*) and a stochastic heat transfer coefficient (*b*) when $\mathcal{L}/W=0.125$ at $x=0$

air velocities. In the region where the preform has necked down close to the size of the final fiber, it is unlikely to affect the fluid flow.

Acknowledgment

These results were obtained as part of the research supported by the National Science Foundation through Grant No. 0626533. The authors wish to thank the reviewers for their comments that materially improved the paper.

References

[1] Reeve, H. M., Mescher, A. M., and Emery, A. F., 2004, "Investigation of Steady State Drawing Force and Heat Transfer in Polymer Optical Fiber Manufacturing," ASME J. Heat Transfer, **126**(2), pp. 236–243.
[2] Ghanem, R., and Brzakala, W., 1996, "Stochastic Finite Element Analysis of Soil Layers With Random Interface," J. Eng. Mech., **122**(4), pp. 361–369.
[3] Lin, G., Su, C.-H., and Karniadakis, G. E., 2007, "Random Roughness Enhances Lift in Supersonic Flow," Phys. Rev. Lett., **99**, p. 104501.
[4] Nair, P. B., Mohan, S. P., Bryan, R., Kenae, A. J., and Taylor, M., 2008, "Tackling Geometric Uncertainty: Stochastic Projection Schemes," ECCOMAS Conference, Venice, Italy.
[5] Xiu, D., and Tartakovsky, D. M., 2006, "Numerical Methods for Differential Equations in Random Domains," SIAM J. Sci. Comput. (USA), **28**(3), pp. 1167–1185.
[6] Rathish Kumar, B. V., 2000, "A Study of Free Convection Induced by a Vertical Wavy Surface With Heat Flux in a Porous Enclosure," Numer. Heat Transfer, Part A, **37**(5), pp. 493–510.
[7] Vanmarcke, E., and Grigoriu, M., 1983, "Stochastic Finite Element Analysis of Simple Beams," J. Eng. Mech., **109**(5), pp. 1203–1214.
[8] Li, C.-C., and Der Kiureghian, A., 1993, "Optimal Discretization of Random Fields," J. Eng. Mech., **119**(6), pp. 1136–1154.
[9] Ghanem, R. G., and Spanos, P. D., 2003, *Stochastic Finite Elements*, Dover, Mineola, NY.
[10] Sakamoto, S., and Ghanem, R., 2002, "Polynomial Chaos Decomposition for the Simulation of Non-Gaussian Nonstationary Stochastic Processes," J. Eng. Mech., **128**(2), pp. 190–201.
[11] Phoon, K. K., Huang, H. W., and Quek, S. T., 2005, "Simulation of Strongly Non-Gaussian Processes Using Karhunen-Loeve Expansion," Probab. Eng. Mech., **20**, pp. 188–198.
[12] Spanos, P. D., Beer, M., and Red-Horse, J., 2007, "Karhunen-Loéve Expansion of Stochastic Processes With a Modified Exponential Covariance Kernel," J. Eng. Mech., **133**(7), pp. 773–779.
[13] Jackson, J. E., 1991, *A User's Guide to Principal Components*, Wiley, New York.
[14] Le Maitre, O. P., Reagan, M. T., Najm, H. N., and Ghanem, R. G., 2002, "A Stochastic Projection Method for Fluid Flow II Random Processes," J. Comput. Phys., **181**, pp. 9–44.
[15] Xiu, D., and Karniadakis, G. E., 2002, "Modeling Uncertainty in Steady State Diffusion Problems Via Generalized Polynomial Chaos," Comput. Methods Appl. Mech. Eng., **191**, pp. 4927–4948.
[16] Hurtado, J. E., and Barbat, A. H., 1998, "Monte Carlo Techniques in Computational Stochastic Mechanics," Arch. Comput. Methods Eng., **5**(1), pp. 3–29.
[17] 2009, COMSOL Multiphysics Ver. 3.5, COMSOL, Inc., Palo Alto, CA.
[18] Emery, A. F., and Bardot, D., 2007, "The Determination of the Sensitivity of Heat Transfer Systems Using Global Sensitivity and Gaussian Processes," ASME Trans. J. Heat Transfer, **129**(8), pp. 1075–1081.
[19] Klimke, A., and Wohlmuch, B., 2005, "Algorithm 847: Spinterp: Piecewise Multilinear Hierarchical Sparse Grid Interpolation in MATLAB," ACM Trans. Math. Softw., **31**(4), pp. 561–579.
[20] Heiss, F., and Winschel, V., 2008, "Likelihood Approximation by Numerical Integration on Sparse Grids," J. Econometr., **144**, pp. 62–80.

R. Wälchli
IBM Research GmbH,
Zurich Research Laboratory,
8803 Rüschlikon, Switzerland;
Department of Mechanical and Process Engineering,
Laboratory of Thermodynamics in Emerging Technologies,
ETH Zürich,
8092 Zürich, Switzerland
e-mail: eto@zurich.ibm.com

T. Brunschwiler

B. Michel

IBM Research GmbH,
Zurich Research Laboratory,
8803 Rüschlikon, Switzerland

D. Poulikakos
Department of Mechanical and Process Engineering,
Laboratory of Thermodynamics in Emerging Technologies,
ETH Zürich,
8092 Zürich, Switzerland

Self-Contained, Oscillating Flow Liquid Cooling System for Thin Form Factor High Performance Electronics

A self-contained, small-volume liquid cooling system for thin form-factor electronic equipment (e.g., blade server modules) is demonstrated experimentally in this paper. A reciprocating water flow loop absorbs heat using mesh-type microchannel cold plates and spreads it periodically to a larger area. From there, the thermal energy is interchanged via large area, low pressure drop cold plates with a secondary heat transfer loop (air or liquid). Four phase-shifted piston pumps create either a linearly or radially oscillating fluid flow in the frequency range of 0.5–3 Hz. The tidal displacement of the pumps covers 42–120% of the fluid volume, and, therefore, an average flow rate range of 100–800 ml/min is tested. Three different absorber mesh designs are tested. Thermal and fluidic characteristics are presented in a time-resolved and a time-averaged manner. For a fluid pump power of 1 W, a waste heat flux of 180 W/cm^2 ($\Delta T = 67$ K) could be dissipated from a 3.5 cm^2 chip. A linear oscillation flow pattern is advantageous over a radial one because of the more efficient heat removal from the chip and lower hydraulic losses. The optimum microchannel mesh density is determined as a combination of low pump losses and high heat transfer rates. [DOI: 10.1115/1.4000456]

Keywords: microchannel, liquid cooling, thermal packaging, oscillating flow

1 Introduction: Transition to Liquid Cooling

With the continuous increase in power dissipation and advances in packaging technology of electronics equipment, the industry is increasing its product development efforts toward effective heat removal concepts. For blade servers, which are optimized to minimize physical space, effective heat removal from high performance central processing units (CPU) and memory cards is of vital importance. Blade modules are typically restricted to the minimum size requirements of a standard server-rack configuration (1*U*: one rack unit, 19″ wide and 1.75″ tall) while still having all the functional components to be considered in a computer [1,2]. Heat spreading concepts such as heat pipes and vapor chambers are traditionally used to distribute excess heat from the processors to a larger area within the blade. There, thermal energy is absorbed by means of high performance air-moving devices blowing subcooled air across the blade. Air heat exchangers are employed to increase the active heat transfer area. This requires a considerable amount of power for the data center air conditioning and air blower operation. Furthermore, the air cooling for both the blade modules and the data center implies a sophisticated air-flow management [3–6].

As an alternative to air cooling, which reaches its cooling capacity at ~100 W/cm^2 [7] liquid cooling using microchannel cold plates, has been demonstrated to be a viable solution for future applications. From the very first demonstrations to enhanced packages, various approaches have been reported resulting in cooling capacities of 350 W/cm^2 and higher [8–12]. One broad field of cooling schemes that has received increased interest recently employs oscillatory flows. Early work on enhanced heat transfer using high frequency oscillatory/pulsating flows can be found in Refs. [13,14]. High heat transfer coefficients from a heated floor of a rectangular duct employing low frequency, large tidal reciprocating flows were demonstrated by Cooper et al. [15]. In Ref. [16], the heat transfer rate could be enhanced by 100% for reciprocating air flows, as compared with standard cooling fans. Furthermore, Sert and Beskok [17] discuss in a numerical study a single-phase, closed microfluidic system that utilizes reciprocating flow forced convection.

Compared with air, water has 4000× higher volumetric heat capacity and is simpler to direct within a highly populated electronic package. In contrast, an all liquid cooled computing system requires a significant amount of supplementary equipment, such as piping, hoses, and pumping station. High investment costs are expected when adapting data centers to liquid cooling. Furthermore, a liquid inside an electronic equipment can cause significant damage in case of leakage. The working fluid volume embedded in the computing system should therefore be minimized to limit damage to a minimum, in case of flooding. In a blade server system, one could think of a primary, closed fluid loop integrated into each individual blade unit to cool the CPUs and spread the heat to a peripheral area where a second, data center-scale fluid loop collects the waste heat from each blade, and finally, in a preferred scenario, reuses it, for example for district heating [18]. The connection between the local and the global fluid loop is done by means of conduction through a large area interface. This opens up a variety of innovative and highly efficient centralized pumping schemes for an all liquid cooled data center.

The basic idea of an effectively spread heat from a small source to a large area could also be fulfilled by means of a passive phase-change device such as vapor chambers or heat pipes. Compared with active liquid cooling systems, they are more convenient in operation since no active pumping device is required. This makes this technology very interesting from a cost and maintenance per-

Contributed by the Heat Transfer Division of ASME for publication in the JOURNAL OF HEAT TRANSFER Manuscript received April 2, 2009; final manuscript received August 26, 2009; published online March 8, 2010. Assoc. Editor: S. J. Kim.

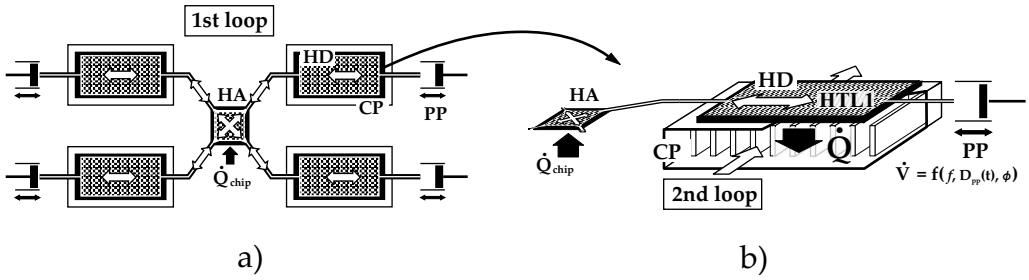

Fig. 1 Illustration of the oscillating liquid cooling principle. (*a*) Heat spreading system with a chip waste heat absorber (HA) in the center and the four heat dissipator (HD) cold plates in the periphery. The fluid oscillations are created by means of phase-shifted piston pumps (PP). (*b*) Heat exchange from the chip via the oscillating fluid to the collector plane (CP) of the secondary heat transfer loop.

spective. However, they might not be able to handle very high heat fluxes (e.g., >150 W/cm^2); thermal spreading distance is limited and they are optimized to a fixed design point, and therefore, less flexible for variable thermal loads.

1.1 Principle of Operation. In this paper, we introduce a hybrid (combined liquid-air) cooling system exploiting the effectiveness of liquid cooling to transport thermal energy from the chip via a microchannel heat absorber to a peripheral location. A self-contained, blade-level liquid cooling circuit spreads heat from the source to a larger area. Liquid-to-air heat exchangers dissipate the heat to the environment using traditional air fans blowing across the blade module. This can be seen as a soft transition to all liquid cooling. No central pump and fluid distribution network is needed, and the system assembly corresponds to a traditional air heat sink. Therefore, small additional investment costs incur for a data center. Alternatively, the air cooling can be replaced by a secondary, data center-level fluid heat transfer loop that aims at collecting thermal energy from each individual blade module. In this case, a collector plane in between the blades is in thermal contact with the peripheral heat exchangers of the primary heat transfer loop. The risk of flooding is reduced to the amount of liquid contained in the closed cooling circuit inside a blade.

In the following, we demonstrate a self-contained, hermetic liquid cooling system using oscillating fluid flows to spread heat from a small source to a large area, Fig. 1. This is defined as the primary heat transfer loop (HTL1) inside the blade. Efficient heat spreading has been demonstrated with effective thermal conductivities of 20× and 50× over copper for spreader plates and interconnecting tubes respectively [19]. A low volume, high performance microchannel heat absorber (HA) is in thermal contact with the heat source. Adiabatic channels connect to four large area heat dissipators (HD), which are placed in available space areas of the blade module around the primary heat source. The oscillating fluid flow is established using reciprocating piston pumps (PP) connected to the outward-facing side of the HDs. Within a pumping cycle, the working fluid takes up heat from the source, carries it to the peripheral HDs, exchanges it via the collector planes (CP) with a secondary heat transfer loop (HTL2), and returns again cooled to the HA. The base area ratio of the dissipator plates to the absorber plate A_{HD}/A_{HA} is greater than 30. The four piston pumps operate with identical displacements (D_{PP}) and frequencies (f). However, depending on the phase shift, the oscillation flow pattern changes. The position of each individual pump i is defined as

$$x_i(t) = D_{PP} \cdot \sin(2\pi \cdot f \cdot t + \phi_i), \quad i = 1 \ldots 4 \tag{1}$$

In a linearly oscillating flow (lin), a pair of actuators on either side operate with a phase shift of 180 deg, whereas in a radially oscillating flow (rad), each piston pump has a 90 deg phase shift to its adjoining pumps. The idea behind a radially oscillating flow pattern is to create a constant flow rate at the source that changes its flow direction by 360 deg within an oscillation cycle. This constant mass flow rate results from the accumulation of the four sinusoidal actuated flows. Thereby, constant high heat transfer rates can be expected, which result in minimized temperature fluctuations of the heat source, i.e., the microprocessor [20]. However, this requires more complex pumping installations. In a linearly oscillating flow, only one reciprocating pump would be required (push-pull piston).

The purpose of the present experimental study is to demonstrate the effectiveness of the above described self-contained, oscillating flow liquid cooling system. In the sections below, experimental details and manufacturing issues will be discussed, followed by specific experimental results on the time-resolved and averaged hydraulic and thermal behavior, along with their analysis and discussions. Finally, specific conclusions will be drawn.

2 Device Fabrication, Experimental Apparatus and Procedure

2.1 Microchannel Cold Plates: HA and HD. Figure 2 shows the design of the absorber and dissipator microchannel cold plates, which are manufactured in a *direct copper bonding* (DCB) process. Therein, 200 μm thick copper sheets are patterned using photolithography and wet etching. A chemical oxidation process builds a defined copper oxide layer. Finally, the layers are stacked and fused at a temperature above the liquidus temperature of the oxide, but below solidus temperature of the copper. This results in an interface-free bond because of interlayer grain growth [21,22]. The manufacturing of the DCB microchannel cold plates was done by Curamik (Eschenbach, Germany).

The HA cold plate (Fig. 2(*a*)) is $30 \times 30 \times 2$ mm^3, with a heat transfer mesh base of 20×20 mm^2. By varying the aspect ratio of the microchannels in a unit cell (see Fig. 2(*b*)), three different mesh porosities

$$\varphi = \frac{V_{void}}{V_{cell}} \tag{2}$$

are realized. The three HA versions are referred to as $V1$ ($\varphi_{V1} = 56\%$, $V_{HA,V1} = 85$ μl), $V2$ ($\varphi_{V2} = 52\%$, $V_{HA,V2} = 81$ μl), and $V3$ ($\varphi_{V3} = 46\%$, $V_{HA,V3} = 76$ μl). To facilitate the generation of the flow patterns mentioned above (lin and rad), the layout of the HA and its corresponding heat transfer mesh create a fourfold symmetry (two diagonal and two normal planes). All four ports are identical, and fluid entering one port can exit the other three ports with a similar pressure drop. This is facilitated by the diagonal manifolds and guarantees a uniform flow distribution. The mesh layout is designed with respect to the unique nature of the radially oscillating flow pattern. As it can be deduced from the mesh unit cell (Fig. 2(*b*)), perpendicular (perp.) and diagonal (diag.) flow directions are ensured. In the case of linear oscillations, the fluid flows only in the horizontal direction. Herewith, the heat transfer mesh penalizes linear oscillations in a sense, so that it is possible to design it with a higher surface enlargement at similar frictional

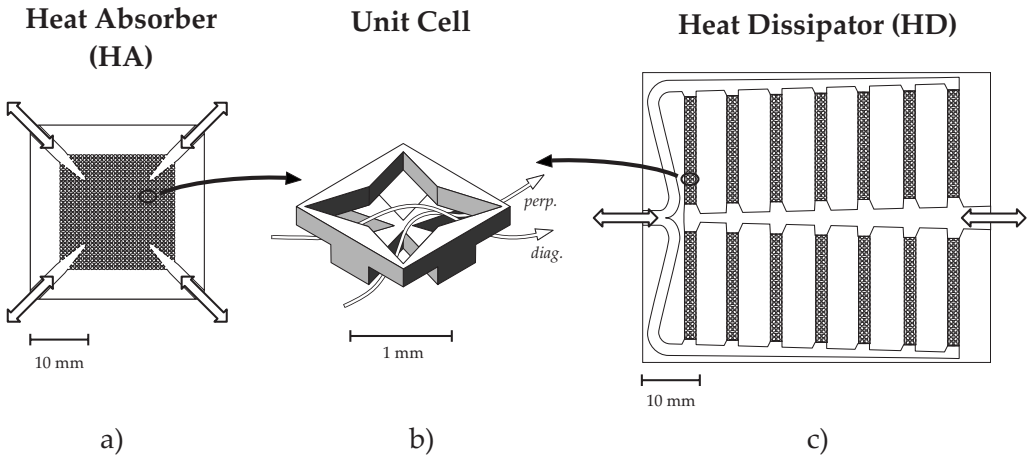

Fig. 2 Microchannel cold plate design of (*a*) the heat absorber (HA) and (c) the heat dissipator (HD). The axially symmetric unit cell heat transfer mesh is displayed in (*b*).

losses. Detailed discussions on the design and characterization of the different microchannel HAs presented here can be found in a previous publication [23].

For the peripheral heat dissipators HD (Fig. 2(*c*)), a large area, low fluid volume cold plate is designed that holds two inlet/outlet manifolds and multiple branching channels. The microchannel heat transfer mesh, which, is analogous to the one used in the HA, is placed in the branching channels. Each flow path has identical pressure loss, and the total inlet to outlet flow resistance is similar for the fluid entering from either side. The HD is $50\times60\times2$ mm^3 in size and contains $V_{HD}=517$ μl of fluid volume. The fluid volume ratio of HD to HA is 6; this illustrates the difference in power density the fluid has to absorb (HA) compared with its dissipation rate (HD). Furthermore, the HD can be designed with low hydrodynamic losses.

The interconnecting tubes between the HA and the HDs are 60 mm long and have a 2.5 mm diameter ($V_{tube}=294$ μl). For flexibility reasons, polyethylene tubes were used. A leak-free connection between the tubes and the heat exchangers (HA and HD) is ensured by using slide-on copper adapters. They are soldered into the manifolds of the microchannel cold plates HA and HD, after the DCB manufacturing.

2.2 Piston Pump Actuators. To carry out an accurate parametric study for different driving frequencies and volume displacements, a piston-type displacement pump is used. A frequency-controlled electric motor (maxon EC 32, maxon DEC 50/5, reduction gear 14:1) powers two disks via a T-type bevel gear (1:1 ratio). The disks feature boreholes with different eccentricities and angular positions. A double-acting hydraulic cylinder is connected to the eccentric locations of each disk and, therefore, creates a sinusoidal motion according to the rotary motion of the disks. Depending on the angular dislocation between the two disks, the appropriate phase shift ϕ_i for radial or linear oscillations can be set. The piston area A_{PP} is 172 mm^2. In this work, four different pump strokes D_{PP} are studied, namely, 0.7 ml, 1.0 ml, 1.5 ml, and 2 ml. We define the averaged flow rate of the oscillating liquid cooling system as

$$\dot{V} = 2 \cdot 2D_{PP} \cdot f(\text{ml/min}) \tag{3}$$

representing the fluid volume passing the HA per cycle time. According to the liquid contents of the HA, the interconnecting tube, and the HDs, each of the four piston pumps displaces 42%, 60%, 90%, and 120% of a quarter of the entire system volume (volume coverage D_{VC}), respectively, as

$$D_{VC} = \frac{D_{PP}}{V_{HA}/2 + 2 \cdot V_{tube} + 2 \cdot V_{HD}} \cdot 100(\%) \tag{4}$$

To emphasize the importance of the volume coverage D_{VC}, it is worth mentioning that as long as $D_{VC} > V_{tube}$, a fraction of the cooling fluid shuttles heat from the HA to the HDs. If that is not the case anymore, the HDs would be useless and the entire system would overheat immediately. The piston pump actuators presented in this work are aimed at establishing a well-controllable flow rate depending on frequency and stroke. Note, however, that this type of actuation is not practical for a real blade server type thermal management system, for which a fully hermetically sealed flow loop using membrane pumps would be a more likely scenario.

2.3 Experimental Setup and Data Reduction. An 18.6×18.6 mm^2 heater/sensor chip represents the blade server's power source to be cooled. Uniform Joule heating power (P_{chip}) of the entire surface A_{chip} is ensured by measuring the current and voltage. Platinum resistance temperature detectors (RTDs) are evenly distributed over the chip surface. The mean chip temperature $T_{j,mean}$ is determined by recording seven RTDs distributed over the entire chip base area and averaging over 50 measurements. RTD1 and RTD4, which are discussed later for the transient measurements, are located in the upper left corner and the center of the heater/sensor chip, respectively.

External temperature measurements are taken using cold-junction compensated T-type thermocouples (TC) (Omega 5 SRTC-TT-(T)I-40–1M, NI SCXI-1102). The fluid temperature T_{fluid} between HA and HD is measured by placing a TC in one of the four interconnecting tubes. The temperature T_{base} is measured between HD and CP by means of thermocouples that are placed in small grooves that have been cut into the top side of the CP.

The system pressure loss is detected using a pressure transducer (Omega PD 23), which determines the amplitude of the pressure oscillations (atmosphere as a reference). The pressure sensor is located at the far end of the primary heat transfer loop, next to one of the double-acting hydraulic cylinders (Fig. 1(*a*)). The difference between the extremes is identified, and the root mean square (RMS) value defines the average pressure drop of the oscillating flow loop, i.e., HTL1

$$\Delta p = \frac{\sqrt{2}}{2} \cdot (p_{max} - p_{min}) \tag{5}$$

As mentioned above the secondary heat transfer loop (HTL2) collects heat from the primary heat transfer loop (HTL1). The CPs are thermally connected with the HA using thermal interface paste (Dow Corning TC-5026). The four CPs are customized, straight channel low aspect ratio solid-to-liquid heat exchangers. Correspondingly, we cut 40 channels (0.5 mm width, 1.25 mm pitch, 60 mm length, and 6 mm depth) into solid brass. An inlet and outlet

manifold ensures a uniform fluid flow rate distribution across the channels. However, in an air cooled blade module, the CPs would be represented by air fin heat exchangers. For all experiments presented in this work, a chiller (Lauda Proline RP 855, ± 0.01°C FS) delivers cold water ($T_{in}=18$°C) at a constant flow rate of $\dot{V}_{HTL2}=600$ ml/min (flow rate sensor: Omega FLR 1000, accuracy: max $\pm 2\%$ FS). In this paper, the HTL2's part of the experimental setup acts solely as a thermal ground and is not discussed in more details. However, the total interface-to-inlet thermal resistance amounts to approximately 0.2 K/W for an area of $A_{CP}=30$ cm^2. This is again discussed later in the Results section.

Two samples of each heat absorber cold plate version (HA *V*1, *V*2, and *V*3) are tested, with the corresponding sets of piston pump frequencies f and displacements D_{pp}. The HAs are connected thermally to the heater/sensor chip at low thermal resistance, utilizing high conductive thermal paste (Dow Corning TC-5026) and a clamping device. The contact pressure is kept constant resulting in $R_{TIM}A_{chip}=12$ K mm^2/W $\pm 8\%$.

For the filling procedure, HTL1 is first flushed for several minutes using an external water loop (deionized water) to remove trapped air bubbles inside the fluid flow system. Next, the external water loop is turned off and HTL1 is closed to become self-contained. The cooling cycles are digitally controlled and data is acquired using a personal computer, corresponding data acquisition hardware, and LABVIEW software.

The data obtained from voltage, current, temperature, flow rate, and pressure measurements were reduced to power, thermal resistance, and hydraulic power. The total thermal resistance (R_{tot}) is the sum of components that account for conduction through the silicon substrate and the thermal interface material (TIM) (R_{Si+TIM}), convection to the fluid at the HA (R_{HA}), and liquid-to-liquid convection from the HD to the CP ($R_{HD}+R_{CP}$)

$$R_{tot} = R_{Si+TIM} + R_{HA} + R_{HD} + R_{CP} = \frac{T_{j,mean} - T_{in}}{P_{chip}} (\mathrm{K/W}) \qquad (6)$$

according to the quadratic error propagation, the measurement uncertainty being $\sigma_{R_{tot}} = \pm 4\%$. The hydraulic power defines the pumping power needed to overcome the system pressure at a given flow rate

$$P_{fluid} = \Delta p \cdot \dot{V} (\mathrm{W}) \qquad (7)$$

Here, the measuring inaccuracy with regards to the quadratic error propagation is $\sigma_{P_{fluid}} = \pm 5\%$.

3 Results and Discussions

3.1 Fluidic Performance. The oscillation frequency adopted in this work varies from $0.5 \le f \le 3$ Hz. Lower frequencies lead to poor thermal performances for the pumps strokes studied in this work. However, frequencies $f > 3$ Hz lead to pressure forces that are not manageable for the piston pumps utilized. Moreover, the pressure level has to be limited to a certain limit, e.g., $\Delta p < 2$ bars, to be feasible for a pump-driven water cooling system, otherwise, the pump power becomes too high.

For oscillatory flows, the transition from a laminar to a turbulent regime differs substantially from steady-flow conditions. Instead of the Reynolds number, the Womersley number $\alpha = D/2 \cdot \sqrt{\omega/\nu}$ and the transition number $\beta = \Delta x \cdot \sqrt{\omega/\nu}$ are used. The variables D, ω, ν, and Δx denote the channel width, the angular velocity, the dynamic viscosity of the fluid, and the maximal axial displacement of the fluid elements, respectively. By recognizing $\sqrt{\nu/\omega}$ as the well-known Stokes-layer thickness due to pure oscillations, the Womersley number α is the ratio of the geometrical half height to the Stokes-layer thickness, and represents a frequency parameter. On the other hand, the transition number β, which has often been used in the oscillatory-flow literature as an indicator for the laminar-turbulent transition, represents the ratio of the tidal displacement to the Stokes-layer thickness. According to Kurzweg, et al. [24], for $\alpha \approx 1$, turbulent flow occurs for $\beta > 3000$. However, a wide range of transition numbers β was reported [25–27]. The frequency and flow range tested in this work results in $0.8 \le \alpha \le 3$ and $80 \le \beta \le 562$. Therefore, we assume a laminar flow regime inside the microchannel heat exchangers.

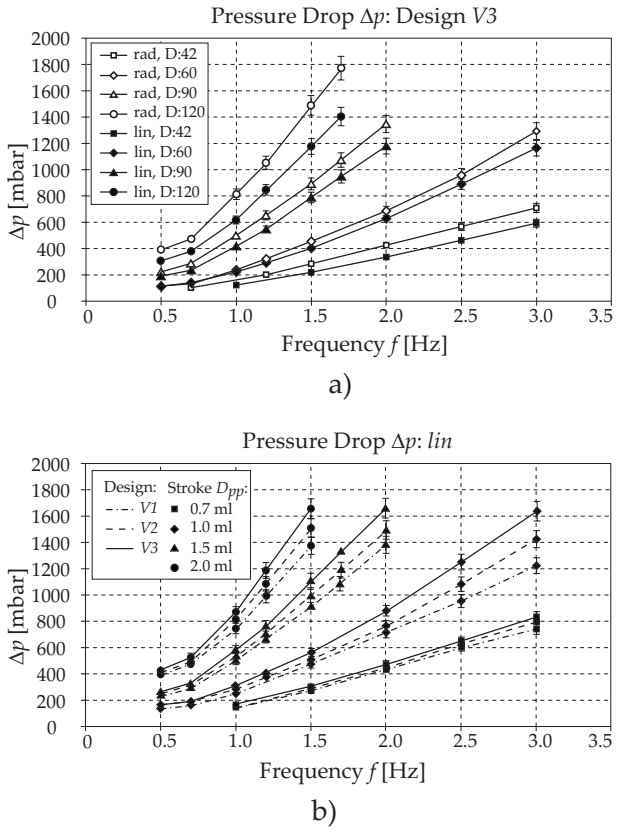

Fig. 3 Averaged (RMS) pressure drop (*a*) for *V*3, various flow patterns (lin and rad), pump displacements D_{pp}, and frequencies f, and (*b*) for various absorber designs V_i, pump displacements D_{pp}, and frequencies f

Depending on the fluid displacement D_{pp}, the frequency was set between 0.5 Hz and 3 Hz. For higher frequencies f and displacements D_{pp}, the pressure drop in the system and the power to drive the piston pump become too high, i.e., $\Delta p \ge 2$ bars. Frequency-dependent pressure drop data with HA *V*3 for lin and rad oscillation flows are shown in Fig. 3(*a*). The comparison of the three different designs, *V*1, *V*2, and *V*3, for linear oscillation flow is presented in Fig. 3(*b*). For both flow patterns, the pressure oscillations follow a clearly sinusoidal behavior. Furthermore, when plotting the pressure drop against the flow rate, the data points for various pump strokes collapse to a single curve. Therefore, we legitimate the decision to define the mean hydraulic losses according to Eq. (5).

Lin exhibits a significantly lower pressure drop than rad. For $D_{pp}=0.7$ ml, the pressure drop in lin flow varies between 100 mbar and 800 mbar, depending on the frequency, and for $D_{pp}=2$ ml, it ranges from 300 mbar to 1400 mbar. For a given frequency f, displacement D_{pp}, and absorber design V_i, rad outperforms lin by 15–25% (Fig. 3(*a*)). This can be explained by the fact that in radial oscillation flow, the fluid momentum forces per cycle are higher. The flow is less directed and more fluid mixing occurs. For example, in the HA, the liquid experiences four primal changes of the planar flow direction per cycle when driven in rad flow, but only two in lin.

Concerning the three different mesh porosities, *V*1, *V*2, and *V*3, the pressure reflect the mesh density (Fig. 3(*b*)). Except for the

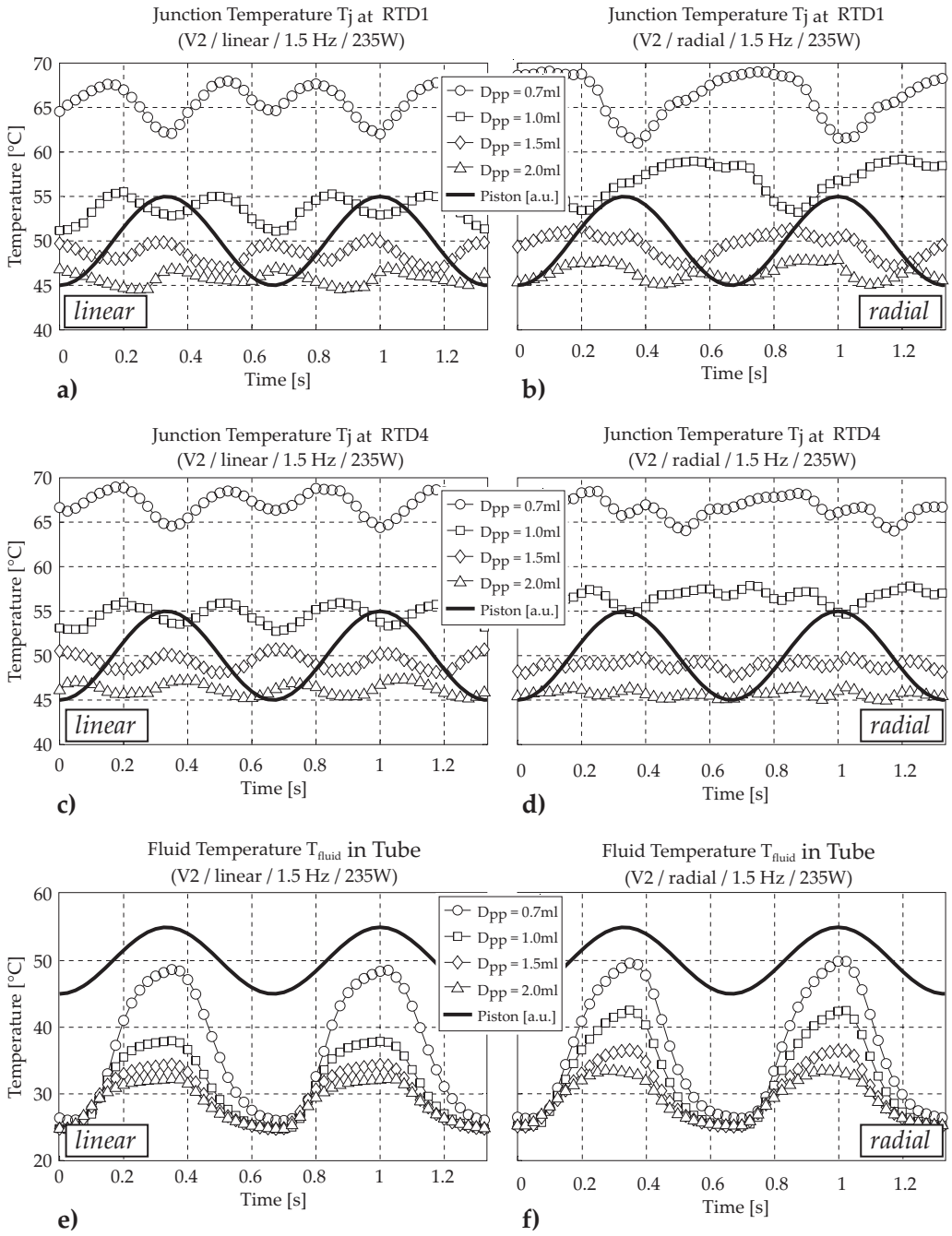

Fig. 4 Temporal temperature oscillations over two cycles at for HA *V*1, P_{chip}=235 W, and *f*=1.5 Hz: Panels (*a–d*) show the chip temperature at two different locations (RTD1: corner region, RTD4: center region) and flow patterns. Panels (*e–f*) give the fluid temperature in the interconnecting tube between the absorber and the dissipator cold plates.

case of $D_{pp}=0.7$ ml, the hydraulic losses for *V*3 are 20% higher than those for *V*1. As will be shown later, a higher heat transfer rate can be achieved at the expense of higher pumping power (denser versus coarser mesh).

3.2 Thermal Performance. As mentioned above, the Womersley number for the entire frequency range is $0.8 \leq \alpha \leq 3$. Small Womersley numbers ($\alpha<1$) result in quasisteady flows with oscillatory parabolic velocity profiles. In turn, large α-values ($\alpha>10$) lead to the "Richardson's annular effect," which results in near-wall velocity overshoots (plug-like velocity profile), where the peak velocity no longer occurs in the symmetry plane of the channel [28,29]. In the present work, the oscillation flow regime is in the transition zone between a parabolic and a plug-like velocity profile. Therefore, we do not expect an enhanced convective heat transfer, owing to a lower velocity boundary layer thickness. Theoretically, for $f>4$, $\alpha>10$ could be reached. However, because of the limited mechanical stability of the pumps, the tidal displacement had to be reduced to $D_{pp}<0.7$ ml. This in turn is insufficient to displace a fluid element from HA to HD in one stroke and leads to a reduced overall thermal performance.

3.2.1 Time-Resolved Measurements. Figure 4 shows the temperature oscillations at various locations (RTD1, RTD4, T_{fluid}) over two cycles for HA *V*2 and a fixed frequency of 1.5 Hz. All measurements were carried out at identical heating power P_{chip}

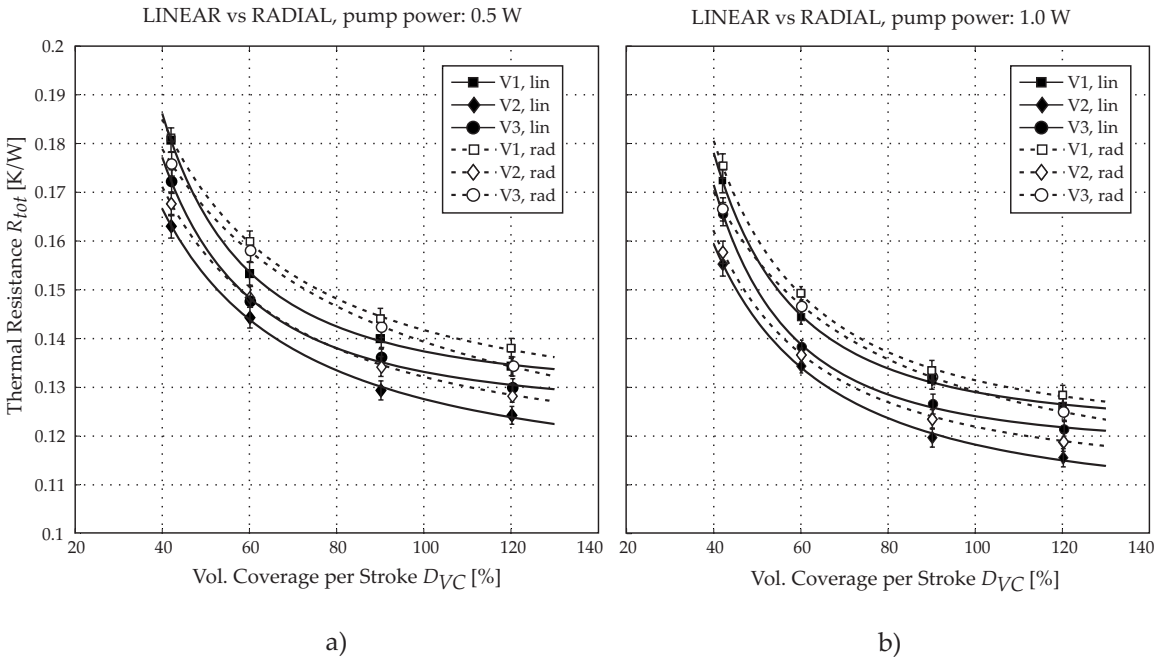

Fig. 5 Dependence of the averaged thermal resistance of the different flow patterns (lin, rad) and heat absorber mesh designs (*V*1, *V*2, *V*3) on the fluid pumping power at (*a*) 0.5 W and at (*b*) 1.0 W)

=235 W. The parameters for the secondary heat transfer loop comply with the descriptions given above. RTD1 is located in the corner of the heater/sensor chip, i.e., below the opening manifold of the HA. RTD4 is slightly offset from the center of the chip, and T_{fluid} is measured inside one of the tubes between HA and HD. In all subplots, the position of the piston pump (solid line) is shown in arbitrary units. A change from low to high values signifies that the pump pushes fluid across the HA through the tube to the corresponding HD. The temperature cycling demonstrates the dependency of the heat transfer rate on the fluid flow rate. High flow rates lead to a higher convective heat transfer coefficient, hence, to lower temperatures and lower inflow/outflow amplitudes, and vice-versa. In the lin flow mode (Fig. 4(*a*)), the temperature exhibits two minima and maxima values per cycle. This is due to the fact that the flow rate peaks twice per cycle (zero crossing of the piston position). The two minima are different (e.g., in Fig. 4(*a*), 62°C and 65°C for $D_{\text{pp}}=0.7$ ml) because the flow can be directed from (outflow, "hot") or to (returnflow, "cold") the heat source HA. The RTD temperature amplitude decreases with increasing stroke D_{pp}, e.g., for RTD4, lin decreases from 5 K to 2.5 K. The slight phase shift between the piston position signal and the RTD temperature is explained by the thermal time constant of the chip/cold plate assembly. Depending on the convective heat transfer rate, the thermal time constant is of the order of $\tau=0.1-0.3$ s (as in pp. 240 in Ref. [30]).

In rad flow (Figs. 4(*b*) and 4(*d*)), the RTD temperature oscillations follow a different characteristic compared with lin. For RTD1, which is located at the corner, the hot period is much more pronounced compared with lin. Only in one quarter of the pumping cycle returnflow from the HD occurs. The second temperature minimum, as detected for lin, is only identifiable for $D_{\text{pp}}=2.0$ ml. The RTD1 temperature amplitude is significantly higher for rad compared with lin, i.e., 40–60%, leading to a higher average temperature. For radial oscillations, however, RTD4 exhibits slight benefits compared with linear oscillations. The average temperature is similar, whereas the temperature amplitude can be reduced by adopting radial oscillation flows. For RTD4 and $D_{\text{pp}}=2.0$ ml, the amplitude is 1 K for rad and 2.5 K for lin. This, in turn, is the only example in the present work in which radially oscillating flows are advantageous over linearly oscillating flows. Locations away from the center (here represented by RTD4) realize a nonsymmetric flow regime over a pump cycle in rad flow. Pure returnflow, as described above, only occurs during a fourth of a pump cycle. We conclude that a constant, but radially oscillating flow regime, could only be established in the very center of the available HA cooling device. Although a design change might improve the situation, it is in the nature of the rad flow principle to transform to a periodic flow characteristic as the point of interest moves away from the center.

Figures 4(*e*) and 4(*f*) illustrates the measured temperature of the thermocouple inserted into the tube between HA and HD. Again, the solid line describes the piston pump position. The phase shift between fluid displacement and fluid temperature is close to zero because the heat transfer is dominated by heat advection (negligible thermal mass of thermocouple tip, $\tau\approx 4$ ms). The temperature is high when fluid flows from HA to HD (outflow), and low in the inverse direction (returnflow). Depending on the pump displacement, the outflow-returnflow temperature difference varies between 8 K and 25 K. For fixed displacements D_{pp}, the measured fluid temperature is always higher for rad than for lin. Moreover, in linear oscillation outflow (Fig. 4(*e*)), a ceiling temperature can be determined for $D_{\text{pp}}\geq 1.0$ ml. This is an indication of a full fluid displacement from one side to the opposite side. In contrast, this is not the case for radial flow. Therefore, we deduce a poorer heat shuttling capability for a radially oscillating flow than for a linearly oscillating flow. After exchanging heat with the HD and flowing back to the HA, the fluid temperature levels at about 25°C. Except for $D_{\text{pp}}=0.7$ ml, the variation in returnflow temperature for the different flow patterns and pump strokes is negligibly small. This indicates that together, the heat dissipator cold plate and the collector plane have a small thermal resistance.

3.2.2 Time-Averaged Measurements. Next, we compare the time-averaged thermal performance for the different HA designs and flow patterns for a fixed pumping power P_{fluid}, Eq. (7). Figure 5 discusses how the total thermal resistance R_{tot} depends on the volume coverage per stroke D_{VC}, Eq. (4). The experimental data are fitted using a power function of the form

$$R_{tot}(D_{VC}) = a \cdot D_{VC}^{b} + c \tag{8}$$

It contrasts the linear oscillation and the radial oscillation flow pattern at 0.5 W (Fig. 5(*a*)) and 1.0 W (Fig. 5(*b*)). First, a clear dependence on the pump power is evident, i.e., a larger volume coverage per stroke D_{VC} leads to a better cooling performance. However, R_{tot} approaches an asymptotic value toward $D_{VC}=120\%$ for linear oscillations. From Eq. (8), the asymptotic value of the total thermal resistance R_{min} can be determined considering the parameter γ. When comparing the volume coverage theoretically required to approach R_{min} by 5%, we find $D_{VC}=100-120\%$ for lin and $D_{VC}>250\%$ for rad. Concerning the pump strokes D_{PP} tested in this work, this range has only been achieved for lin. Again, this shows that heat spreading is much more effective for linearly oscillating flows than for radially oscillating flows. For all fluid displacements D_{VC}, lin performs better than rad. As shown in the hydraulic performance section, the radially oscillating flow exhibits higher hydraulic losses. This is the main reason for the performance difference seen in Fig. 5. However, when considering the flow rate as the independent variable, the discrepancy between the two flow regimes in terms of thermal resistance is marginal and not identifiable within the measuring error. We conclude that for a constant flow rate, the two oscillation patterns compared in this work perform equally well. However, because of a higher pressure loss, more pumping power is needed for radially than for linearly oscillating fluid flows. Furthermore, a self-contained, liquid cooling system with linearly oscillating fluid flows can be established using only one reciprocating pump, in conjunction with a spring-type fluid reservoir on the opposite side of the heat spreading system.

Comparing the three different HA mesh designs, one can see an optimum for *V*2 for the entire pump displacement range presented here. Typically, for steady, laminar, and developing flows in a microchannel, it holds that $\mathrm{Nu}\propto\mathrm{Re}^{\kappa}$, $\kappa\approx 0.5$ and $\Delta p\propto\mathrm{Re}^{\kappa}$, $1.7\leq\kappa\leq 2$ [23], therefore, $\mathrm{Nu}\propto\Delta p^{\kappa}$, $\kappa\approx 0.3$. *V*2 exhibits an optimum combination of thermal and hydraulic performance among the mesh designs presented in this work. Furthermore, the thermal performance of the cooling system presented here reaches an asymptotic value of $R_{tot}=0.11$ K/W, which corresponds to a maximum chip power density of 180 W/cm^2 at $\Delta T=67$ K ($T_{j,max}-T_{in}$, $T_{j,max}=85\,^{\circ}$C, $T_{in}=18\,^{\circ}$C). T_{in} is the chiller-controlled inlet fluid temperature of the secondary heat transfer loop HTL2.

We finalize the discussions with a subdivision of the total thermal resistance R_{tot} into an elemental linear resistor network (cp. insert Fig. 6). Therefore, we employ time-averaged temperatures T_i and a constant heat flux Q_{chip} to calculate the resistor elements of the heat absorber R_{HA}, the heat dissipator R_{HD}, and the collector plane R_{CP}, as

$$R_{Si+TIM}+R_{HA}=\frac{T_{j,mean}-T_{fluid}}{P_{chip}}, R_{HD}=\frac{T_{fluid}-T_{base}}{P_{chip}},$$

$$R_{CP}=\frac{T_{base}-T_{in}}{P_{chip}}(\mathrm{K/W})$$

$$R_{tot}=R_{Si+TIM}+R_{HA}+R_{HD}+R_{CP} \tag{9}$$

The interface resistance between the heater/sensor chip and the HA, as well as the measurement of the different temperature levels, have been discussed above. The interface resistance including conduction resistance in the silicon amounts to $R_{Si+TIM}=0.034$ K/W. In fact, four identical, parallel heat current resistor paths branch off from R_{HA}, each one dissipating a quarter of the total power input. This can be simplified to a single linear resistor network, as presented in Fig. 6. The elemental thermal resistances for *V*2, $f=1.5$ Hz, are presented as a function of the pump displacement D_{PP}, Fig. 6. Again, for a lager flow rate ($D_{PP}\uparrow$), the heat absorber cold plate resistance R_{HA} decreases, which also holds for

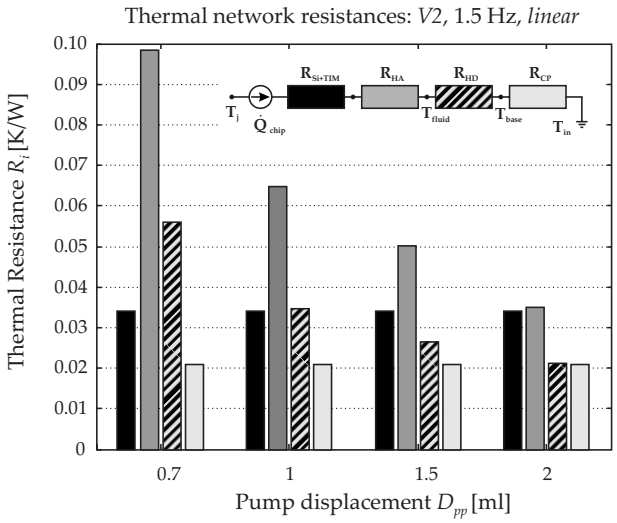

Fig. 6 Division of the overall thermal resistance into a simplified linear resistor network including R_{Si+TIM}, R_{HA}, R_{HD}, and R_{CP}

R_{HD}. However, R_{CP} is independent of the primary flow rate, as expected, because the flow rate of the secondary heat transfer loop (HTL2) is kept constant for all results presented herein. This could be verified by the experimental measurements presented in this work. It is important to note that with $R_{Si+TIM}+R_{HA}\approx 0.65\cdot R_{tot}$, the chip to fluid heat transfer resistance contributes the most to the overall thermal performance of the present cooling system. Therefore, because of an effective heat spreading from the hot chip to a large area, the heat exchangers of HTL2 can be designed in a simple manner. Here, we have chosen low aspect ratio, straight channel cold plates. As mentioned at the beginning, this design could also be replaced by air fin heat exchangers.

4 Summary and Conclusions

We have experimentally demonstrated a high performance thermal management concept for thin form-factor electronic equipment such as a blade server module. By means of a self-contained, reciprocating fluid flow loop, a four-port microchannel cold plate absorbs heat (HA) and delivers the hot fluid via interconnecting tubes to four peripheral dissipating cold plates (HD). There, a periodic heat transfer to a secondary heat transfer loop takes place by thermally attaching the dissipating cold plates to a fluid heat exchanger collecting plane (thermal bus).

To create the fluid oscillations, four piston pumps are actuated, and depending on the phase shift, different oscillation flow patterns (linearly oscillating, lin, and radially oscillating, rad) can be created. The fluid displacement is between 0.7 ml and 2.0 ml, i.e., 42–120% fluid volume coverage per stroke. Depending on the pump stroke, the oscillation frequency ranges between 0.5 Hz and 3 Hz. Higher frequencies cause unacceptably high pressure losses. Three different heat absorber cold plate designs with varying mesh porosities φ were tested.

The fluidic performance studies show a significantly lower pressure drop for lin than for rad (15–25% difference). For rad, the fluid changes its flow direction more frequently per pumping cycle, which results in higher momentum forces. Regarding the different heat absorber mesh designs, the densest (*V*3) features 20% higher pressure drop than the coarsest (*V*1). For a flow range of 100–800 ml/min, the pressure losses are between 100 mbar and 1200 mbar.

Thermal characterization is performed, taking time-resolved and time-averaged measurements. The chip RTD sensors capture the fluid flow oscillations over time. A larger tidal displacement of the piston pump leads to a smaller temperature amplitude. In linear oscillation flow two temperature minima and maxima per

pumping cycle are experienced. For radial fluid oscillations, the cooling performance is less efficient: corner regions of the chip exhibit larger temperature cycling, and only a small spot in the very center of the chip is cooled more efficiently, where the junction temperature is close to constant.

At 1.5 Hz the fluid temperature measured in the interconnecting tube fluctuates between 8 K and 25 K, depending on the pump stroke. In lin, a ceiling temperature can be determined for at least half the time of the outflow phase. This indicates uniform heat transfer. In rad, the heat absorber gets flushed less uniformly.

The averaged thermal performance of the cooling system presented here exhibits a clear dependence on the pump displacement. We have demonstrated a peak cooling performance of 180 W/cm^2 at $\Delta T=67$ K and a pumping power of 1 W. In lin, a pump displacement covering the fluid volume by 100–120% achieves a performance, roughly 5% above the theoretical minimum thermal resistance. Of the three HA designs tested herein, the medium-density mesh performed best ($\varphi_{V2}=52\%$). The optimum is found as a compromise accounting for both, high heat transfer rate and low hydraulic losses, resulting in the best ratio of heat transfer per pressure drop.

A reciprocating pump flow system, as presented here, is simpler in terms of equipment, and more efficient when operated in a linearly oscillating flow mode. The heat spreading from a small source to a large area is more effective for a given pumping power.

Nomenclature

A = area (m^2)
D = channel width (mm)
D_{PP} = piston pump stroke (ml)
D_{VC} = volume coverage (%)
f = piston pump frequency (Hz)
HTL1 = primary heat transfer loop
HTL2 = secondary heat transfer loop
Nu = Nusselt number
p = pressure (Pa)
P = power (W)
R = thermal resistance (K/W)
Re = Reynolds number
RTD(i) = resistance temperature detector at location $i=1,4$
T = temperature (°C)
t = time (s)
V = volume (m^3)
$V1, V2, V3$ = microchannel mesh designs
$\dot{V}$ = fluid flow rate (ml/min)

Greek Letters

α = Womersley number
β = transition number
Δ = difference between two measurements
ϕ = piston pump phase shift (rad)
φ = mesh porosity
κ = exponent
ν = dynamic viscosity (m^2/s)
σ = standard deviation
τ = time constant (s)

Subscripts/Superscripts

cell = unit cell of the heat transfer mesh
chip = heater/sensor chip
fluid = cooling fluid
i = counter for each piston pump ($i=1\ldots4$)
in = inlet
j = chip junction location
max = maximum
mean = averaged value
min = minimum
tot = total, overall
tube = interconnecting tube
void = void volume of a cell of the heat transfer mesh

References

[1] IBM STG Field Skills Education Team, 2009, "IBM BladeCentre and System X Reference Sheet," http://www.redbooks.ibm.com/xref/usxref.pdf
[2] Desai, D. M., Bradicich, T. M., Champion, D., Holland, W. G., and Kreuz, B. M., 2005, "BladeCenter System Overview," IBM J. Res. Dev., **49**(6), pp. 809–821.
[3] Crippen, M. J., Alo, R. K., Champion, D., Clemo, R. M., Grosser, C. M., Gruendler, N. J., Mansuria, M. S., Matteson, J. A., Miller, M. S., and Trumbo, B. A., 2005, "BladeCenter Packaging, Power, and Cooling," IBM J. Res. Dev., **49**(6), pp. 887–904.
[4] Bianchini, R., and Rajamony, R., 2004, "Power and Energy Management for Server Systems," IEEE Trans. Comput., **37**(11), pp. 68–76.
[5] Brey, T., Bigelow, B. E., Bolan, J. E., Cheselka, H., Dayar, Z., Franke, J. M., Johnson, D. E., Kantesaria, R. N., Klodnicki, E. J., Kochar, S., Lardinois, S. M., Morrell, C. A., Rollins, M. S., Wolford, R. R., and Woodham, D. R., 2005, "BladeCenter Chassis Management," IBM J. Res. Dev., **49**(6), pp. 941–961.
[6] Patel, P., Hughes, J., Herman, B., Cases, M., de Araujo, D. N., and Pham, N., 2004, "IBM Bladecenter System Electrical Packaging Design Challenges," *Proceedings of the IEEE 13th Topical Meeting on Electrical Performance of Electronic Packaging*, Portland, OR, pp. 11–14.
[7] Sauciuc, I., Chrysler, G., Mahajan, R., and Szleper, M., 2003, "Air-Cooling Extension—Performance Limits for Processor Cooling Applications," *Proceedings of the SEMITherm*, San Jose, CA, pp. 74–81.
[8] Tuckerman, D. B., and Pease, R. F. W., 1981, "High-Performance Heat Sinking for VLSI," IEEE Electron Device Lett., **2**(5), pp. 126–129.
[9] Vafai, K., and Zhu, I., 1999, "Analysis of Two-Layered Microchannel Heat Sink Concept in Electronic Cooling," Int. J. Heat Mass Transfer, **42**(12), pp. 2287–2297.
[10] Brunschwiler, T., Rothuizen, H., Fabbri, M., Fabbri, M., Kloter, U., Michel, B., Bezama, R. J., and Natarajan, G., 2006, "Direct Liquid Jet-Impingement Cooling With Micron-Sized Nozzle Array and Distributed Return Architecture," *Proceedings of the Tenth Intersociety Conference on Thermal and Thermomechanical Phenomena in Electronic Systems*, San Diego, CA, pp. 196–203.
[11] Colgan, E. G., Furman, B., Gaynes, M., LaBianca, N., Magerlein, J. H., Polastre, R., Bezama, R., Marston, K., and Schmidt, R., 2007, "High Performance and Sub-Ambient Silicon Microchannel Cooling," ASME J. Heat Transfer, **129**(8), pp. 1046–1051.
[12] Zhang, H. Y., Pinjala, D., Wong, T. N., Toh, K. C., and Joshi, Y. K., 2005, "Single-Phase Liquid Cooled Microchannel Heat Sink for Electronic Packages," Appl. Therm. Eng., **25**(10), pp. 1472–1487.
[13] Siegel, R., and Perlmutter, M., 1981, "Heat Transfer for Pulsating Laminar Duct Flow," ASME J. Heat Transfer, **84**, pp. 111–122.
[14] Kurzweg, U. H., and de Zhao, L., 1984, "Heat Transfer by High-Frequency Oscillations: A New Hydrodynamic Technique for Achieving Large Effective Thermal Conductivities," Phys. Fluids, **27**(11), pp. 2624–2627.
[15] Cooper, W. L., Nee, V. W., and Yang, K. T., 1994, "An Experimental Investigation of Convective Heat Transfer From the Heated Floor of a Rectangular Duct to a Low Frequency, Large Tidal Displacement Oscillatory Flow," Int. J. Heat Mass Transfer, **37**(4), pp. 581–592.
[16] Lia, Q. D., Yang, K. T., and Nee, V. W., 1995, "Enhanced Microprocessor Chip Cooling by Channeled Zero-Mean Oscillatory Air Flow," *Proceedings of the INTERpack '95*, Lahaina, HI, pp. 789–794.
[17] Sert, C., and Beskok, A., 2002, "Oscillatory Flow Forced Convection in Micro Heat Spreaders," Numer. Heat Transfer, Part A, **42**, pp. 685–705.
[18] Brunschwiler, T., Smith, B., Ruetsche, E., and Michel, B., 2009, "Toward Zero-Emission Data Centers Through Direct Reuse of Thermal Energy," IBM J. Res. Dev., **53**(3), pp. 11:1–11:13.
[19] Wälchli, R., Linderman, R., Brunschwiler, T., Kloter, U., Rothuizen, H., Bieri, N., Poulikakos, D., and Michel, B., 2008, "Radially Oscillating Flow Hybrid Cooling System for Low Profile Electronics Applications," *Proceedings of the SEMITherm24*, San Jose, CA, pp. 143–149.
[20] Brunschwiler, T. J., Kloter, U., Linderman, R., Michel, B., and Rothuizen, H., 2006, U.S. Patent No. 20070017659A1.
[21] Jillek, W., and Keller, G., 2003, *Handbuch der Leiterplattentechnik-Band 4*, E. G. L. Verlag, eds., Eugen G. Leuze Verlag, Bad Salgau, Germany, pp. 733–755.
[22] Schulz-Harder, J., 2006, "Efficient Cooling of Power Electronics," *Proceedings of the PCIM Conference*, Shanghai, pp. 208–212.
[23] Wälchli, R., Brunschwiler, T., Michel, B., and Poulikakos, D., "Combined Local Microchannel-Scale CFD Modeling and Global Chip Scale Network Modeling for Electronics Cooling Design," Int. J. Heat Mass Transfer, accepted.
[24] Kurzweg, U. H., Lindgren, E. R., and Lothrop, B., 1989, "Onset of Turbulence in Oscillating Flow at Low Womersley Number," Phys. Fluids A, **1**(12), pp. 1972–1975.
[25] Sergeev, S. I., 1966, "Fluid Oscillations in Pipes at Moderate Reynolds Numbers," Fluid Dyn., **1**, pp. 121–122.
[26] Hino, M., Sawamoto, M., and Takasu, S., 1976, "Experiments on Transition to Turbulence in an Oscillating Pipe Flow," J. Fluid Mech., **75**, pp. 193–207.

[27] Merkli, P., and Thomann, H., 1975, "Transition to Turbulence in Oscillating Pipe Flow," J. Fluid Mech., **68**, pp. 567–575.
[28] Zhao, T., and Cheng, P., 1995, "A Numerical Solution of Laminar Forced Convection in a Pipe Subjected to a Reciprocating Flow," Int. J. Heat Mass Transfer, **38**(16), pp. 3011–3022.
[29] Richardson, E. G., and Tyler, E., 1929, "The Transverse Velocity Gradient Near the Mouths of Pipes in Which an Alternating or Continuous Flow of Air Is Established," Proc. Phys. Soc. London, **42**(1), pp. 1–15.
[30] Incropera, F. P., and De Witt, D. P., 2002, *Fundamentals of Heat and Mass Transfer*, 5th ed., Wiley, New York.

The Effect of the Angle of Inclination on the Operation Limiting Heat Flux of Long R-134a Filled Thermosyphons

M. H. M. Grooten

C. W. M. van der Geld
e-mail: c.w.m.v.d.geld@tue.nl

Department of Mechanical Engineering,
Technische Universiteit Eindhoven,
Postbus 513,
5600 MB Eindhoven, Netherlands

When traditional air-to-air cooling is too voluminous, long thermosyphons may offer a way out. For safe operation of heat exchangers equipped with thermosyphons, the limiting heat flux q''_{lim} is an important design parameter. Some literatures are found to deal with the operation limiting heat flux of closed two-phase thermosyphons. However, R-134a filled thermosyphons with large length-to-diameter (188) are hardly investigated up to now. Extrapolation of existing correlations to predict q''_{lim} in this case results in large scatter. The effect of the angle of inclination on q''_{lim} has not been considered until now. Dedicated experiments with a single thermosyphon with a large length-to-diameter ratio (188) and filled with R-134a are presented and analyzed. Effects of saturation temperature, filling ratio, and angle of inclination β on the operational limiting heat flux have been investigated. The thermosyphon functions properly if $\beta < 83$ deg, and q''_{lim} is found to increase with increasing β. With decreasing saturation temperature, q''_{lim} increases. The filling ratio is found not to be crucial if it exceeds 25%. Correlations are presented to accurately predict the operation limiting heat flux for thermosyphons with a L/d ratio up to 188. Because of the accounting for the above new aspects, these correlations are also relevant for filling refrigerants other than R-134a.
[DOI: 10.1115/1.4000441]

Keywords: heat pipe, thermosyphon, heat exchanger, R-134a, limiting heat flux

1 Introduction

Stand-alone electricity power generators are usually cooled with ambient air. In warmer countries, heat pipe equipped heat exchangers provide an alternative for air-to-air heat exchangers at low air temperature differences. In this case, two plate heat exchangers are coupled with multiple wickless heat pipes: so called thermosyphons [1]. Advantages of heat pipes are high heat recovery effectiveness, compactness, no moving parts, light weight, relative economy, no external power requirements, pressure tightness, no cross contamination between streams, and reliability [2,3]. Vasiliev [4,5] gives an overview of applications of heat pipes and thermosyphons.

Safe operation of thermosyphons is principally dependent on knowledge of the limiting heat flux. A number of researchers investigated this maximum heat flux [6–21]. However, a large scatter in results was found. This scatter has several causes: a large variety of working fluids, temperature and pressure ranges, diameters, evaporator length, filling ratios, and the nature of the limit; boiling critical heat flux, entrainment limit, flooding limit, etc.

Research on the effect of the angle of inclination on thermosyphon characteristics is often contradictory [9,16,21,22]. The changes in fluid flow possibly affect the operation limiting heat flux, although no general conclusions on the effects of angle of inclination on the operation limiting heat flux can be drawn from literature. Research on thermosyphons found in literature deals with much shorter thermosyphons than the one considered in the present research. We selected a high L/d ratio in order to highlight and elucidate the effect of the angle of inclination on the limiting heat flux.

The operational heat flux limit of long, R-134a filled thermosyphon has hardly been investigated up to now. Existing correlations to predict the limiting heat flux in thermosyphons result in large scatter if extrapolated to our specific geometry and working fluid. This will be shown in Sec. 4. As stated above, the effect of inclination on the limiting heat flux is not clearly predicted. To promote the commercial use of heat pipe equipped heat exchangers, the limiting heat flux of a single 3 m thermosyphon with a large length-to-diameter ratio of 187.5 should be determined in a wide operating range.

For the above reasons, this study presents measurements and predictions on the operation limiting heat flux of a thermosyphon with a length of 3 m and a large length-to-diameter ratio of 187.5. The thermosyphon is filled with R-134a as working fluid to prevent freezing [1]. The goal of this research is to determine the effect of the angle of inclination on the operation limiting heat flux of the thermosyphon. Relationships between the filling ratio, inclination angle, and operation limiting heat flux will be derived, in order to facilitate future design of heat exchangers equipped with thermosyphons/heat pipes of this type. These main results can be seen as an addition to the many applicability maps existing, see for example the ESDU data item [23]. Conclusions for evaporation and condensation heat transfer in this type of thermosyphon were presented in a previous paper [24].

2 Experimental

The experimental setup is described in detail in Ref. [24]. A schematic overview is shown in Fig. 1. The main features are summarized in Table 1. Note that the length to diameter ratio of the thermosyphon is large: 187.5.

Contributed by the Heat Transfer Division of ASME for publication in the JOURNAL OF HEAT TRANSFER. Manuscript received November 21, 2008; final manuscript received September 18, 2009; published online March 4, 2010. Assoc. Editor: H.-P. Tan.

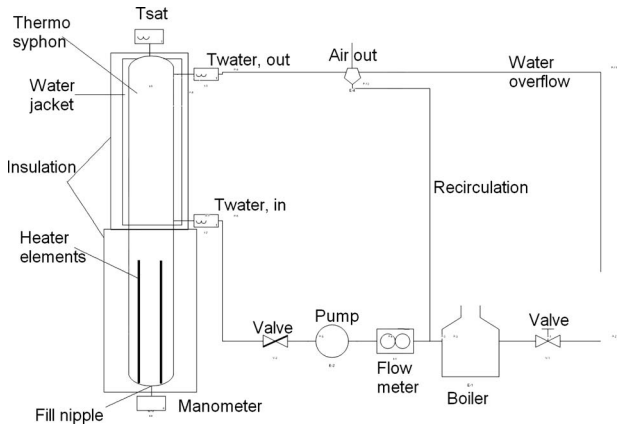

Fig. 1 Schematic view of the experimental setup

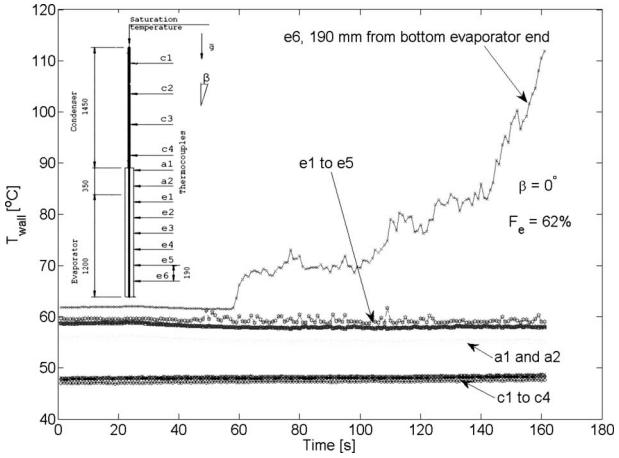

Fig. 2 Temperature history at operating limit. Inset shows thermocouple positions.

Experiments are performed with a filling ratio of 25%, 62%, and 100%. The filling ratio is defined as

$$F_e = \frac{V_f}{V_{\text{evap}}} \tag{1}$$

where the evaporator volume V_{evap} is $\pi r_i^2 L_{\text{evap}}$, r_i is 7.2 mm, and the volume of fluid V_f is the volume of liquid plus the volume that would be obtained if the vapor is condensed to liquid. Measurements are performed at inclination angles β from 0 deg to 87 deg. The angle is determined with Mitutoyo Pro 360 Digital Protractor, which is accurate to 0.2 deg. The saturation temperature inside the thermosyphon is varied between 20°C and 75°C. This corresponds with pressures of 5.7–20.6 bars. The uncertainties of all measured and calculated parameters are estimated according to Ref. [25].

3 Experimental Results

The following results will be presented.

- typical temperature distributions over the thermosyphon at the operation limiting heat flux
- operation limiting heat flux dependencies on saturation temperature and filling ratio
- operation limiting heat flux dependencies on the angle of inclination

Figure 2 shows a typical example of measured wall temperatures at the operation limiting heat flux for a filling ratio of 62%. At inclination angles exceeding 83 deg and saturation temperature of 75°C, the operation limiting heat flux is observed to occur differently, see Fig. 3. All wall temperatures at the evaporator stabilize at a temperature level far above T_{sat}, starting with the evaporator end, and followed by places further away in the direction of the condenser section. The temperature at the bottom end of the evaporator is found to fluctuate, as if the dry out occurs intermittently.

Table 1 Main features of experimental setup

Total length	- 3 m - Copper container
Diameter	- 16 mm (outer) - Wall thickness 0.8 mm - Smooth inner surface
Condenser	- $L_{\text{cond}}=1.45$ m - Tap water cooling, altometer 41BNW15 flow meter, flow rates of $0-0.18\pm0.01$ l/s. Coolant inlet and outlet temperatures measured with Pt-100 (IC Istec ME 1009) sensors. Better than 0.1°C accurate between 0–100°C. - Coolant inlet temperature adjustable with preheater - 20 mm polyethylene foam insulation - 4 K-type thermocouples at outer wall, 0.75°C accurate - Intruding Pt-100 for saturation temperature measurements
Adiabatic section	- $L_{\text{ad}}=0.35$ m - 2 K-type thermocouples at outer wall, 0.75°C accurate
Evaporator	- $L_{\text{evap}}=1.20$ m - Heated uniformly with electrical heater, maximum 1950 ± 1 W, controlled by a Gossen Wattmeter - 40 mm glass wool insulation, heat losses 0.5% of the heat input at worst - 6 K-type thermocouples at outer wall, 0.75°C accurate - WIKA type RB manometer. 0–40 bars, 0.5 bar accurate
Working fluid	- R-134a - Fluid inventory accurate to 0.1 g

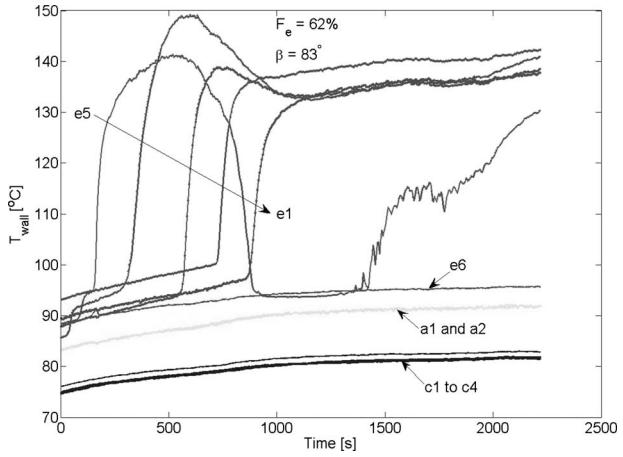

Fig. 3 Temperature history at operating limit at large inclination and high temperatures (see Fig. 2 for thermocouple positions)

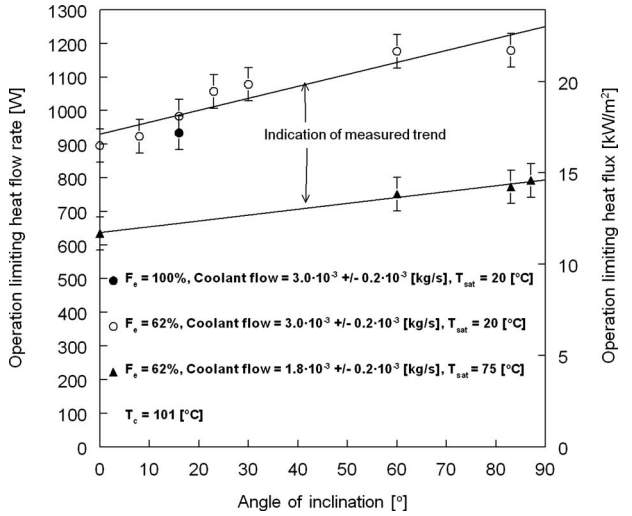

Fig. 5 Operating limit of the thermosyphon versus inclination angle for various filling ratios and saturation temperatures $A_{evap}=0.0543\ m^2$

As shown in Fig. 4, the operation limiting heat flux at vertical orientation at various filling ratios is observed to decrease with increasing saturation temperature. The trend of a decreasing operation limiting heat flux with increasing temperature is coherent for all measurements, also when the thermosyphon is inclined. At a saturation temperature of 20°C, the operation limiting heat flux, based on the evaporator wall area, is 17 kW/m^2, corresponding to a heat flow rate of 900 W. The operation limiting heat flux decreases to 9.2 kW/m^2 around 80°C. Only one point at 25% filling ratio is measured. At higher temperatures, only the gaseous phase is present at this underfilled case. The effect of the filling ratio is found to be negligible, as long as the fluid inventory is sufficient to avoid dry out at normal operations.

A higher operation limiting heat flux is observed at a higher angle of inclination at a saturation temperature of 20°C in Fig. 5: from 17 kW/m^2 in vertical orientation to 22 kW/m^2 in almost horizontal position. The trend of an increasing operation limiting heat flux with increasing inclination is also observed at a saturation temperature of 75°C. The error bars in Figs. 4 and 5 account for the reproducibility of the measurements at the operation limiting heat flux.

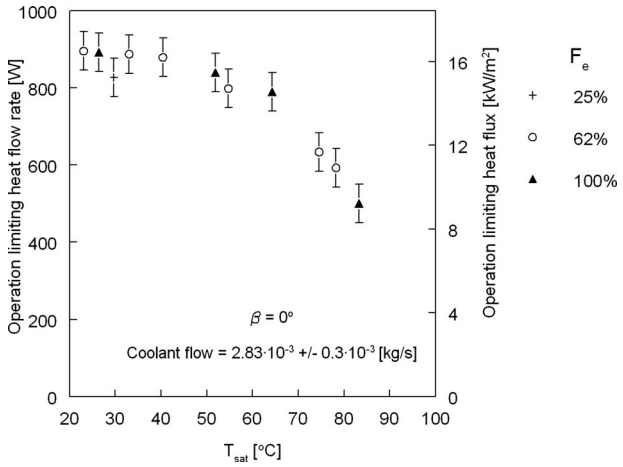

Fig. 4 Operating limit of the thermosyphon versus saturation temperature for various filling ratios $A_{evap}=0.0543\ m^2$. Evaporator heat flux scale is linear.

4 Analysis

4.1 Interpretation of Operation Limiting Heat Flux. Figure 2 shows an entrainment limit; the temperature at the evaporator bottom end increases due to a lack of liquid. The liquid does not reach the end of the evaporator because it evaporates before that time and because vapor shear forces probably entrain the remaining liquid. The occurrence of an entrainment limit at filling ratios of 62% and 100% is in agreement with the findings of Golobic and Gaspersic [6] and Abou-Ziyan et al. [7]. Park et al. [8] observed a boiling limit at filling ratios of 50% and higher. Park et al. did observe entrainment limits, but only at a low filling ratio of 10%.

Shiraishi and co-workers [26,27] visualized the flow behavior almost at a horizontal position with a 13 mm diameter glass tube filled with R-113. The observed flow patterns agree with the measured temperature histories of our measurements in Fig. 3. In an almost horizontal position, liquid can easily flood the condenser. Flooding causes a breakdown of the condensation process and dry patches in the evaporator section due to an increase in void fraction in the evaporation section. Breakdown of the condensation process due to flooding is in agreement with the results of Gross [28]. From the results found by Gross [28] and Shiraishi and co-workers [26,27], it is reasonable to conclude that the measured temperature fluctuations at the evaporator bottom end for angles of inclination larger than 83 deg are due to the boiling limit.

4.2 Operation at Inclination. Since fluid transport in a thermosyphon is gravity driven, the functioning of the thermosyphon would be expected to degrade with increasing β. The contrary is observed: the limiting heat flux increases with increasing β. Proper functioning of the thermosyphon up to large angles of inclination is not surprising with regards to the wall wetting phenomena observed in Fig. 6. In these visualizations, we took care to

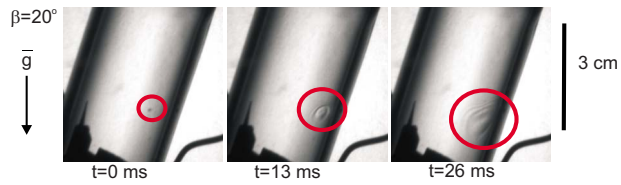

Fig. 6 Proof of wetting of the adiabatic wall at inclination by a liquid film by drop impingement

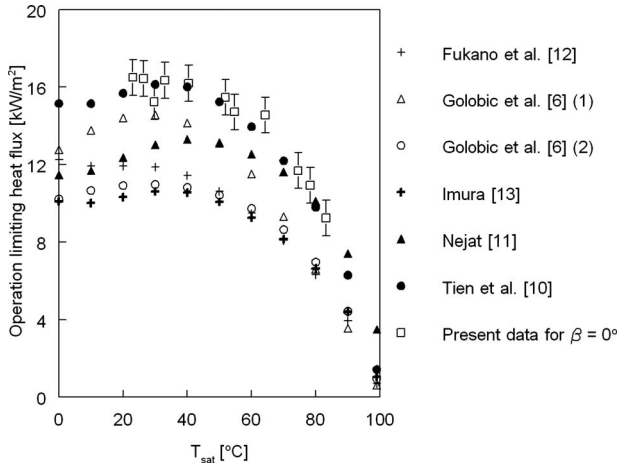

Fig. 7 Predicted operation limiting heat flux by correlations from literature, β=0 deg

have the same contact angle as in the present measurements. Drop impingements from droplets escaping the evaporator section prove that the wall is still fully wet at inclination. A droplet escapes from the evaporator section and hits the adiabatic wall of the thermosyphon. The droplet spreads out and induces waves, proving that a liquid surface and a liquid film are present. This proves that local dry out of the wall does not occur at increasing angle of inclination. Visualizations of flow phenomena in thermosyphons were presented in a previous work [29].

4.3 Application of Existing Correlations to Predict the Limiting Heat Flux. Some correlations from the literature to predict the operation limiting heat flux are shown in Fig. 7. Note that these correlations do not take the angle of inclination into account. The operation limiting heat flux predicted with correlations of Tien and Chung [10] and Nejat [11], agrees to within 1.8 kW/m^2 with the present data, if these correlations are extrapolated to our geometry with $L/d=187.5$ to our working fluid R-134a and taking vertical orientation into account only.

4.4 New Correlation to Predict the Limiting Heat Flux Including Angle of Inclination and for L/d up to 188. Both correlations of Tien and Chung [10] and Nejat [11] are in the form of $q''=a_1\cdot f(\mathrm{Bo}^{1/2})\cdot(d/L_{\mathrm{evap}})^{a_2}$, where a_1 and a_2 are constant and Bo is the Bond number, defined as $\sqrt{\rho_f g d^2/\sigma}$. L_{evap} is the length of the evaporator section: 1.20 m, d is the diameter of the thermosyphon: 16 mm, and q'' is the heat flux per evaporator wall area A_{evap}. The form of these correlations appears to do well to predict the trends in the present data. Both geometrical properties and working fluid properties are incorporated. We have tried to fit the measured data in a correlation of this form. Fit parameters from Tien and Chung [10] are $a_1=0.8$ and $a_2=1$, while fit parameters from Nejat [11] are $a_1=0.09$ and $a_2=0.9$. Equations (2) and (3) are found to be valid for a thermosyphon with R-134a at saturation temperatures between 20°C and the critical temperature (101°C) as

$$\mathrm{Ku}=(0.14\pm0.01)\cdot\left(1-\frac{T_{\mathrm{sat}}}{T_c}\right)^{1/5}\mathrm{Bo}^{1/2}\frac{(d/L_{\mathrm{evap}})^{0.90\pm0.02}}{\left(1+\left(\frac{\rho_v}{\rho_l}\right)^{1/4}\right)^2} \quad (2)$$

$$q''_{\mathrm{lim},0}=\mathrm{Ku}\cdot\Delta h_{fg}\rho_v^{1/2}(\sigma g(\rho_l-\rho_v))^{1/4} \quad (3)$$

with T in K and T_c is the critical temperature of R-134a: 374 K. The two errors in Eq. (2) indicate a 95% confidence interval. The heat flow rate on the evaporator side is for each heat flux given by $Q_{\mathrm{evap}}=q''_{\mathrm{lim},0}\cdot A_{\mathrm{evap}}$, of course. The term $(1-T_{\mathrm{sat}}/T_c)$ in Eq. (2) ensures agreement with the boundary condition $q''=0$ kW/m^2 at the critical temperature T_c. The term (d/L_{evap}) accounts for geometrical properties of the thermosyphon, as in the correlation of Tien and Chung [10] and Nejat [11]. The thermodynamic and transport properties of the working fluid appear in Eq. (2) via the term $(1+(\rho_v/\rho_l)^{1/4})^2$ and via Δh_{fg}, $\rho_v^{1/2}$, σ, and $(\rho_l-\rho_v)$ in Eq. (3).

The correlation coefficient r^2 is defined by [30]

$$r^2=\sum_{i=1}^{N}(\hat{y}_i-\overline{y})^2/\sum_{i=1}^{N}(y_i-\overline{y})^2 \quad (4)$$

where N is the number of measurements with outcome y_i. $\hat{y}_i$ are the corresponding predictions with the fit function and $\overline{y}$ is the average of the set $\{y_i\}$. The number of parameters used in the fit k affects the quality of the fit. Whereas the correlation coefficient should preferably have a value close to 1, the parameter F should, at the same time, have a maximum value, that is

$$F=\left\{\sum_{i=1}^{N}(\hat{y}_i-\overline{y})^2/\sum_{i=1}^{N}(y_i-\hat{y}_i)^2\right\}\cdot(N-k)/(k-1) \quad (5)$$

For Eqs. (2) and (3), fit statistics of data measured at a filling ratio of 100% are $F=29$ and $r^2=0.94$. For data measured with a filling ratio of 62%, fit statistics are found to be $F=130$ and $r^2=0.97$.

Equations (2) and (3) hold for a vertical orientation of the thermosyphon. However, from Fig. 5, we conclude that an increase in the inclination angle increases the operation limiting heat flux at all saturation temperatures. We propose to add this dependency of the operation limiting heat flux on the inclination angle by using

$$q''_{\mathrm{lim}}=q''_{\mathrm{lim},0}\cdot\left(1+\left(b_1\frac{T_{\mathrm{sat}}}{T_c}+b_2\right)\cdot\beta\right) \quad (6)$$

where $q''_{\mathrm{lim},0}$ is the operating limit obtained from Eq. (3). Saturation temperature T is in K and T_c is the critical temperature of R-134a in K. β denotes the inclination with the vertical from 0 deg to 90 deg. A fit of the data of Fig. 5 yields b_1 as $-0.0125\pm10\%$ and b_2 as $1.01\pm10\%$. Fit parameters $F=44$ and $r^2=0.88$ are obtained. The two errors indicated in Eq. (6) are for a 95% confidence interval. Extrapolation of the fit of Eq. (6) to temperatures outside the measured range (20–75°C) should be done with prudence.

5 Conclusions

The operation limiting heat flux q''_{lim} in a 3 m long, R-134a filled thermosyphon, with L/d ratio 188, has been assessed in a wide operating range. The dependencies of q''_{lim} on filling ratio, angle of inclination, and saturation temperature have been determined. Knowledge of these limits is essential for design of heat exchangers equipped with thermosyphons. Maximum heat fluxes at the evaporator of 24 kW/m^2 have been measured, corresponding to heat transfer rates of 1300 W.

The following new trends have been observed.

- The operation limiting heat flux decreased with increasing saturation temperature and with decreasing angle of inclination with the vertical.
- Proper functioning of the thermosyphon is observed up to angles of inclination of $\beta=83$ deg.

Physical explanations for the trends observed have been presented. A new correlation is proposed to take the effect of the angle of inclination on operation limiting heat flux into account. The new correlation predicts this operation limiting heat flux of a thermosyphon as a function of temperature dependent working fluid properties and geometry, including angle of inclination. Because of the accounting for the above trends and because they are based on existing correlations, the new correlations are also relevant for filling refrigerants other than R-134a.

Acknowledgment

The support of H. Hagens of VDL Klima bv., The Netherlands, in facilitating the experimental work is greatly appreciated.

Nomenclature

A = surface area (m^2)
Bo = Bond number ($\sqrt{\rho_f g d^2/\sigma}$)
Fe = filling degree
Ku = Kutateladze number, $(0.14 \pm 0.01)\cdot(1 - T_{sat}/T_c)^{1/5}\mathrm{Bo}^{1/2}(d/L_{evap})^{0.90\pm0.02}/(1 + (\rho_v/\rho_l)^{1/4})^2$
L = length (m)
Q = heat flow rate (W)
T = temperature (°C)
V = volume (m^3)
cp = heat capacity at constant pressure (J/kg K)
d = diameter (m)
g = acceleration due to gravity (m/s^2)
$\Delta h\ fg$ = enthalpy of evaporation (J/kg)
$\dot{m}$ = mass flow rate (kg/s)
q'' = heat flux (W/m^2)
r = radius (m)

Greek

β = inclination angle to the vertical (deg)
ρ = mass density (kg/m^3)
σ = surface tension (N/m)

Subscripts

ad = adiabatic
c = critical
cond = condenser
evap = evaporator
f = fluid
i = inner
l = liquid
lim = limit
sat = saturation
v = vapor

References

[1] Hagens, H., Ganzevles, F. L. A., Van der Geld, C. W. M., and Grooten, M. H. M., 2007, "Air Heat Exchangers With Long Heat Pipes: Experiments and Predictions," Appl. Therm. Eng., **27**(14–15), pp. 2426–2434.
[2] Dunn, P. D., and Reay, D. A., 1994, *Heat Pipes*, 4th ed., Pergamon, New York.
[3] Wadowski, T., Akbarzadeh, A., and Johnson, P., 1991, "Characteristics of a Gravity Assisted Heat Pipe Based Heat Exchanger," Heat Recovery Syst. CHP, **11**(1), pp. 69–77.
[4] Vasiliev, L. L., 2005, "Heat Pipes in Modern Heat Exchangers," Appl. Therm. Eng., **25**(1), pp. 1–19.
[5] Vasiliev, L. L., 1998, "State-of-the-Art on Heat Pipe Technology in Former Soviet Union," Appl. Therm. Eng., **18**(7), pp. 507–551.
[6] Golobic, I., and Gaspersic, B., 1997, "Corresponding States Correlations for Maximum Heat Flux in Two-Phase Closed Thermosyphon," Int. J. Refrig., **20**, pp. 402–410.
[7] Abou-Ziyan, H. Z., Helali, A., Fatouh, M., and Abo El-Nasr, M. M., 2001, "Performance of Stationary and Vibrated Thermosyphon Working With Water and R-134a," Appl. Therm. Eng., **21**, pp. 813–830.
[8] Park, Y. J., Kang, H. K., and Kim, C. J., 2002, "Heat Transfer Characteristics of a Two-Phase Closed Thermosyphon to the Fill Ratio," Int. J. Heat Mass Transfer, **45**, pp. 4655–4661.
[9] Larkin, R. S., 1982, "A Heat Pipe for Control of Heat Sink Temperature," *Proceedings of the Seventh International Heat Transfer Conference*, Munchen, Germany, pp. 319–324.
[10] Tien, C. L., and Chung, K. S., 1979, "Entrainment Limits in Heat Pipes," AIAA J., **17**, pp. 643–646.
[11] Nejat, Z., 1981, "Effects of Density Ratio on Critical Heat Flux in Closed and Vertical Tubes," Int. J. Multiphase Flow, **7**, pp. 321–327.
[12] Fukano, T., Kadoguchi, K., and Tien, C. L., 1988, "Experimental Study on the Critical Heat Flux at the Operating Limit of a Closed Two-Phase Thermosyphon," Heat Transfer-Jpn. Res., **17**, pp. 43–60.
[13] Imura, H., Sasaguchi, K., Kozai, H., and Numata, S., 1983, "Critical Heat Flux in a Closed Two-Phase Thermosyphon," Int. J. Heat Mass Transfer, **26**(8), pp. 1181–1188.
[14] El-Genk, M. S., and Saber, H. H., 1999, "Determination of Operation Envelopes for Closed, Two-Phase Thermosyphons," Int. J. Heat Mass Transfer, **42**, pp. 889–903.
[15] Sugumar, D., and Tio, K.-K., 2009, "The Effects of Working Fluid on the Heat Transport Capacity of a Microheat Pipe," ASME J. Heat Transfer, **131**, pp. 012401.
[16] Negishi, K., and Sawada, T., 1983, "Heat Transfer Performance of an Inclined Two-Phase Closed Thermosyphon," Int. J. Heat Mass Transfer, **26**(8), pp. 1207–1213.
[17] Dobran, F., 1985, "Steady-State Characteristics and Stability Thresholds of a Closed Two-Phase Thermosyphon," Int. J. Heat Mass Transfer, **28**(5), pp. 949–957.
[18] Payakaruk, T., Terdtoon, P., and Ritthidech, S., 2000, "Correlations to Predict Heat Transfer Characteristics of an Inclined Closed Two-Phase Thermosyphon at Normal Operating Conditions," Appl. Therm. Eng., **20**, pp. 781–790.
[19] Noie, S. H., 2005, "Heat Transfer Characteristics of a Two-Phase Closed Thermosyphon," Appl. Therm. Eng., **25**, pp. 495–506.
[20] Mihara, S., and Monde, M., 1998, "Characteristics of Critical Heat Flux in Two Phase Thermosyphon—Relationship Between Maximum Falling Liquid Rate and Instability on Interface of Falling Liquid Film," Heat and Mass Transfer, **34**, pp. 135–142.
[21] Hahne, E., and Gross, U., 1981, "The Influence of the Inclination Angle on the Performance of a Closed Two-Phase Thermosyphon," Heat Recovery Syst. CHP, **1**, pp. 267–274.
[22] Wang, J. C. Y., and Yiwei, M., 1991, "Condensation Heat Transfer Inside Vertical and Inclined Thermosyphons," ASME J. Heat Transfer, **113**, pp. 777–780.
[23] ESDU, 1981, *Heat Pipes—Performance of Two-Phase Closed Thermosyphons*, Engineering Sciences Data Unit, London.
[24] Grooten, M. H. M., and van der Geld, C. W. M., 2009, "Predicting Heat Transfer in Long, R-134a Filled Thermosyphons," ASME J. Heat Transfer, **131**(5), p. 051501.
[25] Kline, S. J., and McKlintock, F. A., 1953, "Describing Uncertainties in Single-Sample Experiments," Mech. Eng. (Am. Soc. Mech. Eng.), **75**, pp. 3–8.
[26] Shiraishi, M., Terdtoon, P., and Murakami, M., 1995, "Visual Study on Flow Behavior in an Inclined Two-Phase Closed Thermosyphon," Heat Transfer Eng., **16**(1), pp. 53–59.
[27] Shiraishi, M., Terdtoon, P., Chailungkar, M., and Ritthidej, S., 1997, "Effects of Bond Numbers on Internal Flow Patterns of an Inclined, Closed, Two-Phase Thermosyphon at Normal Operating Conditions," Exp. Heat Transfer, **10**, pp. 233–251.
[28] Gross, U., 1992, "Reflux Condensation Heat Transfer Inside a Closed Thermosyphon," Int. J. Heat Mass Transfer, **35**(2), pp. 279–294.
[29] Grooten, M. H. M., Van der Geld, C. W. M., and Van Deurzen, L. G. M., 2008, "A Study of Flow Patterns in a Thermosyphon for Compact Heat Exchanger Applications," *Proceedings of the Fifth International Conference on Transport Phenomena in Multiphase Systems*, D. Butrymowicz, T. Skiepko, and J. Soscik, eds., Bialystok, Poland, Vol. 2, pp. 323–328.
[30] Schmidt, J., Giesbrecht, H., and Van der Geld, C. W. M., 2007, "Void Fraction and Distributions in Upward Pipe Flow of Gas and a High-Viscous Liquid," Int. J. Multiphase Flow, **34**(1), pp. 363–374.

A Phase-Sensitive Technique for Measurements of Liquid Thermal Conductivity

Zhefu Wang

Richard B. Peterson
e-mail: richard.peterson@oregonstate.edu

Department of Mechanical Engineering,
Oregon State University,
204 Rogers Hall,
Corvallis, OR 97331

An experimental technique based on the thermal wave approach for measuring the thermal conductivity of liquids is developed in this paper. A stainless steel strip functions as both a heating element and a sealing cover for a chamber containing a test liquid. A periodic current passing through this metal strip generates a periodic Joule heating source. An infrared detector measures the temperature response at the front surface of the stainless steel strip. The phase and magnitude of the temperature response with respect to the heating signal were measured by a lock-in amplifier at various frequencies from 22 Hz to 502 Hz. A one-dimensional, two-layered transient heat conduction model was developed to predict the temperature response on the front surface of the stainless steel strip. The phase information from this temperature response shows high sensitivity to the change in thermal properties of the liquid layer and is employed to match experimental data to find the thermal properties of the test liquid. The measured thermal conductivities of water and ethylene glycol agree quite well with the data from literature and support the validity of this measurement technique. An aqueous fluid consisting of gold nanoparticles is tested and anomalous thermal conductivity enhancement is observed. A discrepancy in the thermal transport behavior between pure liquids and nanofluids is suggested from our experimental results. [DOI: 10.1115/1.3211858]

Keywords: heat conduction, measurement techniques, thermal properties, phase detection, nanofluids

1 Introduction

Potential heat transfer enhancement appears to be the driving force for the study of thermal transport properties of nanofluids over the last decade after the pioneering work of Masuda et al. [1]. This first study showed the anomalous enhancement of the effective thermal conductivity of nanofluids. The majority of the following experimental results reported so far are from the transient hot-wire method [2–6], which is conventionally used to measure the thermal properties of pure liquids. Other measurement techniques found in literature include the temperature oscillation technique [7], optical beam deflection method [8], and 3ω method [9]. However, several important issues about the experimental approach when determining the effective thermal conductivities of nanofluids remain. First, disagreement on the enhancement level of the effective thermal conductivity appears in a number of experimental results among different research teams [3,4,6] and among different measurement techniques [3,7,8]. Although anomalous enhancement was reported in most of the studies [3,5,7,9–13], others [4,6,8] report findings in line with predictions. Second, although the mechanisms of heat transfer enhancement in nanofluids were studied extensively, such as Brownian motion [14–17], interfacial layers [18,19], aggregation [20,21], and thermophoresis [22], the role of measurement techniques on the experimental results was not examined in detail. A recent study suggests that applying a measurement technique conventionally used for pure liquids to a composite liquid such as a nanofluid may lead to misinterpretation of experimental data [23]. It will be desirable if independent experimental techniques can be developed to provide new information concerning the thermal transport process of nanofluids and, therefore, help to explain the discrepancy among the measurement results.

The classical theory of particle/fluid systems originally proposed by Maxwell [24] successfully describes the thermal transport process of the composite system with micrometer or larger particle sizes. The composite system is treated as homogeneous and isotropic. Two important assumptions are zero thermal resistance at the solid/liquid interfaces and no relative motion between liquid and particle. With these assumptions the so-called effective thermal conductivity is introduced into the formula of Fourier's law. Although this theory fails to explain a nanofluid's abnormal capability for transferring heat, the concept of this effective thermal conductivity continues to be used in the experimental study of nanofluids. However, Vadasz [23] argued that this kind of effective thermal conductivity may not exist in a transient process, which is typical for current measurement techniques, such as the transient hot-wire method. By introducing a heat transfer coefficient at the solid-liquid interface, he suggested that the transient hot-wire method may tend to overestimate the measured thermal conductivity of a composite fluid. However, no experimental data are available to provide a quantitative measure of the heat transfer coefficient at the solid-liquid interface to verify his theory up to now. Therefore, if the effective thermal conductivity were still employed as a measure of the thermal transport process in nanofluids under the framework of Fourier's law, a single constant value may not be adequate.

The factors that impact nanofluid thermal conductivity measurements can be categorized into two groups. One concerns the material characteristics, such as thermal properties of base liquid and particles, volume fraction, particle size, and surface treatment. The second is associated with the experimental approach (processing parameters), such as temperature, temperature gradient, pressure, and other parameters. For example, the high temperature gradient, which is common in the hot-wire measurement technique may lead to the redistribution of the nanoparticles [22]. The

Contributed by the Heat Transfer Division of ASME for publication in the JOURNAL OF HEAT TRANSFER. Manuscript received August 29, 2008; final manuscript received June 22, 2009; published online March 5, 2010. Review conducted by Roger Schmidt. Paper presented at the 2008 ASME Heat Transfer, Fluids, Energy, Solar, and Nano Conferences (HTFESN2008), Jacksonville, FL, August 10–14.

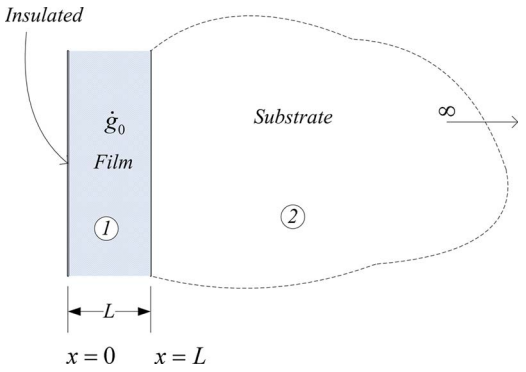

Fig. 1 Schematic sketches of the principles of the measurement

first class of factors was studied extensively [3,4,18–20] while only the temperature effect in the second class was examined [7,9]. A natural question to ask is that given a well characterized nanofluid, what will its effective thermal conductivity be? Is it a constant similar to a pure liquid or could it be a function of temperature as suggested by Das et al. [7]? Other parameters may also enter into consideration. These questions will be important for building an empirical formula of effective thermal conductivity and expediting the process of nanofluid applications in heat transfer. Due to the close relationship between the processing parameters and measurement results, data inconsistency problems mentioned above need to be studied with the processing parameters taken into account.

In light of the above discussion, a technique based on a thermal wave approach is developed to measure thermal conductivities of liquids with application to nanofluids. It is based on surface temperature oscillations and a sustained solution (periodic) to the transient heat conduction equation, hence, it has similar characteristics to the temperature oscillation technique of Czarnetzki and Roetzel [25] and further detailed and developed by Bhattacharya et al. [26]. The validity of this measurement approach was assessed by using water and ethylene glycol as the test references. A gold nanofluid with a gold concentration of 0.058 g/l and average particle size of 4.5 nm was also tested giving interesting results. Because of the higher frequencies used in the approach described here in comparison with other techniques, testing regimes that have been previously inaccessible may now be expanded somewhat, such as higher rate-of-temperature-change regimes due to the use of higher frequencies.

2 Principle of Measurement

The phase detection measurement method employed here was modified from the phase-sensitive measurement technique for determining thermal properties of a dielectric thin film [25]. Figure 1 shows the principle of thermal conductivity measurements of fluids.

This is a one-dimensional, two-layered transient heat conduction model with a periodic volume heating generation source in the first layer. The first layer is a stainless steel strip with a thickness of 12.5 μm. The fluid layer is the liquid that is being tested, such as water, ethylene glycol, or the nanofluid.

Important assumptions of this model include the following:

1. one-dimensional only; two-dimensional effect is neglected
2. no convection occurs; pure conduction only
3. the liquid layer is modeled as a stagnant, semi-infinite material domain
4. the front surface of the stainless steel strip is assumed to be thermally insulted
5. no thermal resistance between the stainless steel layer and the liquid layer
6. constant thermal properties for both layers

The governing differential equation for the first layer is

$$\frac{\partial^2 T_1}{\partial x^2} + \frac{g(t)}{k} = \frac{1}{\alpha_1}\frac{\partial T}{\partial t} \tag{1}$$

and the governing equation for the second layer is

$$\frac{\partial^2 T_2}{\partial x^2} = \frac{1}{\alpha_2}\frac{\partial T_2}{\partial t} \tag{2}$$

The square wave positive-going heating source can be expressed as

$$g(t) = \frac{g_0}{2} + \sum_{n=1}^{\infty} \frac{2g_0}{(2n-1)\pi}\sin[(2n-1)\omega t] \tag{3}$$

Because of the linear nature of our heat conduction model, the solution can be decomposed into ac and dc parts corresponding to the ac and dc heating source components. The dc part of the solution is the steady-state solution of the heat conduction problem with the constant heating source $g_0/2$. It can be used to estimate maximum temperature differences. Each harmonic sinusoidal function in the ac part of the heating source term leads to a solution at the same frequency. The sum of these solutions at different frequencies comprises the ac part of the final solution. Because the solutions at different frequencies can be decoupled from one another, we focus on the solution at the fundamental frequency only and explore the relationship between the temperature signal and the thermal properties of the liquid.

Both of the governing equations are linear and all the boundary conditions are homogeneous except for the heating source term. With the above assumptions, the analytical solution becomes piecewise continuous across the interface. Therefore, the method of complex combination can be applied to both domains and the solution format is assumed as

$$T(x,t) = \overline{T}(x)e^{i\omega t} \tag{4}$$

After Eq. (4) is substituted into Eqs. (1) and (2), the analytical solution of the above differential equations can be easily obtained because the partial differential equation is converted to the ordinary differential equation. The temperature expression of the heating layer T_1 and that of the liquid layer T_2 is shown in Eqs. (5) and (6).

$$T_1(x,t) = (A_1 e^{-\xi_1 x} + B_1 e^{\xi_1 x} + G_0)e^{i\omega t} \tag{5}$$

$$T_2(x,t) = A_2 e^{-\xi_2 x} e^{i\omega t} \tag{6}$$

where

$$A_1 = \frac{-G_0}{(e^{-\xi_1 L} + e^{\xi_1 L}) + \dfrac{k_1\xi_1}{k_2\xi_2}(e^{\xi_1 L} - e^{-\xi_1 L})} \tag{7}$$

$$A_2 = \frac{k_1\xi_1(e^{-\xi_1 L} - e^{\xi_1 L})}{k_2\xi_2 e^{-\xi_2 L}}A_1 \tag{8}$$

$$B_1 = A_1 \tag{9}$$

$$G_0 = \frac{\alpha_1 g_0}{i\omega k_1} \tag{10}$$

$$\xi_1 = \sqrt{i\frac{\omega}{\alpha_1}} \tag{11}$$

$$\xi_2 = \sqrt{i\frac{\omega}{\alpha_2}} \tag{12}$$

The temperature on the front surface of this heating layer in the complex form can be expressed as

$$T_1(x=0,t) = e^{i\omega t} G_0 \left(1 - \frac{2}{(e^{-\xi_1 L} + e^{\xi_1 L}) + \frac{k_1 \xi_1}{k_2 \xi_2}(e^{\xi_1 L} - e^{-\xi_1 L})} \right) \tag{13}$$

This expression is a complex function as indicated both by the $e^{i\omega t}$ term and the form for G_0, ξ_1, and ξ_2. In order to connect the model to the experiment, the complex expression of Eq. (13) can be conceptually written in the form of

$$T_1(x=0,t) = T_{\text{mag}} \sin[\omega t + \psi] \tag{14}$$

where T_{mag} is the magnitude of the temperature oscillation and ψ is the phase shift between the heating signal and the temperature signal. Note that the magnitude and phase could be explicitly written as $\sqrt{R^2+I^2}$ and $\tan^{-1}(I/R)$, respectively, if the real and imaginary components could be isolated from Eq. (13). This has not been accomplished to date. In place of an analytical expressions for T_{mag} and ψ, a computational software is available that can evaluate Eq. (13) and return the real and imaginary components. This is the approach taken in the present study. Assuming that all the experimental parameters except the liquid thermal conductivity k_2 are known and constant, both the magnitude and the phase of the temperature signal can be expressed as functions of the liquid thermal conductivity k_2. Therefore, by measuring the magnitude or the phase of the temperature signal, the thermal conductivity of the liquid can be obtained. By changing the heating frequency, a curve of the magnitude and phase shift under various frequencies is generated and the curve fitting method can be used to derive the liquid thermal conductivity.

Early in the development stage of the technique, amplitude versus frequency and phase versus frequency curves were generated analytically to determine which approach provided a more sensitive route for determining thermal diffusivity. The analytical curves generated clearly indicated that the method developed here was relatively insensitive to the amplitude of the temperature oscillations, i.e., a curve of amplitude versus frequency for one liquid varied only marginally from that of another fluid. This is demonstrated later by inspection of Figs. 2 showing, for the diffusivity range of interest in this work, little difference between water ($\alpha = 0.1445 \times 10^{-6}$ m^2/s) and ethylene glycol ($\alpha = 0.0918 \times 10^{-6}$ m^2/s). However, the phase shift results showed significant differentiation between the two liquids, over 5 deg difference under most of the heating frequencies used. This difference in phase is very measurable with a lock-in amplifier. Added benefits of exploiting this phase shift approach are that (1) only a temperature indicator is now needed for the detection of the signal (not a quantitatively accurate temperature measurement) and (2) phase shift information is often not very sensitive to instrument function changes such and drifts in detector sensitivity.

In the process of designing the test cell and measurement apparatus, consideration of several basic assumptions is very important. First, the pure conduction assumption implies no nature convection inside and outside of the liquid chamber. The maximum temperature difference between the heating element and the fluid can be estimated from the steady-state heat conduction study mentioned above. With the given geometry and this temperature difference, the Nusselt number can be estimated. The Nusselt number obtained is less than unity, which indicates that the effect of nature convection can be ignored and pure conduction assumption is valid. Second, in order to ensure that the semi-infinite material domain assumption applies, the thickness of the chamber needs to be much larger than the penetration depth of the thermal wave in our experiment [26]. According to our estimation at a lower frequency limit of 50 Hz, we set the thickness of the liquid chamber to 1.5 mm to satisfy the penetration depth consideration. Third, because the stainless steel strip is adhesively attached to the delrin support structure at its edge, this edge effect may invalidate our one-dimensional modeling assumption. However, a wider stainless steel strip lowers the electrical resistance. The resistance of the heating element needs to be high enough to secure a detectable temperature signal at the front surface of the stainless steel strip. A compromise between the above two considerations suggests a width of approximately 6 mm. Also, during measurements, we find an acceptable point for acquiring the signal by matching the measurement (through minor lens translation movement) to the model at a frequency within the measurement range and then fix this configuration through all other measurements. This process is validated using two independent test liquids, i.e., when water phase shift data is matched to its model with this procedure, the ethylene glycol data are very accurately predicted by the model (and vice versa).

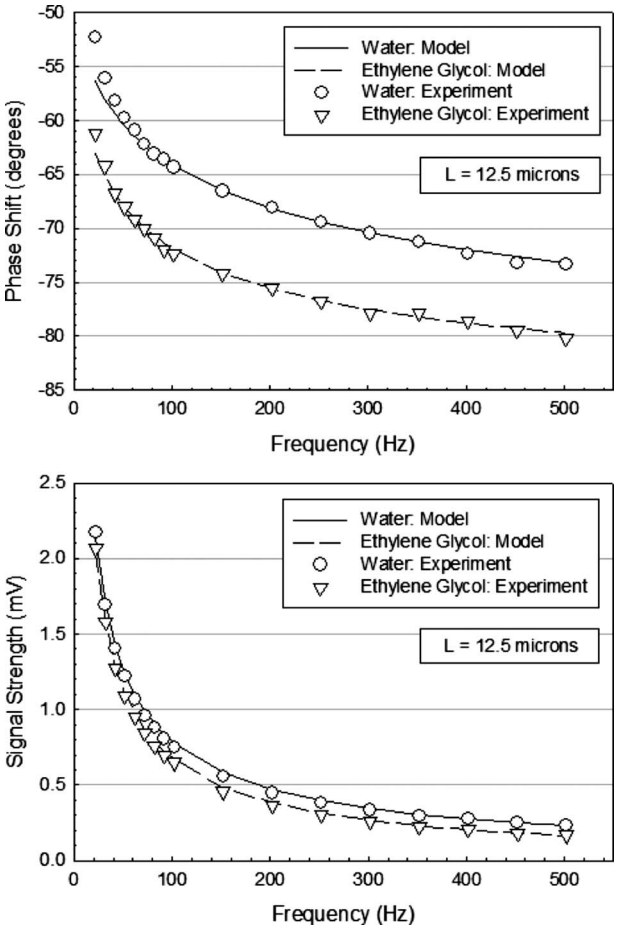

Fig. 2 Normalized amplitude and phase shift—water and ethylene glycol

3 Test Cell Preparation and Experimental Setup

3.1 Test Cell Preparation. The test cell holds the liquid being measured. The cell is constructed by machining an open chamber ($10 \times 6 \times 1.5$ mm^3) into the front surface of a piece of delrin plate ($35 \times 20 \times 10$ mm^3), as shown in Fig. 3. A stainless steel strip (30 mm $\times$ 8 mm $\times$ 12.5 μm) is adhesively bonded onto the delrin surface through use of a transfer tape. This covers the open side of the chamber. This metal strip works as both the heating element and the sealing surface of the test cell. Two small copper bars are soldered on the two ends of the strip to reduce the electrical noise and the contact resistance between this heating strip and the contact pad. Two small stainless steel tubes connect the chamber to the outside supply lines for liquid purging and

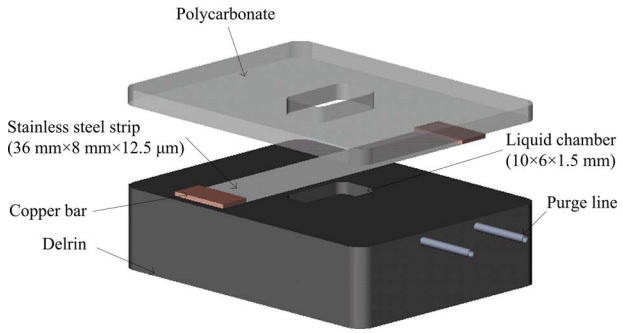

Fig. 3 Test cell design

refill. A polycarbonate plate covers the stainless steel strip for protection. The sample mounting arrangement is the same as that in Ref. [25] except that the specimen is replaced by the test cell.

Figure 4 shows the electric resistance of one of the stainless steel strips used in our experiment. The measured resistance is 0.418 Ω. This low electrical resistance has two effects on our measurement systems. First, a large current up to 2 A is needed to deliver a heating effect high enough to make temperature oscillations detectable, especially at the high end of the frequency range. Second, the low voltage across the heating strip due to the low resistance prohibits the direct sampling of the heating voltage signal as the reference signal to the lock-in amplifier.

3.2 Apparatus. The instrumentation diagram for the experiment is shown in Fig. 5, which can be divided into three sections: electrical heating, temperature sensing, and signal processing sections.

A periodic Joule heating source is generated by a periodic current passing through the stainless steel strip. This periodic current is provided by the MOSFET-based power switch, as shown in Fig. 6. The TTL square waveform from the lock-in amplifier (Stanford research systems Model SR830) is the trigger signal to the MOSFET, while the programmable power supply (Tek Model PS2520G) provides a constant voltage to the power switch. With this design, a very clear voltage square waveform up to 500 Hz can be obtained across the stainless steel strip as viewed by an oscilloscope.

This periodic heating source in the metal strip causes the temperature oscillation on the front surface of the strip, which in turn leads to an oscillating infrared radiation signal. A Zinc Selenide infrared lens (Janos Technology Model A1200-012) focuses this oscillating thermal radiation signal onto an infrared detector

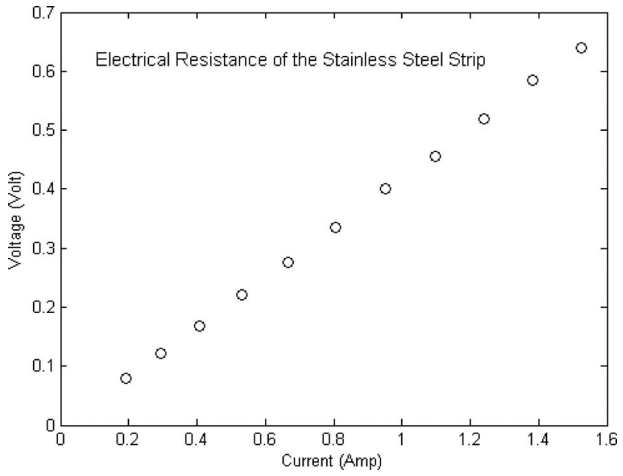

Fig. 4 Resistance of the stainless steel strip

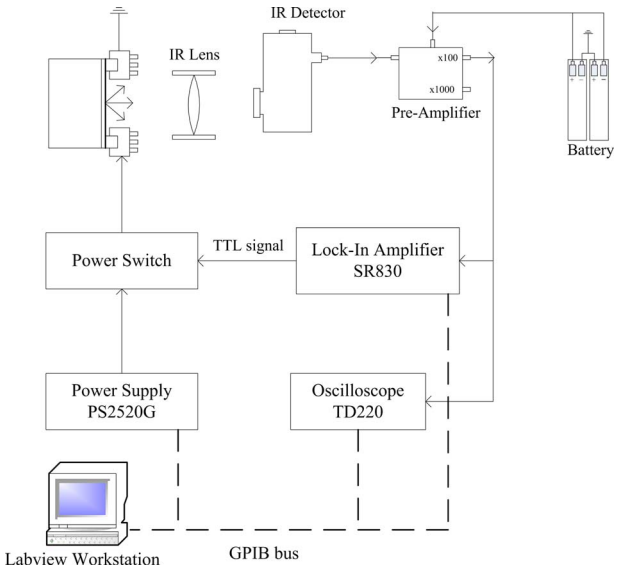

Fig. 5 The schematic of the experimental apparatus

(EG&G Judson Model J15D12-M204-S01M). With a bias current circuit, this Mercury Cadmium Telluride (HgCdTe) photoconductive detector converts the absorbed radiation energy into a voltage signal. Then, a low noise voltage preamplifier (EG&G Judson Model PA-101) increases the signal strength by a factor of 100 or 1000, depending on the gain setting. The resulting voltage signal is supplied to the lock-in amplifier for further signal processing. Note that the preamplifier filters out the dc component so that the lock-in amplifier receives an ac signal only.

The signal processing section includes the lock-in amplifier, an oscilloscope (Tek Model TDS220), and a LABVIEW workstation. The lock-in amplifier and the oscilloscope are connected to the LABVIEW workstation through a GPIB bus for data logging. There are two separate paths to record and process the temperature signals. The first is to use the lock-in amplifier to record the magnitude and phase shift of the temperature signal as input with respect to the TTL trigger signal as reference. The second uses the oscilloscope to record the time-varying waveforms of the temperature signal. The recorded data are then sent to the LABVIEW workstation for further analysis.

3.3 Discussion of the Signal Path. One important issue that needs to be addressed is the signal transducing path. As discussed in the last section, the TTL trigger signal from the lock-in amplifier leads to the heating signal through the power switch. Then the temperature signal in the form of radiation energy caused by the periodic heating source is converted to a low voltage ac signal by the infrared detector. Finally, the pre-amplifier boosts this low voltage ac signal to a voltage level compatible with the lock-in amplifier.

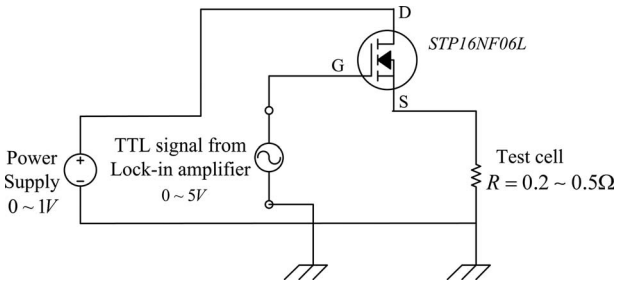

Fig. 6 Diagram of the power switch

However, there are two facts that prevent the direct measurement of the phase difference between the heating signal and the temperature signal using the lock-in amplifier. First is the radiation energy nature of the temperature signal. The temperature signal, in the form of infrared radiation, needs to be converted to an electrical signal, such as a voltage signal, and this electrical signal must be compatible to the lock-in amplifier. The conversion may introduce some additional phase shift into the measurements. Second, the low signal strength and high noise level of the heating signal precludes its direct use as the reference input to the lock-in amplifier.

With the above considerations, the first step of our measurement process is to find the total phase shift of the signal path by designating the TTL trigger as reference and the pre-amplifier output as the signal input to the lock-in amplifier. After this, two compensation phase shifts need to be determined. One is the phase difference between the TTL signal and the heating signal, which is caused by the power switch and can be measured directly. Another one is the phase difference between the pre-amplifier output and the temperature signal, which is induced by the pre-amplifier and can be estimated from the circuit diagram of the pre-amplifier. Therefore, combining the above total phase shift and the two compensation phase differences together, the phase shift between the heating signal and the temperature signal are determined. The phase shift data in the following section are all obtained according to the above procedure.

4 Results and Discussion

The recorded temperature signal is the ac component with an operating frequency varying from 22 Hz to 502 Hz. The maximum amplitude of the temperature oscillation is about 0.2°C at the lower end of the frequency range. According to the steady-state heat conduction analysis of our two-layer structure, the absolute temperature on the stainless steel surface, or the dc component, is about 28°C and 33°C with water and ethylene glycol as the test liquid, respectively.

4.1 Validation of Experimental Apparatus. The experimental apparatus requires validation using liquids with well documented thermal properties. Water and ethylene glycol were chosen for this calibration process. The basic concept behind this two-fluid approach is that experimentally matching the magnitude and phase shift of one fluid through use of Eq. (13), and using experimentally derived parameters for the apparatus, should then allow the prediction of the same experimental data collected for a second fluid.

To demonstrate this approach, the magnitudes of the ac temperature signal for water and ethylene glycol are shown in the bottom graph of Fig. 2. Both the modeling results (lines) and the measurement data (symbols) are given. For the experimental data, the amplitudes at different frequencies are given in terms of signal strength (in millivolts) from the lock-in amplifier. For the modeling results, the amplitudes at different frequencies are matched for one of the fluids through taking into account signal train effects, stainless steel heating strip thickness, and lens positioning. Once these parameters are set using, e.g., water, the same model computations are utilized to generate results for ethylene glycol (with the known thermal properties for the fluid). For this two-fluid calibration methodology, the experimental amplitudes match the model prediction very well as shown in Fig. 2.

The upper graph of Fig. 2 shows the phase shift data for the temperature signal. For both water and ethylene glycol, the model fits the data well except at low frequencies. At these lower frequencies, i.e., below 52 Hz, the large penetration depth causes the phase shift measurements to diverge from the model because the semi-infinite domain assumption of the liquid layer becomes problematic. In these validation tests where model results where matched with experimental phase shift and magnitude data, a stainless steel heating strip thickness of 12.5 μm was used. Several different heating strips were fabricated and used during the course of several months of experimentation development and data collection.

In the model developed for this study, by shifting the magnitude of the thermal conductivity a small amount from the nominal value, the sensitivity of the amplitude and phase shift to the value of thermal conductivity was assessed. This simple analysis approach showed that the phase shift is much more sensitive to the variance of thermal conductivity than the amplitude, especially when taking into account the phase shift measurement capability of the lock-in amplifier. Therefore, the phase shift data were employed for follow-on determinations of the thermal conductivity using nonlinear regression analysis and curve fitting. More details will be discussed in Sec. 4.3.

The procedure for finding the nominal value and the confidence interval of the measured thermal conductivity is as follows. First, frequency values within the range from 52 Hz to 502 Hz was chosen by observation to avoid the outliners (e.g., at 60 Hz and its harmonics) and retain useful signal strength (at the higher end of the frequency range). Second, the standard least-squares method was employed to find the nominal value of thermal conductivity by matching the model to the experimental data using Eq. (13). Third, the standard error of the fit was calculated with the experimental data and the model using the nominal value found in previous step and, then, the 95% confidential interval of the phase shift was obtained. Last, the 95% confidence interval for the thermal conductivity was derived from the phase shift using the least-squares method again.

The nominal values of thermal conductivity for water and ethylene glycol measured here are 0.614 W/m K and 0.253 W/m K. The 95% confidential interval is below $\pm 3\%$ for both the cases. The thermal conductivity of water and ethylene glycol in literatures [27] are 0.613 W/m K and 0.252 W/m K at 30°C.

Another way to look at the present measurement technique is to compare the temperature signal waveform recorded from an oscilloscope to that from a simulation model. Recall that the heating signal is a square wave and can be decomposed into a series of sinusoidal functions according to Fourier series expansion. Because of the linearity of our heat transfer system, each sinusoidal component in the heating signal will generate a temperature oscillation sinusoidal signal at the same frequency. The total temperature response will be the sum of those temperature signal sinusoidal functions with their respective amplitudes and phase shifts.

Figure 7 shows the temperature signal waveforms at 22 Hz, 52 Hz, 102 Hz, and 502 Hz from the experiment and the simulation of the water case. The experimental part is recorded using an oscilloscope and LABVIEW, and the modeled curve is synthesized using the above method. The temperature scale is normalized by the maximum temperature difference found in each case. The two waveforms presented, i.e., the experimental and simulated, share almost the same characteristics. As the frequency increases, little overall shape change is observed in the experimentally recorded waveform, which is consistent with the predictions of the simulated waveform. With increasing frequency, the signal strength falls in the experimentally derived waveform and a significant contribution from noise enters the recorded signal. The presented waveforms also provide an indicator of the degree of signal-to-noise present in this experiment. In some cases, the signal is dominated by noise at the higher frequencies where little signal can be observed from the oscilloscope traces. Even in such situations, the lock-in amplifier is successful in measuring useful amplitude and phase shift data.

4.2 Measurement Results From a Nanofluid. The test nanofluid consisted of an aqueous solution with gold nanoparticles dispersed throughout the liquid. The liquid/particle mixture was generated via the citrate chemical synthesis route [28]. The concentration of gold was 0.058 g/l and the average particle size was 4.5 nm with a standard deviation of 1.5 nm. Before the measure-

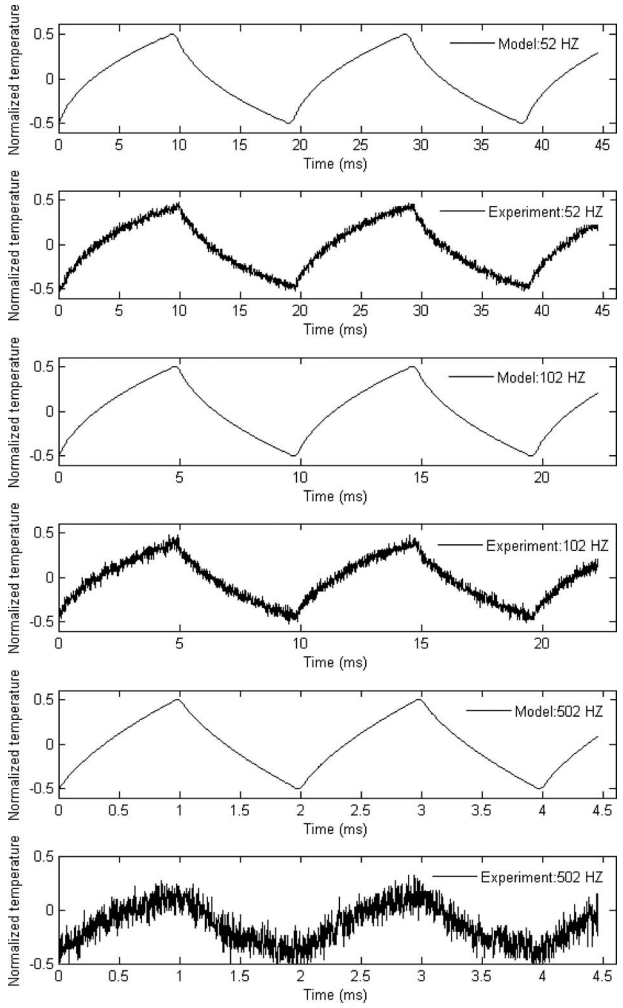

Fig. 7 The waveform of temperature signal

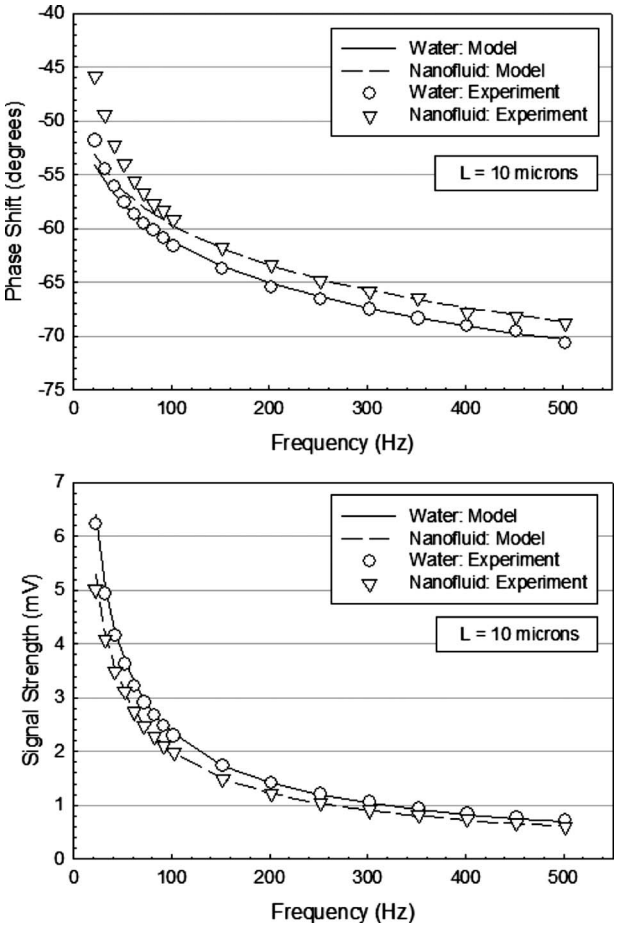

Fig. 8 Normalized amplitude and phase shift—water and nanofluid

ment, the test liquid sample was ultrasonicated for over two hours and a stable and uniform liquid was observed by visual inspection. Since the work presented here focuses on the development of a measurement technique, characterization and preparation of nanofluid will not be covered in this paper.

Before the measurements were performed on the nanofluid, deionized water was used to calibrate the experimental apparatus and provide a reference standard for the nanofluid. After the measurement with water, the test chamber is purged with dry nitrogen and then recharged with nanofluid through the two supply lines. All the other experimental settings were kept the same during this process in order to avoid unaccounted errors introduced into the measurement results.

An implicit assumption so far is that the density and heat capacity of our test liquid are fixed. By observing the temperature expression for the front surface of the heating strip, Eq. (13), we have determined that the thermal conductivity and heat capacity of the test liquid cannot be measured separately by our current apparatus with the frequency range used for this study. Because of the small volume fraction of nanoparticles, the density and heat capacity of the nanofluid are assumed to be the same as that of the base fluid. Murshed et al. [5] conducted a measurement study of the effective thermal diffusivity and thermal conductivity of nanofluids simultaneously using the transient hot-wire technique and suggested that the effective heat capacity of nanofluids shows little variance from the base fluid under small volume fraction conditions. Making this assumption leads to the thermal conductivity of the nanofluid being the only unknown in our model. This permitted a prediction of this quantity using the least-squares curve fitting method from the experimental data [29].

The phase shift data is presented in the upper graph of Fig. 8. Again, the experimental data (symbols) for pure water are modeled well (by the solid line) using the analytical expression for phase shift derived from Eq. (13) and experimental signal train parameters with a stainless steel strip thickness of 10 μm. The fit is quite good although some small deviations appear at low frequencies. For the nanofluid, a good match is found at frequencies higher than approximately 152 Hz. However, for the low frequency regime from 22 Hz to 152 Hz, the derivation between the experimental data and the theoretical model grows when the operating frequency decreases. Although some error was expected due to the large penetration depth at low frequency, the magnitude of this discrepancy is higher than expected. The enhancement in thermal conductivity of the nanofluid using the data between 152 Hz and 502 Hz predicts a 30.4% increase with the above assumptions, i.e., specific heat and density of the nanofluid being assigned the values of the base fluid water. Eastman et al. [11] claimed a 40% enhancement with copper nanoparticles in ethylene glycol while Putnam et al. [8] reported almost no enhancement of gold nanofluids with toluene and ethanol as the base fluids.

The lower graph of Fig. 8 shows the measured signal strength of the front surface temperature for water and the nanofluid in millivolts. Both measurements are consistently well described by the model using the procedures outlined above. This amplitude information is not used for an estimation of the thermal conductivity enhancement, but is presented for the purposes of showing a complete data set from our experimental measurements.

Our strategy in understanding the experimental data is to apply the concept of the effective thermal conductivity to modeling first, and then identify the divergence between the theoretical model and the experimental data. For the phase shift data in Fig. 8, the phase curve fits the model of effective thermal conductivity quite well at the higher frequencies, above 152 Hz. Below this frequency value, the phase shift diverges from the predictions of the model. By applying the same curve fitting method to the low frequency zone, we obtain a higher effective thermal conductivity compared with that in the high frequency range. If this observation has validity, this suggests that the heat transport process in the tested nanofluid is more effective at low operating frequencies than under the high operating frequency in our particular apparatus. These experimental results might imply that a single value of the effective thermal conductivity may not be enough to describe the thermal transport process in a solid/fluid composite system, such as nanofluids.

4.3 Error Analysis. The measurement procedure and the parameters involved provide a guideline of our error analysis. Equation (15) gives the relative parameters in our phase shift measurement and Eq. (16) implies that the thermal conductivity of liquid is found from the measured phase shift using the curve fitting method.

Equation (15) states that the final phase shift used to calculate the thermal conductivity of the test liquid is a function of several parameters: the measured phase of the voltage signal from the pre-amplifier, the phase shift of the power switch, the phase shift of the pre-amplifier, thermal properties of the stainless steel, thermal properties of the liquid, the thickness of the stainless steel, and the operating frequency. A scaling analysis of each of the above parameters was performed to identify the main error sources first. Then, the model was employed to determine how the error propagates from the phase shift data to the resulting value of thermal conductivity [30].

$$\psi = \psi[\psi_m, \psi_{\text{ps}}, \psi_{\text{amp}}, k_s, \rho_s, (c_p)_s, \rho_l, (c_p)_l, L, \omega] \tag{15}$$

$$k_l = k_l(\psi) \tag{16}$$

First, a simple simulation showed that the thermal properties of the stainless steel did not significantly influence the phase shift of the temperature signal at a relative sensitivity level compared with the other model parameters and, hence, they were eliminated from further consideration.

The power switch introduced an additional phase shift into the signal transfer path and needed to be quantified. With the heating signal as the input and the TTL trigger signal as reference, this phase shift was experimentally measured. The standard deviation of the measurement resulted is very low uncertainty from this source of error and was also no longer considered. The pre-amplifier introduced phase shift into the measurement process, as well. The phase shift can be calculated from the electrical circuit diagram for the pre-amplifier. The calculation showed that very small error will enter into the final result and can be neglected too.

The four 1/2 digit resolution of the TTL signal generated by the lock-in amplifier implies the error from the trigger frequency f is insignificant and does not need to be considered in the error analysis. Since the thermal conductivity of the liquid is the desired property, the density, and the heat capacity are assumed constant at this development stage of the technique and no error from these liquid properties values were considered further.

Therefore, the above equations are reduced to

$$\psi = \psi(\psi_m, L) \tag{17}$$

$$k_l = k_l(\psi) = k_l(\psi_m, L) \tag{18}$$

The tolerance of the stainless steel strip provided by the manufacturer is 2% and will be treated as a systematic error. The error of the measured phase shift is the random uncertainty that will propagate into the final result. The 0.01 degree phase resolution of the lock-in amplifier suggests that the systematic error for this component can be ignored compared with that of the random error. Using the root-sum-squares (RSS) method, the uncertainty in the mean value of the thermal conductivity u_k is estimated from

$$u_k = \left[\left(\frac{\partial k}{\partial L} \Delta L \right)^2 + \left(t_{v,95} \frac{\partial k}{\partial \psi} \Delta \psi \right)^2 \right]^{1/2} \tag{19}$$

By assigning different thickness values L to the model, the sensitivity index of the thickness $\partial k / \partial L$ can be determined. Using the same method, we can find the sensitivity index of the phase shift $\partial k / \partial \psi$.

The uncertainty from the measurement of random error is fitted to be 0.0296 W/m K and that from the thickness tolerance of the stainless steel strip is 0.0288 W/m K. Therefore, the total uncertainty of the thermal conductivity measurement is 0.0413 W/m K or approximately 5% of the nominal value.

5 Conclusions

This work describes an experimental technique that can determine the thermal conductivity of liquids from experimental phase shift versus frequency data. The technique requires a reference test liquid, such as water, and was validated using another liquid with well characterized thermal properties. Matching experimental phase shift data to model results for this two-fluid validation and calibration portion of the presented work demonstrated a well characterized experiment. Application of the technique to a gold particle nanofluid with a gold concentration of 0.058 g/l produced interesting but ambiguous results. Even though the technique produced good results through a wide range of frequencies for single component fluids, this was not the case for the nanofluid. For these preliminary results, a high frequency analysis where the temperature oscillation strength is low showed a 30% increase in thermal conductivity compared with the base fluid, water, with a 5% uncertainty range. In a lower frequency range where data from a single component fluid test indicated the technique should still be valid, anomalous phase shift data for nanofluid thermal conductivity resulted. The data could suggest a divergence of thermal transport behavior between nanofluids and pure liquids. For future experimental studies in this area of heat transport processes in nanofluids, the role of the measurement technique requires more attention before unambiguous conclusions can be draw from the measurement data.

Acknowledgment

The authors gratefully acknowledge the support of the Oregon Nanoscience and Microtechnology Institute (ONAMI) and the Army Research Laboratory (ARL) for contributing to the support of this work.

Nomenclature

A = parameter defined in Eq. (6)
B = parameter defined in Eq. (8)
c_p = specific heat, J/kg K
k = thermal conductivity, W/m K
g_0 = volume heating source, W/m^3
G_0 = parameter defined in Eq. (4)
L = thickness of the layer, m
T = temperature, °C
t = time, s
u = uncertainty, %
x = coordinate, m

Greek

α = thermal diffusivity, m^2/s
ρ = density, kg/m^3
ψ = phase, degree
ω = frequency, radian
ξ = parameter defined in Eqs. (5) and (6)

Subscript

- 1 = layer one
- 2 = layer two
- amp = preamplifier
- k = thermal conductivity
- l = liquid
- m = measured
- ps = power switch
- s = solid
- v = degree of freedom

References

[1] Masuda, H., Ebata, A., Teramae, K., and Hishinuma, N., 1993, "Alteration of Thermal Conductivity and Viscosity of Liquid by Dispersing Ultra-Fine Particles," Netsu Bussei, **7**(4), pp. 227–233.

[2] Choi, U. S., 1995, "Enhancing Thermal Conductivity of Fluids With Nanoparticles, Developments and Applications of Non-Newtonian Flows," D. A. Siginer and H. P. Wang, eds., American Society of Mechanical Engineers, New York, FED-Vol. 231/MD-Vol. 66, pp. 99–105.

[3] Lee, S., Choi, S. U. S., Li, S., and Eastman, J. A., 1999, "Measuring Thermal Conductivity of Fluids Containing Oxide Nanoparticles," ASME J. Heat Transfer, **121**, pp. 280–289.

[4] Zhang, X., Gu, H., and Fujii, M., 2006, "Experimental Study on the Effective Thermal Conductivity and Thermal Diffusivity of Nanofluids," Int. J. Thermophys., **27**, pp. 569–580.

[5] Murshed, S. M. S., Leong, K. C., and Yang, C., 2006, "Determination of the Effective Thermal Diffusivity of Nanofluids by the Double Hot-Wire Technique," J. Phys. D, **39**, pp. 5316–5322.

[6] Eapen, J., Williams, W. C., Buongiorno, J., Hu, L., and Yip, S., 2007, "Mean-Field Versus Microconvection Effects in Nanofluids Thermal Conduction," Phys. Rev. Lett., **99**, p. 095901.

[7] Das, S. K., Putra, N., Thiesen, P., and Roetzel, W., 2003, "Temperature Dependence of Thermal Conductivity Enhancement for Nanofluids," ASME J. Heat Transfer, **125**, pp. 567–574.

[8] Putnam, S. A., Cahill, D. G., Braun, P. V., Ge, Z., and Shimmin, R. G., 2006, "Thermal Conductivity of Nanoparticle Suspensions," J. Appl. Phys., **99**, p. 084308.

[9] Wang, Z. L., Tang, D. W., Liu, S., Zheng, X. H., and Araki, N., 2007, "Thermal-Conductivity and Thermal-Diffusivity Measurements of Nanofluids by 3ω Method and Mechanism Analysis of Heat Transport," Int. J. Thermophys., **28**, pp. 1255–1268.

[10] Liu, M., Lin, M., Tsai, C. Y., and Wang, C. C., 2006, "Enhancement of Thermal Conductivity With Cu for Nanofluids Using Chemical Reduction Method," Int. J. Heat Mass Transfer, **49**, pp. 3028–3033.

[11] Eastman, J. A., Choi, S., Li, S., Yu, W., and Thompson, L. J., 2001, "Anomalously Increased Effective Thermal Conductivities of Ethylene Glycol-Based Nanofluids Containing Copper Nanoparticles," Appl. Phys. Lett., **78**, pp. 718–720.

[12] Choi, S. U. S., Zhang, Z. G., Yu, W., Lockwood, F. E., and Grulke, E. A., 2001, "Anomalous Thermal Conductivity Enhancement in Nano-Tube Suspension," Appl. Phys. Lett., **79**, pp. 2252–2254.

[13] Liu, M. S., Lin, M., Huang, I. T., and Wang, C. C., 2006, "Enhancement of Thermal Conductivity With CuO for Nanofluids," Chem. Eng. Technol., **29**, pp. 72–77.

[14] Prasher, R., Bhattacharya, P., and Phelan, P. E., 2005, "Thermal Conductivity of Nanoscale Colloidal Solutions (Nanofluids)," Phys. Rev. Lett., **94**, p. 025901.

[15] Jang, S. P., and Choi, S. U. S., 2004, "Role of Brownian Motion in the Enhanced Thermal Conductivity of Nanofluids," Appl. Phys. Lett., **84**, pp. 4316–4318.

[16] Jang, S. P., and Choi, S. U. S., 2007, "Effects of Various Parameters on Nanofluid Thermal Conductivity," ASME J. Heat Transfer, **129**, pp. 617–623.

[17] Prasher, R., Bhattacharya, P., and Phelan, P. E., 2006, "Brownian-Motion-Based Convective-Conductive Model for the Effective Thermal Conductivity of Nanofluids," ASME J. Heat Transfer, **128**, pp. 588–595.

[18] Keblinski, P., Phillpot, S. R., Choi, S. U. S., and Eastman, J. A., 2002, "Mechanisms of Heat Flow in Suspensions of Nano-Sized Particles (Nanofluids)," Int. J. Heat Mass Transfer, **45**, pp. 855–863.

[19] Xie, H., Fujii, M., and Zhang, X., 2005, "Effect of Interfacial Nanolayer on the Effective Thermal Conductivity of Nanoparticle-Fluid Mixture," Int. J. Heat Mass Transfer, **48**, pp. 2926–2932.

[20] Evans, W., Prasher, R., Fish, J., Meakin, P., Phelan, P., and Keblinski, P., 2008, "Effect of Aggregation and Interfacial Thermal Resistance on Thermal Conductivity of Nanocomposites and Colloidal Nanofluids," Int. J. Heat Mass Transfer, **51**, pp. 1431–1438.

[21] Hong, K. S., Hong, T. K., and Yang, H. S., 2006, "Thermal Conductivity of Fe Nanofluids Depending on the Cluster Size of Nanoparticles," Appl. Phys. Lett., **88**, p. 031901.

[22] Buongiorno, J., 2006, "Convective Transport in Nanofluids," ASME J. Heat Transfer, **128**, pp. 240–250.

[23] Vadasz, P., 2006, "Heat Conduction in Nanofluid Suspensions," ASME J. Heat Transfer, **128**, pp. 465–477.

[24] Maxwell, J. C., 1873, *Electricity and Magnetism*, Clarendon, Oxford, UK.

[25] Czarnetzki, W., and Roetzel, W., 1995, "Temperature Oscillation Techniques for Simultaneous Measurement of Thermal Diffusivity and Conductivity," Int. J. Thermophys., **16**, pp. 413–423.

[26] Bhattacharya, P., Nara, S., Vijayan, P., Tang, T., Lai, W., Phelan, P. E., Prasher, R. S., Song, D. W., and Wang, J., 2006, "Characterization of the Temperature Oscillation Technique to Measure the Thermal Conductivity of Fluids," Int. J. Heat Mass Transfer, **49**, pp. 2950–2956.

[27] Incropera, F. P., Dewitt, D. P., and Bergman, T. L., 2006, *Fundamental of Heat and Mass Transfer*, 6th ed., Wiley, New York.

[28] Jackson, J. E., Borgmeyer, B. V., Wilson, C. A., Cheng, P., and Bryan, J. E., 2006, "Characteristics of Nucleate Boiling With Gold Nanoparticles in Water," *Proceedings of IMECE2006*, *ASME International Mechanical Engineering Congress and Exposition*, Chicago, IL, Nov. 5–10.

[29] Indermuehle, S. W., and Peterson, R. B., 1999, "A Phase-Sensitive Technique for the Thermal Characterization of Dielectric Thin Films," ASME J. Heat Transfer, **121**, pp. 528–536.

[30] Myers, G. E., 1998, *Analytical Methods in Conduction Heat Transfer*, 2nd ed., AMCHT, Madison, WI.

Temperature Measurements of Diesel Fuel Combustion With Multicolor Pyrometry

Tairan Fu[1]
Department of Thermal Engineering,
Key Laboratory for Thermal Science and Power Engineering of Ministry of Education,
Tsinghua University,
Beijing 100084, P. R. China
e-mail: trfu@mail.tsinghua.edu.cn

Zhe Wang
Department of Thermal Engineering,
State Key Laboratory of Power Systems,
Tsinghua University,
Beijing 100084, P. R. China

Xiaofang Cheng
Department of Thermal Science and Energy Engineering,
University of Science and Technology of China,
Hefei 230026, P. R. China

Optical diagnostics techniques to measure diesel combustion flame temperatures are useful for evaluation and control of combustion processes. In this paper, diesel combustion flame temperatures are measured based on a multicolor pyrometry method respectively adopting an optical fiber spectrometer and a color charge coupled device (CCD). The intensity ratios for various wavelengths/wavebands are utilized as the analytical variables to deduce the temperatures to avoid the need to calibrate each system for the specific geometry conditions. The measured multicolor data can determine the temperature T and the soot factor KL. Extra data collected at many wavelengths is used to reduce the noise and random fluctuations in the measurements. To improve the solving precision, a data-processing method based on the least-squares technique is proposed to fit the data for approximate solutions. Verification experiments using the multicolor pyrometry were conducted in a 54–120 kW test furnace with diesel fuel. Data for 16 wavelengths detected by a fiber optic spectrometer from a diesel flame is analyzed to determine how to choose a suitable combination of three wavelengths for three-color pyrometry. The CCD-based three-color measurements, which would be much more practical in field measurements, are compared with the spectrometer-based results. [DOI: 10.1115/1.4000467]

Keywords: temperature, pyrometry, optical diagnostics, diesel combustion flame

1 Introduction

Detailed temperature and soot distributions of diesel flames in integrated circuit (IC) engines are needed to understand the basic physics underlying the flame evolution and emission formation during the combustion processes. The combustion efficiency can be evaluated from temperature measurements. Optical diagnostics techniques for measuring combustion flame temperatures have rapidly developed [1–7], with two-color pyrometry being a well-known optical radiation pyrometry technique used to measure diesel flame-temperature and soot distributions. This technique utilizes the thermal radiation intensity emitted by the soot particles in the flame at two different wavelengths to calculate the flame temperature and the soot factor, which is the product of the equivalent soot concentration and the optical path. Diesel fuel combustion has soot particles and gaseous products. The soot incandescence dominates the flame radiation emissions during most of the heat release period. The temperatures of the soot particles and the surrounding gas differ. This difference is negligible when the soot particles and gas products are in thermal equilibrium, so the measured temperatures of the soot particles based on two-color pyrometry is an appropriate estimate of the flame temperature [3,8].

Zhao and Ladommatos [3] reviewed the research on the two-color method for optical diagnostics of in-cylinder soot and combustion temperatures in diesel engines, focusing on the selection of wavelengths, calibration, data acquisition, effects of soot deposition on the window, effects of nonuniform temperatures and soot, and temperature and soot imaging. Li and Wallace [9] used three optical fiber probes installed in the cylinder head to measure soot temperatures and concentrations in a diesel engine at three points in the combustion chamber. Vattulainen et al. [5] described a system for quantitative imaging diagnostics and its application to in-cylinder flame-temperature measurements in large diesel engines. Tian et al. [10] investigated the combustion process of ethanol injected into the intake port and ignited with the diesel fuel with the two-color method, and discussed combining data for two wavelengths. However, with two-color pyrometry, the system needs to be calibrated beforehand to determine the apparent temperature at the chosen wavelength to establish a relationship between the apparent temperatures and the corresponding sensor outputs using the same geometry for the system and the measured object [3,8]. Obviously, the calibration is only applicable for the same geometry. The literature on two-color pyrometry has mainly used two-wavelength measurements, with many discussions on the choice of wavelengths. The analyses have shown that both visible and infrared wavelengths may be used in two-color systems, but the visible wavelengths are preferred [3,8].

This paper presents a multicolor pyrometry system respectively based on a fiber optic spectrometer and a color charge coupled device (CCD), which does not require geometry calibrations, as an extension of the two-color pyrometer. The radiation intensity ratio (the relative intensity) of different wavelengths/wavebands is utilized to calculate the solutions, eliminating the need to calibrate beforehand for the geometry. At least three wavelengths are required for the temperature and soot calculations. The multiwavelength measurements use an improved data-processing method based on the nonlinear least-squares technique for the solutions. These results are used to identify the best combination of three wavelengths to provide the necessary reference information for a three-color pyrometer for optical diagnostics in an IC engine. Finally, the result differences between the multicolor system based on a fiber optic spectrometer and the pyrometer based on a color CCD for measuring diesel flame-temperature and soot distributions are analyzed.

2 Principle of Multicolor Pyrometry

2.1 Two-Color Pyrometry. Multicolor pyrometry is based on the relationship between the temperature and the emitted thermal

[1]Corresponding author.

Contributed by the Heat Transfer Division of ASME for publication in the JOURNAL OF HEAT TRANSFER. Manuscript received May 20, 2009; final manuscript received August 27, 2009; published online March 9, 2010. Assoc. Editor: H.-P. Tan.

radiation intensity. The spectral intensity of a blackbody is a function of the wavelength and temperature alone as described by Planck's law

$$I_{b,\lambda}(T) = \frac{C_1}{\pi \cdot \lambda^5[\exp(C_2/\lambda T) - 1]} \tag{1}$$

where C_1 and C_2 are the first and second Planck law constants, $C_1 = 1.1910439 \times 10^{-16}$ W m^2 sr^{-1} and $C_2 = 1.4388 \times 10^{-2}$ m K. For values of λT less than 3000 μm K, $I_{b,\lambda}(T)$ may be described using Wien's radiation law with an accuracy of around 1% [11]

$$I_{b,\lambda}(T) = 1/\pi \cdot C_1 \lambda^{-5} \cdot \exp(-C_2/\lambda T) \tag{2}$$

The spectral emissivity ε_λ is defined as the ratio of the actual intensity I_λ emitted by an actual body at a given wavelength to the black body intensity

$$I_\lambda = \varepsilon_\lambda I_{b,\lambda}(T) \tag{3}$$

For soot particles in a diesel flame, ε_λ is estimated by the widely used empirical correlation [3]

$$\varepsilon_\lambda = 1 - \exp(-KL/\lambda^\alpha) \tag{4}$$

where K (m^{-1}) is the absorption coefficient proportional to the number density of the soot particles, L (m) is the geometric thickness of the flame along the optical axis of the imaging system (length of the optical path) and α is an empirical parameter depending on the physical and optical properties of the soot in the flame. In the visible spectrum, α has a fixed value of 1.39 for diesel flames [3].

The measured intensity signal at the wavelength λ_i obtained by a multicolor pyrometry system is given by

$$V_i = \Phi \cdot I_{\lambda_i} = \Phi \cdot (1 - \exp(-KL/\lambda_i^\alpha)) I_{b,\lambda_i}(T) \tag{5}$$

where V_i is the output value (for an 8 bit sensor, the value range is from 0 to 255); Φ $(1/(\text{W m}^{-2}\,\text{sr}^{-1}))$ is an instrument constant obtained by calibration, which is a function of various factors in the system including the radiation attenuation, observation distance, observation angle, lens properties, and analog-to-digital signal conversion.

In a traditional two-color system, the effect of the unknown instrument constant Φ is usually eliminated by calibrating with a blackbody or a standard tungsten lamp to determine the relationship between the intensity I_{λ_i} and the sensor output V_i [3,8]. The calibrated I_{λ_i} may also be expressed in terms of the apparent temperature $T_{a,i}$, which is defined as the temperature of a blackbody that emits the same radiation intensity as the nonblackbody at temperature T, which is $I_{\lambda_i}(T) = I_{b,\lambda}(T_{a,i})$. Combining Eqs. (2)–(5) gives

$$KL = -\lambda_i^\alpha \ln\left(1 - \frac{\exp(-C_2/\lambda_i T)}{\exp(-C_2/\lambda_i T_{a,i})}\right) \tag{6}$$

The unknown product KL can be eliminated by equating Eq. (6) for two specific wavelengths λ_1 and λ_2

$$\lambda_1^\alpha \ln\left(1 - \frac{\exp(-C_2/\lambda_1 T)}{\exp(-C_2/\lambda_1 T_{a,1})}\right) = \lambda_2^\alpha \ln\left(1 - \frac{\exp(-C_2/\lambda_2 T)}{\exp(-C_2/\lambda_2 T_{a,2})}\right) \tag{7}$$

An iterative solution of Eqs. (6) and (7) will give the temperature T and the soot factor KL. However, the calculations require that the geometric conditions for the instrument constant Φ remain the same for the calibration experiments and the actual measurements. In two-color systems, the choice of the two wavelengths is also a key issue. Generally, the visible wavelengths are preferred due to the higher sensitivity and signal to noise (S/N) ratio in the visible range than in the infrared range. In addition, the chosen wavelengths should be far from the radiation or absorption bands of the gas molecules and free radicals in the reaction zone of the flame such as OH, CH, C_2, HCO, NH, NH_2, CO_2, CO, water vapor, and fuel vapor, which may give appreciable emissions in the visible and near-ultraviolet regions. Thus, the wavelengths most often used by researchers with two-color pyrometry are: 549 nm, 750 nm; 529 nm, 624 nm; 550 nm, 700 nm; 460 nm, 640 nm; 550 nm, 650 nm; 450 nm, 640 nm; 581 nm, 631 nm; 540 nm, 643 nm; and 470 nm, 650 nm.

2.2 Multicolor Pyrometry

2.2.1 Principle. The calibration needed to relate V_i and I_{λ_i} in Eq. (5) can be eliminated by a noncalibration mode that utilizes the radiation intensity ratio of two wavelengths λ_i and λ_j as a relative intensity $M_{i,j} = V_i/V_j$

$$M_{i,j} = \frac{V_i}{V_j} = \frac{[1 - \exp(-KL/\lambda_i^\alpha)] \cdot \lambda_i^{-5} \exp(-C_2/\lambda_i T)}{[1 - \exp(-KL/\lambda_j^\alpha)] \cdot \lambda_j^{-5} \exp(-C_2/\lambda_j T)} \tag{8}$$

Thus, $M_{i,j}$ is the function of the temperature T and the soot factor KL. The derivative of $M_{i,j}$ is

$$dM_{i,j} = \frac{\partial M_{i,j}}{\partial T} \cdot dT + \frac{\partial M_{i,j}}{\partial (KL)} \cdot d(KL) \quad \text{or} \quad \Delta M_{i,j} = \frac{\partial M_{i,j}}{\partial T} \cdot \Delta T + \frac{\partial M_{i,j}}{\partial (KL)} \cdot \Delta (KL) \tag{9}$$

where the variables $\partial M_{i,j}/\partial(KL)$ and $\partial M_{i,j}/\partial T$ are

$$\frac{\partial M_{i,j}}{\partial (KL)} = \frac{\partial (V_i/V_j)}{\partial (KL)} = \left(\frac{\lambda_i^{-\alpha} \exp(-KL/\lambda_i^\alpha)}{(1 - \exp(-KL/\lambda_j^\alpha))} - \frac{\lambda_j^{-\alpha} \exp(-KL/\lambda_j^\alpha) \cdot (1 - \exp(-KL/\lambda_i^\alpha))}{(1 - \exp(-KL/\lambda_j^\alpha))^2} \right) \cdot \lambda_i^{-5}/\lambda_j^{-5} \cdot \exp(C_2/T \cdot (1/\lambda_j - 1/\lambda_i)) \tag{10}$$

$$\frac{\partial M_{i,j}}{\partial T} = \frac{\partial (V_i/V_j)}{\partial T} = \frac{1 - \exp(-KL/\lambda_i^\alpha)}{1 - \exp(-KL/\lambda_j^\alpha)} \cdot \frac{\lambda_i^{-5}}{\lambda_j^{-5}} \cdot \exp(C_2/T \cdot (1/\lambda_j - 1/\lambda_i)) \cdot \frac{C_2}{T^2} \cdot \left(\frac{1}{\lambda_i} - \frac{1}{\lambda_j}\right)$$

Equation (9) shows the sensitivity of the radiation intensity ratio to the temperature and the soot factor. If a small change in $\Delta M_{i,j}$ brings about a great change of $[\Delta T/T, \Delta(KL)/(KL)]$ when solving for (T, KL), then the solution (T, KL) is very sensitive to $M_{i,j}$. The issues about the sensitivity were analyzed in detail by Fu et al. [12].

Multicolor pyrometry requires that radiation intensity measurements be made at many wavelength combinations, the number of which is not less than the degrees of freedom in Eq. (8). Thus, at least two combinations are needed, that is, three different wavelengths. Consider an example of a three-color pyrometry with the typical wavelengths $(\lambda_1, \lambda_2, \lambda_3)$ as 500 nm, 600 nm, and 700 nm, respectively, each with a bandwidth of 20 nm. The investigated temperature range is 1500–2500 K, and the KL range is 0.2–2.0. The complex relationship between the intensity ratios $M_{1,2}$ and $M_{1,3}$ and the variables T and KL can be uniquely determined by numerical simulations, as shown in Fig. 1, where the abscissa represents the intensity ratio $M_{1,2} = V_1/V_2$ and the ordinate represents the intensity ratio $M_{1,3} = V_1/V_3$. This distribution can be recorded in a database relating $(M_{1,2}, M_{1,3})$ and (T, KL) for convenient use in the measurement calculations.

Measured multicolor data for a larger number of wavelengths will also give the solutions for the temperature T and the soot factor KL. Generally, with multiple intensity ratios, the least-squares technique is used to fit the data for the solutions. The extra data should reduce the noise and the effects of random fluctuations in the measurements.

2.2.2 Nonlinear Least-Squares Method. Since the emissivity in Eq. (4) is not a linear exponential function of the wavelength,

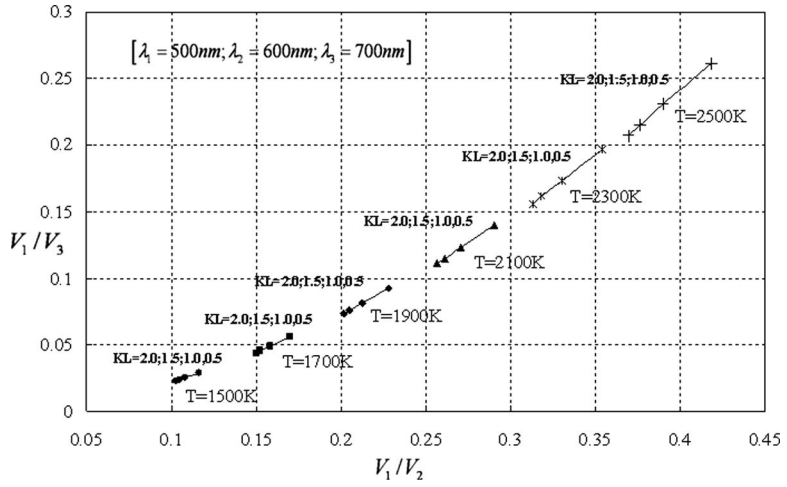

Fig. 1 Distribution of (T, KL) in the measurement coordinates $(M_{1,2}, M_{1,3})$

the nonlinear least-squares method is used to analyze the data [13]. Assume N combinations of wavelengths, and then the error function α is defined as

$$\alpha(T,KL) = \sum_{(i,j)}^{N} (M_{i,j}(T,KL) - f_{i,j})^2 \tag{11}$$

where $f_{i,j}$ is the measured intensity ratio for wavelengths λ_i and λ_j. Minimizing the error function α gives the solutions T^* and KL^*. The least-squares principle gives

$$\frac{\partial \alpha}{\partial T} = 0, \quad \frac{\partial \alpha}{\partial (KL)} = 0 \tag{12}$$

We expand $M_{i,j}$ in a Taylor series around the initial data (T_0, KL_0) and define the vector $\Delta \boldsymbol{z} = (T^* - T_0, KL^* - KL_0)$. An iterative solution of Eq. (12) reduces $\Delta \boldsymbol{z}$ until $\Delta \boldsymbol{z}$ is negligible to obtain the approximate solutions T^* and KL^*.

2.2.3 Improved Data-Processing Method. The magnitude $\partial M_{i,j}/\partial T$ of the intensity ratio sensitivity to the temperature is greatly different from the magnitude $\partial M_{i,j}/\partial (KL)$ of the sensitivity to the soot factor. This usually results in large measurement uncertainties when iteratively solving for (T^*, KL^*) using the least-squares in Eq. (11). Therefore, to account for the relative changes of T and KL arising from the deviation value $(M_{i,j} - f_{i,j})$, Eq. (11) should be rewritten as

$$\beta(T,KL) = \sum_{(i,j)}^{N} \left[\left((M_{i,j} - f_{i,j}) \cdot \frac{\partial T}{\partial M_{i,j}} \cdot \frac{1}{T} \right)^2 + \left((M_{i,j} - f_{i,j}) \cdot \frac{\partial (KL)}{\partial M_{i,j}} \cdot \frac{1}{KL} \right)^2 \right] \tag{13}$$

The solutions are then obtained by minimizing $\beta(T, KL)$. Approximate solutions for (T^*, KL^*) can be found by calculating β at every temperature T and soot factor KL within the specified range $[T \in (1500\ \text{K}, 2500\ \text{K}),\ KL \in (0.2, 2.0)]$ appropriate for diesel flames for most working conditions to find the minimum. This modified calculation method will be used in the following analyses. Due to involving iterations in the process, the time taken for a solution may be longer, especially for the case with more combinations N. It may cause difficulties for real-time measurement. Therefore, for the following experiment applications, we will give some discussions.

3 Experiments and Discussions

The diesel fuel combustion temperatures and soot factors were measured using the multicolor pyrometry respectively based on a fiber optic spectrometer and a color CCD.

3.1 Temperature Measurements Based on a Fiber Optic Spectrometer. An AvaSpec-2048 fiber optic spectrometer with a spectral range (200–1100 nm) and a spectral resolution (0.6 nm) was used for the multiwavelength measurements. The spectral response of the spectrometer was calibrated using a standard source. The effectiveness of the multicolor pyrometry with the fiber optic spectrometer was evaluated in experiments conducted in a 54–120 kW test furnace with diesel fuel, as shown in Fig. 2. After starting up the RIELLO 40 G10 burner of the furnace and working at standard conditions, the spectrometer was aimed at the No. 3 optical window of the furnace. After 10 min of steady working conditions and normal combustion, the spectral radiation intensities at 16 wavelengths from 500 nm to 690 nm were simultaneously recorded at wavelength intervals of 10 nm or 20 nm, with the results shown in Fig. 3. The measured intensity curve was smooth without obvious absorption valleys or emission crests. This choice of wavelengths avoids the effects of the radiation or absorption bands of the gas molecules and free radicals in the flame reaction zone. This data gives 120 combinations of dual-wavelength rela-

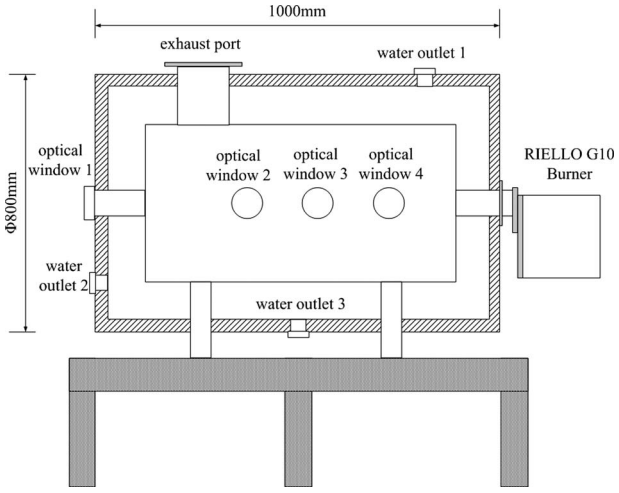

Fig. 2 Diesel fuel test furnace

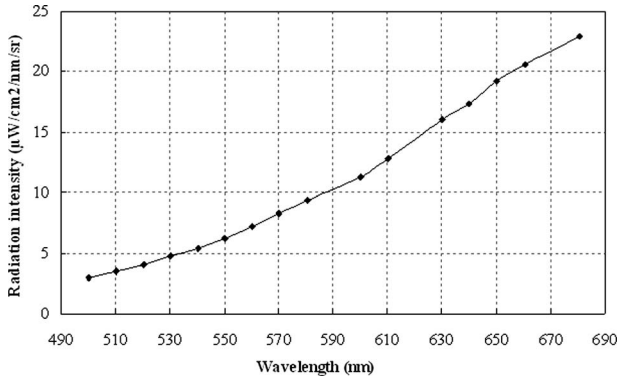

Fig. 3 Spectral radiation intensities at 16 wavelengths

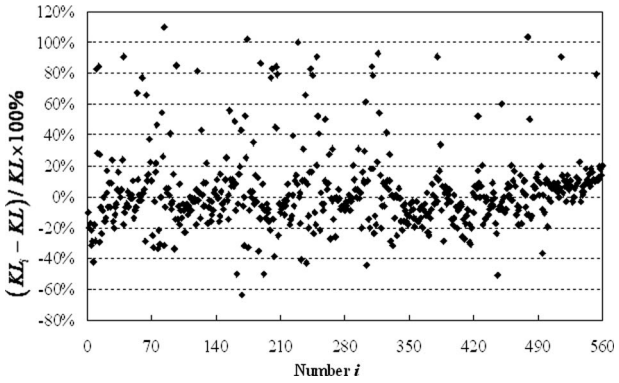

Fig. 5 Relative soot factor errors

tive intensity ratios $M_{i,j}$. The solutions ($T=2020$ K, $KL=0.88$) were then obtained by searching the entire range [$T \in (1500\ \text{K}, 2500\ \text{K})$, $KL \in (0.2, 2.0)$] based on Eqs. (8) and (13). This temperature result using the multicolor inverse method agrees with the standard value.

Although the 16-wavelength measurements will be more accurate, this method is not suitable for the online analyses of dynamic diesel flames with high-frequency fluctuations due to the long data-processing time needed to solve a minimum of Eqs. (11)–(13). Therefore, as with the three-color pyrometer, three wavelengths can be used to calculate the solutions, which greatly improves the computing time. There are 560 combinations of three wavelengths for $\lambda_1<\lambda_2<\lambda_3$ within 16 different wavelengths. Each of the three-wavelength groups can be used to form two intensity ratios ($M_{1,2}, M_{1,3}$), which satisfy the mathematical requirements to uniquely determine the solutions (T, KL). With ideal measurements, the solutions obtained from the three-wavelength pyrometry are the same as the solutions from the 16-wavelength pyrometry. However, there are measurement uncertainties from many sources, including the sensor, the emissivity model, and environmental noise. Thus, the 16-wavelength pyrometry should be more accurate than the three-wavelength pyrometry, since the improved least-squares technique reduces the measurement uncertainties to some extent. Therefore, for the three-wavelength pyrometry, three wavelengths should be carefully chosen to achieve the optimum results. The 16-wavelength data provide an important experimental reference. The solutions T_i and KL_i for each three-wavelength combination i of the 560 combinations were calculated and compared with ($T=2020$ K, $KL=0.88$) from the 16-wavelength measurements as the true solutions. The distribution of the relative temperature error $(T_i-T)/T$ for the 560 combinations is shown in Fig. 4. The range of the relative temperature errors was −10–13%. The relative soot factor error $(KL_i-KL)/KL$ for the 560 combinations shown in Fig. 5 has a much wider range of −62–115%, which again indicates that the soot factor KL is more sensitive to measurement uncertainties than the temperature T.

The conditions for the choice of the best three wavelengths were then restricted to

$$|(T_i-T)/T|<1\%, \quad |(KL_i-KL)/KL|<3\%, \quad \lambda_2-\lambda_1 \geq 20\ \text{nm}, \quad \lambda_3-\lambda_2 \geq 20\ \text{nm} \tag{14}$$

The results in Figs. 4 and 5 give the 36 combinations ($\lambda_1, \lambda_2, \lambda_3$) shown in Fig. 6, which is about 6.4% of the entire 560 combinations. The ordinate in Fig. 6 represents the combination number. Each "circle" represents the wavelength in the combination i. Actual three-wavelength pyrometry measurements based on these intensity ratios can use any of the suitable three-wavelength combinations given here.

3.2 Temperature Measurements Based on a Color CCD. Optical pyrometers are now being produced with a CCD sensor for temperature measurements through optical visualizations [5–8,14–16]. A CCD is a light-sensitive integrated circuit that stores and displays the data for an image by converting each pixel of the image. CCD sensors can conveniently enable temperature field measurements that overcome the shortcomings of traditional spot pyrometers that only detect a few points. Existing CCD-based pyrometer systems use various means to separate the measurement wavelengths/wavebands with a single CCD or multiple CCDs. In single CCD systems, images for different colors are sequentially formed on the same monochrome sensor array

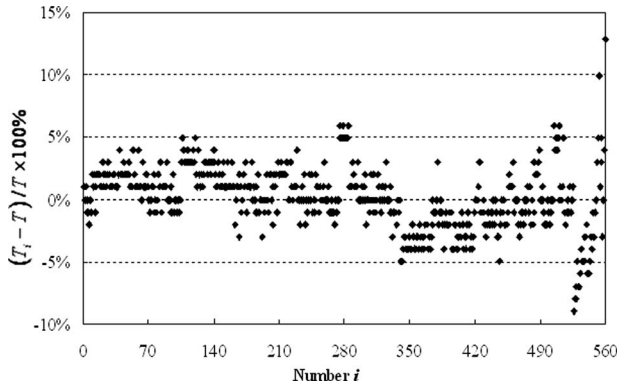

Fig. 4 Relative temperature errors

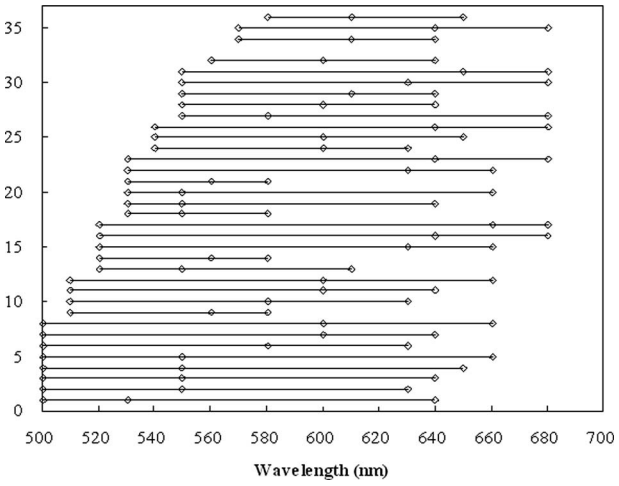

Fig. 6 Three-wavelength combinations

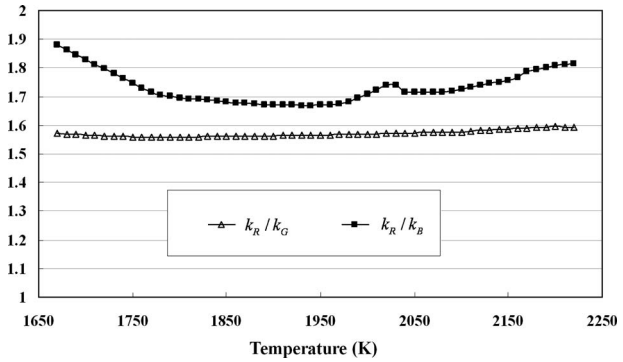

Fig. 7 Ratios of calibration coefficients at different temperatures

through a beam splitting/filtering assembly with narrow-band interference filters [8,14,17] or are simultaneously recorded on a color CCD sensor array with a R-G-B waveband mosaic pixel filter [18,19], with the flame-temperature and soot distributions then calculated.

This research used an established R-G-B waveband measurement system based on a color CCD with an ICX285AL chip (progressive scanning, 1,450,000 pixels, 1392 (H) $\times$ 1036 (V), cell size 6.45×6.45 μm^2, 12 bit data depth, S/N ratio >56 dB, and 20 frames per second at the maximum resolution) for the temperature field measurements of a diesel flame. This pyrometer system has been evaluated [20] through an integrating sphere and a high-temperature blackbody source. The equation relating the spectral radiation intensity to the pixel output for the frame image of a diesel flame is

$$V_R = \Phi \cdot \int_{380\ \mathrm{nm}}^{780\ \mathrm{nm}} F_R(\lambda) \cdot \varepsilon_\lambda \cdot I_{b,\lambda}(T) d\lambda$$

$$V_G = \Phi \cdot \int_{380\ \mathrm{nm}}^{780\ \mathrm{nm}} F_G(\lambda) \cdot \varepsilon_\lambda \cdot I_{b,\lambda}(T) d\lambda \tag{15}$$

$$V_B = \Phi \cdot \int_{380\ \mathrm{nm}}^{780\ \mathrm{nm}} F_B(\lambda) \cdot \varepsilon_\lambda \cdot I_{b,\lambda}(T) d\lambda$$

where (V_R, V_G, V_B) are the pixel values calibrated by the instrument parameters used as the three-waveband measurement outputs of the system and $[F_R(\lambda), F_G(\lambda), F_B(\lambda)]$ are the spectral response functions of the CCD-based pyrometer. The radiation intensity ratios are defined as

$$M_{R,G} = V_R/V_G, \quad M_{R,B} = V_R/V_B \tag{16}$$

The R-G-B waveband measurements described by Eq. (15) may be approximatively treated as three representative wavelength measurements of $(\lambda_R, \lambda_G, \lambda_B) = (475\ \mathrm{nm}, 535\ \mathrm{nm}, 590\ \mathrm{nm})$ for this CCD system. However, the representative wavelengths may be differently adopted for different CCD systems [19,21]. Thus, the intensity ratios for a blackbody $\varepsilon_\lambda = 1$ are rewritten as

$$V_{R,b}/V_{G,b} = \frac{\int_{380\ \mathrm{nm}}^{780\ \mathrm{nm}} F_R(\lambda) \cdot I_{b,\lambda}(T) d\lambda}{\int_{380\ \mathrm{nm}}^{780\ \mathrm{nm}} F_G(\lambda) \cdot I_{b,\lambda}(T) d\lambda} = \frac{k_R \cdot I_{b,\lambda_R}(T)}{k_G \cdot I_{b,\lambda_G}(T)}$$

$$V_{R,b}/V_{B,b} = \frac{\int_{380\ \mathrm{nm}}^{780\ \mathrm{nm}} F_R(\lambda) \cdot I_{b,\lambda}(T) d\lambda}{\int_{380\ \mathrm{nm}}^{780\ \mathrm{nm}} F_B(\lambda) \cdot I_{b,\lambda}(T) d\lambda} = \frac{k_R \cdot I_{b,\lambda_R}(T)}{k_B \cdot I_{b,\lambda_B}(T)} \tag{17}$$

where (k_R, k_G, k_B) are the calibration coefficients for the simplification processing, and the coefficient ratios are obtained through a blackbody source at various temperatures, as shown in Fig. 7. The coefficient ratios slightly change with the temperature.

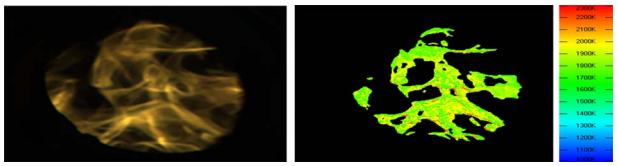

Fig. 8 Original diesel flame image and calculated temperature distributions (from left to right) for an exposure time of 100 μs

Since the wavelength bandwidths of $[F_R(\lambda), F_G(\lambda), F_B(\lambda)]$ are not very wide and less than 200 nm, Eq. (16) may be approximately expressed as follows with $(\lambda_R, \lambda_G, \lambda_B)$:

$$M_{R,G} = \frac{V_R}{V_G} = \frac{\varepsilon_{\lambda_R} \cdot k_R \cdot I_{b,\lambda_R}(T)}{\varepsilon_{\lambda_G} \cdot k_G \cdot I_{b,\lambda_G}(T)}, \quad M_{R,B} = \frac{V_R}{V_B} = \frac{\varepsilon_{\lambda_R} \cdot k_R \cdot I_{b,\lambda_R}(T)}{\varepsilon_{\lambda_B} \cdot k_B \cdot I_{b,\lambda_B}(T)} \tag{18}$$

Equations (18) and (13) can be obtained to calculate the temperature. In actual measurements using the CCD-based system, (V_R, V_G, V_B) are the quantification values. For an 8 bit output, this value range is from 0 to 255. Therefore, we can, beforehand, iteratively calculate the temperature T based on Eqs. (13) and (18) for every combination (V_R, V_G, V_B) within the range from 0 to 255. In addition, the relationship results between (V_R, V_G, V_B) or $(M_{R,G}, M_{R,B})$ and T are recorded in the database format. In applications, we could conveniently obtain the temperature T through searching the database, which avoids the iteration processing and greatly reduces the calculation time. It could well satisfy the requirement of real-time measurements.

The CCD-based system was properly positioned and the iris aperture was adjusted for the same diesel combustion flame testing environments as in Sec. 3.1. The alignment guaranteed that the system optic axial was perpendicular to the plane of the No. 3 optical window of the furnace with the exit radiation in the field of view. The diesel flame images were recorded with the appropriate instrument parameters with an example of the diesel flame-temperature field shown in Fig. 8. The calculation steps are the same as the above descriptions, by, beforehand, establishing the relationship database between (V_R, V_G, V_B) and T.

The average temperature $\overline{T}$ of the diesel flame in Fig. 8 is 1882 K based on

$$\overline{T(p,q)} = \frac{1}{N \times M} \cdot \sum_{p,q=1}^{N,M} T(p,q) \tag{19}$$

where $N \times M$ is the effective pixel number of a frame image, and (p,q) are the coordinates of each pixel in the image. The degree of temperature nonuniformity in the flame image may be described as

$$\frac{1}{\overline{T(p,q)}} \left[\frac{1}{N \times M} \cdot \sum_{p,q=1}^{N,M} (T(p,q) - \overline{T(p,q)})^2 \right]^{0.5} \tag{20}$$

The nonuniformity of the diesel flame image in Fig. 8 is 5.51%, which means that the average range of temperature distribution is 1882 K $\pm$ 104 K.

A comparison of the fiber optic spectrometer and the color CCD pyrometer system show the following.

(i) The multicolor pyrometer based on a fiber optic spectrometer can only realize single point measurements. The temperature solution $T_{\mathrm{FOS}} = 2020$ K of the measured point is acceptable, but it is inconvenient for measuring two-dimensional temperature distributions.

(ii) The three-color pyrometer system based on the color CCD provides full two-dimensional measurements and is, thus, much more convenient. The measured average temperature $T_{CCD}=1882$ K is less than the point result $T_{FOS}=2020$ K for several reasons:

(a) The R-G-B waveband measurements described in Eq. (15) are simplified to three representative wavelength measurements $(\lambda_R,\lambda_G,\lambda_B)=(475\ \text{nm},535\ \text{nm},590\ \text{nm})$ by the calibration coefficients, which causes some error for diesel flame measurements even though the conversion relationship is obtained from a calibration with a blackbody. However, since the determination relationship of the representative wavelengths and the calibration coefficients depends on the temperature, the waveband, and the emissivity function, the relationship calibrated with blackbody measurements are not always accurate for actual measurements with a specified emissivity. It is addressed that the maximum temperature error based on this simplification may be up to 6% in a specified example [22]. Therefore, we think that this simplification may be the major error source, which will be further evaluated in future work. However, such a process of three-wavelength measurements could bring a merit that avoids the calculation's complexity of the coupling between the waveband measurements and the emissivity function. In addition, the results based on this simplification are still acceptable and the relative difference is about 6.83% comparing with the result $T_{FOS}=2020$ K based on multicolor methods using a fiber optic spectrometer.

(b) The choice of the three wavelengths affects the solution precision due to the measurement uncertainties, as shown in Sec. 3.1. Even though the effective wavelengths $(\lambda_R,\lambda_G,\lambda_B)=(475\ \text{nm},535\ \text{nm},590\ \text{nm})$ used for the color CCD pyrometer system are accurate, those are not optimum combinations to minimize the temperature measurement uncertainties.

(iii) The solution accuracy of the CCD-based system can be improved by directly deducing the solutions from the waveband measurement equations combining the emissivity function after the CCD-based system spectral response functions $[F_R(\lambda),F_G(\lambda),F_B(\lambda)]$ are known. This will reduce the error (a) arising from the wavelength simplification. However, the inversion solving of integration equations from waveband measurements needs to be studied in order to minimize the uncertainty effects. In addition, the spectrum responses also need to be reasonably designed as the wavelength combination is optimized for wavelength measurements.

(iv) Another scheme would be to use three CCDs in an integrated system for the three-wavelength measurements through a beam splitter with three optimum response narrow-band interference filters. Although this three-CCD system would be more complex than a single CCD system, it could reduce the error (b).

4 Conclusion

A multicolor pyrometry was used to measure the temperature of diesel combustion flames. Unlike the traditional two-color pyrometry, multicolor pyrometry uses the intensity ratios at different wavelength/wavebands to eliminate the need for calibrations for each geometry condition. For the inverse determination of (T,KL), the extra multicolor information will improve the solutions by reducing the effects of noise and random fluctuations. An improved data-processing method based on the least-squares technique was used to fit the data to obtain the solutions. Verification experiments using the multicolor pyrometry were conducted in a 54–120 kW test furnace with diesel fuel adopting the spectrometer-based system and the CCD-based system. The fiber optic spectrometer was used to record the spectral radiation intensity of the diesel flame at 16 wavelengths from 500 nm to 690 nm with wavelength intervals of 10 nm or 20 nm. These results were used to choose three suitable wavelengths to accurate measurements of diesel flame temperatures. A three-color pyrometer based on a color CCD was then used in the same test environment to measure the diesel flame temperatures. This technique has the advantage of measuring the temperature and soot distributions. The calculated average temperature $T_{CCD}=1882$ K was less than the temperature $T_{FOS}=2020$ K at a specific location obtained from the fiber optic spectrometer, but the differences can be well explained leading to the means to reduce the temperature error.

Acknowledgment

This paper is supported by the National Natural Science Foundation of China (Grant No. 50606033) and the National High Technology Research and Development Program of China (Grant No. 2007AA04Z178).

References

[1] Quoc, H. X., Vignon, J.-M., and Brun, M., 1991, "A New Approach of the Two-Color Method for Determining Local Instantaneous Soot Concentration and Temperature in a D.I. Diesel Combustion Chamber," SAE Technical Paper No. 910736.

[2] Dec, J., 1997, "A Conceptual Model of DI Diesel Combustion Based on Laser-Sheet Imaging," SAE Trans., **106**, pp. 1319–1348.

[3] Zhao, H., and Ladommatos, N., 1998, "Optical Diagnostics for Soot and Temperature Measurement in Diesel Engines," Prog. Energy Combust. Sci., **24**, pp. 221–255.

[4] Bhattacharjee, S., King, M., Cobb, W., Altenkirch, R. A., and Wakai, K., 2000, "Approximate Two-Color Emission Pyrometry," ASME Trans. J. Heat Transfer, **122**(1), pp. 15–20.

[5] Vattulainen, J., Nummela, V., Hernberg, R., and Kytola, J., 2000, "A System for Quantitative Imaging Diagnostics and Its Application to Pyrometric In-Cylinder Flame-Temperature Measurements in Large Diesel Engines," Meas. Sci. Technol., **11**, pp. 103–119.

[6] Fu, T. R., Cheng, X. F., Shi, C. L., Zhong, M. H., Liu, T. M., and Zheng, X. B., 2006, "The Set-Up of a Vision Pyrometer," Meas. Sci. Technol., **17**, pp. 659–665.

[7] Payri, F., Pastor, J. V., Garćıa, J. M., and Pastor, J. M., 2007, "Contribution to the Application of Two-Colour Imaging to Diesel Combustion," Meas. Sci. Technol., **18**, pp. 2579–2598.

[8] Lu, G., and Yan, Y., 2006, "Temperature Profiling of Pulverized Coal Flames Using Multicolor Pyrometric and Digital Imaging Techniques," IEEE Trans. Instrum. Meas., **55**(4), pp. 1303–1308.

[9] Li, X., and Wallace, J. S., 1995, "In-Cylinder Measurement of Temperature and Soot Concentration Using the Two-Colour Method," SAE Paper No. 950848.

[10] Xin, T., Bangquan, H., Jianxin, W., and Liwen, W., 2004, "Research on the Combustion Process of Ethanol Injected in the Intake Port Ignited by Diesel Fuel by Means of Two-Color Method," Trans. CSICE, **22**(1), pp. 39–44.

[11] Dewitt, D. P., and Nutter, G. D., 1989, *Theory and Practice of Radiation Thermometry*, Wiley, New York.

[12] Fu, T. R., Cheng, X. F., and Yang, Z. J., 2008, "Theoretical Evaluation of Measurement Uncertainties of Two-Color Pyrometry Applied to Optical Diagnostics," Appl. Opt., **47**(32), pp. 6112–6123.

[13] Khan, M. A., Allemand, C., and Eagar, T. W., 1991, "Noncontact Temperature Measurement. II. Least Squares Based Techniques," Rev. Sci. Instrum., **62**(2), pp. 403–409.

[14] Cignoli, F., De Iuliis, S., Manta, V., and Zizak, G., 2001, "Two-Dimensional Two-Wavelength Emission Technique for Soot Diagnostics," Appl. Opt., **40**(30), pp. 5370–5378.

[15] Lu, G., Yan, Y., Riley, G., and Bheemul, H. C., 2002, "Concurrent Measurements of Temperature and Soot Concentration of Pulverized Coal Flames," IEEE Trans. Instrum. Meas., **51**(5), pp. 990–995.

[16] Ranc, N., Pina, V., Sutter, G., and Philippon, S., 2004, "Temperature Measurement by Visible Pyrometry: Orthogonal Cutting Application," ASME Trans. J. Heat Transfer, **126**(6), pp. 931–936.

[17] Hampson, G. J., and Reitz, R. D., 1998, "Two-Colour Imaging of In-Cylinder Soot Concentration and Temperature in a Heavy-Duty DI Diesel Engine With Comparison to Multidimensional Modelling for Single and Split Injections," SAE Technical Paper No. 980524.

[18] Lu, S. S., Cheng, X. F., and Wang, A. Q., 2003, "Primary Color Measurement for Luminous Flame Temperature," Combust. Sci. Technol., **9**(2), pp. 178–182.

[19] Luo, Z. X., and Zhou, H. C., 2007, "A Combustion-Monitoring System With 3-D Temperature Reconstruction Based on Flame-Image Processing Technique," IEEE Trans. Instrum. Meas., **56**(5), pp. 1877–1882.
[20] Fu, T. R., Yang, Z. J., Wang, L. P., Cheng, X. F., Zhong, M. H., and Shi, C. L., "Measurement Performance of Optical CCD-Based Pyrometer System," Opt. Laser Technol. (to be published).
[21] Sun, Y. P., Lou, C., Jiang, Z. W., and Zhou, H. C., 2009, "Experimental Research of Representative Wavelengths of Tricolor for Color CCD Camera," J. Huazhong Univ. Sci. Technol., **37**(2), pp. 108–111.
[22] Fu, T. R., Yang, Z. J., and Cheng, X. F., 2009, "Calculation Errors of Flame Temperature Field Measurement Based on Color CCD," Proc. Chin. Soc. Electr. Eng., **29**(2), pp. 81–86.

Superior Convective Heat Transport for Laminar Boundary Layer Flow Over a Flat Plate Using Binary Gas Mixtures With Light Helium and Selected Heavier Gases

Antonio Campo[1]
Department of Mechanical Engineering,
The University of Texas at San Antonio,
San Antonio, TX 78249
e-mail: antonio.campo@utsa.edu

Salah Chikh
Faculté de Génie Mécanique et Génie des Procédés,
Université des Sciences et de la Technologie Houari Boumediène,
B.P. 32, El-Alia-Bâb-Ezzouar,
Algiers 16311, Algeria

Mohammad M. Papari

Mohammad R. Mobinipouya

Department of Chemistry,
Faculty of Sciences,
Shiraz University of Technology,
Shiraz 71555-313, Iran

This paper addresses the laminar boundary layer flow of certain binary gas mixtures along a heated flat plate. To form the binary gas mixtures, light helium (He) is the primary gas and the heavier secondary gases are nitrogen (N_2), oxygen (O_2), xenon (Xe), carbon dioxide (CO_2), methane (CH_4), tetrafluoromethane (CF_4), and sulfur hexafluoride (SF_6). The central objective of this paper is to investigate the potential of this group of binary gas mixtures for heat transfer intensification. From fluid physics, two thermophysical properties, i.e., viscosity η and density ρ, influence the fluid flow, whereas four thermophysical properties, i.e., viscosity η, thermal conductivity λ, density ρ, and heat capacity at constant pressure C_p, affect the forced convective heat transfer. The heat transfer augmentation from the flat plate is pursued by stimulating the forced convection mode as a whole. In this regard, it became necessary to construct a specific correlation equation to handle binary gas mixtures owing Prandtl number $Pr \in (0.1, 1)$. Whenever there is heat transfer invigoration in forced flow, drag force accretion seems to be inevitable. A standard formula for estimating the drag force F_d exerted on the flat plate is available from the fluid dynamics literature. The descriptive equations for the heat transfer rate Q_{mix} and drag force $F_{d,mix}$ associated with the seven binary gas mixtures are channeled through the four thermophysical properties, i.e., density ρ_{mix}, viscosity η_{mix}, thermal conductivity λ_{mix}, and heat capacity at constant pressure $C_{p,mix}$, which depend on the molar gas composition w. Two case studies suffice to elucidate the modified convective heat and momentum transport that the binary gas mixtures bring forward. At a film temperature $T_f = 300$ K and 1 atm, the $He + SF_6$ mixture delivers the absolute maximum for the relative heat transfer $Q_{mix,abs\ max}/B = 16.71$ at an optimal molar gas composition $w_{opt} = 0.96$. When compared with the light primary He gas with a relative heat transfer rate $Q_{He}/B = 12.04$, the $He + SF_6$ mixture generates a significant heat transfer enhancement of 39%. At a film temperature $T_f = 600$ K and the same 1 atm, the relative heat transfer Q_{He}/B for the light primary gas He comes down to 10.77. In reference to this, the $He + SF_6$ mixture furnishes an absolute maximum heat transfer $Q_{mix,abs\ max}/B = 18.11$ at an optimal molar gas composition $w_{opt} = 0.96$, yielding a remarkable heat transfer enhancement of 68%. In the global context, the usage of exotic binary gas mixtures with light helium and selected heavier gases may be envisioned for special tasks in industries that demand high heat transfer rates. [DOI: 10.1115/1.4000433]

Keywords: boundary layer flow, helium gas, binary gas mixtures, heat transfer enhancement

1 Introduction

From the dual standpoints of fundamental and applied researches, laminar boundary layer flows of incompressible fluids with heat transfer is considered a topic of prominence in heat transfer engineering because of its direct impact in a multitude of industrial processes, e.g., petroleum, chemical, metallurgical, nuclear, food, etc.

Aside from the aspect of general interest, a great amount of effort has been devoted lately to the important issue of heat transfer intensification. State-of-the-art review articles on heat transfer enhancement authored by Bergles [1] and Manglik [2] have appeared in specialized handbooks regularly. To attain high levels of heat transfer augmentation in internal or external forced convection, deformation or destruction of the boundary layer by active or passive method is a necessary condition. In general, heat transfer enhancing schemes have been classified in Refs. [1,2] into two broad categories: (a) passive schemes requiring no external power or (b) active schemes, which demand the use of external power. For instance, the application of fluid injection or suction to the fluid flow is an active scheme, whereas the attachment of an array of longitudinal fins onto a flat plate is a passive scheme.

[1]Corresponding author.

Contributed by the Heat Transfer Division of ASME for publication in the JOURNAL OF HEAT TRANSFER. Manuscript received December 13, 2007; final manuscript received September 16, 2009; published online March 4, 2010. Assoc. Editor: S. A. Sherif.

As stated in Refs. [1,2], it is of great interest to explore new passive schemes that, while conducive to heat transfer invigoration, are power-independent, and on the other hand, do not modify the solid surfaces in contact with the moving fluid. Further, it is also imperative that in evaluating any active or passive scheme for enhanced heat transfer related to external boundary layer flow, attention must be given to the attendant drag force, which is intimately connected to the power requirements of the blower that sustains the incoming flow. Optimization of laminar flow over a heated flat plate has been performed by Bejan [3] using methods based on the second law of thermodynamics. Relying on the Blasius–Pohlhausen solutions for $u(x,y)$ and $T(x,y)$ available in the literature, he found the total rate of entropy generation S' produced by fluids with $\mathrm{Pr}=1$.

It appears that no attention has been given in the past to the analysis of laminar boundary layer flows with heat transfer along flat plates using incompressible binary gas mixtures as working fluids. Because of this limitation, the heat/fluid flow characteristics of binary gas mixtures remain unknown. Correspondingly, the central objective in this study is to investigate the behavior of laminar boundary layers of binary gas mixtures over heated flat plates maintained at uniform temperatures. In this respect, the primary gas chosen is light helium (He) and the secondary heavier gases chosen (listed in alphabetical order) are carbon dioxide (CO_2), methane (CH_4), nitrogen (N_2), oxygen (O_2), sulfur hexafluoride (SF_6), tetrafluoromethane or carbon tetrafluoride (CF_4), and xenon (Xe). As a by-product, a collateral objective relates to discover which binary gas mixtures are able to yield reasonable heat transport magnification without excessive drag force penalties that are unattainable by the light He gas or by the companion heavier gases. In general, it is expected that the outcome of the present theoretical study will warrant maximum heat transport in laminar boundary layer flows of some binary gas mixtures over heated solid bodies coupled with moderate drag force in an inexpensive way. Notwithstanding, the usage of these He-based binary gas mixtures may provide a desirable alternative to conventional air for heat exchange devices in industrial settings. This information will provide valuable guidance to engineers that engage in design activities.

The body of the paper is divided into four sections. Section 2 describes the detailed correlation equations for convection heat transfer and drag forces connected to laminar boundary layer flows. The accurate formulas that predict the thermophysical properties of the binary gas mixtures are explained in Sec. 3. The way in which the heat transfer rates and drag forces vary with the molar composition of the binary gas mixtures is put forward in Sec. 4. Lastly, those binary gas mixtures that are capable of delivering maximum heat transfer rates are identified in Sec. 5.

2 Laminar Regime

Attention is directed at the ample spectrum of laminar boundary layers of incompressible air, pure gas, or vapor flowing over a uniformly heated flat plate at a fixed temperature T_w. As usual, the incoming fluid has freestream velocity u_∞ and freestream temperature T_∞. The flat plate is thin, so that the transition Reynolds number Re_{cr} stays near 5×10^5.

2.1 Convective Heat Transfer. The rate of heat transfer Q between a heated plate and a fluid is calculated with Newton's "equation of cooling"

$$Q=\overline{h}A_S(T_w-T_\infty) \tag{1}$$

If the surface area A_S together with the temperature difference T_w-T_∞ are specified, the only possible way for increasing the rate of heat transfer Q is by enlarging the magnitude of the average heat transfer coefficient $\overline{h}$. Conceptually, this idea implies the stimulation of the forced convection mode as a whole, and this is precisely the goal to be pursued in the present paper.

From forced convection theory [4], the average heat transfer coefficient $\overline{h}$ in laminar boundary layer flows of incompressible fluids along heated flat plates depends on the fluid temperature gradient at the plate, say $\theta'(0)$ in dimensionless form. The $\overline{h}$ dependence, normally represented by the so-called Prandtl number function $\theta'(0)=f(\mathrm{Pr})$, gives way to a correlation equation for the average Nusselt number $\overline{\mathrm{Nu}}_L$ of general form

$$\overline{\mathrm{Nu}}_L=\frac{\overline{h}L}{\lambda}=\mathrm{Re}_L^{1/2}\times f(\mathrm{Pr}) \tag{2}$$

which is valid for all Reynolds numbers $\mathrm{Re}_L\leq\mathrm{Re}_{cr}=5\times10^5$. The thermophysical properties of the fluid are evaluated at the film temperature $T_f=(T_w+T_\infty)/2$.

On the side, it is known that binary gas mixtures possess Prandtl numbers that are squeezed between the lower subgroup for metallic liquids with $\mathrm{Pr}\ll1$ and the middle subgroup for air, pure gases, and vapor sharing $\mathrm{Pr}\sim1$, but closer to the latter subgroup.

Attention is turned back to the Prandtl number function $f(\mathrm{Pr})$ appearing in Eq. (2). As cited in Ref. [4], Pohlhausen [5] numerically calculated a small group of dimensionless fluid temperature gradients $\theta'(0)$. If the fluids have $\mathrm{Pr}>0.5$, they are adequately correlated by the cubic parabola

$$\theta'(0)=f(\mathrm{Pr})=0.332\ \mathrm{Pr}^{1/3} \tag{3}$$

On the contrary, when the fluids have $\mathrm{Pr}<0.5$ a different correlation equation for $f(\mathrm{Pr})$ must be constructed. Because this information is missing, we applied nonlinear regression to the tabulated Pr data that extends from 0.001 to 1000 [6]. The outcome of this operation leads to the precise three-part power correlation equation

$$f(\mathrm{Pr})=0.810\ \mathrm{Pr}^{0.454},\quad \mathrm{Pr}\in(0.001,0.1) \tag{4a}$$

$$f(\mathrm{Pr})=0.678\ \mathrm{Pr}^{0.377},\quad \mathrm{Pr}\in(0.1,1) \tag{4b}$$

$$f(\mathrm{Pr})=0.664\ \mathrm{Pr}^{0.333},\quad \mathrm{Pr}\in(1,1000) \tag{4c}$$

In here, R-square is $\sim$99.9% at the global level, while at the local level, the maximum absolute error ascends to 2.25% when $\mathrm{Pr}=0.005$. The software MINITAB [7] facilitated the calculations.

As it is explicitly revealed in Eq. (4), Eq. (4*a*) handles all liquid metals, Eq. (4*b*) handles air, pure gases, vapor, and binary gas mixtures, whereas Eq. (4*c*) handles water, and light and heavy liquids.

2.2 Fluid Flow. A quantity of keen interest in laminar boundary layer flows of incompressible fluids is the drag force F_d exerted on a stationary flat plate. Its magnitude is directly related to the power requirement of the blower to sustain a desired flow level. For a flat plate with surface area A_S, the drag force F_d is defined by the product

$$F_d=\overline{\tau_w}A_S \tag{5a}$$

where the average wall shear stress $\overline{\tau_w}$ and the freestream velocity u_∞ are linked through the expression

$$\overline{\tau_w}=\overline{C_f}\left(\rho\frac{u_\infty^2}{2}\right) \tag{5b}$$

In here, the average skin friction coefficient $\overline{C_f}$ depending on the Reynolds number Re_L is obtained from the formula [4]

$$\overline{C_f}=\frac{1.328}{\mathrm{Re}_L^{1/2}} \tag{5c}$$

Similar to the limitations of Eq. (2), Eq. (5*c*) covers all $\mathrm{Re}_L\leq\mathrm{Re}_{cr}=5\times10^5$. Again, the thermophysical properties of the fluid are evaluated at the film temperature $T_f=(T_w+T_\infty)/2$.

3 Laminar Regime of Binary Gas Mixtures

From theoretical concepts, heat transport happens by the convection mode, which is comprised by the heat conduction mode plus fluid movement [4]. This statement, when rewritten in terms of the acting driving forces, is synonymous with the relation

$$\text{Convection} = \text{Conduction in } \underbrace{\text{moving media}}_{\text{Inertial forces, Viscous forces}} \tag{6}$$

As a point of reference, let us consider the laminar boundary layer flow of incompressible air over a heated flat plate. Disregarding changes in (1) the size of the surface area A_S, (2) the intensity of the freestream velocity u_∞, and (3) the level of temperature difference $T_w - T_\infty$, the improvement of heat transfer from the flat plate to the moving air responds to the stimulation of the convection mode as a whole, that is, elevating the magnitude of $\overline{h}$. Focusing on this singular aspect, a viable option seeks to replace the air with a better pure gas, or perhaps with a better binary gas mixture. In this work, we focused our attention on the latter option simply because by doing so the former option becomes a particular case.

In light of the foregoing arguments, it is expected that the interaction between the intervening thermophysical properties of the light primary He gas when paired with those for the heavier secondary gases N_2, O_2, Xe, CO_2, CH_4, CF_4, and SF_6 could modify in a favorable manner the velocity and temperature of some of the seven binary gas mixtures flowing along the heated flat plate. As a result, this behavioral alteration could ultimately lead to reasonable degrees of heat transfer enhancement.

3.1 Convective Heat Transfer. Introducing Eq. (4*b*) into Eq. (2) provides the appropriate average Nusselt number for binary gas mixtures $\overline{\text{Nu}}_{L,\text{mix}}$. Let $\overline{h}_{\text{mix}}$ designate the average heat transfer coefficient for a prototypical binary gas mixture in Eq. (1), creating the proportionality

$$Q_{\text{mix}} \propto \frac{\lambda_{\text{mix}}^{0.623} \rho_{\text{mix}}^{0.500} C_{p,\text{mix}}^{0.377}}{\eta_{\text{mix}}^{0.123}} \tag{7a}$$

or the equation

$$Q_{\text{mix}}/B = \frac{\lambda_{\text{mix}}^{0.623} \rho_{\text{mix}}^{0.500} C_{p,\text{mix}}^{0.377}}{\eta_{\text{mix}}^{0.123}} \tag{7b}$$

where the subscript "mix" in the variables signifies binary gas mixture. Each of the four thermophysical properties ρ_{mix}, η_{mix}, λ_{mix}, and $C_{p,\text{mix}}$ depends on the molar gas composition w. The overall parameter B in Eq. (7*b*) absorbs the surface area A_S (a geometric quantity) and the freestream velocity u_∞ (a hydrodynamic quantity) directly, while the film temperature T_f (a thermal quantity) is reflected indirectly, that is

$$B = 0.678 \;\; W(u_\infty L)^{0.5}(T_w - T_\infty) \tag{7c}$$

with units of $\text{m}^2\ \text{K}\ \text{s}^{-0.5}$.

3.2 Fluid Flow. Attention is now directed to the drag force exerted by a prototypical binary gas mixture flow past the stationary flat plate $F_{d,\text{mix}}$. The combination of (5) and (6) gives rise to the proportionality

$$F_{d,\text{mix}} \propto \rho_{\text{mix}}^{0.50} \eta_{\text{mix}}^{0.50} \tag{8a}$$

or the equation

$$F_{d,\text{mix}}/C = \rho_{\text{mix}}^{0.50} \eta_{\text{mix}}^{0.50} \tag{8b}$$

where again the subscript "mix" in the variables refers to binary gas mixture. Each of the two thermophysical properties depends on the molar gas composition w. As was done before, the overall coefficient C in Eq. (8*b*) embraces the surface area A_S (a geometric quantity) and the freestream velocity u_∞ (a hydrodynamic quantity) directly, but the film temperature T_f (a thermal quantity) appears indirectly, that is

$$C = 0.664 \;\; W(u_\infty L)^{0.5} \tag{8c}$$

with units of $\text{m}^2\ \text{s}^{-0.5}$.

In reality, the objective of this paper is to increase Q while keeping F_d at a low-to-moderate level. In the context of binary gas mixtures, let us pause here momentarily to describe the ideal thermophysical properties that the binary gas mixtures bring forth in harmony with the structure of Eqs. (7*b*) and (8*b*). First, it is clear that to enhance the heat transfer Q_{mix}, the trio λ_{mix}, ρ_{mix}, and $C_{p,\text{mix}}$ in the numerator of Eq. (7*b*) has to be large, and η_{mix} in the denominator has to be small. Second, to keep $F_{d,\text{mix}}$ at low-to-moderate values, a small η_{mix} and/or a small ρ_{mix} in Eq. (8*b*) will do the job. In addition, it is recognizable that a large ρ_{mix} for Q_{mix} in Eq. (7*b*) contradicts a small ρ_{mix} for $F_{d,\text{mix}}$ in Eq. (8*b*). In other words, this means that a large ρ_{mix} affects $F_{d,\text{mix}}$ adversely in Eq. (8*b*) and a small ρ_{mix} affects Q_{mix} adversely in Eq. (7*b*). Therefore, to settle this matter, an intermediate ρ_{mix} seems to be a reasonable compromise.

4 Thermophysical Properties of Binary Gas Mixtures

Heat convection theory [4] predicts that laminar velocity and temperature boundary layers of incompressible gases depend on four thermophysical properties, i.e., density ρ, viscosity η, thermal conductivity λ, and heat capacity at constant pressure C_p. In principle, for the case of a binary gas mixture, each of the four thermophysical properties varies with temperature T, pressure p, and molar gas composition w by way of the triple-valued functions $f(w,p,T)$ [8]. In practice, if T and p are fixed, a single-valued functions $f(w)$ surfaces up. Accordingly, accurate formulas for the quartet $\eta_{\text{mix}}(w)$, $\lambda_{\text{mix}}(w)$, $\rho_{\text{mix}}(w)$, and $C_{p,\text{mix}}(w)$ are gathered from the literature on applied thermodynamics and physical chemistry and are presented in Secs. 4.1–4.5.

4.1 Molar Gas Composition. The molar gas composition w_i of a certain binary gas mixture is defined as the mass fraction of the single gas i

$$w_i = x_i\left(\frac{M_i}{M_{\text{mix}}}\right), \quad \text{for } i = 1,2 \tag{9}$$

where x_i is the mole fraction, M_i is the molar mass of gas i, and $M_{\text{mix}} = x_1 M_1 + x_2 M_2$ is the molar mass of the gas-gas mixture [8].

4.2 Viscosity. Based on the kinetic theory of gases [9,10], the viscosity of a binary gas mixture η_{mix} is calculated from the determinant ratio formula

$$\eta_{\text{mix}} = -\frac{\begin{vmatrix} H_{AA} & H_{AB} & x_A \\ H_{BA} & H_{BB} & x_B \\ x_A & x_B & 0 \end{vmatrix}}{\begin{vmatrix} H_{AA} & H_{AB} \\ H_{AB} & H_{BB} \end{vmatrix}} \tag{10}$$

First, the elements H_{AA} and H_{BB} along the main diagonal are

$$H_{AA} = \frac{x_A^2}{\eta_A} + \frac{2x_A x_B}{\eta_{AB}} \frac{m_A m_B}{(m_A + m_B)^2}\left(\frac{5}{3A_{AB}^*} + \frac{m_B}{m_A}\right) \tag{11a}$$

The expression for H_{BB} is obtained from the one for H_{AA} interchanging the subscripts A and B. Second, the elements off the main diagonal H_{AB} and H_{BA} are

$$H_{AB}(A \neq B) = -\frac{2x_A x_B}{\eta_{AB}} \frac{m_A m_B}{(m_A + m_B)^2}\left(\frac{5}{3A_{AB}^*} - 1\right) \tag{11b}$$

In here, the interaction viscosity η_{AB} is evaluated from the complex relation

$$\eta_{AB} = \frac{5}{16}\left[\left(\frac{2m_A m_B}{m_A + m_B}\right)\frac{kT}{\pi}\right]^{1/2} \frac{1}{\sigma_{AB}^2 \Omega_{AB}^{*(2,2)}(T_{AB}^*)} \tag{12}$$

in which the subscripts A and B identify the heavier and lighter gases of the A-B pair, m_A and m_B are the masses of A and B, x_A and x_B are the mole fraction of A and B, and A_{AB}^* is the ratio collision integral defined by Bzowski et al. [11]. The functional correlation equations deduced in Ref. [11] facilitate the estimation of the reduced viscosity collision integral $\Omega_{ij}^{*(2,2)}$ in Eq. (12).

The above approach guarantees that the viscosity η_{mix} for binary gas mixtures can be estimated with a maximum error of 1% when compared against experimental data.

4.3 Thermal Conductivity. For a binary gas mixture, Schreiber at al. [12] developed the following determinant ratio formula for the estimation of the thermal conductivity λ_{mix}

$$\lambda_{\text{mix}} = -\frac{\begin{vmatrix} L_{AA} & L_{AB} & x_A \\ L_{AB} & L_{BB} & x_B \\ x_A & x_B & 0 \end{vmatrix}}{\begin{vmatrix} L_{AA} & L_{AB} \\ L_{AB} & L_{BB} \end{vmatrix}} \tag{13}$$

Here, the elements L_{AA}, L_{BB}, and L_{AB} are given by

$$L_{AA} = \frac{x_A^2}{\lambda_A} + \frac{25 x_A x_B}{8 A_{AB}^* \lambda_{AB}}\left(\frac{R}{C_{p,A}^0}\right)^2 \times \left[\frac{25}{4}y_B^4 + \frac{15}{2}y_A^4 - 3y_B^4 B_{AB}^* + 4y_A^2 y_B^2 A_{AB}^* + \left(\frac{C_{p,A}^0}{R} - 2.5\right)\right] \tag{14a}$$

$$L_{BB} = \frac{x_B^2}{\lambda_B} + \frac{x_A x_B}{2 A_{AB}^* \lambda_{AB}}\left(\frac{25}{4}y_A^4 + \frac{15}{2}y_B^4 - 3y_A^4 B_{AB}^* + 4y_A^2 y_B^2 A_{AB}^*\right) \tag{14b}$$

$$L_{AB} = -\frac{5 x_A x_B y_A^2 y_B^2}{4 A_{AB}^* \lambda_{AB}}\left(\frac{R}{C_{p,A}^0}\right)\left(\frac{55}{4} - 3B_{AB}^* - 4A_{AB}^*\right) \tag{14c}$$

where λ_A and λ_B are the thermal conductivity of the molecular gases A and B, and λ_{AB} is the interaction thermal conductivity. In Eqs. (14*a*) and (14*c*), C_p^0 stands for the isobaric heat capacity of gas A from the ideal gas calculated from statistical thermodynamics, R is the gas constant and A^* and B^* are collision integral ratios. Also, y_p is the mass ratio of species q, which is obtained from

$$y_p^2 = \frac{M_q}{M_A + M_B} \tag{15}$$

where M_q is the molar mass of species q. The interaction thermal conductivity λ_{AB} is calculated by the relation

$$\lambda_{AB} = \frac{15}{8}R\left(\frac{M_A + M_B}{M_A M_B}\right)\eta_{AB} \tag{16}$$

in which the interaction viscosity η_{AB} is obtained from Eq. (12).

The thermal conductivity for binary gas mixtures λ_{mix} may be estimated with excellent precision within a 1% error band.

4.4 Density. At low pressures, the molar density of a binary gas mixture ρ_{mix} is determined with the truncated virial equation of state

$$Z = \frac{p}{RT\rho_{\text{mix}}} = 1 + B_2 \rho_{\text{mix}} \tag{17}$$

where Z is the compressibility factor, p is the pressure, R is the gas constant, and B_2 is the second virial coefficient. Using phase equilibrium concepts for a general binary gas mixture consisting of m gases, B_m is calculated by the double summation [13]

$$B_m = \sum_{i=1}^{m}\sum_{j=1}^{m} x_i x_j B_{ij} \tag{18}$$

where B_{ii} is the second virial coefficient of pure gas i, B_{jj} is the second virial coefficient of pure gas j, and B_{ij} is the interaction of the second virial coefficients. To evaluate B_2, we used the simple correlation proposed by Tsonopoulos [14]

$$\frac{B_2 p_c}{RT_c} = B^{(0)} + \omega B^{(1)} \tag{19}$$

where ω is the Pitzer acentric factor. The values of $B^{(0)}$ and $B^{(1)}$ are computed from the relations

$$B^{(0)} = 0.1445 - \frac{0.33}{T_r} - \frac{0.1385}{T_r^2} - \frac{0.0121}{T_r^3} - \frac{0.000607}{T_r^8} \tag{20}$$

and

$$B^{(1)} = 0.0637 + \frac{0.331}{T_r^2} - \frac{0.423}{T_r^3} - \frac{0.008}{T_r^8} \tag{21}$$

where $T_r = T/T_c$, and T_c, p_c, and ω for the pure gases are taken from Ref. [8].

The uncertainty in determining the density of binary gas mixtures ρ_{mix} with this methodology stays around 0.1%.

4.5 Heat Capacity at Constant Pressure. The molar heat capacity at constant pressure $C_{p,\text{mix}}^0$ of binary gas mixtures at low densities may be adequately predicted by the mixing rule [8]

$$C_{p,\text{mix}}^0 = \sum_{i=1}^{2} x_i C_{p,i}^0 \tag{22}$$

where x_i is the mole fraction and $C_{p,i}^0$ is the molar heat capacity at constant pressure of gas i. In Eq. (22), the molar heat capacity at constant pressure C_p^0 and constant volume C_v^0 of pure gases are quantified by the pair of equations

$$C_p^0 - C_v^0 = R \tag{23}$$

and

$$\frac{C_v^0}{R} = S + \sum_{j=1}^{k}\left(\frac{\Theta_{vj}}{T}\right)^2 \frac{\exp\left(\frac{\Theta_{vj}}{T}\right)}{\left[\exp\left(\frac{\Theta_{vj}}{T}\right)\right]^2} \tag{24}$$

In the last equation, the symbol Θ_{vj} stands for the characteristic vibrational temperature for the vibrational degree of freedom j. Besides, S assumes values of 5/2 for linear molecules and 3 for nonlinear molecules [15].

The uncertainty in calculating the heat capacity at constant pressure $C_{p,\text{mix}}^0$ of binary gas mixtures with the combination of the mixing rule and Statistical Thermodynamics is of the order of 1%.

5 Maximization of Heat Transfer With Binary Gas Mixtures

When the accurate formulas for the four thermophysical properties $\eta_{\text{mix}}(w)$, $\lambda_{\text{mix}}(w)$, $\rho_{\text{mix}}(w)$, and $C_{p,\text{mix}}(w)$ given by Eqs. (10), (13), (17), and (22) at a certain p and T are introduced into Eqs. (7) and (8), the heat transfer rate Q_{mix} and the drag force $F_{d,\text{mix}}$ respond to continuous changes in the molar gas composition w of the seven binary gas mixtures $He+N_2$, $He+O_2$, $He+Xe$, $He+CO_2$, $He+CF_4$, $He+CH_4$, and $He+SF_6$ in the proper w-domain [0,1]. Using small steps $\Delta w = 0.01$, the methodical algebraic calculations for the pair Q_{mix} and $F_{d,\text{mix}}$ associated with the seven binary gas mixtures are carried out with the spreadsheet software EXCEL [16].

The objective of the subsection is to search for the absolute maximum of the objective function, namely, the relative heat

Table 1 Thermophysical properties of the pure gases at 300 K and 1 atm

Gas	M (g/mol)	ρ (kg/m^3)	η (μPa s)	λ (mW/mK)	C_p^0 (J/kg K)
He	4.00	0.1624	19.92	**155.70**	**5199.11**
CH_4	16.04	0.6553	**11.19**	34.89	2230.47
N_2	28.01	1.1379	17.96	25.88	1039.66
O_2	32.00	1.3004	20.78	26.64	918.21
CO_2	44.01	1.7964	15.08	16.79	848.40
CF_4	88.00	3.5410	17.34	15.16	699.36
Xe	131.29	5.3610	23.20	5.52	158.49
SF_6	146.06	**5.8585**	29.70	13.20	671.39

transfer rate $Q_{mix}(w)/B$ in Eq. (7*b*). Conceptually, a point $w = w_{opt}$ is an absolute maximum of a single-valued function $Q_{mix}(w)/B$ if

$$Q_{mix}(w_{opt})/B \geq Q_{mix}(w)/B \tag{25}$$

for all w values inside the w-domain [0,1]. In other words, the location of the optimal molar gas composition w_{opt} corresponds to the w value that renders an absolute maximum $Q_{mix,abs\ max}/B$ for all computed ranges of $Q_{mix}(w)/B$ contained in [0,1]. Correspondingly, the companion relative drag force $F_{d,mix}/C$ in Eq. (8*b*) must be evaluated at the same w_{opt}.

6 Presentation of Numerical Results

From a qualitative standpoint, it was deemed appropriate to contrast the united characteristics for convective heat and momentum transport of the seven binary gas mixtures moving along a heated flat plate against those of light helium, the primary gas in binary gas mixtures. Recall that the latter constitutes the baseline case, knowing that the transition Reynolds number Re_{cr} stays near 5×10^5.

First, the numerical values of the thermophysical properties η, λ, ρ, and C_p for the eight single gases He, N_2, O_2, Xe, CO_2, CH_4, CF_4, and SF_6 at two different film temperatures T_f=300 K and 600 K, both sharing 1 atm, are listed in Tables 1 and 2. At this point, it is instructive to inspect the items in Table 1 to notice the variability of the four thermophysical properties for the seven heavy secondary gases with respect to the light primary gas He. Among the eight gases, He has the highest λ_{He} =155.70 mW/mK, the highest $C_{p,He}$=5199.11 J/kg K, the lowest ρ_{He}=0.1624 kg/m^3, and an intermediate η_{He}=19.92 μPa s. As a consequence, in reference to Eq. (7*b*) the lowest ρ_{He} needs to be compensated by a high ρ for the heavy secondary gas(es) and the intermediate η_{He} needs to be compensated with a low η for the heavy secondary gas(es).

A set of four figures has been prepared to illustrate how the two target parameters, i.e., the relative heat transfer rate Q_{mix}/B and the relative drag force $F_{d,mix}/C$ for the binary gas mixtures, are vulnerable to the molar gas composition w in the w-domain [0,1]. In the figure format, the abscissa associates the left extreme w =0 with the light primary gas He, whereas the right extreme w =1 is connected to each of the seven heavier secondary gases N_2, O_2, Xe, CO_2, CH_4, CF_4, and SF_6.

At T_f=300 K and 1 atm, Fig. 1 discloses the family of curves for the relative heat transfer rate Q_{mix}/B changing with w in [0,1], which exhibits skewed-to-the-right shapes. Among the group of seven binary gas mixtures tested, it is seen that only one subgroup of three He+SF_6, He+CF_4, and He+Xe yields maxima $Q_{mix,max}/B$. Further, the three optimal molar gas compositions w_{opt} for them are located near the heavier secondary gases at w =1. The point of reference is the light primary gas He, who owns a relative heat transfer rate Q_{He}/B=12.04. Certainly, the He +SF_6 mixture produces the absolute maximum for the relative heat transfer $Q_{mix,abs\ max}/B$=16.71 that happens at the optimal molar gas composition w_{opt}=0.96. As compared with He, the He +SF_6 mixture generates a remarkable heat transfer enhancement of order 39%. Subsequently, the first relative maximum for the relative heat transfer $Q_{mix,rel\ max}/B$=14.98 is provided by the He +CF_4 mixture, which takes place at w_{opt}=0.90. Herewith, the heat transfer enhancement for the He+CF_4 mixture with respect to He amounts to a significant 24%. Lastly, the He+Xe mixture is responsible for a second relative maximum for the relative heat transfer $Q_{mix,rel\ max}/B$=13 operating in the narrow w-subinterval $0.75\leq w_{opt}\leq 0.80$. Thereby, the heat transfer enhancement supplied by the He+Xe mixture with respect to He resulted in a modest 8%. As the maximum for the relative heat transfer decreases from the best He+SF_6 mixture, the optimal molar composition w_{opt} shifts to the left. As a supplement to this information, Table 3 contains the items pertinent to the other extreme Q/B values associated with the three heavier secondary gases of marked relevance SF_6, CF_4, and Xe. The remaining four Q_{mix}/B curves for the subgroup He+N_2, He+O_2, He+CO_2, and He +CH_4 form a tight cluster, exhibiting a common monotonic decreasing trend with w in [0,1] with no maxima. In synthesis, it is better to use the light primary gas He instead of any of the four above-cited binary gas mixtures.

Plotted in Fig. 2 is the family of curves for the relative drag force $F_{d,mix}/C$ generated by the same seven binary gas mixtures, varying with the molar gas composition w in [0,1]. Without ex-

Table 2 Thermophysical properties of the pure gases at 600 K and 1 atm

Gas	M (g/mol)	ρ (kg/m^3)	η (μPa s)	λ (mW/mK)	C_p^0 (J/kg K)
He	4.00	0.0802	32.22	**252.40**	**5192.87**
CH_4	16.04	0.3215	**19.43**	88.92	3273.02
N_2	28.01	0.5613	29.60	43.92	1075.14
O_2	32.00	0.6413	34.67	50.74	1003.25
CO_2	44.01	0.8825	28.00	41.55	1076.23
CF_4	88.00	1.7632	30.06	40.32	989.21
Xe	131.29	2.6331	**42.92**	10.26	158.58
SF_6	146.06	**2.9284**	23.65	32.70	933.23

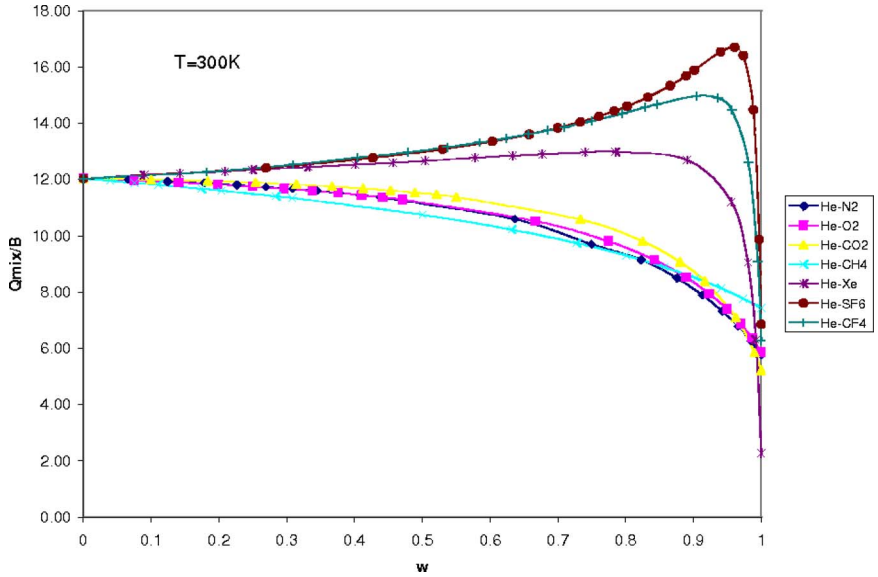

Fig. 1 Influence of the molar gas composition w on the relative heat transfer rate Q_{mix}/B for the binary gas mixtures at 300 K and 1 atm

ception, the entire family of $F_{d,\mathrm{mix}}/C$ curves displays a monotonic increasing behavior from $w=0$ for the light primary gas He toward $w=1$ for the seven heavier secondary gases. As a point of reference, the relative drag force $F_{d,\mathrm{mix}}/C$ for He is 0.002. The uppermost curve corresponds to the $He+SF_6$ mixture, followed by the He+Xe mixture in second place, and the $He+CF_4$ mixture in third place. The respective optimal gas composition w_{opt} are as follows: 0.009 for the $He+SF_6$ mixture at $w_{opt}=0.96$, 0.0055 for

Table 3 Relative heat transfer rates Q_{mix}/B for the best three binary gas mixtures at 300 K and 1 atm

$Q_{He}/B=12.04$	$Q_{SF_6}/B=6.86$	$Q_{mix,abs\ max}/B=16.71$ at $w_{opt}=0.96$ for $He+SF_6$	$\frac{Q_{He+SF_6}-Q_{He}}{Q_{He}}=39\%$
$Q_{He}/B=12.04$	$Q_{CF_4}/B=6.29$	$Q_{mix,rel\ max}/B=14.98$ at $w_{opt}=0.90$ for $He+CF_4$	$\frac{Q_{He+CF_4}-Q_{He}}{Q_{He}}=24\%$
$Q_{He}/B=12.04$	$Q_{Xe}/B=2.27$	$Q_{mix,rel\ max}/B=13$ at $0.75\leq w_{opt}\leq 0.80$ for He+Xe	$\frac{Q_{He+Xe}-Q_{He}}{Q_{He}}=8\%$

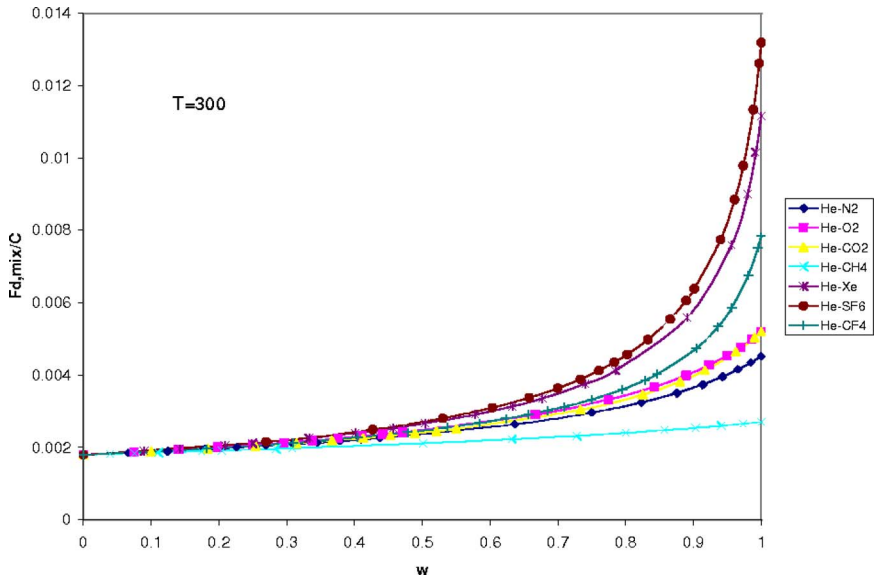

Fig. 2 Influence of the molar gas composition w on the relative drag force $F_{d,\mathrm{mix}}/C$ for the binary gas mixture at 300 K and 1 atm

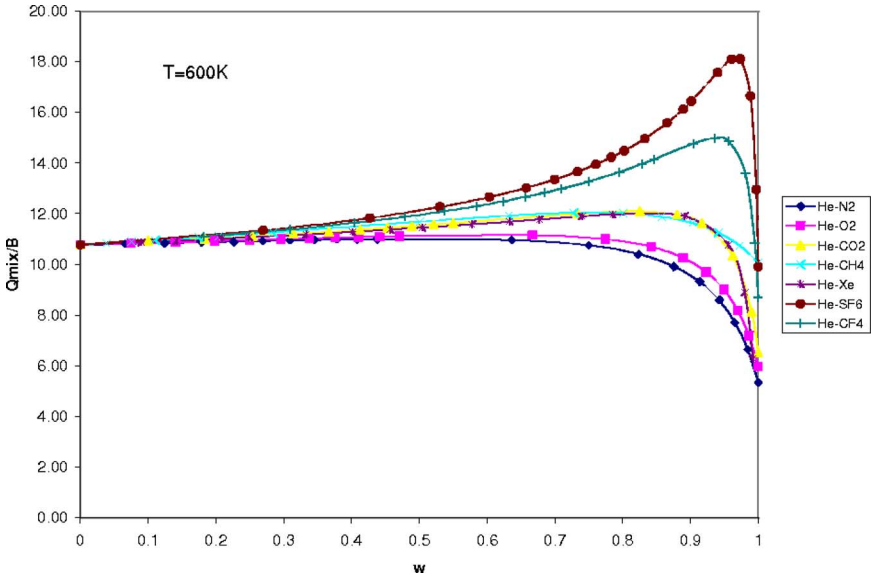

Fig. 3 Influence of the molar gas composition w on the relative heat transfer rate Q_{mix}/B for the binary gas mixtures at 600 K and 1 atm

the $He+Xe$ mixture at $w_{opt}=0.75$, and 0.0045 for the $He+CF_4$ mixture at $w_{opt}=0.9$. The lowermost curve connected to the $He+CH_4$ mixture is a straight line with a mild positive slope.

As a figure-of-merit for those favorable binary gas mixtures discovered, let us consider the ratio between the maximum for the relative heat transfer Q_{mix}/B at the optimal molar composition w_{opt} and the relative drag force $F_{d,mix}/C$ at the same w_{opt}. The $He+CF_4$ mixture owing a ratio $(Q_{mix,abs\ max}/B/F_{d,mix}/C)=15/0.0045=3333$ turns out to be the best among the seven binary gas mixtures under study. The second best corresponds to the $He+SF_6$ mixture with a ratio $(Q_{mix,rel\ max}/B/F_{d,mix}/C)=16.71/0.009=1857$.

Displayed in Fig. 3 is the family of curves for the relative heat transfer rate Q_{mix}/B changing with the molar gas composition w in [0,1] at $T=600$ K and 1 atm. It is observable that for all curves the skewed-to-the-right shapes prevail. Among the seven binary gas mixtures, it turns out that four of them yield maxima $Q_{mix,max}/B$ at various optimal molar gas compositions w_{opt} located near $w=1$. For comparison purposes, the relative heat transfer Q_{He}/B for the light gas He equates to 10.77. The $He+SF_6$ mixture furnishes the absolute maximum heat transfer $Q_{mix,abs\ max}/B=18.11$ at the optimal gas composition $w_{opt}=0.96$. When contrasted against He, the $He+SF_6$ mixture brings forth a high heat transfer enhancement of 68%. A first relative maximum heat transfer $Q_{mix,rel\ max}/B=15$ is provided by the $He+CF_4$ mixture, which takes place at $w_{opt}=0.93$. Herewith, the heat transfer enhancement delivered by the $He+CF_4$ mixture with respect to He amounts to 39%. The trio of $He+Xe$, $He+CH_4$, and $He+CO_2$ mixtures share the second relative maximum heat transfer $Q_{mix,rel\ max}/B=11.97$ that happens in the narrow w-interval $0.74\leq w_{opt}\leq 0.87$. With regards to Q_{He}/B, the heat transfer enhancement supplied by this trio of binary gas mixtures delivers a modest 11%. Table 4 contains supplementary information for $Q_{mix,max}/B$ belonging to the three heavier secondary gases SF_6, CF_4, and Xe. As noted before, as $\overline{h}_{mix,max}/B$ increases from the $He+Xe$ mixture toward the $He+SF_6$ mixture passing through the $He+CF_4$ mixture, the trajectory of w_{opt} moves in the northeast direction. Actually, the equal contribution of the pair of $He+N_2$ and $He+O_2$ mixtures relative to He is negligible. The remaining two Q_{mix}/B curves for the $He+N_2$ and $He+O_2$ mixtures are close to each other evidencing a common monotonic decreasing trend with w in [0,1]. In view of this comportment, it is beneficial to use the light primary gas He instead of those two mixtures.

In Fig. 4 the family of curves for the relative drag force $F_{d,mix}/C$ of the binary gas mixtures is shown varying with the molar gas composition w in [0,1]. Categorically, the entire family of $F_{d,mix}/C$ curves displays a monotonic increasing route from $w=0$ for the light primary He toward the seven heavier secondary gases at $w=1$. For proper guidance, the relative drag force $F_{d,mix}/C$ for He is fixed at 0.0016. The uppermost curve corresponds to the $He+Xe$ mixture, followed by the $He+SF_6$ mixture

Table 4 Relative heat transfer rates Q_{mix}/B for the best five binary gas mixtures at 600 K and 1 atm

$Q_{He}/B=10.77$	$Q_{SF_6}/B=9.91$	$Q_{mix,abs\ max}/B=18.11$ at $w_{opt}=0.96$ for $He+SF_6$	$\frac{Q_{He+SF_6}-Q_{He}}{Q_{He}}=68\%$
$Q_{He}/B=10.77$	$Q_{CF_4}/B=8.70$	$Q_{mix,rel\ max}/B=15$ at $w_{opt}=0.93$ for $He+CF_4$	$\frac{Q_{He+CF_4}-Q_{He}}{Q_{He}}=39\%$
$Q_{He}/B=10.77$	$Q_{Xe}/B=2.17$ $Q_{CH_4}/B=8.70$ $Q_{CO_2}/B=6.53$	$Q_{mix,rel\ max}/B=11.97$ at $0.73\leq w_{opt}\leq 0.86$ for $He+Xe$, $He+CH_4$, and $He+CO_2$	$\frac{Q_{mix}-Q_{He}}{Q_{He}}=11\%$ for $He+Xe$, $He+CH_4$, and $He+CO_2$

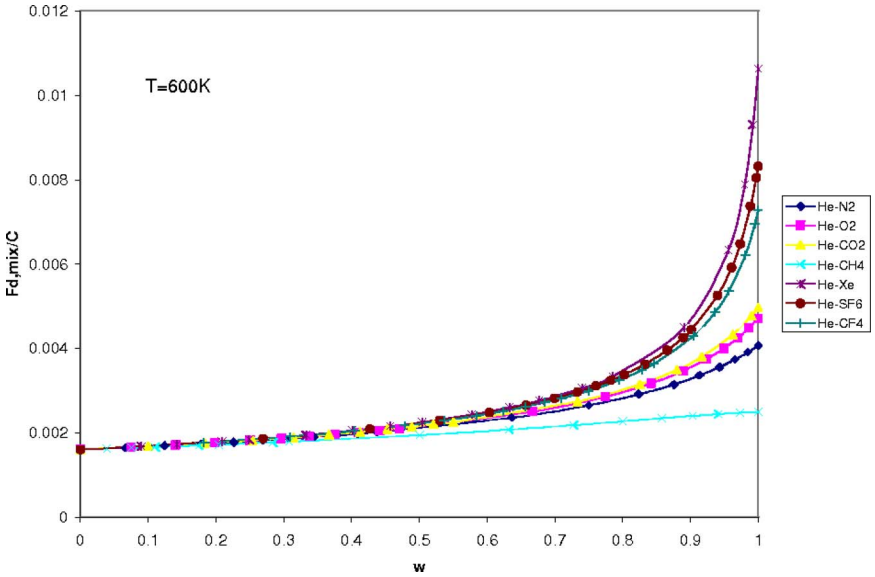

Fig. 4 Influence of the molar gas composition w on the relative drag force $F_{d,\mathrm{mix}}/C$ for the binary gas mixtures at 600 K and 1 atm

in second place, and the $He+CF_4$ mixture in third place. The magnitude of the relative drag forces $F_{d,\mathrm{mix}}/C$ at their respective optimal gas composition w_{opt} are as follows: 0.006 for the $He+SF_6$ mixture at $w_{\mathrm{opt}}=0.96$, 0.0049 for the $He+CF_4$ mixture at $w_{\mathrm{opt}}=0.93$, 0.0033 for the He+Xe mixture at $w_{\mathrm{opt}}=0.74$, 0.0032 for the $He+CO_2$ mixture at $w_{\mathrm{opt}}=0.74$, and 0.0022 for the $He+CH_4$ mixture at $w_{\mathrm{opt}}=0.74$.

7 Trends Manifested by the Binary Gas Mixtures

From the numbers appearing in the figures and tables, it is recognizable that maxima heat transfer rates $Q_{\mathrm{mix,max}}/B$ are provided by some of the seven binary gas mixtures, wherein the secondary gases have the heaviest molar masses (see Tables 1 and 2). As indicated in Table 5, the large molar mass differences $\Delta M_{\mathrm{large}}$ contained between 84 g/mol and 142 g/mol corresponding to the trio of $He+SF_6$, $He+CF_4$, and He+Xe mixtures are capable of maximizing the heat transfer rate. In contrast, the remaining quartet of $He+N_2$, $He+O_2$, $He+CO_2$, and $He+CH_4$ mixtures holding small-to-moderate molar mass differences $\Delta M_{\mathrm{small}}$ grouped between 12 g/mol and 40 g/mol are unable to maximize the heat transfer rate Q_{mix}/B. As a consequence, it may be inferred that their heat transfer attributes are inferior to those of the light primary He.

8 Concluding Remarks

First and foremost, a special correlation equation for binary gas mixtures owing $\mathrm{Pr}\in(0.1,1)$ had to be constructed from the original tabulated data for the broad Prandtl number spectrum spanning from 0.001 to 1000. Based on the seven He-based binary gas mixtures analyzed in this paper at film temperatures of 300 K and 600 K, sharing a pressure of 1 atm, the principal conclusion that may be drawn is that the $He+SF_6$ mixture is unequivocally the best binary gas mixture for laminar boundary layer flows with $\mathrm{Re}<5\times10^5$. This is so regardless of the operating temperature considered. Based on the light primary He gas, the heat transfer enhancement jumps up to 39% for 300 K and up to 68% for 600 K, both quantities being of great significance. As the secondary conclusion, the $He+CF_4$ mixture is the second best binary gas mixture at the two operating temperatures too. In this case, the heat transfer enhancement when referred to He amounts to 24% at 300 K, while at 600 K it is slightly higher reaching 39%. For the same pair of binary gas mixtures $He+SF_6$ and $He+CF_4$, it is evident that the heat transfer enhancements show improvement with elevations in the operating temperature.

Table 5 Molar mass difference ΔM (in ascending order) of the binary gas mixtures

Binary gas mixture	ΔM (g/mol)
$He+CH_4$	12.04
$He+N_2$	24.01
$He+O_2$	28.00
$He+CO_2$	40.01
$He+CF_4$	84.00
He+Xe	127.29
$He+SF_6$	142.06

Nomenclature

A_S = surface area of flat plate (m^2)
B = overall parameter related to Q
B_2 = second virial coefficient (m^3 mol^{-1})
C = overall parameter related to F_d
C_p = mass heat capacity at constant pressure ($J\ kg^{-1}\ K^{-1}$)
C_p^0 = molar heat capacity of an ideal gas at constant pressure ($J\ mol^{-1}\ K^{-1}$)
C_v^0 = molar heat capacity of an ideal gas at constant volume ($J\ mol^{-1}\ K^{-1}$)
$\overline{C_f}$ = average skin friction factor, $\overline{\tau_w}/(\rho u_\infty^2/2)$
F_d = drag force (N)
h = average heat transfer coefficient ($W\ m^{-2}\ K^{-1}$)
L = flat plate length (m)
m = molecular mass (kg)
M_i = molar mass of gas i ($kg\ mol^{-1}$)
$\overline{\mathrm{Nu}_L}$ = average Nusselt number, $\overline{hL}/\lambda$
p = pressure (bar)
P_c = critical pressure (bar)
Pr = Prandtl number, $\eta C_p/\lambda$
Q = heat transfer rate (W)
R = gas constant ($J\ mol^{-1}\ K^{-1}$)

Re_L = length-based Reynolds number, $\rho u_\infty L/\eta$
T = temperature (K)
T_c = critical temperature (K)
T_f = film temperature (K)
T_w = wall temperature (K)
T_∞ = freestream temperature (K)
u_∞ = freestream velocity (m/s)
w = molar gas composition of a binary gas mixture
w_{opt} = optimal molar gas composition of a binary gas mixture
W = flat plate width (m)
x = mole fraction
Z = compressibility factor

Greek Letters

η = viscosity (μPa s)
λ = thermal conductivity (W m^{-1} K^{-1})
ρ = density (kg m^{-3})
$\theta'(0)$ = dimensionless temperature gradient at the plate
$\overline{\tau_w}$ = average wall shear stress (Pa)
ω = Pitzer acentric factor

Subscripts

a = air
mix = binary gas mixture
max = maximum

References

[1] Bergles, A. E., 1999, "Techniques to Enhance Heat Transfer," *Handbook of Heat Transfer*, W. M. Rosehnow and J. P. Hartnett, eds., McGraw-Hill, New York, Chap. 11.
[2] Manglik, R. M., 2003, "Heat Transfer Enhancement," *Heat Transfer Handbook*, A. Bejan and A. D. Kraus, eds., Wiley, New York, Chap. 14.
[3] Bejan, A., 1977, "Study of Entropy Generation in Fundamental Convective Heat Transfer," ASME J. Heat Transfer, **101**, pp. 718–725.
[4] Schlichting, H., and Gersteen, K., 2004, *Boundary Layer Theory*, 8th ed., Springer, Berlin, Germany.
[5] Pohlhausen, K., 1921, "Der Warmeaustausch zwichen festen Korpem und Flussigkeiten mit kleiner Reibung und kleiner Warmeleitung," Z. Angew. Math. Mech., **1**, pp. 115–121.
[6] Suryanarayana, N. V., 1995, *Engineering Heat Transfer*, West Publishing Co., New York.
[7] www.minitab.com
[8] Poling, B. E., Prausnitz, J. M., and O'Connell, J. P., 2001, *The Properties of Gases and Liquids*, McGraw-Hill, New York, pp. A5–A19.
[9] Hirschfelder, J. O., Curtis, C. F., and Bird, R. B., 1964, *Molecular Theory of Gases and Liquids*, Wiley, New York.
[10] Chapman, S., and Cowling, C. F., 1970, *The Mathematical Theory of Non-Uniform Gases*, Cambridge University Press, London, UK.
[11] Bzowski, J., Kestin, J., Mason, E. A., and Uribe, F. J., 1990, "Equilibrium and Transport Properties of Gas Mixtures at Low Density: Eleven Polyatomic Gases and Five Noble Gases," J. Phys. Chem. Ref. Data, **19**, pp. 1179–1232.
[12] Schreiber, M., Vesovic, V., and Wakeham, W. A., 1997, "Thermal Conductivity of Atom-Molecule Dilute Gas Mixtures," High Temp. - High Press., **29**, pp. 653–658.
[13] Dymond, J. H., and Smith, E. B., 1980, *The Virial Coefficients of Pure Gases and Mixtures: A Critical Compilation*, Oxford University Press, London, UK.
[14] Tsonopoulos, C., 1974, "An Empirical Correlation of Second Virial Coefficients," AIChE J., **20**, pp. 263–272.
[15] McQuarrie, D. A., 2000, *Statistical Mechanics*, Harper and Row, New York, pp. 95–137.
[16] www.office.microsoft.com

Forced Convection Heat Transfer Enhancement by Porous Pin Fins in Rectangular Channels

Jian Yang

Min Zeng

Qiuwang Wang[1]
e-mail: wangqw@mail.xjtu.edu.cn

State Key Laboratory of Multiphase Flow in Power Engineering,
School of Energy and Power Engineering,
Xi'an Jiaotong University,
Xi'an, Shaanxi 710049, China

Akira Nakayama
Department of Mechanical Engineering,
Shizuoka University,
3-5-1 Johoku,
Hamamatsu 432-8561, Japan

The forced convective heat transfer in three-dimensional porous pin fin channels is numerically studied in this paper. The Forchheimer–Brinkman extended Darcy model and two-equation energy model are adopted to describe the flow and heat transfer in porous media. Air and water are employed as the cold fluids and the effects of Reynolds number (Re), pore density (PPI) and pin fin form are studied in detail. The results show that, with proper selection of physical parameters, significant heat transfer enhancements and pressure drop reductions can be achieved simultaneously with porous pin fins and the overall heat transfer performances in porous pin fin channels are much better than those in traditional solid pin fin channels. The effects of pore density are significant. As PPI increases, the pressure drops and heat fluxes in porous pin fin channels increase while the overall heat transfer efficiencies decrease and the maximal overall heat transfer efficiencies are obtained at PPI = 20 for both air and water cases. Furthermore, the effects of pin fin form are also remarkable. With the same physical parameters, the overall heat transfer efficiencies in the long elliptic porous pin fin channels are the highest while they are the lowest in the short elliptic porous pin fin channels. [DOI: 10.1115/1.4000708]

Keywords: porous pin fin channel, forced convection, heat transfer enhancement, CFD simulation

1 Introduction

Pin fins have a variety of applications in industry due to their excellent heat transfer performance, e.g., in cooling of electronic components, in cooling of gas turbine blades, and recently, in hot water boilers of central heating systems, etc. [1]. In the two early studies by Sahiti et al. [2,3], it was demonstrated that pin fin arrays offer the most effective way of enhancing the heat transfer rate within a particular heat exchanger volume. However, the pressure drops in such heat exchangers are usually much higher than those in others [1]; this defect greatly lowers the overall heat transfer performances of pin fin heat exchangers and as a result, their applications are restricted. In order to reduce the pressure drops and improve the overall heat transfer performances for pin fin heat exchangers, porous metal pin fin arrays may be used instead of traditional solid metal pin fin arrays.

As porous media can significantly intensify the mixing of fluid flow and increase the contact surface area with fluid inside, it has been regarded as an effective way to enhance heat transfer by using porous media [4]. The flow and heat transfer in porous pin fin heat exchangers for present study can be modeled as forced convective heat transfer in partially filled porous channels. The researches on forced convection with partially filled porous configurations have been investigated extensively in the last years. Hadim [5] studied the laminar forced convection in a fully or partially filled porous channel containing discrete heat sources on the bottom wall. The Brinkman–Forchheimer extended Darcy model were used for the computations. He found that when the width of the heat source and the space between the porous layers were of same magnitudes as the channel height, the heat transfer enhancement in the partially filled channel was almost the same as that in the fully filled porous channel while the pressure drop was much lower. Hadim and Bethancourt [6] later studied the similar problem in a partially filled porous channel. They found that when the heat source width was decreased, there was a moderate increase in heat transfer enhancement and a significant decrease in pressure drop. Huang and Vafai [7] presented a detailed investigation of forced convection in a channel filled with multiple emplaced porous blocks. With comparison of the local Nusselt number distributions between the channel with and without porous blocks, they found that significant heat transfer augmentation can be achieved through the emplacement of porous blocks. Huang et al. [8] later presented a similar investigation in cooling of multiple heated blocks covered with porous media. The results showed that significant cooling augmentation of the blocks can be achieved through the cover of finite-sized porous substance. Other similar studies of forced convection in a channel filled with porous blocks can also be found in Refs. [9,10]. Besides porous block, porous baffles are also popular for heat transfer enhancement applications. Ko and Anand [11] experimentally studied the heat transfer enhancement in a rectangular channel by using a porous baffle made up of aluminum foam. The experiments showed that the use of porous baffles resulted in heat transfer enhancement as high as 300% compared with heat transfer in straight channel with no baffles and the heat transfer enhancement ratio was found to be higher for taller and thicker porous baffles. Furthermore, Yang and Huang [12] presented a numerical prediction on the turbulent fluid flow and heat transfer characteristics for rectangular channel with porous baffles. They found that, both the solid and porous baffles walls enhanced the heat transfer relative to the smooth channel while the porous baffle channel has a lower friction factor due to less channel blockage.

According to above studies, it can be concluded that with proper selection of governing parameters, significant heat transfer augmentation and pressure drop reduction can be achieved simultaneously in partially filled porous channels. Therefore, we could believe that the overall heat transfer performance of porous pin fin heat exchangers with proper configurations would be better than that of traditional solid pin fin heat exchangers. On account of this

[1]Corresponding author.

Contributed by the Heat Transfer Division of ASME for publication in the JOURNAL OF HEAT TRANSFER. Manuscript received January 8, 2009; final manuscript received November 7, 2009; published online March 5, 2010. Assoc. Editor: S. A. Sherif.

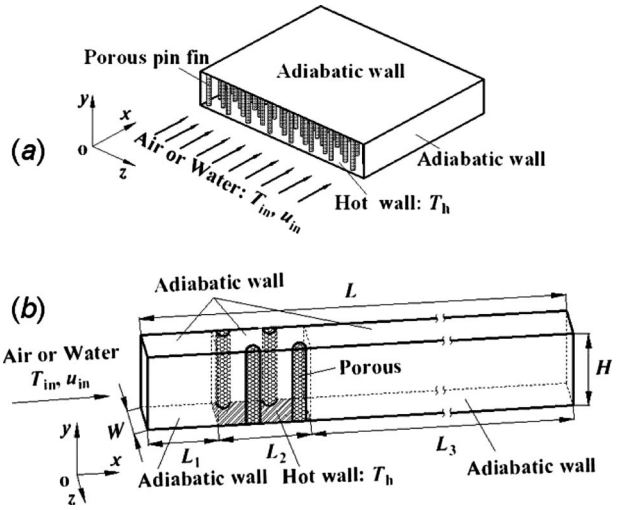

Fig. 1 Physical model: (*a*) porous pin fin heat sink and (*b*) representative computational domain

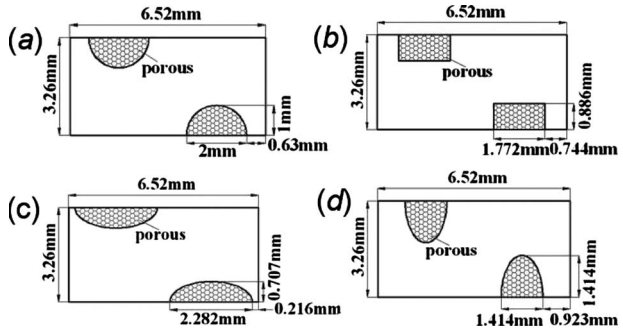

Fig. 2 Different forms of porous pin fin cross-section: (*a*) circular form, (*b*) cubic form, (*c*) long elliptic form, and (*d*) short elliptic form

reason, in our previous study as reported by Yang et al. [13], we performed a comprehensive numerical study on forced convection heat transfer in three-dimensional (3D) porous pin fin channels with air as the cold fluid. We found that with the proper selection of governing parameters, the pressure drops in porous pin fin channels were much lower than those in solid pin fin channels while the heat fluxes and the overall heat transfer efficiencies were much higher. The overall heat transfer efficiencies in long elliptic porous pin fin channels were the best and the maximal values were obtained at $K=2\times10^{-7}$ m^2. These findings could be useful for understanding and optimizing the flow and heat transfer performances in porous pin fin heat exchangers. However, it was noted that, in our previous study [13], the permeability (K) and inertial coefficient (c_F) in the momentum equation were modeled with Ergun equation [14] and the volumetric heat transfer coefficient (h_v) in the energy equation was calculated with Wakao equation [15]. This would be reasonable for the flow and heat transfer in the packed beds of particles while for the porous media with high porosity ($\phi=0.9$), such as metal foams, the applicability of the Ergun equation and Wakao equation would be questionable. Furthermore, in the work of Yang et al. [13], only air was investigated and the performances for other fluids are still unknown, which would also be important for applications. With these motivations in the present study, we further study the forced convection heat transfer in three-dimensional porous pin fin channels and the performances for both air and water are carefully compared. According to the authors' knowledge, almost no such attentions have been paid on this subject before. The Forchheimer–Brinkman extended Darcy model and two-equation energy model with more reasonable model parameters (K, c_F, and h_v) for porous media are employed and the effects of Reynolds number, pore density, and pin fin form are studied in detail.

2 Physical Model and Computational Method

2.1 Physical Model and Dimensions. As shown in Fig. 1(*a*), the physical model is derived from traditional pin fin heat sink, which generally consists of a bottom wall, two side walls, a top wall, and a pin fin array. The bottom wall is hot and its temperature is kept at T_h. The side and the top walls are kept adiabatic. The pin fin array is made of high porosity metal foams (aluminum) and arranged in stagger; air and water are used as the cold fluids. In order to obtain a basic understanding of flow and heat transfer performances in porous pin fin heat exchangers, a simplified porous pin fin channel with appropriate boundary conditions is adopted for the computations, which can be regarded as forced convection heat transfer in a partially filled porous channel (Hadim [5], Huang and Vafai [7], and Yang et al. [13]). The computational domain is depicted in Fig. 1(*b*), which is composed of a developing inlet block ($L_1=10$ mm), two pin fin array unit cells ($L_2=2\times6.52$ mm), and a developing outlet block ($L_3=70$ mm). The dimensions of the computational domain are $L(93.04\ \text{mm})\times W(3.26\ \text{mm})\times H(10\ \text{mm})$ for air and $L(93.04\ \text{mm})\times W(3.26\ \text{mm})\times H(2\ \text{mm})$ for water, where the channel height (H) for water is much lower due to its higher heat transfer capacity. The total area of pin fin cross-sections over the base wall area in single pin fin array unit cell is 15%, which is reasonable for industry applications. The temperature and velocity of inlet are kept at T_{in} and u_{in}, respectively. The bottom wall of pin fin array unit cells is the hot wall and the temperature is kept at T_h. Two other bottom walls and all top walls are kept adiabatic. The symmetry boundary conditions are adopted for two side walls and the flow and heat transfer of outlet are considered to be fully developed. Furthermore, four different kinds of porous pin fins with circular, cubic, long elliptic, and short elliptic cross-section forms are employed to investigate the pin fin configuration effects and the cross-section areas of different pin fins are identical with each other ($A_{pin}=3.14\ \text{mm}^2$). The physical dimensions and cross-section forms of different porous pin fins are presented in Fig. 2.

2.2 Governing Equations and Computational Method. The flow in the computational domain is considered to be three-dimensional, laminar, incompressible, and steady for both clear fluid and porous regions. For clear fluid region, the flow and heat transfer are modeled with Navier–Stokes and energy equations. For porous region, the metal foams are assumed to be homogeneous, isotropic, high porosity ($\phi=0.9$), and high thermal conductivity (aluminum: $k_s=238\ \text{W m}^{-1}\text{K}^{-1}$). The Forchheimer–Brinkman extended Darcy model [16] is adopted to simulate the flow in porous media, where the inertia and viscosity effects are considered. Furthermore, the porous matrix is assumed to be in local thermal nonequilibrium with fluid phase inside due to their large thermal conductivity difference. Therefore, the two-equation energy model [16] is employed to account for the heat transfer between porous matrix and fluid inside. The conservation equations for mass, momentum, and energy are as follows.

Continuity

$$\nabla \cdot \boldsymbol{V} = 0 \tag{1}$$

Momentum

$$\begin{cases} \text{Clear fluid region: } \boldsymbol{V}\cdot\nabla\boldsymbol{V} = -\dfrac{1}{\rho_f}\nabla p + v_f\nabla^2\boldsymbol{V} \\ \text{Porous region: } \dfrac{1}{\phi^2}(\boldsymbol{V}\cdot\nabla)\boldsymbol{V} = -\dfrac{1}{\rho_f}\nabla p + \dfrac{v_f}{\phi}\nabla^2\boldsymbol{V} - \dfrac{v_f}{K}\boldsymbol{V} - \dfrac{c_F}{\sqrt{K}}|\boldsymbol{V}|\boldsymbol{V} \end{cases} \tag{2}$$

Energy

$$\begin{cases} \text{Clear fluid region: } (\rho c_p)_f(\boldsymbol{V}\cdot\nabla T_f) = \nabla\cdot(k_f\nabla T_f) \\ \text{Porous region: } \begin{cases} \text{fluid phase: } (\rho c_p)_f(\boldsymbol{V}\cdot\nabla T_f) = \phi\nabla\cdot(k_f\nabla T_f) + h(T_s - T)_f \\ \text{porous matrix: } 0 = (1\text{-}\phi)\nabla\cdot(k_s\nabla T_s) + h_v(T_f\text{-}T_s) \end{cases} \end{cases} \tag{3}$$

where $\boldsymbol{V}$ is the velocity vector. T_f and T_s are the temperatures of the fluid and porous matrix, respectively. ϕ is the porosity. The permeability (K), Forchheimer coefficient (c_F), and volumetric heat transfer coefficient (h_v) are calculated with following correlations developed from high porosity metal foams by Bhattacharya et al. [17] and Calmidi and Mahajan [18].

$$\begin{cases} K = 0.00926\cdot\dfrac{\phi}{\chi - 1}\cdot d_p^2 \\ c_F = 0.0095\cdot G^{-0.8}\sqrt{\dfrac{\phi}{3(\chi-1)}}\left(1.18\sqrt{\dfrac{(1-\phi)}{3\pi}}\dfrac{1}{G}\right)^{-1} \\ h_v = \dfrac{3\pi d_f G}{(0.59 d_p)^2}\cdot\dfrac{k_f(0.52\mathrm{Pr}^{0.37}(|\boldsymbol{V}|d_f/\nu_f)^{0.5})}{d_f} \end{cases} \tag{4}$$

where Pr is the Prandtl number with the definition of Pr $= \nu_f/(k/\rho\cdot c_p)_f$. ν_f is the kinetic viscosity of fluid and k_f is the thermal conductivity of fluid. d_p and d_f are the pore size and fiber diameter of the metal foams, respectively. χ is the tortuosity of the porous matrix and G is a shape function that takes into account the variation in fiber cross-section with porosity. The definitions of d_p, d_f, χ, and G are as follows:

$$d_p = 0.0254/\mathrm{PPI}; \quad d_f = 1.18\sqrt{\frac{(1-\phi)}{3\pi}}\frac{d_p}{G};$$

$$\chi = \left[\frac{\pi}{4\phi}\left(1 - \left(1.18\sqrt{\frac{(1-\phi)}{3\pi}}\frac{1}{G}\right)^2\right)\right]^{-1};$$

$$G = 1 - \exp(-(1-\phi)/0.04) \tag{5}$$

where PPI is the pore density of the metal foams.

Boundary conditions

$$\begin{cases} x = 0 & T_f = T_{\mathrm{in}}, \quad u = u_{\mathrm{in}}, \quad v = w = 0 \\ x = L & \dfrac{\partial T_f}{\partial x} = 0, \quad \dfrac{\partial u}{\partial x} = \dfrac{\partial v}{\partial x} = \dfrac{\partial w}{\partial x} = 0 \\ y = 0 & \dfrac{\partial T_f}{\partial y} = 0 (0 < x < L_1, L_2 < x < L), \quad T_f = T_h (L_1 \le x \le L_2) \\ & T_s = T_h \text{ (porous region)}, \quad u = v = w = 0 \\ y = H & \dfrac{\partial T_f}{\partial y} = 0, \quad \dfrac{\partial T_s}{\partial y} = 0 \text{ (porous region)}, \quad u = v = w = 0 \\ z = 0, W & \dfrac{\partial T_f}{\partial z} = 0, \quad \dfrac{\partial T_s}{\partial z} = 0 \text{ (porous region)}, \quad \dfrac{\partial u}{\partial z} = \dfrac{\partial v}{\partial z} = 0, w = 0 \end{cases}$$

The thermal physical quantities of interest in present investigation are the heat flux of the hot wall (q), the pressure drop (Δp), the overall heat transfer efficiency (γ), and the heat transfer performance ratio (γ'), which are defined as follows:

$$q = \frac{(\rho c_p)_f\cdot u_{\mathrm{in}}\cdot A_{\mathrm{in}}\cdot(T_{\mathrm{out}} - T_{\mathrm{in}})}{A_h}; \quad \Delta p = p_{\mathrm{in}} - p_{\mathrm{out}}; \quad \gamma = \frac{q}{\Delta p};$$

$$\gamma' = \frac{(\mathrm{Nu}_{\mathrm{hav},p}/\mathrm{Nu}_{\mathrm{hav},s})}{(f_p/f_s)^{1/3}} \tag{6}$$

where A_{in} is the area of inlet. A_h is the base area of hot wall and T_{out} is the average temperature of outlet. $\mathrm{Nu}_{\mathrm{hav}}$ is the average Nusselt number of the hot wall. f is the friction factor. The subscripts "p" and "s" represent values obtained in porous and solid

Table 1 Hot wall heat flux, pressure drop, and overall heat transfer efficiency in circular porous pin fin channel with different grids (ϕ=0.9, PPI=30, T_{in}=293 K, T_h=343 K, Pr=0.7, Re=2291)

Total elements	94,809	297,864	766,080
q/kW m^{-2}	25.17	25.05	25.02
Δp/Pa	5.59	5.86	5.93
γ/kW m^{-2} Pa^{-1}	4.50	4.27	4.22

pin fin channels, respectively. The Nusselt number (Nu_{hav}) and friction factor (f) are defined as follows:

$$Nu_{hav} = \frac{q \cdot D}{(T_h - (T_{in} + T_{out})/2) \cdot k_f}; \quad f = \frac{(\Delta p/L) \cdot D}{1/2 \cdot (\rho_f u_{in}^2)} \tag{7}$$

where $D=2H$ is the hydraulic diameter of inlet.

The Reynolds number (Re) is defined as follows:

$$Re = \frac{u_{in} \cdot D}{\nu_f} \tag{8}$$

The Darcy Number (Da) and average Nusselt number (Nu_{av}) in the middle section ($z=0.5W$) of each heater for model validations (see Figs. 4 and 5) are defined as follows:

$$Da = \frac{K}{H^2}; \quad Nu_{av} = \left. \frac{q' \cdot H}{(T_{hav} - T_{in}) \cdot k_f} \right|_{y=0, \quad z=0.5W} \tag{9}$$

where K is the permeability of porous blocks, H is the channel height, q' is the constant heat flux of each heater, k_f is the thermal conductivity of fluid, T_{in} is the temperature of inlet, and T_{hav} is the average temperature in the middle section ($y=0$, $z=0.5W$) of each heater.

The governing equations (Eqs. (1)–(3)) for the computational domain are solved with commercial code CFX10. The convective term in momentum equations is discretized with high resolution scheme. The continuity and momentum equations are solved together with coupled solver based on finite control volume method and the discrete equations are solved with multigrid accelerated incomplete lower upper factorization technique (CFX 10 [19]). The user-define expressions for the additional energy equation of porous matrix (T_s) and source terms of interphase heat transfer in both energy equations of fluid and porous matrix (T_f and T_s, Eq. (3)) are developed and compiled with CFX expression language. Furthermore, the conservative interface flux conditions for mass, momentum, and heat transfer are adopted at the interfaces between clear fluid and porous regions. For convergence criteria, the relative variations in temperature and velocity between two successive iterations are demanded to be smaller than the previously specified accuracy levels of 1.0×10^{-6}.

3 Grid Independence Test and Model Validation

Before proceeding further, the grids used for present study are checked at first. As shown in Fig. 2(a), the circular porous pin fin model is selected for the test and the computational parameters are kept constant with ϕ=0.9, PPI=30, T_{in}=293 K, T_h=343 K, Pr=0.7, and Re=2291 (Air: u_{in}=2 m s^{-1}). In present test, a multiblock, O-type, structural grid with hexahedral elements is used and the grid is intensified on solid walls and pin fin regions. The total numbers of grid elements vary from 94,809 to 766,080 and the computational results are presented in Table 1. It shows that, the grid with total element number of 297,864 is good enough for the test case with the maximal lengths of the grid elements of being 0.47 mm for central flow region and 0.1 mm for near wall flow region. Therefore, similar grids are finally employed for the following studies and the total numbers of grid elements for different pin fin models are listed in Table 2.

Table 2 Computational grids for different pin fin models

Pin fin models	Circular	Cubic	Long elliptic	Short elliptic
Total elements (air)	297,864	320,040	298,410	316,512
Total elements (water)	147,920	173,580	179,200	179,120

Furthermore, the reliability and accuracy of present computational models and method are validated. According to the authors' knowledge, most studies of forced convection heat transfer in partially filled porous channels were based on two-dimensional (2D) model and almost no three-dimensional researches have been reported on this subject before. Therefore, a two-dimensional similar problem as reported by Hadim [5] (see Fig. 3(a)) is finally selected for the validations. In the present study, the 2D partially filled porous channel [5] is extended along z coordinate with width of $W=10H$ and a reasonable 3D physical model is finally obtained for the computation (see Fig. 3(b)). The 3D partially filled porous channel with dimensions of $L \times H \times W$ is equipped with four porous blocks and each block is heated at bottom with constant heat flux. The inlet temperature and velocity are kept constant and all other walls are kept adiabatic. The computational model and method used for this problem are similar to those presented in Sec. 2 and the predicted average Nusselt numbers (Nu_{av}) in the middle sections ($y=0$, $z=0.5W$) of different heaters are compared with those as reported in Ref. [5] (see Fig. 4). The average deviation of Nu_{av} is 3.5%. This indicates that the computational models and method presented in the present study are reliable and capable of modeling flow and heat transfer phenomena in 3D partially filled porous channels.

4 Results and Discussion

4.1 Performance Comparison for Solid and Porous Pin Fin Models. First, the flow and heat transfer performances in solid and porous pin fin channels are compared. The circular pin fin form (see Fig. 2(a)) is selected for present study. Air (Pr=0.7) and water (Pr=3.9) are used as cold fluids and the Reynolds number (Re) varies from 1000 to 2291 with ϕ=0.9, PPI=30, T_{in}=293 K, and T_h=343 K.

The temperature distributions in solid and porous pin fin channels are shown in Fig. 5. It shows that the internal temperatures of

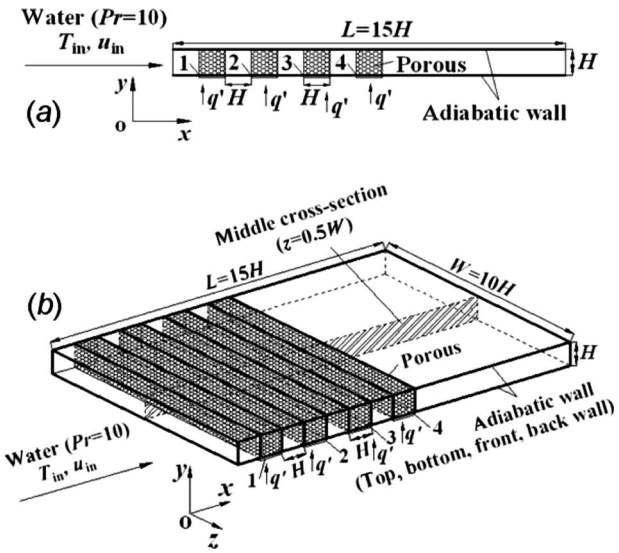

Fig. 3 Physical models for model validation: (*a*) 2D physical model reported in Ref. [5] and (*b*) 3D physical model used for present computation (based on (*a*))

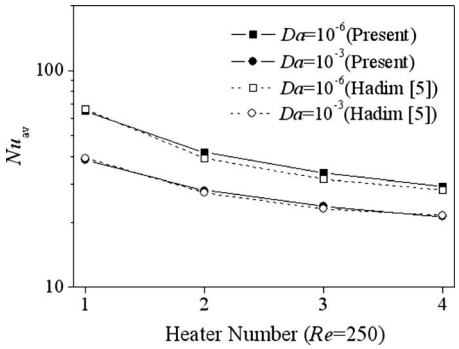

Fig. 4 Comparison of average Nusselt number of each heater with Ref. [5]

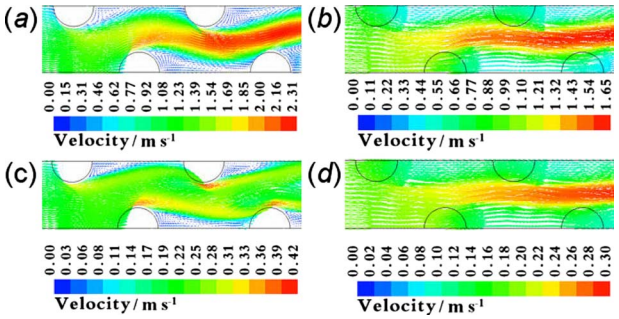

Fig. 6 Velocity vector distributions in solid and porous pin fin channels (ϕ=0.9, PPI=30, Re=1000): (*a*) solid pin fin channel (air: *y*=5 mm), (*b*) porous pin fin channel (air: *y*=5 mm), (*c*) solid pin fin channel (water: *y*=0.5 mm), and (*d*) porous pin fin channel (water: *y*=0.5 mm)

solid pin fins are quite uniform and the average temperatures are high, which are 342.0 K for air case and 340.4 K for water case, respectively, while the internal temperatures of porous pin fins are not so uniform and the average temperatures are much lower, which are 330.1 K for air case and 308.2 K for water case, respectively. However, the fluid temperatures in porous pin fin channels are higher than those in solid pin fin channels. The average fluid temperatures in porous pin fin channels are 311.0 K for air and 297.7 K for water while they are 308.2 K and 296.4 K in solid pin fin channels. These results indicate that more heats can be transported away by using porous pin fins and their heat transfer performances would be better. This is because the porous pin fins can greatly enlarge the contact surface areas and mix the fluid flow inside, which may lead to significant heat transfer enhancements. The velocity vector distributions in solid and porous pin fin channels are presented in Fig. 6. It shows that with the same Reynolds number, the fluid velocities in solid pin fin channels are much higher than those in porous pin fin channels for both air and water cases. Large vortices are formed behind solid pin fins while no such vortices are found in porous pin fin channels. In solid pin fin channels, the solid pin fins are totally impermeable and this would narrow the flow passages and enhance the flow tortuosities inside. While in porous pin fin channels, the porous pin fins are permeable and the fluid can flow through them directly. This would widen the flow passages and lower the flow tortuosities inside. Therefore, the flow resistances and pressure drops in porous pin fin channels would be lower.

The variations in pressure drop (Δp), hot wall heat flux (q), overall heat transfer efficiency (γ), and heat transfer performance ratio (γ') with Reynolds number are presented in Fig. 7. It shows that the pressure drops in porous pin fin channels are much lower than those in solid pin fin channels (36.9% lower for air and 9.5% lower for water at Re=2291, see Fig. 7(*a*)) while the heat fluxes in porous pin fin channels are much higher than those in solid pin fin channels (38.6% higher for air and 45.7% higher for water at Re=2291, see Fig. 7(*a*)). Therefore, the overall heat transfer efficiencies in porous pin fin channels are much higher (119.5% higher for air and 37.9% higher for water at Re=2291, see Fig. 7(*b*)). It is also obvious that as Re increases from 1000 to 2291, all

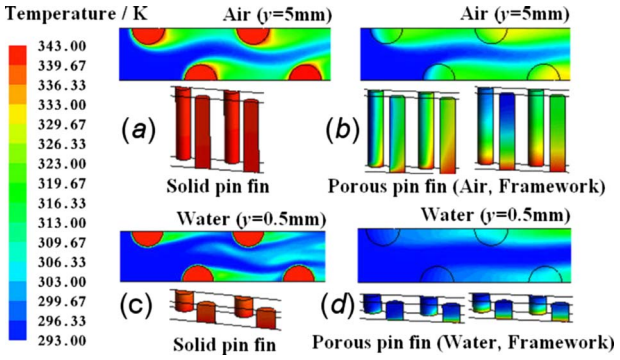

Fig. 5 Temperature distributions in solid and circular porous pin fin channels (ϕ=0.9, PPI=30, Re=1000): (*a*) solid pin fin channel with air, (*b*) porous pin fin channel with air, (*c*) solid pin fin channel with water, and (*d*) porous pin fin channel with water

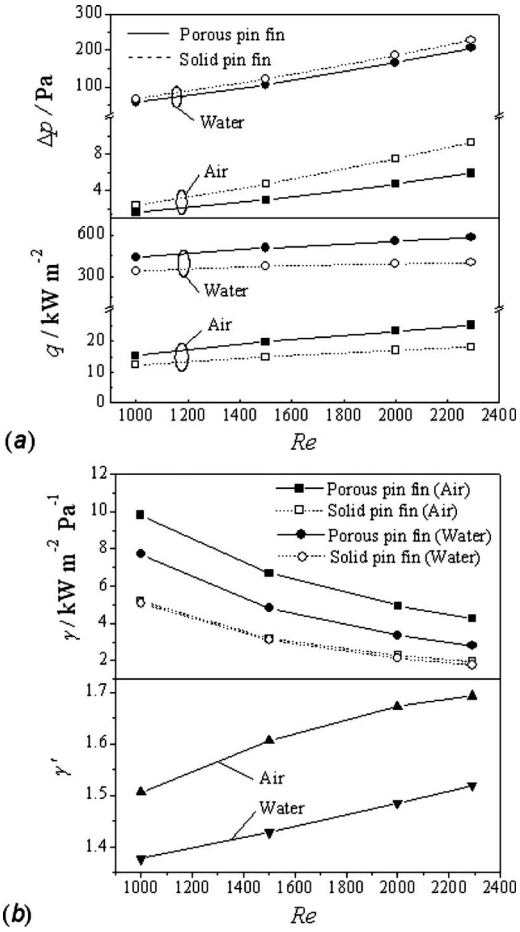

Fig. 7 Variations in pressure drop, hot wall heat flux, overall heat transfer efficiency, and heat transfer performance ratio with Re in solid and porous pin fin channels (ϕ=0.9, PPI=30): (*a*) pressure drop and hot wall heat flux and (*b*) overall heat transfer efficiency and heat transfer performance ratio

Table 3 Characteristics of metal foams

Sample	ϕ	PPI	d_p/m	d_f/m	K/m^2	c_f	k_s/W m^{-1} K^{-1}
1	0.9	20	1.3×10^{-3}	1.7×10^{-4}	7.91×10^{-8}	0.102	238
2	0.9	25	1.0×10^{-3}	1.3×10^{-4}	5.06×10^{-8}	0.102	238
3	0.9	30	8.5×10^{-4}	1.1×10^{-4}	3.51×10^{-8}	0.102	238
4	0.9	35	7.3×10^{-4}	9.6×10^{-5}	2.58×10^{-8}	0.102	238
5	0.9	40	6.4×10^{-4}	8.4×10^{-5}	1.98×10^{-8}	0.102	238

the values of heat transfer performance ratios (γ') are larger than unit for both air and water cases (see Fig. 7(*b*)), which means that with the same pumping powers, the heat transfer performances in porous pin fin channels are also much better than those in solid pin fin channels. These results are consistent with the former analysis of temperature and flow variations, which confirms the point that with proper selection of physical parameters, the heat transfer augmentations and flow resistance reductions can be achieved simultaneously and the overall heat transfer performances will be significantly improved by using porous pin fins. Furthermore, it can be found that with different fluids, the flow and heat transfer performances are different. With the same Reynolds number, the pressure drops and heat fluxes in porous pin fin channels for water are much higher than those for air while the overall heat transfer efficiencies and heat transfer performance ratios are much lower. Due to the intrinsic thermophysical differences between air and water, the viscosity and heat transfer capacity of water are much higher, which would lead to higher pressure drops and heat fluxes. However, due to the same reasons, when water is used as cold fluid, most heats will be transported away just through the lower parts of the porous pin fins and the heat transfers in the upper parts of the porous pin fins are inactive (see Fig. 5(*d*)). Therefore, the overall utilization ratios of the porous fins are low for water, which would lead to lower overall heat transfer efficiencies and heat transfer performance ratios.

4.2 The Effect of Pore Density. In this section, the effect of pore density (PPI) for different metal foams is investigated. The circular pin fin form (see Fig. 2(*a*)) is selected again for present computations. Both air (Pr=0.7) and water (Pr=3.9) are used as cold fluids. In the present study, five different kinds of high porosity metal foams with $20\leq \text{PPI}\leq 40$ are selected for the computations, which are similar to those as studied by Bhattacharya et al. [17] and Calmidi and Mahajan [18]. These metal foams would also be common in industry applications and their characteristics are presented in Table 3. Furthermore, besides PPI, the other parameters are kept at constant with $\phi=0.9$, $T_{\text{in}}=293$ K, $T_h=343$ K, and Re=2291.

The variations in pressure drop (Δp), hot wall heat flux (q), and overall heat transfer efficiency (γ) with pore density (PPI) are presented in Fig. 8. It shows that, as PPI increases from 20 to 40, the pressure drops and heat fluxes in porous pin fin channels increase for both air and water cases while the overall heat transfer efficiencies decrease. This is because, as PPI increases, the permeability (K) decreases rapidly and the viscosity effects inside porous media increase, which would lead to increases in pressure drops. Meanwhile, as PPI increases, the solid-fluid interfacial surface areas inside porous media also increase quickly and the volumetric heat transfer coefficient (h_v) between porous matrix and fluid phase increases, which would lead to increases in heat fluxes. As PPI increases from 20 to 40, the pressure drops in the porous pin fin channels increase by 52.9% and 24.2% for air and water, respectively, and the corresponding heat fluxes increase by 15.6% and 21.1%. It is obvious that the increase rates of pressure drops are much higher than those of heat fluxes, especially when air is used as cold fluid. Therefore, as PPI increases, the overall heat transfer efficiencies decrease. Furthermore, with different pore densities ($20\leq \text{PPI}\leq 40$), the pressure drops in porous pin fin channels are lower than those in solid pin fin channels (50.5% lower for air and 20.2% lower for water at PPI=20) while the heat fluxes in porous pin fin channels are higher (23.4% higher for air and 30.1% higher for water at PPI=20). Therefore, the overall heat transfer efficiencies (γ) in porous pin fin channels are much higher and their maximal values are obtained at PPI=20, which are 149.2% and 63.1% higher than those in solid pin fin channels for air and water cases, respectively. These results indicate that with proper selection of pore density, the flow and heat transfer performances in porous pin fin channels will be improved.

4.3 The Effect of Porous Pin Fin Form. Finally, the effect of porous pin fin form is examined. Four different kinds of porous pin fins are compared here, including circular, cubic, long elliptic, and short elliptic cross-section forms (see Fig. 2). Air (Pr=0.7) and water (Pr=3.9) are used as cold fluids and the Reynolds number (Re) varies from 1000 to 2291 with $\phi=0.9$, PPI=40, $T_{\text{in}}=293$ K, and $T_h=343$ K.

The temperature distributions in different porous pin fin channels are presented in Figs. 9 and 10. It shows that, the temperature distributions in circular and cubic porous pin fin channels are similar while they are quite different in long elliptic and short elliptic porous pin fin channels for both air and water cases. The average temperatures of air are 311.09 K, 311.30 K, 307.07 K, and 316.18 K in circular, cubic, long elliptic, and short elliptic porous pin fin channels, respectively, and they are 298.13 K, 298.11 K, 297.75 K, and 298.50 K for water, respectively. It is obvious that, the average temperatures of air and water in short elliptic porous pin fin channels are the highest and they are the lowest in long elliptic porous pin fin channels. The flows in short elliptic porous pin fin channels are intensively mixed and most of the fluids in the channels, including central flow regions, have taken part in heat transfer actively while in long elliptic porous pin fin channels, the

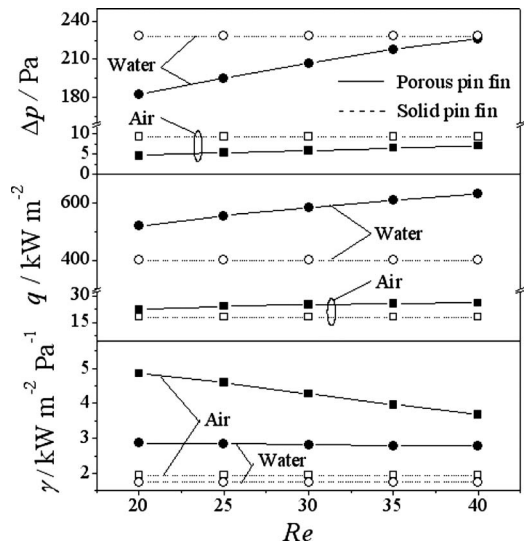

Fig. 8 Variations in pressure drop, hot wall heat flux, and overall heat transfer efficiency with pore density ($\phi=0.9$, Re=2291)

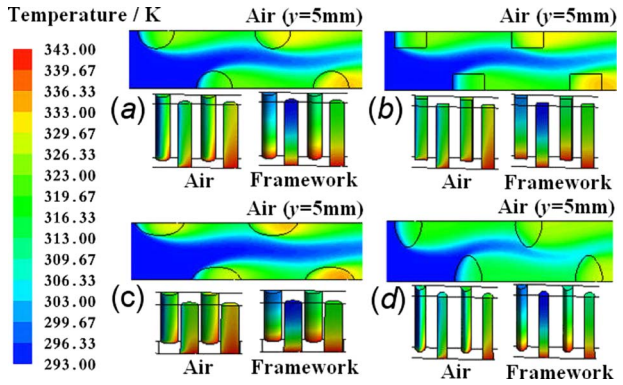

Fig. 9 Temperature distributions in different porous pin fin channels with air (ϕ=0.9, PPI=40, Pr=0.7, Re=1000): (*a*) circular pin fin channel, (*b*) cubic pin fin channel, (*c*) long elliptic pin fin channel, and (*d*) short elliptic pin fin channel

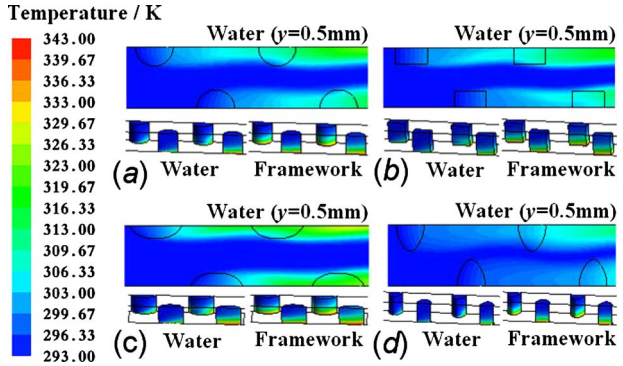

Fig. 10 Temperature distributions in different porous pin fin channels with water (ϕ=0.9, PPI=40, Pr=3.9, Re=1000) (*a*) circular pin fin channel, (*b*) cubic pin fin channel, (*c*) long elliptic pin fin channel, and (*d*) short elliptic pin fin channel

flows are less mixed, the central flow regions are almost not disturbed. Therefore, the heat transfers in short elliptic porous pin fin channels would be the highest. However, with the same reasons, the pressure drops in short elliptic porous pin fin channels would also be the highest.

The variations in pressure drop (Δp), hot wall heat flux (q), and overall heat transfer efficiency (γ) with Reynolds number are presented in Figs. 11 and 12. It shows that with the same Reynolds number, the pressure drops and heat fluxes in short elliptic porous pin fin channels are the highest and they are the lowest in long elliptic porous pin fin channels. The differences in pressure drops between each other are 95.9% and 48.7% for air and water cases at Re=2291, respectively, and the corresponding differences in heat fluxes are 60.6% and 14.3%. However, the variations in overall heat transfer efficiencies (γ) are reverse, which are the highest in long elliptic porous pin fin channels and lowest in short elliptic porous pin fin channels and the differences between each other are 21.9% and 30.1% for air and water cases at Re=2291, respectively. These results indicate that, with proper selection of porous pin fin forms, the overall heat transfer performances in porous pin fin channels will be greatly improved and optimized.

5 Conclusions

The forced convective heat transfer in three-dimensional porous pin fin channels is numerically studied in this paper. Both air and water are used as the cold fluids and the effects of Reynolds number, pore density, and pin fin form are carefully investigated.

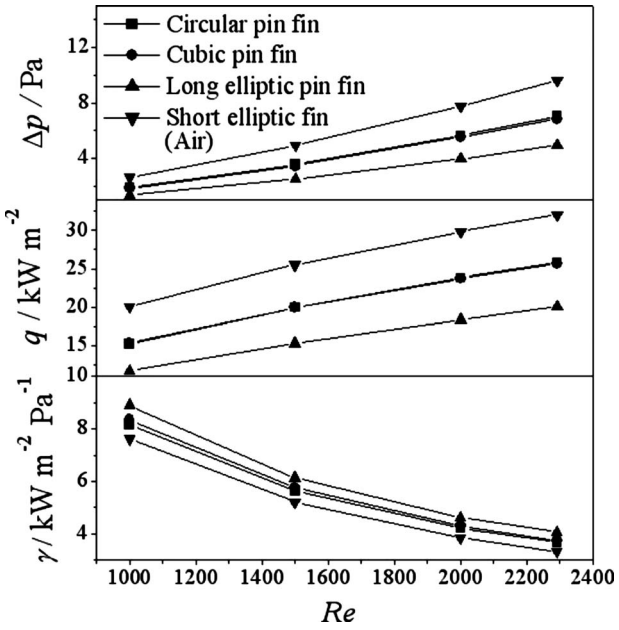

Fig. 11 Variations in pressure drop, hot wall heat flux and overall heat transfer efficiency with Re in different porous pin fin channels (ϕ=0.9, PPI=40, Pr=0.7)

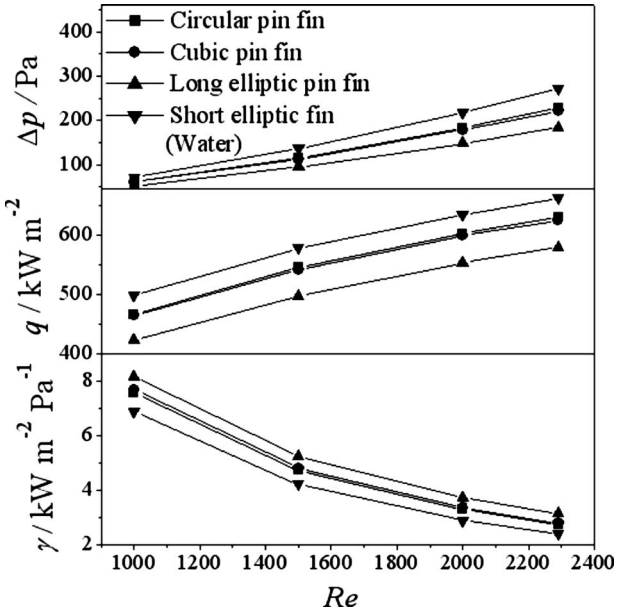

Fig. 12 Variations in pressure drop, hot wall heat flux and overall heat transfer efficiency with Re in different porous pin fin channels (ϕ=0.9, PPI=40, Pr=3.9)

The flow and heat transfer performances in porous pin fin channels are also compared with those in traditional solid pin fin channels in detail. The major findings are as follows.

(1) With proper selection of metal foams, such as PPI=30, significant heat transfer enhancements and pressure drop reductions can be achieved simultaneously by using porous pin fins for both air and water cases, and the overall heat transfer efficiencies in porous pin fin channels are much higher than those in solid pin fin channels, which are 119.5% and 37.9% higher for air and water cases at Re=2291, respectively.

(2) The effects of pore density are significant. As pore density increases from 20 to 40, the maximal overall heat transfer efficiencies are obtained at PPI=20 for both air and water cases, which are 149.2% and 63.1% higher than those in solid pin fin channels at Re=2291, respectively.
(3) The effects of pin fin form are also remarkable. With same physical parameters, the pressure drops and heat fluxes are the highest in short elliptic porous pin fin channels and lowest in long elliptic porous pin fin channels while the overall heat transfer performances are the highest in long elliptic porous pin fin channels and lowest in short elliptic porous pin fin channels. The differences in overall heat transfer efficiencies between each other are 21.9% for air case and 30.1% for water case at PPI=40 and Re=2291, respectively.

Acknowledgment

We would like to acknowledge financial support for this work provided by the National Natural Science Foundation of China (Grant No. 50821064).

Nomenclature

A = area (m^2)
c_F = Forchheimer coefficient, Eq. (4)
c_p = specific heat at constant pressure ($J\ kg^{-1}\ K^{-1}$)
D = hydraulic diameter of inlet (m)
Da = Darcy number, Eq. (9)
d_f = fiber diameter of metal foam (m)
d_p = pore size of metal foam (m)
f = friction factor, Eq. (7)
G = shape function for metal foam, Eq. (5)
H = channel height (m)
h_v = volumetric heat transfer coefficient, Eq. (4) ($W\ m^{-3}\ K^{-1}$)
K = permeability, Eq. (4) (m^2)
k = thermal conductivity ($W\ m^{-1}\ K^{-1}$)
L = total channel length (m)
L_1 = length of developing inlet block (m)
L_2 = length of hot wall (m)
L_3 = length of developing outlet block (m)
Nu_{av} = average Nusselt number, Eq. (9)
Nu_{hav} = average Nusselt number of hot wall, Eq. (8)
p = pressure (Pa)
PPI = pore density
Pr = Prandtl number
q = heat flux of hot wall, Eq. (6) ($W\ m^{-2}$)
q' = constant heat flux of each heater, Eq. (9)
Re = Reynolds number, Eq. (8)
T = temperature (K)
u,v,w = velocity in x, y, z directions ($m\ s^{-1}$)
$\boldsymbol{V}$ = velocity vector ($m\ s^{-1}$)
W = channel width (m)
x,y,z = coordinate directions (m)

Greek Symbols

γ = overall heat transfer efficiency, Eq. (6) ($W\ m^{-2}\ Pa^{-1}$)
γ' = heat transfer performance ratio, Eq. (6)
ν = kinetic viscosity ($m^{-2}\ s^{-1}$)
ρ = density ($kg\ m^{-3}$)
ϕ = porosity
χ = tortuosity of porous matrix, Eq. (5)

Subscripts

f = fluid phase, fiber
h = hot wall
hav = average value of each heater
in = inlet
out = outlet
p = value obtained in porous pin fin channel
pin = pin fin cross-section
s = solid phase, value obtained in solid pin fin channel

References

[1] Sahiti, N., Lemouedda, A., Stojkovic, D., Durst, F., and Franz, E., 2006, "Performance Comparison of Pin Fin In-Duct Flow Arrays With Various Pin Cross-Sections," Appl. Therm. Eng., **26**, pp. 1176–1192.
[2] Sahiti, N., Durst, F., and Dewan, A., 2005, "Heat Transfer Enhancement by Pin Elements," Int. J. Heat Mass Transfer, **48**, pp. 4738–4747.
[3] Sahiti, N., Durst, F., and Dewan, A., 2006, "Strategy for Selection of Elements for Heat Transfer Enhancement," Int. J. Heat Mass Transfer, **49**, pp. 3392–3400.
[4] Jiang, P. X., Li, M., Lu, T. J., Yu, L., and Ren, Z. P., 2004, "Experimental Research on Convection Heat Transfer in Sintered Porous Plate Channels," Int. J. Heat Mass Transfer, **47**, pp. 2085–2096.
[5] Hadim, A., 1994, "Forced Convection in a Porous Channel With Localized Heat Sources," ASME J. Heat Transfer, **116**, pp. 465–472.
[6] Hadim, A., and Bethancourt, A., 1995, "Numerical Study of Forced Convection in a Partially Porous Channel With Discrete Heat Sources," ASME J. Electron. Packag., **117**, pp. 46–51.
[7] Huang, P. C., and Vafai, K., 1994, "Analysis of Forced Convection Enhancement in a Channel Using Porous Blocks," J. Thermophys. Heat Transfer, **8**, pp. 563–573.
[8] Huang, P. C., Yang, C. F., Hwang, J. J., and Chui, M. T., 2005, "Enhancement of Forced-Convection Cooling of Multiple Heated Blocks in a Channel Using Porous Covers," Int. J. Heat Mass Transfer, **48**, pp. 647–664.
[9] Fu, W., Huang, H., and Lion, W., 1996, "Thermal Enhancement in Laminar Channel Flow With a Porous Block," Int. J. Heat Mass Transfer, **39**, pp. 2165–2175.
[10] Ould-Amer, Y., Chikh, S., Bouhadef, K., and Lauriat, G., 1998, "Forced Convection Cooling Enhancement by Use of Porous Materials," Int. J. Heat Fluid Flow, **19**, pp. 251–258.
[11] Ko, K. H., and Anand, N. K., 2003, "Use of Porous Baffles to Enhance Heat Transfer in a Rectangular Channel," Int. J. Heat Mass Transfer, **46**, pp. 4191–4199.
[12] Yang, Y. T., and Hwang, C. Z., 2003, "Calculation of Turbulent Flow and Heat Transfer in a Porous-Baffled Channel," Int. J. Heat Mass Transfer, **46**, pp. 771–780.
[13] Yang, J., Zeng, M., and Wang, Q. W., 2008, "Numerical Study on Forced Convective Heat Transfer in Porous Pin Fin Channels," ASME Paper No. HT2008-56216.
[14] Ergun, S., 1952, "Fluid Flow Through Packed Columns," Chem. Eng. Prog., **48**, pp. 89–94.
[15] Wakao, N., and Kaguei, S., 1982, *Heat and Mass Transfer in Packed Beds*, McGraw-Hill, New York.
[16] Nield, D. A., and Bejan, A., 2006, *Convection in Porous Media*, 3rd ed., Springer, New York.
[17] Bhattacharya, A., Calmidi, V. V., and Mahajan, R. L., 2002, "Thermophysical Properties of High Porosity Metal Foams," Int. J. Heat Mass Transfer, **45**, pp. 1017–1031.
[18] Calmidi, V. V., and Mahajan, R. L., 2000, "Forced Convection in High Porosity Metal Foams," ASME J. Heat Transfer, **122**, pp. 557–565.
[19] CFX Inc., 2005, User Guide, CFX 10.

Modeling the Effects of System Rotation on the Turbulent Scalar Fluxes

B. A. Younis[1]
Department of Civil and Environmental Engineering,
University of California,
Davis, CA 95616
e-mail: bayounis@ucdavis.edu

B. Weigand

F. Mohr[2]

M. Schmidt[2]

Institut für Thermodynamik der Luft- und Raumfahrt,
Universität Stuttgart,
70569 Stuttgart, Germany

A proposal for modeling the effects of system rotation on the turbulent scalar fluxes is presented. It is based on extension to rotating frames of an explicit algebraic model derived using tensor-representation theory. The model is formulated to allow for the turbulent scalar fluxes to depend on the details of the turbulence field and on the gradients of both the mean-velocity and the scalar. Such dependence, which is absent from conventional models, is required by the exact equations governing the transport of the scalar fluxes. The model's performance is assessed, both a priori and by actual computations, by comparisons with results from recent direct numerical simulations (DNS) of flows in heated channels rotated about their streamwise, spanwise, and wall-normal axes. To place the new model's performance in context, additional comparisons are made with predictions obtained from three alternative models, namely, the conventional gradient-transport model, a model that is implicit in the scalar fluxes derived by simplification of the modeled transport equations for the scalar fluxes, and a differential scalar-flux transport model. The results show that the present model yields predictions that are substantially in better agreement with the DNS results than the algebraic models, and which are indistinguishable from those obtained with the more complex differential model. However, important differences remain and reasons for these are discussed.
[DOI: 10.1115/1.4000446]

1 Introduction

System rotation is known to significantly modify the rate of heat, mass, and momentum transport by turbulence. In the flow in a straight channel rotated about its spanwise axis, for example, experiments show that relative to the case of no rotation, the turbulence activity is significantly enhanced on the leading (pressure) side and diminished on the trailing (suction) side [1]. On the other hand, an initially turbulent flow in a circular pipe undergoes reverse transition to a laminarlike state when the pipe is strongly rotated about its longitudinal axis [2]. The prediction of flows subjected to system rotation has proved to be beyond the capabilities of turbulence closures based on linear stress-strain assumptions. The reasons for this become apparent from the examination of the exact equations describing the conservation of the individual normal stresses. These equations contain "extra" generation terms associated with the rotation-rate vector Ω_m. For the rotation of a channel about the streamwise (ST) axis ($m=x$, see Fig. 1 for coordinates and notation), the rotational terms that appear in the equations for $\overline{u^2}$, $\overline{v^2}$, and $\overline{w^2}$ are 0, $4\Omega_x\overline{vw}$, and $-4\Omega_x\overline{vw}$, respectively. Thus by taking the trace of these equations to obtain the equation for the turbulence kinetic energy (k), all the rotation-dependent terms vanish, and the resulting form of this equation is identical to that appropriate to a nonrotating flow. The same occurs for the cases where the axis of rotation is aligned with the wall-normal (WN) ($m=y$) or the spanwise directions ($m=z$), where the rotation-dependent terms in the normal stresses are obtained as ($-4\Omega_y\overline{uw}$, 0, and $4\Omega_y\overline{uw}$) and ($4\Omega_z\overline{uv}$, $-4\Omega_z\overline{uv}$, and 0), respectively. In the absence of rotation-dependent terms in the k-equation, the equation for dissipation rate similarly takes on a form which is identical to that appropriate to zero rotation. Consequently, the eddy-viscosity remains unaffected by rotation and models which employ this parameter to determine the rate of momentum transport obtain results for rotated flows that are exactly identical to the stationary cases [3].

In contrast, Reynolds-stress turbulence closures which retain the rotation-dependent generation terms have been shown to successfully capture the main features of flows subjected to system rotation [4,5]. The success of Reynolds-stress transport models in these and in other flows which are subjected to body forces (such as buoyancy and streamline curvature) has contributed to their increased acceptance as a practical option in engineering calculations. But the progress in modeling turbulent momentum transport has not been matched by progress in the related problem of modeling the turbulent scalar fluxes which continue to be obtained from gradient-transport hypotheses, namely, Fourier's law in the case of heat transfer and Fick's law for mass transfer. Thus the turbulent scalar-flux $\overline{u_i\theta}$, which governs the rate of transport of a scalar Θ is obtained from

$$-\overline{u_i\theta} = \frac{\nu_t}{\sigma_t}\frac{\partial\Theta}{\partial x_i} \tag{1}$$

where θ is the fluctuating component of the scalar, ν_t is the eddy-viscosity, and σ_t is the turbulent Prandtl or Schmidt number.

The shortcoming of eddy-diffusivity models become apparent from inspection of Eq. (1). These models enforce the alignment of the scalar-flux in a particular coordinate direction with the gradients of the scalar in the same direction. Thus, for example, in two-dimensional fully-developed channel flows with temperature gradients nonzero only in the direction normal to the walls, Eq. (1) predicts both the streamwise and spanwise scalar-flux components to be zero. As will be seen later, both components are in fact nonzero, with the streamwise component typically 2–3 times greater than that in the direction of the scalar gradient. The accurate prediction of these flux components is essential for cases where buoyancy effects are important. Another defect is the assumption that the turbulent Prandtl number σ_t is constant while recent results from Direct Numerical Simulations (DNS) of rotat-

[1]Corresponding author.
[2]Present address: ALSTOM (Switzerland) Ltd., Brown Boveri Strasse 7, 5401 Baden, Switzerland.

Contributed by the Heat Transfer Division of ASME for publication in the JOURNAL OF HEAT TRANSFER. Manuscript received March 9, 2009; final manuscript received August 28, 2009; published online March 8, 2010. Editor: Yogesh Jaluria.

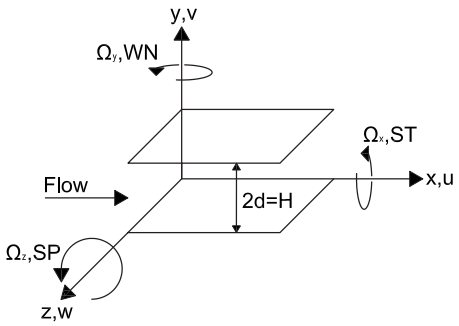

Fig. 1 Geometry and coordinates system

ing flows show that this parameter is spatially variable and can depend strongly on rotation. But the most important defect in Eq. (1) is that it does not allow for the dependence of $\overline{u_i\theta}$ on the rotation-rate vector Ω_m. As will be shown later, this dependence is required if the model for $\overline{u_i\theta}$ is to be consistent with the exact equations governing the conservation of these quantities. In the absence of an explicit dependence on Ω_m, it is not surprising that gradient-transport models fail badly to capture the effects of rotation on the turbulent scalar fluxes.

The present study is motivated by the need for a model for the turbulent scalar fluxes that can obtain these to the same degree of accuracy with which the Reynolds stresses are obtained using second-order closure models. Specifically, the aim is to devise an algebraic model that retains the simplicity, robustness, and ease of implementation in complex computational procedures of the simple gradient-transport hypothesis but yet can correctly capture the significant modification to the turbulent scalar fluxes wrought by system rotation. The proposed model is presented in the next section. Its performance is evaluated by using recent results of direct numerical simulations of flows in channels rotated in orthogonal modes. Comparisons will also be made with alternative scalar-flux closures in order to put the present contribution in proper perspective.

2 Model Formulation

The effects of system rotation on the turbulence can be clearly seen from inspection of the exact equations for transport of Reynolds stresses ($\overline{u_iu_j}$) and the turbulent scalar fluxes ($\overline{u_i\theta}$) in rotating frames

$$\frac{D\overline{u_iu_j}}{Dt} = \text{diff}(\overline{u_iu_j}) + P_{ij} + G_{ij} + \Phi_{ij} - \epsilon_{ij} \tag{2}$$

$$\frac{D\overline{u_i\theta}}{Dt} = \text{diff}(\overline{u_i\theta}) + P_{i\theta} + G_{i\theta} + \Phi_{i\theta} - \epsilon_{i\theta} \tag{3}$$

In the above, the terms diff( ), Φ, and ϵ represent diffusion, fluctuating pressure-gradient correlations, and viscous dissipation, respectively. The precise forms of these terms are not relevant to the subsequent analysis and will not therefore be elaborated upon here (the interested reader may refer to Refs. [6,7] for details). The terms P and G represent the rates of production of the transported quantity by mean shear and by rotational effects. They are given by

$$P_{ij} = -\left(\overline{u_iu_k}\frac{\partial U_j}{\partial x_k} + \overline{u_ju_k}\frac{\partial U_i}{\partial x_k}\right) \tag{4}$$

$$G_{ij} = -2\Omega_k(\overline{u_ju_m}\epsilon_{ikm} + \overline{u_iu_m}\epsilon_{jkm}) \tag{5}$$

$$P_{i\theta} = -\left(\overline{u_k\theta}\frac{\partial U_i}{\partial x_k} + \overline{u_ku_i}\frac{\partial \Theta}{\partial x_k}\right) \tag{6}$$

$$G_{i\theta} = -2\epsilon_{ijk}\Omega_j\overline{u_k\theta} \tag{7}$$

Inspection of these terms reveals that the effects of rotation on the turbulent scalar fluxes enter indirectly through modification of the Reynolds stresses and more directly via the appearance of the rotation-rate vector Ω_m. A properly-formulated model for the fluxes must therefore explicitly account for these separate agencies to stand any chance in capturing the effects of rotation about any given axis.

The modeling strategy pursued here is based on extending the model of Younis et al. [8] for the turbulent scalar fluxes. This model was derived by first writing the functional relationship for $\overline{u_i\theta}$ implied by the exact equation (3). For incompressible, nonrotating, and nonbuoyant flows, this is obtained as

$$-\overline{u_i\theta} = f_i(\overline{u_iu_j}, S_{ij}, W_{ij}, \Theta_j, \tau) \tag{8}$$

where τ is the scalar time-scale which was taken to be proportional to the mechanical time-scale k/ϵ, and S_{ij} and W_{ij} are the strain rate and rotation tensors

$$S_{ij} = \frac{1}{2}\left(\frac{\partial U_i}{\partial x_j} + \frac{\partial U_j}{\partial x_i}\right) \tag{9}$$

$$W_{ij} = \frac{1}{2}\left(\frac{\partial U_i}{\partial x_j} - \frac{\partial U_j}{\partial x_i}\right) \tag{10}$$

Results from tensor-representation theory were then used to find the general expression for $\overline{u_i\theta}$ in terms of its functionals. The outcome was an algebraic model for the scalar fluxes which is explicit in these variables. Being explicit is a particularly desirable feature of the model since it means that the unknown fluxes can be obtained directly without the need for iterations which can add to the computational effort and which are frequently the source of convergence difficulties. After simplification, the model takes the form

$$-\overline{u_i\theta} = C_1\frac{k^2}{\epsilon}\frac{\partial\Theta}{\partial x_i} + \left(C_2\frac{k}{\epsilon}\overline{u_iu_j} + C_3\frac{k^3}{\epsilon^2}\frac{\partial U_i}{\partial x_j} - C_4\frac{k^2}{\epsilon^2}P_{ij}\right)\frac{\partial\Theta}{\partial x_j} \tag{11}$$

The model contains four coefficients given in the original reference as $(C_1, C_2, C_3, C_4) = (-0.0455, 0.373, -0.00373, -0.0235)$. While these values proved satisfactory in unbounded flows, it was found necessary to modify the coefficient C_1 to correctly reproduce the damping effects associated with the presence of a solid wall. This is done here following the proposal of Younis et al. [9]

$$C_1 = -0.0455(1 - e^{-A\beta Pe^{\alpha}}) \tag{12}$$

where

$$\begin{aligned}
\text{Re}_t &= \frac{k^2}{\nu\epsilon} \\
P_e &= \text{Re}_t\ \text{Pr} \\
A_{ij} &= \frac{\overline{u_iu_j}}{k} - \frac{2}{3}\delta_{ij} \\
A_2 &= A_{ij}A_{ij} \\
A_3 &= A_{ij}A_{jk}A_{ik} \\
A &= 1 - \tfrac{9}{8}(A_2 - A_3) \\
\alpha &= -0.02 \\
\beta &= 1.9
\end{aligned} \tag{13}$$

With the basic model for $\overline{u_i\theta}$ in place, we turn to consideration of how best to introduce the effects of system rotation in Eq. (11).

The most direct way to make the scalar fluxes depend on Ω_k, the rotation-rate vector, is to extend the definition of the rate of production by shear, which appears in Eq. (11), to include the rate of production of the Reynolds stresses due to rotation (G_{ij}), i.e.,

$$P_{ij} = P_{ij} + G_{ij} \tag{14}$$

The rationale for this extension is that the magnitude of the turbulent scalar fluxes is closely related to the overall turbulence activity; thus rotation, which would enhance the turbulence levels (by increasing the Reynolds stresses), will also directly enhance the scalar fluxes.

Launder et al. [4], in their Reynolds-stress closure study of rotating channel flow, point out that the requirement that the substantial derivative of the Reynolds stresses ($D\overline{u_i u_j}/Dt$) be frame independent requires that $1/2G_{ij}$ be assigned to the convection term. Thus with only $1/2G_{ij}$ remaining in Eq. (14), the effects of rotation enter Eq. (11) exclusively via the C_4 term, which now reads

$$C_4 \frac{k^2}{\epsilon^2}\left(\overline{u_i u_k}\left(\frac{\partial U_j}{\partial x_k} + \epsilon_{jmk}\Omega_m\right) + \overline{u_j u_k}\left(\frac{\partial U_i}{\partial x_k} + \epsilon_{imk}\Omega_m\right)\right) \tag{15}$$

An alternative view of how best to sensitize the scalar fluxes to rotation is to recognize that the vorticity (W_{ij}), which enters the formulation of the model of Eq. (11), is replaced in rotating frames by the absolute (or intrinsic) vorticity, viz.

$$W_{ij}^{*} = W_{ij} + \epsilon_{mji}\Omega_m \tag{16}$$

The direct effect of employing the intrinsic vorticity in the derivation of the model is that the velocity gradients, which appear in Eq. (11), are now modified to read

$$\frac{\partial U_i}{\partial x_j} = \frac{\partial U_i}{\partial x_j} + \epsilon_{mji}\Omega_m \tag{17}$$

Substitution of this expression for the velocity gradient in Eq. (11) modifies the C_3 and C_4 terms as follows:

$$C_3 \frac{k^3}{\epsilon^2}\left(\frac{\partial U_i}{\partial x_j} + \epsilon_{mji}\Omega_m\right) + C_4 \frac{k^2}{\epsilon^2}\left(\overline{u_i u_k}\left(\frac{\partial U_j}{\partial x_k} + \epsilon_{jmk}\Omega_m\right) + \overline{u_j u_k}\left(\frac{\partial U_i}{\partial x_k} + \epsilon_{imk}\Omega_m\right)\right) \tag{18}$$

It is immediately apparent that the two approaches give identical results for the C_4 term while it is only by adopting the transformed vorticity approach that the C_3 term is sensitized to rotational effects. The latter approach, as well as being consistent with the requirement of coordinates invariance, provides a more complete description of the effects of rotation on the turbulent scalar fluxes. Therefore, the rotation-sensitized model we propose here can be written as

$$-\overline{u_i\theta} = C_1 \frac{k^2}{\epsilon}\frac{\partial \Theta}{\partial x_i} + \left[C_2 \frac{k}{\epsilon}\overline{u_i u_j} + C_3 \frac{k^3}{\epsilon^2}\left(\frac{\partial U_i}{\partial x_j} + \epsilon_{mji}\Omega_m\right) + C_4 \frac{k^2}{\epsilon^2}\left(\overline{u_i u_k}\left(\frac{\partial U_j}{\partial x_k} + \epsilon_{jmk}\Omega_m\right) + \overline{u_j u_k}\left(\frac{\partial U_i}{\partial x_k} + \epsilon_{imk}\Omega_m\right)\right)\right]\frac{\partial \Theta}{\partial x_j} \tag{19}$$

In what follows, the results obtained with the model given by Eq. (19) will be referred to as "explicit." The expressions for the various scalar-flux components, as given by the model for the case of rotation around any coordinate axis, are listed in the Appendix.

To put the present model's results in perspective, we compare its predictions with those obtained from two very different alternatives. The first of these is the simple gradient-transport closure given by Eq. (1). Following the usual practice in models which utilize eddy-viscosity closures, the turbulent viscosity in Eq. (1) was evaluated from $C_\mu k^2/\epsilon$ with $C_\mu = 0.09$. The turbulent Prandtl number Pr_t was set equal to 0.85. The second model used for these comparisons closely mirrors the model developed by Gibson [10] to account for the effects of streamline curvature on the turbulent scalar fluxes. Thus the differential transport equations for $\overline{u_i\theta}$ (Eq. (3)) are reduced to a set of algebraic equations via the approximation

$$\frac{D\overline{u_i\theta}}{Dt} - D(\overline{u_i\theta}) = \frac{\overline{u_i\theta}}{(k\overline{\theta^2})^{0.5}}\left[\frac{D(k\overline{\theta^2})^{0.5}}{Dt} - D((k\overline{\theta^2})^{0.5})\right] = \frac{\overline{u_i\theta}}{2k}(P-\epsilon) + \frac{\overline{u_i\theta}}{2\overline{\theta^2}}(P_\theta - \epsilon_\theta) \tag{20}$$

where P_θ and ϵ_θ are the rates of production and dissipation of the scalar variance $\overline{\theta^2}$.

Gibson [10] modeled $\Phi_{i\theta}$ in Eq. (3) as the sum of two terms, one containing only turbulence correlations and another containing gradients of mean-velocity and scalar, with corrections to each to account for wall damping effects, viz.

$$\Phi_{i\theta} = \Phi_{i\theta,1} + \Phi_{i\theta,2} + \Phi'_{i\theta,1} + \Phi'_{i\theta,2} \tag{21}$$

$$\Phi_{i\theta,1} = -C_{1\theta}\frac{\epsilon}{k}\overline{u_i\theta} \tag{22}$$

$$\Phi_{i\theta,2} = -C_{2\theta}P_{i\theta} \tag{23}$$

$$\Phi'_{i\theta,1} = -C'_{1\theta}\frac{\epsilon}{k}\overline{u_k\theta}n_i n_k f \tag{24}$$

$$\Phi'_{i\theta,2} = C'_{2\theta}C_{2\theta}P_{k\theta}n_i n_k f \tag{25}$$

The effects of curvature were introduced in Ref. [10] by treating $G_{i\theta}$, the term representing the rate of generation of $u_i\theta$ due to streamline curvature, in exactly the same way as P_{i_θ}, i.e., by the addition of a term which reads

$$\Phi_{i\theta,3} = -C_{3\theta}G_{i\theta} \tag{26}$$

with coefficient $C_{3\theta}$ set equal to $C_{2\theta}$.

In extending this modeling approach to the case of rotating flows, the same argument regarding the noninvariance of the substantial derivative applies here as well and thus the appropriate way to introduce the effects of rotation into the pressure correlations term is to substitute for $G_{i\theta}$ in Eq. (26) by one-half its value. The outcome of this substitution would be identical to what would be obtained if the velocity gradients appearing in the expression for $P_{i\theta}$ in Eq. (23) were replaced by the rotation-dependent expression for velocity gradient given by Eq. (17).

With this treatment of $G_{i\theta}$, the differential equations are reduced to the following set of algebraic relations for the turbulent scalar fluxes:

$$-\overline{u_i\theta} = \frac{k}{\epsilon}\psi_{\theta 1}\left(\overline{u_k\theta}\left(\frac{\partial U_i}{\partial x_k} + \epsilon_{imk}\Omega_m\right) + \overline{u_i u_k}\frac{\partial \Theta}{\partial x_k}\right) + \psi_{\theta 2}n_i n_k \overline{u_k\theta} \tag{27}$$

where

$$\psi_{\theta 1} = \frac{(1-C_{2\theta})}{\frac{1}{2}\left(\frac{P}{\epsilon}-1\right) + C_{1\theta}} \tag{28}$$

$$\psi_{\theta 2} = \frac{C'_{1\theta}}{\frac{1}{2}\left(\frac{P}{\epsilon}-1\right) + C_{1\theta}} \tag{29}$$

and the coefficients ($C_{1\theta}$, $C_{2\theta}$, $C'_{1\theta}$, and $C'_{2\theta}$) are assigned their original values (0.3, 0.33, 0.5, and 0).

The algebraic expression of Eq. (27), together with the above values for the model coefficients, will hereafter be referred to as the "implicit" model. This designation refers to the appearance of

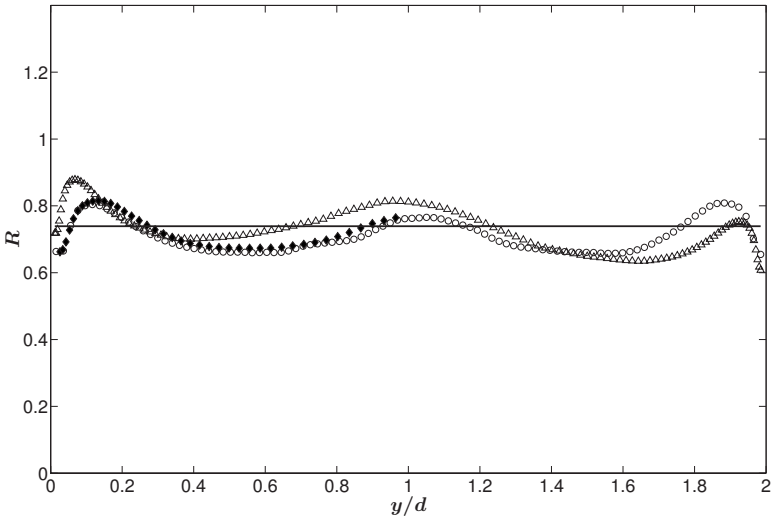

Fig. 2 DNS results for spatial variation of time-scale ratio *R* with and without rotation: no rotation (○) [13], streamwise (△) [15], wall-normal (♦) [17], and average value (—)

the unknown fluxes on both sides of the expression thereby requiring iterations to be performed for their determination.

3 Model Assessment

The DNS results used for the purpose of model assessment are for heated channel flows that are nominally fully-developed in the x-direction (refer to Fig. 1). Thus, on long-time average basis, only the y-direction gradients of mean-velocity and temperature are nonzero. In these conditions, and for the general case of rotation around all three axes, the nonzero components of the velocity gradient are

$$\frac{\partial U_i}{\partial x_j} = \begin{bmatrix} 0 & \dfrac{\partial U}{\partial y} - \Omega_z & \Omega_y \\ \Omega_z & \dfrac{\partial V}{\partial y} & -\Omega_x \\ -\Omega_y & \dfrac{\partial W}{\partial y} + \Omega_x & 0 \end{bmatrix} \tag{30}$$

The explicit-model equations for the case of a fully-developed flow with nonzero gradients of velocity and scalar in the y-direction and which is subjected to rotation around all three coordinate directions are

$$-\overline{u\theta} = \left\{ C_2 \frac{k}{\epsilon}\overline{uv} + C_3 \frac{k^3}{\epsilon^2}\left(\frac{\partial U}{\partial y} - \Omega_z\right) + C_4 \frac{k^2}{\epsilon^2}\left(\overline{v^2}\left(\frac{\partial U}{\partial y} - \Omega_z\right) + \overline{u^2}\Omega_z - \overline{uw}\Omega_x + \overline{vw}\Omega_y\right)\right\}\frac{\partial \Theta}{\partial y} \tag{31}$$

$$-\overline{v\theta} = \left\{ C_1 \frac{k^2}{\epsilon} + C_2 \frac{k}{\epsilon}\overline{v^2} + C_4 \frac{k^2}{\epsilon^2}(2\overline{uv}\Omega_z - 2\overline{vw}\Omega_x)\right\}\frac{\partial \Theta}{\partial y} \tag{32}$$

$$-\overline{w\theta} = \left\{ C_2 \frac{k}{\epsilon}\overline{vw} + C_3 \frac{k^3}{\epsilon^2}\Omega_x + C_4 \frac{k^2}{\epsilon^2}(\overline{uw}\Omega_z - \overline{w^2}\Omega_x - \overline{uv}\Omega_y + \overline{v^2}\Omega_x)\right\}\frac{\partial \Theta}{\partial y} \tag{33}$$

We examine first the validity of the modeling assumption that the time-scale for the fluctuations of the scalar field τ_θ $(=\overline{\theta^2}/2\epsilon_\theta)$ is proportional to τ_m, the mechanical time-scale $(=k/\epsilon)$. This assumption is often made in modeling the scalar fluxes, as it has the advantage of eliminating the scalar variance and its dissipation rate—two unknowns, which would require additional modeling. The validity of this approach rests on the assumptions that R, the time-scale ratio (τ_θ/τ_m), is constant across the shear layer and that this parameter is not significantly affected by rotation. We test these assumptions here by plotting the value of R implied by the DNS results for channel flows with no rotation, as well as for channels rotated about their streamwise and wall-normal axes. The results are displayed in Fig. 2. It is immediately apparent that the variations in R across the channel and its dependence on the mode of rotation are sufficiently small to justify the assumption that the scalar time-scale is proportional to the mechanical time-scale and can therefore be replaced by it. The spatially-averaged value of R obtained by the DNS for all the cases shown in Fig. 2 is 0.74. This compares very favorably with the value of about 0.7 implied by the measurements of Bremhorst and Bullock [11,12] in heated pipe flow.

3.1 Stationary Channel. The model's performance is first assessed in relation to the baseline flow, namely, that in a heated plane channel with no rotation. The DNS results are those of Debusschere and Rutland [13]. The nondimensional temperatures of the top and bottom walls were kept constant and set equal to one and zero, respectively. The Prandtl number was 0.7 and Re_τ, the Reynolds number based on friction velocity and the half width, was 186.

The scalar fluxes $\overline{u\theta}$ and $\overline{v\theta}$ are compared in Figs. 3 and 4. In this and all subsequent comparisons, the heat fluxes were nondimensionalized using the friction temperature and the friction velocity. The most striking feature of the results is the relative magnitude of the streamwise component of heat-flux (a quantity, which is obtained as zero by Fourier's law) compared with that in the direction of the temperature gradient. Close to the wall, this ratio attains a value of nearly 7. The explicit model captures the correct maximum value of $\overline{u\theta}$ though the predictions then appears to decay at a much faster rate than is suggested by the DNS. This behavior, which will be observed in all subsequent comparisons involving this parameter, is due, in part, to the absence from the model predictions of a contribution from the streamwise gradient $\partial\Theta/\partial x$. The absence of such contribution is not due to the absence in the explicit model on a dependence on the streamwise gradients (which it clearly does, as can be seen in the Appendix) but, rather, because the archived DNS results do not permit the evaluation of these gradients.

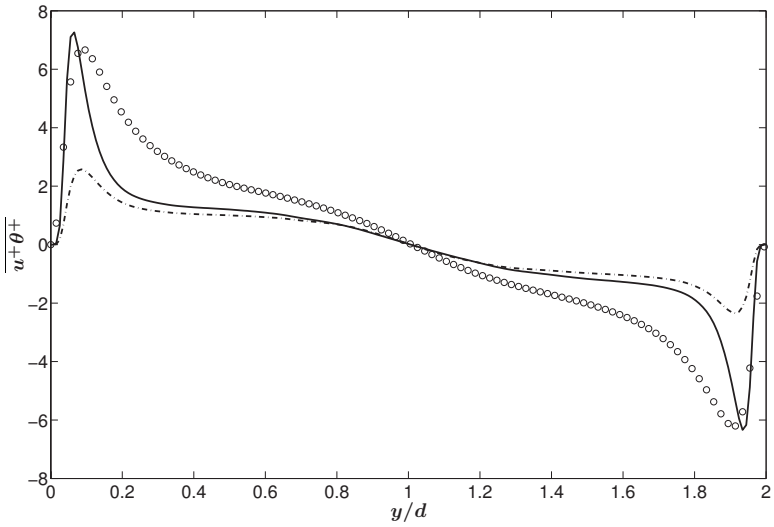

Fig. 3 $\overline{u\theta}$ in stationary channel. DNS of Debusschere and Rutland [13]. DNS (○), explicit (—), and implicit (·–·).

In sharp contrast, the profile of $\overline{v\theta}$ is far better predicted by the explicit model, whereas the implicit-model underestimates this quantity quite significantly. The conventional gradient-transport model also seriously underpredicts this component. Note that in applying this model, the eddy-viscosity, which appears in Eq. (1) was damped close to the wall in accordance with the low turbulence Reynolds number proposals of Chien [14].

Even though the turbulent Prandtl number no longer enters into the explicit model's formulation, it is still instructive to compare the values of this parameter implied by the DNS and the model. This parameter is evaluated from

$$\mathrm{Pr}_t \equiv \frac{\overline{uv}}{\overline{v\theta}} \frac{\partial \Theta/\partial y}{\partial U/\partial y} \tag{34}$$

Figure 5 compares the DNS and model's predictions of Pr_t. Both results show that this parameter attains a value close to unity near the wall and then drops to about 0.8 at the channel centerline. Typical values of Pr_t used in connection with eddy-diffusivity closures are of the order of 0.85 [6].

3.2 Streamwise Rotation. The next case considered is that of flow in a channel rotated about its streamwise axis. The time-averaged flow is symmetric about the channel's center. According to the DNS results of El-Samni and Kasagi [15], the effects of rotation on the mean flow are to induce a large mean-velocity component (W) in the spanwise direction. As a result, all six components of the Reynolds-stress tensor assume nonzero values in this mode of rotation. The present model was assessed by comparisons with results from two DNS studies differing substantially in the relative strength of the imposed rotation. The first study is that of Wu and Kasagi [16] for rotation number Ro_τ ($\equiv 2\Omega_x d/u_{\tau_o}$ where d is the channel half width) of 2.5 and $\mathrm{Pr}=0.71$. The lower wall ($y/d=0$) was heated, and the upper wall ($y/d=2$) was cooled. The Reynolds number of the simulations, based on wall friction velocity and half width, was $\mathrm{Re}_\tau=300$. The results are plotted in Figs. 6–8. The maximum value of the streamwise heat-flux $\overline{u\theta}$ is again well predicted with the explicit model though, as with the stationary flow, the model shows a more rapid drop in

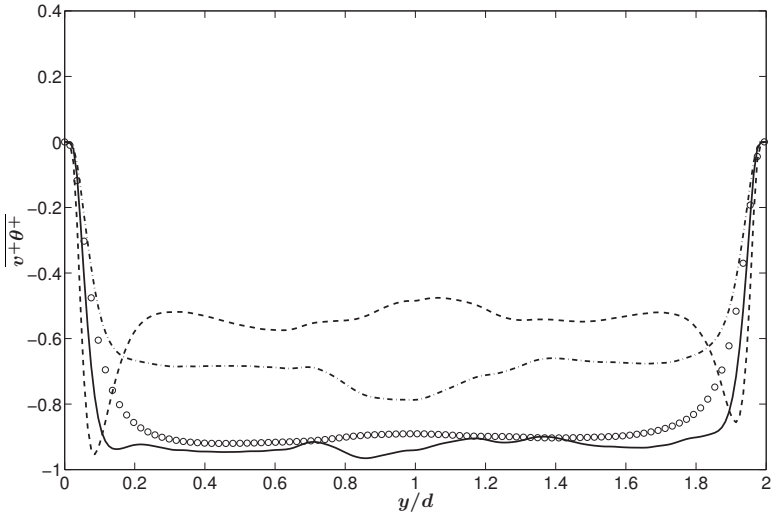

Fig. 4 $\overline{v\theta}$ in stationary channel. DNS of Debusschere and Rutland [13]. DNS (○), explicit (—), implicit (·–·), and gradient-transport (– – –).

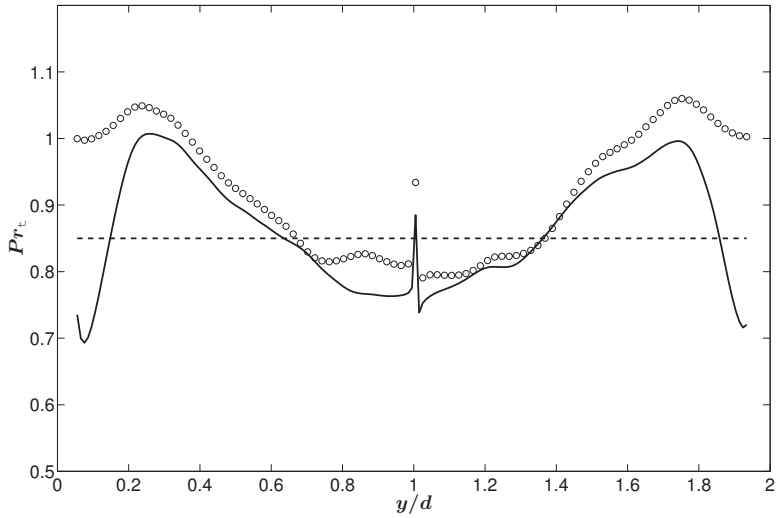

Fig. 5 Pr_t in stationary channel. DNS of Debusschere and Rutland [13]. DNS (○), explicit (—), and Pr_t=0.85(– – –).

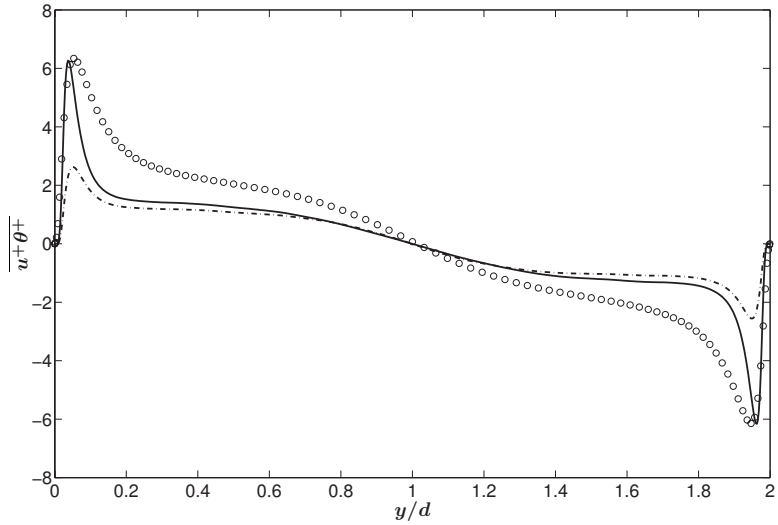

Fig. 6 $\overline{u\theta}$ in channel with streamwise rotation. DNS of Wu and Kasagi [16] for Ro_τ=2.5. DNS (○), explicit (—), and implicit (·–·).

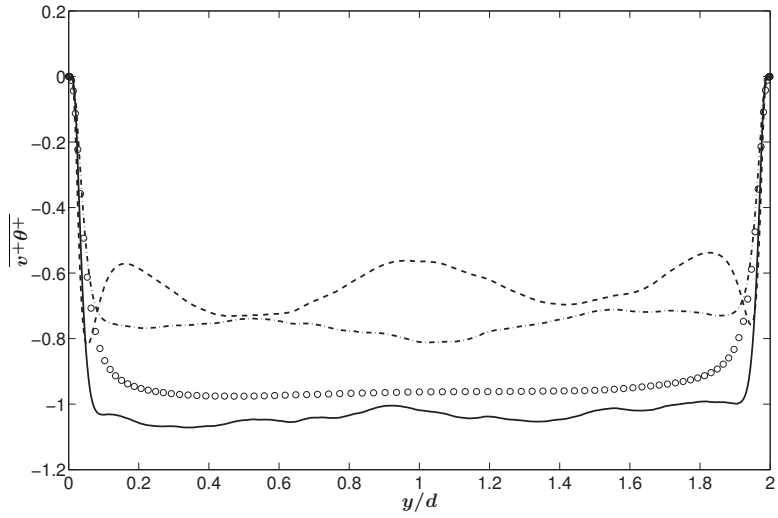

Fig. 7 $\overline{v\theta}$ in channel with streamwise rotation. DNS of Wu and Kasagi [16] for Ro_τ=2.5. DNS (○), explicit (—), implicit (·–·), and gradient-transport (– – –).

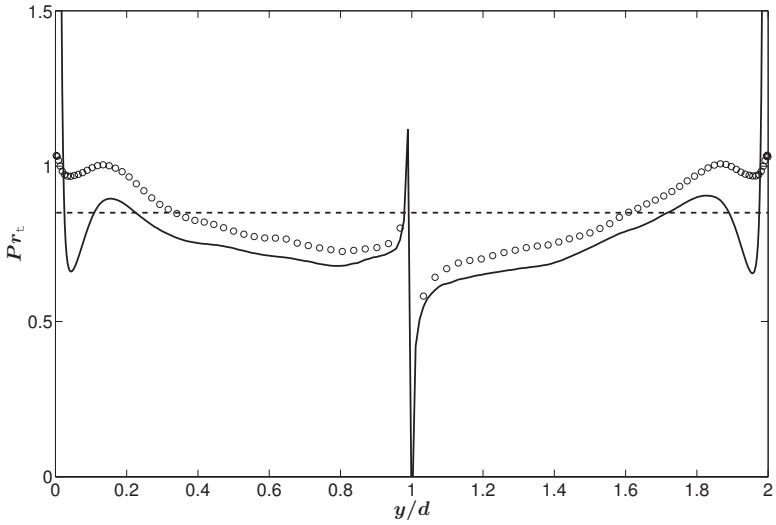

Fig. 8 Pr_t in channel with streamwise rotation. DNS of Wu and Kasagi [16] for Ro_τ=2.5. DNS (○), explicit (—), and Pr_t=0.85(– – –).

this quantity away from the walls than is obtained in the DNS. With the assumption of fully-developed mean flow, the effects of streamwise rotation on the heat-flux component $\overline{v\theta}$ in the explicit model enter via the term $2\overline{vw}\Omega_x \partial\Theta/\partial y$ (see Eq. (32)), which has the effect of increasing its magnitude with respect to the $\Omega_x=0$ case. This is clearly obtained both in the DNS and by the explicit model. In contrast, both the implicit-model and the gradient-transport closure significantly underestimate the enhancement of this component with both yielding results that are quite similar to those obtained for the no rotation case. From the definition of the turbulent Prandtl number (Eq. (34)), an increase in the level of $\overline{v\theta}$ would lead to a decrease in Pr_t relative to the stationary flow. This is borne out in Fig. 8. The discontinuities at the centerline are a consequence of the mean-velocity gradient becoming zero there.

The second case considered is by El-Samni and Kasagi [15] for Re_τ=150 and the much higher rotation number Ro_τ=15. The Prandtl number was again set equal to 0.71 but now with the top wall heated and the bottom wall cooled. The DNS and the models' results, which are displayed in Figs. 9–11, show significantly different trends and are not in close correspondence with each other as was the case for the weaker-rotation flow. Thus, for example, the DNS results show that relative to the stationary flow, the maximum value of $\overline{u\theta}$ is slightly reduced by rotation, while the explicit model shows that this quantity is significantly increased by rotation. The explanation for this model's result can again be found from inspection of the model equation (Eq. (31)). There, it can be seen that the effects of rotation enter through a term proportional to $\overline{uw}\Omega_x$. Now $\overline{uw}$, which is zero in the stationary case, becomes nonzero in the presence of streamwise rotation with the DNS results showing its level increasing with Ω_x. This is what is obtained by the explicit model. Significant differences are also apparent in the DNS results and the models' predictions of the heat-flux component $\overline{v\theta}$, especially away from the wall (note that the DNS results for this were only available for one-half of the channel). In this respect it should be noted that the shape of the $\overline{v\theta}$ profile obtained with the explicit model mirrors quite closely the shape of the spanwise velocity (W) obtained by the DNS. The DNS profile, on the other hand, shows no difference from the stationary and the weakly-rotated case.

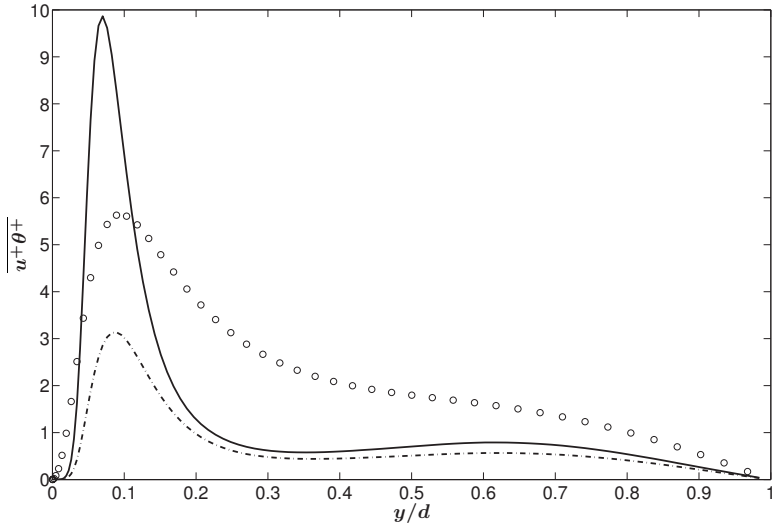

Fig. 9 $\overline{u\theta}$ in channel with streamwise rotation. DNS of El-Samni and Kasagi [15] for Ro_τ=15. DNS (○), explicit (—), and implicit (·–·).

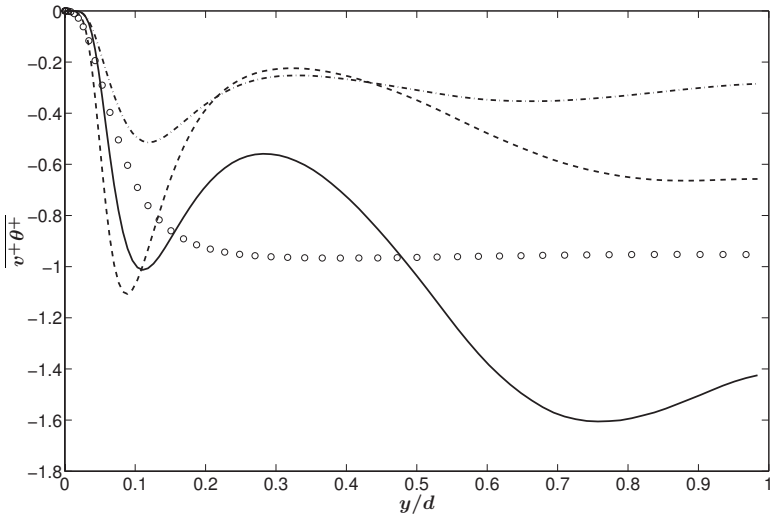

Fig. 10 $\overline{v\theta}$ in channel with streamwise rotation. DNS of El-Samni and Kasagi [15] for Ro_τ=15. DNS (○), explicit (—), implicit (·–·), and gradient-transport (– – –).

An interesting feature of this flow is that the imposition of a temperature gradient in the y direction leads to the generation of a heat-flux component in the z direction. This is clearly seen in Fig. 11 where both the DNS results show $\overline{w\theta}$ to be of the same order as $\overline{v\theta}$. In gradient-transport models, $\overline{w\theta}$ is obtained as zero. With the explicit model, it is given by the expression

$$-\overline{w\theta} = \frac{k^2}{\epsilon^2}(C_3 k - C_4(\overline{w^2} - \overline{v^2}))\Omega_x \frac{\partial \Theta}{\partial y} \tag{35}$$

Thus with $\overline{w\theta}$ directly proportional to Ω_x, the magnitude of this component of the heat-flux is predicted to increase with the rate of rotation Ω_x. The explicit model again succeeds in capturing the near-wall variations fairly accurately but seems to depart from the DNS result away from the wall. In contrast, the implicit-model incorrectly obtains both the sign of this component and the shape of its profile.

3.3 Wall-Normal Rotation. The DNS results used for this case are those of El-Samni and Kasagi [17] with Ro_τ=0.04 and Re_τ=160.1. The models' results for the heat-flux component $\overline{u\theta}$ are compared with the DNS in Fig. 12. Here again, as was the case for the other modes of rotation, as well as for the no rotation case, the explicit model obtains the correct maximum level of this quantity but then shows a much more rapid decrease in the levels of this quantity toward the channel's centerline. Possible causes for this discrepancy have already been discussed in connection with the no rotation case. The implicit-model fails entirely in capturing the peak level but then obtains a similarly fast decay rate away from the wall. The fact that two models that were formulated from entirely different approaches yield similar trends lends support to the suggestion that the streamwise gradients of velocity and temperature make an important contribution to the levels of $\overline{u\theta}$ away from the wall. In sharp contrast to this outcome, the explicit model yields very accurate predictions of $\overline{v\theta}$, as can be seen in Fig. 13. The figure also shows that both the implicit and the gradient-transport models yield predictions that significantly differ, qualitatively and quantitatively, from the DNS results.

3.4 Spanwise Rotation. The case of a channel rotated about its spanwise axis is next considered. Here, the effects of rotation

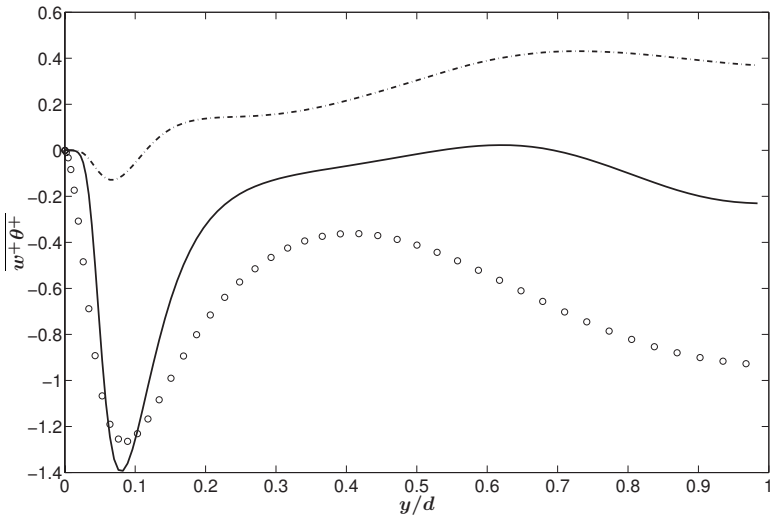

Fig. 11 $\overline{w\theta}$ in channel with streamwise rotation. DNS of El-Samni and Kasagi [15] for Ro_τ=15. DNS (○), explicit (—), and implicit (·–·).

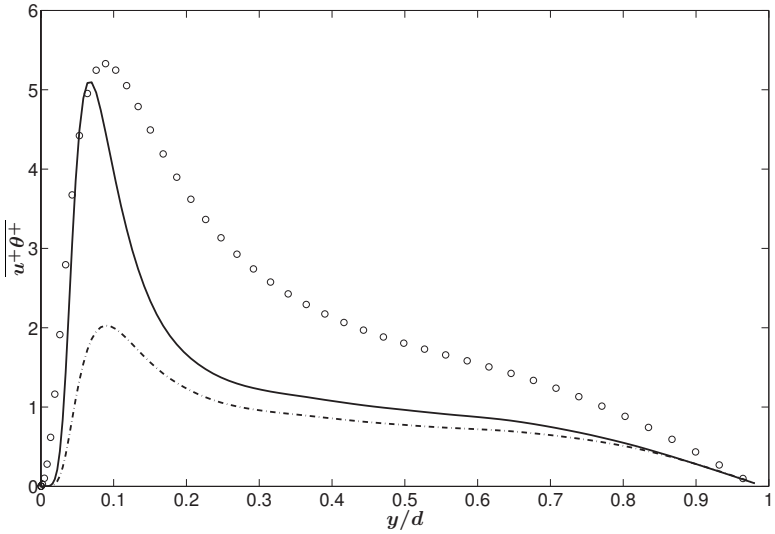

Fig. 12 $\overline{u\theta}$ in channel with wall-normal rotation. DNS of El-Samni and Kasagi [17] for Ro_τ=0.04. DNS (○), explicit (—), and implicit (·–·).

are to induce strong asymmetry in the flow field due to enhancement of the turbulence activity on the pressure side and its suppression on the suction side. The rate of heat transfer to the wall is similarly affected by rotation. Comparisons are made with the results of Wu and Kasagi [16], which were obtained with $Ro_\tau(=(2\Omega_z d)/u_\tau^*)=2.5$, $Re_\tau^*(=(u_\tau^* d)/\nu)=295.5$, and $Pr=0.71$, where u_τ^* is the friction velocity calculated from the wall shear stress averaged on the two walls. The wall temperatures were kept constant with the lower wall heated and the top wall cooled. The rotation-induced asymmetry is clearly evident in Figs. 14 and 15. Note, in particular, the steepening of the $\overline{v\theta}$ profile near the pressure side: this indicates quite significant increase in the value of the Nusselt number compared with the no rotation case. The present model correctly captures this increase though it appears to overestimate the absolute value of $\overline{v\theta}$. This is, in part, due to the fact that in this flow, very strong secondary flows are set-up in the form of large-scale longitudinal roll cells associated with the Taylor–Goertler instability. These introduce significant spanwise variations in the velocity and temperature fields such that gradients in that direction can no longer be assumed to be negligible. Unfortunately the available DNS do not include data to allow for the evaluation of these gradients whose effects on $\overline{v\theta}$ cannot therefore be determined. The DNS and model results for the turbulent Prandtl number are compared in Fig. 16, where the effects of rotation can be seen to be quite significant and are manifested by large departures from the constant value.

In a further test of the new model's performance, the model was implemented in a finite-volume calculation method and used in actual computation of a rotating flow. In these computations, the prediction of the mean-velocity and the turbulence field was achieved using a complete Reynolds-stress transport closure in which a modeled differential transport equation is solved for each component of the Reynolds-stress tensor. This level of closure was previously found necessary to correctly capture the effects of rotation on turbulence [4]. The turbulence closure used is that of Gerolymos and Vallet [18], which is of the low turbulence Reynolds number variety, to allow for the simulations to be carried out through the viscous sublayer to the bounding walls. Details of

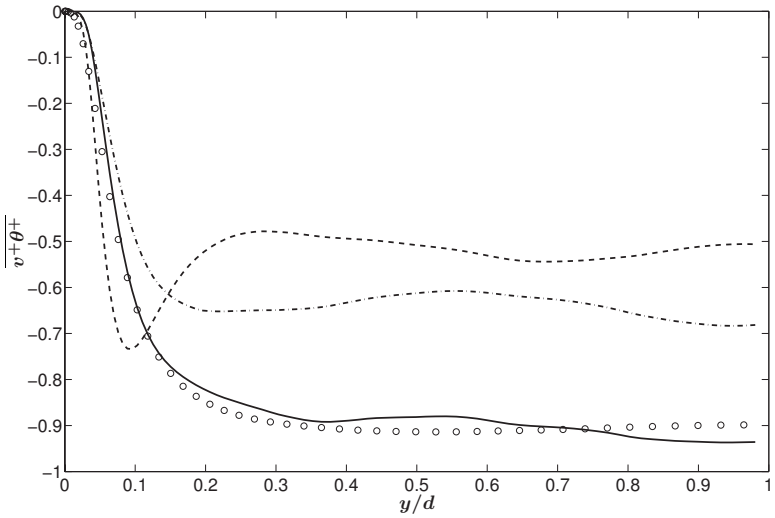

Fig. 13 $\overline{v\theta}$ in channel with wall-normal rotation. DNS of El-Samni and Kasagi [17] for Ro_τ=0.04. DNS (○), explicit (—), implicit (·–·), and gradient-transport (– – –).

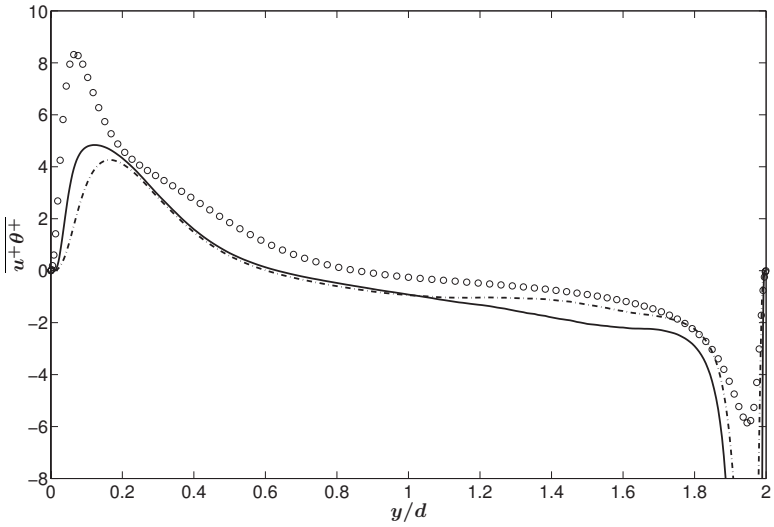

Fig. 14 $\overline{u\theta}$ in channel with spanwise rotation. DNS of Wu and Kasagi [16] for Ro_τ=2.5. DNS (○), explicit (—), and implicit (·–·).

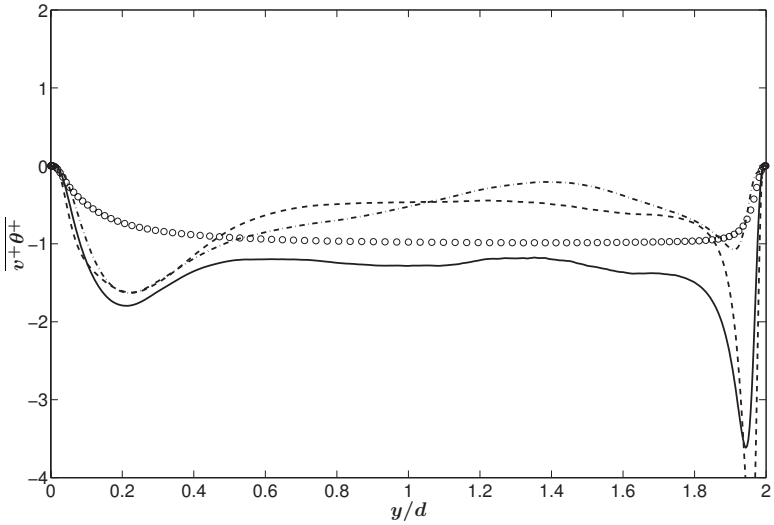

Fig. 15 $\overline{v\theta}$ in channel with spanwise rotation. DNS of Wu and Kasagi [16] for Ro_τ=2.5. DNS (○), explicit (—), implicit (·–·), and gradient-transport (– – –).

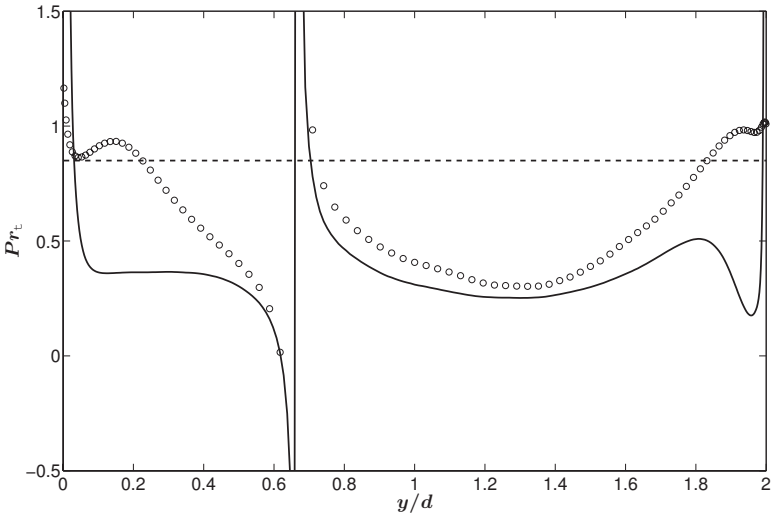

Fig. 16 Pr_t in channel with spanwise rotation. DNS of Wu and Kasagi [16] for Ro_τ=2.5. DNS (○), explicit (—), and Pr_t=0.85(– – –).

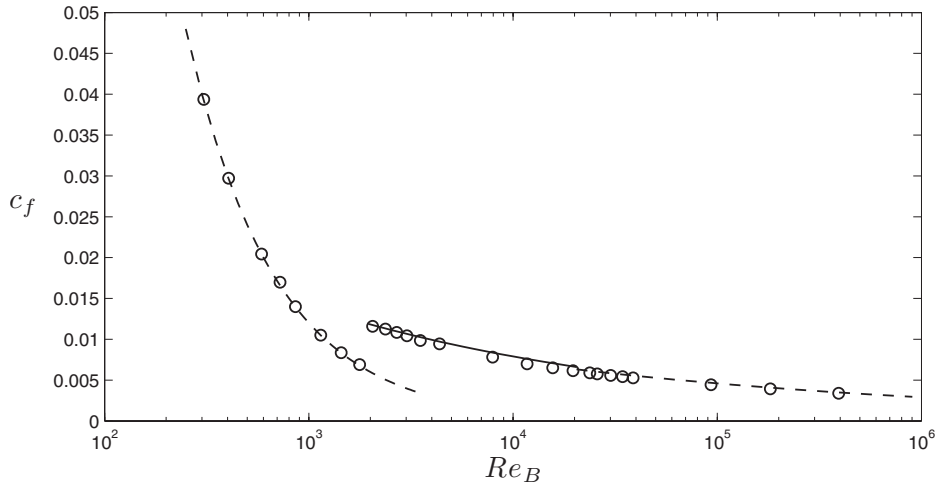

Fig. 17 Skin-friction coefficient in stationary channel. Laminar solution (- -) and Turbulent correlations [20] (- -). Predictions: Gerolymos and Vallet [18] (○).

this model are given in the original reference and are not reproduced here. To assess the explicit model's performance in relation to a considerably more elaborate closure, predictions were also obtained using a differential heat-flux transport closure based on the solution of Eq. (3) for the individual heat-flux components. The unknown correlations were modeled, as described in Eqs. (21)–(25). The finite-volume solution procedure is based on the EXPRESS code [19], which is second-order accurate in space and iteratively solves the time-averaged forms of the equations governing conservation of mass, momentum, and thermal energy. Details of the solution methodology are provided in Refs. [9,19]. Treatment of the rotation terms, which appear explicitly in the Reynolds-stress transport equations, follows the practice described in Ref. [4]. Grid-independent solutions were obtained using 139 grid nodes, unevenly distributed, with 20 nodes located within each viscous sublayer.

As the effects of rotation reduce the turbulence levels on the stabilized side of a rotating channel, leading eventually to flow relaminarization, it is important to first check the models' performance in a range of flow conditions spanning the transition regime. This is done here in a heated stationary channel. The results for the skin-friction coefficient C_f are compared in Fig. 17 with the experimental correlations for this parameter [20]. The Gerolymos–Vallet [18] model captures very accurately the discontinuity in C_f at the point of transition. Also notable is this model's ability to exactly reproduce the analytical solution for the laminar regime. The predicted variation in Nu with Re is compared in Fig. 18 with the analytical solution for the laminar regime and with the experimental correlation [21]. Plotted there are the results obtained with both the explicit and the differential models. There are no clear differences between the models' results with both producing a close match to the experimental correlations.

For the flow in a heated channel rotated about its spanwise axis, the effects of rotation are most clearly seen in the changes they bring about in the values of the wall shear stress on the suction and pressure sides. These are shown in Fig. 19, where the ratio of friction velocity in the presence of rotation to that at the same Reynolds number but with no rotation (u_τ/u_{τ_0}) is plotted for various values of the rotation parameter Ro. For moderate values of Ro $(0<\mathrm{Ro}<0.1)$, the model yields results in reasonable agreement with the measurements of Johnston et al. [1] though, for the suction side, the correspondence between the two deteriorates for higher rotation rates.

Comparisons with the DNS results of Nishimura and Kasagi [22] for the heated rotating channel with $\mathrm{Re}_\tau=150$ and Ro

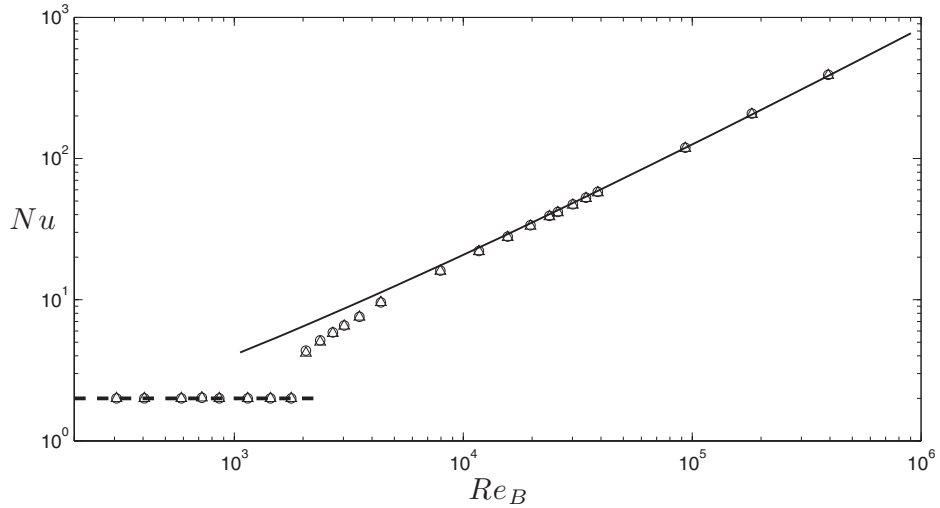

Fig. 18 Nusselt number in stationary channel. Laminar solution (- -), turbulent correlations [21] (—), explicit (○), and differential flux model (△).

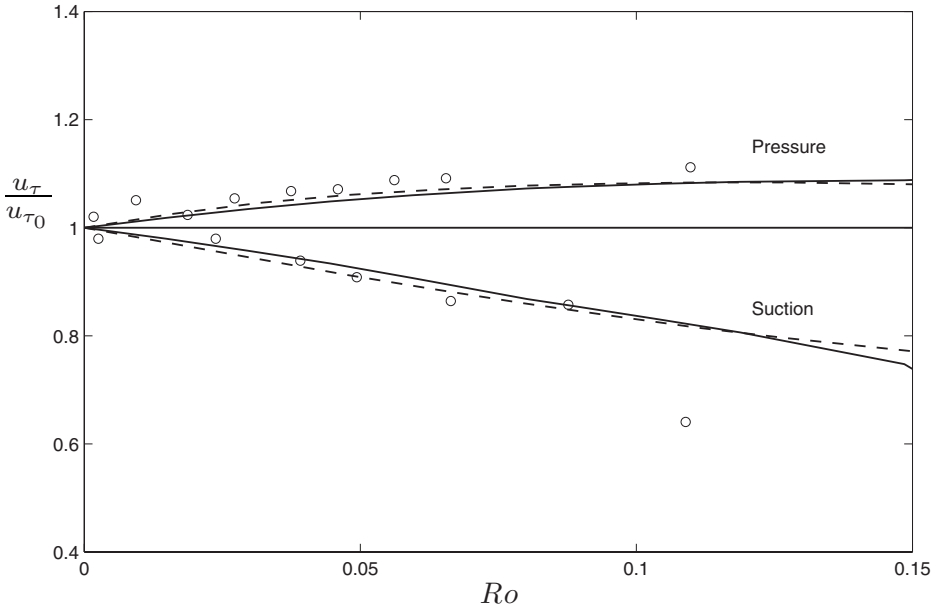

Fig. 19 Friction velocities in spanwise-rotating channel. Data of Johnston et al. [1] (○) and Gerolymos and Vallet [18] (—).

=0.159 are presented in Fig. 20. Predictions obtained with the gradient-transport model Eq. (1) are included for comparison. In general, the explicit model yields the closest correspondence with the DNS results though significant differences are apparent in the central region of the channel. The heat-flux component $\overline{v\theta}$ is well predicted there, but both the explicit and the differential models show it to essentially collapse in the stabilized region of the flow. This is reflected by the predicted value of Nusselt number, which is obtained there by the explicit and differential models as 5.87 and 5.78, respectively. These values compare well with the DNS value of 5.98. In contrast, Fourier's law predicts this quantity as being equal to 5.12.

4 Concluding Remarks

An explicit algebraic model for the turbulent scalar fluxes, derived from tensor-representation theory, has been extended here to account for the effects of system rotation. The resulting model accounts directly for the rates of rotation around all three orthogonal axes in a manner that is consistent with the effects of rotation on the rates of production of the Reynolds stresses and with the principle of coordinates invariance. In order to put this model's performance in the context of what is obtainable from alternative closure strategies, an alternative model was derived using an approach that has proved successful in other complex flows; specifically by the reduction to algebraic form of modeled differential transport equations for the scalar fluxes. Even though the outcome here was a model which is implicit in the scalar fluxes—an undesirable feature from a numerical implementation standpoint—the model nevertheless contains direct dependence on the rotation rates and can thus provide meaningful basis for models comparisons. Moreover, since the gradient-transport model still forms the basis of many practical computations, its results are also included in the assessment.

The models' performance was assessed using recent results from direct numerical simulations of heated flows in channels subjected to different modes of rotation. DNS results for a stationary channel were also considered. It was found that the explicit model performed substantially better than the implicit and the gradient-transport models in all the cases examined while yielding results that are on par with those obtained from the more complicated differential model. The correspondence between this model's predictions and the DNS results was generally satisfactory except in the cases where the mode of rotation leads to the establishment of strong secondary flows in planes normal to the main flow. The effects on the scalar fluxes of these secondary flows (more specifically, the spanwise gradients of mean-velocity and temperature that they give rise to) are directly accounted for in the DNS, and the tabulated values reported from these studies are obtained by time-averaging fully three-dimensional, time-dependent velocity, and temperature fields in which the gradients of instantaneous velocities and temperature were nonzero in all three directions. These gradients will thus have entered into determination of the DNS results for the heat fluxes. However, only the time-averaged velocities and temperature are usually made available from DNS studies and, even then, these are only available along a single direction (the y direction in the cases considered here) and only at the channel's midplane. It was therefore not possible to evaluate either the streamwise or spanwise gradients of velocities and temperature for use in this study. These gradients contribute to the modeled values of $\overline{u_i\theta}$, as can be seen in the equations in the Appendix. It is therefore to be expected that differences between DNS and model results will arise and that the source of such differences will be hard to identify in the absence of sufficient details from the DNS results. As the provision of data suitable for model development is often one of the motivations for DNS, this study highlights the need for documentation of the time-averaged gradients of instantaneous velocities and temperature in all three directions.

Acknowledgment

F.M. and M.S. gratefully acknowledge the financial support provided by the Erich Becker Foundation—Fraport AG.

Nomenclature

$C_1, C_2, \ldots$ = model coefficients
C_f = skin-friction coefficient
G_{ij} = Reynolds stress rotation production rate
k = turbulence kinetic energy
Nu = Nusselt number
P_{ij} = Reynolds-stress shear production rate
$P_{i\theta}$ = scalar-flux production rate
Pr = Prandtl number
Re = Reynolds number

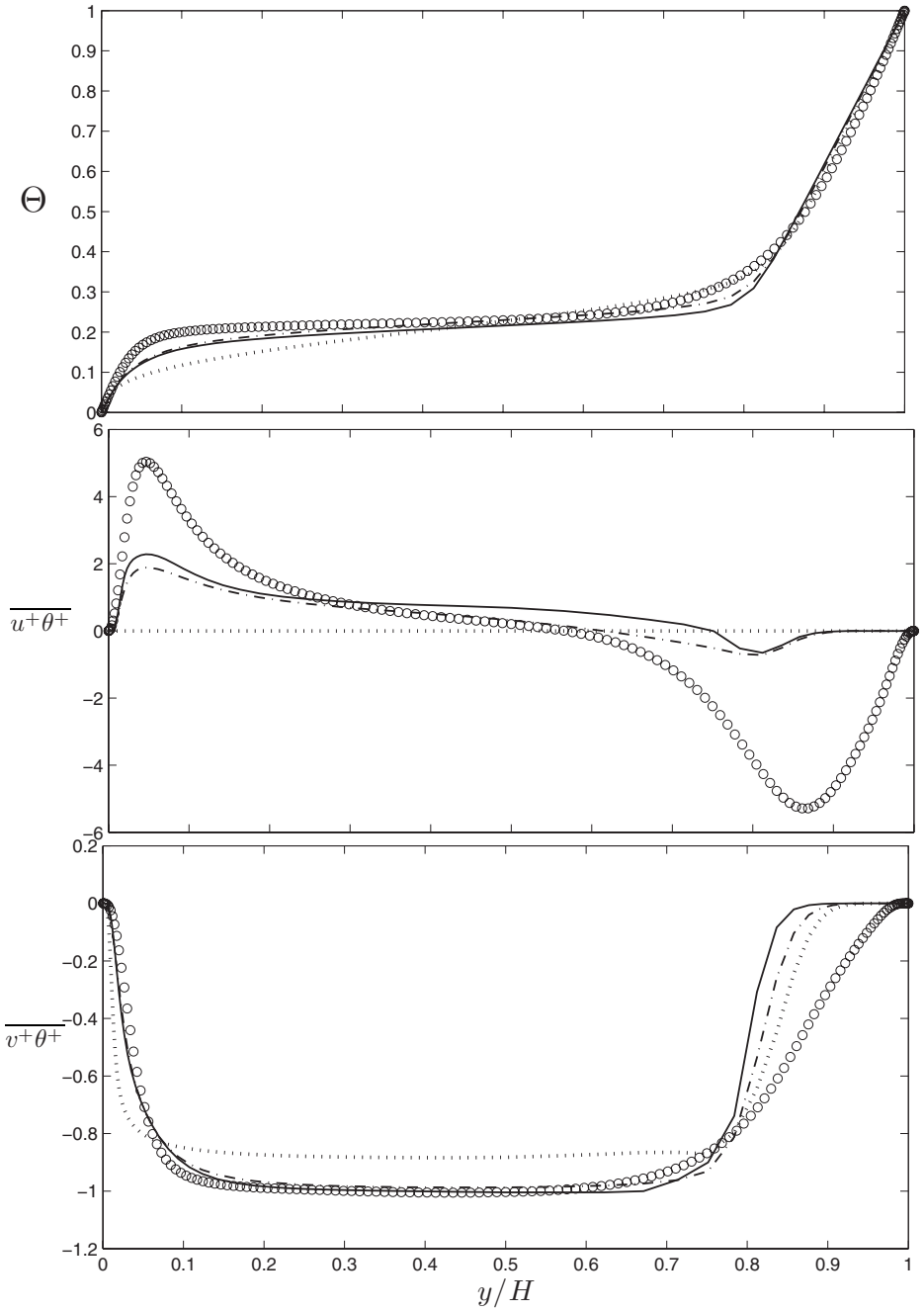

Fig. 20 Rotating channel flow with Re_τ=150 and Ro=0.159. DNS (○), explicit (—), differential flux model (–·–·–), and gradient-transport (···).

Ro = rotation parameter
S_{ij} = mean rate of strain
U_τ = friction velocity
$\overline{u_i u_j}$ = Reynolds stresses
$\overline{u_i\theta}$ = scalar fluxes
W_{ij} = mean vorticity

Greek Symbols

ϵ = viscous dissipation rate
ν_t = eddy-viscosity
Ω = rotation-rate vector
σ_t = turbulent Prandtl number
Θ = mean scalar

Appendix: Model Equations for General Rotation

For the case of rotation around all three axes, the explicit model equations (Eq. (19)) are obtained as

$$-\overline{u\theta} = +C_1\frac{k^2}{\epsilon}\frac{\partial\Theta}{\partial x} + C_2\frac{k}{\epsilon}\left(\overline{u^2}\frac{\partial\Theta}{\partial x} + \overline{uv}\frac{\partial\Theta}{\partial y} + \overline{uw}\frac{\partial\Theta}{\partial z}\right)$$
$$+C_3\frac{k^3}{\epsilon^2}\left(\frac{\partial U}{\partial x}\frac{\partial\Theta}{\partial x} + \left(\frac{\partial U}{\partial y} - \Omega_z\right)\frac{\partial\Theta}{\partial y} + \left(\frac{\partial U}{\partial z} + \Omega_y\right)\frac{\partial\Theta}{\partial z}\right)$$
$$+C_4\frac{k^2}{\epsilon^2}\left[\left(2\overline{u^2}\frac{\partial U}{\partial x} + 2\overline{uv}\left(\frac{\partial U}{\partial y} - \Omega_z\right) + 2\overline{uw}\left(\frac{\partial U}{\partial z} + \Omega_y\right)\right)\frac{\partial\Theta}{\partial x}\right.$$

$$+\left(\overline{u^2}\left(\frac{\partial V}{\partial x}+\Omega_z\right)+\overline{uv}\frac{\partial V}{\partial y}+\overline{uw}\left(\frac{\partial V}{\partial z}-\Omega_x\right)+\overline{uv}\frac{\partial U}{\partial x}+\overline{v^2}\left(\frac{\partial U}{\partial y}-\Omega_z\right)+\overline{vw}\left(\frac{\partial U}{\partial z}+\Omega_y\right)\right)\frac{\partial\Theta}{\partial y}+\left(\overline{u^2}\left(\frac{\partial W}{\partial x}-\Omega_y\right)+\overline{uv}\left(\frac{\partial W}{\partial y}+\Omega_x\right)+\overline{uw}\frac{\partial W}{\partial z}+\overline{uw}\frac{\partial U}{\partial x}+\overline{vw}\left(\frac{\partial U}{\partial y}-\Omega_z\right)+\overline{w^2}\left(\frac{\partial U}{\partial z}+\Omega_y\right)\right)\frac{\partial\Theta}{\partial z}\right] \tag{A1}$$

$$-\overline{v\theta}=C_1\frac{k^2}{\epsilon}\frac{\partial\Theta}{\partial y}+C_2\frac{k}{\epsilon}\left(\overline{uv}\frac{\partial\Theta}{\partial x}+\overline{v^2}\frac{\partial\Theta}{\partial y}+\overline{vw}\frac{\partial\Theta}{\partial z}\right)+C_3\frac{k^3}{\epsilon^2}\left(\left(\frac{\partial V}{\partial x}+\Omega_z\right)\frac{\partial\Theta}{\partial x}+\frac{\partial V}{\partial y}\frac{\partial\Theta}{\partial y}+\left(\frac{\partial V}{\partial z}-\Omega_x\right)\frac{\partial\Theta}{\partial z}\right)+C_4\frac{k^2}{\epsilon^2}\left[\left(\overline{uv}\frac{\partial U}{\partial x}+\overline{v^2}\left(\frac{\partial U}{\partial y}-\Omega_z\right)+\overline{vw}\left(\frac{\partial U}{\partial z}+\Omega_y\right)+\overline{u^2}\left(\frac{\partial V}{\partial x}+\Omega_z\right)+\overline{uv}\frac{\partial V}{\partial y}+\overline{uw}\left(\frac{\partial V}{\partial z}-\Omega_x\right)\right)\frac{\partial\Theta}{\partial x}+\left(2\overline{uv}\left(\frac{\partial V}{\partial x}+\Omega_z\right)+2\overline{v^2}\frac{\partial V}{\partial y}+2\overline{vw}\left(\frac{\partial V}{\partial z}-\Omega_x\right)\right)\frac{\partial\Theta}{\partial y}+\left(\overline{uv}\left(\frac{\partial W}{\partial x}-\Omega_y\right)+\overline{v^2}\left(\frac{\partial W}{\partial y}+\Omega_x\right)+\overline{vw}\frac{\partial W}{\partial z}+\overline{uw}\left(\frac{\partial V}{\partial x}+\Omega_z\right)+\overline{vw}\frac{\partial V}{\partial y}+\overline{w^2}\left(\frac{\partial V}{\partial z}-\Omega_x\right)\right)\frac{\partial\Theta}{\partial z}\right] \tag{A2}$$

$$-\overline{w\theta}=C_1\frac{k^2}{\epsilon}\frac{\partial\Theta}{\partial z}+C_2\frac{k}{\epsilon}\left(\overline{uw}\frac{\partial\Theta}{\partial x}+\overline{vw}\frac{\partial\Theta}{\partial y}+\overline{w^2}\frac{\partial\Theta}{\partial z}\right)+C_3\frac{k^3}{\epsilon^2}\left(\left(\frac{\partial W}{\partial x}-\Omega_y\right)\frac{\partial\Theta}{\partial x}+\left(\frac{\partial W}{\partial y}+\Omega_x\right)\frac{\partial\Theta}{\partial y}+\frac{\partial W}{\partial z}\frac{\partial\Theta}{\partial z}\right)+C_4\frac{k^2}{\epsilon^2}\left[\left(\overline{uw}\frac{\partial U}{\partial x}+\overline{vw}\left(\frac{\partial U}{\partial y}-\Omega_z\right)+\overline{w^2}\left(\frac{\partial U}{\partial z}+\Omega_y\right)+\overline{u^2}\left(\frac{\partial W}{\partial x}-\Omega_y\right)+\overline{uv}\left(\frac{\partial W}{\partial y}+\Omega_x\right)+\overline{uw}\frac{\partial W}{\partial z}\right)\frac{\partial\Theta}{\partial x}+\left(\overline{uw}\left(\frac{\partial V}{\partial x}+\Omega_z\right)+\overline{vw}\frac{\partial V}{\partial y}+\overline{w^2}\left(\frac{\partial V}{\partial z}-\Omega_x\right)+\overline{uv}\left(\frac{\partial W}{\partial x}-\Omega_y\right)+\overline{v^2}\left(\frac{\partial W}{\partial y}+\Omega_x\right)+\overline{vw}\frac{\partial W}{\partial z}\right)\frac{\partial\Theta}{\partial y}+\left(2\overline{uw}\left(\frac{\partial W}{\partial x}-\Omega_y\right)+2\overline{vw}\left(\frac{\partial W}{\partial y}+\Omega_x\right)+2\overline{w^2}\frac{\partial W}{\partial z}\right)\frac{\partial\Theta}{\partial z}\right] \tag{A3}$$

References

[1] Johnston, J. P., Halleen, R. M., and Lezius, D. K., 1972, "Effects of Spanwise Rotation on the Structure of Two-Dimensional Fully Developed Turbulent Channel Flow," J. Fluid Mech., **56**, pp. 533–557.

[2] Weigand, B., and Beer, H., 1989, "Heat-Transfer in an Axially Rotating Pipe in the Thermal Entrance Region: 1. Effect of Rotation on Turbulent Pipe Flow," Waerme- Stoffuebertrag., **24**(4), pp. 191–202.

[3] Speziale, C. G., Younis, B. A., and Berger, S. A., 2000, "Analysis and Modelling of Turbulent Flow in an Axially Rotating Pipe," J. Fluid Mech., **407**, pp. 1–26.

[4] Launder, B. E., Tselepidakis, D. P., and Younis, B. A., 1987, "A Second-Moment Closure Study of Rotating Channel Flow," J. Fluid Mech., **183**, pp. 63–75.

[5] Younis, B. A., Speziale, C. G., and Berger, S. A., 1998, "Accounting for Effects of a System Rotation on the Pressure-Strain Correlation," AIAA J., **36**, pp. 1746–1748.

[6] Launder, B. E., 1976, "Heat and Mass Transport," *Turbulence*, P. Bradshaw, ed., Springer-Verlag, Berlin, pp. 231–287.

[7] Malin, M., and Younis, B. A., 1997, "The Prediction of Turbulent Transport in an Axially Rotating Pipe," Int. Commun. Heat Mass Transfer, **24**, pp. 89–99.

[8] Younis, B. A., Speziale, C. G., and Clark, T. T., 2005, "A Rational Model for the Turbulent Scalar Fluxes," Proc. R. Soc. London, Ser. A, **461**, pp. 575–594.

[9] Younis, B. A., Weigand, B., and Spring, S., 2007, "An Explicit Algebraic Model for Turbulent Heat Transfer in Wall-Bounded Flow With Streamline Curvature," ASME J. Heat Transfer, **129**, pp. 425–433.

[10] Gibson, M. M., 1978, "An Algebraic Stress and Heat-Flux Model for Turbulent Shear Flow With Streamline Curvature," Int. J. Heat Mass Transfer, **21**, pp. 1609–1617.

[11] Bremhorst, K., and Bullock, K. J., 1970, "Spectral Measurements of Temperature and Longitudinal Velocity Fluctuations in Fully Developed Pipe Flow," Int. J. Heat Mass Transfer, **13**, pp. 1313–1329.

[12] Bremhorst, K., and Bullock, K. J., 1973, "Spectral Measurements of Turbulent Heat and Momentum Transfer in Fully Developed Pipe Flow," Int. J. Heat Mass Transfer, **16**, pp. 2141–2154.

[13] Debusschere, B., and Rutland, C. J., 2004, "Turbulent Scalar Transport Mechanisms in Plane Channel and Couette Flows," Int. J. Heat Mass Transfer, **47**, pp. 1771–1781.

[14] Chien, K.-Y., 1982, "Predictions of Channel and Boundary-Layer Flows With a Low Reynolds-Number Model," AIAA J., **20**, pp. 33–38.

[15] El-Samni, O. A., and Kasagi, N., 2001, "The Effects of System Rotation With Three Orthogonal Rotating Axes on Turbulent Channel Flow," *Proceedings of the ICFDP7: Seventh International Conference of Fluid Dynamics and Propulsion*, Sharm El-Sheik, Egypt, Dec. 19–21.

[16] Wu, H., and Kasagi, N., 2004, "Effects of Arbitrary Directional System Rotation on Turbulent Channel Flow," Phys. Fluids, **16**, pp. 979–990.

[17] El-Samni, O. A., and Kasagi, N., 2000, "Heat And Momentum Transfer In Rotating Turbulent Channel Flow," *Proceedings of the Fourth JSME-KSME Thermal Engineering Conference*, Kobe, Japan, Oct. 1–6.

[18] Gerolymos, G. A., and Vallet, I., 2001, "Wall-Normal-Free Reynolds-Stress Closure for Three-Dimensional Compressible Separated Flows," AIAA J., **39**, pp. 1833–1842.

[19] Younis, B. A., 1996, "EXPRESS: Accelerated Parabolic Reynolds Stress Solver," City University London, Hydraulics Section Report No. HDBAY1.

[20] Kakac, S., Shah, R. K., and Aung, W., 1987, *Handbook of Single-Phase Convective Heat Transfer*, Wiley, New York.

[21] Kays, W. M., Crawford, M., and Weigand, B., 2004, *Convective Heat and Mass Transfer*, 4th ed., McGraw-Hill, New York.

[22] Nishimura, M., and Kasagi, N., 1996, "Direct Numerical Simulation of Combined Forced and Natural Turbulent Convection in a Rotating Plane Channel," *Proceedings of the Third KSME-JSME Thermal and Fluids Engineering Conference*, Kyongju, Korea, Vol. 3, pp. 77–82.

Computational Fluid Dynamics Evaluation of Heat Transfer Correlations for Sodium Flows in a Heat Exchanger

Seok-Ki Choi[1]
e-mail: skchoi@kaeri.re.kr

Seong-O Kim

Fast Reactor Development Division,
Korea Atomic Energy Research Institute,
150-1 Deokjin-dong,
Yuseong-gu, Daejeon 305-353, Korea

Hoon-Ki Choi
Department of Mechanical Engineering,
Changwon National University,
7 Sarim-dong,
Changwon, Gyeongnam 641-773, Korea

*A numerical study for the evaluation of heat transfer correlations for sodium flows in a heat exchanger of a fast breeder nuclear reactor is performed. Three different types of flows such as parallel flow, cross flow, and two inclined flows are considered. Calculations are performed for these three typical flows in a heat exchanger changing turbulence models. The tested turbulence models are the shear stress transport (SST) model and the SSG-Reynolds stress turbulence model by Speziale, Sarkar, and Gaski (1991, "Modelling the Pressure-Strain Correlation of Turbulence: An Invariant Dynamical System Approach," J. Fluid Mech., **227**, pp. 245–272). The computational model for parallel flow is a flow past tubes inside a circular cylinder and those for the cross flow and inclined flows are flows past the perpendicular and inclined tube banks enclosed by a rectangular duct. The computational results show that the SST model produces the most reliable results that can distinguish the best heat transfer correlation from other correlations for the three different flows. It was also shown that the SSG-RSTM high-Reynolds number turbulence model does not deal with the low-Prandtl number effect properly when the Peclet number is small. According to the present calculations for a parallel flow, all the old correlations do not match with the present numerical solutions and a new correlation is proposed. The correlations by Dwyer (1966, "Recent Developments in Liquid-Metal Heat Transfer," At. Energy Rev., **4**, pp. 3–92) for a cross flow and its modified correlation that takes into account of flow inclination for inclined flows work best and are accurate enough to be used for the design of the heat exchanger.*
[DOI: 10.1115/1.4000707]

1 Introduction

The heat exchanger of a liquid metal nuclear power reactor is a shell-and-tube heat exchanger and on the shell side of the heat exchanger a liquid metal such as sodium flows across the tube bundles in all directions from parallel to perpendicular. Thus, a proper heat transfer coefficient for these flow conditions should be provided for a better heat exchanger design. However, the experimental correlations for a heat transfer of a liquid metal are very rare in literature since the sodium experiment is very expensive and difficult. The most difficult thing is that the differences among the correlations are so grave that it is difficult to decide which correlation should be used for a particular flow situation. In the present study, we propose a computational fluid dynamics (CFD) evaluation of the existing heat transfer correlations for sodium flows in a heat exchanger so that an appropriate heat transfer correlation is used for a particular flow situation.

It is useful to outline the previous heat transfer correlations for parallel flow, cross flow, and inclined flows. For a parallel flow without a baffle, many correlations have been proposed in the past mainly for the design of a fuel assembly. Those are the Westinghouse and modified-Schad correlations by Tang et al. [1], Graber and Rieger [2], Borishansky et al. [3], and Kisohara et al. [4]. The comparisons of these correlations with experimental data are given by Tang et al. [1]. It is shown that for P/D values of 1.1 and 1.2, the modified-Schad (by Tang et al. [1]) and Borishansky et al. [3] correlations agree best with the experimental data while the correlation by Graber and Rieger [2] overpredicts the heat transfer coefficient when the P/D value is 1.1. They also reported that the Westinghouse correlation (by Tang et al. [1]) underestimates the heat transfer coefficient when the P/D value is 1.2. These observations indicate that the performance of each correlation is strongly dependent on the value of P/D and care should be paid in choosing a proper correlation for a particular problem. For example, the P/D range of the Westinghouse correlation is $1.15 \leq P/D \leq 1.3$ and that of the modified-Schad correlation is $1.05 \leq P/D \leq 1.15$. Thus, the above conclusions cannot be applied to a parallel flow in an intermediate heat exchanger of a liquid metal reactor where the P/D values are relatively high; for example, the P/D value is 1.6 for the Korea Advanced Liquid Metal Reactor design.

For a cross flow, Hsu [5] published analytic solutions for a heat transfer coefficient based on the following assumptions: (a) the physical properties are constant, (b) the flow is two-dimensional and steady, (c) the flow is incompressible, inviscid, and irrotational, (d) there is no contact resistance at a solid-liquid interface, (e) a negligible eddy conductivity compared with a molecular conduction, (f) the hydrodynamic potential distribution on the surface of a tube is linear, and (f) there is no interaction between the boundary layers of adjacent tubes. The assumption of a negligible eddy conductivity compared with a molecular conduction is a good assumption when the Peclet number is small. Using these assumptions, Hsu [5] developed two correlations for the condition of a simple cosine surface temperature distribution around a tube and for the condition of a uniform heat flux from a tube. These correlations show linear profiles on the log-log plot of Nusselt number (Nu) versus Peclet number (Pe). ($\mathrm{Nu} = a(\mathrm{Pe})^b_{v,\max}$). Later, Dwyer [6] presented the experimental results by Hoe et al. [7], Rickard et al. [8], and Subbotin et al. [9] and claimed that the

[1]Corresponding author.

Contributed by the Heat Transfer Division of ASME for publication in the JOURNAL OF HEAT TRANSFER. Manuscript received December 3, 2008; final manuscript received November 3, 2009; published online March 4, 2010. Assoc. Editor: S. A. Sherif.

profiles should be concave upward and explained that the linear profile on a log-log plot of Nu versus Pe in the theoretical study by Hsu [5] was due to the assumption of inviscid and irrotational flow in its derivation. Dwyer and co-worker [6,7] modified Hsu's correlation to remedy this problem. They derived another correlation for a concave upward type of correlation. ($\mathrm{Nu}=a+b(\mathrm{Pe})^{c}_{v,\max}$).

In estimating the heat transfer coefficients for inclined flows, it is a good approximation to assume that they are the same as the cross flow through a bundle of elliptically shaped rods. Hsu [11] developed such a correlation using the same assumptions as those for a cross flow. Thus, this correlation gives a straight line on a log-log plot of Nu versus Pe, whereas the true curve is presumably one of increasing slope as the Peclet number is increased, which gives a concave upward shape on a log-log plot of Nu versus Pe. Dwyer [6] modified Hsu's correlation to account for the flow inclination effect by a function of the inclined angle. Kalish and Dwyer [10] later devised a different correlation from their NaK experimental data.

It is evident that the heat transfer correlations for a liquid metal flow are not abundant compared with those of water or air. In the present study a CFD evaluation of a sodium heat transfer coefficient is proposed. The CFD at present is mature enough to calculate complex flows and the existing sodium heat transfer correlations for the design of a heat exchanger are evaluated by the CFD results and the compared results are presented. The CFD code used in the present study is CFX-11 code and four different turbulence models such as the shear stress transport model (SST), the renormalization group (RNG) $k-\varepsilon$ model, the SSG-Reynolds stress turbulence model (SSF-RSTM), and the omega-Reynolds stress turbulence model (omega-RSTM), which are available in CFX-11 code are tested to see the impact of a turbulence model on the solutions.

In what follows, we present the existing heat transfer correlations for parallel flow, cross flow, and inclined flows. Then, the numerical method is briefly explained and the numerical evaluation of the heat transfer coefficients is presented, followed by a conclusion.

2 Heat Transfer Correlations for Liquid Metal Flows

2.1 Parallel Flow. The liquid metal heat transfer correlations for a parallel flow are relatively abundant, mainly due to the design of a fuel assembly, and in this case the range of P/D value is very small ($P/D=1.15-1.35$) compared with that of a parallel flow in a heat exchanger. Among them, the following six correlations are considered in the present study:

(1) Graber–Rieger [2] correlation

$$\mathrm{Nu}=0.25+6.20\left(\frac{P}{D}\right)+\left(-0.007+0.032\frac{P}{D}\right)(\mathrm{Pe})^{\left(0.8-0.024\frac{P}{D}\right)} \tag{1}$$

(2) Lubarsky–Kaufman [12] correlation

$$\mathrm{Nu}=0.625(\mathrm{Pe})^{0.4} \tag{2}$$

(3) Seban–Shimazaki [13] correlation

$$Nu=5.0+0.025(Pe)^{0.8} \tag{3}$$

(4) Kisohara et al. [4] correlation

$$\mathrm{Nu}=4.77+0.728(\mathrm{Pe})^{0.454} \tag{4}$$

(5) Westinghouse correlation by Tang et al. [1]:

$$\mathrm{Nu}=4.0+0.33\left(\frac{P}{D}\right)^{3.8}\left(\frac{\mathrm{Pe}}{100}\right)^{0.86}+0.16\left(\frac{P}{D}\right)^{5.0} \tag{5}$$

(6) Present correlation

$$\mathrm{Nu}=0.16+4.03\left(\frac{P}{D}\right)+\left(-0.005+0.021\frac{P}{D}\right)(\mathrm{Pe})^{(0.8-0.024(P/D))} \tag{6}$$

2.2 Cross Flow. Three liquid metal heat transfer correlations for a cross flow are considered.

(1) Hsu [5] correlation

$$\mathrm{Nu}=0.958\left(\frac{\phi_1}{D}\right)^{0.5}\left(\frac{P-D}{P}\right)^{0.5}(\mathrm{Pe}_{v,\max})^{0.5} \tag{7}$$

(2) Kalish and Dwyer [10] correlation

$$\mathrm{Nu}=\left(\frac{\phi_1}{D}\right)^{0.5}\left(\frac{P-D}{P}\right)^{0.5}(6.19+0.2665[\mathrm{Pe}_{v,\max}]^{0.635}) \tag{8}$$

(3) Dwyer [6] correlation

$$\mathrm{Nu}=\left(\frac{\phi_1}{D}\right)^{0.5}\left(\frac{P-D}{P}\right)^{0.5}(5.36+0.1974[\mathrm{Pe}_{v,\max}]^{0.682}) \tag{9}$$

2.3 Inclined Flows. Only three liquid metal heat transfer correlations for an inclined flow exist within the present author's knowledge and they are as follows:

(1) Kalish and Dwyer [10] correlation

$$\mathrm{Nu}=\left(\frac{\phi_1}{D}\right)^{0.5}\left(\frac{P-D}{P}\right)^{0.5}\left[\frac{\sin\beta+\sin^2\beta}{1+\sin^2\beta}\right]^{0.5}(5.44+0.228[\mathrm{Pe}_{v,\max}]^{0.614}) \tag{10}$$

(2) Dwyer [6]) correlation

$$\mathrm{Nu}=0.958\left(\frac{\phi_1}{D}\right)^{0.5}\left(\frac{P-D}{P}\right)^{0.5}\left[\frac{\sin\beta+\sin^2\beta}{1+\sin^2\beta}\right]^{0.5}[\mathrm{Pe}_{v,\max}]^{0.5} \tag{11}$$

(3) Modified Dwyer [6] correlation

$$\mathrm{Nu}=\left(\frac{\phi_1}{D}\right)^{0.5}\left(\frac{P-D}{P}\right)^{0.5}\left[\frac{\sin\beta+\sin^2\beta}{1+\sin^2\beta}\right]^{0.5}(5.36+0.1974[\mathrm{Pe}_{v,\max}]^{0.682}) \tag{12}$$

In the above equations, β is the inclined angle and ϕ_1 is a hydrodynamic potential function and its value for many different cases of the P/D are tabulated by Hsu [5].

3 Turbulence Models

The selection of turbulence model is very important for accurate prediction of thermal-hydraulic problems. Four turbulence models, which are available in CFX-11 code [14], are considered and they are the SST, the RNG $k-\varepsilon$ model, the SSG-RSTM, and the omega-RSTM. The SST model and RNG $k-\varepsilon$ model are commonly used two-equation turbulence models, which have been validated for various problems in literature and these two models are known to perform better than the conventional $k-\varepsilon$ model, especially for the problems involving separation and curvature effect such as the present problem. The SSG-RSTM turbulence model is chosen here due to its theoretically sound derivation of the pressure-strain term [15] and is also due to the best performance among the high-Reynolds number Reynolds stress models available in CFX-11 code. The omega-RSTM model is tested here to investigate the performance of the low-Reynolds number second-moment closure for the present problem. The SST and omega-RSTM models are the low-Reynolds number models in which calculations are carried out all the way to the wall, while the RNG $k-\varepsilon$ and SSG-RSTM models are the high-Reynolds number models and use the wall functions near the wall. A preliminary test of the above four turbulence models was performed and it was shown that for a low-Reynolds number model the SST model gives nearly same solutions as the omega-RSTM. It was

also shown that the SSG-RSTM model outperforms the RNG $k-\varepsilon$ model for the present problem. The results of these tests lead us to use the SST model and the SSG-RSTM for the present purpose. As details of these two models are given in CFX-11 code [14] only a brief description of them is given here.

The transport equations for the turbulence kinetic energy and its specific dissipation rate in the SST model can be written as follows:

$$\frac{\partial}{\partial t}(\rho k)+\frac{\partial(\rho U_j k)}{\partial x_j}=\frac{\partial}{\partial x_j}\left[\left(\mu+\frac{\mu_T}{\sigma_{k*}}\right)\frac{\partial k}{\partial x_j}\right]+P_k-\beta'\rho k\omega \quad (13)$$

$$\frac{\partial}{\partial t}(\rho\omega)+\frac{\partial(\rho U_j\omega)}{\partial x_j}=\frac{\partial}{\partial x_j}\left[\left(\mu+\frac{\mu_T}{\sigma_\omega}\right)\frac{\partial\omega}{\partial x_j}\right]+\alpha\frac{\omega}{k}P_k-\rho\beta\omega^2+(1-F_1)\frac{2\rho}{\sigma_{\omega 2}\omega}\frac{\partial k}{\partial x_j}\frac{\partial\omega}{\partial x_j} \quad (14)$$

In this model, a blending function (F_1) is used to activate the Wilcox $k-\omega$ model close to the wall and the $k-\varepsilon$ model in the outer region. By this approach, the SST model overcomes the deficiencies of both $k-\varepsilon$ and $k-\omega$ models. The advantage of the ω-equation is that it allows for a more accurate near wall treatment with an automatic switch from a wall function to a low-Reynolds number formulation based on the grid spacing.

The governing equations for the Reynolds stresses and their dissipation rate in the SSG-RSTM can be written as follows:

$$\frac{\partial}{\partial t}(\rho\overline{u_iu_j})+\frac{\partial(\rho U_k\overline{u_iu_j})}{\partial x_k}=\frac{\partial}{\partial x_k}\left[\left(\mu+\frac{2}{3}C_s\frac{k^2}{\varepsilon}\right)\frac{\partial\overline{u_iu_j}}{\partial x_k}\right]+P_{ij}+\phi_{ij}-\frac{2}{3}\delta_{ij}\rho\varepsilon \quad (15)$$

$$\frac{\partial}{\partial t}(\rho\varepsilon)+\frac{\partial(\rho U_k\varepsilon)}{\partial x_k}=\frac{\partial}{\partial x_k}\left[\left(\mu+\frac{\mu_T}{\sigma_\varepsilon}\right)\frac{\partial\varepsilon}{\partial x_k}\right]+\frac{\varepsilon}{k}(C_{\varepsilon 1}P_k-C_{\varepsilon 2}\rho\varepsilon) \quad (16)$$

In the SSG-RSTM, the pressure-strain term (ϕ_{ij}) is treated by that given by Speziale et al. [15].

4 Results and Discussion

Let us consider a flow situation where the sodium (liquid Na) flows inside a circular cylinder or rectangular duct in which several tubes are placed as shown in Fig. 1. The energy balance equation can be written as follows:

$$hA_w(T_b-T_w)=\dot{m}C_p(T_{\text{in}}-T_{\text{out}}) \quad (17)$$

The overall Nusselt number can be obtained as follows if the outlet temperature (T_{out}) and the bulk temperature (T_b) are known from the numerical results:

$$\text{Nu}=\frac{h}{k}D=\frac{\dot{m}C_pD(T_{\text{in}}-T_{\text{out}})}{kA_w(T_b-T_w)} \quad (18)$$

The inlet temperature of sodium (T_{in}) is 818 K and the wall temperature of the tube (T_w) is 598 K for all cases considered in the present study. The working fluid in the present study is a liquid Na and the physical properties of the liquid Na are based on the average temperature of inlet and tube wall (=708 K). The outer diameter of the tube is 12.7 mm. The bulk temperature (T_b) is obtained from the volume average of the temperature in the tube region.

For boundary conditions, the temperature and mass flow rate are specified at the inlet and at the outlet the pressure boundary condition and the zero gradient temperature condition are imposed. The adiabatic wall condition was imposed for the outer cylinder in the parallel flow computation and the same condition was imposed at the top and bottom boundaries for the cross and inclined flows. The symmetry condition can be imposed at the top and bottom walls for the cross and inclined flows and it was shown that the calculated heat transfer coefficients were nearly same between two different impositions of boundary condition. The symmetry condition was imposed at the lateral (left and right) boundaries

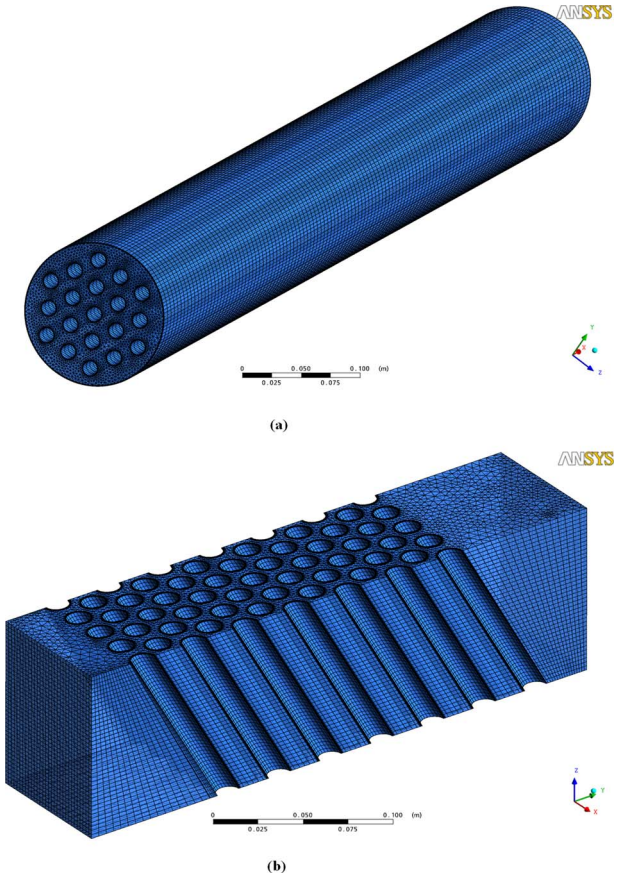

Fig. 1 Numerical grids: (*a*) parallel flow and (*b*) inclined flow

Typically 350,000–560,000 numerical grids are generated using the WORKBENCH program in CFX-11 code. The shapes of typical numerical grids are shown in Fig. 1 for a parallel flow and an inclined flow where the inclined angle is 60 deg. In this figure, the pitch to tube diameter ratio (P/D) is 1.85 for the parallel flow and is 1.6 for the cross and inclined flows. Calculations are performed changing the inlet mass flow rate. The inlet mass flow rate is divided by eight intervals in a range between 0.54 kg/s and 5.4 kg/s, and this corresponds to the Peclet number in a range of $40 \le \text{Pe} \le 400$. In the initial phase of the present study, the grid sensitivity on the numerical solutions are performed. Figure 2 shows the predicted Nusselt number using two different numerical grids for the 60 deg inclined flow. This figure shows that the predicted heat transfer coefficient is not so sensitive to the numerical grid when the numerical grids are properly refined near the wall. All the numerical solutions presented in this paper are those using the fine grids. In order to check whether the first grid point from the tube wall is placed within the logarithmic layer when the wall function method is used in the calculations by the SSG-RSTM high-Reynolds number model, the value of $y+$ was checked for the whole tube walls. The maximum value of $y+$ for a cross flow when the Peclet number is maximum (Pe=400) was 62.25, indicating that the grid refinement near the wall is properly done in the calculations by the SSG-RSTM. In CFX-11 code, the typical convergence is declared when all the root-mean-square of the residuals of momentum equations and energy equation is less than 10^{-4} and we adopt this criterion for all calculations. Due to using

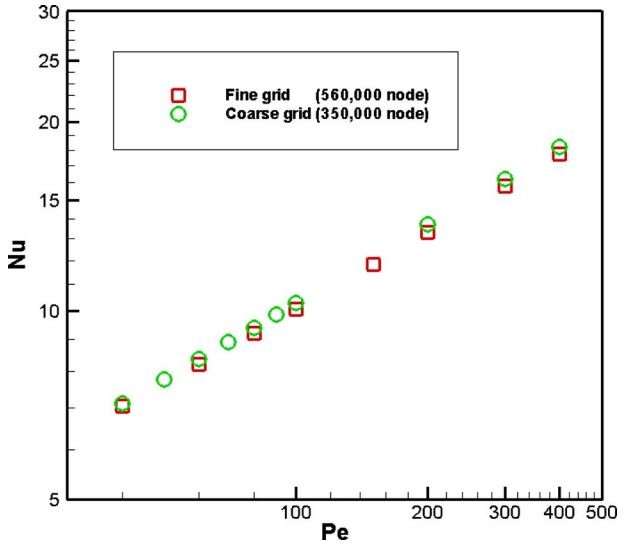

Fig. 2 Grid dependency test (SST model, $Pe_{v,max}$=400, and β =60 deg)

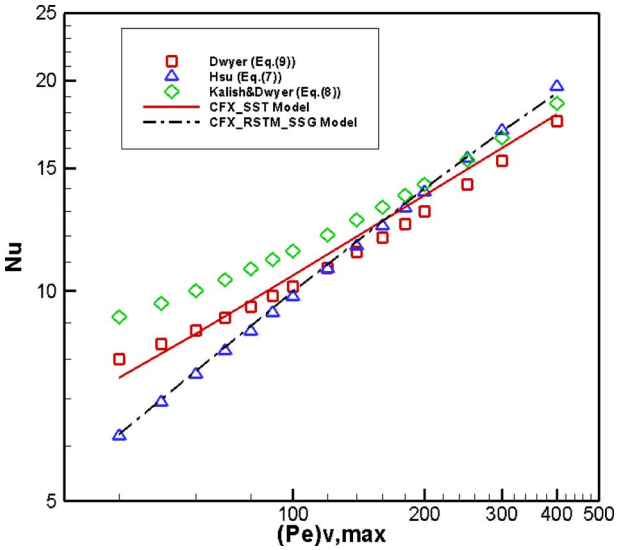

Fig. 4 Comparison of correlations and CFD results for a cross flow (β=90 deg)

the coupled method in CFX-11 code, the convergence is reached within 50 iterations for all cases.

4.1.1 Parallel Flow. Figure 3 shows the predicted Nusselt number profiles by the two turbulence models together with the previous correlations for a parallel flow. The Pe number in this figure is that based on the average inlet velocity. We can observe that the Graber and Rieger [2] correlation predicts the Nusselt number much larger than the present solutions using the two different turbulence models. The differences in the magnitude of the Nusselt number between the Graber and Rieger [2] correlation and the present numerical results are very large. It may be partly due to the different imposition of temperature boundary condition at the tube wall (q_w=constant by Graber and Rieger [2] and T_w=constant in the present study). However, the trend of increase in the Nusselt number versus the Peclet number is nearly the same as the present predictions. The correlation by Kisohara et al. [4] and the Westinghouse correlation by Tang et al. [1] predicted the Nusselt number nearly the same and the predicted Nusselt numbers increases rapidly as the Peclet number increase when compared with other correlations. Their predictions are nearly the same as the present numerical results only when the Peclet number is very small (Pe$\approx$40) and the differences become more grave when the Peclet number becomes larger. It is observed that the correlations by Lubarsky–Kaufman [12] and Seban–Shimazaki [13] predicted the Nusselt number much smaller than the present numerical results in the whole range of the Peclet number considered (40$\leq$Pe$\leq$400). If the Peclet number is relatively small, the heat transfer is dictated by the molecular conduction due to the high conductivity of the sodium and the heat transfer curve should be flat or concave [6] as is observed in the results by the SST model. It is noted that the SSG-RSTM is a high-Reynolds number model and this model use the wall functions near the wall, thus the near wall turbulence is not modeled properly especially when the Peclet number is small and that is observed in the Fig. 3. When the Peclet number is rather large (Pe$\geq$140) and the flow become fully turbulent, the two models result in nearly the same magnitude for the heat transfer coefficient. We can observe that the SSG-RSTM produce a little convex curve when the Peclet number is very small (Pe$\leq$60), which is a contradiction to the physical phenomenon explained before. The SST model predicts the proper behaviors and a new correlation based on the predictions by the SST model is proposed (Eq. (6)) since no previous correlations match with our predictions. It is noted that the correlations by Graber and Rieger [2], Seban–Shimazaki [13], and the proposed correlation showed the same trends of increase in Nusselt number versus the Peclet number, as shown in Fig. 3, although the magnitudes of Nusselt number are different. It is noted that when one considers a conservative design based on the our proposed correlation, one may choose the correlation by Seban–Shimazaki [13] and it was done recently by Mochizuki and Takano [16] in their heat transfer analysis of heat exchanger in a sodium cooled fast reactor.

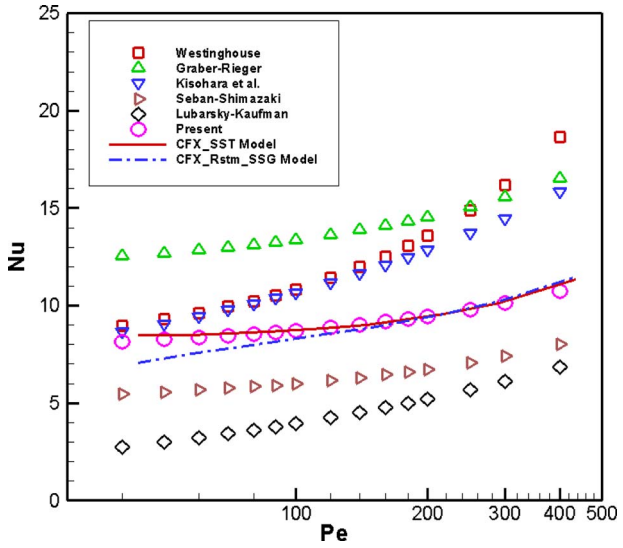

Fig. 3 Comparison of correlations and CFD results for a parallel flow

4.1.2 Cross Flow. Fig. 4 shows the log-log plot of the Nusselt number versus the Peclet number for a cross flow (β=90 deg). The Peclet number in this figure ($(Pe)_{v,max}$) is the Peclet number based on the maximum inlet velocity. The prediction by the SSG-RSTM follows the theoretical correlation by Hsu [5] while that of the SST model follows the Dwyer's correlation. The Hsu's correlation is based on the assumptions such that the flow is two-dimensional, incompressible, inviscid, and irrotational as mentioned earlier. The fact that the prediction by the SSG-RSTM matches with Hsu's correlation means that the high Reynolds

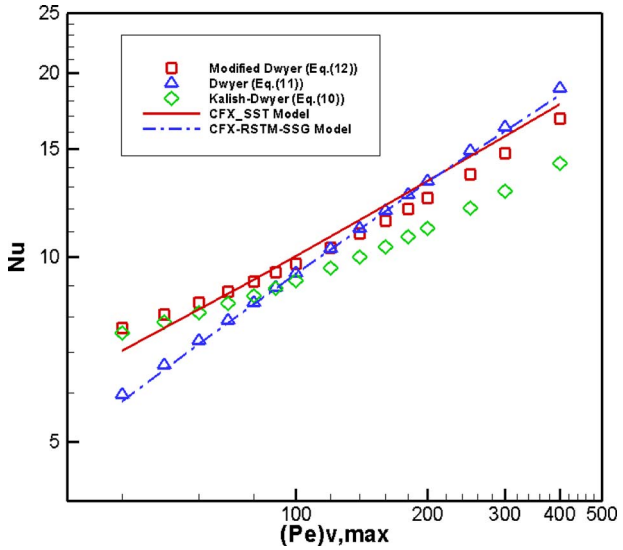

Fig. 5 Comparison of correlations and CFD results for an inclined flow (β=60 deg)

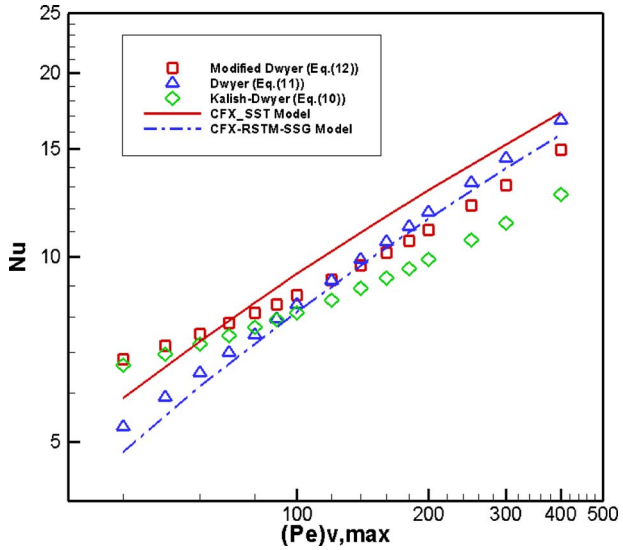

Fig. 6 Comparison of correlations and CFD results for an inclined flow (β=30 deg)

number model SSG-RSTM with the wall function method behaves like an inviscid and irrotational flow when the Peclet number is small. The inaccurate behavior of the high Reynolds number turbulence model is due to the use of the wall function method near the wall and is also due to the fact that the high Reynolds number model does not properly deal with the low-Prandtl number effect when the Peclet number is small. The SST model predicts a little larger magnitude of the heat transfer coefficient than that by the SSG-RSTM when the Peclet number is small ($(\mathrm{Pe})_{v,\max} \leq 100$). The predictions by the SST model agrees well with the correlation by Dwyer [6] in Eq. (9), when the Peclet number is small and they also agree well with the correlation by Kalish and Dwyer [10] in Eq. (8), when the Peclet number is large. Note that the SST model calculates the momentum and energy equations all the way to the wall and properly model the near wall behavior. The difference between the present predictions by the SST model and the correlation by the Dwyer [6] is small and the Dwyer's correlation (Eq. (9)) can be used for the design of a heat exchanger in a liquid metal nuclear reactor. Note that the correlation by Kalish and Dwyer [10] overpredicts the heat transfer coefficient when the Peclet number is small.

4.1.3 Inclined Flows. Figures 5 and 6 show the predicted Nusselt number versus the Peclet number on the log-log plot for the inclined flows where the inclined angles are 60 deg and 30 deg, respectively. The heat transfer correlations for the inclined flows of a liquid metal are very rare in literature. We could only find three correlations such as those by Kalish and Dwyer [10] in Eq. (10), and Dwyer [6] in Eq. (11), and the modified Dwyer correlation in Eq. (12). The Dwyer's correlation is based the theoretical study by Hsu [11]. Dwyer [6] modified Hsu's correlation to account for the flow inclination effect by multiplying a function based on the inclined angle. Thus, this correlation gives a straight line on the log-log plot of the Nusselt number versus the Peclet number whereas the true curve from the experimental data is a concave upward shape [6]. The correlation by Kalish and Dwyer [10] is based on their NaK experimental data. Figure 5 shows the predictions by the two turbulence models and the experimental correlations for an inclined flow where the inclined angle is 60 deg. It is observed that the numerical result by the SSG-RSTM follows the correlation by Dwyer [6] in Eq. (11). The prediction by the SST model agrees well with the modified correlation by Dwyer [6] in Eq. (12) and they also agree well with the correlation by Dwyer [6] when the Peclet number is large. Similar behaviors have been observed for cross flow. It should be noted that the correlation by Kalish and Dwyer [6] severely underpredicted the heat transfer coefficient when the Peclet number is larger than 150. When the inclined angle is small (β=30 deg), the computational results for the heat transfer coefficient follow a very similar trend although some differences in the magnitude of Nusselt number exist, which can be seen in Fig. 6. The heat transfer coefficient by the SSG-RSTM follows the correlation by Dwyer [6] in Eq. (11) as expected. The predicted Nusselt number by the SST model generally follows that of the modified correlation by Dwyer [6] in Eq. (12) and a small difference in magnitude of heat transfer coefficient exists. This may be due to the numerical error originated from using strongly nonorthogonal numerical grids. It is observed that the correlation by Kalish and Dwyer [10] in Eq. (10) underpredicted the heat transfer coefficient when the Peclet number is large. All of these results recommend us to use the modified correlation by Dwyer [6] in Eq. (12) for inclined flows.

5 Conclusions

The results of the present numerical study for the evaluation of heat transfer correlations for liquid metal fluid flows in a heat exchanger are presented. The computations were performed for parallel flow, cross flow, and inclined flows changing turbulence models. The turbulence models employed in the present study are the SST model and the SSG-Reynolds stress model. The following conclusions are drawn from the present study.

(1) The high-Reynolds model SSG-RSTM does not behave properly in a region where the Peclet number is small while the SST model results in reliable solutions for a whole region ($40 \leq \mathrm{Pe} \leq 400$).
(2) For parallel flow, no previous correlations match well with the present computational results and a new correlation is proposed based on the present results by the SST model in Eq. (6).
(3) For cross flow, the correlation by Dwyer [6] in Eq. (9) can be used for the design of the heat exchanger without a significant error.
(4) For inclined flows, the modified Dwyer model [6] in Eq. (12) was reliable and accurate enough to be used in a real design. The Kalish and Dywer correlation in Eq. (10) underpredicts the heat transfer coefficient when the Peclet number is large.

Acknowledgment

This study has been supported by the Nuclear Research and Development Program of the Ministry of Education, Science, and Technology of Korea.

Nomenclature

a, b, c = constants
A_w = total rod heat transfer area
C_P = specific heat
C_s = constant in the Reynolds stress model
$C_{\varepsilon 1}, C_{\varepsilon 2}$ = constants in the ε-equation of the Reynolds stress model
D = outer diameter of tube
F_1 = blending function in the SST model
h = heat transfer coefficient
k = turbulent kinetic energy or conductivity
$\dot{m}$ = mass flow rate
Nu = Nusselt number
P = pitch, distance between tube centers
Pe = Peclet number
$\mathrm{Pe}_{v,\max}$ = Peclet number based on maximum velocity
P_{ij} = production rate of Reynolds stress
P_k = production rate of turbulent kinetic energy
Pr = Prandtl number
Re = Reynolds number
T_b = bulk temperature
T_{in} = inlet temperature
T_{out} = outlet temperature
T_w = tube wall temperature
$\underline{U_i}$ = time mean velocity components
$\overline{u_i u_j}$ = Reynolds stresses

Greek

$\alpha, \beta', \sigma_\omega, \sigma_{k*}, \sigma_\varepsilon, \sigma_{\omega 2}$ = constants in the model transport equations
β = inclined angle or turbulent model constant
δ_{ij} = Kronecker delta
ε = dissipation rate of turbulent kinetic energy
μ = dynamic viscosity
μ_T = dynamic turbulent viscosity
ρ = density
ϕ_1 = hydrodynamic potential function, which is a function of P/D
ϕ_{ij} = pressure-strain term
ω = specific dissipation rate of turbulent kinetic energy

References

[1] Tang, Y. S., Coffied, R., and Markley, R. A., 1978, "Thermal Analysis of Liquid Metal Fast Breeder Reactors," American Nuclear Society.
[2] Graber, H., and Rieger, M., 1973, "Experimental Study of Heat Transfer to Liquid Metals Flowing In-Line Through Tube Bundles," Prog. Heat Mass Transfer, **7**, pp. 151–166.
[3] Borishansky, V. M., Gotorsky, M. A., and Firsova, E. V., 1969, "Heat Transfer to Liquid Metal Flowing Longitudinally in Wetted Bundle of Rods," At. Energy, **27**, pp. 1347–1350.
[4] Kisohara, N., Nakai, S., Sato, H., and Yatabe, T., 2001, "Development of a Double-Wall-Tube Steam Generator-Evaluation of Thermal Hydraulic Tests on High Mass Flow Rate Condition," JNC Report No. TN-9400.
[5] Hsu, C. J., 1964, "Analytical Study of Heat Transfer to Liquid Metals in Cross-Flow Through Rod Bundles," Int. J. Heat Mass Transfer, **7**, pp. 431–446.
[6] Dwyer, O. E., 1966, "Recent Developments in Liquid-Metal Heat Transfer," At. Energy Rev., **4**, pp. 3–92.
[7] Hoe, R. J., Dropkin, D., and Dwyer, O. E., 1957, "Heat Transfer Rates to Cross-Flowing Mercury in a Staggered Tube Bank-I," Trans. ASME, **79**, pp. 899–907.
[8] Rickard, C. L., Dwyer, O. E., and Dropkin, D., 1958, "Heat Transfer Rates to Cross-Flowing Mercury in a Staggered Tube Bank-II," Trans. ASME, **80**, pp. 642–652.
[9] Subbotin, V. I., Minashin, V. E., and Deniskin, E. I., 1963, "Heat Exchange in Flow Across Tube Banks," Teplofiz. Vys. Temp., **1**, pp. 238–258.
[10] Kalish, S., and Dwyer, O. E., 1967, "Heat Transfer to NaK Flow Through Unbaffled Rod Bundle," Int. J. Heat Mass Transfer, **10**, pp. 1533–1558.
[11] Hsu, C. J., 1965, "Heat Transfer to Liquid Metals Flowing Past Spheres and Elliptic Rod Bundles," Int. J. Heat Mass Transfer, **8**, pp. 303–315.
[12] Lubarsky, B., and Kaufmani, S. J., 1955, "Review of Experimental Investigations of Liquid-Metal Heat Transfer," NACA TN 3336.
[13] Seban, R. A. and Shimazaki, T., 1950, "Heat Transfer to a Fluid Flowing Turbulently in a Smooth Pipe With Walls at Constant Temperature," ASME Paper No. 50-A-128.
[14] ANSYS Inc., 2006, ANSYS CFX 11.0-Solver Theory Guide.
[15] Speziale, C. G., Sarkar, S., and Gaski, T. B., 1991, "Modelling the Pressure-Strain Correlation of Turbulence: An Invariant Dynamical System Approach," J. Fluid Mech., **227**, pp. 245–272.
[16] Mochizuki, H., and Takano, M., 2009, "Heat Transfer in Heat Exchangers of Sodium Cooled Fast Reactor Systems," Nucl. Eng. Des., **239**, pp. 295–307.

A Design and Rating Method for Shell-and-Tube Heat Exchangers With Helical Baffles

Jian-Fei Zhang

Ya-Ling He

Wen-Quan Tao[1]
e-mail: wqtao@mail.xjtu.edu.cn

School of Power and Energy Engineering,
Xi'an Jiaotong University,
Xi'an 710049, China

A method for design and rating of shell-and-tube heat exchanger with helical baffles (STHXHB) has been developed in present study based on the public literatures and the widely used Bell–Delaware method for shell-and-tube heat exchanger with segmental baffles (STHXSB). A number of curve-type factors in the literature have all been replaced by mathematical expressions for the convenience of engineering design. The detailed calculation procedure of the method is provided. The accuracy of present method is validated with some experimental data. Four design cases of replacing original STHXsSB by STHXsHB are supplied, and the comparison results show that all of the STHXsHB have better performance than the original heat exchangers with segmental baffles.
[DOI: 10.1115/1.4000457]

Keywords: shell-and-tube heat exchanger, helical baffle, pressure drop, heat transfer, design and rating method

1 Introduction

Shell-and-tube heat exchangers (STHXs) are widely used in many industrial areas, and more than 35–40% of heat exchangers are of this type due to their robust geometry construction, easy maintenance, and possible upgrades [1]. Besides supporting the tube bundles, the baffles in shell-and-tube heat exchangers form flow passage for the shell-side fluid in conjunction with the shell. The most-commonly used baffle is the segmental baffle, which forces the shell-side fluid going through in a zigzag manner, hence, improves the heat transfer with a large pressure drop penalty. This type of heat exchanger has been well-developed [2–6] and probably is still the most-commonly used type of the shell-and-tube heat exchangers. But there are three major drawbacks in the conventional shell-and-tube heat exchangers with segmental baffles (STHXsSB): (1) the large shell-side fluid pressure drop; (2) the dead zone in each compartment between two adjacent segmental baffles, which lead to an increase of fouling resistance; and (3) the dramatic zigzag flow pattern and longer unsupported tube spans, which lead to high risk of vibration failure of tube bundle. A number of improved structures were proposed for the purposes of higher heat transfer coefficient, low possibility of tube vibration, and reduced fouling factor with a mild increase in pumping power [7–11].

However, the principal shortcomings of the conventional segmental baffle still remain in the improved structures of the above-mentioned studies. A new type of baffle, called the helical baffle, provides further improvement. This type of baffle was first developed by Lutcha and Nemcansky [12]. They investigated the flow field patterns produced by such helical baffle geometry with different helix angles. They found that these flow patterns were very close to the plug flow condition, which was expected to reduce shell-side pressure drop and to improve heat transfer performance. Stehlik et al. [13] compared heat transfer and pressure drop correction factors for a heat exchanger with an optimized segmental baffle based on the Bell–Delaware method [2–4] with those for a heat exchanger with helical baffles. Kral et al. [14] discussed the performance of heat exchangers with helical baffles based on test results of various baffles geometries. One of the most important geometric factors of the STHXHB is the helix angle. Recently a comprehensive comparison between the test data of shell-side heat transfer coefficient versus shell-side pressure drop was provided for five helical baffles and one segmental baffle measured for oil-water heat exchanger [15]. It is found that based on the heat transfer per unit shell-side fluid pumping power or unit shell-side fluid pressured drop, the case of 40 deg helix angle behaves the best.

For the convenience of manufacturing, up to now all helical baffles actually used in STHXs are noncontinuous approximate helicoids. The noncontinuous helical baffles are usually made by four elliptical sector-shaped plates joined in succession. The elliptical sector-shaped plates are arranged in a pseudohelical (noncontinuous) manner, with each baffle occupying one-quarter of the cross section of the heat exchanger and being angled to the axis of the heat exchanger. The two adjacent baffles may be joined end to end at the perimeter of each sector, forming a continuous helix at the outer periphery (Fig. 1(*a*)); this structure of connecting baffles together is called a single helix manner. Another connection between two adjacent sectors is the middle-overlapped connection, as shown in Fig. 1(*b*), where the helix angle, designated by β, helical pitch, B, and baffle thickness, S_p, are presented. As shown in Fig. 1(*c*), the helix angle is referred to as the angle between the normal line of the elliptical sector-shaped plates and the heat exchanger axis. For heat exchangers with large shell diameters, such structures can reduce the helical pitch to shorten the length of heat exchanger and can also reduce the cross-flow area to obtain a higher shell-side velocity. Hence such connection is more popular in engineering practice. Typical publications on experimental study of STHXsHB since the year 2000 can be referred to in Refs. [15–19]. With the rapid advances in computer hardware numerical simulation plays an increasingly important role. Typical progresses in the shell-and-tube heat exchanger performance simulations can be found in Refs. [20–39].

The research results of experimental measurements and numerical simulations provide the bases of engineering design method, for which the primary objects are to determine the required heat transfer surfaces and the fluid pressure drops of shell-and-tube sides. In the design method, the input data are flow rates and at least three of the inlet and outlet temperatures of both sides in heat exchanger. After primary guessing for the heat exchanger structure, the over-all heat transfer coefficient and the pressure drop

[1]Corresponding author.

Contributed by the Heat Transfer Division of ASME for publication in the JOURNAL OF HEAT TRANSFER. Manuscript received May 7, 2009; final manuscript received August 23, 2009; published online March 9, 2010. Assoc. Editor: G. Lorenzini.

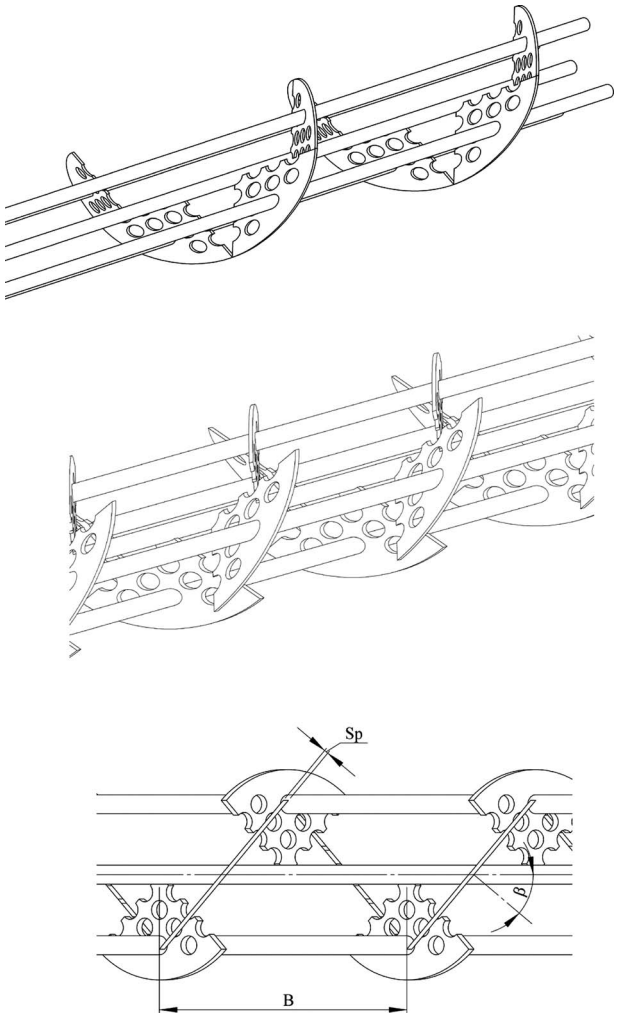

Fig. 1 Helical baffle arrangement and parameters definition

can be determined by adopting correlations obtained from tests or simulations. If the calculated heat transfer rate and pressure drops cannot satisfy the design requirements, the heat exchanger is reconstructed, and the calculation is repeated again until the calculated heat transfer rate and the pressure drops can satisfy the prespecified conditions. It can be seen that the heat transfer and pressure drop correlations are the basis for the design method.

The above-mentioned engineering design method has been quite well-developed for the conventional segmental baffled shell-and-tube heat exchangers (STHXsSB) [2–6,11,40–51]. However, for STHXsHB, the situation is totally different. Except the early work published by Stehlik et al., we can hardly find papers related to the design method of STHXsHB. Reference [37] is the only one known to the present authors. In Ref. [13] a comprehensive comparison was made for the flow and heat transfer characteristics of STHXsSB and STHXsHB, and based on the design method for the STHXsSB, a series of correction curves were provided for the calculation of pressure drop and heat transfer coefficient of STHXsHB. But, the complete design method and procedure for determination of geometry parameters of both sides in STHXsHB were not provided in Ref. [13]. Of course this is not convenient to the engineering application. In Ref. [37], part of the design methods is based on the results in Ref. [13], but the detailed design procedure and the determination of geometry parameters of both sides in STHXsHB were not supplied either. This situation is obviously not convenient for a good engineering design of a STHXHB.

Stimulated by the above-mentioned situation, in this paper the present authors propose a complete calculating method for the design of a STHXHB in detail via a number of equations based on the study results in Ref. [13] and the Bell–Delaware method [2–6]. The accuracy of this method is validated by comparison with the experiment data in Ref. [15]. Finally, some application cases of this method are presented.

2 Correlations for Flow and Heat Transfer Characteristics in Shell Side of STHXsHB

Based on Refs. [2–6,13] the correlations for flow and heat transfer in shell side of STHXsHB are proposed and collected in this section. Most of the symbols used the following presentation are the same as what were used in Ref. [13] for the sake of convenience.

2.1 Correlations for Heat Transfer Coefficient in Shell Side of STHXsHB. The average Nu number for the shell side of STHXsHB [13] is determined by

$$\mathrm{Nu}_s = 0.62 \times (0.3 + \sqrt{\mathrm{Nu}_{\mathrm{lam}}^2 + \mathrm{Nu}_{\mathrm{turb}}^2}) \times Y_2 \times Y_3 \times Y_4 \times Y_7 \times Y_8 \times Y_9 \times Y_{10} \quad (1)$$

where

$$\mathrm{Nu}_{\mathrm{lam}} = 0.664\ \mathrm{Re}^{0.5}\ \mathrm{Pr}^{0.33} \quad (2)$$

$$\mathrm{Nu}_{\mathrm{turb}} = \frac{0.037\ \mathrm{Re}^{0.7}\ \mathrm{Pr}}{1 + 2.433\ \mathrm{Re}^{-0.1}(\mathrm{Pr}^{0.67} - 1)} \quad (3)$$

In Eq. (1) coefficients Y_i are the correction factors. Their physical meanings are defined as follows [13]. Y_2 accounts for the thermal-physics properties effects; Y_3 accounts for the scale-up from a single tube row to a bundle of tubes; Y_4 accounts for the adverse temperature gradient; Y_7 accounts for the bundle-shell bypass streams; Y_8 accounts for the baffle spacing in inlet and outlet sections; Y_9 accounts for the change in the cross-flow characteristics in heat exchanger; and Y_{10} accounts for the turbulent enhancement.

Average heat transfer coefficient for shell side of STHXsHB [13] is

$$h_s = \frac{\mathrm{Nu}_s \times \lambda_s}{l} \quad (4)$$

where

$$l = \frac{\pi d_o}{2} \quad (5)$$

where d_o is the outside diameter of the tube; and λ_s is thermal conductivity of shell-side fluid. The application ranges of Eqs. (1)–(5) are $10 < \mathrm{Re} < 10^6$, $10 < \mathrm{Pr} < 10^3$, $n_{rc} > 10$, and $5 \leq \beta \leq 45$ deg, where

$$n_{rc} = n_{rp}(n_p - 1) \quad (6)$$

n_{rp} is the number of tube rows in the cross section of heat exchanger; and n_p is the number of baffles.

2.2 Correlations for Pressure Drop in Shell Side of STHXsHB. According to Stehlik et al. [13], the pressure drop cross the bundle per unit cycle without bypass flow can be determined by

$$\Delta p_{t0}^1 = 2\lambda_{22} n_r^1 \rho_2 u_2^2 Z_2 Z_6 Z_7 \quad (7)$$

The pressure drop cross the whole bundle zone with bypass flow is [13]

$$\Delta p_{t0} = \Delta p_{t0}^1 \frac{l_{t0}}{B} Z_3 \quad (8)$$

The pressure drop in the inlet and outlet zones [13]

$$\Delta p_{tn} = \Delta p_{t0}^{1} Z_5 \tag{9}$$

where n_r^1 is the number of tube rows on the center stream line within one cycle. λ_{22} is the friction factor of ideal cross-flow through tube bundle, which can be determined by referring to [6,52]. l_{to} is the baffled length of tube bundle.

In Eqs. (7)–(9) correction factors are defined as [13] follows. Z_2 accounts for the thermal-physics properties effects; Z_3 accounts for the bundle-shell bypass streams; Z_5 accounts for the baffle spacing in inlet and outlet sections; Z_6 accounts for the change in the cross-flow characteristics in heat exchanger; and Z_7 accounts for the turbulent enhancement.

The pressure drop in the inlet and outlet nozzles can be calculated by [53,54]

$$\Delta p_{\text{nozzle}} = \xi \times 0.5 \times \rho v_{s,\text{nozzle}}{}^2 \tag{10}$$

where ξ is taken as 1.5 or 2.0 by referring to Refs. [53,54].

The over-all pressure drop of the shell-side fluid

$$\Delta p_{s,\text{all}} = \Delta p_{tn} + \Delta p_{\text{nozzle}} + \Delta p_{t0} \tag{11}$$

From above presentation it can be seen that the determination of factors Y_i and Z_i is the key issue to obtain the shell-side fluid heat transfer coefficient and pressure drop. Section 2.3 is for this purpose.

2.3 Determination of Factors. *Y_2 and Z_2* [6,13].

$$Y_2 = \left(\frac{\eta_s}{\eta_{s,w}}\right)^{0.14} \tag{12}$$

$$Z_2 = \left(\frac{\eta_s}{\eta_{s,w}}\right)^{-0.14} \tag{13}$$

where $\eta_{s,w}$ is the dynamic viscosity at average temperature of tube wall.

The determination of average temperature of tube wall is conducted by [6]

$$t_w = t_{t,\text{avg}} + \left(\frac{t_{s,\text{avg}} - t_{t,\text{avg}}}{1 + h_t/h_s}\right) \tag{14}$$

where $t_{t,\text{avg}}$ and $t_{s,\text{avg}}$ are the averaged inlet and outlet temperatures of tube side and shell side in the heat exchanger, respectively. h_t and h_s are heat transfer coefficients for tube side and shell side, respectively.

Y_3 [13,52]. For in-line arrangement,

$$Y_3 = 1 + \frac{0.7}{\varepsilon^{1.5}} \frac{b/a - 0.3}{(b/a + 0.7)^2} \tag{15}$$

For staggered arrangement,

$$Y_3 = 1 + \frac{2}{3b} \tag{16}$$

where a is the ratio of distance between the tube normal to the flow direction and the central tube pitch, b, is the ratio of distance between tube in the flow direction and the central tube pitch, as shown in Fig. 2, and the parameter ε is determined by

$$\text{if } b \geq 1: \quad \varepsilon = 1 - \frac{\pi}{4a} \tag{17}$$

$$\text{if } b < 1: \quad \varepsilon = 1 - \frac{\pi}{4ab} \tag{18}$$

Y_7 and Z_3 [13]. Y_7 and Z_3 are functions of $t_t \cdot n_{pt}/D_1$ and S_{ss}/S_{2z}, as shown in graphs presented by Stehlik et al. [13]. These curves have been fitted to the following equations (using x and y, respectively, to substitute $t_t \cdot n_{pt}/D_1$ and S_{ss}/S_{2z} for simplicity):

$$Y_7 = \exp[-1.343x(1-(2y)^{0.338})] \tag{19}$$

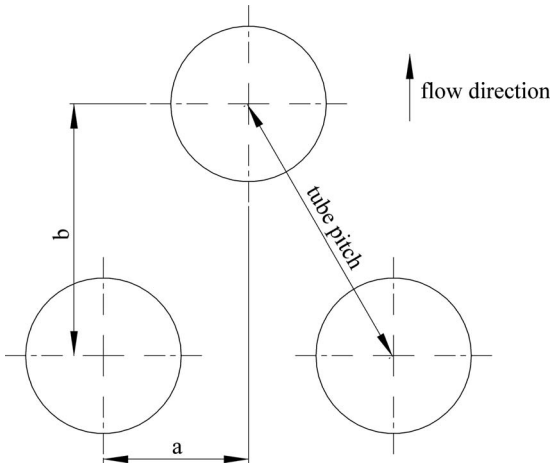

Fig. 2 Definition of parameters used in Y_3

$$Z_3 = \exp[-3.56x(1-(2y)^{0.363})] \tag{20}$$

where

$$S_{ss} = 0.5(B - S_p/\cos\beta)[D_1 - D_s - S_{tt}] \tag{21}$$

$$S_{2z} = 0.5(B - S_p/\cos\beta)\left[D_i - D_1 + \frac{D_1 - d_o}{t_t}(t_t - d_o)\right] \tag{22}$$

In the above equations, t_t is the tube pitch, D_1 is the inner diameter of shell, S_p is the thickness of baffle, S_{tt} is distance between the two tubes' outside surfaces, n_{pt} is the number of stealing strip pairs, and D_s is the diameter of tube bundle. It should be emphasized that for the STHXsHB because the shell-side flow pattern resulted from the helical-type structure is close to helical flow, the cross section area, S_{2z}, is actually only half of the entire cross section at the shell centerline of the heat exchanger.

Y_8 and Z_5 [13]. Y_8 and Z_5 are functions of $(l_{tc}-l_{to})/l_{tc}$ and $B/D1$, as shown in graphs presented by Stehlik et al. [13]. Again, the present authors have made curve-fitting for the convenience of design as follows (using x and y, respectively, to substitute $(l_{tc}-l_{to})/l_{tc}$ and $B/D1$ for simplicity):

$$Y_8 = 1.079y^{0.0487} - 0.445y^{-0.301}x^{1.2} \tag{23}$$

$$Z_5 = (-0.0172 + 0.0899y)x^{-1.2} \tag{24}$$

where l_{tc} is the effective length of the tube bundle, and l_{to} is the baffled length of tube bundle.

Figure 3 illustrates the definitions of l_{to} and l_{tc}. The helical pitch B can be calculated with D_1 and β at hand (see Eq. (25)) [55], and then the maximum number of baffle numbers can be determined

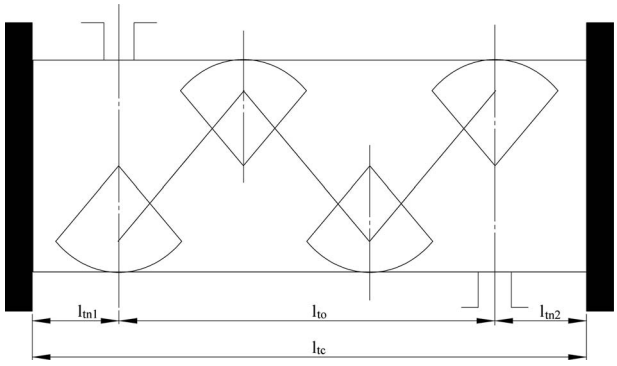

Fig. 3 Definition of parameters used in Y_8 and Z_5

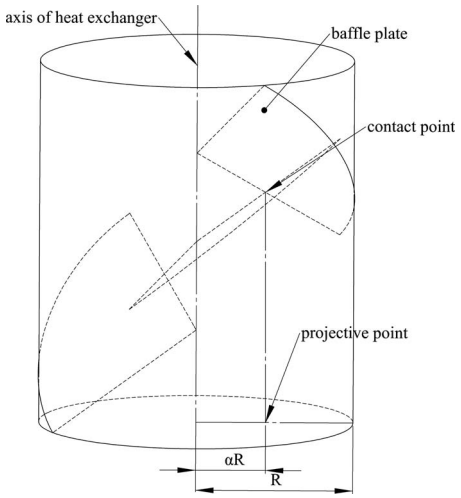

Fig. 4 Definition of overlapped rate α

with specified value of l_{tc} The baffle number is an integral. Then l_{to} and the distances between inlet and outlet baffles to tube sheet, l_{tn1} and l_{tn2}, can be determined with ease

$$B = \alpha n \cdot D_1 \sin\frac{\pi}{n} \cdot \tan\beta, \quad n \geq 2, \quad 0 < \alpha \leq 1 \tag{25}$$

where α is the dimensionless radius of the contacting point of the two successive helical baffles (see Fig. 4).

Y_9 and Z_6 [13]. From the graphs presented by Stehlik et al. [13], Y_9 and Z_6 are only influenced by helical angle. The curves in [13] can be fitted to the following equations:

$$Y_9 = 0.977 + 0.00455x - 0.0001821x^2 \quad (18 \text{ deg} \leq x \leq 45 \text{ deg}) \tag{26}$$

$$Y_9 = 1 \quad (x < 18 \text{ deg}) \tag{27}$$

$$Z_6 = 0.289 - (5.06 \times 10^{-4})x - (4.53 \times 10^{-5})x^2 \tag{28}$$

where x represents the helical angle β.

Y_{10} and Z_7 [13]. Y_{10} and Z_7 are also only influenced by the helical angle, as shown in the graphs presented by Stehlik et al. [13]. The following curve-fitted equations are obtained by the present authors:

$$Y_{10} = -56.39 + 8.28x - 0.46x^2 + 0.012x^3 - (1.64 \times 10^{-4})x^4 + (8.19 \times 10^{-7})x^5 \quad (25 \text{ deg} < x < 45 \text{ deg}) \tag{29}$$

$$Y_{10} = 1 \quad (x < 25 \text{ deg}) \tag{30}$$

$$Z_7 = -5.411 + 0.379x - 0.00402x^2 \quad (22 \text{ deg} < x < 45 \text{ deg}) \tag{31}$$

$$Z_7 = 1 \quad (x < 22 \text{ deg}) \tag{32}$$

where x represents the helical angle β.

3 Correlations for the Flow and Heat Transfer in Tube Side of STHXsHB

3.1 Correlations for Heat Transfer Coefficient in Tube Side of STHXsHB. The average heat transfer coefficient of tube side is calculated by the Gnielinski equation in turbulence condition or the Sieder–Tate equation in laminar condition [56–58].

3.2 Correlations for Pressure Drop in Tube Side of STHXsHB [53,54].

$$\Delta p_{t,\text{all}} = \frac{1}{2}\xi\rho v_{t,\text{nozzle}}^2 + \frac{1}{2}\rho u_t^2\left[\frac{f_t L_{tc}}{d_i}\frac{1}{(\phi_t)^r} + k_c + k_e + 4\right]N_p \tag{33}$$

where ξ is taken as 1.5 or 2.0 [53,54]; k_c and k_e are friction factors for the sudden contraction and expansion effects, respectively, when the tube side fluid flows into and out of the tubes; N_p is the number of tube passes; and if there is only one tube pass in the heat exchanger, the number "4" in Eq. (33) should be omitted. The friction factor f_t can be determined by referring to Refs. [53,54].

4 Design Procedures

In heat transfer textbooks heat exchanger design is often classified by the design mode and rating mode [54,56,57]. Simply speaking, in the design mode the heat transfer rate is given and the required heat transfer surface area is searched for, while the rating mode is applied for an existing heat exchanger to find its capability of heat transfer at some given condition. The present design method can be used for both design mode and rating mode. For the convenience of presentation the procedure of the design mode is first presented in detail. For the design mode the task is to determine all the geometry parameters of one heat exchanger, which can satisfy the request heat duty and maximum allowable pressure drop.

Procedure for design mode is listed as follows:

(1) Define the heat duty of each side by Eqs. (34) and (35), respectively

$$\Phi_s = M_s \times c_{ps} \times |t_{s,\text{in}} - t_{s,\text{out}}| \tag{34}$$

$$\Phi_t = M_t \times c_{pt} \times |t_{t,\text{in}} - t_{t,\text{out}}| \tag{35}$$

The deviation between the heat duties of both sides, Φ_s and Φ_t, should be lower than 5% for a conventional engineering design.

(2) Determine the tube layout pattern such as 30 deg, 45 deg, and 90 deg layout pattern.

(3) Determine the thermophysical properties of the tube side and shell-side fluids at its reference temperature, which is usually taken as the average magnitude of the inlet and outlet temperatures of corresponding sides.

(4) Guess the primary over-all heat transfer coefficient K_0 and calculate the primary requested heat transfer area A_o by Eq. (36), and Δt_m is the logarithmic mean temperature difference

$$A_o = \frac{\Phi_s}{K_0 \cdot \Delta t_m} \tag{36}$$

(5) Fix the tube effective length or the inner diameter of the shell; if the tube effective length is fixed, the tube number can be determined by Eq. (37)

$$A_o = N_t \cdot \pi d_o l_{tc} \tag{37}$$

and the diameter of tube bundle can be carried out by referring to graphs or empirical formula in Ref. [6].Then the inner diameter of shell can be defined based on the diameter of tube bundle.

If the inner diameter of shell is fixed, the diameter of tube bundle can be defined at first, and the tube number also can be determined by referring to graphs or empirical in Ref. [6].

(6) Choose the helical angle and overlap ratio of helical baffles.

(7) Calculate the shell-side velocity and tube side velocity, determine the Re number of each side, then calculate the value of correction factors according to the discussion in Sec. 2.3.

(8) Carry out the heat transfer coefficient and pressure drop for each side under present geometry and obtain the over-all heat transfer coefficient by Eq. (36)

Table 1 Helical baffled shell-and-tube heat exchanger geometry

Item		Dimensions and description		
Shell-side parameters	D_o/D_i/mm	325/313	325/313	223/211
	Material	0Cr18Ni9	0Cr18Ni9	0Cr18Ni9
Tube parameters	d_o/d_i/mm	19/15	19/15	19/15
	Effective length/mm	1194	1608	1703
	No.	97	97	37
	Layout pattern	45 deg	45 deg	45 deg
	Tube pitch/mm	25	25	25
	Material	0Cr18Ni9	0Cr18Ni9	0Cr18Ni9
Baffle parameters	Baffle pitch/mm	161	255	250
	Helix angle	20 deg	30 deg	40 deg
	Thickness/mm	3	3	3
	No.	24	24	24

$$\frac{1}{k} = \frac{1}{h_t}\frac{d_o}{d_i} + \frac{d_o}{2\lambda_w}\ln\frac{d_o}{d_i} + \frac{1}{h_s} \tag{38}$$

(9) Carry out the heat duty, Φ, of the heat exchanger at present geometry. If Φ is around 15% greater than Φ_0, then it means that the designed heat exchanger has a safety margin of 15% for the heat transfer. As an engineering design, usually 15 % extra heat transfer area (i.e., 15% redundancy) is acceptable for safe operation. Then the design procedure can be considered finished. If not, repeat steps (4)–(8), until the specified redundancy is satisfied.

For the rating mode, all the geometries are specified; the task is to evaluate the heat duty and pressure drop of heat exchanger, and steps (4)–(8) can be used for the rating mode.

5 Validations

As indicated above, one of the major contributions of the present paper is the replacement of the curves in Ref. [13] with the equations shown in Sec. 2.3. Such a replacement was conducted with certain errors by reading the data from the graphs. Thus it is of crucial importance to validate whether such transformation can keep the unavoidable error within the acceptable range. As such a validation of the experimental data in Ref. [15] is adopted to validate the accuracy of the present method. Since the geometry parameters (see Table 1) and operation conditions are all known, rating calculation is performed to predict the over-all heat transfer coefficient and over-all pressure drop. The comparison between test data and calculation results is listed in Tables 2–4. It can be observed from the tables that the prediction accuracy of the present method is adequate for the engineering application.

6 Application of the Proposed Method

6.1 The Replacement of a Tube Core With SB by That With HB for a Common Shell. Because STHXsSB cause higher pressure drop or pump power, sometimes the heat transfer capacity of it has to be weakened with the increase in baffle spacing to meet the maximum allowable pressure drop. STHXsHB can reduce the pressure drop or pump power significantly and has a better comprehensive performance: At a fixed flow rate, the heat transfer coefficient per unit pressure drop or per unit pump power of STHXsHB is much higher than that of STHXsSB [12–15]. When a STHXHB is used to replace a STHXSB, if the reconstructed equipment has an equal pressure drop as the original heat exchanger, its heat transfer capacity must be larger than that of the original one; and if the reconstructed equipment has an equal heat transfer capacity, then it can definitely save pumping power. In the following presentation we will provide such engineering examples.

6.2 Replacement Examples. Four cases are provided to show the application of the present method, and the purpose of the design cases is to replace the original STHXSB with STHXHB. All the data for STHXSB come from heat exchangers in practical usage. In all the replacement design cases, the inner diameters of

Table 2 Validation of 20 deg helical baffled heat exchanger

	Experimental data		Calculation results		Deviation	
	Over-all heat transfer coefficient ($W(m^2\,K)^{-1}$)	Over-all pressure drop for shell side (kPa)	Over-all heat transfer coefficient ($W(m^2\,K)^{-1}$)	Over-all pressure drop for shell side (kPa)	Over-all heat transfer coefficient %	Over-all pressure drop for shell side %
1	134.4	1.29	165.9	0.96	23.4	−25.6
2	150.5	1.86	179.2	1.47	19.1	−21.0
3	175.7	4.32	202.1	3.65	15.0	−15.5
4	197.7	7.89	218.6	6.85	10.6	−13.2
5	201.6	10.9	228.3	9.69	13.2	−11.1

Table 3 Validation of 30 deg helical baffled heat exchanger

	Experimental data		Calculation results		Deviation	
	Over-all heat transfer coefficient ($W(m^2\,K)^{-1}$)	Over-all pressure drop for shell side (kPa)	Over-all heat transfer coefficient ($W(m^2\,K)^{-1}$)	Over-all pressure drop for shell side (kPa)	Over-all heat transfer coefficient %	Over-all pressure drop for shell side %
1	140.8	1.38	152.0	1.39	8.0	0.7
2	150.2	1.94	160.3	1.96	6.7	1.0
3	164.3	3.34	170.9	3.44	4.0	3.0
4	183.0	5.69	183.4	5.91	0.2	3.9
5	196.7	7.36	189.3	7.61	−3.8	3.4

Table 4 Validation of 40 deg helical baffled heat exchanger

	Experimental data		Calculation results		Deviation	
	Over-all heat transfer coefficient ($W(m^2\ K)^{-1}$)	Over-all pressure drop for shell side (kPa)	Over-all heat transfer coefficient ($W(m^2\ K)^{-1}$)	Over-all pressure drop for shell side (kPa)	Over-all heat transfer coefficient %	Over-all pressure drop for shell side %
1	280.7	20.0	337.3	23.15	20.2	15.8
2	298.5	25.4	353.4	28.65	17.7	12.8
3	305.8	32.0	366.5	35.27	19.8	10.2
4	324.3	41.3	384.2	44.3	18.5	7.3
5	339.8	49.3	398.9	53.9	17.4	9.3

shells and the tube layout pattern (excluding the tube effective length) remained unchanged to save the cost of manufacture modification.

6.2.1 Case 1. The original design data and comparison results are listed in Table 5. It shows that the comprehensive performance is greatly improved by using tube-core with 40 deg middle-overlapped helical baffles, and the pressure drop of STHXHB is 39% lower than that of original unit with 16% decrease in heat transfer area.

6.2.2 Case 2. Table 6 lists the original data and the comparison results. The usage of tube-core with 40 deg middle-overlapped helical baffles can reduce the over-all pressure drop by 46% compared to the original STHXSB, and the heat transfer area is 13% lower than that of original unit.

6.2.3 Case 3. The original data and comparison results are shown in Table 7. It shows that although the pressure drop of the heat exchanger with 40 deg middle-overlapped helical baffles is equivalent to that of the original STHXSB, the heat transfer area reduced by around 33% compared to the original STHXSB.

6.2.4 Case 4. In this case, 20 deg middle-overlapped helical baffles were adopted to replace the original unit (see Table 8, and the pressure drop in STHXHB is 33% lower than that of the original unit with 10% decrease in heat transfer area.

7 Conclusions

A method for the design and rating of STHXsHB is developed in the present paper based on the study results in Ref. [13] and the

Table 6 Design result for heat exchanger Case 2

Parameters	Unit	Original STHXSB	Designed STHXHB
Shell-side fluid		Water	Water
Tube side fluid		Water	Water
Shell-side flow rate	kg/h	133,242	133,242
Tube side flow rate	kg/h	25,278.6	25,278.6
Inlet/outlet temperature of shell side	°C	85/95	85/95
Inlet/outlet temperature of shell side	°C	210/160	210/160
d_o/d_i	mm	19×2	19×2
Tube arrangement		45 deg	45 deg
Tube effective length	mm	3000	2600
Tube No.		213	213
Inner diameter of shell	mm	500	500
Baffle spacing/helical pitch	mm	300	592.67
Over-all pressure drop for shell side	bar	0.225	0.12
Over-all heat transfer coefficient	$W/m^2\ K$	317.4	323.0
Heat transfer area	m^2	38.14	33.04

Table 5 Design result for heat exchanger Case 1

Parameters	Unit	Original STHXSB	Designed STHXHB
Shell-side fluid		Lean TEG	Lean TEG
Tube side fluid		Sea water	Sea water
Shell-side flow rate	kg/h	8195.6	8195.6
Tube side flow rate	kg/h	21,803.8	21,803.8
Inlet/outlet temperature of shell side	°C	81.1/41	81.1/41
Inlet/outlet temperature of shell side	°C	29.4/37.8	29.4/37.8
d_o/d_i	mm	19.05/15.75	19.05/15.75
Tube arrangement		30 deg	30 deg
Tube effective length	mm	5181	4445
Tube No.		90	90
Inner diameter of shell	mm	330	330
Baffle spacing/helical pitch	mm	184.9	391.4
Over-all pressure drop for shell side	bar	0.024	0.014
Over-all heat transfer coefficient	$W/m^2\ K$	406.0	471.3
Heat transfer area	m^2	28.58	23.92

Table 7 Design result for heat exchanger Case 3

Parameters	Unit	Original STHXSB	Designed STHXHB
Shell-side fluid		Mixture fluid	Mixture fluid
Tube side fluid		Mixture fluid	Mixture fluid
Shell-side flow rate	kg/h	177,328.4	177,328.4
Tube side flow rate	kg/h	35,470.3	35,470.3
Inlet/outlet temperature of shell side	°C	64.5/76	64.5/76
Inlet/outlet temperature of shell side	°C	210/160	210/160
d_o/d_i	mm	19×2	19×2
Tube arrangement		45 deg	45 deg
Tube effective length	mm	3000	2100
Tube No.		321	321
Inner diameter of shell	mm	600	600
Baffle spacing/helical pitch	mm	400	711.2
Over-all pressure drop for shell side	bar	0.13	0.12
Over-all heat transfer coefficient	$W/m^2\ K$	296.9	329.0
Heat transfer area	m^2	57.48	38.3

Table 8 Design result for heat exchanger Case 4

Parameters	Unit	Original STHXSB	Designed STHXHB
Shell-side fluid		320 conduction oil	320 conduction oil
Tube side fluid		Water	Water
Shell-side flow rate	kg/h	33,250.00	33,250.00
Tube side flow rate	kg/h	37,734.00	37,734.00
Inlet/outlet temperature of shell side	°C	55/40	55/40
Inlet/outlet temperature of shell side	°C	26/32	26/32
d_o/d_i	mm	10×1	10×1
Tube arrangement		30 deg	30 deg
Tube effective length	mm	2385	2150
Tube No.		440	440
Inner diameter of shell	mm	309	309
Baffle spacing/helical pitch	mm	250	160
Over-all pressure drop for shell side	bar	1.5	1.03
Over-all heat transfer coefficient	W/m^2 K	477.8	607.0
Heat transfer area	m^2	32.97	31.09

Bell–Delaware method. The calculation procedure of the design method for STHXsHB is provided in detail, seemingly first in the public literature. One of the major contributions of the present paper is the replacement of those graphs in Ref. [13] by mathematical formulation with enough accuracy. From method validation and application examples, the following conclusions can be made.

1. The accuracy of the present method can meet the requirement of engineering design.
2. With an appropriate selection of geometric parameters the replacement of STHXsSB with STHXsHB usually can appreciably reduce shell-side pressure drop and reduce the heat transfer area at the same over-all heat transfer rate.

Acknowledgment

This work is supported by the National Fundamental Research Program of China (973 Program) (Grant No. 2007CB206902), the Key Project of Chinese Ministry of Education (Grant No. 306014), and the National Natural Science Foundation of China (Grant No. 50806057).

Nomenclature

Latin Symbols

A_o = heat exchange area based on the outer diameter of tube, m^2
a = the ratio of distance between tube normal to the flow direction and the central tube pitch
B = helical pitch for helical baffles, m
b = the ratio of distance between tube in the flow direction and the central tube pitch
c = specific heat, kJ kg K
D_1 = inside diameter of the shell, m
D_{ctl} = the diameter of the circle through the centers of the tube located within the outermost tubes
D_s = outside diameter of shell, m
d_i = tube inner diameter, m
d_o = outer diameter of tube, m
ft = friction factor
h = heat transfer coefficient, $W(m^2\ K)^{-1}$
k = over-all heat transfer coefficient, $W(m^2\ K)^{-1}$
k_c and k_e = friction factors for the sudden contraction or expansion effects when the tube side fluid flows into and out of the tubes
l = characteristic dimension, m
l_{tc} = the effective length of tube bundle, m
l_{tn} = the nonbaffled length of tube bundle, m
l_{to} = the baffled length of tube bundle, m
M = mass flux, kg/s
N = tube number
N_p = the number of tube passes
N_t = number of tube rows
Nu = Nusselt number
n_r^1 = the number of tube rows on the center stream line within 1 cycle
n_{rp} = the number of rows of tubes
n_p = the number of baffles
n_{pt} = the number of stealing strip pairs
Δp = pressure drop, kPa
Δp_{nozzle} = pressure drop in the inlet and outlet nozzles, kPa
Δp_{t0}^1 = pressure drop cross the bundle per unit cycle without bypass flow, kPa
Δp_{t0} = pressure drop cross the whole bundle zone with bypass flow, kPa
Δp_{tn} = pressure drop in inlet and outlet zone, kPa
Re = Reynolds number
S_{ss} = bundle-to-tube cross-flow bypass area per baffle, m^2
S_{2z} = the cross-flow area at the shell centerline, m^2
S_p = the thickness of baffle, mm
S_{tt} = distance between two tube outside surfaces, m
t = temperature, °C
Δt_m = logarithmic mean temperature difference, K
t_t = tube pitch, mm
v_{nozzle} = fluid velocity in nozzles, m s^{-1}
Y_i and Z_i = correction factor for heat transfer coefficient and pressure drop, respectively

Greek Symbols

β = helix angle
Φ = heat duty, W
λ = conductivity factor of tube wall, $W(m\ K)^{-1}$
λ_{22} = the friction factor of ideal cross-flow through tube bundle
ρ = density of shell-side fluid, kg m^{-3}
η = dynamics viscosity of shell-side fluid, Pa s
ξ = nozzle pressure drop coefficient

Subscripts

in = inlet
lm = laminar
out = outlet
s = shell side
t = tube side
turb = turbulence
w = wall

References

[1] Master, B. I., Chunangad, K. S., and Pushpanathan, V., 2003, "Fouling Mitigation Using Helixchanger Heat Exchangers," *Proceedings of the ECI Conference on Heat Exchanger Fouling and Cleaning: Fundamentals and Applications*, Santa Fe, NM, May 18–22, pp. 317–322.
[2] Bell, K. J., 1981, "Delaware Method for Shell Side Design," *Heat Exchangers Thermal Hydraulic Fundamentals and Design*, S. Kakac, A. E. Bergles, and F. Mayinger, eds., Taylor & Francis, Washington, DC.
[3] Bell, K. J., 1986, "Delaware Method of Shell Side Design," *Heat Exchanger Sourcebook*, J. W. Pallen, ed., Hemisphere, Washington, DC.
[4] Bell, K. J., 1988, "Delaware Method of Shell-Side Design," *Heat Transfer Equipment Design*, R. K. Shah, E. C. Sunnarao, and R. A. Mashelkar, eds., Taylor & Francis, New York.
[5] Bell, K. J., 2004, "Heat Exchanger Design for the Process Industries," ASME

J. Heat Transfer, **126**(6), pp. 877–885.
[6] Schlünder, E. U., ed., 1983, *Heat Exchanger Design Handbook*, Vol. 3, Hemisphere, Washington, DC.
[7] Mukherjee, R., 1992, "Use Double-Segmental Baffles in the Shell-and-Tube Heat Exchangers," Chem. Eng. Prog., **88**, pp. 47–52.
[8] Saffar-Avval, M., and Damangir, E., 1995, "A General Correlation for Determining Optimum Baffle Spacing for All Types of Shell and Tube Exchangers," Int. J. Heat Mass Transfer, **38**(13), pp. 2501–2506.
[9] Li, H. D., and Kottke, V., 1998, "Effect of Baffle Spacing on Pressure Drop and Local Heat Transfer in Shell-and-Tube Heat Exchangers for Staggered Tube Arrangement," Int. J. Heat Mass Transfer, **41**(10), pp. 1303–1311.
[10] Stehlík, P., and Wadekar, V. V., 2002, "Different Strategies to Improve Industrial Heat Exchange," Heat Transfer Eng., **23**(6), pp. 36–48.
[11] Khalifeh Soltan, B., Saffar-Avval, M., and Damangir, E., 2004, "Minimization of Capital and Operating Costs of Shell and Tube Condensers Using Optimum Baffle Spacing," Appl. Therm. Eng., **24**(17–18), pp. 2801–2810.
[12] Lutcha, J., and Nemcansky, J., 1990, "Performance Improvement of Tubular Heat Exchangers by Helical Baffles," Trans. Inst. Chem. Eng., Part A, **68**, pp. 263–270.
[13] Stehlik, P., Nemcansky, J., and Kral, D., 1994, "Comparison of Correction Factors for Shell-and-Tube Heat Exchangers With Segmental or Helical Baffles," Heat Transfer Eng., **15**(1), pp. 55–65.
[14] Kral, D., Stelik, P., Van Der Ploeg, H. J., and Masster, B. I., 1996, "Helical Baffles in Shell-and-Tube Heat Exchangers, Part One: Experimental Verification," Heat Transfer Eng., **17**(1), pp. 93–101.
[15] Zhang, J. F., Li, B., Huang, W. J., Lei, Y. G., He, Y.-L., and Tao, W. Q., 2009, "Experimental Performance Comparison of Shell Side Heat Transfer for Shell-and-Tube Heat Exchangers With Middle-Overlapped Helical Baffles and Segmental Baffles," Chem. Eng. Sci., **64**, pp. 1643–1653.
[16] Shuli, W., 2002, "Hydrodynamic Studies on Heat Exchangers With Helical Baffles," Heat Transfer Eng., **23**(3), pp. 43–49.
[17] Zhnegguo, Z., Tao, X., and Xiaoming, F., 2004, "Experimental Study on Heat Transfer Enhancement of a Helically Baffled Heat Exchanger Combined With Three-Dimensional Finned Tubes," Appl. Therm. Eng., **24**(14–15), pp. 2293–2300.
[18] Peng, B., Wang, Q. W., Zhang, C., Xie, G. N., Luo, L. Q., Chen, Q. Y., and Zeng, M., 2007, "An Experimental Study of Shell-and-Tube Heat Exchangers With Continuous Helical Baffles," ASME J. Heat Transfer, **129**, pp. 1425–1431.
[19] Lei, Y. G., He, Y. L., Chu, P., and Li, R., 2008, "Design and Optimization of Heat Exchangers With Helical Baffles," Chem. Eng. Sci., **63**, pp. 4386–4395.
[20] Patankar, S. V., and Spalding, D. B., 1974, "A Calculation Procedure for the Transient and Steady State Behavior of Shell-and-Tube Heat Exchanger," *Heat Exchanger Design and Theory Source Book*, N. F. Afgan and E. U. Schlunder, eds., McGraw-Hill, New York.
[21] Butterworth, D., 1978, "A Model for Heat Transfer During Three-Dimensional Flow in Tube Bundles," Sixth International Heat Transfer Conference, Toronto, Canada, Paper No. HX-6.
[22] Sha, W. T., 1980, "An Overview on Rod-Bundle Thermal-Hydraulic Analysis," Nucl. Eng. Des., **62**, pp. 1–24.
[23] Sha, W. T., Yang, C. I., Kao, T. T., and Cho, S. M., 1982, "Multi-Dimensional Numerical Modeling of Heat Exchangers," ASME J. Heat Transfer, **104**, pp. 417–425.
[24] Prithiviraj, M., and Andrews, M. J., 1998, "Three-Dimensional Numerical Simulation of Shell-and-Tube Heat Exchanger. Part I: Foundation and Fluid Mechanics," Numer. Heat Transfer, Part A, **33**, pp. 799–816.
[25] Prithiviraj, M., and Andrews, M. J., 1998, "Three-Dimensional Numerical Simulation of Shell-and-Tube Heat Exchanger. Part II: Heat Transfer," Numer. Heat Transfer, Part A, **33**, pp. 817–828.
[26] Prithiviraj, M., and Andrews, M. J., 1999, "Comparison of a Three-Dimensional Numerical Model With Existing Methods for Prediction of Flow in Shell-and-Tube Heat Exchangers," Heat Transfer Eng., **20**(2), pp. 15–19.
[27] Deng, B., 2003, "Experimental and Numerical Study of Flow and Heat Transfer in the Shell Side of Heat Exchangers," Ph.D. thesis, Xi'an Jiaotong University, Xi'an, China.
[28] Andrews, M. J., and Master, B. I., 1999, "3-D Modeling of the ABB Lummus Heat Transfer Helixchanger Using CFD," International Conference on Compact Heat Exchangers, Banff, Canada.
[29] Andrews, M. J., and Master, B. I., 2005, "Three-Dimensional Modeling of a Helixchanger® Heat Exchanger Using CFD," Heat Transfer Eng., **26**, pp. 22–31.
[30] Schröder, K., and Gelbe, H., 1999, "Two- and Three-Dimensional CFD-Simulation of Flow-Induced Vibration Excitation in Tube Bundles," Chem. Eng. Process., **38**, pp. 621–629.
[31] Mohr, U., and Gelbe, H., 2000, "Velocity Distribution and Vibration Excitation in Tube Bundle Heat Exchangers," Int. J. Therm. Sci., **39**, pp. 414–421.
[32] Philpott, C., and Deans, J., 2004, "The Enhancement of Steam Condensation Heat Transfer in a Horizontal Shell and Tube Condenser by Addition of Ammonia," Int. J. Heat Mass Transfer, **47**, pp. 3683–3693.
[33] Karlsson, T., and Vamling, L., 2005, "Flow Fields in Shell-and-Tube Condensers: Comparison of a Pure Refrigerant and a Binary Mixture," Int. J. Refrig., **28**, pp. 706–713.
[34] Lee, S. H., and Hur, N., 2007, "Numerical Analysis of the Fluid Flow and Heat Transfer in a Shell and Tube Heat Exchanger," *Proceedings of the First Asian Symposium on Computational Heat Transfer and Fluid Flow*, Xi'an, China.
[35] Shen, R. J., Feng, X., and Gao, X. D., 2004, "Mathematical Model and Numerical Simulation of Helical Baffles Heat Exchanger," J. Enhanced Heat Transfer, **11**, pp. 461–466.
[36] Lei, Y. G., He, Y. L., Li, R., and Gao, Y. F., 2008, "Effects of Baffle Inclination Angle on Flow and Heat Transfer of a Heat Exchanger With Helical Baffles," Chem. Eng. Process., **47**(12), pp. 2336–2345.
[37] Jafari Nasr, M. R., and Shafeghat, A., 2008, "Fluid Flow Analysis and Extension of Rapid Design Algorithm for Helical Baffle Heat Exchangers," Appl. Therm. Eng., **28**, pp. 1324–1332.
[38] Zhang, J. F., He, Y. L., and Tao, W. Q., 2009, "3D Numerical Simulation on Shell-and-Tube Heat Exchangers With Middle-Overlapped Helical Baffles and Continuous Baffles—Part I: Numerical Model and Results of Whole Heat Exchanger With Middle-Overlapped Helical Baffles," Int. J. Heat Mass Transfer, **52**(23-24), pp. 5371–5380.
[39] Zhang, J. F., He, Y. L., and Tao, W. Q., 2009, "3D Numerical Simulation on Shell-and-Tube Heat Exchangers With Middle-Overlapped Helical Baffles and Continuous Baffles—Part II: Simulation Results of Periodic Model and Comparison Between Continuous and Noncontinuous Helical Baffles," Int. J. Heat Mass Transfer **52**(23-24), pp. 5381–5389.
[40] Kern, D. Q., 1950, *Process Heat Transfer*, McGraw-Hill, New York.
[41] Tinker, T., 1958, "Shell-Side Characteristics of Shell-and-Tube Heat Exchangers: A Simplified Rating System for Commercial Heat Exchangers," Trans. ASME, **80**, pp. 36–52.
[42] Palen, J. W., and Taborek, J., 1969, "Solution of Shell Side Flow Pressure Drop and Heat Transfer by Stream Analysis Method," Chem. Eng. Prog., Symp. Ser., **65**(93), pp. 53–63.
[43] Reppich, M., and Zagermann, S., 1995, "A New Design Method for Segmentally Baffled Heat Exchangers," Comput. Chem. Eng., **19**, pp. S137–S142.
[44] Serna, M., and Jimmenez, A., 2004, "An Efficient Method for the Design of Shell and Tube Heat Exchangers," Heat Transfer Eng., **25**(2), pp. 5–16.
[45] Kara, Y. A., and Güraras, Ö., 2004, "A Computer Program for Designing of Shell-and-Tube Heat Exchangers," Appl. Therm. Eng., **24**(13), pp. 1797–1805.
[46] Del Col, D., Muzzolon, A., Piubello, P., and Rosetto, L., 2005, "Measurement and Prediction of Evaporator Shell-Side Pressure Drop," Int. J. Refrig., **28**, pp. 320–330.
[47] Ayub, Z. H., 2005, "A New Chart Method for Evaluating Single-Phase Shell Side Heat Transfer Coefficient in a Single Segmental Shell and Tube Heat Exchanger," Appl. Therm. Eng., **25**(14–15), pp. 2412–2420.
[48] Selbas, R., Önder, K., and Reppich, M., 2006, "A New Design Approach for Shell-and-Tube Heat Exchangers Using Genetic Algorithms From Economic Point of View," Chem. Eng. Process., **45**(4), pp. 268–275.
[49] Caputo, A. C., Pelagagge, P. M., and Salini, P., 2008, "Heat Exchanger Design Based on Economic Optimization," Appl. Therm. Eng., **28**(10), pp. 1151–1159.
[50] Fesanghary, M., Damangir, E., and Soleimani, I., 2009, "Design Optimization of Shell and Tube Heat Exchangers Using Global Sensitivity Analysis and Harmony Search Algorithm," Appl. Therm. Eng., **29**(5–6), pp. 1026–1031.
[51] Ponce-Ortega, J., Serna-González, M., and Jiménez-Gutiérrez, A., 2009, "Use of Genetic Algorithms for the Optimal Design of Shell-and-Tube Heat Exchangers," Appl. Therm. Eng., **29**(2–3), pp. 203–209.
[52] Schlünder, E. U., ed., 1983, *Heat Exchanger Design Handbook*, Vol. 2, Hemisphere, Washington, DC.
[53] Gaddis, E. S., and Gnielinski, V., 1997, "Pressure Drop on the Shell Side of Shell-and-Tube Heat Exchangers With Segmental Baffles," Chem. Eng. Process., **36**(2), pp. 149–159.
[54] Kuppan, T., 2000, *Heat Exchanger Design Handbook*, Marcel Dekker, New York.
[55] Li, B., 2007, "Numerical Simulation and Experimental Study on Heat Transfer Enhancement in Air and Oil Heat Transfer Equipment," Ph.D. thesis, Xi'an Jiaotong University, Xi'an, China.
[56] Incropera, F. P., and DeWitt, D. P., 2002, *Heat and Mass Transfer*, 5th ed., Wiley, New York.
[57] Yang, S. M., and Tao, W. Q., 1998, *Heat Transfer*, 3rd ed., High Education, Beijing, China.
[58] Gnielinski, V., 1976, "New Equations for Heat and Mass Transfer in Turbulent Pipe and Channel Flows," Int. Chem. Eng., **16**, pp. 359–368.

Daniel Baker
P. O. Box 124,
Lemont, PA 16851

George S. Dulikravich[1]
Professor
Department of Mechanical and Materials Engineering,
Multidisciplinary Analysis, Inverse Design, Robust Optimization and Control (MAIDROC),
Florida International University,
10555 West Flagler Street,
EC 3474, Miami, FL 33174
e-mail: dulikrav@fiu.edu

Brian H. Dennis
Department of Mechanical and Aerospace Engineering,
University of Texas at Arlington,
UTA Box 19018,
Arlington, TX 76019

Thomas J. Martin
Pratt & Whitney Engine Company,
Turbine Discipline Engineering and Optimization Group,
M/S 169-20,
400 Main Street,
East Hartford, CT 06108

Inverse Determination of Eroded Smelter Wall Thickness Variation Using an Elastic Membrane Concept

A novel algorithm has been developed for the nondestructive determination of the shape of the interface between a melt and a refractory material wall in smelter furnaces. This method uses measurements of temperature and heat flux at a number of points on the outer surface of the furnace, and assumes that the inner (guessed) surface of the furnace wall is isothermal. The temperature field is then predicted in the entire furnace wall material by numerically solving a steady state heat conduction equation subject to the measured temperature values on the external surface and the isothermal melt material solidus temperature on the inner surface of the wall. The byproduct of this analysis is the computed heat flux on the external surface. The difference between the measured and the computed heat fluxes on the outer surface of the furnace is then used as a forcing function in an elastic membrane motion concept to determine perturbations to the inner (melt-refractory) surface motion. The inverse determination of the melt-refractory interface shape can be achieved by utilizing this algorithm and any available analysis software for the temperature field in the refractory wall. The initial guess of the inner shape of the wall can be significantly different from the final (unknown) wall shape. The entire wall shape determination procedure requires typically 5–15 temperature field analyses in the furnace wall material. [DOI: 10.1115/1.4000436]

Keywords: inverse problems, shape determination, refractory wall, wall erosion, shape design, hearth wear

1 Introduction

Walls of furnaces that contain molten materials (metal, glass, etc.) are made of layers of bricks of high-temperature resistive refractory material. High thermal gradients inside the melt create very strong circulations of the melt that causes erosion of the inner wall surface of the furnace. This erosion can lead to the complete depletion of the protective refractory material at certain locations of the furnace wall. At such points, the molten material can easily soften the outer steel casing of the furnace and break it, causing a major industrial disaster. It is therefore highly desirable to continuously monitor the actual thickness of the entire furnace wall so that the furnace can be shut down and the wall material repaired before the breakout happens. The use of any sensors imbedded in the inner surface of the wall (the melt-wall interface surface) is unacceptable because the strong melt velocity field would wash such sensors away very quickly. One method for the determination of the refractory wall thickness utilizes nondestructive measurement techniques and inverse shape determination concepts. Notice that this class of inverse problems is fundamentally different from inverse problems dealing with the determination of unknown boundary conditions on a known geometry [1,2].

Shape inverse determination involves the ability to determine the shape of a configuration satisfying the governing field equation(s) subject to specified surface boundary conditions and certain geometric constraints. A multitude of shape inverse determination techniques have been developed in various fields of science and engineering. Several research teams in countries with strong steel industries have been working on developing and applying such nondestructive monitoring technologies.

Some of the pioneering work was performed in Japan. Yoshikawa and co-workers [3–5] considered axisymmetric configurations of blast furnaces. They attempted to incorporate the effects of the solidified melt layer in their inverse formulation, based on the use of boundary element methods for heat conduction analysis, and a shape optimization algorithm that could handle only a relatively small number of design variables. Shin and Lee [6] used an inverse formulation of a nonlinear heat conduction equation, while Takatani et al. [7] used three-dimensional computational fluid dynamics to predict the temperature field in the wall and consequently the wall erosion topology.

Another significant effort in the development of inverse methods for the determination of the inner wall surface shape was performed in the ex-USSR (Ukraine) by a research team of Matsevity [8–11]. It is concerned with the bottom of the flash smelting furnace, which is the multilayer structure consisting of refractory and heat-insulating materials. Two upper layers are built from chromomagnesite bricks and act as working and insulating lining. Underneath are the layers of refractory bricks and light refractory bricks, which are the heat insulators. The lower refractory brick layer lies on the concrete raft, which is cast on the horizontal steel plate that leans against the columnar concrete supports of the furnace foundation. The width of the wall domain in this problem is much larger than the wall thickness, practically symmetric, relative to the transverse axis, and has a low heat conductivity of the component materials. These facts were used to justify the assumption of the two-dimensionality of the temperature field in the furnace bottom wall. Apparently, this team has not considered a simultaneous prediction of the inner surface of the furnace bottom and sidewalls.

[1]Corresponding author.

Contributed by the Heat Transfer Division of ASME for publication in the JOURNAL OF HEAT TRANSFER. Manuscript received September 21, 2008; final manuscript revised September 17, 2009; published online March 4, 2010. Assoc. Editor: B. Q. Lee.

Preuer et al. [12], Druckenthaner et al. [13], and Radmoser [14], in the Austria/Germany region of central Europe, reported on a more mathematically involved method of simultaneously determining the thickness of the bottom and the sidewall of the blast furnaces that involved the use of a regularization technique, in order to prevent the ill-posed inverse problem from developing exponentially large errors. However, their approach did not appear to be flexible enough to treat realistic irregular inner wall surface configurations.

Sorli and Skaar [15] from Norway reported on a very exact and mathematically sound inverse methodology that converges quite rapidly because it utilizes an adjoint operator formulation. However, the method was demonstrated only for very simple smooth shapes of the inner surface of the wall that were not significantly different from the initially guessed wall surface configurations.

The team of Tanaka [16,17] utilized a sophisticated Kalman filtering technique and boundary element method to deal with axisymmetric configurations of the blast furnaces. Katamine et al. [18], also from Japan, developed a method based on the distributed sensitivity function that uses adjoint variables. Their approach is able to predict quite realistic shapes of the inner surface of the furnace walls, but does not seem to offer a consistently high accuracy in the prediction of the wall wear configuration.

Huang et al. [19] and Roldan [20] in the United States recently reported efforts to predict the configuration of an eroded smelter hearth wall using computational fluid mechanics and an inverse heat conduction approach.

It should be pointed out that despite the separate efforts of several independent research teams, none of the published work utilizing different inverse shape determination approaches has been demonstrated to work reliably when realistic values of temperature and heat flux measurement errors are included. In conclusion, reliable and affordable methodology for continuous sensing and monitoring of realistic three-dimensional variation in refractory wall thickness in smelters is still unavailable. Those available are the several methods for the prediction of the furnace wall thickness variation in a two-dimensional horizontal or vertical plane, assuming a perfect symmetry of the furnace inner and outer walls with respect to the vertical axis.

Furthermore, the existing methods do not offer simultaneously high accuracy, reliability, and speed of the prediction of the wall thickness distribution. The objective of this paper is to elaborate on an alternative method for predicting realistic two-dimensional furnace wall wear configurations reliably and accurately. The new method [21] is based on the authors' concept for inverse design of aerodynamic shapes [22–24] and could be conceptually extended to three dimensions [22].

2 General Approaches to Inverse Determination of Shapes

There exists a multitude of inverse techniques that are useful in solving different types of engineering problems. Two major classes of inverse tools for shape determination can be defined as methods with coupled field analysis and shape modification, and methods with uncoupled field analysis and shape modification. The coupled methods require an intimate understanding of the original field analysis code in order to make specific changes in the boundary condition enforcement subroutines. This is time consuming and hard to accomplish if the original analysis code is not well documented and if the original developers are not available. When a designer uses a commercially available analysis code, he/she cannot perform its conversion to an inverse shape determination code since only a compiled version of the code is available.

The uncoupled inverse methods require no modification to a field analysis code. Thus, any reliable field analysis code or even experimental field measurements data can be used in the shape determination process, without a need for alterations of such a field analysis tool. The field analysis code will be called during the inverse shape determination process as a large subroutine to compute boundary values of certain field variables. These boundary values will then be fed into the master inverse shape determination code that will compute new geometry updates. This means that even a compiled version of a commercially available field analysis code is perfectly acceptable, since it requires only the updated geometry computed by the inverse shape determination master code. This entire procedure constitutes one iteration in the global inverse shape determination process. The uncoupled shape determination techniques have the added benefits of simplicity, relative ease of programming, and versatility.

3 Thermal Boundary Conditions

The essence of all inverse shape determination algorithms is that they require the boundary conditions for field problems to be overspecified on at least some portions of the known part of the boundary. In the problem of inverse determination of the inner surface of the refractory wall in smelters, this means that both temperature T_o and normal temperature derivatives $(dT/dn)_o$ should be provided on the external surface of the refractory wall. A continuous reading of temperature T_o on this surface can be accomplished by placing inexpensive and reliable temperature measuring probes on the outer surface of the furnace refractory wall. The normal derivatives of temperature on the outer surface of the refractory wall of a blast furnace could be measured inexpensively by placing another temperature probe, a few centimeters radially inward from each of the outer surface temperature probes. The difference between the temperatures read by each probe in such a pair of temperature probes can be divided by the known distance between the two probes in a pair to provide the needed outer surface local normal temperature gradient. Values of T_o and $(dT/dn)_o$ can then be interpolated at other surface points by using, for example, B-splines.

The inner surface of the refractory wall of the furnace is of an unknown shape, but the temperature of this surface T_i is assumed to be known and equal to the solidification temperature of the melt, which is recirculating in the furnace. The assumption of the isothermal solidus temperature on the unknown inner surface of the refractory wall is reasonable, although not exact, because there could be layers of solidified melt and slag on some parts of this surface. However, these details could possibly be resolved only by performing a highly accurate conjugate heat transfer analysis [25,26] of the melt flow field and the refractory wall. Despite several attempts at using computational fluid dynamics and conjugate heat transfer analysis [7,12,19,20] to predict shapes of the eroded hearth inner surface, such complex analysis is not sufficiently reliable at the present time because of the stringent requirements on its high accuracy and speed of execution. Hence, the isothermal surface condition on the melt/wall interface is the widely accepted thermal boundary condition.

4 Elastic Membrane Concept for Shape Evolution

Inverse determination of the inner surface shape of the refractory wall of a blast furnace is based on the use of measured T_o and $(dT/dn)_o$ (the overspecified boundary conditions), and on the postulated isothermal value of T_i. These boundary conditions are used in the following manner.

Garabedian and McFadden [27] first proposed the elastic membrane approach for inverse design of aerodynamic shapes, where the body surface is treated as an elastic membrane that deforms under certain surface loads $\Delta C_p(s)$ until it achieves a desired distribution of surface loads. The original nonphysical model for the evolution of, for example, a two-dimensional aerodynamic shape, was given by [27]

$$\beta_0 \Delta n + \beta_1 \frac{d\Delta n}{ds} + \beta_2 \frac{d^2 \Delta n}{ds^2} = \Delta C_p(s) \tag{1}$$

Here, Δn is defined as the shape correction normal to the membrane surface, while the membrane contour-following coordinate

is s. The ordinary differential equation with constant coefficients (Eq. (1)) is analogous to a linear forced spring-damper-mass-spring system, where the monotonically increasing time coordinate has been traded for the surface-contour-following coordinate s. Coefficients β_0, β_1, and β_2 are the user-supplied constants that control the rate of convergence of the iterative shape determination process.

Equation (1) is traditionally solved for shape corrections Δn by evaluating its derivatives using finite differencing. The major problem with this approach is its slow convergence, in conjunction with the field analysis codes of increasing nonlinearity [21]. In an attempt to alleviate these problems, we have developed a new formulation of the elastic membrane design concept, which allows a Fourier series analytical solution to the shape evolution equation [21–24].

4.1 Fourier Series Solution of Shape Evolution Equation. It should be noticed that there is an analogy between the forcing function $\Delta C_p(s)$ in the aerodynamic shape design application, which varies arbitrarily with the contour-following coordinate s and the smelter outer wall surface heat flux difference

$$\Delta q_o = \left(\frac{dT}{dn}\right)_o^{\text{measured}} - \left(\frac{dT}{dn}\right)_o^{\text{computed}} \tag{2}$$

which varies arbitrarily with the circumferential contour-following coordinate θ. Notice also a global periodicity of the mass-damper-spring forcing function and the outer surface heat flux difference Δq_o that repeats its value at the starting and the ending contour-following θ-coordinate.

Thus, on the inner surface of the furnace wall configuration, this elastic membrane surrogate model for inverse shape determination leads to the shape evolution equation [24]

$$\beta_0 \Delta n + \beta_1 \frac{d\Delta n}{d\theta} + \beta_2 \frac{d^2 \Delta n}{d\theta^2} = \Delta q_o \tag{3}$$

which has a homogeneous solution of the general form [24]

$$\Delta n_h = F e^{\lambda_1 \theta} + G e^{\lambda_2 \theta} \tag{4}$$

where F and G are (as yet) undetermined coefficients, and eigenvalues are determined from

$$\lambda_{1,2} = \frac{-\beta_1 \pm \sqrt{\beta_1^2 + 4\beta_0 \beta_2}}{-2\beta_2} \tag{5}$$

A particular solution of the elastic membrane model (Eq. (3)) can be represented in terms of a Fourier series as

$$\Delta n_p = A_0 + \sum_{N=1}^{N_{\max}} [A_N \cos N\theta + B_N \sin N\theta] \tag{6}$$

The forcing function Δq_o can also be represented in terms of another Fourier series as

$$\Delta q_o = a_0 + \sum_{N=1}^{N_{\max}} [a_N \cos N\theta + b_N \sin N\theta] \tag{7}$$

Then, from Eq. (6), it follows that

$$\frac{d\Delta n_p}{d\theta} = \sum_{N=1}^{N_{\max}} [-A_N N \cos N\theta + B_N N \sin N\theta] \tag{8}$$

$$\frac{d^2 \Delta n_p}{d\theta^2} = -\sum_{N=1}^{N_{\max}} [A_N N^2 \cos N\theta + B_N N^2 \sin N\theta] \tag{9}$$

Substitution of Eqs. (6), (8), and (9) into the general evolution (Eq. (3)) and collection of like terms yields analytical links among the coefficients of the two Fourier series

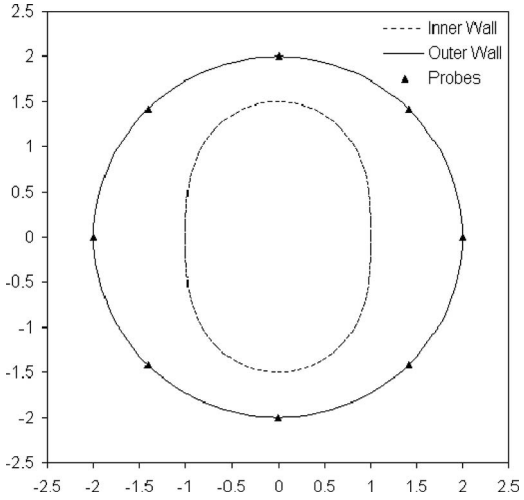

Fig. 1 Symmetric test geometry: target shape of the inner surface (vertical oval) and the outer surface (circle of radius 2.0 m) of the furnace wall with indication of the locations of eight temperature and heat flux probes

$$A_N = \frac{a_N(N^2\beta_2 - \beta_0) - b_N(\beta_1 N)}{(N^2\beta_2 - \beta_0)^2 + (\beta_1 N)^2}, \quad N = 0,1,2,\ldots,N_{\max} \tag{10}$$

$$B_N = \frac{b_N(N^2\beta_2 - \beta_0) + a_N(\beta_1 N)}{(N^2\beta_2 - \beta_0)^2 + (\beta_1 N)^2}, \quad N = 0,1,2,\ldots,N_{\max} \tag{11}$$

Thus, the complete solution for geometry corrections Δn in the locally normal direction to the outside surface of the furnace wall can be represented analytically as

$$\Delta n = F e^{\lambda_1 \theta} + G e^{\lambda_2 \theta} + A_0 + \sum_{N=1}^{N_{\max}} [A_N \cos N\theta + B_N \sin N\theta] \tag{12}$$

The unknown constants, F and G, are determined to be zero from the closure conditions $\Delta n(0) = \Delta n(2\pi)$. This form of solution of the elastic membrane model equation has significant advantages over the standard finite difference approach, since any errors due to finite differencing are removed because the formulation is exact. Consequently, the Fourier series formulation for the elastic membrane concept in inverse shape determination converges faster than the finite difference formulation [21–24].

5 Numerical Results in Horizontal Plane

The Fourier series formulation of the elastic membrane inverse shape determination concept was tested for accuracy and speed of convergence on horizontal cross sections of an idealized furnace, using two simple geometries with outer surface radius $R_o = 2.0$ m. The first test geometry had an oval doubly symmetric inner boundary shape, given as $R_i = 1.0 + 0.5 \sin^2 \theta$ (Fig. 1). The second test geometry had only one axis of symmetry with the inner surface represented by a fourth order polynomial, where slope was discontinuous at the point $R_i(0) = R_i(2\pi)$ (Fig. 2)

$$R_i = 1.0 + 0.5\left\{\left[\frac{(2\pi - \theta)}{2\pi}\right]^4 + \frac{\theta}{2\pi}\right\} \tag{13}$$

Thermal boundary conditions were $T_i = 2000.0$ K and $T_o = 350.0$ K. For simplicity, the furnace wall was assumed to be made of an isotropic homogeneous material. In principle, the analysis of the steady heat conduction could account for a wall made of a finite number of subdomains, each having a different coefficient of thermal conductivity. This is treated easily by the finite element method and could be treated equally easily by the

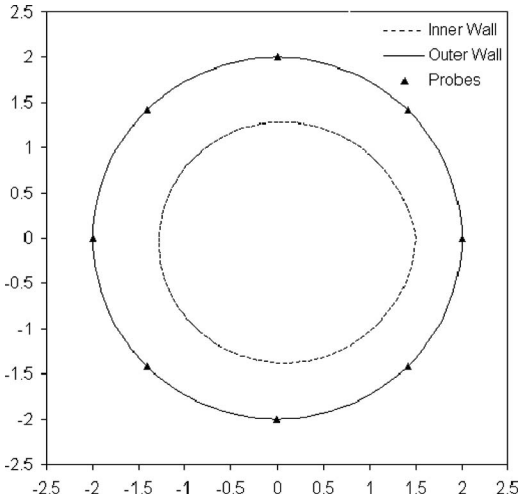

Fig. 2 Asymmetric test geometry: target shape of the inner surface and the outer surface (circle of radius 2.0 m) of the furnace wall with indication of the locations of eight temperature and heat flux probes

boundary element method. Even the realistic situation where the local thermal conductivities are temperature-dependent can be treated relatively easily by both numerical methods [1].

We used a highly accurate boundary element heat conduction analysis code [1] to solve Laplace's equation for a steady thermal field in the annular region. The entire inverse shape determination procedure consisted of the following steps.

1. The "measured" outer surface heat flux corresponding to the inner surface target shape was determined by solving for the temperature field subject to $T_i=2000$ K and $T_o=350$ K, and computing dT/dr on the outer boundary. These boundary values were considered to be errorless.
2. Then, the inner surface was changed to a guessed shape, which was a unit circle in both test cases.
3. Using the analysis code for heat conduction, steady thermal field was solved in this perfectly circular concentric annular region subject to $T_i=2000$ K and $T_o=350$ K.
4. The computed values of dT/dr on the outer boundary were then treated as initial dT/dr computed values.
5. The elastic membrane forcing function Δq_o was then created by the difference between the measured and the initial values of dT/dr on the outer boundary.
6. After several different choices for the values of the elastic membrane coefficients, we used $\beta_0=5000.0$, $\beta_1=0.0$, and $\beta_2=0.0$ that provided the fastest convergence.
7. The inverse design code solved Eq. (3) for corrections in the wall thickness and updated the shape of the inner surface of the furnace wall as $R_i^{\text{new}}=R_i^{\text{old}}+\Delta n$.
8. This shape was then treated as the new initial shape and the entire procedure was automatically repeated.
9. The difference between the computed and the measured heat flux on the outer surface was used as a convergence indicator, and the shape update process was stopped when the heat flux difference reached an acceptably low value (Fig. 3).

The shape of the inner surface of the furnace wall was also used as an indicator of convergence (Fig. 4). After ten iterations in the symmetric test case, the RMS error of dT/dr on the outer surface of the furnace wall decreased to 0.2% of its initial value (Fig. 5), while the RMS error of the radial location of the inner surface decreased to 1.0% of its initial value (Fig. 5).

In the asymmetric geometry test case, the elastic membrane coefficients were chosen as $\beta_0=5000.0$, $\beta_1=0.0$, and $\beta_2=0.0$. After ten iterations, the external surface heat flux difference practically disappeared (Fig. 6), and the inner surface of the furnace wall converged to the target shape (Fig. 7). The RMS error of dT/dr on the outer surface of the furnace wall decreased to 0.1% of its initial value (Fig. 8), while the RMS error on the inner surface of the furnace wall decreased to 0.8% of its initial value (Fig. 8).

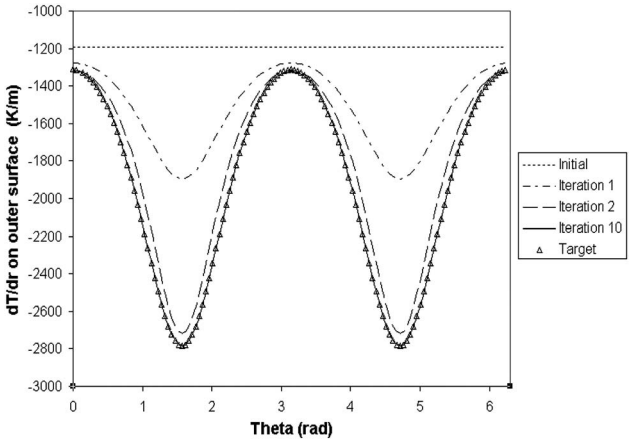

Fig. 3 Symmetric case: convergence history of the outer surface heat flux

6 Effect of Measurement Errors

An actual furnace was not available to evaluate the accuracy of this inverse shape determination method. In an actual field operation of the proposed method, the thermocouples will read local values of temperature on the outer surface of the furnace wall. These readings will inevitably be in error and this error will be randomly distributed among the thermocouples. It is desirable to get maximum information out of as few thermocouples as possible. Consequently, we simulated measurement of the flux at only eight points on the outer surface of the furnace (Figs. 1 and 2). Then, an unbiased error was applied to those eight measurements by using a Gaussian probability distribution (Fig. 9).

These eight randomly perturbed flux values were then spline fitted and interpolated to the remainder of the outer surface of the wall. In a similar fashion, the random error was applied to the computed external temperature, thus simulating actual field measurements with errors. Then, the inverse shape determination procedure was performed while measuring the difference between the

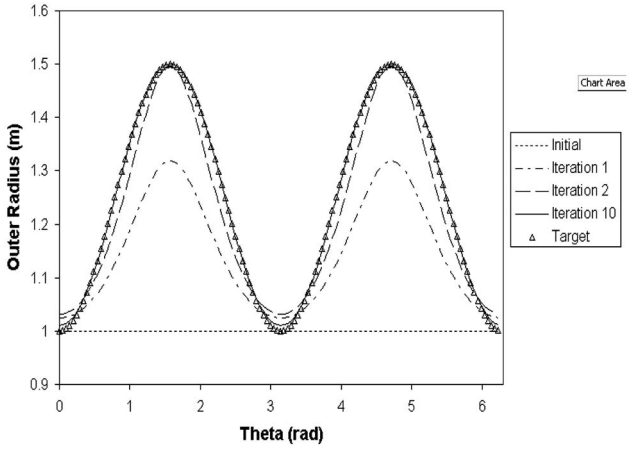

Fig. 4 Symmetric case: convergence history of the inner surface geometry

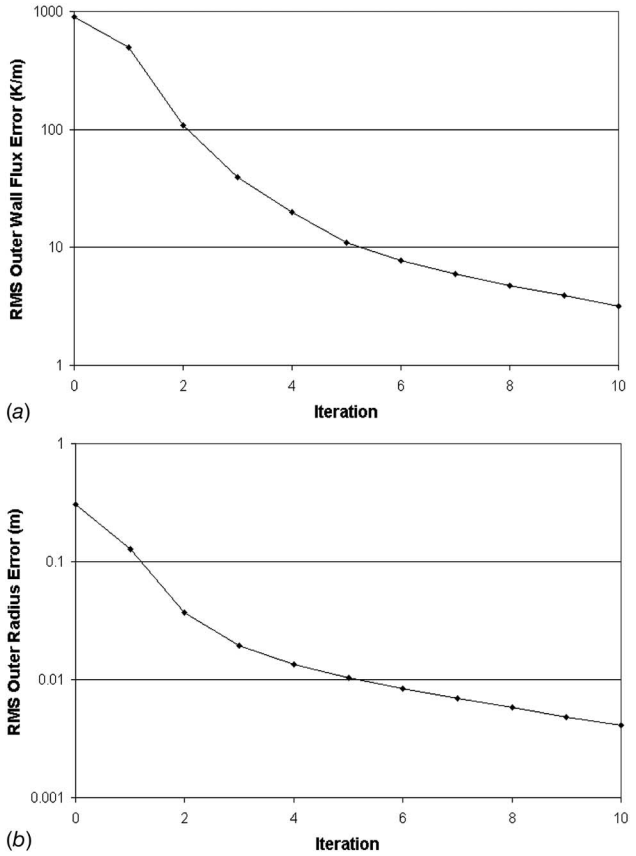

Fig. 5 Symmetric case: convergence history of the RMS error of the outer surface heat flux and of the inner surface geometry

converged shape (subject to the perturbed thermal boundary conditions) and the correct shape. The entire process was repeated a number of times (20 in this case), and the average amount of error in the geometry of the predicted inner surface of the furnace wall was determined.

The effect of different levels of measurement error on the accuracy of furnace inner surface shape prediction is shown in Table 1. The RMS errors, where the average wall thickness used was 0.75 m, were computed as

$$\Delta R_i = (R_i^{\text{target}} - R_i^{\text{predicted}})/(R_o - R_i)_{\text{average}} \tag{14}$$

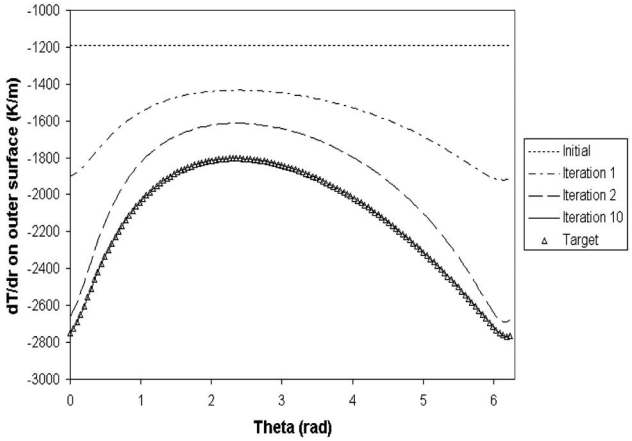

Fig. 6 Asymmetric case: convergence history of the outer surface heat flux

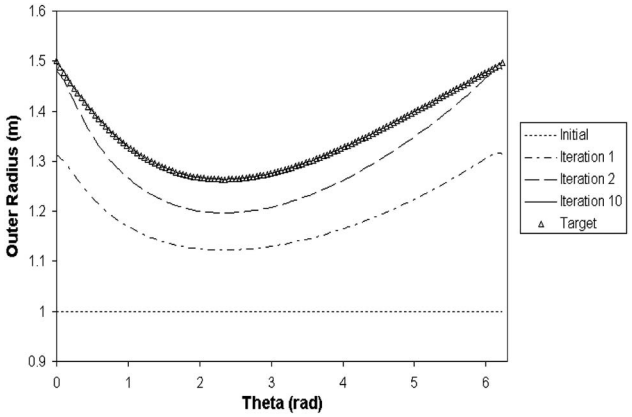

Fig. 7 Asymmetric case: convergence history of the inner surface geometry

7 Numerical Results in Meridional Plane

In the case when the blast furnace configuration is treated as an axisymmetric shape, only half of the vertical (meridional) plane needs to be considered (Figs. 10 and 11). The same elastic membrane concept and Fourier series analytical solution used in the horizontal plane was now applied to the determination of the eroded furnace inner wall shape in the meridional plane.

In this example, there were two material domains: The hearth

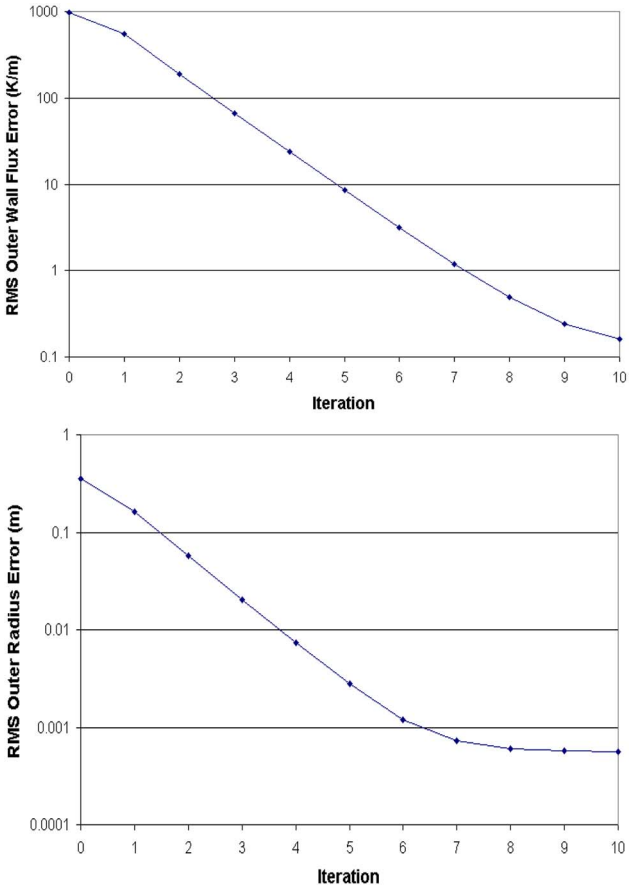

Fig. 8 Asymmetric case: convergence history of the RMS error of the outer surface heat flux and of the inner surface geometry

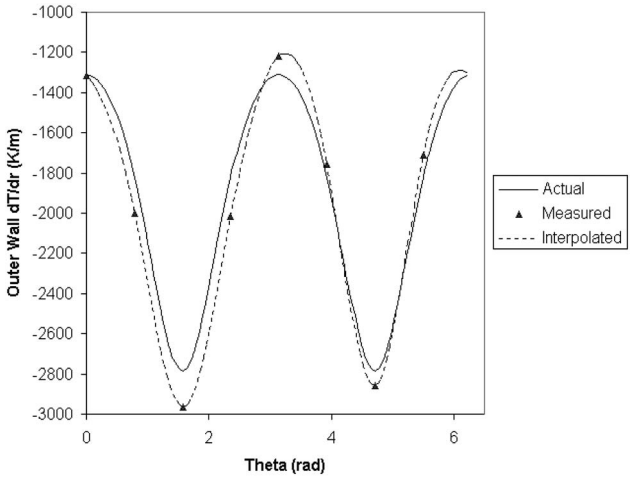

Fig. 9 An example of actual (solid line), measured (actual with stochastically added noise at only eight locations on the outer surface of the furnace wall), and interpolated measured heat fluxes (dashed line) for the geometrically symmetric test case

bottom, the lower 2.5 m of the furnace, had thermal conductivity $k=10.0\ \mathrm{W\,m^{-1}\,K^{-1}}$. Everything above that line (i.e., the side wall) had conductivity $k=13.0\ \mathrm{W\,m^{-1}\,K^{-1}}$.

The cold face of the hearth bottom is the furnace bottom surface where natural convective cooling takes place in air, with ambient air temperature assumed to be $T_{\mathrm{air}}=310.0$ K and convective heat transfer coefficient was assumed to be $h_{\mathrm{air}}=30.0\ \mathrm{W\,m^{-2}\,K^{-1}}$. Temperature probes were assumed to be located at 40 points, spaced evenly in the radial direction on the bottom surface.

Table 1 Relative errors in the predicted inner surface radius due to different levels of the simulated measurement errors of temperature and heat flux on the outer surface

Simulated measurement errors		Expected RMS error in predicted values of R_i	
T_o (%)	$(dT/dr)_o$ (%)	Symmetric (%)	Asymmetric (%)
5.0	5.0	4.2	4.9854
0.0	5.0	4.14	4.7852
5.0	0.0	1.21	0.6373
0.0	0.0	0.84	0.6372

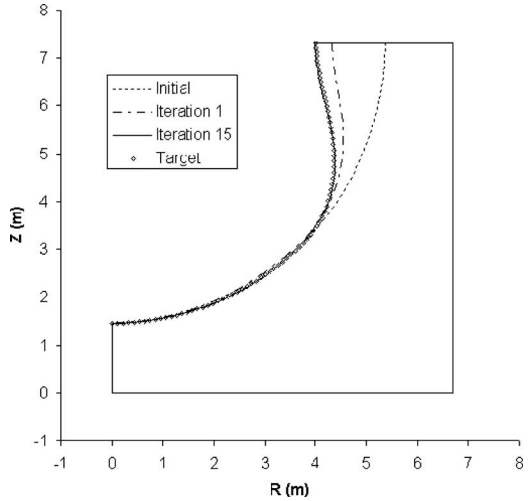

Fig. 10 Initial, target, intermediate, and final shapes of the inner surface of the smelter wall in meridian plane

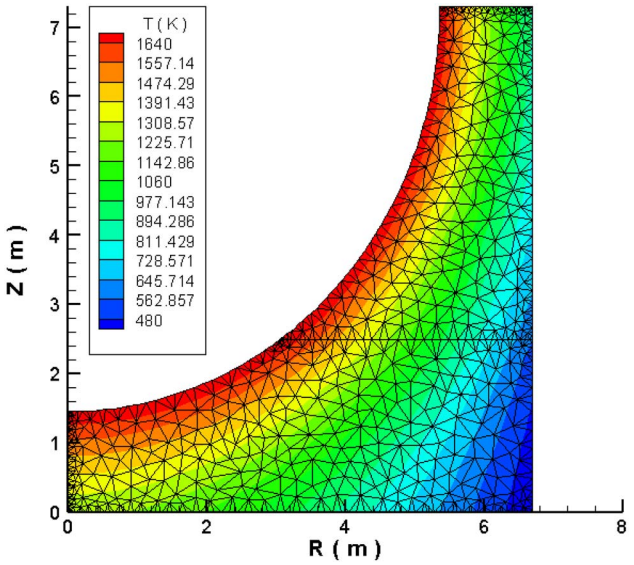

Fig. 11 Initial configuration, temperature field computed using least-squares finite element method [28] and nonstructured computational grid [29]

The steel shell that contacts the cold face of the hearth sidewall had forced convective cooling by water, where the ambient water temperature was assumed to be $T_{\mathrm{water}}=300.0$ K and the convective heat transfer coefficient was assumed to be $h_{\mathrm{water}}=150.0\ \mathrm{W\,m^{-2}\,K^{-1}}$. Temperature probes were assumed to be located at 40 points, spaced evenly in the vertical direction on this surface.

The top boundary was treated as thermally insulated. The left boundary is the furnace vertical symmetry line; thus, the boundary condition there was treated as adiabatic.

The curved wall (Figs. 10 and 11) is the melt/furnace interface surface, assumed to be maintained at a constant temperature of $T_i=1720.0$ K.

Here, we used a fast and accurate finite element method [28] to analyze the steady temperature field in the smelter wall. The forcing function in Eq. (3) was the difference between the measured temperatures on the vertical sidewall, on the bottom wall, and FEM calculated temperatures on these walls. In actual applications, the measured surface temperatures and heat fluxes would be provided at a relatively small number of locations and then interpolated at the larger number (in this example, 40+40=80) surface grid points by using, for example, B-splines.

Inner surface shape corrections were performed along the rays emanating from the imaginary point where the top boundary and furnace centerline intersect. Boundary conditions on Eq. (3) were set, such that $d\Delta n/ds=0$ at the end points so that shape deformation is described with a Fourier cosine series. User-specified coefficients in Eq. (3) were: $\beta_0=200.0$, $\beta_1=0.0$, and $\beta_2=-1.0$, leading to fast and accurate results (Figs. 10–14).

Shape error (Fig. 13) was calculated at 80 evenly spaced points on the design surface (melt-refractory interface) by finding the minimum distances between these points and the target contour (considered to be made up of line segments). RMS and max values are based on that set of 80 individual shape error values.

Temperature errors (Fig. 14) were calculated at each of the 40 evenly spaced points on the vertical sidewall and 40 evenly spaced points on the bottom, as $\mathrm{Err}=|T_{\mathrm{calculated}}-T_{\mathrm{measured}}|$. RMS and max values were based on that set of 80 individual error values.

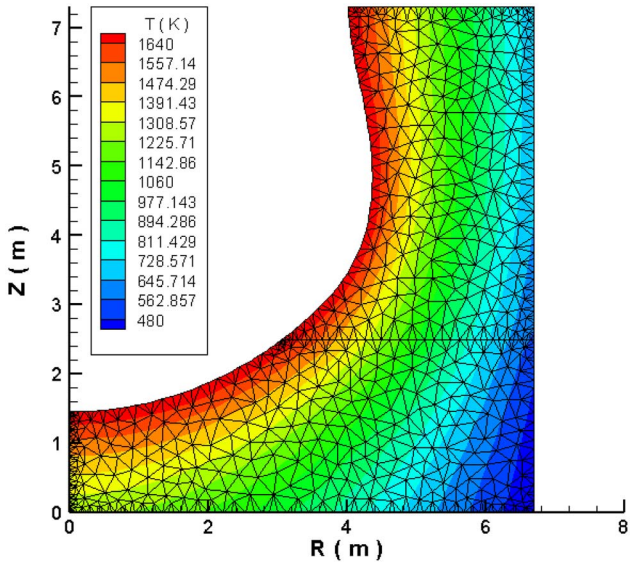

Fig. 12 Final configuration, temperature field computed using least-squares finite element method [28], and computational grid [29]

8 Summary

A new method was developed and tested for the nondestructive determination of wall thickness distribution in blast furnaces and smelters. This technique utilizes external surface measurements of temperature and heat flux and employs a Fourier series solution of an elastic membrane model to evolve the shape of the inner furnace wall. The method accepts any available computer code capable of analyzing the steady temperature field in the furnace wall. It also requires a relatively small number of inexpensive thermocouples. The entire procedure is computationally efficient, highly accurate even under the simulated conditions of measurement noise, and could be extended to the prediction of realistic three-dimensional eroded furnace wall configurations, with sections having different temperature-dependent thermal properties.

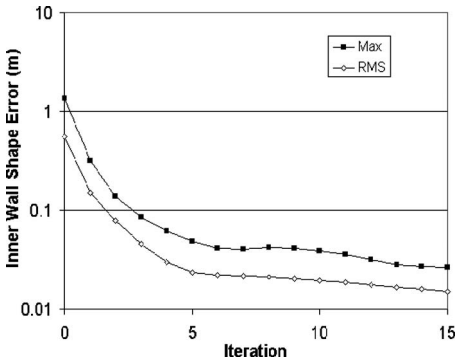

Fig. 13 Convergence history of the inner surface shape error

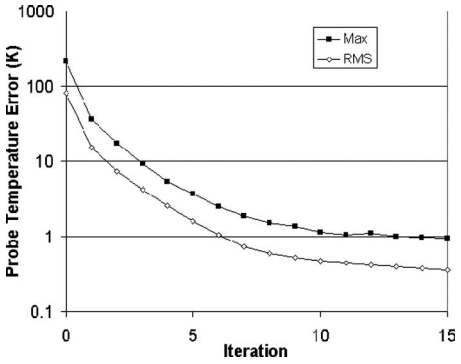

Fig. 14 Convergence history of the inner surface temperature error

Acknowledgment

The authors are grateful for useful comments and suggestions provided by Dr. Keqian (Ken) Liu of U.S. Steel, Technical Center, Monroeville, PA and by the reviewers of the original manuscript. G.S.D. and B.H.D. are grateful for the partial support provided for this research by the U.S. NSF under Grant No. DMS-0073698, administered through the Computational Mathematics program.

Nomenclature

A_N, B_N = Fourier series coefficients for Δn
a_N, b_N = Fourier series coefficients for Δq_o
h = convective heat transfer coefficient (W m^{-2} K^{-1})
k = thermal conductivity (W m^{-1} K^{-1})
N = a term in a Fourier series
n = normal direction to the surface (m)
R = radius of the wall surface (m)
r = radial distance (m)
s = surface-following coordinate (m)
T = temperature (K)
β_0, β_1, β_2 = coefficients in mass-damper-spring model of the elastic membrane
$\Delta C_p(s)$ = difference between target and actual surface pressure (N m^{-2})
Δn = shape correction normal to the surface (m)
Δq_o = outer surface heat flux difference (K m^{-1})
θ = circumferential angle (rad)

Subscripts

h = homogeneous part of solution
i = inner surface of the wall
max = maximum number
o = outer surface of the wall
p = particular part of solution

Superscripts

old = old (previous) value
new = new (updated) value
target = desired (target) value
predicted = actual (predicted) value

References

[1] Dulikravich, G. S., and Martin, T. J., 1996, "Inverse Shape and Boundary Condition Problems and Optimization in Heat Conduction," *Advances in Numerical Heat Transfer*, W. J. Minkowycz and E. M. Sparrow, eds., Taylor & Francis, London, Vol. 1, pp. 381–426.
[2] Dennis, B. H., and Dulikravich, G. S., 1999, "Simultaneous Determination of Temperatures, Heat Fluxes, Deformations, and Tractions on Inaccessible Boundaries," ASME J. Heat Transfer, **121**, pp. 537–545.
[3] Yoshikawa, F., and Szekely, J., 1981, "Mechanism of Blast Furnace Hearth Erosion," Ironmaking Steelmaking, **8**, pp. 159–168.
[4] Yoshikawa, H., et al., 1984, "Estimation of Erosion Line of Refractory and Solidification Layer in Blast Furnace Hearth," *Proceedings of the Fourth Conference on Simulation Technology*, Japan Society for Simulation Technology, pp. 75–78.
[5] Yoshikawa, F., Nigo, S., Kiyohara, S., Taguchi, S., Takahashi, H., and Ichimiya, M., 1987, "Estimation of Refractory Wear and Solidified Layer Distribution in the Blast Furnace Hearth and Its Application to the Operation," Tetsu to Hagane, **73**(15), pp. 2068–2075.
[6] Shin, M., and Lee, J.-W., 2000, "Prediction of the Inner Wall Shape of an Eroded Furnace by the Nonlinear Inverse Heat Conduction Technique," JSME Int. J., Ser. B, **43**(4), pp. 544–549.
[7] Takatani, K., Inada, T., and Takata, K., 2001, "Mathematical Model for Transient Erosion Process of Blast Furnace Hearth," ISIJ Int., **41**(10), pp. 1139–1145.
[8] Matsevity, Y. M., Moultanovsky, A. V., and Nemirovsky, I. A., 1988, "Simu-

lation of Thermal State Discretely Cooled Constructions of Units of Non-Ferrous Metallurgy," Promenergetika, **1**, pp. 42–44.
[9] Matsevity, Y. M., Moultanovsky, A. V., and Timchenko, V. M., 1991, "Diagnostics of Destruction of Cooled Caisson Wall Units on the Base of Identification of Heat Transfer Conditions," Promyshlennaya Teplotekhnika, **13**(3), pp. 3–12.
[10] Kostikov, A. O., and Matsevity, Y. M., 1998, "Determination of Thickness of Heat Transferring Wall With the Help of Solving Geometrical Inverse Heat Conduction Problem," Problemy Mashinostroeniya, **1**(3–4), pp. 52–59.
[11] Matsevity, Y. M., Timchenko, V. M., and Kostikov, A., 2001, "Identification of Destruction in Metallurgical Equipment by Solving the Inverse Heat Conduction Problems," *Proceedings of the ICHMT Symposium CHT'01—Advances in Computational Heat Transfer*, Davis G. de Vahl and E. Leonardi, eds., Begell House Inc., New York, Vol. 2, pp. 1145–1152.
[12] Preuer, A., Winter, J., and Hiebler, H., 1992, "Computation of the Erosion in the Hearth of a Blast Furnace," Steel Res., **63**(4), pp. 147–151.
[13] Druckenthaner, H., et al., 1998, "Online Simulation of the Blast Furnace," *Advanced Steel*, pp. 58–61.
[14] Radmoser, E., 1998, "Security-Related Parts of a Blast Furnace Model," ECMI Newsletter No. 23.
[15] Sorli, K., and Skaar, I. M., 1999, "Monitoring the Wear-Line of a Melting Furnace," *Proceedings of the 3ICIPE, Third International Conference on Inverse Problems in Engineering*, K. Woodbury, ed., ASME, New York.
[16] Tanaka, M., Matsumoto, T., and Oida, S., 1998, "Identification of Unknown Boundary Shape of Rotationally Symmetric Body in Steady Heat Conduction Via BEM and Filter Theories," *Inverse Problems in Engineering Mechanics—ISIP '98*, M. Tanaka, and G. S. Dulikravich, eds., Elsevier, New York pp. 121–130.
[17] Tanaka, M., Matsumoto, T., and Yano, T., 2000, "A Combined Use of Experimental Design and Kalman Filter-BEM for Identification of Unknown Boundary Shape for Axisymmetric Bodies Under Steady-State Heat Conduction," *Proceedings of the Inverse Problems in Engineering Mechanics—ISIP '00*, M. Tanaka and G. S. Dulikravich, eds., Elsevier, New York pp. 3–12.
[18] Katamine, E., Azegami, H., and Kojima, M., 1999, "Boundary Shape Determination on Steady-State Heat Conduction Fields," JSME Int. J., Ser. B, **65**(629), pp. 275–281.
[19] Huang, D., Chaubal, P., Abramowitz, H., and Zhou, C., 2005, "Hearth Skulls and Hearth Wear Investigation of ISPAT Inland's #7 Blast Furnace," *Proceedings of the AIST 2005*, Charlotte, NC, Vol. 1, pp. 101–112.
[20] Roldan, D., 2005, "Numerical Investigation of the Erosion in a Blast Furnace Hearth," MS thesis, Purdue University Calumet, IN.
[21] Dulikravich, G. S., and Baker, D. P., 1998, "Fourier Series Analytical Solution for Inverse Design of Aerodynamic Shapes," *Inverse Problems in Engineering Mechanics—ISIP '98*, M. Tanaka and G. S. Dulikravich, eds., Elsevier, UK, pp. 427–436.
[22] Dulikravich, G. S., and Baker, D. P., 1999, "Using Existing Flow-Field Analysis Codes for Inverse Design of Three-dimensional Aerodynamic Shapes," *Recent Development of Aerodynamic Design Methodologies—Inverse Design and Optimization*, K. Fujii and G. S. Dulikravich, eds., Vol. 68, Springer, New York, pp. 89–112.
[23] Baker, D. P., 1999, "A Fourier Series Approach to the Elastic Membrane Inverse Shape Design Problem in Aerodynamics," MS thesis, Department of Aerospace Engineering, Pennsylvania State University, University Park, PA.
[24] Baker, D. P., Dulikravich, G. S., Martin, T. J., and Dennis, B. H., 2003, "Inverse Determination of Smelter Wall Erosion Shapes Using a Fourier Series Method," *Proceedings of the International Symposium on Inverse Problems in Engineering Mechanics—ISIP '03*, Nagano, Japan, Feb. 18–21.
[25] Han, Z.-X., Dennis, B. H., and Dulikravich, G. S., 2001, "Simultaneous Prediction of External Flow-Field and Temperature in Internally Cooled 3-D Turbine Blade Material," Int. J. Turbo Jet Engines, **18**(1), pp. 47–58.
[26] Dulikravich, G. S., 1999, "Electro-Magneto-Hydrodynamics and Solidification," *Advances in Flow and Rheology of Non-Newtonian Fluids, Part B*, D. A. Siginer, D. De Kee, and R. P. Chhabra, eds., Elsevier, New York, Vol. 8, pp. 677–716.
[27] Garabedian, P., and McFadden, G., 1982, "Design of Supercritical Swept Wings," AIAA J., **20**(3), pp. 289–291.
[28] Dennis, B. H., Eberhart, R. C., Dulikravich, G. S., and Radons, S. W., 2003, "A Finite Element Simulation of Cooling of 3-D Human Head and Neck," J. Biomech. Eng., **125**, pp. 832–840.
[29] Marcum, D. L., and Weatherhill, N. P., 1995, "Unstructured Grid Generation Using Iterative Point Insertion and Local Reconnection," AIAA J., **33**(9), pp. 1619–1625.

Numerical Simulation of Transient Thermal Transport on a Rotating Disk Under Partially Confined Laminar Liquid Jet Impingement

Jorge C. Lallave

Muhammad M. Rahman

Department of Mechanical Engineering,
University of South Florida,
Tampa, FL 33620

This paper considers the transient conjugate heat transfer characterization of a partially confined liquid jet impinging on a rotating and uniformly heated solid disk of finite thickness and radius. A constant heat flux was imposed at the bottom surface of the solid disk at $t=0$, and heat transfer was monitored for the entire duration of the transient until the steady state condition was reached. Calculations were done for a number of disk materials using water as the coolant, covering a range of Reynolds numbers (225–900), Ekman numbers ($7.08\times10^{-5}-\infty$), nozzle-to-target spacing ($\beta=0.25-1.0$), confinement ratios ($r_p/r_d=0.2-0.75$), disk thicknesses to nozzle diameter ratios ($b/d_n=0.25-1.67$), and solid to fluid thermal conductivity ratios (36.91–697.56). It was found that a higher Reynolds number decreases the time to achieve the steady state condition and increases the local and average Nusselt number. The duration of the transient increases with the increment of the Ekman number and disk thickness, and the reduction in the thermal diffusivity of the disk material. [DOI: 10.1115/1.4000442]

Keywords: partially confined liquid jet impingement, transient conjugate heat transfer, rotating disk

1 Introduction and Literature Review

Impinging jet is an attractive means of providing high heat or mass transfer rate. Rotation is an effective and powerful way to generate a secondary flow that enhances the convective transport. Therefore, jet impingement, in combination with rotation, is used in various processes in mechanical, manufacturing, electrical, and chemical engineering such as metal etching, fabrication of printed wiring boards, rinsing or washing, surface preparation or coating, and microgravity fluid handling. Particularly in a microgravity environment, the body force generated by rotation is extremely useful to transport the fluid over the heat transfer surface. The primary motivation for this study was to calculate fundamental heat transfer coefficient distribution that can be useful to design high heat flux heating and cooling systems for space applications. Both steady state and transient heat transfer coefficients are needed to optimize the design of these systems.

The liquid jet considered in this study is axisymmetric. The jet nozzle is attached to a confinement plate parallel to the impingement surface with a separation distance of H_n. The diameter of the confinement disk is smaller than the impingement disk, and therefore, the fluid comes out of confinement and spreads downstream with a free surface exposed to the ambient environment. This partially confined liquid jet impingement in the presence of disk rotation and thermal boundary layer behaviors that control the transient convective heat transfer process during startup of power will be examined in detail.

Reviews of fluid flow and heat transfer during jet impingement over a stationary surface were presented by Polat et al. [1] and Garimella [2]. Experimental studies of a single round jet impinging on a rotating disk were conducted by Metzger and Grochowsky [3]. Carper and Deffenbaugh [4] conducted experiments to determine the average convective heat transfer coefficient for the rotating solid fluid interface at uniform temperature, cooled by a single liquid jet of oil impinging normal to the rotating disk. A nondimensional correlation was given in terms of jet and rotational Reynolds numbers. Carper et al. [5] conducted further experiments to consider the Prandtl number effects on the average heat transfer coefficient at the rotating disk. They documented the effects of the rotational Reynolds number on the average Nusselt number for various jet Reynolds numbers.

Popiel and Boguslawski [6] reported measurements of heat transfer rate for a range of rotational and jet Reynolds numbers. Thomas et al. [7] measured the film thickness across a stationary and rotating horizontal disk using the capacitance technique, where the liquid was delivered to the disk by a controlled impinging jet. Saniei et al. [8] investigated the heat transfer coefficients from a rotating disk with jet impingement. The jet was placed perpendicular to the disk surface at four different distances from the center of the disk. The characterization of a thin film of water from an axisymmetric controlled impinging jet on stationary and rotating disk surfaces was done by Ozar et al. [9,10]. The authors measured the thickness of the liquid film on the disk surface by an optical method, and characterized the hydraulic jump. In a later study, Rice et al. [11] presented an analysis of the liquid film and heat transfer characteristics of a free surface controlled liquid jet impingement onto a rotating disk. Computations were performed using a two-dimensional axisymmetric Eulerian mesh, while the free surface was calculated with the volume of the fluid method. An integral analysis of hydrodynamics and heat transfer in a thin liquid film flowing over a rotating disk surface was presented by Basu and Cetegen [12]. The model considered constant temperature and constant heat flux boundary conditions over a range of Reynolds and Rossby numbers, covering both inertia and rotation dominated regimes. Lallave and Rahman [13] numerically studied

Contributed by the Heat Transfer Division of ASME for publication in the JOURNAL OF HEAT TRANSFER. Manuscript received November 26, 2008; final manuscript received July 24, 2009; published online March 5, 2010. Assoc. Editor: G. Biswas.

the conjugate heat transfer for a partially confined liquid jet impinging on a rotating and uniformly heated solid disk of finite thickness and radius. The present investigation is an advancement over this study to explore the transient heat transfer effect during the startup of power.

There have only been a few studies on transient heat transfer associated with jet impingement cooling. The transient freezing of water during circular jet impingement on a disk at subzero temperature was studied experimentally by Moallemi and Naraghi [14]. Steady state and transient methods were used by Owens and Liburdy [15], in order to study jet impingement cooling of surfaces. Thermochromic liquid crystals were employed to measure the surface temperature. Kumagai et al. [16] investigated the transient boiling heat transfer rate of a two-dimensional impinging water jet on a rectangular surface for jet subcooling from 14 K to 50 K. Francis and Wepfer [17] investigated the thermal characteristics of jet impingement drying of a moist porous solid using a numerical solution employing a one-dimensional transient model. Fujimoto et al. [18] presented a numerical simulation of transient cooling of a solid by an impinging circular free surface liquid jet. The flow and thermal fields in the liquid, as well as the temperature distributions in the hot solid, were predicted. Rahman et al. [19] presented the transient analysis of a free jet of high Prandtl number fluid impinging on a stationary solid disk of finite thickness. Liu et al. [20] presented a numerical simulation of transient convective heat transfer during air jet impingement cooling of a confined multichip module disk. They found that a large rate of decrease in chip temperature and average Nusselt number happens in the earlier part of the transient. Sarghini and Ruocco [21] presented a transient numerical analysis of a planer jet impingement on a finite thickness substrate at low volumetric flow rate including the effects of buoyancy. They found that conduction plays a very significant role at the initial part of the transient process. A series of experimental investigations on transient and steady state cooling performance of heat sinks with a confined slot jet impingement were done by Lin et al. [22].

Although the above investigations provided very useful information, only a few attempted to produce local heat transfer distribution for a rotating disk, in combination with free or confined liquid jet impingement. There have only been a few studies on transient heat transfer, and most of them are experimental work on free jet impingement. None of these studies considered transient heat transfer during partially confined liquid jet impingement. The present study attempts to carry out a comprehensive investigation of transient conjugate heat transfer for a partially confined liquid jet impingement over a spinning solid disk. The variation in disk temperature, as well as local and average heat transfer coefficients during the transient heating process, are explored for different combinations of flow rate, spin rate of the target disk, nozzle height, confinement ratio, disk thickness, and disk material. The results are expected to be valuable toward the design of cooling or heating systems for engineering applications.

2 Modeling and Computation

A schematic of the physical problem is shown in Fig. 1. An axisymmetric liquid jet is discharged through a nozzle and impinges at the center of the top surface of a solid circular disk, spinning with a uniform angular velocity about the z-axis. The confinement plate attached to the nozzle is smaller in diameter than the disk, which allows the formation of free surface flow when the fluid exits the confined region. After an isothermal fluid flow has been established on the disk, at $t=0$, the power source is turned on to deliver a uniform heat flux at the bottom surface of the disk, while the confinement plate is kept insulated. Due to symmetry of the problem about the axis of rotation, all $\partial/\partial\theta$ terms can be dropped out. The equations for the conservation of mass, momentum (r, θ, and z directions, respectively), and energy for incompressible flow of a Newtonian fluid with temperature dependant properties can be written as [23]

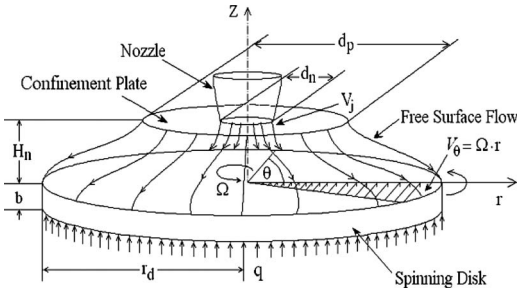

Fig. 1 Three-dimensional schematic of axisymmetric semi-confined liquid jet impingement on a uniformly heated spinning disk

$$\frac{\partial \rho_f}{\partial t} + \frac{1}{r}\frac{\partial}{\partial r}(\rho_f r V_r) + \frac{\partial}{\partial z}(\rho_f V_z) = 0 \tag{1}$$

$$\rho_f\left(\frac{\partial V_r}{\partial t} + V_r\frac{\partial V_r}{\partial r} + V_z\frac{\partial V_r}{\partial z} - \frac{V_\theta^2}{r}\right) = -\frac{\partial p}{\partial r} + \frac{1}{r}\frac{\partial}{\partial r}\left[\frac{2}{3}\cdot\mu_f r\left(2\frac{\partial V_r}{\partial r} - \frac{V_r}{r} - \frac{\partial V_z}{\partial z}\right)\right] + \frac{\partial}{\partial z}\left[\mu_f\left(\frac{\partial V_r}{\partial z} + \frac{\partial V_z}{\partial r}\right)\right] + \frac{2}{3}\cdot\frac{\mu_f}{r}\left(\frac{\partial V_r}{\partial r} + \frac{\partial V_z}{\partial z} - \frac{2\cdot V_r}{r}\right) \tag{2}$$

$$\rho_f\left(\frac{\partial V_\theta}{\partial t} + V_r\frac{\partial V_\theta}{\partial r} + V_z\frac{\partial V_\theta}{\partial z} + \frac{V_r V_\theta}{r}\right) = \frac{1}{r^2}\frac{\partial}{\partial r}\left[r^2\mu_f\left[r\frac{\partial}{\partial r}\left(\frac{V_\theta}{r}\right)\right]\right] + \frac{\partial}{\partial z}\left[\mu_f\left(\frac{\partial V_\theta}{\partial z}\right)\right] \tag{3}$$

$$\rho_f\left(\frac{\partial V_z}{\partial t} + V_r\frac{\partial V_z}{\partial r} + V_z\frac{\partial V_z}{\partial z}\right) = -\rho_f g - \frac{\partial p}{\partial z} + \frac{1}{r}\frac{\partial}{\partial r}\left[r\mu_f\left(\frac{\partial V_r}{\partial z} + \frac{\partial V_z}{\partial r}\right)\right] + \frac{\partial}{\partial z}\left[\frac{2}{3}\mu_f\left(2\frac{\partial V_Z}{\partial z} - \frac{V_r}{r} - \frac{\partial V_r}{\partial r}\right)\right] \tag{4}$$

$$\rho_f\left(\frac{\partial T_f}{\partial t} + V_r\frac{\partial (Cp_f T_f)}{\partial r} + V_z\frac{\partial (Cp_f T_f)}{\partial z}\right) = \left[\frac{1}{r}\frac{\partial}{\partial r}\left(k_f r\frac{\partial T_f}{\partial r}\right) + \frac{\partial}{\partial z}\left(k_f\frac{\partial T_f}{\partial z}\right)\right] + 2\cdot\mu_f\left[\left(\frac{\partial V_r}{\partial r}\right)^2 + \left(\frac{V_r}{r}\right)^2 + \left(\frac{\partial V_Z}{\partial z}\right)^2 + \frac{1}{2}\left(\frac{\partial V_\theta}{\partial r} - \frac{V_\theta}{r}\right)^2 + \frac{1}{2}\left(\frac{\partial V_\theta}{\partial z}\right)^2 + \frac{1}{2}\left(\frac{\partial V_r}{\partial z} + \frac{\partial V_Z}{\partial r}\right)^2 - \frac{1}{3}\left(\frac{\partial V_r}{\partial r} + \frac{V_r}{r} + \frac{\partial V_Z}{\partial z}\right)^2\right] \tag{5}$$

The variation in properties of solids with temperature was not significant. Therefore, the conservation of energy inside the solid can be characterized by the following equation:

$$\frac{\partial T_S}{\partial t} = \alpha_s\left[\frac{\partial^2 T_S}{\partial r^2} + \frac{1}{r}\left(\frac{\partial T_S}{\partial r}\right) + \frac{\partial^2 T_S}{\partial z^2}\right] \tag{6}$$

The following boundary conditions were used to complete the physical problem formulation:

$$\text{At} \quad r = 0, \quad -b \le z \le 0: \frac{\partial T_S}{\partial r} = 0 \tag{7}$$

$$\text{At} \quad r = 0, \quad 0 \le z \le H_n: V_\theta = V_r = 0, \quad \frac{\partial V_z}{\partial r} = 0, \quad \frac{\partial T_f}{\partial r} = 0 \tag{8}$$

$$\text{At} \quad r = r_d, \quad -b \le z \le 0: \frac{\partial T_S}{\partial r} = 0 \tag{9}$$

$$\text{At} \quad r = r_d, \quad 0 \le z \le \delta: p = p_{\text{atm}} \tag{10}$$

$$\text{At} \quad z = -b, \quad 0 \le r \le r_d: -k_s \frac{\partial T_s}{\partial z} = q_w \tag{11}$$

$$\text{At} \quad z = 0, \quad 0 \le r \le r_d: V_\theta = \Omega \cdot r, \quad V_r = V_z = 0,$$

$$T_s = T_f, \quad k_s \frac{\partial T_s}{\partial z} = k_f \frac{\partial T_f}{\partial z} \tag{12}$$

$$\text{At} \quad z = H_n, \quad 0 \le r \le r_n: V_z = -V_j, \quad V_r = V_\theta = 0, \quad T_f = T_j \tag{13}$$

$$\text{At} \quad z = H_n, \quad r_n \le r \le r_p: V_\theta = V_r = V_z = 0, \quad \frac{\partial T_f}{\partial z} = 0 \tag{14}$$

The boundary condition at the free surface outside the confinement can be expressed as [24]

$$\text{At} \quad z = \delta, \quad r_p \le r \le r_d: \frac{\partial \delta}{\partial r} = \frac{V_z}{V_r},$$

$$p = p_{\text{atm}} - \frac{\sigma \dfrac{d^2\delta}{dr^2}}{\left[1 + \left(\dfrac{d\delta}{dr}\right)^2\right]^{3/2}}, \quad \frac{\partial V_s}{\partial n} = 0, \quad \frac{\partial T_f}{\partial n} = 0 \tag{15}$$

where V_S is the component of fluid velocity along the free surface and n is the coordinate normal to the free surface. The boundary conditions at the free surface $r_p \le r \le r_d$ include the kinematic condition and balance of normal and shear stresses. The kinematic condition relates the velocity components to the local slope of the free surface. The normal stress balance takes into account the effects of surface tension. In the absence of any significant resistance from the ambient gas, the shear stress encountered at the free surface is essentially zero. Similarly, the heat loss from the fluid film to the ambient gas is negligible, resulting in a zero temperature gradient at the free surface.

The solid disk was assumed to be at thermal equilibrium with jet fluid before the heating of the plate was turned on. The velocity field at this condition was determined by solving only the continuity and momentum equations in the fluid region. Thus

$$\text{at} \quad t = 0: T_f = T_s = T_j, \quad \mathbf{V}_i = \mathbf{V}(\text{isothermal}) \tag{16}$$

The average heat transfer coefficients can be defined as

$$h_{\text{av}} = \frac{2}{r_d^2 \cdot (\overline{T}_{\text{int}} - T_j)} \int_0^{r_d} hr(T_{\text{int}} - T_j) dr \tag{17}$$

where $\overline{T}_{\text{int}}$ is the average temperature at the solid-liquid interface.

The properties of the solid materials used for the numerical simulation, such as density, thermal conductivity, and specific heat, were obtained from Özisik [25] and assumed to remain constant over the working temperature range. Fluid (H_2O) properties were obtained from Bejan [26] and were correlated by the following equations. Between 300 K $< T <$ 411 K; $Cp_f = 9.5 \times 10^{-3} T^2 - 5.9299T + 5098.1$; $k_f = -7.0 \times 10^{-6} T^2 + 5.8 \times 10^{-3} T - 0.4765$; $\rho_f = -2.7 \times 10^{-3} T^2 + 1.3104T + 848.07$; and $\ln(\mu_f) = -3.27017 - 0.0131T$. Here, the absolute temperature T is in K. The nozzle opening and the heated target disk have radii of 0.6 mm and 6.0 mm, respectively. The heat flux (q) was kept constant at 125 kW/m^2. The incoming fluid temperature (T_j) was set to 310 K. The thickness of the disk (b) was varied over the following values: 0.30 mm, 0.60 mm, 1.0 mm, 1.5 mm, and 2.0 mm. The jet impingement height or the distance between the nozzle and disk was set at the following values: 3×10^{-4}, 6×10^{-4}, 9.0×10^{-4}, and 1.2×10^{-3} m. The spinning rate (Ω) was varied from 0 rad/s to 78.54 rad/s or 0 rpm to 750 rpm. The flow rate was varied from 6.65×10^{-7} m^3/s to 2.72×10^{-6} m^3/s. These provided the ranges of Reynolds and Ekman numbers of: Re = 225 to 900 and Ek $= 7.08 \times 10^{-5}$ to ∞. Using the laminar-turbulent transition criterion used by Popiel and Boguslawski [6] and Vanyo [27], all runs used in the paper were checked and found out to be laminar.

The governing equations, along with the boundary and initial conditions, were solved using the Galerkin finite element method [28]. Four node quadrilateral elements were used. For each element, the velocity, pressure, and temperature fields were approximated, which led to a set of discretized equations that defined the continuum. The Newton–Raphson algorithm was used to solve these nonlinear algebraic equations. An iterative procedure was used to arrive at the solution for the velocity and temperature fields. In order to determine the initial velocity field (V_i), the equations for the conservation of mass and momentum were solved. Since the solution of the momentum equation required only two out of the three boundary conditions at the free surface, the third condition that relates the slope of the free surface to local velocity components at the free surface was used to upgrade the position of the free surface at the end of each iteration step. The solver used spines to track the free surface and rearranged grid distribution with the movement along the free surface. The spines are straight lines passing through the free surface nodes and connect the remaining nodes underneath the free surface. The movement of the free surface affected only the nodes along the spine. Once the final free surface height distribution and the flow field for the isothermal equilibrium condition were reached, the power was turned on and heat began to flow. Then the computation domain included both solid and fluid regions. The continuity, momentum, and energy equations were solved simultaneously as a conjugate problem, taking into account the variation in fluid properties with temperature. The computation covered the entire transient period all the way to the steady state condition. Because of large changes at the outset of the transient and very small changes when the solution approached the steady state condition, a fixed time step was used to cover the earlier part of the transient up to 25 s, and a variable time step was used for the rest of the computation. At each time step, the solution was considered converged when relative change in field values from a particular iteration to the next, and the sums of the residuals for each variable became less than 10^{-6}. The computation was done using CFD software FIDAP 8.7, along with significant user coding.

To determine the number of elements for accurate numerical solution, computation was performed for several grids or combinations of number of elements in the horizontal and vertical directions covering the solid and fluid regions, as shown in Fig. 2. It may be noted that the local Nusselt number obtained using a 14 $\times$ 39 grid is significantly different from those obtained using other grid structures. The numerical solution becomes grid independent when the number of divisions equal to 28×63 in the axial (z) and radial (r) directions, respectively, is used. Comparing the numerical results for the 32×72 and 45×100 grids with a 28×63 grid showed an average difference of 0.72%. Therefore, all further computations were carried out using 28×63 grid. In addition, computations were performed to calculate a suitable fixed time step to determine the sensitivity of the transient solution. These transient computations showed that the variation in the local Nusselt number is not sensitive to time step size when an increment of 0.075 s or less is chosen. For this study, the time increment of 0.05 s was selected to ensure a smooth variation.

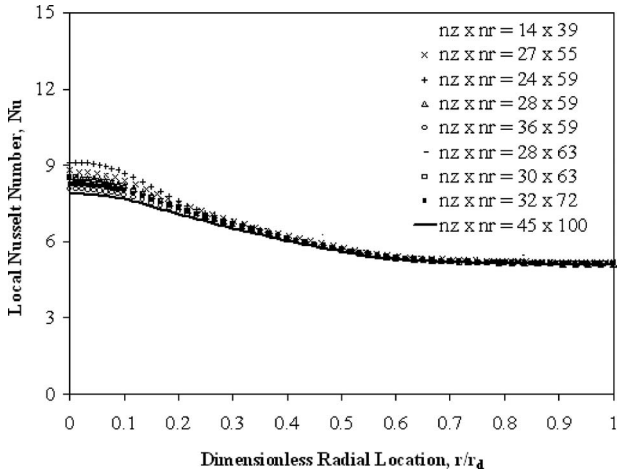

Fig. 2 Local Nusselt number distributions for different number of elements in r and z directions (Re=750, b/d_n=0.5, Ek =4.25×10^{-4}, β=0.5, and r_p/r_d=0.667)

3 Results and Discussion

Figure 3 shows the local Nusselt number and the dimensionless interface temperature variation for different time instants. It can be observed that at the earlier part of the transient heat transfer process, the solid-fluid interface maintains a more uniform temperature. The difference of dimensionless maximum and minimum temperature at the solid-fluid interface increases from 0.016 at Fo=0.051 to 0.05 when the steady state condition is reached at Fo=0.369. After the power is turned on, the heat is first absorbed by the solid as it is transmitted through the solid and dissipated to the fluid. At the solid-fluid interface, the fluid absorbs heat and carries it as it moves downstream. At the start of the transient, the thickness of the thermal boundary layer is zero. As time goes on, the thickness of the thermal boundary layer increases, and therefore, the temperature rises. The interface temperature responds to the boundary layer thickness that increases downstream. Therefore, the temperature becomes minimum at the impinging point and maximum at the outer edge of the spinning disk. The local Nusselt number is controlled by local temperature and heat flux at the solid-fluid interface. It shows a higher value at early stages of the transient process due to a smaller temperature difference between the liquid jet and disk solid-fluid interface. This essentially means that all heat reaching the solid-fluid interface via conduction through the solid is more efficiently convected out as the local fluid temperature is low everywhere at the interface. The local Nusselt number is at maximum at the center of the disk and decreases along the radial distance as the boundary layer thickness increases downstream. The local Nusselt number decreases with time until it reaches the steady state equilibrium distribution.

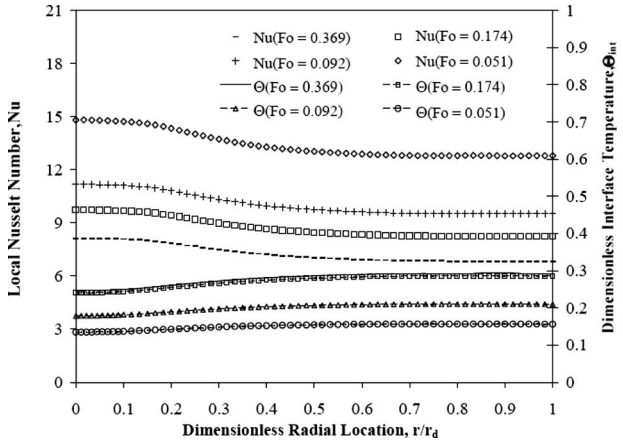

Fig. 3 Local Nusselt number and dimensionless interface temperature distributions for a silicon disk with water as the cooling fluid for different Fourier numbers (Re=275, Ek=4.25 ×10^{-4}, β=0.5, b/d_n=0.5, and r_p/r_d=0.667)

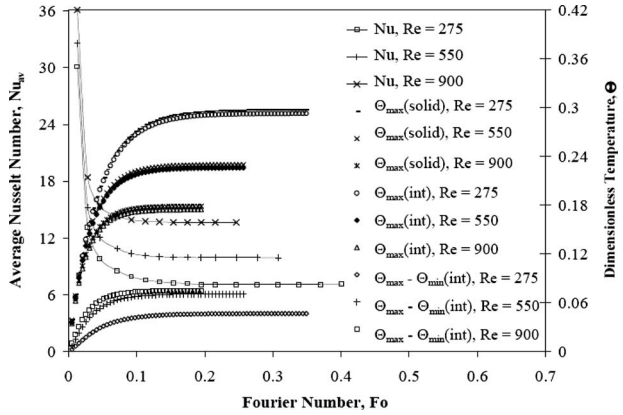

Fig. 4 Average Nusselt number and dimensionless temperature variations with time for different Reynolds numbers (Ek =4.25×10^{-4}, β=0.5, silicon disk, b/d_n=0.5, and r_p/r_d=0.667)

The integrated average Nusselt number and the variation in dimensionless maximum temperature at the interface, maximum temperature inside the solid, and maximum-to-minimum temperature difference at the interface for different Fourier numbers at different values of Reynolds number are shown in Fig. 4. The average Nusselt number is large at the early part of the transient and monotonically decreases with time, ultimately reaching the value for the steady state condition. A higher Reynolds number increases the magnitude of fluid velocity near the solid-fluid interface that controls the convective heat transfer, and therefore, increases the average Nusselt number. The control of maximum temperature is important in many critical thermal management applications, including electronic packaging. As expected, the temperature increases everywhere with time, starting from the initial isothermal condition. A rapid increment is seen at the earlier part of the transient and it levels off as the thermal storage capacity of the solid diminishes and become zero at the steady state condition. It may be noted that the time required to reach the steady state condition is lower at a higher Reynolds number because the higher velocity of the fluid helps to enhance the convective heat transfer process. This is due to quicker dissipation of heat with higher flow rate. The steady state Fourier number (Fo_{ss}) was defined as the time needed to approach 99.99% of the steady state local Nusselt number over the entire solid-fluid interface. It was found that Fo_{ss} decreases from 0.369 at Re=275 to 0.195 at Re=900.

Figure 5 provides the variations of the average Nusselt number and the dimensionless maximum temperature at the interface, maximum temperature inside the solid, and maximum-to-minimum temperature difference at the interface with the progression of time at different Ekman numbers. The average Nusselt number is large at the early part of the transient and monotonically decreases with time, ultimately reaching the value for the steady state condition. Throughout the transient heating process, the average Nusselt number is more at larger spinning rate or smaller Ekman number. As the Ekman number decreases from ∞ to 7.08 $\times 10^{-5}$, the average Nusselt number increases by an average of 27.47% when the Reynolds number is kept constant at 550. The maximum temperature within the solid was encountered at the outlet adjacent to the heated surface ($z=-b$, $r=r_d$). The temperatures rise with time as the solid disk and the fluid store heat, showing a rapid response at the earlier part of the heating process

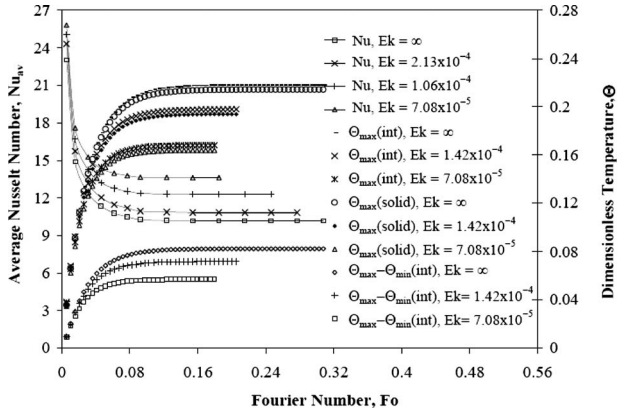

Fig. 5 Average Nusselt number and dimensionless temperature variations with time for different Ekman numbers (Re =550, β=0.25, silicon disk, b/d_n=0.5, and r_p/r_d=0.667)

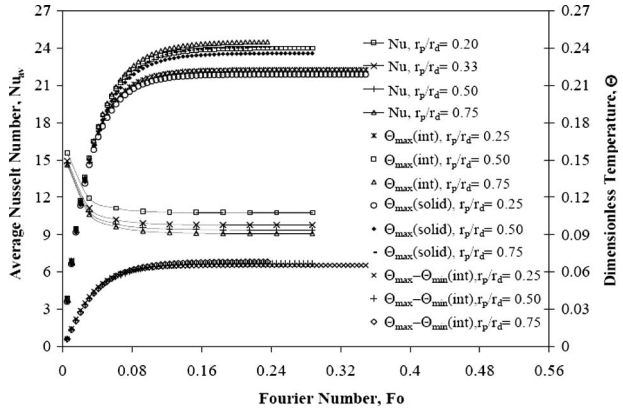

Fig. 7 Average Nusselt number and dimensionless temperature variations with time for different plate to disk confinement ratios (Re=450, Ek=4.25×10^{-4}, β=0.5, silicon disk, and b/d_n =0.5)

until the thermal storage capacity reaches its limit at the steady state condition. It may be noted that the magnitude of the dimensionless temperature, as well as the time required to reach the steady state condition, become smaller as the Ekman number decreases. This is because the magnitude of fluid velocity near the solid-fluid interface that controls the convective heat transfer rate increases with the increment of the rotational rate of the disk or the reduction in the Ekman number. These observations are in agreement with the numerical solutions of Rice et al. [11].

The effects of nozzle-to-target spacing for water as the coolant and silicon as the disk material at a spinning rate of 125 rpm or Ek=4.25×10^{-4} and Reynolds number of 750, is demonstrated in Fig. 6. It may be noticed that a higher average Nusselt number and a smaller maximum temperature are obtained over the entire transient process when the nozzle is brought closer to the heated disk. The smaller gap between the nozzle and the target disk provides a higher fluid velocity between the target disk and the confinement plate, and therefore, results in a larger rate of convective heat transfer. As the nozzle-to-target spacing decreases from 1 to 0.25, the average Nusselt number increases by an average of 12.71% when the Reynolds number is kept constant at 750.

Different plate-to-disk confinement ratios (r_p/r_d) from 0.2 to 0.75 were investigated for water as the coolant and silicon as the disk material. The effects of plate-to-disk confinement ratio on the variation in dimensionless maximum temperature at the interface, maximum temperature inside the solid, and maximum-to-minimum temperature difference at the interface and average Nusselt number are shown in Fig. 7. The average Nusselt number increases with the reduction in the plate-to-disk confinement ratio. When r_p is increased, the frictional resistance from both walls slows down the momentum and results in higher film thickness at the free surface region for any given spin rate and flow rate. A lower fluid velocity obviously results in a smaller convective heat transfer rate. As the plate-to-disk confinement ratio decreases from 0.75 to 0.2, the average Nusselt number increases by an average of 18.07%, when the Reynolds and Ekman numbers are kept constant at 450 and 4.25×10^{-4}, respectively. For the same conditions, the maximum temperature inside the solid decreases by 8.96%, when the confinement ratio is reduced from 0.75 to 0.25.

The effects of solid material properties on transient heat transfer are presented in Fig. 8. The studied materials were aluminum, Constantan, copper, silicon, and silver, having different thermophysical properties. For all materials, the temperature changes occur faster at the earlier part of the heating process, and the slopes gradually decrease as the steady state condition approaches. It can be observed that a material having a lower thermal conductivity, such as Constantan, maintains a higher temperature at the solid disk interface and within the solid as the thermal conductivity controls how effectively the heat flows and distributes through the material. For the same reason, the maximum temperature within the solid and that at the interface are significantly different for Constantan, whereas it is about the same for both silver and aluminum. The thermal diffusivity of the material also contributes to

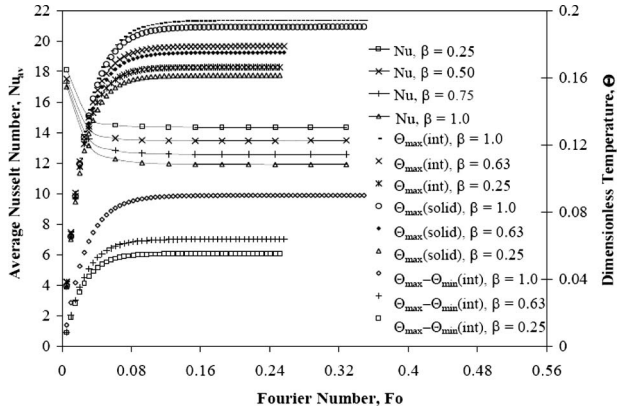

Fig. 6 Average Nusselt number and dimensionless temperature variations with time for different nozzle to target spacing (Re=750, Ek=4.25×10^{-4}, silicon disk, b/d_n=0.5, and, r_p/r_d =0.667)

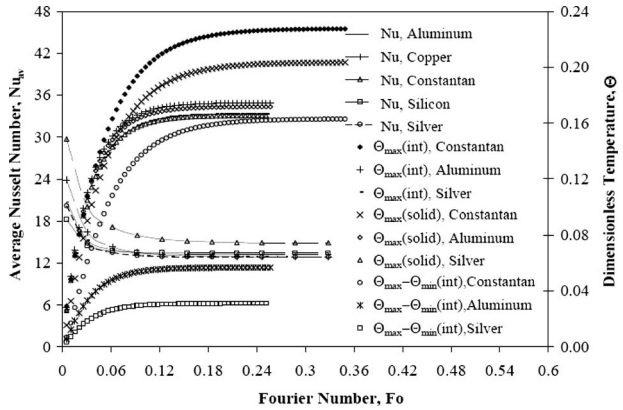

Fig. 8 Average Nusselt number and dimensionless temperature variations with time for different solid materials (Re=875, Ek=2.13×10^{-4}, b/d_n=0.5, β=0.5, and r_p/r_d=0.667)

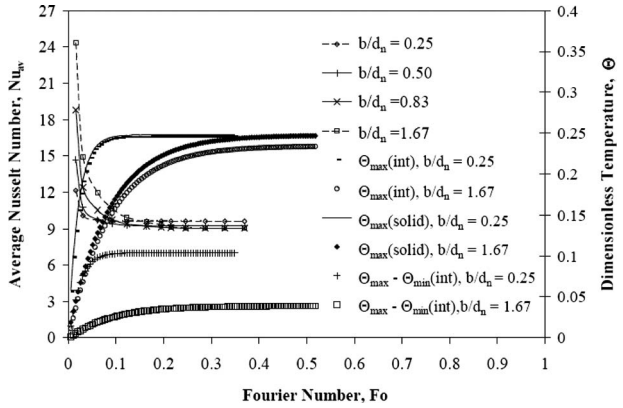

Fig. 9 Average Nusselt number and dimensionless temperature variations with time for different silicon disk thicknesses (Re=450, Ek=4.25×10^{-4}, β=0.5, and r_p/r_d=0.667)

the transient heat transfer process. Silver and aluminum reach the steady state faster than Constantan due to their higher thermal diffusivity. The values of thermal diffusivity for these materials at 303 K are $\alpha_{\text{silver}}=1.74\times10^{-4}$ m^2/s, $\alpha_{\text{aluminum}}=8.33\times10^{-5}$ m^2/s, and $\alpha_{\text{Constantan}}=6.20\times10^{-6}$ m^2/s. The magnitude of the temperature nonuniformity at the interface at steady state is controlled by thermal conductivity of the material. It may be noted that Constantan ($k_{\text{Constantan}}=22.7$ W/m K) has an average maximum-to-minimum temperature difference of 17.24 K, whereas silver ($k_{\text{silver}}=429$ W/m K) has only an average of 3.34 K temperature difference at the interface. Figure 8 also shows the distribution of average Nusselt numbers with time for the five materials used in this study. Constantan shows a higher average heat transfer coefficient compared with the other materials over the entire transient process due to its lower thermal conductivity. In addition, the average Biot number for Constantan at different time intervals range from 0.216 to 0.341, showing the highest values compared with the other materials. The lowest Biot number was obtained for silver, and it ranged from 0.009 to 0.02. Therefore, the variation in temperature within the solid was very significant to justify the conjugate analysis presented in this paper.

Another important factor that controls the transient heat transfer process is the thickness of the disk. Its effects on the variation in the dimensionless maximum temperature at the interface, maximum temperature inside the solid, and maximum-to-minimum dimensionless temperature difference at the interface and average Nusselt number are shown in Fig. 9. In these plots, silicon has been used as the disk material, and water as the cooling fluid. The disk thickness significantly affects the temperature distribution. It may be noted that as the thickness of the solid disk increases, the time needed to achieve the steady state condition increases. This is due to more thermal storage capacity within the solid. The radial conduction becomes stronger as the disk thickness increases, generating a more uniform temperature distribution at the interface. The average Nusselt number is higher for a thinner disk. The increment of silicon disk thickness from 0.3 mm to 2 mm increases the average Biot number from 0.011 to 0.178.

Figure 10 shows the development of isothermal lines within the solid at different time instants. It may be noticed that at the early stages of the transient heat transfer process, the isothermal lines grow parallel to the bottom heated surface of the solid disk. As time progresses and heat reaches the solid-fluid interface, they start to form concentric lines around the stagnation point and expand further downstream into the solid until a steady state condition is achieved. Figure 10(*d*) shows that a maximum temperature range of 29.63 K is obtained at the steady state condition.

A comparison of the present numerical results with the experimental data of Ozar et al. [10] for various spinning rates of the

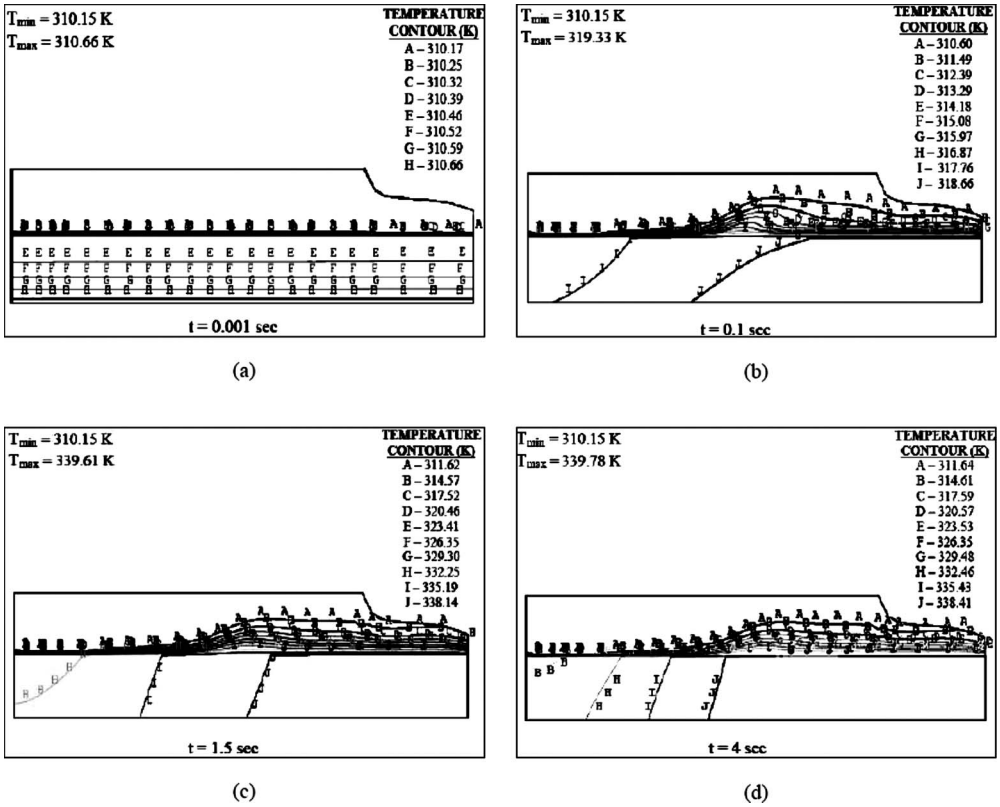

Fig. 10 Isothermal lines at different instants for a silicon disk with water as the cooling fluid (Re=450, Ek=4.25×10^{-4}, β=0.5, b/d_n=0.5, r_p/r_d=0.667, and q_w=125 kW/m^2)

Table 1 Local Nusselt number comparison between experimental data of Ozar et al. [10] and present numerical results (T_j=293 K, q=32 kw/m^2, b=0.00635 m, Re=238, H_n=0.000254 m, b/d_n=0.125, $r_{hin}=r_p$=0.0508 m, r_p/r_d=0.25)

Confinement ratio (r/r_{hin})	Spinning rate (50 rpm) Numerical	Experimental	Percent difference
1.8	193.40	185	4.34
2.15	166.56	175	−5.07
2.7	135.80	155	−14.14
	Spinning rate (100 rpm)		
	Numerical	Experimental	
1.8	217.58	215	1.19
2.15	197.39	205	−6.39
2.7	152.78	169	−10.62
	Spinning rate (200 rpm)		
	Numerical	Experimental	
1.8	261.09	260	0.42
2.15	224.86	249	−10.73
2.7	183.33	205	−11.82
		Average	6.91

target disk is presented in Table 1. To match with the experimental conditions, the following combination of the parameters was used: q_w=32 kW/m^2, Re=238, T_j=293 K, H_n=0.00254 m, d_n=0.0508 m, r_p=0.051 m, r_d=0.2032 m, and b=0.00635 m. Water was used as the working fluid. The disk was made of aluminum; a material with a thermal conductivity of 202.4 W/m K. As seen in Table 1, the differences in the value of local Nusselt number results are in the range of −14.14 to +4.34%, with an average difference of 6.91%. Considering the uncertainty of experimental measurements and round off and discretization errors in numerical computation, the overall comparison between test data and numerical results can be considered to be quite satisfactory.

4 Conclusions

A number of conclusions can be made based on the results of the present investigation. Local Nusselt numbers show a higher value at earlier stages of the transient process. The duration of the transient heat transfer process and the maximum temperature inside the solid decreases as the Reynolds number increases. As the Ekman number decreases from ∞ to 7.08×10^{-5}, the average Nusselt number increases by an average of 27.47%. As the dimensionless nozzle-to-target spacing decreases from 1 to 0.25, the average Nusselt number increases by an average of 12.71%. The increment of confinement ratio (r_p/r_d) decreases the convective heat transfer rate over the entire transient period. The increment of disk thickness decreases the maximum temperature at the interface and within the solid, and increases the time needed to achieve the steady state condition. A lower thermal conductivity material maintains a higher average Nusselt number and a higher maximum temperature within the solid, over the entire transient process. A disk material with higher thermal diffusivity reaches the steady state faster.

Nomenclature

b = disk thickness (m)
Bi = Biot number ($h_{av}\cdot b/k_S$)
Cp = specific heat (J/kg K)
d_n = diameter of the nozzle (m)
Ek = Ekman number ($\nu_f/(4\cdot\Omega\cdot r_d^2)$)
Fo = Fourier number ($\alpha_f t/d_n^2$)
g = acceleration due to gravity (m/s^2)
h = heat transfer coefficient (W/m^2 K), $q_{int}/(T_{int}-T_j)$
h_{av} = average heat transfer coefficient (W/m^2 K), defined by Eq. (17)
H_n = distance of the nozzle from the plate (m)
k = thermal conductivity (W/m K)
nr = number of elements in the radial direction
nz = number of elements in the axial direction
Nu = Nusselt number ($(h\cdot d_n)/k_f$)
Nu_{av} = average Nusselt number for the entire surface ($(h_{av}\cdot d_n)/k_f$)
p = pressure (Pa)
Pr = Prandtl number (ν_f/α_f)
q = heat flux (W/m^2)
r = radial coordinate (m)
r_d = disk radius (m)
r_p = plate radius (m)
r_p/r_d = confinement plate to disk radius ratio (confinement ratio)
Re = Reynolds number ($(V_j\cdot d_n)/\nu_f$)
t = time (s)
T = temperature (K)
$\bar{T}_{int}$ = average interface temperature (K), $(2/r_d^2)\int_0^{r_d} T_{int} r dr$
V_j = jet velocity (m/s)
$V_{r,z,\theta}$ = velocity component in the r-, z-, and θ-direction (m/s)
z = axial coordinate (m)

Greek Symbols

α = thermal diffusivity (m^2/s)
β = dimensionless nozzle to target spacing (H_n/d_n)
δ = liquid film thickness (m)
ε = thermal conductivity ratio (k_S/k_f)
μ = dynamic viscosity (kg/m s)
ν = kinematic viscosity (m^2/s)
θ = angular coordinate (rad)
Θ = dimensionless temperature ($(2\cdot k_f\cdot(T_{int}-T_j)/(q\cdot d_n)$)
ρ = density (kg/m^3)
σ = surface tension (N/m)
Ω = angular velocity (rad/s)

Subscripts

atm = ambient
av = average
f = fluid
i = initial condition
int = solid-fluid interface
j = jet or inlet
max = maximum
n = nozzle
s = solid
ss = steady state
w = bottom surface of the disk

References

[1] Polat, S., Huang, B., Mujumdar, A. S., and Douglas, W. J. M., 1989, "Numerical Flow and Heat Transfer Under Impinging Jets: A Review," Annu. Rev. Numer. Fluid Mech. Heat Transfer, **2**(2), pp. 157–197.
[2] Garimella, S. V., 2000, "Heat Transfer and Flow Fields in Confined Jet Impingement," Annu. Rev. Heat Transfer, **11**, pp. 413–494.
[3] Metzger, D. E., and Grochowsky, L. D., 1977, "Heat Transfer Between an Impinging Jet and a Rotating Disk," ASME J. Heat Transfer, **99**, pp. 663–667.
[4] Carper, H. J., Jr., and Deffenbaugh, D. M., 1978, "Heat Transfer From a

Rotating Disk With Liquid Jet Impingement," *Proceedings of the Sixth International Heat Transfer Conference*, Hemisphere, Washington, DC, Vol. 4, pp.113–118.
[5] Carper, H. J., Jr., Saavedra, J. J., and Suwanprateep, T., 1986, "Liquid Jet Impingement Cooling of a Rotating Disk," ASME J. Heat Transfer, **108**(3), pp. 540–546.
[6] Popiel, C. O., and Boguslawski, L., 1986, "Local Heat Transfer From a Rotating Disk in an Impinging Round Jet," ASME J. Heat Transfer, **108**(2), pp. 357–364.
[7] Thomas, S., Faghri, A., and Hankey, W. L., 1991, "Experimental Analysis and Flow Visualization of a Thin Liquid Film on a Stationary and Rotating Disk," ASME J. Fluids Eng., **113**(1), pp. 73–80.
[8] Saniei, N., Yan, X., and Schooley, W., 1998, "Local Heat Transfer Characteristics of a Rotating Disk Under Jet Impingement Cooling," *Proceedings of the 11th International Heat Transfer Conference*, J. S. Lee, ed., Korean Society of Mechanical Engineers, Kyongju, Korea, Vol. 5, pp. 445–450.
[9] Ozar, B., Cetegen, B. M., and Faghri, A., 2003, "Experiments on the Flow of a Thin Liquid Film Over a Horizontal Stationary and Rotating Disk Surface," Exp. Fluids, **34**(5), pp. 556–565.
[10] Ozar, B., Cetegen, B. M., and Faghri, A., 2004, "Experiments on Heat Transfer in a Thin Liquid Film Flowing Over a Rotating Disk," ASME J. Heat Transfer, **126**(2), pp. 184–192.
[11] Rice, J., Faghri, A., and Cetegen, B. M., 2005, "Analysis of a Free Surface Film From a Controlled Liquid Impinging Jet Over a Rotating Disk Including Conjugate Effects, With and Without Evaporation," Int. J. Heat Mass Transfer, **48**(25–26), pp. 5192–5204.
[12] Basu, S., and Cetegen, B. M., 2006, "Analysis of Hydrodynamics and Heat Transfer in a Thin Liquid Film Flowing Over a Rotating Disk by the Integral Method," ASME J. Heat Transfer, **128**(3), pp. 217–225.
[13] Lallave, J. C., and Rahman, M. M., 2008, "Modeling of Convective Cooling of a Rotating Disk by Partially Confined Liquid Jet Impingement," ASME J. Heat Transfer, **130**(10), pp. 102201–102211.
[14] Moallemi, M. K., and Naraghi, M. N., 1994, "An Experimental and Analytical Investigation of Ice Formation From a Circular Water Jet Impinging on a Horizontal Cold Surface," ASME J. Heat Transfer, **116**(4), pp. 1016–1027.
[15] Owens, R., and Liburdy, J. A., 1995, "Use of Thermochromatic Liquid Crystals in the Study of Jet Impingement Cooling: Sensitivity of Transient Heating Methods," *Proceedings of the SPIE, International Society of Optical Engineering*, San Diego, CA, Vol. 2546, pp. 136–144.
[16] Kumagai, S., Suzuki, S., Kubo, R., and Kawazoe, M., 1995, "Transient Cooling of a Hot Metal Plate With an Impinging Water Jet," Heat Transfer-Jpn. Res., **24**(6), pp. 538–550.
[17] Francis, N. D., and Wepfer, W. J., 1996, "Jet Impingement Drying of a Moist Porous Solid," Int. J. Heat Mass Transfer, **39**(9), pp. 1911–1923.
[18] Fujimoto, H., Takuda, H., Hatta, N., and Viskanta, R., 1999, "Numerical Simulation of Transient Cooling of a Hot Solid by an Impinging Free Surface Jet," Numer. Heat Transfer, Part A, **36**(8), pp. 767–780.
[19] Rahman, M. M., Bula, A. J., and Leland, J. E., 2000, "Analysis of Transient Conjugate Heat Transfer to a Free Impinging Jet," J. Thermophys. Heat Transfer, **14**(3), pp. 330–339.
[20] Liu, L. K., Su, W. S., and Hung, Y. H., 2004, "Transient Convective Heat Transfer of Air Jet Impinging Onto a Confined Ceramic Based MCM Disk," ASME J. Electron. Packag., **126**(1), pp. 159–172.
[21] Sarghini, F., and Ruocco, G., 2004, "Enhancement and Reversal Heat Transfer by Competing Modes in Jet Impingement," Int. J. Heat Mass Transfer, **47**(8–9), pp. 1711–1718.
[22] Lin, T. W., Wu, M. C., Liu, L. K., Fang, C. J., and Hung, Y. H., 2006, "Cooling Performance of Using a Confined Slot Jet Onto Heated Heat Sinks," ASME J. Electron. Packag., **128**(1), pp. 82–91.
[23] Burmeister, L. C., 1993, *Convective Heat Transfer*, 2nd ed., Wiley, New York, pp. 581–590.
[24] White, F. M., 2003, *Fluid Mechanics*, 5th ed., McGraw-Hill, New York.
[25] Özisik, M. N., 1993, *Heat Conduction*, 2nd ed., Wiley, New York, pp. 657–660.
[26] Bejan, A., 1995, *Convection Heat Transfer*, 2nd ed., Wiley, New York, pp. 595–602.
[27] Vanyo, J. P., 1993, *Rotating Fluids in Engineering and Science*, Butterworth, MA, Chap. 14, pp. 233–264.
[28] Fletcher, C. A. J., 1984, *Computational Galerkin Methods*, Springer-Verlag, New York.

Effects of Variable Viscosity and Thermal Conductivity of CuO-Water Nanofluid on Heat Transfer Enhancement in Natural Convection: Mathematical Model and Simulation

Eiyad Abu-Nada
Intitut für Technishe Verbrennung,
Leibniz Universtät Hannover,
Welfengarten 1a,
Hannover 30167, Germany;
Department of Mechanical Engineering,
Hashemite University,
Zarqa 13115, Jordan
e-mail: eiyad@hu.edu.jo

Heat transfer enhancement in horizontal annuli using variable thermal conductivity and variable viscosity of CuO-water nanofluid is investigated numerically. The base case of simulation used thermal conductivity and viscosity data that consider temperature property dependence and nanoparticle size. It was observed that for $Ra \geq 10^4$*, the average Nusselt number was deteriorated by increasing the volume fraction of nanoparticles. However, for* $Ra = 10^3$*, the average Nusselt number enhancement depends on aspect ratio of the annulus as well as volume fraction of nanoparticles. Also, for* $Ra = 10^3$*, the average Nusselt number was less sensitive to volume fraction of nanoparticles at high aspect ratio and the average Nusselt number increased by increasing the volume fraction of nanoaprticles for aspect ratios* ≤ 0.4*. For* $Ra \geq 10^4$*, the Nusselt number was deteriorated everywhere around the cylinder surface especially at high aspect ratio. However, this reduction is only restricted to certain regions around the cylinder surface for* $Ra = 10^3$*. For* $Ra \geq 10^4$*, the Maxwell–Garnett and the Chon et al. conductivity models demonstrated similar results. But, there was a deviation in the prediction at* $Ra = 10^3$ *and this deviation becomes more significant at high volume fraction of nanoparticles. The Nguyen et al. data and the Brinkman model give completely different predictions for* $Ra \geq 10^4$*, where the difference in prediction of the Nusselt number reached 50%. However, this difference was less than 10% at* $Ra = 10^3$*.* [DOI: 10.1115/1.4000440]

Keywords: nanofluid, viscosity, thermal conductivity, natural convection, annulus

1 Introduction

Natural convection heat transfer is an important phenomenon in thermal engineering due to its wide applications in thermal systems such as electronic cooling, heat exchangers, and thermal systems. Enhancement of heat transfer in such systems is very essential from the industrial and energy saving perspectives. The low thermal conductivity of conventional heat transfer fluids, such as water, is considered a primary limitation in enhancing the performance and the compactness of such thermal systems. An innovative technique for improvement of heat transfer using nanoscale particle dispersed in a base fluid, known as nanofluid, has been studied extensively during the past decade [1–3] mainly for forced convection applications. However, natural convection heat transfer research using nanofluids has received relatively less attention and there is still a debate on the effect of nanoparticles on heat transfer enhancement in natural convection applications.

Examples of these controversial results are the works conducted by Khanafer et al. [4], who studied copper-water nanofluids in a two-dimensional rectangular enclosure. They showed that the heat transfer rate increased with the percentage of the suspended nanoparticles. Oztop and Abu-Nada [5] supported the findings of Khanafer et al. [4], where an enhancement in heat transfer was registered with the additions of nanoparticles. However, contrary experimental findings were reported by Putra et al. [6] Wen and Ding [7], Nnanna [8], and Ho and Lin [9]. More recently, Abu-Nada et al. [10] showed that the enhancement in heat transfer in natural convection depends mainly on the Rayleigh number, and for certain Rayleigh numbers $Ra = 1 \times 10^4$, the heat transfer was not sensitive to nanoparticles concentration, whereas at higher values of the Rayleigh number, an enhancement in heat transfer was taking place. More theoretical studies on natural convection enhancement were also reported by Hwang et al. [11] and Ho et al. [12]. Therefore, there is still a controversy on the effect of nanofluids on heat transfer in natural convection and the numerical simulations seem to overestimate the enhancement of heat transfer in natural convection.

Conceptually, natural convection heat transfer is affected by fluid properties such as viscosity and thermal conductivity. Most of the previous mentioned numerical works used the Brinkman model for the viscosity. This model is shown to underestimate the effective viscosity of the nanofluid [13–15]. The Brinkman model does not account for nanofluid temperature or nanoparticle sizes. On the other hand, for the thermal conductivity, most of mentioned numerical simulations used the Maxwell–Garnett (MG) model for the prediction of thermal conductivity. This model does account for main mechanisms for heat transfer in nanofluids such as the Brownian motion; also, it neglects nanoparticle size or temperature dependence. Therefore, numerical simulations need to incorporate more robust models for viscosity and thermal conductivity that consider temperature dependence and nanoparticle size.

Contributed by the Heat Transfer Division of ASME for publication in the JOURNAL OF HEAT TRANSFER. Manuscript received November 7, 2008; final manuscript received September 30, 2009; published online March 4, 2010. Assoc. Editor: P. E. Phelan.

Recently, Angue Minsta et al. [16] studied the effect nanoparticles concentration and nanoparticles size on nanofluids viscosity under a wide range of temperatures experimentally. They showed that viscosity drops sharply with temperature, especially for high concentration of nanoparticles. Moreover, the effect of temperature, nanoparticle size, and nanoparticles volume fraction on nanofluids thermal conductivity was studied experimentally by Chon et al. [17] and they showed that nanofluid thermal conductivity is affected by temperature, volume fraction of nanoparticles, and nanoparticle size. Thus, such physics cannot be ignored and the dependence of nanofluid properties on temperature and volume fraction of nanoparticles must be taken into account in order to predict the correct role of nanoparticles on heat transfer enhancement in natural convection. Therefore, the scope of the current research is to implement more realistic models for nanofluid properties to predict heat transfer enhancement in natural convection. The experimental results reported by Nguyen et al. [14] will be used to derive a correlation for nanofluid viscosities as a function of temperature and nanoparticle concentrations. Also, the model of Chon et al. [17] will be used for the thermal conductivity. The current research will evaluate the role of both viscosity and thermal conductivity, derived from experimental data, on heat transfer in natural convection. Besides, these models will be compared with frequent used models in literature, namely, the Brinkman model for viscosity and the MG model for thermal conductivity. The enhancement in heat transfer will be evaluated under wide ranges of temperatures and volume fraction of nanoparticles.

2 Governing Equations and Problem Formulation

Figure 1 shows a schematic diagram of differentially heated annulus. The fluid in the annulus is a water based nanofluid containing CuO nanoparticle. The nanofluid is assumed incompressible and the flow is assumed to be laminar. It is assumed that water and nanoparticles are in thermal equilibrium and no slip occurs between them. The thermophysical properties of the nanofluid are given in Table 1. The inner cylinder is maintained at a constant temperature (T_H) higher than the outer cylinder (T_C). The density of the nanofluid is approximated by the Boussinesq model. The viscosity as well as the thermal conductivity of the nanofluid is considered variable properties that vary with temperature as well as volume fraction of nanoparticles.

The following dimensionless groups are introduced:

$$\Omega = \frac{\omega L^2}{\alpha f_o}, \quad \Psi = \frac{\psi}{\alpha f_o}, \quad V = \frac{vL}{\alpha f_o}, \quad U = \frac{uL}{\alpha f_o}, \quad T = \frac{\tilde{T} - T_C}{T_H - T_C},$$

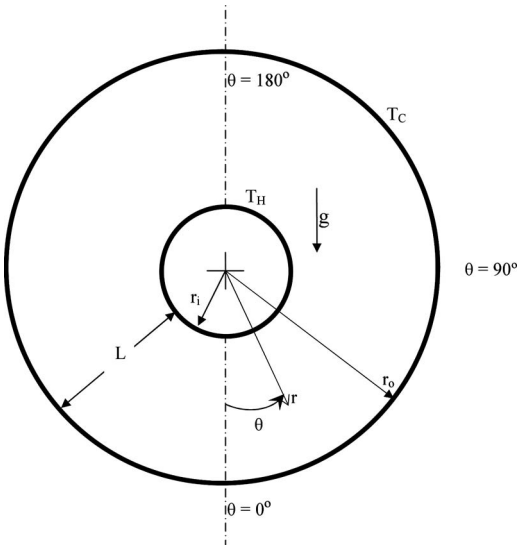

Fig. 1 Sketch of the problem geometry

Table 1 Thermophysical properties of fluid and CuO nanoparticles

Physical properties	Fluidphase (water)	CuO
C_p (J/kg K)	4179	540
ρ (kg/m^3)	997.1	6500
K (W/m K)	0.613	18.0
$\beta \times 10^{-5}$ (1/K)	21	0.85
D_p (nm)	0.384	29

$$\text{and} \quad r = \frac{\tilde{r} - r_i}{L}, \quad k = \frac{k_{nf}}{k_{fo}}, \quad \alpha = \frac{\alpha_{nf}}{\alpha_{fo}}, \quad \mu = \frac{\mu_{nf}}{\mu_{f_o}} \tag{1}$$

By using the dimensionless quantities given in Eq. (1), the governing equations in terms of stream-function-vorticity formulation are written as follows:

Vorticity equation:

$$\begin{aligned}
\frac{\partial}{\partial r}\left(\Omega\frac{\partial \Psi}{\partial \theta}\right) - \frac{\partial}{\partial \theta}\left(\Omega\frac{\partial \Psi}{\partial r}\right) = {} & \frac{\Pr}{(1-\varphi) + \varphi\dfrac{\rho_p}{\rho_f}}\left(\frac{\partial}{\partial r}\left(\mu\left(r + \frac{r_i}{L}\right)\frac{\partial \Omega}{\partial r}\right) + \frac{\partial}{\partial \theta}\left(\mu\frac{1}{\left(r + \dfrac{r_i}{L}\right)}\frac{\partial \Omega}{\partial \theta}\right)\right) \\
& + \mathrm{Ra}\,\Pr\left[\frac{1}{\dfrac{(1-\varphi)}{\varphi}\dfrac{\rho_f}{\rho_p} + 1}\frac{\beta_s}{\beta_f} + \frac{1}{\dfrac{\varphi}{(1-\varphi)}\dfrac{\rho_f}{\rho_p} + 1}\right]\left(\frac{\partial T}{\partial r}\left(r + \frac{r_i}{L}\right)\sin\theta + \frac{\partial T}{\partial \theta}\cos\theta\right) \\
& + \frac{\Pr}{(1-\varphi) + \varphi\dfrac{\rho_p}{\rho_f}}\left(-U + \left(r + \frac{r_i}{L}\right)\frac{\partial U}{\partial r} + \frac{\partial V}{\partial \theta}\right)\left(\frac{\partial^2 \mu}{\partial r^2} - \frac{1}{\left(r + \dfrac{r_i}{L}\right)^2}\frac{\partial^2 \mu}{\partial \theta^2}\right) \\
& + \frac{4\,\Pr}{(1-\varphi) + \varphi\dfrac{\rho_p}{\rho_f}}\left(\frac{\partial V}{\partial r}\frac{\partial^2 \mu}{\partial r\,\partial\theta}\right) + \frac{\Pr}{(1-\varphi) + \varphi\dfrac{\rho_p}{\rho_f}}\left(\left(r + \frac{r_i}{L}\right)\frac{\partial \Omega}{\partial r}\frac{\partial \mu}{\partial r} + \frac{1}{\left(r + \dfrac{r_i}{L}\right)}\frac{\partial \Omega}{\partial \theta}\frac{\partial \mu}{\partial \theta}\right)
\end{aligned} \tag{2}$$

Energy equation:

$$\frac{\partial}{\partial r}\left(T\frac{\partial \Psi}{\partial \theta}\right)-\frac{\partial}{\partial \theta}\left(T\frac{\partial \Psi}{\partial r}\right)=\frac{1}{(1-\varphi)+\varphi\dfrac{(\rho c_p)_p}{(\rho c_p)_{f_o}}}\left(\frac{\partial}{\partial r}\left(k\left(r+\frac{r_i}{L}\right)\frac{\partial \Omega}{\partial r}\right)+\frac{\partial}{\partial \theta}\left(k\frac{1}{\left(r+\frac{r_i}{L}\right)}\frac{\partial \Omega}{\partial \theta}\right)\right) \quad (3)$$

Kinematics equation:

$$\frac{1}{\left(r+\frac{r_i}{L}\right)}\left(\frac{\partial}{\partial r}\left(\left(r+\frac{r_i}{L}\right)\frac{\partial \Psi}{\partial r}\right)+\frac{\partial}{\partial \theta}\left(\frac{1}{\left(r+\frac{r_i}{L}\right)}\frac{\partial \psi}{\partial \theta}\right)\right)=-\Omega \quad (4)$$

where the dimensionless number are given as

$$\mathrm{Ra}=\frac{g\beta(T_H-T_C)L^3}{\upsilon_{f_o}\alpha_{f_o}},\quad \mathrm{Pr}=\frac{\nu_{f_o}}{\alpha_{f_o}} \quad (5)$$

where the subscript *o* stands for the reference temperature, which is taken as 22°C in the current study. The temperature difference between the hot and cold surfaces is kept constant at 30°C. The ratio between the length of the gap between the inner and outer cylinders divided by the inner cylinder diameter, i.e., L/D, is called the aspect ratio. The dimensionless radial and tangential velocities are given respectively as

$$V=\frac{1}{\left(r+\frac{r_i}{L}\right)}\frac{\partial \psi}{\partial \theta},\quad U=-\frac{\partial \psi}{\partial r} \quad (6)$$

The thermal diffusivity, density, and heat capacitance of the nanofluid are given as, respectively,

$$\alpha_{nf}=\frac{k_{nf}}{(\rho c_p)_{nf}} \quad (7)$$

$$\rho_{nf}=(1-\varphi)\rho_f+\varphi\rho_p \quad (8)$$

$$(\rho c_p)_{nf}=(1-\varphi)(\rho c_p)_f+\varphi(\rho c_p)_p \quad (9)$$

The effective thermal conductivity of the nanofluid is calculated by the model of Chon et al. [17]

$$\frac{k_{nf}}{k_{bf}}=1+64.7\varphi^{0.7640}\left(\frac{d_f}{d_p}\right)^{0.3690}\left(\frac{k_f}{k_p}\right)^{0.7476}\mathrm{Pr}^{0.9955}\,\mathrm{Re}^{1.2321} \quad (10)$$

The results using Eq. (10) will be compared with the results using the MG model given by

$$\frac{k_{nf}}{k_f}=\frac{k_p+(n-1)k_f-(n-1)(k_f-k_p)\varphi}{k_p+(n-1)k_f+(k_f-k_p)\varphi} \quad (11)$$

The Pr and Re in Eq. (10) are given respectively as [17]

$$\mathrm{Pr}=\frac{\mu_f}{\rho_f\alpha_f},\quad \mathrm{Re}=\frac{\rho_f k_b T}{3\pi\mu_f^2 l_f} \quad (12)$$

where *f* stands for the base fluid, which is water in the current study, k_b is the Boltzmann constant 1.3807×10^{-23} J/K, and l_f is the mean path of base fluid particles given as 0.17 nm [17]. This model considers the effect of nanoparticle size and temperature on nanofluids thermal conductivity with a wide range of temperature between 21°C and 70°C. This model was further tested experimentally by Angue Minsta et al. [16] for Al_2O_3 and CuO nanoparticles and found to predict the thermal conductivity of nanofluid accurately up to a volume fraction of 9% for both CuO and Al_2O_3 nanoparticles. Therefore, the current study adopted the model of Chon et al. to predict the thermal conductivity of CuO-water nanofluid.

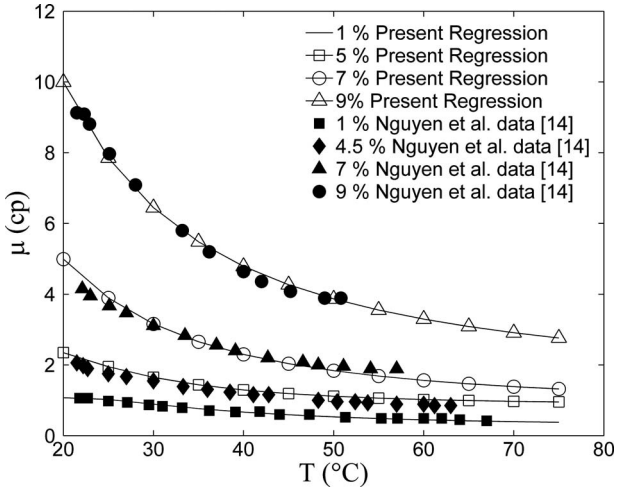

Fig. 2 Comparison between viscosities calculated using Eq. (13) and the data of Nguyen et al. [14]

The correlation for dynamic viscosity of CuO-water nanofluid is derived using the available experimental data of Nguyen et al. [14]. Actually, no explicit correlation is given in Ref. [14] that defines the viscosity of CuO-water nanofluid as a multifunction of temperature and volume fraction of nanoparticles. Therefore, in the recent work, a two-dimensional regression is used to develop such a correlation. The R^2 of the regression is 99.8% and a maximum error is 5%. The correlation obtained from the two-dimensional regression is given as

$$\mu_{\mathrm{CuO}}(cp)=-0.6967+\frac{15.937}{\tilde{T}}+1.238\varphi+\frac{1356.14}{\tilde{T}^2}-0.259\varphi^2-30.88\frac{\varphi}{\tilde{T}}-\frac{19652.74}{\tilde{T}^3}+0.01593\varphi^3+4.38206\frac{\varphi^2}{\tilde{T}}+147.573\frac{\varphi}{\tilde{T}^2} \quad (13)$$

Figure 2 presents a plot for the viscosity of CuO-water nanofluid as a function of temperature and concentration of nanoparticles calculated by using Eq. (13). Also, the figure plots the measured

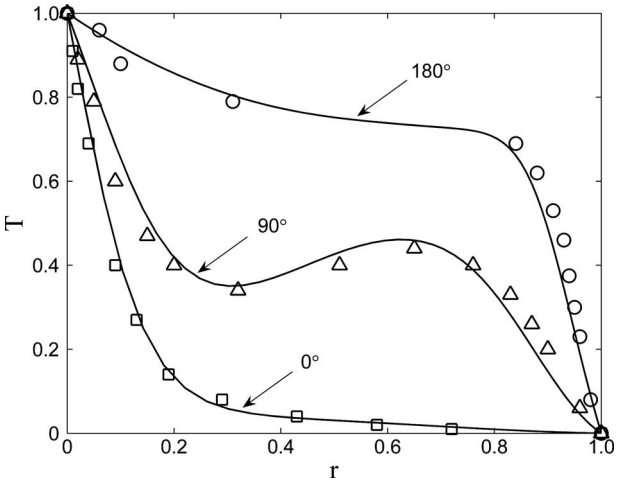

Fig. 3 Comparison of the present work (solid lines) and the experimental results of Kuehn and Goldstein [22]; experimental data points: □: 0 deg, ◇: 90 deg, ○: 180 deg (Ra=4.7×10⁴, Pr=0.706, and L/D=0.8)

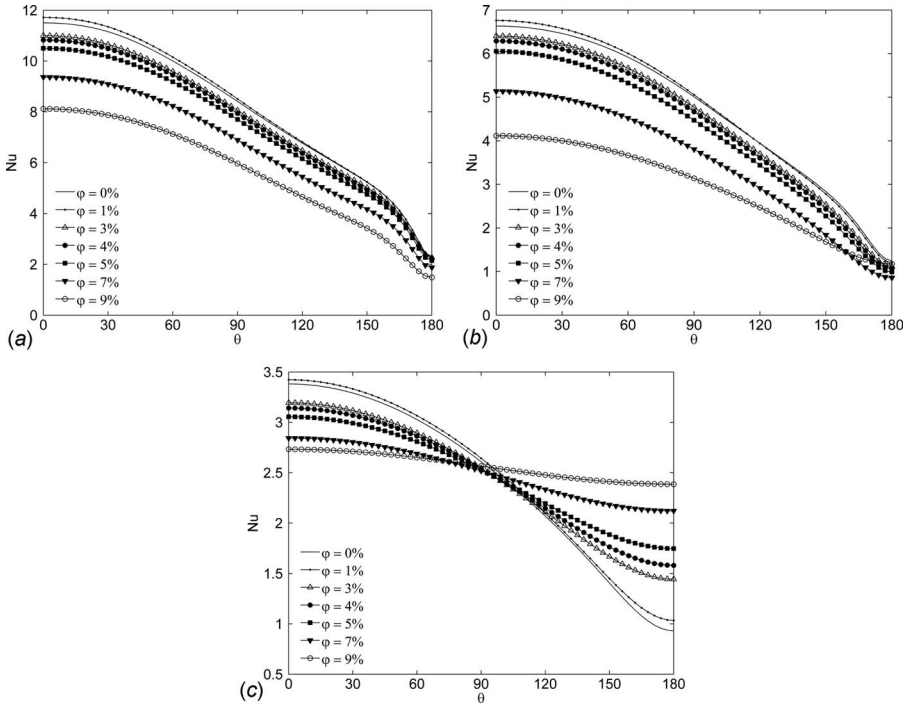

Fig. 4 Nusselt number distribution around the inner cylinder surface using various volume fractions of CuO nanoparticles ($L/D=0.8$): (*a*) $Ra=10^5$, (*b*) $Ra=10^4$, and (*c*) $Ra=10^3$

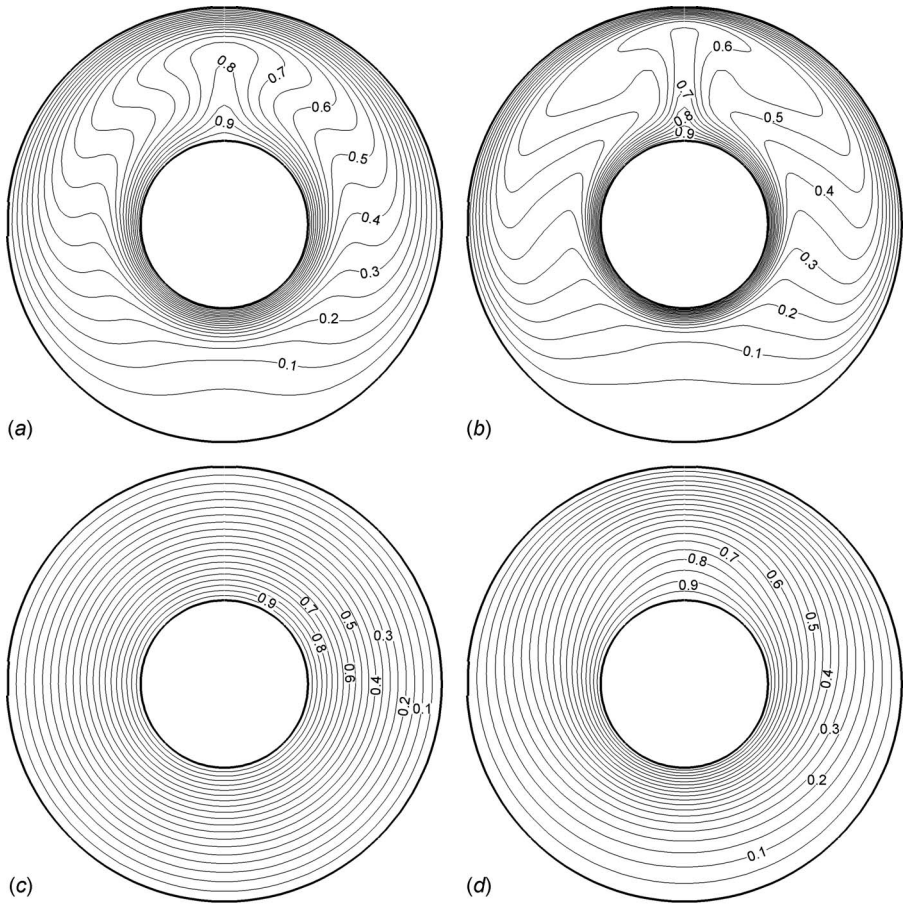

Fig. 5 Temperature isotherms for $L/D=0.8$: (*a*) $Re=10^5$ ($\varphi=9\%$), (*b*) $Re=10^5$ ($\varphi=1\%$) (*c*) $Re=10^3$ ($\varphi=9\%$), and (*d*) $Re=10^3$ ($\varphi=1\%$)

data from the experiment of Nguyen et al. [14]. It is very clear that the derived equation (Eq. (13)) predicts the viscosity of nanofluids accurately. The results, using Eq. (13), will be compared with the Brinkman model given by

$$\mu_{nf} = \frac{\mu_f}{(1-\varphi)^{2.5}} \tag{14}$$

It is worth mentioning that the viscosity of the base fluid (water) is considered to be variable with temperature and the flowing equation is used to evaluate the viscosity of water, which is still derived from the measurements of Nguyen et al. [14]

$$\mu_{H_2O}(cp) = -81.1 + 98.75\ln(T) - 45.23\ln^2(T) + 9.71\ln^3(T) - 0.946\ln^4(T) + 0.03\ln^5(T) \tag{15}$$

3 Numerical Implementation

Equations (2) and (3), absorbing the variable properties correlations given in Eqs. (10) and (13), are solved using the finite volume approach [18,19]. For full details of numerical implementation, the reader is referred to Abu-Nada et al. [10].

After solving Ψ, Ω, and T, further useful quantities are obtained. For example, the Nusselt number at the inner cylinder surface is expressed as

$$\mathrm{Nu} = -\left(\frac{k_{nf}}{k_f}\right)\frac{\partial T}{\partial r} \tag{16}$$

where (k_{nf}/k_f) is calculated using Eq. (10). The average Nusselt number is calculated as

$$\mathrm{Nu}_{avg} = \frac{1}{\pi}\int_{\theta=0}^{\theta=\pi} \mathrm{Nu}(\theta)d\theta \tag{17}$$

The integration of Eq. (17) is evaluated using the 1/3 Simpson's rule of integration. A normalized Nusselt number is defined as the ratio of Nusselt number at any volume fraction of nanoparticles to that of pure water and is given as

$$\overset{*}{\mathrm{Nu}}_{avg} = \frac{\mathrm{Nu}(\varphi)}{\mathrm{Nu}(\varphi=0)} \tag{18}$$

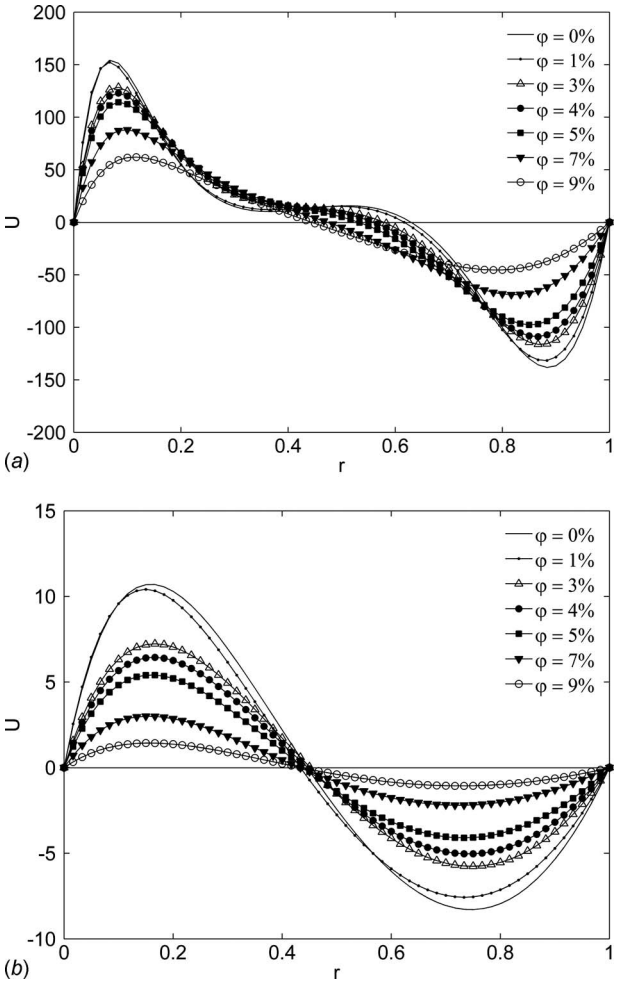

Fig. 6 Tangential velocity for Re=10^5, L/D=0.8, and θ=90 deg: (*a*) Ra=10^5 and (*b*) Ra=10^3

4 Grid Testing and Code Validation

The present code was tested for grid independence by calculating the average Nusselt number around the inner cylinder surface. It was found that a grid size of 61×61 guarantees a grid independent solution for both cases. The Nusselt number for the grid independent solution is compared with the results of Guj and Stella [20] and Shu et al. [21] for $\mathrm{Ra}=0.53\times10^4$. The calculated average Nusselt number by the current code gives a value of 2.47010, which falls between the results obtained by Guj and Stella ($\mathrm{Nu}_{avg}=2.4220$) and the results of Shu et al. [21] ($\mathrm{Nu}_{avg}=2.5560$). Furthermore, a grid independence test was carried out for the CuO-water nanofluid using $\varphi=9\%$, $\mathrm{Ra}=10^5$, and $L/D=0.8$. It was found that the same grid size 61×61 guarantees a grid independent solution.

The present numerical solution is further validated by the experimental results of Kuehn and Goldstein [22]. The comparisons for three temperature profiles at three different angles are shown in Fig. 3. It is clear that present results are in good agreement with other published data.

5 Results and Discussion

The range of the Rayleigh number, volume fraction of nanoparticles, and aspect ratio are $\mathrm{Ra}=10^3-10^5$, $0\le\varphi\le9\%$, and $0.2\le L/D\le0.8$, respectively. Figure 4 presents Nusselt number distribution around the inner cylinder surface using various volume fractions of CuO nanoparticles for $L/D=0.8$. For the case of $\mathrm{Ra}=10^5$ and $\mathrm{Ra}=10^4$, the increase in the volume fraction of nanoparticles causes a reduction in the Nusselt number everywhere around the inner cylinder surface. However, for $\mathrm{Ra}=10^3$ there is a reduction in the Nusselt number for $\theta<90$ and an enhancement in heat transfer is taking place for $\theta>90$. Also, it is clear that for high volume fraction of nanoparticles, $\varphi=9\%$, and for the case for $\mathrm{Ra}=10^3$, the Nusselt number variation around the inner cylinder surface becomes less pronounced compared with lower volume fraction of nanoparticles. Actually, for $\mathrm{Ra}=10^3$, the more addition of nanoparticles reduces the difference between the maximum and minimum Nusselt numbers around the cylinder surface and the distribution of the Nusselt number, or the temperature gradient at the cylinder surface, becomes nearly uniform for $\varphi=9\%$ (maximum Nusselt number is 2.7 and minimum is 2.4). This is best illustrated by looking at Fig. 5, where the case of $\varphi=9\%$, and for the case for $\mathrm{Ra}=10^3$, the temperature is almost uniform around the inner cylinder surface. Also, Fig. 5 illustrates how the thickness of thermal boundary layer is influenced by the addition of nanoparticles. Also, it is very interesting to note how the plume region is influenced by increasing the volume fraction for nanoparticles, where, for the case of 10^5, as shown in Fig. 5(*a*), the plume region spreads wider, and for the case of $\mathrm{Ra}=10^3$, as shown in Fig. 5(*c*), the plume region disappears completely. This behavior is related to the increased viscosity at high volume fraction of nanoparticles, see Fig. 2, where high φ causes the fluid to become more viscous and this causes the velocity to decrease accordingly, see Fig. 6, which reduces convection. The reduction in velocities and convection will cause the fading of the plume at $\mathrm{Ra}=10^3$ and the spreading of the plume region for the case of $\mathrm{Ra}=10^5$. The increase in

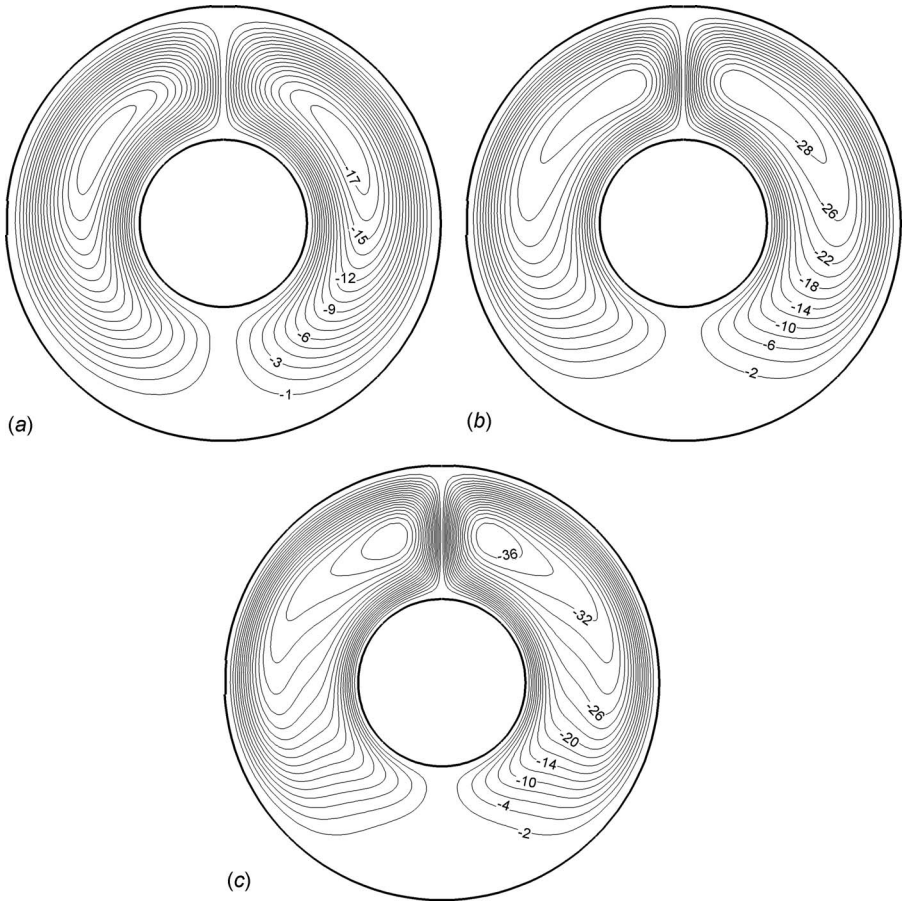

Fig. 7 Streamlines for Re=10^5 and $L/D=0.8$: (*a*) $\varphi=9\%$, (*b*) $\varphi=5\%$, and (*c*) $\varphi=1\%$

thermal boundary layer thickness is responsible for the reduction in temperature gradients at the inner surface, which causes a reduction in the Nusselt number accordingly (see Eq. (16)). It is observed from Fig. 5, for $Ra=10^5$, that the addition of nanoparticles causes an increase in thermal boundary layer thickness, which explains the reduction in the value of the Nusselt number everywhere around the inner cylinder surface. However, for the case of $Ra=10^3$, the addition of nanoparticles causes the thermal boundary layer thickness to increase for $\theta<90$; however, this thickness decreases for $\theta>90$ because of the plume disappearance. This explains the behavior observed in Fig. 4(*c*) for the Nusselt number distribution around the inner surface. Figure 7 shows the streamlines for the case of $Ra=10^5$. It is clear that by increasing the volume fraction of nanoparticles, the magnitudes of streamlines contours are reduced due to the increased viscosity of the nanofluids as mentioned earlier.

Figure 8 studies the effect of aspect ratio on heat transfer enhancement of nanofluids. The figure shows that for the case of $Ra=10^5$, the behavior encountered using smaller aspect ratio is similar to that of high aspect ratio. However, for $Ra=10^4$ and $Ra=10^3$, different behaviors are observed using smaller aspect ratios. For the case of $Ra=10^3$ the angle at which the Nusselt number switches from a reduction to an increase is reduced to 60 deg for $L/D=0.4$ and to 30 deg for $L/D=0.2$ compared with the 90 deg for $L/D=0.8$ (see Fig. 4). Thus, the region around the inner cylinder surface where an enhancement in heat transfer is taking place increases. This leads to an enhancement in the total Nusselt number around the inner cylinder surface, as shown in Fig. 9.

Figure 9 shows the average Nusselt number around the inner cylinder surface. Starting with the large aspect ratio of 0.8, the average Nusselt number is reduced by adding more nanoparticles for the case of $Ra=10^5$ and $Ra=10^4$; however, the Nusselt number is approximately less sensitive to the addition of nanoparticles for case of $Ra=10^3$. For smaller aspect ratios, as shown in Figs. 9(*b*) and 9(*c*), the cases of $Ra=10^5$ and $Ra=10^4$ still has a similar trend to that of $L/D=0.8$. However, for $Ra=10^3$, the addition of nanoparticles causes more enhancement in the Nusselt number, which is related to the point discussed earlier in the last paragraph.

An interesting comparison between various models used for thermal conductivity and viscosity on the average Nusselt number is shown in Fig. 10. This figure shows results obtained using four different approaches. The first approach is using the MG model for the thermal conductivity and the Brinkman model for the viscosity of nanofluids. This combination is used by most researchers in literature. The second approach is using the model of Chon et al. [17] for thermal conductivity and the Brinkman model for the viscosity of the nanofluid. The third approach is using the MG model for the thermal conductivity and the experimental data of Nguyen et al. [14] for viscosity. The fourth approach, the one that is used in the current study as the base case, is using the model of Chon et al. [17] for thermal conductivity and model of Nguyen et al. for viscosity of nanofluids.

From Figs. 10(*a*) and 10(*b*), it is clear that the difference between average Nusselt number calculated using the model of Chon et al. and the MG model is negligible. However, the difference in the Nusselt number when using the data of Nguyen et al. and the Brinkman model is much more significant. This tells that the role of nanofluid viscosity is more significant than thermal conductivity. Also, the prediction of Nusselt number using the Nguyen data is completely different from using the Brinkman model. The Brinkman model shows an overestimation in the en-

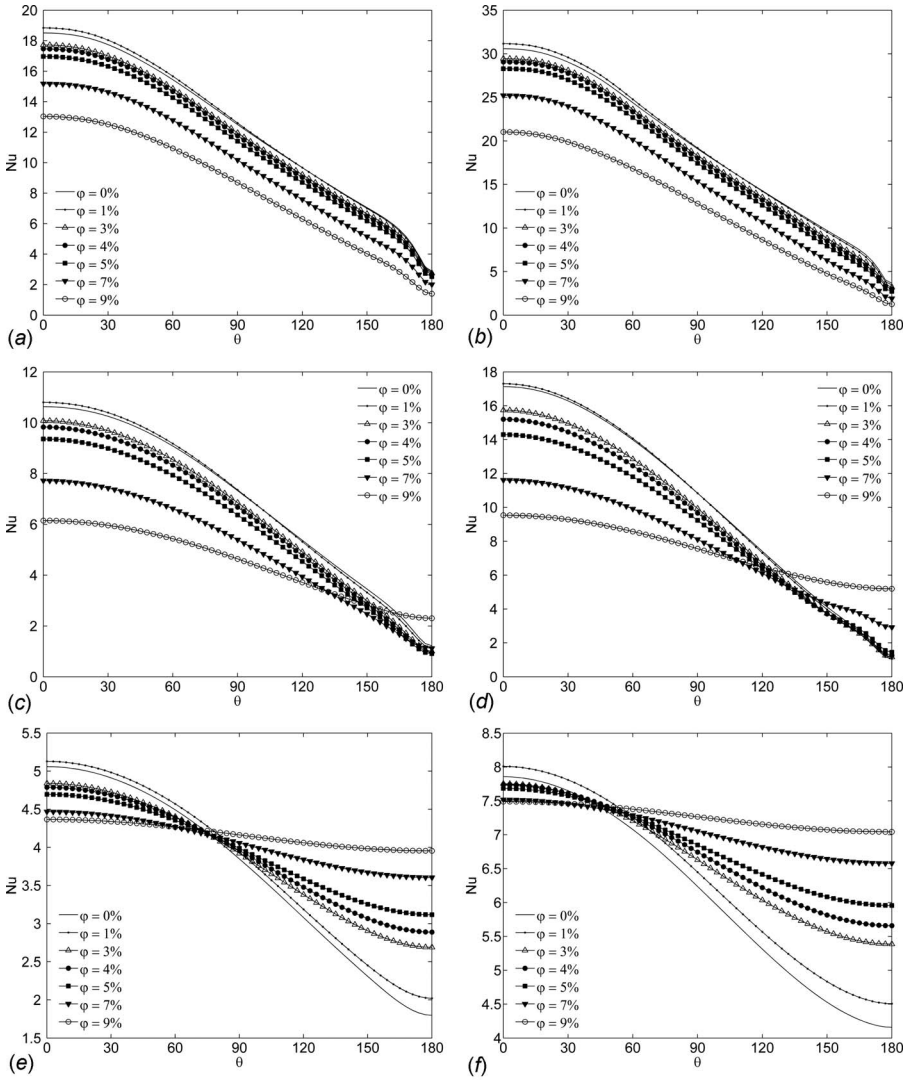

Fig. 8 Nusselt number distribution around the inner cylinder surface using various volume fractions of CuO nanoparticles: (*a*) Ra=10^5 (*L*/*D*=0.4), (*b*) Ra=10^5 (*L*/*D*=0.2), (*c*) Ra=10^4 (*L*/*D*=0.4), (*d*) Ra=10^4 (*L*/*D*=0.2), (*e*) Ra=10^3 (*L*/*D*=0.4), and (*f*) Ra=10^3 (*L*/*D*=0.2)

hancement in the Nusselt number by increasing the volume fraction of nanoparticles. However, the data of Nguyen et al. show deterioration in the Nusselt number by adding nanoparticles. Actually, the Brinkman model is used for dispersed particles in solution with particle size much higher than the nanoscale particles and its applicability to nanoparticles is questionable. On the other hand, for low Reynolds number, i.e., Ra=10^3 when the data of Nguen et al. are used, the Nusselt number is not sensitive to volume fraction less than 5%; however, for higher volume fractions, an enhancement in heat transfer is observed, which is opposite to the behavior registered at high Rayleigh number (using the data of Nguyen et al.). The convection currents at low Rayleigh number (Ra=10^3) are small compared with high Rayleigh numbers, and therefore, it is obvious that the role of nanofluid viscosity becomes less significant. It is interesting to note that for this Rayleigh number all of the four approaches predict an enhancement in heat transfer. Also, the difference in Nusselt prediction between the Brinkman model and the data of Nguyen et al. is small compared with high Rayleigh numbers. For example, this difference, at φ=9%, is approximately10% compared with 50% at Ra=10^5.

Also, Fig. 10 shows that the deviation between the model of Chon et al. and the MG model becomes more pronounced for Ra=10^3, especially at high volume fractions of nanoparticles. This tells that such difference becomes more appreciable at high volume fraction of nanoparticles and this difference cannot be neglected. In general the MG model overpredicts the enhancement in heat transfer compared with the model of Chon et al. at high volume fractions of nanoparticles ($\varphi > 5\%$). Figure 10 is very useful to identify when the MG model is appropriate for natural convections applications and when its applicability becomes less accurate. Besides, it tells that for higher Rayleigh numbers, the Brinkman model prediction deviates considerably from the measured data prediction and this difference cannot be neglected, which limits the applicability of the Brinkman model at high Rayleigh numbers. However, this difference is less pronounced at lower Rayleigh number and the Brinkman model could be used with approximately 10% deviation in prediction from the measured data.

A closer look at Fig. 10 reveals that for the MG model and the experimental data of Nguyen et al. (also the data of Chon et al. and Nguyen et al.), heat transfer increases up to 1% then decreased up to 3% and again it increases. To discuss this behavior it is useful to break the explanation into three parts: the first part is for $0 \leq \varphi \leq 1\%$, the second part is for $1\% < \varphi < 3\%$, and the third

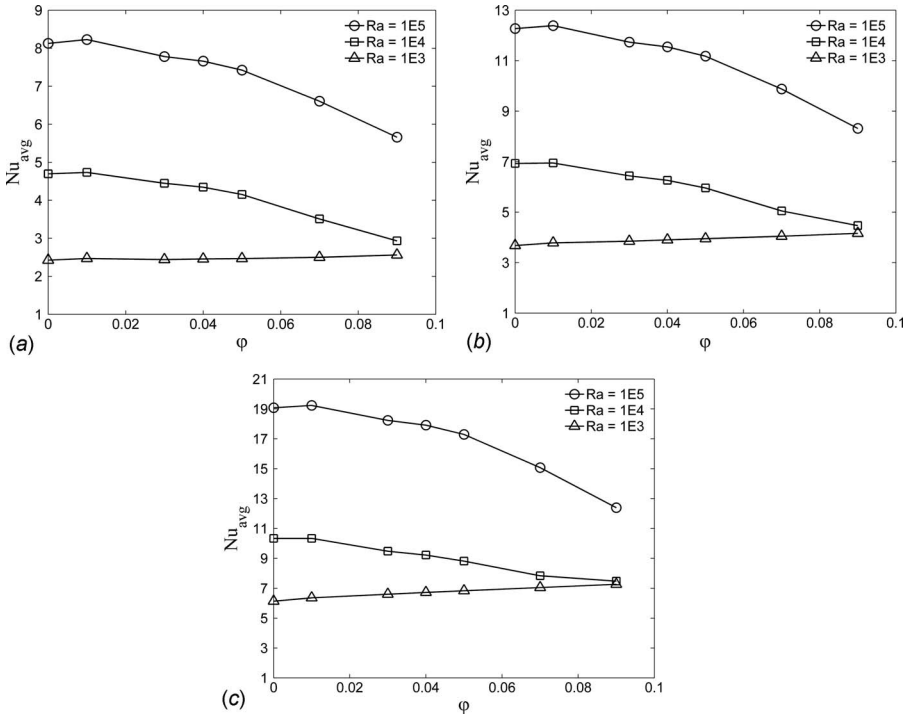

Fig. 9 Average Nusselt number: (*a*) *L*/*D*=0.8, (*b*) *L*/*D*=0.4, and (*c*) *L*/*D*=0.2

part is for $\varphi > 4\%$. For the first part, this behavior is related to the regression employed. The regression given in Eq. (13) was employed for $1 < \varphi < 9\%$. However, the viscosity of pure water was calculated from Eq. (15). This creates inconsistency in viscosity estimation near $\varphi = 1\%$. However, for the second part, this behavior is related to the dual role of thermal conductivity and viscosity on heat transfer enhancement. In general, the influence of nanoparticles elucidates two opposing effects on the Nusselt number: a favorable effect that is driven by the presence of high thermal conductivity nanoparticles, and an undesirable effect promoted by the high level of viscosity experienced at high volume fractions of nanoparticles. Therefore, for $\mathrm{Ra} = 10^3$, the presence of nanoparticles increases the nanofluid viscosity, which reduces Nusselt number at the heated surface due to the increased viscosity. This phenomenon is accompanied by some enhancement in heat transfer due to the high thermal conductivity of nanoparticles but, such

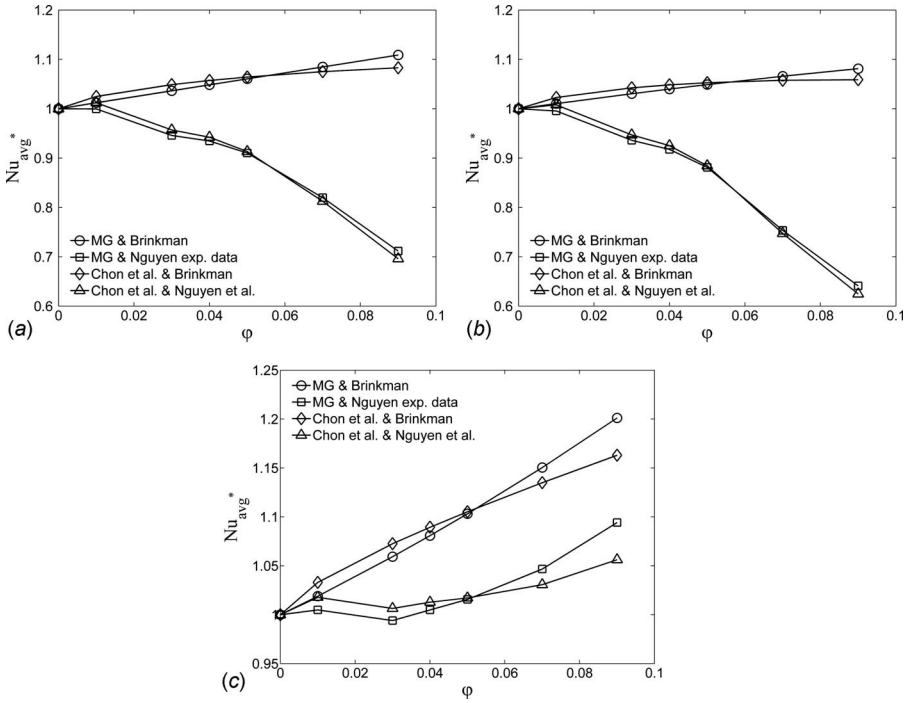

Fig. 10 Effects of the conductivity and viscosity models on the Nusselt number (*L*/*D* =0.8): (*a*) Ra=10^5, (*b*) Ra=10^4, and (*c*) Ra=10^3

enhancement at low volume fraction of nanoparticles is very minimal compared with the deterioration brought by the viscosity. For the third piece, as the volume fraction of nanoparticles increase beyond 4%, the role of thermal conductivity becomes dominant and enhancement in the Nusselt number is observed, as shown in Fig. 10.

6 Conclusions

For $Ra \geq 10^4$, the average Nusselt number is reduced by increasing the volume fraction of nanoparticles. However, for $Ra = 10^3$, the average Nusselt number enhancement depends on aspect ratio as well as volume fraction of nanoparticles. For $Ra = 10^3$, the average Nusselt number is not sensitive to nanoparticles at high aspect ratio $L/D = 0.8$, and the average number is enhanced by increasing the volume fraction of nanoaprticles for $L/D \leq 0.4$. For $Ra \geq 10^4$, the Nusselt number is deteriorated everywhere around the cylinder surface especially at high aspect ratio. However, this reduction is only limited to certain regions around the cylinder surface at $Ra = 10^3$. For $Ra \geq 10^4$, the MG model and model of Chon et al. give similar results. However, there is a deviation at $Ra = 10^3$ and this deviation becomes more significant at high volume fraction of nanoparticles. The data of Nguyen et al. and the Brinkman model give completely different predictions for $Ra \geq 10^4$, where the difference in the prediction of the Nusselt number could reach 50%. However, this difference reduces to less than 10% at $Ra = 10^3$.

Acknowledgment

The author would like to thank Dr. Ziyad Masoud for his huge efforts in preparing the final figures of the manuscript.

Nomenclature

- c_p = specific heat at constant pressure (J/kg K)
- D = diameter of inner cylinder (m)
- g = gravitational acceleration (m/s^2)
- h = local heat transfer coefficient (W/m^2 K)
- k = thermal conductivity (W/m K)
- L = gap between inner and outer cylinder, i.e., $L = r_o - r_i$ (m)
- Nu = Nusselt number
- Pr = Prandtl number
- q_w = heat transfer at the inner cylinder surface (W/m^2)
- Ra = Rayleigh number
- Re = Reynolds number
- $\tilde{r}$ = radial coordinate measured from the inner cylinder surface (m)
- r = nondimensional radial distance
- $\tilde{T}$ = dimensional temperature (K)
- T = nondimensional temperature
- u = dimensional tangential velocity (m/s)
- U = nondimensional tangential velocity
- v = dimensional radial velocity (m/s)
- V = nondimensional radial velocity

Greek Symbols

- α = thermal diffusivity (m^2/s)
- β = thermal expansion coefficient (1/K)
- φ = nanoparticle volume fraction
- ν = kinematic viscosity (m^2/s)
- θ = angle measured from the lower symmetry plane
- Ψ = nondimensional stream function
- ψ = dimensional stream function (m^2/s)
- Ω = nondimensional vorticity
- ω = dimensional vorticity (1/s)
- ρ = density (kg/m^3)
- μ = dynamic viscosity ($N\,s/m^2$)

Subscripts

- avg = average
- C = cold
- f = fluid
- H = hot
- nf = nanofluid
- p = particle

References

[1] Choi, U. S., 1995. "Enhancing Thermal Conductivity of Fluids With Nanoparticles," FED (Am. Soc. Mech. Eng.), **231**(66), pp. 99–105.

[2] Daungthongsuk, W., and Wongwises, S., 2007, "A Critical Review of Convective Heat Transfer Nanofluids," Renewable Sustainable Energy Rev., **11**, pp. 797–817.

[3] Trisaksri, V., and Wongwises, S., 2007, "Critical Review of Heat Transfer Characteristics of Nanofluids," Renewable Sustainable Energy Rev., **11**, pp. 512–523.

[4] Khanafer, K., Vafai, K., and Lightstone, M., 2003. "Buoyancy-Driven Heat Transfer Enhancement in a Two-Dimensional Enclosure Utilizing Nanofluids," Int. J. Heat Mass Transfer, **46**, pp. 3639–3653.

[5] Oztop, H. F., and Abu-Nada, E., 2008, "Numerical Study of Natural Convection in Partially Heated Rectangular Enclosure Filled With Nanofluids," Int. J. Heat Fluid Flow, **29**(5), pp. 1326–1336.

[6] Putra, N., Roetzel, W., and Das, S. K., 2003, "Natural Convection of Nano-Fluids," Heat Mass Transfer, **39**, pp. 775–784.

[7] Wen, D., and Ding, Y., 2004, "Experimental Investigation into Convective Heat Transfer of Nanofluids at the Entrance Region Under Laminar Flow Conditions," Int. J. Heat Mass Transfer, **47**(24), pp. 5181–5188.

[8] Nnanna, A. G. A., 2007, "Experimental Model of Temperature-Driven Nanofluid," ASME J. Heat Transfer, **129**, pp. 697–704.

[9] Ho, C. J., and Lin, C. C., 2006, "Experiments on Natural Convection Heat Transfer of a Nanofluid in a Square Enclosure," *Proceedings of the 13th International Heat Transfer Conference*, Sydney, Australia.

[10] Abu-Nada, E., Masoud, Z., and Hijazi, A., 2008, "Natural Convection Heat Transfer Enhancement in Horizontal Concentric Annuli Using Nanofluids," Int. Commun. Heat Mass Transfer, **35**(5), pp. 657–665.

[11] Hwang, K. S., Lee, J. H., and Jang, S. P., 2007, "Buoyancy-Driven Heat Transfer of Water-Based Al2O3 Nanofluids in a Rectangular Cavity," Int. J. Heat Mass Transfer, **50**, pp. 4003–4010.

[12] Ho, C. J., Chen, M. W., and Li, Z. W., 2008, "Numerical Simulation of Natural Convection of Nanofluid in a Square Enclosure: Effects Due to Uncertainties of Viscosity and Thermal Conductivity," Int. J. Heat Mass Transfer, **51**, pp. 4506–4516.

[13] Pak, B. C., and Cho, Y. I., 1998, "Hydrodynamic and Heat Transfer Study of Dispersed Fluids With Submicron Metallic Oxide Particles," Exp. Heat Transfer, **11**, pp. 151–170.

[14] Nguyen, C. T., Desgranges, F., Roy, G., Galanis, N., Mare, T., Boucher, S., and Angue Minsta, H., 2007, "Temperature and Particle-Size Dependent Viscosity Data for Water-Based Nanofluids—Hystresis Phenomenon," Int. J. Heat Fluid Flow, **28**, pp. 1492–1506.

[15] Polidori, G., Fohanno, S., and Nguyen, C. T., 2007, "A Note on Heat Transfer Modeling of Newtonian Nanofluids in Laminar Free Convection," Int. J. Therm. Sci., **46**(8), pp. 739–744.

[16] Angue Minsta, H., Roy, G., Nguyen, C. T., and Doucet, D., 2008, "New Temperature and Conductivity Data for Water-Based Nanofluids," Int. J. Therm. Sci., **48**(2), pp. 363–373.

[17] Chon, C. H., Kihm, K. D., Lee, S. P., and Choi, S. U. S., 2005, "Empirical Correlation Finding the Role of Temperature and Particle Size for Nanofluid (Al_2O_3) Thermal Conductivity Enhancement," Appl. Phys. Lett., **87**(15), pp. 153107.

[18] Patankar, S. V., 1980, *Numerical Heat Transfer and Fluid Flow*, Hemisphere, Washington, DC.

[19] Versteeg, H. K., and Malalasekera, W., 1995, *An Introduction to Computational Fluid Dynamic: The finite Volume Method*, Wiley, New York.

[20] Guj, G., and Stella, F., 1995, "Natural Convection in Horizontal Eccentric Annuli: Numerical Study," Numer. Heat Transfer, **27**, pp. 89–105.

[21] Shu, C., Yeo, K. S., and Yao, Q., 2000, "An Efficient Approach to Simulate Natural Convection in Arbitrary Eccentric Annuli by Vorticity Stream Function Formulation," Num. Heat Transfer, Part A, **38**, pp. 739–756.

[22] Kuehn, T. H., and Goldstein, R. J., 1976, "An Experimental and Theoretical Study of Natural Convection in the Annulus Between Horizontal Concentric Cylinders," J. Fluid Mech., **74**, pp. 695–719.

Monte Carlo Study of Phonon Heat Conduction in Silicon Thin Films Including Contributions of Optical Phonons

Arpit Mittal

Sandip Mazumder[1]
Mem. ASME
e-mail: mazumder.2@osu.edu

Department of Mechanical Engineering,
Ohio State University,
201 West 19th Avenue,
Columbus, OH 43210

The Monte Carlo method has found prolific use in the solution of the Boltzmann transport equation for phonons for the prediction of nonequilibrium heat conduction in crystalline thin films. This paper contributes to the state-of-the-art by performing a systematic study of the role of the various phonon modes on thermal conductivity predictions, in particular, optical phonons. A procedure to calculate three-phonon scattering time-scales with the inclusion of optical phonons is described and implemented. The roles of various phonon modes are assessed. It is found that transverse acoustic (TA) phonons are the primary carriers of energy at low temperatures. At high temperatures ($T>200$ K), longitudinal acoustic (LA) phonons carry more energy than TA phonons. When optical phonons are included, there is a significant change in the amount of energy carried by various phonons modes, especially at room temperature, where optical modes are found to carry about 25% of the energy at steady state in silicon thin films. Most importantly, it is found that inclusion of optical phonons results in better match with experimental observations for silicon thin-film thermal conductivity. The inclusion of optical phonons is found to decrease the thermal conductivity at intermediate temperatures (50–200 K) and to increase it at high temperature (>200 K), especially when the film is thin. The effect of number of stochastic samples, the dimensionality of the computational domain (two-dimensional versus three-dimensional), and the lateral (in-plane) dimension of the film on the statistical accuracy and computational efficiency is systematically studied and elucidated for all temperatures. [DOI: 10.1115/1.4000447]

Keywords: Monte Carlo, Boltzmann transport equation, thin film, thermal conductivity, optical phonon, silicon

1 Introduction

In recent years, aggressive scale-down in the feature sizes of electronic devices, coupled with faster processing speeds, has resulted in large quantity of heat being generated per unit volume in these devices. The efficient removal of heat from such devices is a daunting task, and overheating is one of the most common causes of device failure. Accordingly, there has been an increasing interest in modeling thermal transport in micro- and nanoscale semiconductor devices to gain a better fundamental understanding of the mechanism of heat conduction in crystalline thin films.

Nonequilibrium heat conduction in thin films has been successfully modeled in the past using the semiclassical Boltzmann transport equation (BTE) for phonons. Numerical solution of the BTE has previously been obtained both stochastically [1,2] and deterministically [3–5], and the thermal conductivity of thin films made of silicon and other semiconductor materials has been predicted successfully. The relative advantages and disadvantages of stochastic versus deterministic techniques for solution of the BTE is discussed in detail elsewhere [1,3,6–8] and is not the primary subject of this paper.

The first formal Monte Carlo (MC) procedure for phonon transport was presented by Peterson [9]. Peterson's study did not consider phonon dispersion and did not account for the various phonon polarizations. Mazumder and Majumdar [1] presented the first comprehensive algorithm to solve the BTE for phonons by the MC method with the inclusion of phonon dispersion and polarization. In their approach, statistical samples (phonons) are drawn from six individual stochastic spaces: three wave vector and three position vector components. The sampled phonons first undergo drift (ballistic motion) and then undergo scattering events. Lacroix et al. [2] presented a transient MC algorithm that modified the scattering algorithm used by Mazumder and Majumdar [1] to enforce Kirchhoff's law during the scattering phase. This modified algorithm has later been used by other researchers [10–13], and has been found to accurately predict transient heat conduction in thin films in both ballistic and diffusive regimes.

Although Mazumder and Majumdar [1] accounted for the acoustic modes of phonon propagation, the contribution of optical phonons toward energy transport was neglected based on the presumption that they have slow group velocities and, therefore, do not contribute to energy transport [14]. Although this contention is intuitive, it is well known [5] that interaction between optical and acoustic phonons alters the effective relaxation rates of the acoustic phonons and, thereby, affects energy transport in an indirect manner. Narumanchi [5] suggested that optical phonons must be considered even in steady-state thermal predictions. While the group velocity of optical phonons is small at small and large values of the wave-vector, **K**, it is not negligible for intermediate values of **K**. For longitudinal optical (LO) phonons, the group velocity can be comparable to the slower acoustic modes [3]. Therefore, further systematic studies are necessary to understand the effect of optical phonons on thermal transport.

Narumanchi and co-workers [4,5] and Wang [3] considered optical phonons in their deterministic finite-volume formulation for

[1]Corresponding author.

Contributed by the Heat Transfer Division of ASME for publication in the JOURNAL OF HEAT TRANSFER. Manuscript received March 24, 2009; final manuscript received September 23, 2009; published online March 8, 2010. Assoc. Editor: Kenneth Goodson.

solving the BTE. Narumanchi's work invoked two simplifying assumptions while taking optical phonons into consideration in his model. First, similar to the assumptions made in the past [1], the optical phonons were assumed to have zero group velocities. Second, all the optical phonons were clubbed into a single band and no distinction was made between LO and transverse optical (TO) modes. Though Wang [3] removed the first assumption made in Narumanchi's work, the two polarizations of the optical phonons have not been considered in calculating phonon lifetimes. The result of their work, therefore, does not bring out explicitly the role of optical phonons in silicon thermal conductivity prediction and the subsequent impact on energy transport in semiconductor thin films. Recently, Kazan et al. [15] studied the role of optical phonon decay into acoustic modes using the modified Callaway theory for germanium and found that the inclusion of optical phonons increases the accuracy in predicting the thermal conductivity of semiconductors. Therefore, these studies make a compelling case for inclusion of optical phonons in the numerical solution of the BTE for phonons. The current work seeks to build on the works of Mazumder and Majumdar [1] and Lacroix et al. [2] to solve the BTE for phonons with full phonon dispersion including LO and TO phonons using the MC method. First, the BTE is solved considering only LA and TA modes, and the thermal conductivity of silicon thin films are computed. Subsequently, optical modes are also considered and the thermal conductivity results, thus obtained, are compared with the results obtained without considering optical phonons, as well as experimental results obtained by Asheghi [16].

The biggest roadblock in incorporating optical phonons in the numerical solution of the BTE for phonons is the lack of three-phonon scattering time-scales for the optical modes. Using the expressions given by Han and Klemens [17], Narumanchi and co-workers [4,5] presented a methodology for calculating the three-phonon interaction time-scales for the various phonon modes undergoing Umklapp (U) scattering, including optical phonons. In Narumanchi's work, however, the contribution of Normal (N) processes toward phonon relaxation time calculation has not been considered. Narumanchi and co-workers [4,5] considered only a subset of the possible interactions between different phonon modes for the phonon lifetime calculations. The interactions considered embody the low-temperature assumption, thereby allowing simplifications to be made to the phonon conservation laws. While removing this assumption is desirable, it would imply consideration of a very large number of three-phonon interactions and rigorous implementation of the energy and momentum conservation laws to calculate the three-phonon interaction time-scales over the whole wave-vector space [3]. This would increase the complexity of the numerical simulation dramatically. Therefore, this has not been attempted in the present work. As a start, the phonon lifetimes for U processes of various phonon modes have been calculated using the expressions given by Han and Klemens [17] and interactions considered by Narumanchi et al. [4,5]. The contribution of the N processes to the phonon lifetime data is calculated from the expressions given by Holland [18]. Therefore, in order to calculate the overall phonon relaxation time, a hybrid approach derived from the works of Holland [18] and Han and Klemens [17] has been employed in the present work. The objective of this study is to shed some light, albeit preliminary, on the effect of optical phonons on energy transport and thermal conductivity predictions in silicon thin films.

Ever since the development of the first comprehensive Monte Carlo procedure by Mazumder and Majumdar [1], significant advances have been made toward the improvement of such algorithms. These include alternative and, perhaps, better procedures for the treatment of scattering [2,19], alternative formulations for sampling phonons [20], and steady-state approaches aimed toward the reduction of computational time and memory [12]. Despite these advances, a few critical questions remain unanswered. For Monte Carlo simulations aimed toward prediction of through-plane thermal conductivity of thin films, the lateral (or in-plane) dimensions (Y and Z) (see Fig. 1) of the film are free parameters. Ideally, if the lateral (or nonthermalizing) boundaries are made perfectly specular, the effect of the lateral dimension is irrelevant because in that case these boundaries would pose no resistance (i.e., they are symmetry planes). In the actual physical scenario, the thermal conductivity at low temperature is dictated by boundary scattering, and the boundary must be made partially specular to keep the thermal conductivity finite in the ballistic limit. This is done by calibrating the degree of specularity (α) against experimental data, as originally proposed by Mazumder and Majumdar, and later used by almost all subsequent studies [12,19]. Therefore, the choice of the lateral dimension would affect the calibrated value of α, and it is important to ensure that the calibration of α and the choice of lateral dimensions has no bearing on the predicted thermal conductivity. Furthermore, it is important to understand the effect of the choice of lateral dimension on the computational efficiency.

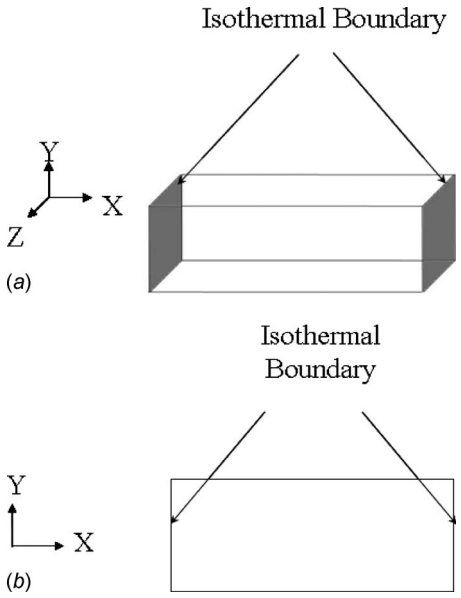

Fig. 1 Computational domain (*a*) 3D and (*b*) 2D

Mazumder and Majumdar [1] used a two-dimensional (2D) computational domain to predict thin-film thermal conductivity, whereas later studies [2,12,19] carried out their simulations on a three-dimensional (3D) computational domain. Whether a 2D or 3D computational domain should be used is still a matter of debate, and systematic studies are required to elucidate the *pros* and *cons* of either choice. Statistical errors are inherent to any MC simulation. In this particular case, the statistical noise in the heat flux (or thermal conductivity) data depends on the number of stochastic samples used for the MC simulation. The number of stochastic samples, in turn, determines the computational cost. This work, in addition to exploring the role of optical phonons, systematically explores the correlation between the above-mentioned numerical issues through careful analysis of the statistical errors and the associated computational cost.

2 Theory and Numerical Procedure

Quantized lattice vibrations or phonons are the predominant carriers of thermal energy in semiconductor devices [6]. If the mean free path of the traveling phonons is larger than the film thickness, thermodynamic equilibrium ceases to exist and, thus, the Fourier law of heat conduction is invalid. In this scenario, bulk thermal conductivity values, which are experimentally determined by inversion of the Fourier law itself, cannot be used for analysis.

The Boltzmann transport equation is a semiclassical equation and has been successfully used to model particles that interact with each other via short range forces and follow a statistical distribution [3]. Phonons follow Bose–Einstein statistics and interact with each other via scattering processes and, therefore, can be modeled using the BTE, which may be written as [21]

$$\frac{\partial f}{\partial t} + \boldsymbol{v}_g \cdot \nabla f = \left[\frac{\partial f}{\partial t}\right]_{\text{scattering}} \tag{1}$$

where f is the distribution function of an ensemble of phonons, and $\boldsymbol{v}_g$ is the group velocity. The left side of Eq. (1) represents change of the distribution function due to motion (or drift), whereas the right-hand side represents the change in the distribution function due to collisions (or scattering). Drift causes the phonon energy distribution function to deviate from equilibrium, while collisions tend to restore equilibrium.

2.1 Phonon-Phonon Scattering. Prior to solution of the BTE for phonons, it is necessary to formulate the right-hand-side of Eq. (1). This scattering term is complicated if all possible scattering mechanisms are considered rigorously. Due to the complexity of the scattering term, simplifications and approximations have to be made to the BTE before it can be solved. The most common approximation used to simplify the BTE is the relaxation time approximation, whereby the scattering term is expressed as

$$\left[\frac{\partial f}{\partial t}\right]_{\text{scattering}} = \frac{f - f_0}{\tau} \tag{2}$$

where f_0 is the equilibrium distribution function (i.e., the Bose–Einstein distribution function), and τ is the overall scattering time-scale of the phonon due to all scattering processes in combination. This approximation essentially linearizes the scattering term of the BTE and implies that whenever a system is not in equilibrium, the scattering term will restore the system to equilibrium following an exponential decay law: $f - f_0 = \exp(-t/\tau)$. In the relaxation time approximation, scattering between different wave-vectors is not explicitly accounted for. Instead, the phonons relax to the equilibrium distribution [6].

Scattering of three or more phonons with each other occurs due to the anharmonic nature of the interatomic forces and the discrete nature of the lattice structure. Phonon-phonon scattering involving four or more phonons is important only at temperatures much higher than the Debye temperature [6] (645 K for silicon) and is not considered here since 645 K is much higher than the operating temperature of most electronic devices.

Three-phonon interactions can be classified as Normal processes and Umklapp processes. Both N and U processes are governed by energy and momentum conservation rules given by [14]

$$\omega + \omega' \leftrightarrow \omega'' \quad \text{(Normal and Umklapp)}$$

$$\mathbf{K} + \mathbf{K}' \leftrightarrow \mathbf{K}'' \quad \text{(Normal)}$$

$$\mathbf{K} + \mathbf{K}' \leftrightarrow \mathbf{K}'' + \mathbf{b} \quad \text{(Umklapp)} \tag{3}$$

where ω, ω', and ω'' are the angular frequencies of the interacting phonons, and $\mathbf{K}$, $\mathbf{K}'$, and $\mathbf{K}''$ are their wave-vectors. During these interactions, two phonons may merge to form a third phonon, or a single phonon may break up into two phonons. In an Umklapp process, momentum is not conserved—the difference in phonon wave-vectors resulting in the reciprocal lattice vector, $\mathbf{b}$.

A critical component for solving the BTE for phonons is the computation of the relaxation times for the three-phonon interactions. The difficulty in determining these time-scales is borne from the fact that the expressions for calculating these time-scales are not available due to complex nature of the anharmonic interatomic forces. As a result, much of the published literature use only approximate relaxation times, which are typically derived either by using curve-fits to bulk thermal conductivity [18] or by making low-temperature approximations that allow simplifications to the conservation rules [17]. It is critical to note that although both N and U processes are important, only U processes pose resistance to thermal transport. On the other hand, N processes indirectly affect thermal energy transport, especially at low temperatures, by creating sufficient number of high-**K** phonons that affect U processes [6]. Therefore, it is essential to consider the contribution of both N and U processes for the calculation of the overall relaxation time.

Holland [18], using perturbation analysis in combination with calibration to experimental data, developed frequency and temperature dependent expressions for the relaxation times of scattering for LA and TA phonons

$$\tau_{NU}^{-1} = B_L \omega^2 T^3 \quad \text{(LA, Normal + Umklapp)}$$

$$\tau_N^{-1} = B_{TN} \omega T^4 \quad \text{(TA, Normal)} \tag{4a}$$

$$\tau_U^{-1} = \begin{cases} 0 & \text{(TA, Umklapp for } \omega < \omega_{1/2}\text{)} \\ B_{TU}\omega^2/\sinh\left(\dfrac{\hbar\omega}{k_B T}\right) & \text{(TA, Umklapp for } \omega > \omega_{1/2}\text{)} \end{cases} \tag{4b}$$

where $\omega_{1/2}$ is the frequency corresponding to $K/K_{\max} = 0.5$, and B_L, B_{TN}, and B_{TU} are constants [18] that need to be obtained through calibration against experimental data, and the values suggested by Holland [18] and used later by Mazumder and Majumdar [1] have been used in the present study. For silicon, $\omega_{1/2} = 2.417 \times 10^{13}$ rad/s. Previous MC studies of the phonon BTE [1,2] have used these time-scales for thermal conductivity calculations as a preliminary step. Holland made two important assumptions for calculating these time-scales: (1) only high-frequency TA phonons undergo Umklapp processes and (2) LA phonons do not undergo U processes at all. Therefore, in effect, Eq. (4*a*) gives the time-scale for N processes, whereas the expression in Eq. (4*b*) gives the phonon interaction time-scales for U processes. Despite these assumptions, the expressions provided by Holland continue to be popular because of their simplicity and the ease of their implementation.

Klemens [22], starting from perturbation theory, considered scattering processes due to anharmonicities, and derived a set of expressions for U processes at low temperatures. Based on the work of Klemens [22] and Han and Klemens [17], Narumanchi et al. [4] provided a methodology for calculating frequency and temperature dependent phonon lifetimes for both optical and acoustic modes for the U processes. The advantage of using the expressions given in Narumanchi's work is that unlike the expressions given by Holland [18], only a single fitting parameter, called the Gruneisen constant, is used to calculate the phonon lifetimes.

In the present study, a hybrid approach is used to calculate the phonon time-scales wherein the time-scale for N processes is calculated from Holland's expressions, as given by Eq. (4*a*). The procedure for calculating the time-scale of U processes, as derived from Narumanchi et al. [5] and Han and Klemens [17], is described next. For silicon, the three-phonon interactions that are believed to be important [4,5] are shown in Table 1, wherein BZB refers to phonons corresponding to the first Brillouin zone boundary. The relaxation time, τ_{ij}, for the interactions of the type LA + TA(BZB) $\leftrightarrow$ LA, TA + TA(BZB) $\leftrightarrow$ LA, and TA + LA(BZB) $\leftrightarrow$ LA and for the optical modes is calculated from Ref. [17] using similar expressions proposed by Narumanchi and co-workers [4,5]

$$\frac{1}{\tau_{ij}} \approx \frac{\chi\gamma^2}{3\pi\rho v_{\text{ph}}^2 v_g} \omega_i \omega_{tr} \omega_j r_c^2 \left| \left[\frac{1}{(e^{\hbar\omega_{tr}/k_B T} - 1)} - \frac{1}{(e^{\hbar\omega_j/k_B T} - 1)} \right] \right| \tag{5}$$

where i refers to the phonon for which the time-scale needs to be calculated, henceforth referred to as the incoming mode, j refers to the resultant or the translated mode, and tr refers to the mode by which the incoming mode is translated to the resultant mode

Table 1 Three-phonon interactions considered in this study for the calculation of scattering time-scales for each type of phonon

Longitudinal acoustic phonons
LA+TA(BZB)↔LA
LA+TA↔LO(BZB)
LA+TA↔TO(BZB)
LA+LA↔LO(BZB)
LA+TA↔TO(BZB)
Longitudinal optical phonons
LO↔LA+TA(BZB)
LO↔LA+LA(BZB)
LO↔TA+LA(BZB)
Transverse acoustic phonons
TA+TA(BZB)↔LA
TA+LA(BZB)↔LA
TA+LA↔LO(BZB)
TA+LA↔TO(BZB)
Transverse optical phonons
TO↔LA+TA(BZB)
TO↔LA+LA(BZB)
TO↔TA+LA(BZB)

(referred to as the translational mode). The phase velocity of the incoming mode is denoted by $v_{\mathrm{ph}}(=\omega/k)$, and $v_g(=|\boldsymbol{v}_g|)$ is the magnitude of the group velocity of the resultant mode. ρ is the density of the solid (i.e., bulk silicon). ω_i is the frequency of the incoming phonon in rad/s, ω_j is the frequency of the resultant mode, while ω_{tr} is the frequency of the translational mode at the BZB. χ is the degeneracy of the translated mode, γ is the Grunesen constant and has been taken to be 0.59 for silicon [5], and r_c denotes the effective radius. For the [100] direction, r_c is calculated as [17]

$$r_c = \frac{2\pi/a - k_i}{2\sqrt{2}} \tag{6}$$

where a is the lattice constant, and k_i is the wave-vector of the phonon for which the time-scale needs to be calculated.

For the interaction of the type LA/TA+LA/TA↔LO/TO(BZB), the time-scales are calculated using the expression

$$\frac{1}{\tau_{ij}} \approx \frac{\chi\gamma^2}{3\pi\rho v_{\mathrm{ph}}^2 v_g}\omega_i\omega_O\omega_{tr}^3\left[\frac{1}{(e^{\hbar\omega_{tr}/k_BT}-1)} - \frac{1}{(e^{\hbar\omega_O/k_BT}-1)}\right] \tag{7}$$

where ω_O is the frequency of the optical mode at the BZB, ω_i is the incoming phonon frequency, and $\omega_{tr}(=\omega_O-\omega_i)$ is the translated phonon frequency.

For a given incoming phonon frequency and polarization, the time-scale for all the possible interactions are calculated. If the various phonon-phonon interaction processes are assumed to be independent, their scattering probabilities can be added together. The overall scattering time-scale is then given by Mathiessen's rule

$$\frac{1}{\tau_{U,i}} = \sum_j \frac{1}{\tau_{ij}} \tag{8}$$

where τ_{ij} is the relaxation time for a single scattering process (as calculated using Eqs. (5) and/or Eq. (7)), and $\tau_{U,i}$ is the relaxation time for all U processes combined. The overall relaxation time τ is then calculated as

Table 2 Curve-fit parameters for silicon dispersion data [29]

Phonon polarization	ω_0 (10^{13} rad/s)	v_s (10^2 m/s)	c (10^{-7} m^2/s)
LA	0.00	9.01	−2.00
TA	0.00	5.23	−2.26
LO	9.88	0.00	−1.60
TO	10.20	−2.57	1.12

$$\frac{1}{\tau} = \frac{1}{\tau_N} + \frac{1}{\tau_U} \tag{9}$$

and is used as an input for solution of Eq. (1), with the scattering term expressed by Eq. (2).

2.2 Dispersion Relationships. Prior to the solution of the BTE, information regarding phonon dispersion is required. Phonon dispersion plays an important part in thermal conductivity calculations and is necessary to model polarization and frequency-dependent behavior [3]. It has been observed that the inclusion of phonon dispersion has a significant effect on the phonon mean free path [23]. The phonon dispersion relationships for a given material and a specified direction are determined by neutron scattering experiments [24,25]. They may also be calculated from lattice dynamics either by solving the Schrödinger equation for lattice vibrations [26] or using semiclassical approaches under the harmonic approximation [27]. For bulk silicon, the experimental dispersion data have been well documented by Brockhouse [24] and Dolling [25]. For nanoscale films, the use of bulk dispersion relationships is inappropriate due to the folding of the Brillouin zone, also referred to as phonon confinement. According to Heino [13], the effect of phonon confinement becomes appreciable only in very thin structures of around 10–20 nm thick. For the present study, since the film thicknesses considered are relatively thick, it was deemed appropriate to use bulk dispersion relationships. Chung et al. [28] discussed the impact of various curve-fits for phonon dispersion data on thermal conductivity calculations and proposed a model that uses quadratic curve-fits for LA phonons and a cubic curve-fit for TA phonons. In the present study each phonon dispersion branch is treated under the isotropic Brillouin zone (BZ) approximation by a quadratic curve-fit given by [29]

$$\omega_\kappa = \omega_o + v_s k + ck^2 \tag{10}$$

For the acoustic modes, the constants v_s and c are chosen so as to capture the slope of the dispersion curve near the center of the Brillouin zone and the maximum frequency at the edge of the BZ. For longitudinal optical phonons, these values ensure that the LO frequency at the BZ boundary equals the maximum LA frequency. For both TA and transverse optical phonons, the curves are fitted such that the slope at the edge of the BZ is zero [30]. Quadratic curve-fits have been used as they give an accurate approximation to the phonon dispersion data and are easy to invert in order to get the phonon wave vector and the phonon group velocity data. The phonon group velocity is calculated using the expression

$$v_g = \nabla_k \omega \tag{11}$$

Table 2 lists the values of the curve-fit parameters for silicon in the [100] direction [29]. The dispersion relationship in the [100] direction calculated from the curve-fit is shown in Fig. 2. These data are provided as input into the Monte Carlo code in the form of constants in Table 2. In this particular study, since an isotropic Brillouin zone is assumed, the group velocity obtained using Eq. (11) is essentially the slope of the dispersion curves, and it is codirectional with the wave vector.

2.3 Monte Carlo Procedure. The Monte Carlo procedure used in this study is adapted directly from the work of Mazumder

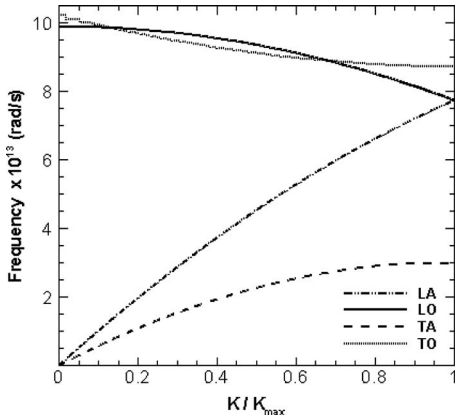

Fig. 2 Curve-fit data for dispersion curves for silicon in [100] direction

and Majumdar [1], and only issues that are different from the original work and issues that illustrate concepts discussed in this paper are highlighted in this section.

The first step in the MC solution technique is to determine the number of phonons per unit volume that are present in the computational domain, N_{actual}. For a given material, N_{actual} is only a function of the initial temperature and the physical dimensions of the computational domain. When optical phonons are included [2]

$$N_{\text{actual}} = \sum_{p} \sum_{i=1}^{N_b} \frac{1}{\left[\exp\left(\frac{\hbar\omega_{0,i}}{k_B T}\right) - 1\right]} \left(\frac{k^2}{2\pi^2}\right) \left.\frac{dk}{d\omega}\right|_{\omega_{0,i}} \Delta\omega_i \chi_p \tag{12}$$

where N_b is the number of frequency intervals into which the phonon frequency space is divided. In the present study, the frequency range $[0, \omega_{\max,TO}]$ has been discretized into 1000 spectral bins. Another trial was conducted with 1250 spectral bins with $[0, \omega_{\max,LA}]$ accounting for 1000 bins while an additional 250 bins were used for the optical modes. This had no impact on the results obtained during validation of the code in diffusion and ballistic limits. Hence, it was considered appropriate to use 1000 spectral bins as it is computationally less expensive to do so. $\omega_{0,i}$ and $\Delta\omega_i$ are the central frequency and the bandwidth of the ith spectral bin, respectively. The summation is done over all the polarizations p with χ being the degeneracy factor for each of the polarizations. Equation (12) is valid only for an isotropic Brillouin zone, with k being the component of the wave vector in any direction.

The actual number of phonons calculated using Eq. (12) can be quite large and, therefore, a weight factor, W, is introduced. The weight factor is defined as the ratio of the actual number of phonons, N_{actual}, to the prescribed number of phonons (stochastic samples) to be traced during the Monte Carlo simulation

$$W = \frac{N_{\text{actual}}}{N_{\text{prescribed}}} \tag{13}$$

The value of $N_{\text{prescribed}}$ is provided as an input to the MC calculation. Once the weight factor has been calculated, sampled phonons are allowed to drift and undergo scattering events.

Phonons traveling in a solid may be scattered by a variety of mechanisms, including lattice imperfections, such as vacancies, dislocations, and impurities, interactions with electrons or other phonons, and boundaries. Interchange of energy between lattice waves occurs in these processes. These scattering phenomena fall into two categories, namely elastic scattering and inelastic scattering. Phonon scattering due to vacancies and dislocations can be neglected if the crystal is considered to be perfect. As the primary focus of this study is to investigate the role of various phonon modes on energy transport and thermal conductivity prediction, only phonon-phonon (or intrinsic) scattering events have been considered here.

The computation of phonon-phonon scattering time-scales has already been discussed in an earlier section. In the MC procedure, once the time-scale of scattering of phonons has been calculated, the probability of scattering of the phonon between time t and $t + \Delta t$ may be calculated as [1]

$$P_{\text{scat}} = 1 - \exp\left(\frac{-\Delta t}{\tau}\right) \tag{14}$$

A random number R_{scat} is drawn, and if the probability of scattering, P_{scat}, is greater than R_{scat}, then the phonon is scattered. The duration of the time step, Δt, was varied with film thickness but kept constant during a simulation. The time step was chosen such that it is smaller than the minimum scattering time for any of the phonons sampled during the simulation. For a 0.42 μm film, the time step was chosen to be 1 ps for all temperatures (10–300 K). Scattering of the phonon is implemented by resampling the frequency, polarization, and direction of the phonon from the cumulative number density function modulated by the probability of scattering. In the present study the scattering algorithm proposed by Lacroix et al. [2] has been used. This algorithm enforces Kirchhoff's law for phonons, i.e., the rate of formation of phonons of a certain state equals its rate of destruction, thereby retaining equilibrium if the initial state is already in equilibrium. The reason the outgoing phonon state(s) are sampled from an equilibrium distribution is because, by definition, collisions restore equilibrium. Thus, each time a phonon scatters, the local thermodynamic state is little bit closer to equilibrium. If the phonons were in a box and colliding over an infinite time interval, the current algorithm will guarantee that the Bose–Einstein distribution is recovered. The alternative to this procedure is to pair phonons and have them engage in the selection rules directly. However, this procedure will result in a scheme that will produce huge statistical errors because the number of phonons contained in a spatial bin is generally quite small and not adequate to address all collision possibilities. Attempts to use such a scheme showed that the Bose–Einstein distribution is never recovered with any practically feasible sample size. At the end of the scattering algorithm, the local equilibrium temperature is obtained for each spatial bin and the thermal gradient across the thin film is calculated. The net flux through the boundaries is calculated, and the "effective" thermal conductivity is then obtained by inverting the Fourier law of heat conduction. Other than the procedure used to resample the states of scattered phonons for which the algorithm of Lacroix et al. [2] is used, the procedure used here is an extension (inclusion of optical phonons) to the algorithm proposed by Mazumder and Majumdar [1].

3 Results and Discussion

This section presents results of MC simulations in silicon films of various thicknesses with and without taking optical phonons into consideration. The predicted results (thermal conductivity) are compared against experimental data, and the role of various phonon modes on thermal transport is discussed.

Prior to computation of the through-plane thermal conductivity, the Monte Carlo code was verified against analytical solutions for limiting scenarios. In the ballistic limit, i.e., for the case when the phonon mean free path is much larger than the film thickness, the code reproduced a medium temperature equal to the average of the fourth power of the two boundary temperatures. In the diffusion limit, i.e., for the case when the phonon mean free path is much smaller than the film thickness, the code reproduced a linear temperature profile between the two boundary temperatures. The effect of boundary scattering was also verified by altering the degree of specularity, α, of the lateral (nonthermalizing bound-

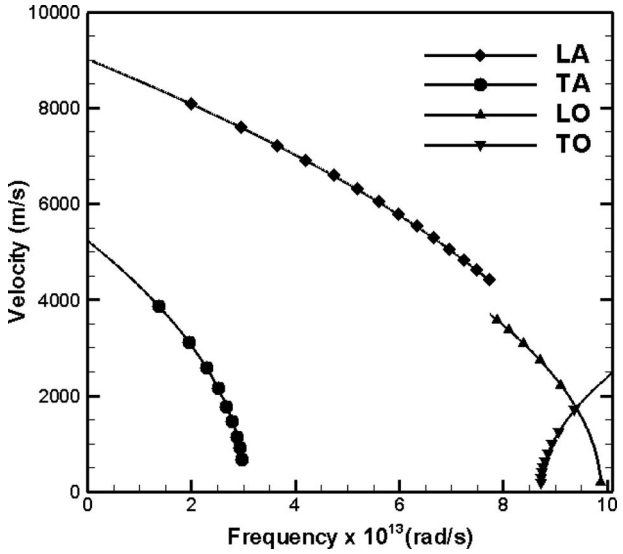

Fig. 3 Group velocity of the various phonon modes

aries), and previously reported results [1,2] were reproduced. These results are not shown here as they have been reported in a previous publication [1] by the same group.

3.1 Thermal Conductivity and Role of Various Phonon Modes. Computation of the thermal conductivity of silicon thin films requires computation of the group velocities of the various phonon modes from the dispersion relationship. Figure 3 shows the variation in group velocity of the various phonon modes with frequency calculated using the dispersion relationship shown in Fig. 2 (as adapted from Ref. [25]). The important point to note is that contrary to popular belief (and assumptions made by many past researchers), the group velocities of both LO and TO phonons are of the same order of magnitude as the acoustic phonons, although the frequency ranges for the acoustic modes and optical modes are different.

Another important quantity that gets altered due to the inclusion of optical phonons is the cumulative phonon occupation number at equilibrium, as computed from the Bose–Einstein distribution. This cumulative distribution function is critical for assigning phonon frequency and polarization when phonons are initialized within the computational domain, or when phonons are added to or deleted from the domain after a scattering event. Figure 4 illustrates the cumulative distribution function with and without optical phonons for various temperatures. Clearly, optical phonons alter the high-frequency part of the distribution function for temperatures greater than 100 K. It can also be seen from the cumulative distribution function that the number density of optical phonons is small at low temperatures (<100 K). Therefore, optical phonons are not expected to directly influence thermal energy transport at these temperatures. At higher temperatures, though, the number density of optical phonons is quite significant and they are expected to contribute toward thermal energy transport.

Figure 5 shows a comparison between the phonon lifetimes for the acoustic modes computed using two different approaches: (1) using expressions provided by Holland (Eqs. (4*a*) and (4*b*)) and (2) using the hybrid approach based on the works of Holland [18] and Han and Klemens [17] (Eqs. (5) and (7)) presented in this work. While the computed time-scales are somewhat different, it is encouraging to see that the time-scales computed using the hybrid approach are of the same order of magnitude as the time-scales computed using Holland's data. If that were not the case, these new time-scales would result in thermal conductivity that is significantly different from those predicted by Mazumder and Majumdar [1]. It is also seen that the time-scales predicted by the two

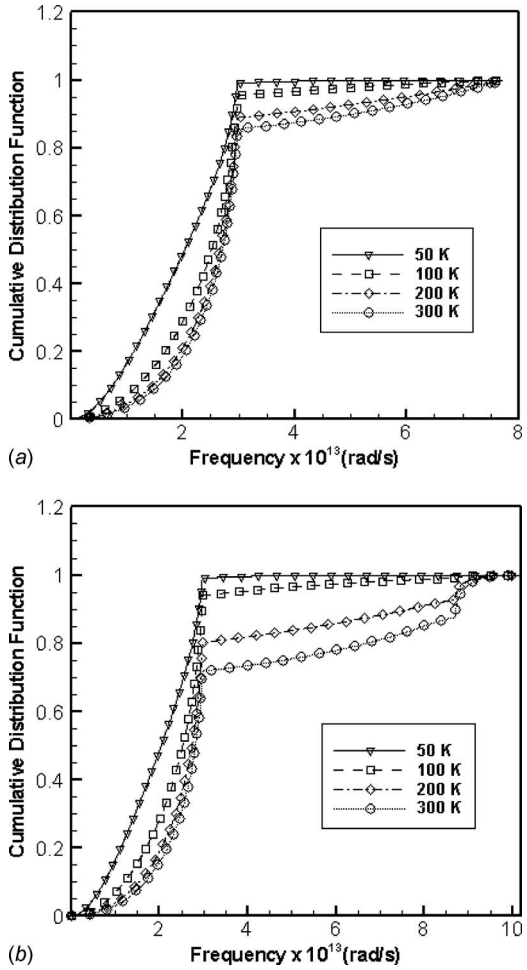

Fig. 4 Normalized cumulative distribution function: (*a*) without optical phonons and (*b*) with optical phonons

methods match almost exactly at high temperatures (300 K). This result is consistent with the fact that Holland's assumption of "near equilibrium" transport is more valid at 300 K than at 100 K and, therefore, the time-scales computed by Holland are expected to be more accurate at higher temperatures. Following these observations, the hybrid approach was deemed suitable for the computation of timescales of all phonon modes. Figure 6 shows the computed mean free paths of all four phonon modes, where the mean free path is defined as the product of the scattering time-scale and the group velocity. As shown in Fig. 6, the computed mean free paths for various phonon polarizations are of the same order of magnitude and follow similar behavior, as calculated by Henry and Chen [31] using molecular dynamics.

The thermal conductivity predicted by the MC simulations with and without the inclusion of optical phonons has been plotted in Figs. 7–9 for three different silicon film thicknesses. In each case, the experimental thermal conductivity values obtained by Asheghi [16] have also been plotted. It is clear that the inclusion of optical phonons does have an effect on the predicted thermal conductivity of silicon thin films. At low temperature (<50 K), thermal conductivity predictions are dominated by boundary scattering. Thus, inclusion of optical phonons has no impact on the predicted thermal conductivity. At intermediate temperatures (50–200 K), the occupation number of optical phonons is quite low. Few optical phonons are present, and they carry little energy themselves. However, they decrease the scattering time-scales of the acoustic phonons via collisions (Fig. 5(*a*)), thereby resulting in a decrease in the value of thermal conductivity. At high temperature

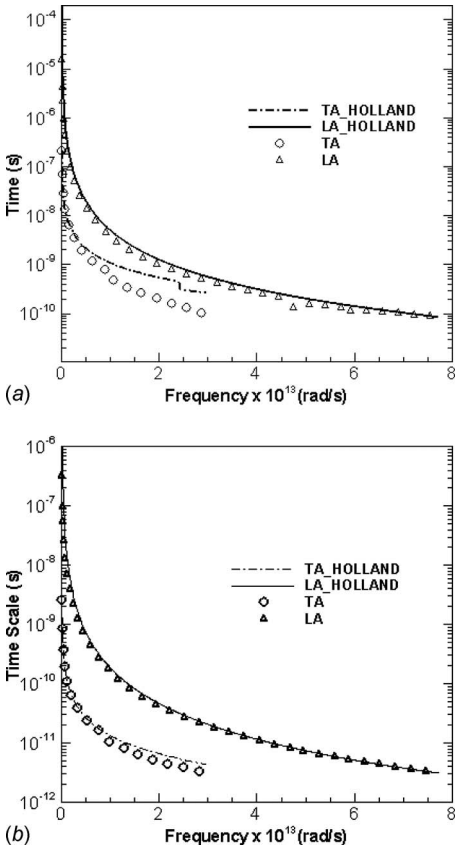

Fig. 5 Phonon-phonon scattering time-scales computed using the present hybrid approach and Holland's model at (*a*) 100 K and (*b*) 300 K

(>200 K), optical phonons are excited, and a significant fraction of the energy is carried by optical phonons themselves. Thus, their inclusion enhances the thermal conductivity and is evident in Fig. 7 for 300 K. It is also noteworthy that the high-temperature effect is more pronounced in thin films (Fig. 7) than in thick films (Fig. 9). For example, for a 3 μm film at 300 K, collisions between phonons are so abundant that it does not matter what phonons are considered in the simulation because transport is almost in the diffusion regime. The alteration of thermal conductivity shown by

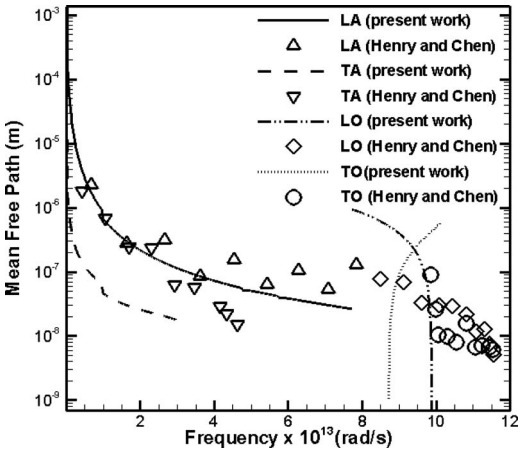

Fig. 6 Comparison of mean free paths of all four phonon modes at 300 K computed using the present hybrid approach, and data obtained using molecular dynamics by Henry and Chen [31]

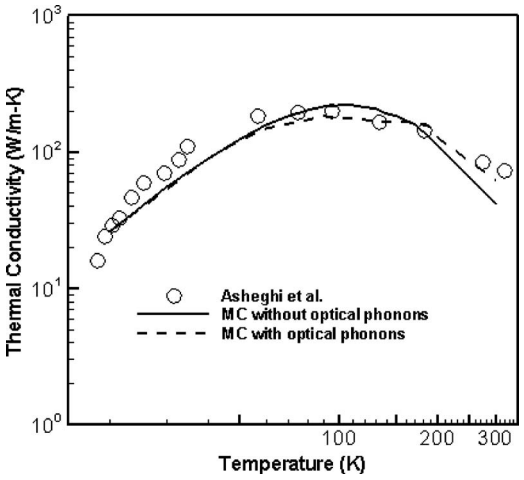

Fig. 7 Predicted and measured [16] through-plane thermal conductivity for a 0.42 μm silicon film

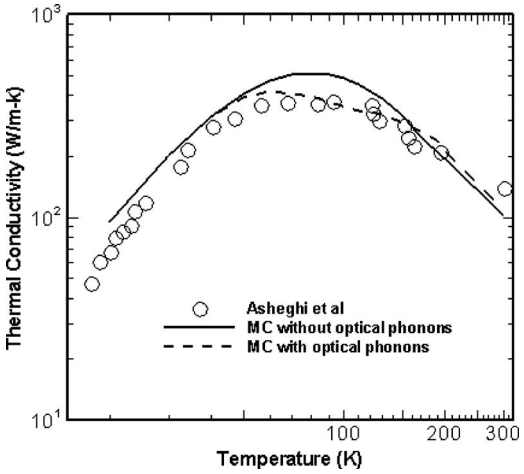

Fig. 8 Predicted and measured [16] through-plane thermal conductivity for a 1.6 μm silicon film

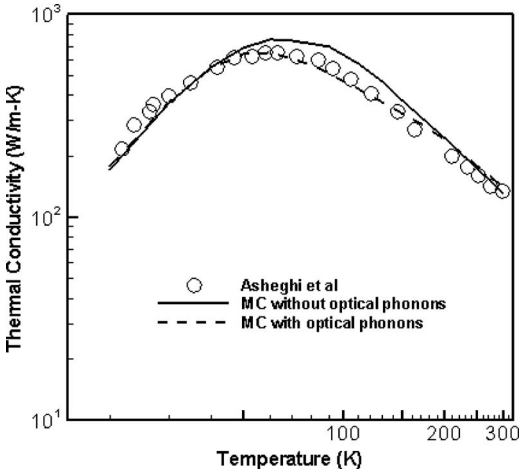

Fig. 9 Predicted and measured [16] through-plane thermal conductivity for a 3 μm silicon film

Table 3 Contribution (%) of various phonon modes toward thermal energy transport when both acoustic and optical modes are considered. Film thickness is 0.42 μm.

T (K)	LA	TA	LO	TO
100	30.00	66.50	2.60	0.83
200	42.15	41.00	12.16	4.69
300	43.27	30.87	19.21	6.65

these results discounts earlier assumptions [1] that optical phonons can be neglected for silicon thin-film thermal conductivity prediction.

Tables 3 and 4 show the contribution of the various phonon modes toward thermal transport. Different temperatures are considered, and the contributions with and without the inclusion of optical phonons are noted. The results shown are for a 0.42 μm film. The relative contribution of various phonon modes toward thermal energy transport has been discussed extensively in the past. Holland [18], Mazumder and Majumdar [1], and Hamilton and Parrot [32] predicted that TA phonons are the predominant carriers of thermal energy, whereas Ju and Goodson [23] and Henry and Chen [31] reported that LA phonons are the predominant carriers of thermal energy. In the present work, it is found that at lower temperatures TA phonons carry more energy than LA phonons. At 100 K, acoustic modes account for over 95% of the total thermal energy transport, the contribution of LA phonons being 30%. As the temperature increases, contribution of LA phonons increases. Above 200 K, the contribution of LA phonons has been found to be more than TA phonons. At 300 K, acoustic modes contribute about 75% of the total energy transport, of which about 30% is contributed by TA phonons. The contribution of optical modes has been found to be about 25% with the contribution of LO phonons accounting for about 19%. At stated earlier, these findings are for a 0.42 μm thick film. For thicker films, the contribution of optical phonons was found to be smaller. For example, for a 3 μm film at 300 K, the contribution of optical phonons was found to be about 10%. Recent studies by Goicochea et al. [33] also reported similar findings: The contribution of optical phonons decrease with increase in film thickness. For very thick films (bulk material), Henry and Chen [31] and Broido et al. [34] found the contribution of optical phonons to be about 5% at 300 K. The findings of the present study suggest that even though optical phonons have slower group velocities than LA or TA modes, their contribution to thermal energy transport could be significant, especially at room temperature and if the film is sufficiently thin. The results obtained in this work corroborate the results obtained by Wang [3], who suggested that one-fifth of the energy transfer rate in hot spots is contributed by optical phonons.

3.2 Numerical Issues. As discussed earlier, one of the critical parameters in the calculation of the through-plane thermal conductivity of thin films is the lateral dimension of the film. Ideally, the in-plane dimension of the film should be much larger than the film thickness (or through-plane dimension). Since boundary scattering dictates the thermal conductivity at low temperature (ballistic regime), it is necessary to calibrate the degree of specularity of the boundary to replicate the exact boundary resistance, as has been proposed by Mazumder and Majumdar [1] and used in subsequent studies [3,5]. If the chosen lateral dimension is small, the phonons will strike the boundary more often and a larger value of the degree of specularity will be necessary, than in a case where the lateral dimension of the film is large. The same idea is applicable to thin films treated using a 2D versus 3D computational domain. In a 2D simulation, only two lateral boundaries pose resistance to the phonons, while in a 3D simulation, four boundaries pose resistance to the phonons. Thus, the calibrated degree of specularity in 2D versus 3D is expected to be significantly different. For example, Mazumder and Majumdar [1] reported using a value of 0.6 for a 2D thin-film calculation, while Wang [3], in his finite-volume formulation, used a value of 0.4 for the specularity parameter, α. In the present study, we have performed both 2D and 3D simulations, with the lateral dimension being one-tenth of the film thickness, and it was found that the calibrated value of α is 0.885 for the 2D and 0.965 for the 3D case. When the lateral dimension is made equal to the film thickness, in 2D case, α changes to 0.14 whereas in the 3D case, it changes to 0.67. Figure 10 shows the comparison between the thermal conductivity predicted using a 2D versus a 3D computational domain for a silicon film 0.42 μm thick. It is evident that within the limits of statistical errors, the thermal conductivity predicted by the 2D calculation, as well as the 3D calculation is approximately the same. Also, the statistical variations in the thermal conductivity at different temperatures are also comparable for the two cases. Thus, it can be concluded that the lateral dimension of the film and/or the dimensionality of the computational domain are truly free parameters that, once calibrated, has no impact on the physical results or their statistical accuracy.

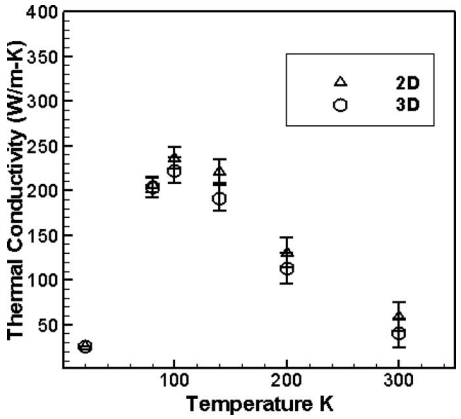

Fig. 10 Predicted thermal conductivity using 2D versus 3D computational domains

Figure 11 shows the CPU time comparisons for the 2D case versus the 3D case. The timing study has been carried out on a 2.13 GHz Dell Optiplex machine with approximately 50,000 phonons ($=N_{\text{prescribed}}$) simulated in each case. Although the 3D MC simulations are more expensive than the 2D case at low temperatures, at high temperatures (>100 K) the CPU time for both 2D and the 3D cases has been found to be within a few percent of each other. Therefore, for the usual operating range of semiconductor devices, there is not much disadvantage in performing 3D simulations. At low temperatures, phonon transport is dominated by ballistic motion, and there are more phonon-boundary interactions in the 3D case than in the 2D case. Since line-surface intersections are more expensive to compute in three dimensions than in two dimensions, the overall CPU is higher for 3D computations in the ballistic case. High temperature transport, on the other hand, is dominated by scattering events, which are point events and, therefore, the CPU times are not affected by the extra CPU

Table 4 Contribution (%) of various phonon modes toward thermal energy transport when only acoustic modes are considered. Film thickness is 0.42 μm.

T (K)	LA	TA
100	31.14	68.86
200	50.45	49.55
300	58.08	41.92

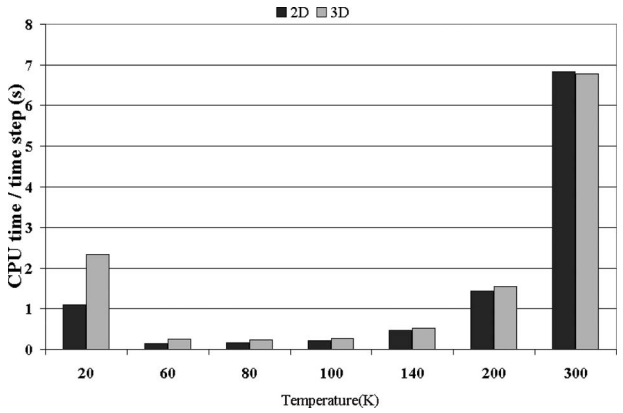

Fig. 11 CPU time taken for 2D versus 3D simulations with $N_{prescribed}$=50,000

time taken for phonon-boundary intersection calculations. In summary, these studies clearly show that the statistical accuracy is comparable in 2D versus 3D simulations, and the computational efficiency is also comparable above 100 K (scattering dominated regimes). These results imply that in strong contrast with deterministic methods for solving the BTE, stochastic methods for solving the BTE do not require any additional computational time in going from two dimensions to three dimensions. While these attributes of the Monte Carlo method, i.e., easy scalability to three dimensions, has been known, in general, these studies provide hard evidence to corroborate this general notion.

Having resolved the longstanding issue of the suitability of 2D versus 3D simulations, we proceeded to carefully analyze the statistical errors as a function of the prescribed number of stochastic samples, $N_{prescribed}$. Table 5 shows the statistical noise or variation in the thermal conductivity for a 0.42 μm thin film at 80 K. The fluxes at the left (cold) and the right (hot) boundaries have been plotted in Fig. 12 for two different values of $N_{prescribed}$. With increasing time, the two flux values converge to the same value, as expected for a one-dimensional film at steady state. The fluctuations in the fluxes are associated with probability driven events in the MC calculation and is, therefore, directly related to the number of stochastic samples traced. By increasing the value of $N_{prescribed}$ from 50,000 to 500,000, the standard deviation in the flux decreases from 22% to about 7%. On the other hand, increasing the value of $N_{prescribed}$ from 50,000 to 500,000 increases the computational cost 8 times. It is worth noting that once the system reaches a statistically steady state, a time average of the data is equivalent to an ensemble average (i.e., a case where the simulation is repeated with different initial random number seeds). Thus, to compute the thermal conductivity at steady state, one can use time averaged values of the fluxes rather than ensemble averaged values in order to save computational time. Figure 13 shows the time averaged flux values over ten time steps for $N_{prescribed}$ =50,000. Time averaging over ten time steps reduces the standard deviation in the statistical noise from 22% to about 7%. Worth noting is the similarity in the flux data shown in Figs. 12(*b*) and

Table 5 Statistical noise in the thermal conductivity for both 2D and 3D calculations at 80 K as a function of sample size

	2D	3D
$N_{prescribed}$	σ/κ (%)	σ/κ (%)
50,000	22.39824	23.50699
100,000	15.74578	16.45898
500,000	7.165036	7.487463

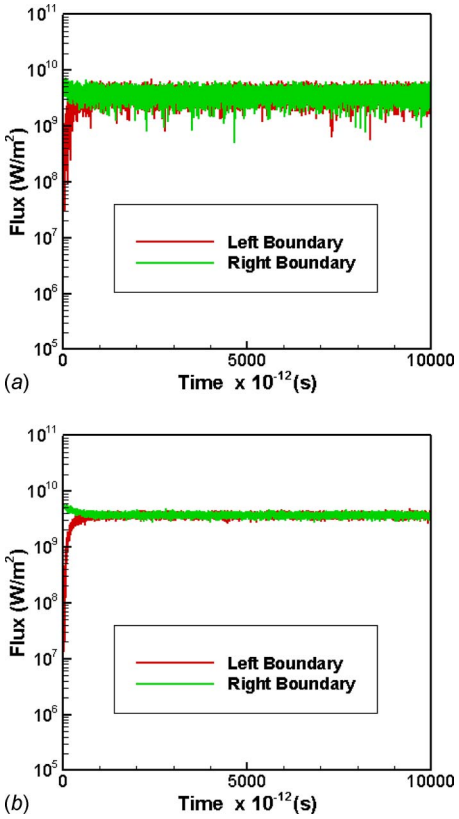

Fig. 12 Time-dependent energy flux at the boundaries for a 0.42 μm thin film with (*a*) $N_{prescribed}$=50,000 and (*b*) $N_{prescribed}$ =500,000

13. One other important finding is that the standard deviation in the flux computed at the boundaries is about the same in the 2D and the 3D case—further corroborating the earlier claim that 2D and 3D computations have the same statistical accuracy as long as $N_{prescribed}$ is the same.

The statistical variation in the flux computed at the boundaries is even more dramatic in the diffusive limit (300 K). Table 6 shows the variation in the thermal conductivity for different values of $N_{prescribed}$ at 300 K. As can be seen, the noise is much higher in this case even when a very large value of $N_{prescribed}$ is used. This is because at higher temperature there are numerous scattering events, all of which are probability driven and involve drawing of several random numbers. This necessitates the time

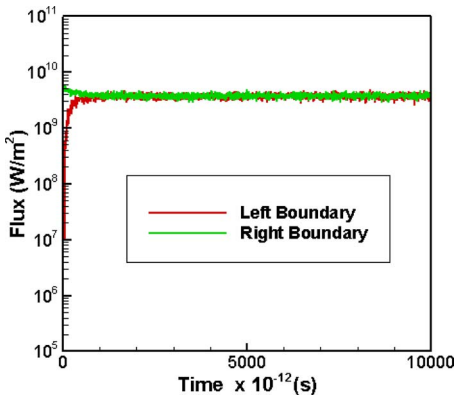

Fig. 13 Time averaged energy flux (average of data presented in Fig. 12(*a*)) at the boundaries for a 0.42 μm thin film computed using $N_{prescribed}$=50,000

Table 6 Statistical noise in the thermal conductivity for 2D calculations at 300 K as a function of sample size

$N_{\text{prescribed}}$	κ (W/m K)	σ/κ (%)
50,000	57.80	187.0303
100,000	52.621	149.245
500,000	55.379	62.57

averaging of the data over a very large number of time steps (~1000) in order to extract the steady-state values. Figure 14(*a*) shows the variation in the flux at the boundaries for a 0.42 μm film at 300 K with $N_{\text{prescribed}}$=50,000. Figure 14(*b*) shows the same flux data averaged over 1000 time steps. It is quite evident that time averaging reduces the noise in the flux data and allows for steady-state predictions to be made using a smaller value of $N_{\text{prescribed}}$. For transient calculations, however, time averaging cannot be used and a higher value of $N_{\text{prescribed}}$ has to be used. The above studies demonstrate that for steady-state calculations, time averaging of the statistically stationary solution is a means to avoid numerous simulations to obtain ensemble averaged data.

4 Summary and Conclusions

The role of various phonon polarizations and modes in thermal energy transport has been investigated by solving the BTE for phonons using the Monte Carlo method between 20 K and 300 K in silicon thin films. A methodology for calculating the lifetimes of various phonon polarizations, including optical phonons, has been implemented. This methodology is an extension of the ideas proposed by Holland [18] and by Han and Klemens [17]. It highlights the role of optical phonons in thermal energy transport and makes a compelling case for their inclusion in predicting silicon thin-film thermal conductivity. Numerical predictions with the inclusion of optical phonons produce results that match experimental results better than when only acoustic modes are considered. Below 50 K, thermal conductivity predictions are unaltered by the inclusion of optical phonons. Between 50 K and 200 K, the inclusion of optical phonons decrease the predicted thermal conductivity, while above 200 K the inclusion of optical phonons increases the predicted thermal conductivity. This behavior was found to be stronger in thin films than in films that are relatively thick. It is also found that at temperatures below 200 K, TA phonons carry more energy than LA phonons, whereas at higher temperatures LA phonons are dominant carriers of thermal energy. The optical phonons alter thermal transport in two ways. At intermediate temperature (<200 K), they slow down the acoustic phonons through additional three-phonon interactions. At high temperature (>200 K), they not only alter the scattering time-scales of the acoustic phonons, but also carry 10–25% of the energy themselves. Overall, their role was found to be most significant at high temperature and for films that are thin.

Several numerical issues pertinent to predicting through-plane thermal conductivity of semiconductor thin films have been investigated and discussed. First, it is found that using 2D versus 3D computational domain is comparable from both accuracy and computational efficiency standpoint except in ballistic regimes (low temperature) where 2D simulations are computationally slightly more efficient. This finding has strong implications in terms of the feasibility of using MC calculations for practical 3D device structures. The statistical errors were carefully analyzed. It is found that statistical errors are high in the diffusion limit where the number of probability driven events is large. It is shown that for steady-state calculations, time averaging of the statistically stationary data can be used to reduce statistical noise and can result in tremendous computational savings.

Future research will focus on removing the assumptions made in calculation of phonon lifetimes by the direct implementation of the energy and momentum conservation laws [3] and the treatment of the anisotropic Brillouin zone. Efforts are also underway in combining deterministic and hybrid methods to address the two disparate regimes of transport, namely, ballistic and diffusive regimes.

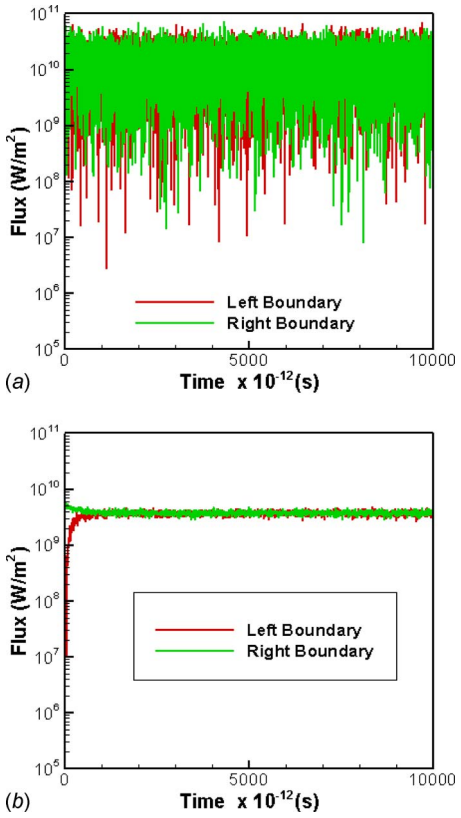

Fig. 14 Energy flux at the boundaries for a 0.42 μm film with (*a*) $N_{\text{prescribed}}$=50,000 and (*b*) flux time averaged over 1000 time steps

Acknowledgment

Financial support for this work was provided by the Department of Energy's Basic Energy Science Program through Grant No. DE-FG02-06ER46330.

Nomenclature

f = distribution function
f_0 = equilibrium distribution function
t = time (s)
τ = overall relaxation time (s)
$\mathbf{K}$ = wave vector (m^{-1})
$k=|\mathbf{K}|$ = magnitude of wave vector (m^{-1})
$\mathbf{b}$ = reciprocal lattice vector (m^{-1})
B_L = constant used in relaxation time calculation
B_{TN} = constant used in relaxation time calculation
B_{TU} = constant used in relaxation time calculation
$\hbar$ = Dirac constant = 1.0546×10^{-34} (m^2 kg s^{-1})
k_B = Boltzmann constant = 1.381×10^{-23} (m^2 kg s^{-2} K^{-1})
r_c = effective radius (m)
p = phonon polarization
a = lattice constant (m)
N_b = number of spectral (frequency) bins
N_{actual} = total number of phonons per unit volume
$N_{\text{prescribed}}$ = number of phonons traced

v_s, c = constants used for calculating phonon dispersion
W = weight factor
P_{scat} = probability of scattering of a phonon
R_{scat} = random number between 0 and 1
Δt = time step (s)
T = thermodynamic temperature (K)

Greek

α = degree of specularity
$\boldsymbol{v}_g$ = phonon group velocity vector (m/s)
v_g = magnitude of phonon group velocity (m/s)
v_{ph} = phase velocity (m/s)
τ_{ij} = relaxation time for interaction between i and j (s)
χ = degeneracy of each phonon polarization
γ = Gruneisen parameter
ρ = density (kg/m^3)
τ_{NU} = combined relaxation time for N and U scattering (s)
τ_N = relaxation time for Normal scattering (s)
τ_U = relaxation time for Umklapp scattering (s)
ω = angular frequency (rad/s)
$\omega_{0,i}$ = central frequency of the ith spectral bin (rad/s)
$\Delta\omega$ = bandwidth of a spectral interval (rad/s)
κ = thermal conductivity (W/m K)
σ = standard deviation in thermal conductivity (W/m K)

References

[1] Mazumder, S., and Majumdar, A., 2001, "Monte Carlo Study of Phonon Transport in Solid Thin Films Including Dispersion and Polarization," ASME J. Heat Transfer, **123**, pp. 749–759.
[2] Lacroix, D., and Joulain, K., and Lemonnier, D., 2005, "Monte Carlo Transient Phonon Transport in Silicon and Germanium at Nanoscale," Phys. Rev. B, **72**, p. 064305.
[3] Wang, T., 2007, "Sub-Micron Thermal Transport in Ultra-Scaled Metal-Oxide Semiconductor Devices," Ph.D. thesis, School of Mechanical Engineering, Purdue University, West Lafayette, IN.
[4] Narumanchi, S. V. J., Murthy, J. Y., and Amon, C. H., 2004, "Submicron Heat Transport Model in Silicon Accounting for Phonon Dispersion and Polarization," ASME J. Heat Transfer, **126**, pp. 946–955.
[5] Narumanchi, S. V. J., 2003, "Simulation of Heat Transport in Sub-Micron Conduction," Ph.D. thesis, Department of Mechanical Engineering, Carnegie Mellon University, Pittsburgh, PA.
[6] Murthy, J. Y., Narumanchi, S. V. J., Pascual-Gutierrez, J. A., Wang, T., Ni, C., and Mathur, S. R., 2005, "Review of Multi-Scale Simulation in Sub-Micron Heat Transfer," Int. J. Multiscale Comp. Eng., **3**, pp. 5–32.
[7] Sinha, S., and Goodson, K. E., 2005, "Review: Multiscale Thermal Modeling in Nanoelectronics," Int. J. Multiscale Comp. Eng., **3**, pp. 107–133.
[8] Cahill, D. G., Ford, W. K., Goodson, K. E., Mahan, G. D., Majumdar, A., Maris, H. J., Merlin, R., and Phillpot, S. R., 2003, "Nanoscale Thermal Transport," J. Appl. Phys., **93**, pp. 793–818.
[9] Peterson, R. B., 1994, "Direct Simulation of Phonon-Mediated Heat Transfer in a Debye Crystal," ASME J. Heat Transfer, **116**, pp. 815–822.
[10] Jeng, M. S., Yang, R. G., Song, D., and Chen, G., 2008, "Modeling the Thermal Conductivity and Phonon Transport in Nanoparticle Composites Using Monte Carlo Simulation," ASME J. Heat Transfer, **130**(4), p. 042410.
[11] Randrianalisoa, J., and Baillis, D., 2008, "Monte Carlo Simulation of Cross-Plane Thermal Conductivity of Nanostructured Porous Silicon Films," J. Appl. Phys., **103**(5), p. 053502.
[12] Randrianalisoa, J., and Baillis, D., 2008, "Monte Carlo Simulation of Steady-State Microscale Phonon Heat Transport," ASME J. Heat Transfer, **130**(7), p. 072404.
[13] Heino, P., 2007, "Thermal Conduction Simulations in the Nanoscale," J. Comput. Theor. Nanosci., **4**(5), pp. 896–927.
[14] Kittel, C., 1996, *Introduction to Solid State Physics*, Wiley, New York.
[15] Kazan, M., Pereira, S., Coutinho, J., Correia, M. R., and Masri, P., 2008, "Role of Optical Phonon in Ge Thermal Conductivity," Appl. Phys. Lett., **92**(21), p. 211903.
[16] Asheghi, M., 2000, "Thermal Transport Properties of Silicon Films," Ph.D. thesis, Stanford University, Standford, CA.
[17] Han, Y. J., and Klemens, P. G., 1993, "Anharmonic Thermal Resistivity of Dielectric Crystals at Low Temperature," Phys. Rev. B, **48**(9), pp. 6033–6042.
[18] Holland, M. G., 1963, "Analysis of Lattice Thermal Conductivity," Phys. Rev., **132**(6), pp. 2461–2471.
[19] Chen, Y., Li, D., Lukes, J. R., and Majumdar, A., 2005, "Monte Carlo Simulation of Silicon Nanowire Thermal Conductivity," ASME J. Heat Transfer, **127**, pp. 1129–1137.
[20] Aubry, S., Kimmer, C., Schelling, P., Piekos, E., and Phinney, L., 2007, "Phonon-Mediated Thermal Transport in Micro-Systems," Proceedings of the Materials Research Society Fall 2007 Meeting, Nov. 28–29, Boston, MA, Paper No. EE1.4.
[21] Majumdar, A., 1997, "Microscale Energy Transport in Solids," *Microscale Energy Transfer* (Series in Chemical and Mechanical Engineering), C. L. Tien, A. Majumdar, and F. Gerner, eds., Taylor & Francis, London, pp. 1–95.
[22] Klemens, P. G., 1969, "Theory of Thermal Conductivity of Solids," *Thermal Conductivity*, Vol. 1, Academic Press, London, pp. 1–68.
[23] Ju, Y. S., and Goodson, K. E., 1999, "Phonon Scattering in Silicon Films With Thickness of Order 100 nm," Appl. Phys. Lett., **74**(20), pp. 3005–3007.
[24] Brockhouse, B. N., 1959, "Lattice Vibrations in Silicon and Germanium," Phys. Rev. Lett., **2**(6), pp. 256–258.
[25] Dolling, G., 1963, "Lattice Vibrations in Crystals With the Diamond Structure," *Symposium* on Inelastic Scattering of Neutrons in Solids and Liquids.
[26] Ghatak, A. K., and Kothari, L. S., 1972, *An Introduction to Lattice Dynamics*, Addison-Wesley, London.
[27] Ziman, J. M., 1960, *Electrons and Phonons*, Oxford University Press, London, UK.
[28] Chung, J. D., McGaughey, A. J. H., and Kaviany, M., 2004, "Role of Phonon Dispersion in Lattice Thermal Conductivity Analysis," ASME J. Heat Transfer, **126**, pp. 376–380.
[29] Pop, E., 2004, "Self-Heating and Scaling of Thin Body Transistors," Ph.D. thesis, Department of Electrical Engineering, Stanford University, Stanford, CA.
[30] Pop, E., Dutton, R. W., and Goodson, K. E., 2004, "Analytic Band Monte Carlo Model for Electron Transport in Si Including Acoustic and Optical Phonon Dispersion," J. Appl. Phys., **96**(9), pp. 4998–5005.
[31] Henry, A. S., and Chen, G., 2008, "Spectral Phonon Transport Properties of Silicon Based on Molecular Dynamics Simulations and Lattice Dynamics," J. Comput. Theor. Nanosci., **5**(2), pp. 141–152.
[32] Hamilton, R. A. H., and Parrott, J. E., 1969, "Variational Calculation of Thermal Conductivity of Germanium," Phys. Rev., **178**(3), pp. 1284–1292.
[33] Goicochea, J. V., Madrid, M., and Amon, C., 2008, "Hierarchical Modeling of Heat Transfer in Silicon-Based Electronic Devices," 11th Intersociety Conference on Thermal and Thermomechanical Phenomena in Electronic Systems, ITHERM 2008, Orlando, FL, pp. 1006–1017.
[34] Broido, D. A., Malorny, M., Birner, G., and Mingo, N., 2007, "Intrinsic Lattice Thermal Conductivity of Semiconductors From First Principles," Appl. Phys. Lett., **91**, p. 231922.

Design and Test of Carbon Nanotube Biwick Structure for High-Heat-Flux Phase Change Heat Transfer

Qingjun Cai
e-mail: qcai@teledyne.com

Chung-Lung Chen

Teledyne Scientific & Imaging,
1049 Camino Dos Rios,
Thousand Oaks, CA 91360

With the increase in power consumption in compact electronic devices, passive heat transfer cooling technologies with high-heat-flux characteristics are highly desired in microelectronic industries. Carbon nanotube (CNT) clusters have high thermal conductivity, nanopore size, and large porosity and can be used as wick structure in a heat pipe heatspreader to provide high capillary force for high-heat-flux thermal management. This paper reports investigations of high-heat-flux cooling of the CNT biwick structure, associated with the development of a reliable thermometer and high performance heater. The thermometer/heater is a 100-nm-thick and 600 μm wide Z-shaped platinum wire resistor, fabricated on a thermally oxidized silicon substrate of a CNT sample to heat a 2 $\times$2 mm^2 wick area. As a heater, it provides a direct heating effect without a thermal interface and is capable of high-temperature operation over 800°C. As a thermometer, reliable temperature measurement is achieved by calibrating the resistance variation versus temperature after the annealing process is applied. The thermally oxidized layer on the silicon substrate is around 1-μm-thick and pinhole-free, which ensures the platinum thermometer/heater from the severe CNT growth environments without any electrical leakage. For high-heat-flux cooling, the CNT biwick structure is composed of 250 μm tall and 100 μm wide stripelike CNT clusters with 50 μm stripe-spacers. Using 1 $\times$1 cm^2 CNT biwick samples, experiments are completed in both open and saturated environments. Experimental results demonstrate 600 W/cm^2 heat transfer capacity and good thermal and mass transport characteristics in the nanolevel porous media.
[DOI: 10.1115/1.4000469]

Keywords: thermometer, carbon nanotube, wick structure

1 Introduction

In new-generation microelectronic systems, the increase in power dissipation requires compact, lightweight, thermally suited, high-heat-flux-capable, and passive cooling technologies to solve the die-level/chip-level thermal management issues. Heat pipe is an extensively used cooling technology in electronic industry. For high-heat-flux cooling, concept of biwick structure was presented to enhance liquid supply and vapor ventilation and to overcome both the capillary and boiling limitations [1]. In the past decade, numerous researches have been conducted to gain deep understanding of phase change mechanism and critical parameters associated with biwick designs [2–7]. Using microbiwick structure sintered by spherical copper powders, 500 W/cm^2 high-heat-flux phase change has been demonstrated by Semenic et al. [8]. Reilly et al. [9] achieved 650 W/cm^2 cooling by introducing an additional monoporous layer into the 800-μm-thick biwick. For higher heat flux cooling, it is necessary to have smaller pore size to supply sufficient liquid to the evaporation area and higher material thermal conductivity to reduce the temperature difference across wick structure/the superheat of boiling. In addition, when operating at higher heat flux cooling, high-speed vapor flow in large pore needs to be optimized so that vapor would not be trapped within the wick structure and lead to dryout.

Different from traditional carbon materials, carbon nanotube (CNT) [10] clusters have nanolevel pore size, large porosity (>95%), and high longitudinal thermal conductivity (>2000 W/m K for each individual CNT) [11], and it can be a good material to make wick structure in a heat pipe. Moreover, CNT can be directly grown on the silicon substrate with height of over 1 mm, which makes direct-cool of silicon-based electronic devices possible and manufacture of silicon-based high-heat-flux heat spreader feasible. In our previous research [12], we presented a stripelike CNT biwick structure for rapid vapor ventilation and experimentally demonstrated a high-heat-flux capability of 400 W/cm^2. However, due to the thickness and poor thermal conductivity of the ceramic heater substrate and the large contact thermal interface, heater temperature increases rapidly with the rise of heat flux. The existence of the thermal interface also causes heat loss and increases the difficulty of precisely measuring the temperature difference between the CNT wick structure and the silicon substrate, especially at high heat flux. Development of microelectromechanical system (MEMS) technologies provides a mature solution to make an interface-free/high-heat-flux-capable heater and thermometer integrated with CNT samples. During the past decade, based on resistance temperature detector (RTD) principles, metallic film has been deposited on a semiconductor substrate and used as both an electrical heater and thermometer. A number of papers have been published to report the technology and applications [13–16]. However, the technology remains a challenge in high-temperature applications in which thermal stress (caused by difference in coefficients of thermal expansion between the metal heater/thermometer and substrate material) may break the adhesion. In addition, fabrication related material defects might introduce a large temperature measurement error [17].

In this paper, we combine MEMS technology with the CNT

Contributed by the Heat Transfer Division of ASME for publication in the JOURNAL OF HEAT TRANSFER. Manuscript received June 19, 2009; final manuscript revised: September 23, 2009; published online March 9, 2010. Assoc. Editor: R. D. Tzou.

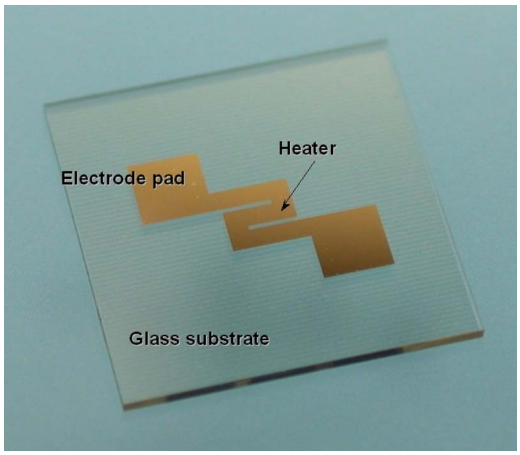

Fig. 1 Platinum heater/thermometer on a glass die

synthesis process to develop thermometers/heaters to integrate with biwick samples without introducing any thermal interface. The thermometers/heaters exhibit good temperature measurement repeatability and accuracy after the annealing process is applied, and survive high-operation-temperature tests at over 800°C. Using these samples, high-heat-flux tests of the CNT biwick structure are conducted in both open and saturated environments. The experimental results demonstrate a phase change heat transfer as high as 600 W/cm^2 on 250-μm-thick CNT wick structures.

2 Development of Thermometer and Heater

Due to the effect of temperature on resistance, a platinum resistor can work as both a thermometer and a heater. As a thermometer, platinum is a remarkable material for temperature measurement. In various forms, it operates over a range of −260°C to 960°C, with accuracies approaching mK. It can be cycled repeatedly over hundreds of °C and still maintain the best temperature resistance characteristics. As a heater, the platinum material has a very high melting point (1772°C) and can be used in high-temperature experiments in microscale heat transfer areas.

Development of platinum resistors involves two types of substrates, glass and surface-oxidized silicon. Samples using the former substrate are made for visualization in the maximum temperature calibration. The latter substrate has higher thermal conductivity and is used for high-heat-flux experimental tests. The platinum resistor on a glass substrate is fabricated by the MEMS e-beam evaporation process. As shown in Fig. 1, a Z-shaped platinum circuit is made in the center of a 500-μm-thick and 1 $\times 1$ cm^2 die (glass 7740), the total heating area being 2 $\times 2$ mm^2. The thickness of platinum layer varies in the range from 10 nm to 200 nm, with a 0.5 nm titanium adhesion layer underneath. The total resistance varies from 10 Ω to 300 Ω. At the diagonal ends of the resistor, two 2×2 mm^2 pads are created for electrode connections. To bond electrodes and avoid self-heating of the electrical pads, a layer of solder material is applied and covers the pads. From the effect of temperature on resistance, the platinum wire resistance can be described as

$$R(T) = R(T_0)(1 + \alpha \Delta T) \tag{1}$$

where α is a linear temperature coefficient of electrical resistance, T_0 is the reference temperature, T is the temperature at which the resistance is measured, and ΔT is the difference between T and T_0. Due to the lattice defects (process related), the $R-T$ performance of platinum resistor is different with solid platinum metal. Even after the annealing process, temperature coefficients can be altered during CNT synthesis process and appear differently among samples. Each sample must be calibrated (resistance versus temperature) before actual measurements.

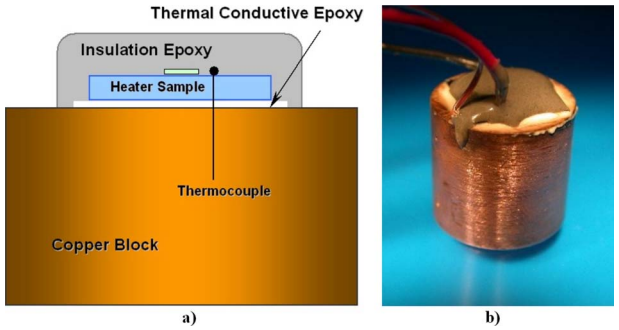

Fig. 2 Calibration of resistance versus temperature of the platinum thermometer: (*a*) schematic diagram and (*b*) sample in calibration

The calibration setup for thermometer/heater development purpose (distinct with experimental measurements of CNT biwick structure) is shown in Figs. 2(*a*) and 2(*b*). A glass sample heater/thermometer is epoxy bonded to a cylindrical copper block. The large thermal mass and high thermal conductivity of the copper block are able to provide steady/uniform heating on the calibrated sample and an identical temperature between a reference thermometer and a platinum resistor. Meanwhile, to prevent heat loss induced temperature differences on the calibrated sample, an approximately 2-mm-thick low thermal conductivity epoxy material covers the top of the sample. Two electrical power leads are connected to the electrode pads of the platinum circuit. In theory, the platinum thermometer can achieve good accuracy in measurement of high temperatures. But for the application discussed in this paper, 0.5°C measurement accuracy is sufficient for high-heat-flux heat transfer investigations. Consequently, an E-type thermocouple associated with an Agilent 34970A data acquisition is chosen as the reference thermometer, having a reading measurement accuracy of 0.1°C. The system level accuracy would be lowered to around 0.5°C. Resistance measurement is conducted through an HP 34401A multimeter by using the four-wire measurement model. The measurement accuracy is in the $\mu\Omega$ range.

The temperature coefficient calibration is first conducted right after the heater/thermometer samples are fabricated by MEMS process. The sample resistance is approximately 350 Ω at room temperature. As the data plotted in Fig. 3, the hysteresis and reduced total resistance appear in two thermal cycles (1 cycle is specified as a whole process of heating up and cooling down). The temperature difference at the resistance 380 Ω reaches 8°C. The hysteresis and calibration deviation come from the sample fabrication process. Because the platinum circuit is fabricated with the e-beam evaporation process, the metal layer is porous with pinholes. Different from the solid platinum material, the porous and

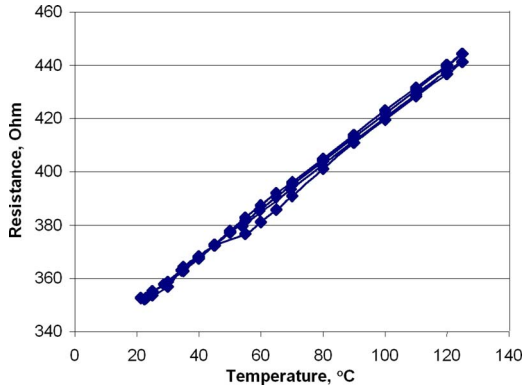

Fig. 3 Resistance versus temperature before annealing

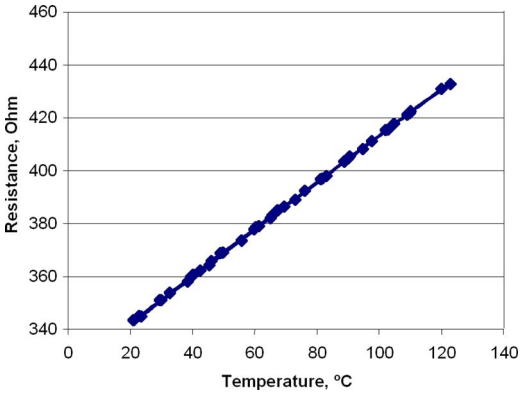

Fig. 4 Resistance versus temperature after annealing

thin layer has numerous lattice defects that introduce an impurity electrical resistance to the resistor. While temperature is elevated in an annealing process, the disorder lattice structure will adjust itself and therefore lead to permanent change (independent of heating sequence) on both electrical impurity resistance (absolute resistance value at reference temperature) and temperature coefficients (curve slope).

The annealing temperature is set at 170°C for 10 min. Since calibrations will be conducted below 120°C, such an annealing temperature is high enough for eliminating the resistance abnormal variation and hysteresis. Multiple experiments prove that good measurement repeatability of the platinum thermometer can be achieved as long as the annealing temperature is higher than the maximum testing temperature. As shown in Fig. 4, after the annealing process, all data collected from 2 cycles is overlapped. Resistance variation with temperature is repeatable and linear. Measurement deviation is less than 0.5°C at each fixed resistance value.

When the resistor is operating at high temperature, thermal stress (caused by different thermal expansion coefficient and temperature between the metal and substrate) could build up in the platinum metal layer. After reaching a maximum value, the metal layer will detach from the substrate and burn the resistor. The burning resistor can be visualized from the other side of transparent substrate (glass). Since the platinum heater/thermometer will be used in high-heat-flux experiments and experience 670°C high-temperature CNT growth process, quantitatively defining the maximum operating temperature is critical for evaluating performance of the thermometer/heater in this research.

Using a glass substrate, the experimental measurements of the maximum operation temperature are conducted by heating the sample element at room temperature under water (functioning as a coolant). An experimental schematic diagram is plotted in Fig. 5.

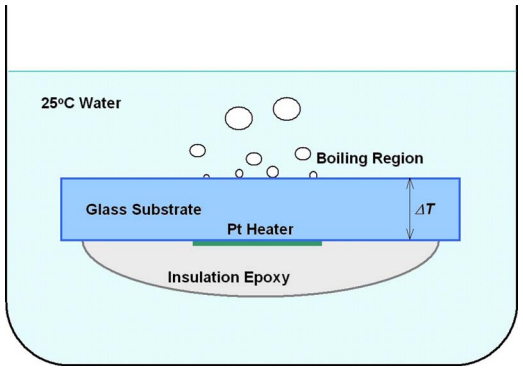

Fig. 5 Test schematic for the maximum operating temperature of the platinum thermometer/heater

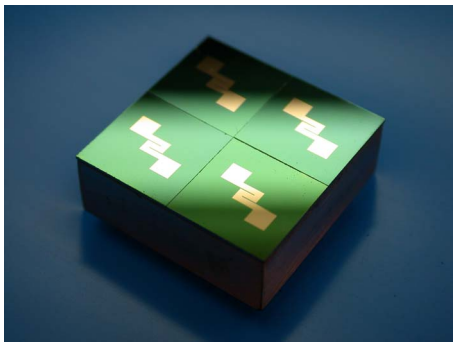

Fig. 6 Silicon substrate samples integrated with the platinum thermometer/heater

We use two approaches to calculate and estimate the maximum operating temperature. The first one is to calibrate temperature coefficient based on the correlation of Eq. (1). Once the resistance variation versus temperature is obtained, the maximum operating temperature can be decided by measuring the resistance at the resistor burning point. The second approach takes advantage of the pool boiling theory from which the boiling surface temperature is inferred in the range 120–130°C at the critical heat flux (CHF)/burning point. Because of the poor thermal conductivity of glass, the in-plane heat spreading is negligible. We can therefore calculate the temperature difference (between the boiling surface and heater) to estimate the resistor temperature based on the 1D heat transfer assumption.

In multiple sample tests, the platinum resistor works well under 800°C. With further increase in input power, the resistor is thermally damaged at 850°C and 175 W/cm^2 heat flux (subcool included) at which point the metal layer detaches from the glass substrate and burns. The resistance rapidly increases, followed by interruption of the circuit. The experimental results indicate the platinum resistor heater can withstand CNT growth temperature (670°C) and high-heat-flux experiments.

3 CNT Biwick Sample Preparations

For high-heat-flux phase change, the capillary limitation is the major bottleneck in delivering sufficient operating liquid to the heating area. The nanosize pores in the CNT biwick structure can provide ultrahigh capillary pressure to overcome high flow resistance in the porous wick structure; meanwhile, the large CNT surface area can significantly increase the total meniscuses, thin-film evaporation area, and evaporation efficiency.

Development of CNT biwick structure sample starts with fabrication of the sample substrate (integrated with a heater/thermometer). For the two aforementioned materials, the glass-type substrate samples are not able to withstand the CNT synthesis temperature (chemical vapor deposition (CVD) 670°C). It deforms and twists during growth, which destroys the catalyst distribution and fails CNT growth eventually. The silicon has a much higher softening point (1365°C) and can bear the high-temperature process of CNT growth. The silicon material also has high thermal conductivity and will significantly lower the heater temperature in high-heat-flux experiments. However, silicon is an electrical semiconductive material. The platinum circuit created on the silicon substrate must be electrically insulated. A 1-μm-thick and pinhole-free SiO_2 layer is therefore created by thermally oxidizing the silicon substrate. Platinum circuit is deposited on the surface of SiO_2 layer afterward. In the later CNT synthesis process, the pinhole-free SiO_2 layer also acts as a shield to prevent amorphous carbon from invading and short circuiting. Limited by the power supply voltage, the total resistance of the platinum layer is lower, within the range 10–40 Ω, in actual high-heat-flux tests. Figure 6 shows the silicon substrate samples

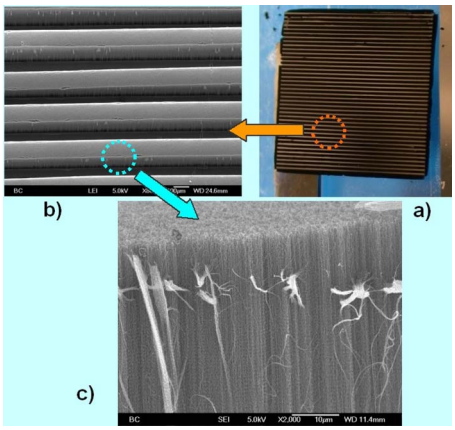

Fig. 7 Development of CNT biwick structure

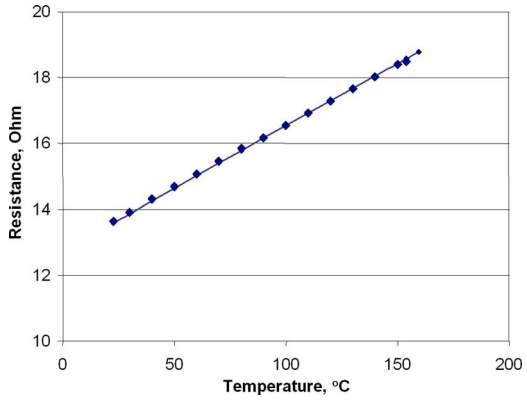

Fig. 8 The *R−T* calibration result of the platinum thermometer/heater for high-heat-flux tests

integrated with heater/thermometer ready for CNT synthesis process.

After the platinum resistors are made on one side of the double polished silicon wafer, the CNT biwick structure development process will be initiated on the other side of the wafer. The process is started with a lithographic process to define various CNT growth patterns, followed by sputtering of the catalyst coating (Fe, Al, and Fe, 10 nm in total) and completed by photoresist lift-off and cleaning processes. Before CNT growth, the silicon wafer is diced into 1×1 cm^2 samples to allow chemical synthesis in a small growth chamber. The following CNT synthesis process is comprised of three main steps [4]. The first step is to anneal the catalyst film at elevated temperature and in a hydrogen environment. A horizontal 1 in. (2.54 cm) inner diameter quartz tube furnace is employed to complete this step. The result of the annealing process is to generate nanocatalyst particles on the surface of silicon substrate. The second step is to grow CNT using a thermal CVD process. Immediately after annealing, the furnace is flushed by flowing gases of hydrogen and C_2H_4 at ambient pressure. At temperature 670°C, carbon atoms dissolve on metal catalyst particles and then precipitate, leading to the formation of tubular carbon solid. CNT growth lasts minutes, depending on growth height. After growth and naturally cooling down, the CNT samples will show hydrophobic properties when soaked in water. The third step is an acid-treatment process to make CNT hydrophilic. In this process, the CNT sample is immersed in 2% hydrochloric acid (HCl) solution for 5 min, then rinsed with de-ionized (DI) water several times to remove the residuals, and completed by air-dry.

The 1×1 cm^2 CNT biwick structure/patterned CNT growth is shown in Figs. 7(*a*)–7(*c*). This sample is approximately 250 μm high, on average. The individual CNT diameter varies in a range from a few nanometers to 20 nm [18]. The parallel CNT stripes are 100 μm wide and 50 μm apart. When operating at high heat flux, the stripelike CNT clusters (shown in Figs. 7(*b*) and 7(*c*)) function as the first order/nanowick structure and provide high capillary pressure and supply liquid for meniscus evaporation. Spacing between every two CNT stripes (shown in Fig. 7(*b*)) is the second order/microwick structure, which acts as a liquid supply (low resistance) and vapor ventilation channels when nucleation boiling begins. As in the calibration experiments, the synthesized CNT biwick structure sample undergoes electrode soldering and epoxy thermal/electrical insulation processes. An E-type thermocouple is mounted on one of electrode pads, so the in-plane heat spreading effect can be monitored.

Because the CNT synthesis is a high-temperature process, it can be looked as an annealing process for platinum thermometers/heaters. After CNT is synthesized on silicon substrate, calibrations are conducted in a temperature-controlled oven. The calibration result of the temperature coefficient of the Pt resistor sample is plotted in Fig. 8. A series of data indicates good repeatability of resistance variation versus temperature. Compared with the solid platinum temperature coefficient, the metal lattice disorder causes additional resistance that lifts the whole line up around 2.0 Ω.

4 Experimental System Setup

High-heat-flux experiments are conducted in both open and saturated environments. The experimental system comprises of a testing subsystem and a data processing subsystem.

The testing subsystem includes a Sorensen DCS 20-50 power supply, a Neslab chiller, a stainless steel testing chamber, and a Zeiss light source used for visualization of phase change. As shown in Fig. 9, the main body of the vacuum chamber is a 5 in. (inner diameter) stainless steel cylinder. The three side openings are located at 120 deg angular intervals. The transparent one (on the left side of the cylinder) is used for sample illumination. The right-side opening holds the test sample and all vacuum feedthroughs for temperature measurements and power connections. The third one is transparent, too, and located behind the cylinder, as shown in Fig. 9, which is for experimental visualiza-

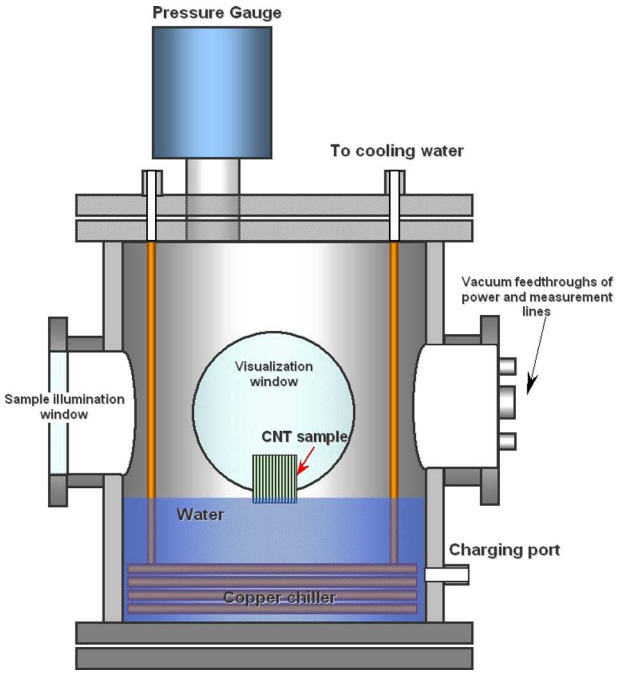

Fig. 9 Test chamber for high-heat-flux experiments

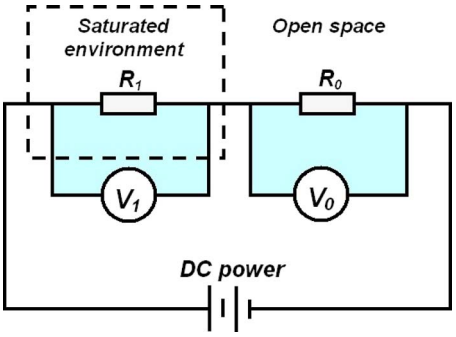

Fig. 10 Resistance measurement circuit of the platinum thermometer/heater

tion. To maintain high vacuum for phase change experiments, a turbo pump capable of 10^{-7} Torr and a high vacuum gauge capable of 10^{-10} Torr are employed. The testing chamber also contains a spiral copper chiller, which is set for control coolant temperature and saturated pressure in the saturated environment through the Neslab chiller. Vacuum and liquid charging ports are located at the bottom of the chamber. In our experiments, DI water is used as operating liquid. The CNT biwick samples are vertically set within the test chamber, as shown in Fig. 9. Liquid altitude in the chamber is slowly increased until it merges the bottom edge of the test samples (CNT biwick structure). Liquid charging is completed through a standard vacuum and backfeeding process [19]. Liquid supply to the sample heating area automatically proceeds with the capillary force effect of the CNT biwick structure.

Within the vacuum chamber, two thermocouples are used for monitoring temperatures of working fluid and the sample substrate. Electrical resistance measurement of the platinum thermometer/heater is conducted through measuring voltage drops across the resistors, as the schematic diagram shown in Fig. 10. R_0 is a known resistor with very small temperature coefficient, and R_1 is the platinum thermometer/heater. To avoid the interference of ac signal on voltage measurement, dc power was used. An Agilent 349710A data acquisition device is used to measure voltage added on the resistors. With the voltage measurements, the resistance R_1 can be calculated as

$$R_1 = \frac{V_1}{V_0} R_0 \tag{2}$$

To quantify the superheat while doing high-heat-flux tests, the wall temperature of substrate, T_w, is defined based on the 1D conduction heat transfer:

$$T_w = T_{\text{thermo}} - (\Delta T_{\text{Si}} + \Delta T_{\text{SiO}_2}) = T_{\text{thermo}} - \frac{Q}{A}\left(\frac{l_{\text{Si}}}{k_{\text{Si}}} + \frac{l_{\text{SiO}_2}}{k_{\text{SiO}_2}}\right) \tag{3}$$

where T_{thermo} is the reading temperature of the platinum thermometer, Q is the input power, A is the heating area, l is the layer thickness, and k is the material thermal conductivity.

The data processing subsystem is composed of a Yokogawa WT200 power-meter, an Agilent 34970A data acquisition, and a data management computer.

5 Experimental Results and Analysis

In this experiment, measurement accuracy of resistor thermometer is limited by the reference thermometer, thermocouple. The measurement uncertainty of the E-type thermocouple system is generally within $\pm 0.5°C$, and the input power varies within ± 0.2 W.

Using ICEPAK as the modeling tool, the heat spreader effect/heat loss in high-heat-flux tests is investigated. As shown in Fig. 11(*a*), the computational domain of the modeling is a 10×4 mm^2 cross

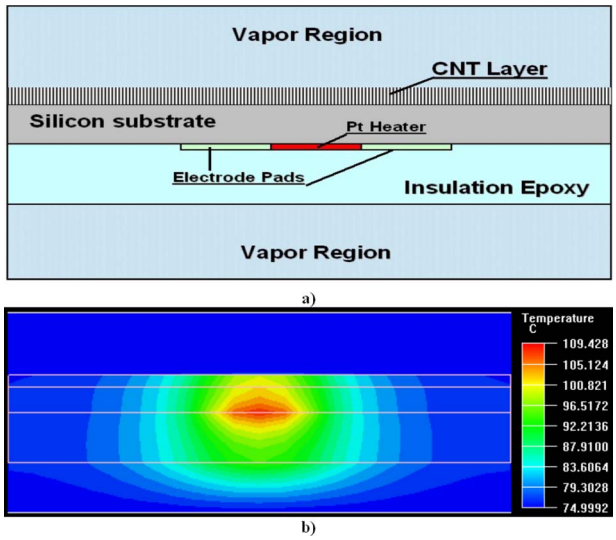

Fig. 11 Modeling of heat spreader effect/heat loss in high-heat-flux tests

section area. From top to bottom in sequence, there is, in thickness, a 1.25 mm vapor region, a 0.25 mm CNT layer, a 0.5 mm silicon substrate, a 1.0 mm epoxy insulation layer, and a 1.0 mm vapor region, respectively. The Pt heater is 2 mm wide and located in the center of the simulation domain. By assuming a reasonable high heat transfer coefficient (40 kW/m^2 K) on phase change surface, the in-plane heat spreading is simulated. At 400 W/cm^2 heat flux and at various ambient temperatures, the maximum heat losses are less than 1% of the total input power. Figure 11(*b*) shows the temperature profile of the simulation domain when the saturated temperature is 75°C. The minor heat loss is experimentally testified by measuring the temperature on a characterized location and by comparing with simulation data. On one of the electrode pads (around 1.0 mm off the heating area), the mounted thermocouple monitors temperature rise in high-heat-flux tests. At the similar test conditions (400 W/cm^2 and 72°C saturated temperature), the experimental temperature rise on this point is approximately 10°C, which is consistent with the simulation results (8–9°C temperature rise at the same location). The measured temperature versus heat flux is plotted in Fig. 12.

Experimental visualization of the CNT biwick phase change is first completed in open environment tests. With around 89°C surrounding liquid, evaporation of the operating liquid starts when

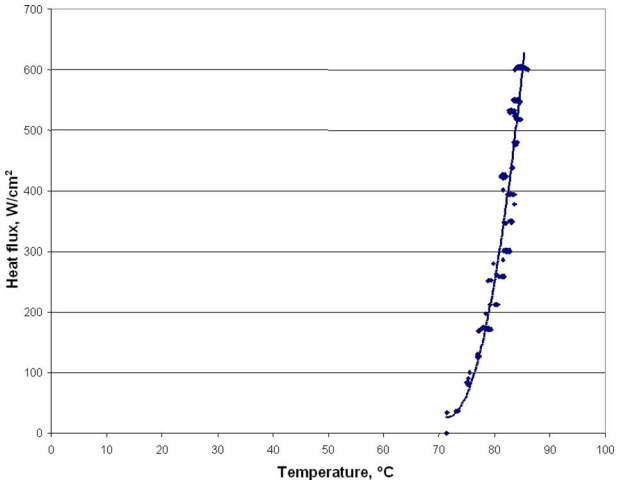

Fig. 12 Temperature measurement on sample electrode pad

Fig. 13 Intensive phase change on CNT biwick structure

heat flux is above 5 W/cm^2 (the sensible heat is needed for warming up subcooled operating liquid). At this power density level, a vapor jet from the heating area is observed and shown in Fig. 13. Above 50 W/cm^2, nucleation boiling happens in the CNT biwick structure. Further increasing the heat flux to 600 W/cm^2, intensive phase change along with vapor-carried liquid splash is observed. We do not see dryout even though the heat flux goes up to 600 W/cm^2. Experiments are stopped at 600 W/cm^2 because the further increase in vapor flow speed/heat flux debonds the stripelike CNT clusters from the silicon substrate. As a result, the dryout happens without functional CNT wick structure, which is indicated by the exposure of bare silicon and significant increase in electrode pad temperature.

By varying operation liquid temperature, the phase change heat transfer characteristics of the CNT biwick structure are revealed, plotted in Fig. 14. The mark names shown in Fig. 14 are liquid temperature in the chiller. Due to the heat loss in the cooling loop, the actual operation liquid temperature is a few degrees lower in the chamber. In all four testing temperatures from 25°C to 95°C, 600 W/cm^2 high-heat-flux cooling is reached. Lower operating liquid temperature consumes more sensible heat to warm the liquid to boiling point. The superheat of phase change at 600 W/cm^2 is in the range 25–45°C.

Without operating liquid precool, experiments in saturated environment also demonstrate 600 W/cm^2 heat transfer capability, as shown in Fig. 15. Liquid starts phase change after heat is added. Torturous curvatures in the figure indicate switches of phase change modes at difference heat flux levels [4]. At heat flux 600 W/cm^2, the maximum superheat in the saturated environment (50°C, 75°C, and 95°C) falls in a range 35–45°C. For data of operating liquid temperature at 25°C, sensible heat is needed

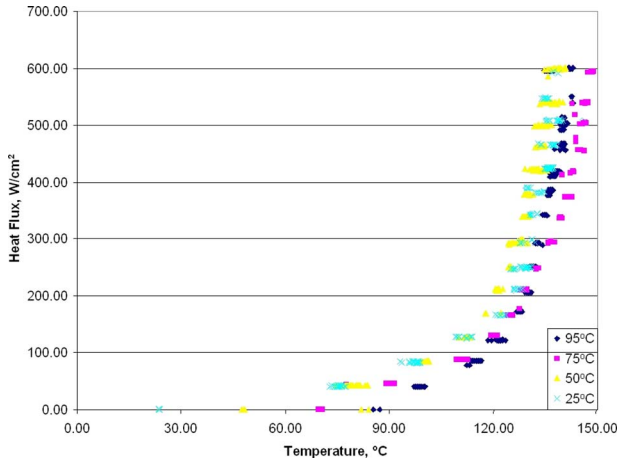

Fig. 14 High-heat-flux experimental results in open environment

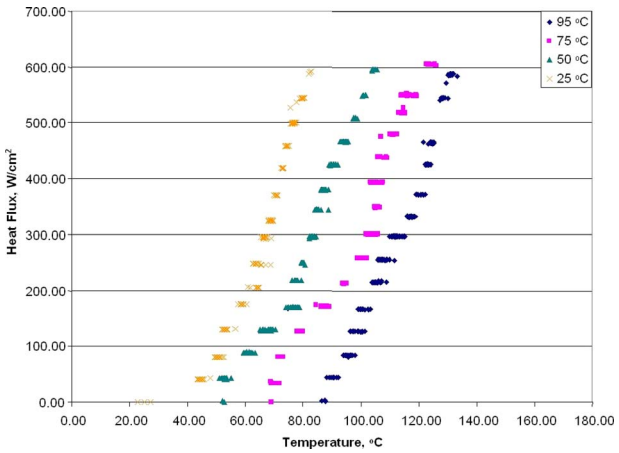

Fig. 15 High-heat-flux experimental results in saturated environment

prior to boiling. Residual noncondensable gas leads to slightly high superheat to 50°C. Improvement of vacuum system will reduce the superheat and gain a higher heat transfer coefficient.

In all relevant literatures, there is no exactly the same (in geometry) metallic wick available for comparisons of heat transfer performance. In general, microwick structure capable of high-heat-flux cooling is much thicker for supplying adequate liquid.

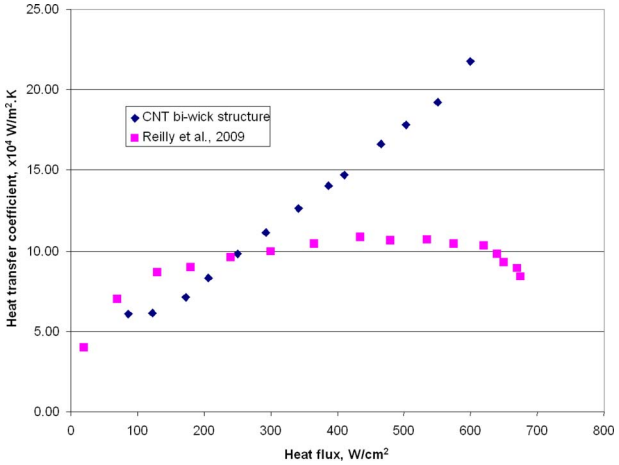

Fig. 16 Comparison of heat transfer coefficient between microcopper and nano-CNT biwick structures

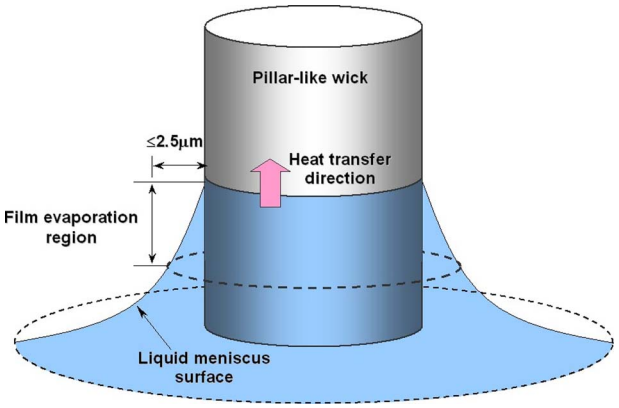

Fig. 17 Schematic diagram of the film evaporation for pillar-like wick structure

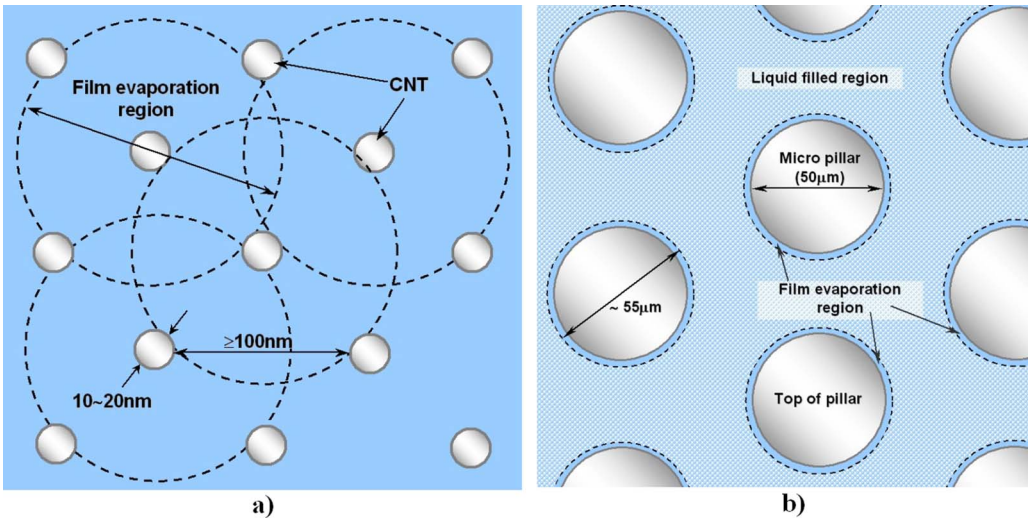

Fig. 18 Total thin-film evaporation area comparisons between nano- and micropillarlike wick structures

For example, microsintered copper powder biwick structure [9], capable of 650 W/cm^2 cooling, is 800 μm thick and more than three times than the CNT wick. To better understand performance merits of the CNT biwick structure, we ignore wick geometrical differences, use the micrometallic wick structure as a reference, and plot heat transfer coefficients versus heat flux. In Fig. 16, when the input heat flux is at the lower level, the heat transfer coefficient is comparable between micrometallic wick and CNT wick. The CNT biwick starts to demonstrate better heat transfer performance when heat flux increases over 250 W/cm^2, where evaporation on small pore interfaces becomes dominant [4]. At the high heat flux 600 W/cm^2, no performance degradation is found on the CNT biwick structure, while the micro biwick structure starts to dryout (heat transfer coefficient starts to decrease with heat flux).

High performance of CNT biwick structure benefits from two key features. First, the stripelike biwick and thin wick design allow vapor to straightly and rapidly escape from the boiling surface and reduce the possibility of dryout caused by trapped vapor in the wick. Second, nanosize pores increase the capillary force and therefore boosts the liquid transport capability of the wick structure. A large amount of nanosize pores also significantly increase film evaporation area and phase change efficiency. To understand this mechanism, evaporation on liquid meniscus is schematically shown in Fig. 17, where the pillar represents individual carbon nanotube of CNT wick or single pillar of silicon wick. When heat transfers from the bottom to the top of the pillar, surround liquid is heated up and evaporates. The thinner the liquid film is, the lower the thermal resistance across it. As a result, more than 90% evaporation heat transfer occurs on the region where liquid film is less than 2–3 μm [20]. In our research, a 2.5-μm-thick liquid film is defined as film evaporation region (to distinguish with the thin-film evaporation region).

The geometric analysis of the film evaporation regions of wick structure denotes that the scale of wick structure affects the evaporation efficiency. As the schematic diagram shown in Fig. 18(*a*) (top view), film evaporation regions of nanopillarlike wick are overlapped among CNTs. Almost 100% area in the *x-y* plane works for high efficient phase change. In contrast, film evaporation regions of microwick only include thin layers around pillars (Fig. 18(*b*)). The area ratio of film evaporation regions can reach over 100, depending on microwick dimensions. Because of the increase in film evaporation area, CNT biwick structure is potentially capable of higher heat flux heat transfer and efficiency.

The next step of work in this research is to improve CNT bonding strength with the silicon substrate so that CNT can survive at higher speed vapor flow/heat flux.

6 Conclusions

Experimental investigations of CNT biwick structure, associated with the development of high performance platinum thermometer/heater, lead to the following conclusions.

1. The e-beam evaporation coated platinum heater/thermometer can withstand over 800 °C experimental testing temperature. The thermometer after the annealing process exhibits good temperature measurement repeatability and accuracy. The results show that the MEMS developed platinum heater/thermometer is an ideal choice for high temperature and high-heat-flux heat transfer experiments.
2. Experimental tests of CNT biwick structure demonstrate up to 600 W/cm^2 heat transfer capacity and indicate that the nanolevel porous media can significantly increase phase change efficiency and potentially be applied in microhigh-heat-flux cooling devices.

Acknowledgment

This research is sponsored by the DARPA/MTO under Contract No. N66001-08-C-2009 with Dr. T. Kenny as the program manager. The authors would like to thank Dr. Hengzhi Wang and Professor Zhifeng Ren for their support and assistance in this study.

Nomenclature

A = heating surface area, m^2
l = silicon substrate thickness, m
k = thermal conductivity, W/m K
Q = heat load, W
R = resistance, Ω
T = temperature, °C

Greek Symbols

α = temperature coefficient, Ω/°C
Δ = difference

Subscripts

0 = reference

1 = measurement
thermo = thermometer
w = wall
Si = silicon
SiO_2 = silicon dioxide

References

[1] Vityaz, P. A., Konev, S. K., Medvedev, V. B., and Sheleg, V. K., 1984, "Heat Pipes With Bidispersed Capillary Structures," *Proceedings of the Fifth International Heat Pipe Conference*, Vol. 1, pp. 127–135.

[2] North, M. T., Rosenfeld, J. H., and Shaubach, R. M., 1995, "Liquid Film Evaporation From Bi-Dispersed Capillary Wicks in Heat Pipe Evaporators," *Proceedings of the Ninth International Heat Pipe Conference*, Albuquerque, NM, May 1–5, pp. 143–147.

[3] North, M. T., Sarraf, D. B., Rosenfeld, J. H., Maidanik, Y. F., and Vershinin, S., 1997, "High Heat Flux Loop Heat Pipes," AIP Conf. Proc., **387**, pp. 561–566.

[4] Wang, J., and Catton, I., 2004, "Vaporization Heat Transfer in Biporous Wicks of Heat Pipe Evaporators," *Proceedings of the 13th International Heat Pipe Conference*, Vol. 2, pp. 76–86.

[5] Cao, X. L., Cheng, P., and Zhao, T. S., 2002, "Experimental Study of Evaporative Heat Transfer in Sintered Copper Bidispersed Wick Structures," J. Thermophys. Heat Transfer, **16**(4), pp. 547–552.

[6] Merilo, E. G., Semenic, T., and Catton, I., 2004, "Experimental Investigation of Boiling Heat Transfer in Bidispersed Media," *Proceedings of the 13th International Heat Pipe Conference*, Vol. 2, pp. 87–93.

[7] Li, C., Peterson, G. P., and Wang, Y., 2006, "Evaporation/Boiling on Thin Capillary Wick (I): Thickness Effects," ASME J. Heat Transfer, **128**, pp. 1312–1319.

[8] Semenic, T., Lin, Y., and Catton, I., 2005, "Biporous Sintered Copper for a Closed Loop Heat Pipe Evaporator," ASME Paper No. IMECE2005-82180.

[9] Reilly, S. W., and Catton, I., 2009, "Improving Biporous Heat Transfer by Addition of Monoporous Interface Layer," ASME Paper No. HT2009-88257.

[10] Dresselhaus, M. S., Dresselhaus, G., and Avouris, P., eds., 2001, *Carbon Nanotubes Synthesis, Structure, Properties and Applications*, Springer, Berlin.

[11] Kim, P., Shi, L., Majumdar A., and McEuen, P. L., 2001, "Thermal Transport Measurement of Individual Multiwalled Nanotubes," Phys. Rev. Lett., **87**, p. 215502.

[12] Cai, Q., Chen, C. L., Xiong, G., and Ren, Z. F., 2008, "Exploration of Carbon Nanotube Wick Structure for High Heat Flux Cooling," ASME Paper No. HT2008-56208.

[13] Jiang, L., Wong, M., and Zohar, Y., 1999, "A Micro-Channel Heat Sink With Integrated Temperature Sensors for Phase Transition Study," *12th IEEE International Conference on Micro ElectroMechanical Systems*, Jan. 17–21, pp. 159–164.

[14] Datta, J. R., 1995, "Heater Integrated Sensor System," *Proceedings of the IEEE International Symposium on Industrial Electronics*, Jul. 10–14, pp. 849–854.

[15] Tait, R. B., Huphries, R., and Lorenz, J., 1994, "Thick Film Heater Elements and Temperature Sensors in Modern Domestic Appliances," IEEE Trans. Ind. Appl., **30**(3), pp. 573–577.

[16] Chen, H. T., Liu, C. W., Liu, S. G., Yang, C. S., and Gau, C., 2007, "Fabrication of a Complicated Heat Transfer Microchannel System for CPU Cooling Study," *Proceedings of the Second IEEE International Conference on Nano/Micro Engineered and Molecular Systems*, Jan. 16–19, pp. 654–658.

[17] Nicholas, J. V., and White, D. R., 2001, *Traceable Temperature*, 2nd ed., Wiley, New York.

[18] Cai, Q., Chen, B. C., Zhao, Y., Mack, J., Ma, Y., Chen, C. L., Wang, H., and Ren, Z. F., 2009, "Thermal Property Measurements of Carbon Nanotube Forest Synthesized by Thermal CVD Process," ASME Paper No. HT2009-88076.

[19] Faghri, A., 1995, *Heat Pipe Science and Technology*, Taylor & Francis, New York.

[20] Wang, H., Garimella, S. V., and Murthy, J. Y., 2007, "Characteristics of an Evaporating Thin Film in a Microchannel," Int. J. Heat Mass Transfer, **50**, pp. 3933–3942.

Constructal Allocation of Nanoparticles in Nanofluids

Chao Bai

Liqiu Wang[1]
e-mail: lqwang@hku.hk

Department of Mechanical Engineering,
The University of Hong Kong,
Pokfulam Road, Hong Kong

We perform a constructal design of heat conduction in a blade-configured disk-shaped domain with uniform heat generation and periphery heat-sink by introducing a transition line from two-path conduction to one-path conduction in the domain. This orderly arranged blade configuration can offer significantly smaller constructal overall temperature difference than that of the dispersed configuration and thus performs much better. The constructal allocation of nanoparticles inside the base fluids and thus the heat-conduction design inside the nanofluids are very important for better system performance. This work shows that the search for heat-flow configuration is a key to performance, and the constructal theory is the strategy for discovering the configuration and the significantly better performance. [DOI: 10.1115/1.4000473]

Keywords: nanofluids, constructal theory, transition line, dispersed configuration, blade configuration, overall temperature difference

1 Introduction

Having a very small amount of nanoparticles in nanofluids can exhibit anomalously higher effective thermal conductivities than those of their base fluids [1–3]. Since the final goal of nanofluids research is to use nanofluids for improving system performance, we should thus take the systems that use nanofluids into consideration in addition to purely improve their effective thermal conductivity [4,5]. As the system performance being considered, the allocation of the two conducting materials in nanofluids (base fluids and nanoparticles) has been proved to be an important issue [4,5]. For the heat-conduction systems considered in Ref. [4], the nanoparticles are dispersed inside the base fluids but are allowed to have different local volume fractions in different parts of the system. The results show that by constructing the nanoparticle volume fraction, smaller overall thermal resistance can indeed be achieved. The present work shows that the system performance can be further improved by a constructal design of continuous high-conductivity paths of nanoparticles inside the base fluid based on the constructal theory [5–8].

2 Constructal Overall Temperature Difference

Consider heat conduction in a disk-shaped domain with periphery heat sink (T_0) (Fig. 1). A uniform volumetric heat generation q''' occurs in this two-dimensional domain and correspondingly the heat generation per unit area is $q'''t$, where t is the disk thickness. In Ref. [4], the Birchak, Landau–Lifshitz, Lichtenecker, and Maxwell nanofluids are used to conduct heat in this disk-shaped domain. Inside these nanofluids, nanoparticles disperse homogeneously in the direction perpendicular to the radius of the domain (dispersed configuration). It has been proven that a uniform distribution of particle volume fraction will lead to the minimal overall temperature difference [4]. Here, instead of dispersing the nanoparticles inside the base fluids, we arrange the nanoparticles one by one to form thin k_p blades (blade configuration), which are positioned radially and equidistantly with one ends touching the center of the domain and the other ends touching the disk periphery of heat sink (Fig. 1), where k_p and k_f are the thermal conductivities of the nanoparticles and the base fluids, respectively, and for each k_p blade, there is one circular sector with adiabatic radial sides.

Like that in the dispersed configuration, the composition of nanoparticles and base fluids is fixed by

$$\phi = \frac{\text{volume of } k_p \text{ material}}{\text{total volume}} \tag{1}$$

Our aim is to examine whether the blade configuration will lead to a smaller constructal overall temperature difference than that of the dispersed configuration for a fixed used amount of materials (nanoparticle and base fluid).

To simplify the analysis, we assume the following.

(1) There are many radial k_p blades positioning equidistantly in the disk-shaped domain such that each circular sector is sufficiently slender and can be approximated by an isosceles triangle whose base and height are $2H$ and R_0, respectively. Figure 2 shows such a circular sector.
(2) The thickness of k_p blades (D) is constant.
(3) The overall particle volume fraction is small ($\phi \ll 1$).
(4) The thermal-conductivity ratio of nanoparticles and base fluids is fixed and large: $\tilde{k}\phi \geq 2/(2-\sqrt{2})$, where $\tilde{k}$ is the thermal-conductivity ratio $\tilde{k}=k_p/k_f$.
(5) The contact resistance is not considered.

Under assumptions (2) and (3), the sufficiently thin k_p blade can be represented by the axis of symmetry of the circular sector, as shown in Fig. 2; the fixed composition of nanoparticles and base fluids can be now expressed as

$$\phi = \frac{DR_0}{HR_0} = \frac{D}{H} \tag{2}$$

Each circular sector is an elemental volume of heat-flow structure due to symmetry of the domain. We can thus obtain the constructal overall temperature difference of the system by analyzing heat conduction in one circular sector. Assumptions (1) and (4) ensure that most of the heat generated near the domain center in a circular sector prefers to flow first perpendicularly to the k_p blade and then along the k_p blade to the periphery (two-path conduction). However, due to the boundary condition of the periphery heat-sink, most of the heat generated near the periphery will flow radially to the heat-sink periphery inside the base fluid (one-path conduction). For each circular sector, there is a transition line in

[1]Corresponding author.

Contributed by the Heat Transfer Division of ASME for publication in the JOURNAL OF HEAT TRANSFER. Manuscript received July 8, 2009; final manuscript received: September 8, 2009; published online March 9, 2010. Assoc. Editor: R. D. Tzou.

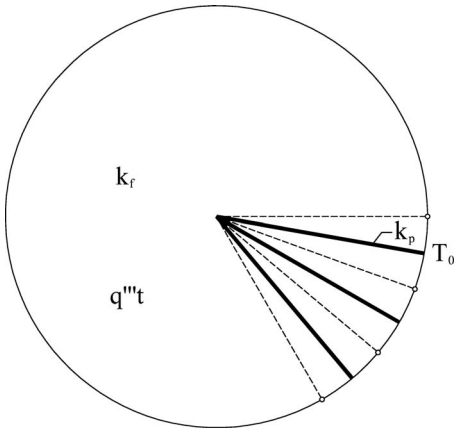

Fig. 1 Blade-configured disk-shaped domain

which the temperature differences along the two ways of heat conduction are equal to each other. Such a transition line divides the sector into two theoretical parts: (a) near the domain center and (b) near the periphery in Fig. 2. While heat also follows along the one-path conduction in part (a) and along the two-path conduction in part (b), we can virtually and equivalently exchange the flow paths of these two parts of heat such that it can be assumed that all heat follows along the two-path conduction in part (a) and along the one-path conduction in part (b). The inequality in assumption (4) ensures that the area of part (a) is always not less than that of part (b), which in turn ensures that the amount of heat assigned theoretically to the two-path conduction equals approximately or is more than the actual amount. Furthermore, it can be proved that for same amount of heat conducted, nonevenly distributed heat load will cause a higher temperature difference than relatively evenly distributed heat load for the same k_p blade. The constructal overall temperature difference found in the present work will thus not underestimate it. After the transition line is determined, the constructal overall temperature difference can be easily obtained.

2.1 Transition Line $f(r)$. Due to the symmetry of heat conduction in each circular sector, the transition line is also symmetric with respect to the symmetry axis of the circular sector. We can thus focus on finding its half. Express the transition line mathematically by $f(r)$ (shown in Fig. 2) and label its intersection points with the radial side and symmetry axis of circular sector as $r=r_m$ and $r=r_n$, respectively, as shown in Fig. 2.

Consider an arbitrary point $(r_0, f(r_0))$ on the transition line. For the two-path conduction, heat first flows perpendicularly inside the base fluid to the k_p blade and obeys the governing equation

$$\frac{d^2T}{dy^2} = -\frac{q'''}{k_f} \tag{3}$$

and boundary conditions

$$y = 0, \quad T = T_c \tag{4}$$

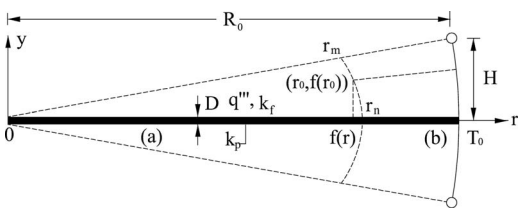

Fig. 2 One circular sector in the disk-shaped domain

$$y = f(r_0), \quad \frac{dT}{dy} = 0$$

where T_c is the temperature at point $(r_0, 0)$. Solving this equation, we obtain

$$T_{r_0,2} = \frac{q'''}{2k_f} f^2(r_0) + T_c \tag{5}$$

Here $T_{r_0,2}$ is the temperature at point $(r_0, f(r_0))$ for the two-path heat conduction. Heat conducted along the k_p blade to the heat-sink periphery can be described by

$$\frac{d^2T}{dr^2} = -\frac{2f(r)q'''}{k_pD} \tag{6}$$

and

$$r = r_0, \quad \frac{dT}{dr} = -\frac{r_m^2 Hq'''}{k_pDR_0} - \frac{2q'''}{k_pD}\int_{r_m}^{r_0} f(r)dr$$

$$r = r_n, \quad T = T_{r_n} \tag{7}$$

where T_{r_n} is the temperature at point $(r_n, 0)$. Integrating Eq. (6) from r_0 to r and substituting the temperature gradient at $r=r_0$ yield

$$\frac{dT}{dr} = -\frac{2q'''}{k_pD}\int_{r_m}^{r_0} f(r)dr - \frac{2q'''}{k_pD}\int_{r_0}^{r} f(r)dr - \frac{r_m^2 Hq'''}{k_pDR_0} \tag{8}$$

Integrating Eq. (8) again from r_0 to r_n and substituting the temperature at $r=r_n$ lead to

$$T_c - T_{r_n} = \frac{2q'''}{k_pD}\int_{r_0}^{r_n}\int_{r_m}^{r} f(r)drdr + \frac{r_m^2 Hq'''}{k_pDR_0}(r_n - r_0) \tag{9}$$

Therefore $T_{r_0,2}$ depends on r_m, r_n, T_{r_n}, and $f(r)$.

For the one-path conduction, heat flows directly along the radial direction inside the base fluid to the heat-sink periphery. Therefore,

$$\frac{d^2T}{dr^2} = -\frac{q'''}{k_f} \tag{10}$$

and

$$r = r_0, \quad \frac{dT}{dr} = 0$$

$$r = R_0, \quad T = T_0 \tag{11}$$

describe this conduction. Solving this equation, we obtain the expression of $T_{r_0,1}$ (the temperature at point $(r_0, f(r_0))$ for the one-path heat conduction):

$$T_{r_0,1} = \frac{q'''}{2k_f}(R_0 - r_0)^2 + T_0 \tag{12}$$

Applying similar procedures to point $(r_n, 0)$, with the temperature at point $(r_n, 0)$ labeled as $T_{r_n,2}$ and $T_{r_n,1}$ for the two-path and the one-path heat conduction, respectively, leads to

$$\frac{T_{r_n,2} - T_0}{R_0 - r_n} = \frac{2q'''}{k_pD}\int_{r_m}^{r_n} f(r)dr + \frac{r_m^2 Hq'''}{k_pDR_0} \tag{13}$$

$$T_{r_n,1} = \frac{q'''}{2k_f}(R_0 - r_n)^2 + T_0 \tag{14}$$

Since point $(r_n, 0)$ is on the transition line, we can equate these two equations to obtain a correlation between r_m and r_n as well as an expression for T_{r_n}:

$$\frac{k_p D q'''}{2k_f}(R_0 - r_n) = 2q''' \int_{r_m}^{r_n} f(r)dr + \frac{r_m^2 H q'''}{R_0} \tag{15}$$

and

$$T_{r_n} - T_0 = \frac{q'''}{2k_f}(R_0 - r_n)^2 \tag{16}$$

The expression for T_{r_n} can reduce the independent variables in $T_{r_0,2}$ to r_m, r_n, and $f(r)$:

$$T_{r_0,2} = \frac{q'''}{2k_f} f^2(r_0) + \frac{2q'''}{k_p D} \int_{r_0}^{r_n} \int_{r_m}^{r} f(r)drdr + \frac{r_m^2 H q'''}{k_p D R_0}(r_n - r_0) + \frac{q'''}{2k_f}(R_0 - r_n)^2 + T_0 \tag{17}$$

Equating $T_{r_0,2}$ in Eq. (17) and $T_{r_0,1}$ in Eq. (12) yields the governing equation for $f(r)$:

$$\frac{q'''}{2k_f}(R_0 - r_0)^2 = \frac{q'''}{2k_f} f^2(r_0) + \frac{2q'''}{k_p D} \int_{r_0}^{r_n} \int_{r_m}^{r} f(r)drdr + \frac{r_m^2 H q'''}{k_p D R_0}(r_n - r_0) + \frac{q'''}{2k_f}(R_0 - r_n)^2 \tag{18}$$

where r_m and r_n satisfy Eq. (15) and the geometry condition

$$f(r_m) = \frac{H}{R_0} r_m \tag{19}$$

Equations (15), (18), and (19) fully determine the transition line $f(r)$, r_m, and r_n.

Differentiating Eq. (18) twice with respect to r_0 yields

$$f(r_0)f''(r_0) + [f'(r_0)]^2 - \frac{2k_f}{k_p D} f(r_0) = 1 \tag{20}$$

In order to ensure that solution of this differential equation is also the solution of the integral equation (18), two initial conditions must be fulfilled [9]:

$$f(r_n) = 0 \tag{21}$$

and

$$\frac{q'''}{k_f}(r_m - R_0) = \frac{q'''}{k_f} f(r_m) f'(r_m) - \frac{r_m^2 H q'''}{k_p D R_0} \tag{22}$$

Since no independent variable appears in differential equation (20), we can consider $f'(r_0)$ to be a function of $f(r_0)$ alone. Labeling $f'(r_0)$ as Z, Eq. (20) can be reduced into

$$Z^2 + \frac{f}{2}\frac{dZ^2}{df} - \frac{2k_f}{k_p D} f = 1 \tag{23}$$

Viewing Z^2 as another function, Eq. (23) is a first-order linear differential equation with the solution

$$Z^2 = \frac{4k_f}{3k_p D} f + 1 + \frac{c_1}{f^2} \tag{24}$$

or

$$[f'(r_0)]^2 = \frac{4k_f}{3k_p D} f(r_0) + 1 + \frac{c_1}{f^2(r_0)} \tag{25}$$

Solving Eq. (25) will yield function $f(r)$ with two integration constants determined by initial conditions (21) and (22). Since r_m and r_n appear in Eqs. (21) and (22), Eqs. (15) and (19) must be used to obtain the final exact expression for $f(r)$.

In principle, we can fix the transition line $f(r)$ precisely by applying the above-mentioned procedures. However, it is difficult to obtain the analytical solution of Eq. (25). However, we can obtain the following features of transition line based on Eq. (25).

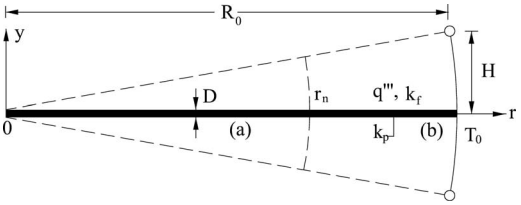

Fig. 3 One circular sector in the disk-shaped domain with the approximated transition line

(i) The constant c_1 must be non-negative since $f(r_n)=0$.

(ii) If $c_1=0$, Eq. (25) can be solved analytically and the final expression for $f(r)$ is

$$f(r) = \frac{k_f}{3k_p D}(r - r_n)^2 - (r - r_n) \tag{26}$$

Then we have

$$\left(r_m - R_0 + \frac{k_f H}{k_p D R_0} r_m^2\right)^2 - \frac{H^2}{R_0^2} r_m^2 - \frac{4k_f H^3}{3k_p D R_0^3} r_m^3 = 0 \tag{27}$$

$$\frac{k_f}{3k_p D}(r_m - r_n)^2 - (r_m - r_n) = \frac{H}{R_0} r_m \tag{28}$$

and

$$\frac{k_p D}{2k_f}(R_0 - r_n) = (r_m - r_n)^2 - \frac{2k_f}{9k_p D}(r_m - r_n)^3 + \frac{H}{R_0} r_m^2 \tag{29}$$

Since these three equations are independent of each other, we cannot obtain the values of r_m and r_n. Therefore, $c_1=0$ is not possible.

(iii) Since $c_1=0$ is not physically possible, c_1 must be a positive constant. Then according to Eq. (25), the smallest slope of the transition line is $-\infty$ at $r_0=r_n$ due to Eq. (21), and the largest slope of the transition line is smaller than -1. Because each circular sector is sufficiently slender, we can reasonably assume that the transition line is just $r=r_n$, as shown in Fig. 3.

2.2 Constructal Overall Temperature Difference. Because the transition line is $r=r_n$ (Fig. 3), Eq. (13) can be written as

$$\frac{T_{r_n,2} - T_0}{R_0 - r_n} = \frac{r_n^2 H q'''}{k_p D R_0} \tag{30}$$

Combining Eq. (30) with Eq. (14) and noting that $T_{r_n,2}=T_{r_n,1}$, we have the r_n equation

$$\frac{k_p D q'''}{2k_f}(R_0 - r_n) = \frac{r_n^2 H q'''}{R_0} \tag{31}$$

which can be transformed further into

$$\frac{\tilde{k}\phi}{2}(1 - \tilde{r}_n) = \tilde{r}_n^2 \tag{32}$$

where $\tilde{r}_n$ is defined as r_n/R_0. Solving Eq. (32) leads to

$$\tilde{r}_n = \sqrt{\frac{\tilde{k}^2\phi^2}{16} + \frac{\tilde{k}\phi}{2}} - \frac{\tilde{k}\phi}{4} \tag{33}$$

Letting the two-path conduction area (a) not less than the one-path conduction area (b) yields

$$\tilde{r}_n \geq \frac{\sqrt{2}}{2} \tag{34}$$

which requires, according to Eq. (33),

$$\tilde{k}\phi \geq \frac{2}{2-\sqrt{2}} \tag{35}$$

This is the one used in assumption (4).

Heat conduction in Part (a) is governed by

$$\frac{d^2T}{dr^2} = -\frac{2Hq'''}{k_p D R_0} r \tag{36}$$

with boundary conditions

$$r = r_0, \quad \frac{dT}{dr} = -\frac{Hq'''r_0^2}{k_p D R_0}$$
$$r = r_n, \quad T = T_{r_n} \tag{37}$$

and

$$\frac{d^2T}{dy^2} = -\frac{q'''}{k_f} \tag{38}$$

with boundary conditions

$$y = 0, \quad T = T_c$$
$$y = \frac{H}{R_0} r_0, \quad \frac{dT}{dy} = 0 \tag{39}$$

Here $(r_0, 0)$ refers to an arbitrary point on the k_p blade, T_c is the temperature at this arbitrary point, and T_{r_n} is the temperature at $r=r_n$ (approximated transition line). Solving these equations yields

$$T_{r_0} = \frac{H^2 q'''}{2k_f R_0^2} r_0^2 + \frac{Hq'''}{3k_p D R_0}(r_n^3 - r_0^3) + T_{r_n} \tag{40}$$

where T_{r_0} is the temperature of the point $(r_0, (H/R_0)r_0)$. Substituting Eq. (16) into Eq. (40) leads to

$$T_{r_0} - T_0 = \frac{H^2 q'''}{2k_f R_0^2} r_0^2 + \frac{Hq'''}{3k_p D R_0}(r_n^3 - r_0^3) + \frac{q'''}{2k_f}(R_0 - r_n)^2 \tag{41}$$

which can be transformed further into a nondimensional form

$$\frac{T_{r_0} - T_0}{q''' R_0^2 / k_f} = \frac{\alpha^2 \tilde{r}_0^2}{2} + \frac{\tilde{r}_n^3 - \tilde{r}_0^3}{3\tilde{k}\phi} + \frac{1}{2}(1 - \tilde{r}_n)^2 \tag{42}$$

Here α is the aspect ratio of circular sector $\alpha=(H/R_0)$, and $\tilde{r}_0$ is defined by $\tilde{r}_0=(r_0/R_0)$. Substituting Eq. (33) into Eq. (42) yields

$$\frac{T_{r_0} - T_0}{q''' R_0^2 / k_f} = \frac{\alpha^2 \tilde{r}_0^2}{2} + \frac{1}{3\tilde{k}\phi}\left[\left(\sqrt{\frac{\tilde{k}^2\phi^2}{16} + \frac{\tilde{k}\phi}{2}} - \frac{\tilde{k}\phi}{4}\right)^3 - \tilde{r}_0^3\right] + \frac{1}{2}\left(1 - \sqrt{\frac{\tilde{k}^2\phi^2}{16} + \frac{\tilde{k}\phi}{2}} + \frac{\tilde{k}\phi}{4}\right)^2 \tag{43}$$

In order to find the maximal temperature of the system, we treat $\tilde{r}_0$ as variable and differentiate Eq. (43) with respect to it. Letting the resultant expression equal to zero leads to two solutions for $\tilde{r}_0$ which are $\tilde{r}_0=0$ and $\tilde{r}_0=\alpha^2\tilde{k}\phi$. It can be proved that they give the minimum and maximum values of Eq. (43), respectively. Therefore, the maximal temperature of the system occurs at $\tilde{r}_0=\alpha^2\tilde{k}\phi$ and will approach the minimum value as the aspect ratio of circular sector tends to zero. Thus, the constructal aspect ratio of circular sector should be as small as possible. Finally, the constructal overall temperature difference is

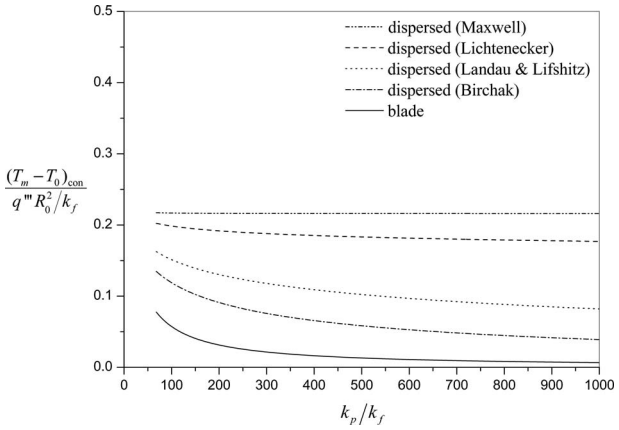

Fig. 4 Comparison between the blade configuration and dispersed configuration at $\phi=0.05$

$$\frac{(T_m - T_0)_{con}}{q''' R_0^2/k_f} \approx \frac{1}{3\tilde{k}\phi}\left(\sqrt{\frac{\tilde{k}^2\phi^2}{16} + \frac{\tilde{k}\phi}{2}} - \frac{\tilde{k}\phi}{4}\right)^3 + \frac{1}{2}\left(1 - \sqrt{\frac{\tilde{k}^2\phi^2}{16} + \frac{\tilde{k}\phi}{2}} + \frac{\tilde{k}\phi}{4}\right)^2 \tag{44}$$

3 Comparison Between Blade and Dispersed Configurations

For the dispersed configuration, the constructal overall temperature difference reads [4]:

In the Birchak nanofluids,

$$\frac{(T_m - T_0)_{con}}{q''' R_0^2/k_f} = \frac{1}{4[1 + \phi(\tilde{k}^{1/2} - 1)]^2} \tag{45}$$

In the Landau–Lifshitz nanofluids,

$$\frac{(T_m - T_0)_{con}}{q''' R_0^2/k_f} = \frac{1}{4[1 + \phi(\tilde{k}^{1/3} - 1)]^3} \tag{46}$$

In the Lichtenecker nanofluids,

$$\frac{(T_m - T_0)_{con}}{q''' R_0^2/k_f} = \frac{1}{4\tilde{k}^{\phi}} \tag{47}$$

In the Maxwell nanofluids,

$$\frac{(T_m - T_0)_{con}}{q''' R_0^2/k_f} = \frac{1}{4\left[1 + \dfrac{3(\tilde{k}-1)\phi}{2 + \tilde{k} - (\tilde{k}-1)\phi}\right]} \tag{48}$$

Keeping the volumetric heat generation q''', domain radius R_0, base fluid, nanoparticle, and nanofluid composition all the same for the four cases of dispersed configuration as well as for the blade configuration, we can examine which configuration is the best for smaller constructal overall temperature difference or equivalently the best system performance. Figures 4–7 compare Eqs. (44)–(48) at $\phi=0.05$, 0.03, 0.01, and 0.005, respectively, and with $\tilde{k}\phi \geq 2/(2-\sqrt{2})$ (a requirement in assumption (4)). The blade configuration is always with the lowest constructal overall temperature difference for all cases. Therefore, the system performance can be further improved by constructal allocation of nanoparticles instead of dispersing them in the base fluids.

4 Discussion

The present work considers a disk-shaped domain with uniform volumetric heat generation and periphery heat-sink. Nanofluids

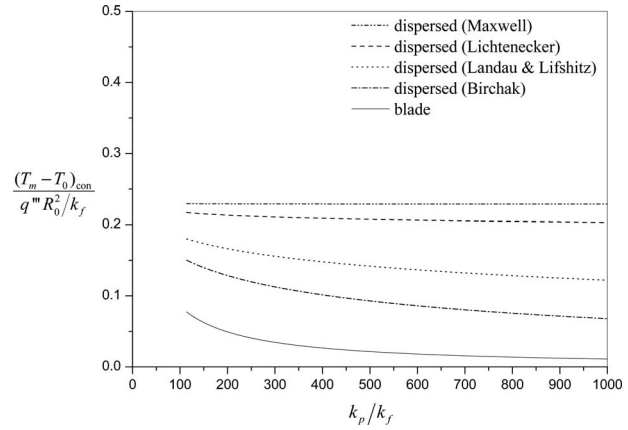

Fig. 5 Comparison between the blade configuration and dispersed configuration at $\phi=0.03$

are used for heat conduction inside this domain. Nanoparticles are assumed to be arranged together to form thin k_p blades positioned radially and equidistantly with one ends touching the center of the domain and the other ends touching the heat-sink periphery of the domain, instead of dispersing inside the base fluids in conventional nanofluids. Our goal is to find whether such orderly arranged nanofluids can offer better system performance than the conventional dispersed nanofluids.

By introducing a transition line that divides the elemental volume of heat-flow structure (circular sector) into the two-path heat-conduction part and one-path heat-conduction part, the constructal overall temperature difference of the blade-configured domain is obtained. Result shows that the constructal aspect ratio of the circular sector should be as small as possible within the valid range of analysis presented here.

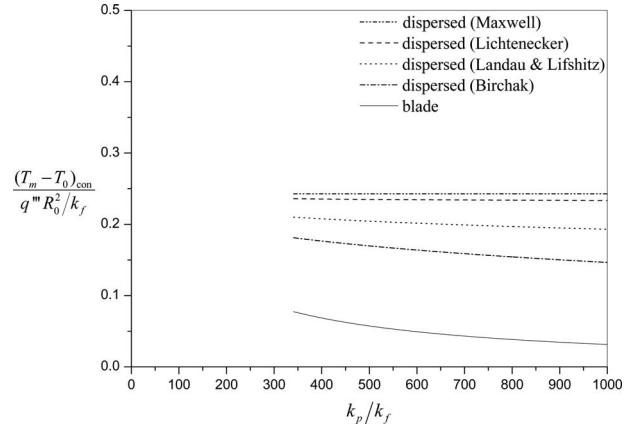

Fig. 6 Comparison between the blade configuration and dispersed configuration at $\phi=0.01$

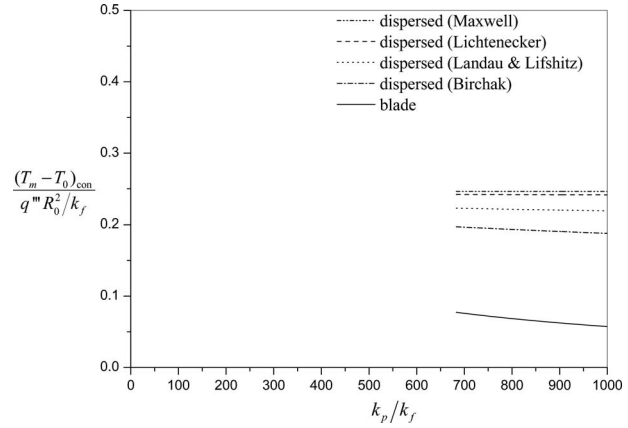

Fig. 7 Comparison between the blade configuration and dispersed configuration at $\phi=0.005$

The constructal overall temperature difference is compared with that for the dispersed-configured disk-shaped domain at $\phi=0.05$, $\phi=0.03$, $\phi=0.01$, and $\phi=0.005$. As the ϕ value decreases, the constructal overall temperature difference increases for both the dispersed configuration and the blade configuration. However, the constructal overall temperature difference of the blade configuration is always significantly smaller than that of dispersed configuration. Thus, the orderly arranged nanofluids indeed can perform better than the conventional dispersed nanofluids for the heat-conduction system considered here. This may be due to the introduction of another kind of conduction mechanism in the blade configuration, which acts just like the tree-shaped high-conductivity path in electronic chips and eddies in turbulent flow [10–12]. Through proper allocation of the two different conduction materials (lower thermal-conductivity base fluid and higher thermal-conductivity k_p blades), a lower constructal overall temperature difference can be obtained. Therefore, our research should also focus on constructal allocation of nanoparticles and heat-conduction channels inside nanofluids.

5 Concluding Remarks

A theoretical analysis is conducted on a blade-configured disk-shaped domain by introducing a concept of transition line from two-path conduction to one-path conduction in order to compare the performance of two nanofluid configurations: dispersed configuration and blade configuration. The system's constructal aspect ratio is found to be as small as possible as long as the analysis is valid. The orderly arranged blade configuration can offer significantly smaller constructal overall temperature difference than that of the dispersed configuration due to the introduction of another kind of conduction mechanism by arranging nanoparticles into blades. The heat-conduction design inside the nanofluids is thus very important for better system performance.

Acknowledgment

The financial support from the Research Grants Council of Hong Kong (Grant Nos. GRF718009 and GRF717508) is gratefully acknowledged.

Nomenclature

c_1 = integration constant
D = thickness of the k_p blade (m)
f = transition line function
H = half base length of circular sector (m)
k = thermal conductivity (W/m·K)
$\tilde{k}$ = thermal-conductivity ratio of nanoparticles and base fluids
q''' = volumetric heat generation rate (W/m^3)
r = coordinate (m)
$\tilde{r}$ = nondimensionalized coordinate
R = radius (m)
T = temperature (K)
t = thickness of the disk-shaped domain
Z = function
y = coordinate (m)

Greek Symbols

α = aspect ratio of circular sector
ϕ = overall particle volume fraction

Subscripts

0 = lower temperature/arbitrary point/outer
1 = one-path conduction

2 = two-path conduction
c = intersection of the two paths in the two-path conduction
f = base fluid
m = intersection point indication of transition line and radial sides of circular sector/maximal
n = intersection point indication of transition line and symmetry axis of circular sector
p = particle
con = constructal

References

[1] Wang, L. Q., and Wei, X. H., 2009, "Nanofluids: Synthesis, Heat Conduction, and Extension," ASME J. Heat Transfer, **131**, p. 033102.
[2] Choi, S. U. S., 2009, "Nanofluids: From Vision to Reality Through Research," ASME J. Heat Transfer, **131**, p. 033106.
[3] Peterson, G. P., and Li, C. H., 2006, "Heat and Mass Transfer in Fluids With Nanoparticle Suspensions," Adv. Heat Transfer, **39**, pp. 257–376.
[4] Bai, C., and Wang, L. Q., 2009, "Constructal Design of Particle Volume Fraction in Nanofluids," ASME J. Heat Transfer, **131**, p. 112402.
[5] Wang, L. Q., and Quintard, M., 2009, "Nanofluids of the Future," Advances in Transport Phenomena, **2009**, pp. 179–243.
[6] Bejan, A., and Lorente, S., 2008, *Design With Constructal Theory*, Wiley, Hoboken, NJ.
[7] Reis, A. H., 2006, "Constructal Theory: From Engineering to Physics, and How Flow Systems Develop Shape and Structure," Appl. Mech. Rev., **59**, pp. 269–282.
[8] Bejan, A., and Lorente, S., 2006, "Constructal Theory of Configuration Generation in Nature and Engineering," J. Appl. Phys., **100**, p. 041301.
[9] Bai, Y. L., 2009, "On Solving Integral Equations With Variables," Development & Innovation of Machinery & Electrical Products, **22**, pp. 34–35.
[10] Bejan, A., 2000, *Shape and Structure: From Engineering to Nature*, Cambridge University Press, Cambridge.
[11] Bejan, A., 2004, *Convection Heat Transfer*, 3rd ed., Wiley, Hoboken, NJ.
[12] Bejan, A., 1997, "Constructal-Theory Network of Conducting Paths for Cooling a Heat Generating Volume," Int. J. Heat Mass Transfer, **40**, pp. 799–816.

D. A. Nield
Department of Engineering Science,
University of Auckland,
Private Bag 92019,
Auckland 1142, New Zealand
e-mail: d.nield@auckland.ac.nz

A. V. Kuznetsov
Department of Mechanical and Aerospace Engineering,
North Carolina State University,
Campus Box 7910,
Raleigh, NC 27695-7910
e-mail: avkuznet@eos.ncsu.edu

The Effect of Local Thermal Nonequilibrium on the Onset of Convection in a Nanofluid

The onset of convection in a horizontal layer of a nanofluid is studied analytically. The model used for the nanofluid incorporates the effects of Brownian motion and thermophoresis, and allows for local thermal nonequilibrium (LTNE) between the particle and fluid phases. The analysis reveals that in some circumstances, the effect of LTNE can be significant, but for a typical dilute nanofluid (with large Lewis number and with small particle-to-fluid heat capacity ratio), the effect is small. [DOI: 10.1115/1.4000474]

Keywords: nanofluid, Brownian motion, thermophoresis, Rayleigh–Bénard problem, local thermal nonequilibrium

1 Introduction

The term "nanofluid" refers to a liquid containing a dispersion of submicronic solid particles (nanoparticles). The term was coined by Choi [1]. The characteristic feature of nanofluids is thermal conductivity enhancement, a phenomenon observed by Masuda et al. [2]. This phenomenon suggests the possibility of using nanofluids in advanced nuclear systems [3]. A comprehensive survey of convective transport in nanofluids was made by Buongiorno [4], who, after considering alternative methods, proposed a model incorporating the effects of the Brownian diffusion and thermophoresis. This model was applied to the Rayleigh–Bénard problem (the onset of convection in a horizontal layer uniformly heated from below) by Tzou [5,6] and Nield and Kuznetsov [7]. The corresponding problem for convection in a porous medium was studied by Nield and Kuznetsov [8,9].

In each of these studies of the onset of convection, it has been assumed that the solid particle phase and the fluid phase are in local thermal equilibrium. One might think that because the particles are very small, this is an obvious assumption to make. However, because the particles are buffeted by the fluid molecules, and the fluid temperature fluctuates rapidly with position on a nanoscale, the situation is more complex. The pioneering investigation by Vadasz [10] has in fact suggested that thermal lagging may provide an explanation for the unexpectedly large thermal conductivity that was observed in experiments with nanofluids. This has motivated the present study. It should be pointed out that the suggestion of Vadasz [10] was made in the context of the application to the transient hot wire experimental method, and therefore, the suggestion was linked to strong transient effects.

In Sec. 2, we have reexamined the conservation equations for a nanofluid, taking into account local thermal nonequilibrium (LTNE). In the following sections, we have applied the new equations to the classical Rayleigh–Bénard problem.

2 Conservation Equations for a Nanofluid

It is assumed that no nanoparticle agglomeration occurs and that the nanoparticle suspension remains stable. According to Anoop at al [11], there are experimental techniques that make it possible to prepare nanoparticle suspensions that remain stable for several weeks.

We treat the nanofluid as a continuum, using quantities averaged over a representative elementary volume (REV), a procedure common in the study of flow in a saturated porous medium (the usefulness of application of concepts developed for porous media to special cases of nanofluid suspensions was demonstrated in a recent paper by Vadasz [12]). Within the REV, we have a fluid phase (labeled with the subscript f) and a particle solid phase (subscript p). We consider the situation where the temperature T_p within the particle solid phase is different from the temperature T_f within the fluid phase. We modify the conservation equations, as formulated by Buongiorno [4] and Tzou [5,6].

The continuity equation for the nanofluid is

$$\nabla \cdot \mathbf{v} = 0 \tag{1}$$

Here, $\mathbf{v}$ is the nanofluid velocity.

The conservation equation for the nanoparticles in the absence of chemical reactions is

$$\frac{\partial \phi}{\partial t} + \mathbf{v} \cdot \nabla \phi = -\frac{1}{\rho_p} \nabla \cdot \mathbf{j}_p \tag{2}$$

where ϕ is the nanoparticle volume fraction, ρ_p is the nanoparticle mass density, and $\mathbf{j}_p$ is the diffusion mass flux for the nanoparticles, given as the sum of two diffusion terms (Brownian diffusion and thermophoresis) by

$$\mathbf{j}_p = \mathbf{j}_{p,B} + \mathbf{j}_{p,T} = -\rho_p D_B \nabla \phi - \rho_p D_T \frac{\nabla T_f}{T_f} \tag{3}$$

Here D_B is the Brownian diffusion coefficient given by the Einstein–Stokes equation

$$D_B = \frac{k_B T_f}{3\pi\mu d_p} \tag{4}$$

where k_B is the Boltzmann constant, μ is the viscosity of the fluid, and d_p is the nanoparticle diameter. Use has been made of the expression

$$\mathbf{V}_T = -\tilde{\beta}\frac{\mu}{\rho}\frac{\nabla T_f}{T_f} \tag{5}$$

for the thermophoretic velocity $\mathbf{V}_T$. Here, ρ is the fluid density and the proportionality factor $\tilde{\beta}$ is given by

$$\tilde{\beta} = 0.26\frac{k}{2k + k_p} \tag{6}$$

where k and k_p are the thermal conductivities of the fluid and the particle material, respectively. Hence, the thermophoretic diffusion flux is given by

Contributed by the Heat Transfer Division of ASME for publication in the JOURNAL OF HEAT TRANSFER. Manuscript received July 21, 2009; final manuscript received September 23, 2009; published online March 9, 2010. Editor: P. Vadasz.

$$\mathbf{j}_{p,T} = \rho_p \phi \mathbf{V}_T = -\rho_p D_T \frac{\nabla T_f}{T_f} \tag{7}$$

where the thermophoretic diffusion coefficient is given by

$$D_T = \tilde{\beta}\frac{\mu}{\rho}\phi \tag{8}$$

Equations (2) and (3) then produce the conservation equation in the form

$$\frac{\partial \phi}{\partial t} + \mathbf{v}\cdot\nabla\phi = \nabla\cdot\left[D_B \nabla\,\phi + D_T \frac{\nabla T_f}{T_f}\right] \tag{9}$$

If one introduces a buoyancy force and adopts the Boussinesq approximation, then the momentum equation can be written as

$$\rho\left(\frac{\partial \mathbf{v}}{\partial t} + \mathbf{v}\cdot\nabla\mathbf{v}\right) = -\nabla p + \mu\nabla^2\mathbf{v} + \rho\mathbf{g} \tag{10}$$

where

$$\rho = \phi\rho_p + (1-\phi)\rho_f \tag{11}$$

The nanofluid density ρ can be approximated by the base-fluid density ρ_f when ϕ is small. Then, when the Boussinesq approximation is adopted, the buoyancy term is approximated by

$$\rho\mathbf{g} \cong [\phi\rho_p + (1-\phi)\{\rho(1-\beta(T_f - T_0))\}]\mathbf{g} \tag{12}$$

Following the argument given by Buongiorno [4], it can be seen that the REV thermal energy balance for the fluid phase can be written as

$$(1-\phi)(\rho c)_f\left[\frac{\partial T_f}{\partial t} + \mathbf{v}\cdot\nabla T_f\right] = (1-\phi)k_f\nabla^2 T_f + (1-\phi) \times (\rho c)_p\left[D_B \nabla\,\phi\cdot\nabla T_f + D_T\frac{\nabla T_f\cdot\nabla T_f}{T_f}\right] + h_{fp}(T_p - T_f) \tag{13}$$

In this expression, each term is based on a unit volume of the REV. Equation (13) is obtained after the use of the equations

$$(1-\phi)(\rho c)_f\left[\frac{\partial T}{\partial t} + \mathbf{v}\cdot\nabla T\right] = (1-\phi)[-\nabla\cdot\mathbf{q} + h_p \nabla\cdot\mathbf{j}_p] + h_{fp}(T_p - T_f) \tag{14}$$

$$\mathbf{q} = -k_f \nabla T + h_p \mathbf{j}_p \tag{15}$$

$$\nabla h_p = c_p \nabla T \tag{16}$$

Here, h_{fp} is an interphase heat transfer coefficient incorporating the specific surface area, $(\rho c)_f$ is the nanofluid heat capacity, h_p is the specific enthalpy of the nanoparticle material, and $\mathbf{q}$ is the energy flux relative to a frame moving with the nanofluid velocity $\mathbf{v}$. Experimental values of h_{fp} can be obtained by an indirect method; see, for example, Ref. [13].

Likewise, the REV thermal energy balance within the solid phase is given by

$$\phi(\rho c)_p\left[\frac{\partial T_p}{\partial t} + \mathbf{v}\cdot\nabla T_p\right] = \phi k_p \nabla^2 T_p + h_{fp}(T_f - T_p) \tag{17}$$

The expression within the square brackets in Eq. (17) is the material derivative of T_p. It is being assumed that the solid particles are being carried along by the fluid in the same way, as if they were particles of fluid. Here, $(\rho c)_p$ and k_p are the heat capacity and the thermal conductivity of the solid phase, respectively.

It will be noted that if one has a local thermal equilibrium so that $T_f = T_p = T$, then on the addition of Eqs. (13) and (17), one has

$$(\rho c)_m\left[\frac{\partial T}{\partial t} + \mathbf{v}\cdot\nabla T\right] = k_m\nabla^2 T_f + (1-\phi)\rho_p c_p\left[D_B \nabla\,\phi\cdot\nabla T + D_T\frac{\nabla T\cdot\nabla T}{T}\right] \tag{18}$$

where

$$(\rho c)_m = (1-\phi)(\rho c)_f + \phi(\rho c)_p, \quad k_m = (1-\phi)k_f + \phi k_p \tag{19}$$

Then if one drops the subscript m and approximates $(1-\phi)$ by 1 (something that is valid for a dilute nanofluid), then one recovers Eq. (16) of Nield and Kuznetsov [7].

3 Application to the Rayleigh–Bénard Problem

We select a coordinate frame in which the z-axis is aligned vertically upwards. We consider a horizontal layer of fluid confined between the planes $z^* = 0$ and $z^* = H$. From now on, asterisks are used to denote dimensional variables (previously, an asterisk has not been needed because all the variables were dimensional). Each boundary wall is assumed to be perfectly thermally conducting. The temperatures at the lower and upper wall are taken to be T_h^* and T_c^*, the former being the greater. The Oberbeck–Boussinesq approximation is employed. Homogeneity of the fluid is assumed. The reference temperature is taken to be T_c^*. In the linear theory being applied here, the temperature change in the fluid is assumed to be small in comparison with T_c^*.

The boundary values of the nanoparticle volume fraction are taken to be ϕ_0^* at the bottom and ϕ_1^* at the top of the layer, and it is assumed that the increment $\phi_1^* - \phi_0^*$ is small in comparison with ϕ_0^*.

The conservation equations then take the form

$$\nabla^*\cdot\mathbf{v}^* = 0 \tag{20}$$

$$\rho\left(\frac{\partial \mathbf{v}^*}{\partial t^*} + \mathbf{v}^*\cdot\nabla\mathbf{v}^*\right) = -\nabla^* p^* + \mu\nabla^{*2}\mathbf{v}^* + [\phi^*\rho_p + (1-\phi^*)\{\rho(1 - \beta(T_f^* - T_c^*))\}]\mathbf{g} \tag{21}$$

$$(\rho c)_f\left[\frac{\partial T_f^*}{\partial t^*} + \mathbf{v}^*\cdot\nabla^* T_f^*\right] = k_f\nabla^{*2}T_f^* + (\rho c)_p\left[D_B\nabla^*\phi^*\cdot\nabla^* T_f^* + D_T\frac{\nabla^* T_f^*\cdot\nabla^* T_f^*}{T_f^*}\right] + \frac{h_{fp}}{(1-\phi_0^*)}(T_p^* - T_f^*) \tag{22}$$

$$(\rho c)_p\left[\frac{\partial T_p^*}{\partial t^*} + \mathbf{v}^*\cdot\nabla^* T_p^*\right] = k_p\nabla^{*2}T_p^* + \frac{h_{fp}}{\phi_0^*}(T_f^* - T_p^*) \tag{23}$$

$$\frac{\partial \phi^*}{\partial t^*} + \mathbf{v}^*\cdot\nabla^*\phi^* = D_B\nabla^{*2}\phi^* + (D_T/T_c^*)\nabla^{*2}T^* \tag{24}$$

We write $\mathbf{v}^* = (u^*, v^*, w^*)$.

We assume that the temperature and the volumetric fraction of the nanoparticles are constant on the boundaries, and one has thermal equilibrium there. Thus, the boundary conditions are

$$w^* = 0, \quad \frac{\partial w^*}{\partial z^*} + \lambda_1 H\frac{\partial^2 w^*}{\partial z^{*2}} = 0, \quad T_f^* = T_h^*, \quad T_p^* = T_h^* \qquad \phi^* = \phi_0^* \quad \text{at} \quad z^* = 0 \tag{25}$$

$$w^* = 0, \quad \frac{\partial w^*}{\partial z^*} - \lambda_2 H\frac{\partial^2 w^*}{\partial z^{*2}} = 0, \quad T_f^* = T_c^*, \quad T_p^* = T_c^* \tag{26}$$

$$\phi^* = \phi_1^* \quad \text{at} \quad z^* = H$$

The parameters λ_1 and λ_2 each take the value 0 for the case of a rigid boundary and ∞ for a free boundary.

We recognize that our choice of boundary conditions imposed on ϕ^* is somewhat arbitrary. It could be argued that zero particle flux on the boundaries is more realistic physically, but then, one is faced with the problem that it appears that no steady-state solution for the basic conduction equations is then possible (we attempted to obtain such a solution but encountered a contradiction), so that in order to make analytical progress, it is necessary to freeze the basic profile for ϕ^*, and at that stage, our choice of boundary conditions is seen to be quite realistic.

We introduce dimensionless variables as follows. We define

$$(x,y,z) = (x^*,y^*,z^*)/H, \quad t = t^*\alpha_f/H^2$$

$$(u,v,w) = (u^*,v^*,w^*)H/\alpha_f, \quad p = p^*H^2/\mu\alpha_f \tag{27}$$

$$\phi = \frac{\phi^* - \phi_0^*}{\phi_1^* - \phi_0^*}, \quad T_f = \frac{T_f^* - T_c^*}{T_h^* - T_c^*}, \quad T_p = \frac{T_p^* - T_c^*}{T_h^* - T_c^*}$$

where

$$\alpha_f = \frac{k_f}{(\rho c)_f} \tag{28}$$

Then, Eqs. (20)–(24) take the form

$$\nabla \cdot \mathbf{v} = 0 \tag{29}$$

$$\frac{1}{\mathrm{Pr}}\left(\frac{\partial \mathbf{v}}{\partial t} + \mathbf{v}\cdot\nabla\mathbf{v}\right) = -\nabla p + \nabla^2\mathbf{v} - \mathrm{Rm}\,\hat{\mathbf{e}}_z + \mathrm{Ra}\,T_f\hat{\mathbf{e}}_z - \mathrm{Rn}\,\phi\hat{\mathbf{e}}_z \tag{30}$$

$$\frac{\partial T_f}{\partial t} + \mathbf{v}\cdot\nabla T_f = \nabla^2 T_f + \frac{N_B}{\mathrm{Le}}\nabla\phi\cdot\nabla T_f + \frac{N_A N_B}{\mathrm{Le}}\nabla T_f\cdot\nabla T_f + N_H(T_p - T_f) \tag{31}$$

$$\frac{\partial T_p}{\partial t} + \mathbf{v}\cdot\nabla T_p = \varepsilon\nabla^2 T_p + \gamma N_H(T_f - T_P) \tag{32}$$

$$\frac{\partial \phi}{\partial t} + \mathbf{v}\cdot\nabla\phi = \frac{1}{\mathrm{Le}}\nabla^2\phi + \frac{N_A}{\mathrm{Le}}\nabla^2 T_f \tag{33}$$

$$w = 0, \quad \frac{\partial w}{\partial z} + \lambda_1\frac{\partial^2 w}{\partial z^2} = 0, \quad T_f = 1, \quad T_p = 1, \quad \phi = 0 \quad \text{at} \quad z = 0 \tag{34}$$

$$w = 0, \quad \frac{\partial w}{\partial z} - \lambda_2\frac{\partial^2 w}{\partial z^2} = 0, \quad T_f = 0, \quad T_p = 0, \quad \phi = 1 \quad \text{at} \quad z = 1 \tag{35}$$

Here

$$\mathrm{Pr} = \frac{\mu}{\rho\alpha_f} \tag{36}$$

$$\mathrm{Le} = \frac{\alpha_f}{D_B} \tag{37}$$

$$\mathrm{Ra} = \frac{\rho g\beta H^3(T_h^* - T_c^*)}{\mu\alpha_f} \tag{38}$$

$$\mathrm{Rm} = \frac{[\rho_p\phi_1^* + \rho(1-\phi_1^*)]gH^3}{\mu\alpha_f} \tag{39}$$

$$\mathrm{Rn} = \frac{(\rho_p - \rho)(\phi_1^* - \phi_0^*)gH^3}{\mu\alpha_f} \tag{40}$$

$$N_A = \frac{D_T(T_h^* - T_c^*)}{D_B T_c^*(\phi_1^* - \phi_0^*)} \tag{41}$$

$$N_B = \frac{(\rho c)_p}{(\rho c)_f}(\phi_1^* - \phi_0^*) \tag{42}$$

$$N_H = \frac{h_{fp}H^2}{(1-\phi_0^*)k_f} \tag{43}$$

$$\gamma = \frac{(1-\phi_0^*)}{\phi_0^*}\frac{(\rho c)_f}{(\rho c)_p} \tag{44}$$

$$\varepsilon = \frac{k_p/(\rho c)_p}{k_f/(\rho c)_f} \tag{45}$$

The parameter Le is a Lewis number and Ra is the familiar thermal Rayleigh number. The new parameters Rm and Rn may be regarded as a basic-density Rayleigh number and a concentration Rayleigh number, respectively. The parameter N_A is a modified diffusivity ratio and is somewhat similar to the Soret parameter that arises in cross diffusion phenomena in solutions, while N_B is a modified particle-density increment, N_H is an interface heat transfer parameter (Vadasz [10] called it the Nield number, while elsewhere in a recent literature, it has been called the Sparrow number), γ is a modified thermal capacity ratio, and ε is a thermal diffusivity ratio. We can observe from Eq. (31) that the order of magnitude of the thermophoresis effect relative to that of the Brownian motion effect is given by the parameter N_A.

In the spirit of the Oberbeck–Boussinesq approximation, Eq. (29) has been linearized by the neglect of a term proportional to the product of ϕ and T. This assumption is likely to be valid in the case of small temperature gradients in a dilute suspension of nanoparticles.

3.1 Basic Solution. We seek a time-independent quiescent solution of Eqs. (29)–(33) with the temperature and nanoparticle volume fraction varying in the z-direction only, that is a solution of the form

$$\mathbf{v} = 0, \quad p = p_b(z), \quad T_f = T_{fb}(z), \quad T_p = T_{pb}(z), \quad \phi = \phi_b(z)$$

Equations (30)–(33) reduce to

$$0 = -\frac{dp_b}{dz} - \mathrm{Rm} + \mathrm{Ra}\,T_{fb} - \mathrm{Rn}\,\phi_b \tag{46}$$

$$\frac{d^2T_{fb}}{dz^2} + \frac{N_B}{\mathrm{Le}}\frac{d\phi_b}{dz}\frac{dT_{fb}}{dz} + \frac{N_A N_B}{\mathrm{Le}}\left(\frac{dT_{fb}}{dz}\right)^2 + N_H(T_p - T_f) = 0 \tag{47}$$

$$\varepsilon\frac{d^2T_{pb}}{dz^2} + \gamma N_H(T_{fb} - T_{pb}) = 0 \tag{48}$$

$$\frac{d^2\phi_b}{dz^2} + N_A\frac{d^2T_{fb}}{dz^2} = 0 \tag{49}$$

Using the boundary conditions (34) and (35), Eq. (49) may be integrated to give

$$\phi_b = -N_A T_{fb} + (1 - N_A)z + N_A \tag{50}$$

and substitution of this into Eq. (47) gives

$$\frac{d^2T_{fb}}{dz^2} + \frac{(1-N_A)N_B}{\mathrm{Le}}\frac{dT_{fb}}{dz} + N_H(T_{pb} - T_{fb}) = 0 \tag{51}$$

The solution of Eqs. (48) and (51) for T_{fb} and T_{pb}, satisfying Eqs. (34) and (35), is readily found but is quite complicated in form in the general case. The remainder of the basic solution can then be found by first substituting in Eq. (50) to obtain ϕ_b, and then using the integration of Eq. (46) to obtain p_b.

According to Buongiorno [4], for most nanofluids investigated so far, $\mathrm{Le}/(\phi_1^* - \phi_0^*)$ is large of the order 10^5 to 10^6, and since the nanoparticle fraction decrement $(\phi_1^* - \phi_0^*)$ is typically no smaller than 10^{-3}, this means that Le is large of the order 10^2 to 10^3, while N_A is no greater than about 10. Then the coefficient $(1 - N_A)N_B/\mathrm{Le}$ is negligible, and so to a good approximation, one obtains the results

$$T_{fb} = T_{pb} = 1 - z \tag{52}$$

and so

$$\phi_b = z \tag{53}$$

Thus, for the case of large Lewis numbers, the basic solution is one in which the temperature and volume fraction gradients are linear and there is a local thermal equilibrium.

3.2 Perturbation Solution. We now superimpose perturbations on the basic solution. We write

$$\mathbf{v} = \mathbf{v}', \quad p = p_b + p', \quad T_f = T_{fb} + T_f', \quad T_p = T_{pb} + T_p'$$
$$\phi = \phi_b + \phi' \tag{54}$$

substitute (50) in Eqs. (29)–(35), and linearize by neglecting products of primed quantities. The following equations are obtained when Eqs. (52) and (53) are used:

$$\nabla \cdot \mathbf{v}' = 0 \tag{55}$$

$$\frac{1}{\mathrm{Pr}}\frac{\partial \mathbf{v}'}{\partial t} = -\nabla p' + \nabla^2 \mathbf{v}' + \mathrm{Ra}\, T'\hat{\mathbf{e}}_z - \mathrm{Rn}\, \phi'\hat{\mathbf{e}}_z \tag{56}$$

$$\frac{\partial T_f'}{\partial t} - w' = \nabla^2 T_f' + \frac{N_B}{\mathrm{Le}}\left(\frac{\partial T_f'}{\partial z} - \frac{\partial \phi'}{\partial z}\right) - \frac{2N_AN_B}{\mathrm{Le}}\frac{\partial T_f'}{\partial z} + N_H(T_p' - T_f') \tag{57}$$

$$\frac{\partial T_p'}{\partial t} - w' = \varepsilon\nabla^2 T_p' + \gamma N_H(T_f' - T_p') \tag{58}$$

$$\frac{\partial \phi'}{\partial t} + w' = \frac{1}{\mathrm{Le}}\nabla^2\phi' + \frac{N_A}{\mathrm{Le}}\nabla^2 T_f' \tag{59}$$

$$w' = 0, \quad \frac{\partial w}{\partial z} + \lambda_1\frac{\partial^2 w}{\partial z^2} = 0, \quad T_f' = 0, \quad T_p' = 0, \quad \phi' = 0 \quad \text{at}$$
$$z = 0 \tag{60}$$

$$w' = 0, \quad \frac{\partial w}{\partial z} - \lambda_2\frac{\partial^2 w}{\partial z^2} = 0, \quad T_f' = 0, \quad T_p' = 0, \quad \phi' = 0 \quad \text{at}$$
$$z = 1 \tag{61}$$

It will be noted that the parameter Rm is not involved in these and in subsequent equations. It is just a measure of the basic static pressure gradient.

The seven unknowns u', v', w', p', T_f', T_p', and ϕ' can be reduced to four by operating on Eq. (56) with $\hat{\mathbf{e}}_z$ curl curl, and using the identity curl curl $\equiv$ grad div $-\nabla^2$ together with Eq. (55). The result is

$$\frac{1}{\mathrm{Pr}}\frac{\partial}{\partial t}\nabla^2 w' - \nabla^4 w' = \mathrm{Ra}\,\nabla_H^2 T_f' - \mathrm{Rn}\,\nabla_H^2\phi' \tag{62}$$

Here, ∇_H^2 is the two-dimensional Laplacian operator on the horizontal plane.

The differential equations (62) and (57)–(59), and the boundary conditions (60) and (61), constitute a linear boundary-value problem that can be solved using the method of normal modes.

We write

$$(w', T_f', T_p', \phi') = [W(z), \Theta_f(z), \Theta_p(z), \Phi(z)]\exp(st + ilx + imy) \tag{63}$$

and substitute into the differential equations to obtain

$$\left((D^2 - \alpha^2)^2 - \frac{s}{\mathrm{Pr}}(D^2 - \alpha^2)\right)W - \mathrm{Ra}\,\alpha^2\Theta_f + \mathrm{Rn}\,\alpha^2\Phi = 0 \tag{64}$$

$$W + \left(D^2 + \frac{N_B}{\mathrm{Le}}D - \frac{2N_AN_B}{\mathrm{Le}}D - \alpha^2 - s - N_H\right)\Theta_f + N_H\Theta_p - \frac{N_B}{\mathrm{Le}}D\Phi = 0 \tag{65}$$

$$W + \gamma N_H\Theta_f + [\varepsilon(D^2 - \alpha^2) - s - \gamma N_H]\Theta_p = 0 \tag{66}$$

$$W - \frac{N_A}{\mathrm{Le}}(D^2 - \alpha^2)\Theta_f - \left(\frac{1}{\mathrm{Le}}(D^2 - \alpha^2) - s\right)\Phi = 0 \tag{67}$$

$$W = 0, \quad DW + \lambda_1 D^2 W = 0, \quad \Theta_f = 0, \quad \Theta_p = 0, \quad \Phi = 0 \quad \text{at}$$
$$z = 0 \tag{68}$$

$$W = 0, \quad DW - \lambda_2 D^2 W = 0, \quad \Theta_f = 0, \quad \Theta_p = 0, \quad \Phi = 0 \quad \text{at}$$
$$z = 1 \tag{69}$$

where

$$D \equiv \frac{d}{dz} \quad \text{and} \quad \alpha = (l^2 + m^2)^{1/2} \tag{70}$$

Thus α is a dimensionless horizontal wavenumber.

For neutral stability, the real part of s is zero. Hence, we now write $s = i\omega$, where ω is real and is a dimensionless frequency.

We now employ a Galerkin-type weighted residuals method to obtain an approximate solution to the system of Eqs. (64)–(69). We choose as trial functions (satisfying the boundary conditions) W_n, Θ_{fn}, Θ_{pn}, and Φ_n; $n = 1, 2, 3, \ldots, N$, and write

$$W = \sum_{n=1}^{N} A_n W_n, \quad \Theta_f = \sum_{n=1}^{N} B_n\Theta_{fn}, \quad \Theta_p = \sum_{n=1}^{N} C_n\Theta_{pn}$$
$$\Phi = \sum_{n=1}^{N} D_n\Phi_n \tag{71}$$

substitute into Eqs. (64)–(67), and make the expressions on the left-hand sides of those equations (the residuals) orthogonal to the trial functions, thereby obtaining a system of $4N$ linear algebraic equations in the $4N$ unknowns A_n, B_n, C_n, and D_n; $n = 1, 2, \ldots, N$. The vanishing of the determinant of coefficients produces the eigenvalue equation for the system. One can regard Ra as the eigenvalue. Thus, Ra is found in terms of the other parameters.

4 Results and Discussion

In the case of local thermal equilibrium, we have $N_H = 0$ and the equations reduce to those investigated by Nield and Kuznetsov [7]. In this paper, we are concerned with the effect of LTNE. Besides N_H, we have γ and ε as new parameters additional to the old parameters Ra, Rn, Pr, Le, N_A, and N_B. Because of the large parameter space, we simplify the analysis. In Ref. [7], both

nonoscillatory and oscillatory convection were investigated, but in this paper, we confine ourselves to the case of nonoscillatory instability, so that we can set $s=0$ in the above equations. We consider free-free and rigid-rigid boundary conditions in turn.

4.1 Free-Free Boundaries. For this case, the boundary conditions are

$$W=0, \quad D^2W=0, \quad \Theta_f=0, \quad \Theta_p=0, \quad \Phi=0 \text{ at}$$
$$z=0 \quad \text{and at} \quad z=1 \tag{72}$$

and the trial functions can be chosen as

$$W_n=\Theta_{fn}=\Theta_{pn}=\Phi_n=\sin n\pi z; n=1,2,3,\ldots \tag{73}$$

For a first approximation, we take $N=1$. This produces the result

$$\mathrm{Ra}\left[1+\frac{(\gamma+1)}{\varepsilon}\frac{N_H}{(\pi^2+\alpha^2)}\right]+\mathrm{Rn}\left[\mathrm{Le}+N_A+\frac{(\gamma+\varepsilon)\mathrm{Le}+(\gamma+1)N_A}{\varepsilon}\frac{N_H}{(\pi^2+\alpha^2)}\right]=\frac{(\pi^2+\alpha^2)^3}{\alpha^2}\left[1+\frac{(\gamma+\varepsilon)}{\varepsilon}\frac{N_H}{(\pi^2+\alpha^2)}\right] \tag{74}$$

In the case of a local thermal equilibrium, this simplifies to

$$\mathrm{Ra}+(\mathrm{Le}+N_A)\mathrm{Rn}=\frac{(\pi^2+\alpha^2)^3}{\alpha^2} \tag{75}$$

As α varies, the right-hand side takes a minimum value of $27\pi^4/4$ at $\alpha=\pi/\sqrt{2}$. In the absence of nanoparticles, one recovers the well-known result $\mathrm{Ra}_c=27\pi^4/4=657.5$ and $\alpha_c=\pi/\sqrt{2}=2.22$ for the critical Rayleigh number and the corresponding critical wave number, respectively. In the general case, if one approximates α by $\pi/\sqrt{2}$, the stability boundary is given by

$$\left[1+\frac{2(\gamma+1)}{3\pi^2\varepsilon}N_H\right]\mathrm{Ra}+\left[\mathrm{Le}+N_A+\frac{2[(\gamma+\varepsilon)\mathrm{Le}+(\gamma+1)N_A]}{3\pi^2\varepsilon}N_H\right]\mathrm{Rn}=\frac{27\pi^4}{4}\left[1+\frac{2(\gamma+\varepsilon)}{3\pi^2\varepsilon}N_H\right] \tag{76}$$

As noted above, for a typical nanofluid, Le is of the order 10^2 to 10^3 and N_A is not much greater than 10. In this case, an approximation to Eq. (76) is

$$\left[1+\frac{2(\gamma+1)}{3\pi^2\varepsilon}N_H\right]\mathrm{Ra}+\mathrm{Le}\left[1+\frac{2(\gamma+\varepsilon)}{3\pi^2\varepsilon}N_H\right]\mathrm{Rn}=\frac{27\pi^4}{4}\left[1+\frac{2(\gamma+\varepsilon)}{3\pi^2\varepsilon}N_H\right] \tag{77}$$

We note that the coefficient of Rn in Eq. (77) is large. Thus, under the approximations we have made so far, we have the result that the presence of nanoparticles lowers the value of the critical Rayleigh number, usually by a substantial amount, in the case when Rn is positive, that is, when the basic nanoparticle distribution is a top-heavy one.

The effect of LTNE appears in Eq. (76) through the parameter N_H. From its definition in Eq. (44), we note that for a dilute nanofluid, the parameter γ will normally have a large value. When γ is large compared with unity and compared with ε, Eq. (77) further reduces to

$$\mathrm{Ra}+(\mathrm{Le}+N_A)\mathrm{Rn}=\frac{27\pi^4}{4} \tag{78}$$

The terms involving N_H have cancelled. The effect of LTNE is then negligible.

It will be noted that in Eq. (76), the parameter N_B does not appear. The instability is almost purely a phenomenon due to buoyancy, coupled with the conservation of nanoparticles. It is independent of the contributions of Brownian motion and thermophoresis to the thermal energy equation. Rather, the Brownian motion and thermophoresis enter to produce their effects directly into the equation expressing the conservation of nanoparticles so that the temperature and the particle density are coupled in a particular way, and that results in the thermal and concentration buoyancy effects being coupled in the same way.

It is emphasized that the simple expression in Eq. (74) arises because the Lewis number has been assumed to be large. In order to estimate the contribution of the terms involving N_B, the two-term Galerkin result has been investigated. The expression in the eigenvalue equation is now complicated and it is difficult to make a statement that is simultaneously precise, simple, and general. However, it is clear that the functions of N_B are of second degree. We conclude that for practical purposes, Eq. (74) is a good approximation.

4.2 Rigid-Rigid Boundaries. Again, we confine our analysis to the one-term Galerkin approximation and to the case of nonoscillatory convection. Appropriate trial functions satisfying the boundary conditions, which are now

$$W=0, \quad DW=0, \quad \Theta_f=0, \quad \Theta_p=0, \quad \Phi=0 \text{ at}$$
$$z=0 \quad \text{and at} \quad z=1 \tag{79}$$

are

$$W_1=z^2(1-z)^2, \quad \Theta_{f1}=z(1-z), \quad \Theta_{p1}=z(1-z), \quad \Phi_1=z(1-z) \tag{80}$$

With this choice of trial functions, the eigenvalue equation takes the form

$$\mathrm{Ra}\left[1+\frac{(\gamma+1)}{\varepsilon}\frac{N_H}{(10+\alpha^2)}\right]+\mathrm{Rn}\left[\mathrm{Le}\left\{1+\frac{(\gamma+\varepsilon)}{\varepsilon}\frac{N_H}{(10+\alpha^2)}\right\}+N_A\left\{1+\frac{(\gamma+1)}{\varepsilon}\frac{N_H}{(10+\alpha^2)}\right\}\right]=\frac{28}{27\alpha^2}(504+24\alpha^2+\alpha^4)(10+\alpha^2)\left[1+\frac{(\gamma+\varepsilon)}{\varepsilon}\frac{N_H}{(10+\alpha^2)}\right] \tag{81}$$

For the case of local thermal equilibrium, the boundary for nonoscillatory instability is

$$\mathrm{Ra}+(N_A+\mathrm{Le})\mathrm{Rn}=\frac{28}{27\alpha^2}(504+24\alpha^2+\alpha^4)(10+\alpha^2) \tag{82}$$

The right-hand side of this equation takes a minimum when $\alpha=3.12$ and its minimum value is 1750. Hence, the onset of nonoscillatory instability is characterized by

$$\mathrm{Ra}+(N_A+\mathrm{Le})\mathrm{Rn}=1750 \tag{83}$$

The value 1750 obtained using the one-term Galerkin approximation is about 3% greater than the well-known exact value 1707.762 for the critical Rayleigh number for the classical Rayleigh–Bénard problem.

For the general case, we will now use the approximate value 3.12 for the critical wavenumber. Then Eq. (81) becomes

$$\left[1+\frac{(\gamma+1)}{19.73\varepsilon}N_H\right]\mathrm{Ra}+\left[\mathrm{Le}\left\{1+\frac{(\gamma+\varepsilon)}{19.73\varepsilon}N_H\right\}+N_A\left\{1+\frac{(\gamma+1)}{19.73\varepsilon}N_H\right\}\right]\mathrm{Rn}=1750\left[1+\frac{(\gamma+\varepsilon)}{19.73\varepsilon}N_H\right] \tag{84}$$

Except for the change in numerical coefficients (namely, 1750 instead of $27\pi^4/4$ and 19.73 instead of $3\pi^2/2$), Eq. (84) is the same as Eq. (76).

4.3 General Discussion. A number of authors, for example in Refs. [13–16], have reported results of experiments on nanofluids.

Particularly, noteworthy are the unexpected high values of the thermal conductivity that have been observed. In our model, these observations can be taken into account, simply by modifying the values of thermal conductivity and viscosity that enter the definition of the Rayleigh number.

To the best of our knowledge, the only available experimental paper concerned with convection in a rectangular container heated from below is that by Hwang et al. [14], who investigated water-based fluids containing alumina. However, their concern was with convection well above critical, with Rayleigh numbers of the order 10^6.

Besides the present paper and those of Tzou [5,6], the only analytical investigation of convective instability in nanofluids known to us is that by Kim et al. [15]. These authors investigate the variation in properties of the nanofluid that are incorporated in the definition of the Rayleigh number. Thus, their investigation is complementary to ours and it is not possible to make any direct meaningful comparison between them.

There appears to be a discrepancy between our results and Fig. 4(b) in Refs. [5,6]. This figure indicates that the analysis in Refs. [5,6] leads to the prediction that the critical Rayleigh number is reduced by a substantial amount in the bottom-heavy case, whereas our analysis leads to a predicted increase in the value of the critical Rayleigh number for nonoscillatory instability in this case. Tzou [5,6] offered no physical explanation for the substantial reduction. Tzou [5,6] used the symbol Le to denote a Lewis number, divided by the nanoparticle fraction decrement rather than a regular Lewis number. This means that his parameter Le tends to infinity as the nanoparticle fraction decrement tends to zero, i.e., in the limit, as the nanofluid is replaced by a regular fluid. Accordingly, we hypothesize that it is possible that the solution obtained by Tzou [5,6] may become singular in some sense in this limit.

5 Conclusions

We have investigated analytically the onset of convection in a horizontal layer of a nanofluid, using a model for the nanofluid that incorporates the effects of Brownian motion and thermophoresis, and that allows for LTNE between the particle and fluid phases. The analysis revealed that in some circumstances, the effect of LTNE can be significant, but for a typical dilute nanofluid (with large Lewis number and with large modified fluid-to-particle heat capacity ratio), the effect is small.

This provides support to our hypothesis that any enhanced effective thermal conductivity due to LTNE, as proposed by Vadasz [10] and explained by him in terms of thermal lagging, is a phenomenon associated with a highly transient situation. Our conclusion is in accord with the results of Zhang and Ma [16], who studied conduction with periodic heat flux and found that the effect of LTNE was important only when the period was short.

Nomenclature

c = nanofluid specific heat at constant pressure (J/kg K)
c_p = specific heat of the nanoparticle material (J/kg K)
d_p = nanoparticle diameter (m)
D_B = Brownian diffusion coefficient, given by Eq. (4) (m^2/s)
D_T = thermophoretic diffusion coefficient, given by Eq. (8) (m^2 K/s)
h_p = specific enthalpy of the nanoparticle material (J/kg)
h_{fp} = fluid-particle interphase heat transfer coefficient (W/m^3 K)
H = dimensional layer depth (m)
$\mathbf{j}_p$ = diffusion mass flux for the nanoparticles, given by Eq. (3) (kg/m^2 s)
$\mathbf{j}_{p,T}$ = thermophoretic diffusion, given by Eq. (7) (kg/m^2 s)
k = thermal conductivity of the nanofluid (W/m K)
k_B = Boltzmann's constant (J/K)
k_p = thermal conductivity of the particle material (W/m K)
Le = Lewis number, defined by Eq. (37)
N_A = modified diffusivity ratio, defined by Eq. (41)
N_B = modified particle-density increment, defined by Eq. (42)
N_H = Nield number, defined by Eq. (43)
p^* = pressure (Pa)
p = dimensionless pressure ($p^* H^2/\mu\alpha_f$)
$\mathbf{q}$ = energy flux relative to a frame moving with the nanofluid velocity $\mathbf{v}$ (W/m^2)
Ra = thermal Rayleigh–Darcy number, defined by Eq. (38)
Rm = basic-density Rayleigh number, defined by Eq. (39)
Rn = concentration Rayleigh number, defined by Eq. (40)
t^* = time (s)
t = dimensionless time ($t^*\alpha_f/H^2$)
T^* = nanofluid temperature (K)
T = dimensionless temperature $(T^*-T_c^*)/(T_h^*-T_c^*)$
T_c^* = temperature at the upper wall (K)
T_h^* = temperature at the lower wall (K)
(u,v,w) = dimensionless velocity components, $(u^*,v^*,w^*)H/\alpha_f$ (m/s)
$\mathbf{v}$ = nanofluid velocity (m/s)
$\mathbf{V}_T$ = thermophoretic velocity (m/s)
(x,y,z) = dimensionless Cartesian coordinates; $(x^*,y^*,z^*)/H$; z is the vertically upward coordinate
(x^*,y^*,z^*) = Cartesian coordinates (m)

Greek

α_f = thermal diffusivity of the fluid, given by Eq. (28) (m/s^2)
$\tilde{\beta}$ = proportionality factor, given by Eq. (6)
γ = modified thermal capacity ratio, defined by Eq. (44)
ε = thermal diffusivity ratio, defined by Eq. (45)
μ = viscosity of the fluid (N s/m^2)
ρ = fluid density (kg/m^3)
ρ_p = nanoparticle mass density (kg/m^3)
ϕ^* = nanoparticle volume fraction
ϕ = relative nanoparticle volume fraction $(\phi^*-\phi_0^*)/(\phi_1^*-\phi_0^*)$

Superscripts

* = dimensional variable (used from Sec. 3 onwards)
$'$ = perturbation variable

Subscripts

b = basic solution
f = fluid
m = mixture
p = particle

References

[1] Choi, S., 1995, "Enhancing Thermal Conductivity of Fluids With Nanoparticles," *Developments and Applications of Non-Newtonian Flows*, D. A. Siginer and H. P. Wang, eds., ASME, FED-MD-Vol. 231, pp. 99–105.
[2] Masuda, H., Ebata, A., Teramae, K., and Hishinuma, N., 1993, "Alteration of Thermal Conductivity and Viscosity of Liquid by Dispersing Ultra-Fine Particles," Netsu Bussei, **7**, pp. 227–233.

[3] Buongiorno, J., and Hu, L.-W., 2005, "Nanofluid Coolants for Advanced Nuclear Power Plants," *Proceedings of the ICAPP '05*, Seoul, May 15–19, Paper No. 5705.
[4] Buongiorno, J., 2006, "Convective Transport in Nanofluids," ASME J. Heat Transfer, **128**, pp. 240–250.
[5] Tzou, D. Y., 2008, "Instability of Nanofluids in Natural Convection," ASME J. Heat Transfer, **130**, p. 072401.
[6] Tzou, D. Y., 2008, "Thermal Instability of Nanofluids in Natural Convection," Int. J. Heat Mass Transfer, **51**, pp. 2967–2979.
[7] Nield, D. A., and Kuznetsov, A. V., "The Onset of Convection in a Nanofluid Layer," Int. J. Therm. Sci., submitted.
[8] Nield, D. A., and Kuznetsov, A. V., 2009, "Thermal Instability in a Porous Medium Layer Saturated by a Nanofluid," Int. J. Heat Mass Transfer, **52**, pp. 5796–5801.
[9] Kuznetsov, A. V., and Nield, D. A., 2009, "Thermal Instability in a Porous Medium Layer Saturated by a Nanofluid: Brinkman Model," Transp. Porous Media, doi:10.1007/s11242-009-9413-2.
[10] Vadasz, P., 2006, "Heat Conduction in Nanofluid Suspensions," ASME J. Heat Transfer, **128**, pp. 465–477.
[11] Anoop, K. B., Sundararajan, T., and Das, S. K., 2009, "Effect of Particle Size on the Convective Heat Transfer in Nanofluid in the Developing Region," Int. J. Heat Mass Transfer, **52**, pp. 2189–2195.
[12] Vadasz, P., 2009, "Nanofluid Suspensions as Derivative of Interface Heat Transfer Modeling in Porous Media," ASME Paper No. HT2009-88295.
[13] Polyaev, V. M., Mozhaev, A. P., Galitseysky, B. A., and Lozhkin, A. L., 1996, "A Study of Internal Heat Transfer in Nonuniform Porous Structures," Exp. Therm. Fluid Sci., **12**, pp. 426–432.
[14] Hwang, K. S., Lee, J. H., and Jang, S. P., 2007, "Buoyancy-Driven Heat Transfer of Water-Based Al_2O_3 Nanofluids in a Rectangular Cavity," Int. J. Heat Mass Transfer, **50**, pp. 4003–4010.
[15] Kim, J., Kang, Y. T., and Choi, C. K., 2004, "Analysis of Convective Instability and Heat Transfer Characteristics of Nanofluids," Phys. Fluids, **16**, pp. 2395–2401.
[16] Zhang, Y., and Ma, H. B., 2008, "Nonequilibrium Heat Conduction in a Nanofluid With Periodic Heat Flux," Int. J. Heat Mass Transfer, **51**, pp. 4862–4874.

Spectral Collocation Method for Transient Combined Radiation and Conduction in an Anisotropic Scattering Slab With Graded Index

Ya-Song Sun

Ben-Wen Li[1]
e-mail: heatli@hotmail.com,
heatli@epm.neu.edu.cn

Key Laboratory of National Education Ministry for Electromagnetic Processing of Materials,
Northeastern University,
P.O. Box 314,
Shenyang 110004, China

The spectral collocation method for transient combined radiation and conduction heat transfer in a planar participating medium with spatially variable refractive index is introduced and formulated. The angular dependence of the problem is discretized by discrete ordinates method and the space dependence is expressed by Chebyshev polynomial and discretized by spectral collocation method. Due to the exponential convergence of spectral methods, very high accuracy can be obtained even using a small resolution for present problem. Numerical results in one-dimensional planar slab by Chebyshev collocation spectral-discrete ordinates method (SP-DOM) are compared with those available data in references. Effects of various parameters such as the variable thermal conductivity, the scattering albedo, the emissivity of boundary, the conduction-radiation parameter, the optical thickness, and the graded index are studied for absorbing, emitting, and anisotropic scattering medium. The SP-DOM has been found to successfully and efficiently deal with transient combined radiation and conduction heat transfer problem in graded index medium. [DOI: 10.1115/1.4000444]

Keywords: spectral collocation method, radiative heat transfer, graded index, anisotropic scattering, transient combined radiation and conduction

1 Introduction

In graded index medium, the ray goes along a curved path determined by the Fermat principle. As a result, the solution of combined radiation and conduction heat transfer in graded index medium is more difficult than that in uniform index medium. During the past decades, the combined radiation and conduction heat transfer in graded index medium has evoked wide interest of many researchers.

After the year 2000, many numerical methods have been proposed to solve combined radiation and conduction heat transfer in graded index medium. For example, Abdallah and Dez [1] presented a curved ray-tracing method (CRT). Xia et al. [2] and Huang and co-workers [3,4] proposed a combined curved ray-tracing and pseudosource adding method (CRT-PSA). Liu et al. [5] employed a meshless local Petrov–Galerkin approach (MLPG). Because of additional mathematical and computational complexities, the above works did not take into account transient effects of heat transfer. For combined radiation and conduction heat transfer in semitransparent medium, transient heat transfer must be analyzed because semitransparency can cause internal temperature responses that are much more rapid and have distributions different form those only due to conduction.

Liu and Tan [6] solved the transient coupled heat transfer problems for a graded index slab with black surfaces and analyze the transient response caused by pulsed irradiation. Yi et al. [7] analyzed the effects of graded refractive index on steady and transient heat transfer in semitransparent slab using ray-tracing/nodal-analyzing method (RTNAM). Tan et al. [8] and Yi et al. [9] adopted RTNAM to solve transient coupled heat transfer in scattering medium with graded refractive index. In Ref. [8], the refractive index varies continuously along the slab thickness and both boundary surfaces are specular and semitransparent. In Ref. [9], the boundaries are one semitransparent surface and the other opaque surface. Mishra et al. [10] used a combined Lattice Boltzmann method (LBM) and discrete transfer method (DTM). In Ref. [10], even the cases of variable thermal conductivity and variable refractive index were considered. Luo et al. [11], Tan et al. [12], and Yi et al. [13] employed RTNAM to solve transient combined radiation and conduction heat transfer in a scattering multilayer composite with specular interfaces.

In the field of numerical simulations, it is well known that the finite element method (FEM) and the finite volume method (FVM) can provide linear convergence while the spectral methods can provide exponential convergence [14,15]. Spectral methods have been widely applied in computational fluid dynamics [16,17], electrodynamics [18] and magnetohydrodynamics [19,20], etc. While early in 1992, Zenouzi and Yener [21] used the Galerkin method to solve the radiative part of a radiation and natural convection combined problem. Later, Kuo et al. [22] made a numerical comparison for spectral methods and FVM to solve the radiation and natural convection combined problem and they concluded that the spectral methods were more accurate. De Oliveira et al. [23] made a combination of spectral method and Laplace transform to solve radiative heat transfer in isotropic scattering media. Recently, the collocation spectral method for radiative part in stellar modeling was carried out [24]. In the work of Modest and Yang [25], the spherical harmonics method was further developed to reduce the number of first-order partial differential equations. Zhao and Liu [26–28] proposed the spectral element method for radiative heat transfer and coupled radiative and conductive heat transfer. The authors would like to mention that the spectral element method is very suitable for irregular geo-

[1]Corresponding author.

Contributed by the Heat Transfer Division of ASME for publication in the JOURNAL OF HEAT TRANSFER. Manuscript received January 18, 2009; final manuscript received July 23, 2009; published online March 8, 2010. Assoc. Editor: H.-P. Tan.

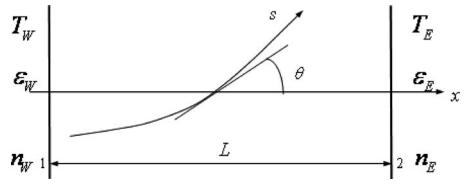

Fig. 1 Physical geometry of slab

metrical systems while its accuracy is still lower than that of pure spectral methods. Li and co-workers [29–32] successfully developed the Chebyshev collocation spectral method for 1D radiative heat transfer even with anisotropic scattering medium [29], 1D radiative heat transfer in graded index medium [30], coupled conduction and radiation in concentric spherical participating medium [31], and combined conduction and radiation in one-dimensional semitransparent medium with graded index [32].

In this paper, we extend the spectral collocation method to solve the transient coupled conduction and radiation heat transfer in graded index medium. In the following of this paper, the physical model and governing equations will be presented in the second section. The SP-DOM formulations for radiative transfer equation (RTE) and energy equation will be presented in detail in the third section. The discretized equations, for radiation and conduction separately, will be simultaneously solved iteratively and the process will be described in the fourth section. Validations by typical case with available numerical results and analysis by the effects of various parameters are made in the fifth section. Finally, the last section gives the conclusions.

2 Physical Model and Governing Equations

We consider a problem of transient combined radiation and conduction heat transfer in one-dimensional semitransparent gray absorbing, emitting, and anisotropic scattering slab with thickness L bounded by two opaque, diffuse, and gray walls (see Fig. 1). The refractive index n varies along the axial coordinate x. Some properties such as density ρ, specific heat c_p, extinction coefficient β, and scattering albedo ω are uniform over the slab but the thermal conductivity λ of medium varies with temperature. The variation in thermal conductivity is taken as

$$\lambda = \lambda_0 + a'(T - T_0) \tag{1}$$

where λ_0 is the reference thermal conductivity, a' is the coefficient of thermal conductivity variation, and T_0 is the reference temperature. The initial temperature of the system is T_0. On both sides of the slab, the emissivities are ε_W and ε_E and the temperatures are T_W and T_E, respectively.

The governing equation for radiative transfer in one-dimensional graded index medium in term of radiation intensity [33] can be written as

$$\mu\frac{\partial I(x,\mu)}{\partial x} + \gamma'(1-\mu^2)\frac{\partial I(x,\mu)}{\partial \mu} + (k_a + k_s - 2\gamma'\mu)I(x,\mu) = n^2 k_a I_b(x) + \frac{k_s}{2}\int_{-1}^{1} I(x,\mu')\Phi(\mu',\mu)d\mu' \tag{2}$$

with the boundary conditions

$$I(x_W) = \varepsilon_W n_W^2\frac{\sigma T_W^4}{\pi} + 2(1-\varepsilon_W)\int_{-1}^{0} I(x_W,\mu')|\mu'|d\mu', \quad \mu > 0 \tag{3a}$$

$$I(x_E) = \varepsilon_E n_E^2\frac{\sigma T_E^4}{\pi} + 2(1-\varepsilon_E)\int_{0}^{1} I(x_E,\mu')|\mu'|d\mu', \quad \mu < 0 \tag{3b}$$

where $I(x,\mu)$ is the radiation intensity at position x and direction cosine μ, $\gamma' = \partial(\ln n)/\partial x$ is the derivative of refractive index, k_a is the absorption coefficient, k_s is the scattering coefficient, $I_b(x)$ is the blackbody radiation intensity, and σ is the Stefan–Boltzmann constant. The anisotropic scattering phase function $\Phi(\mu',\mu)$ is the F2 phase function given by Eq. (4) with asymmetry factor of 0.66972 [34].

$$\Phi(\mu',\mu) = \sum_{j=0}^{8} C_j P_j(\mu) P_j(\mu') \tag{4}$$

where P_j are the Legendre polynomials and C_j are specified coefficients defined as $C_0=1.0$, $C_1=2.00917$, $C_3=1.56339$, $C_4=0.67407$, $C_5=0.04725$, $C_6=0.00671$, $C_7=0.00068$, and $C_8=0.00005$.

From the view of energy conservation, the simplified transient state energy equation in the system reads

$$\rho c_p\frac{dT(x,t)}{dt} = \lambda\frac{\partial^2 T(x,t)}{\partial x^2} - k_a\left[4n^2\sigma T^4(x,t) - 2\pi\int_{-1}^{1} I(x,\mu)d\mu\right] \tag{5}$$

with the initial and boundary conditions

$$T(x,0) = T_0 \tag{6}$$

$$T(x_W,t) = T_W \tag{7a}$$

$$T(x_E,t) = T_E \tag{7b}$$

Similar in Ref. [10], employing dimensionless variables, namely, dimensionless temperature $\Theta = T/T_0$, dimensionless axial coordinate $X = x/L$, dimensionless derivative of refractive index $\gamma = \tau_L^{-1}\partial(\ln n)/\partial X$, dimensionless radiative intensity $G = (\pi I)/(\sigma T_0^4)$, conduction-radiation parameter $N_{cr} = (\lambda_0\beta)/(4\sigma T_0^3)$, optical thickness $\tau_L = \beta L$, scattering albedo $\omega = k_s/\beta$, dimensionless time $\zeta = (\lambda_0\beta^2 t)/(\rho c_p)$, and dimensionless coefficient of thermal conductivity $a = a'T_0/\lambda_0$, the set of dimensionless coupled governing equation for the combined radiation and conduction problem in graded index medium can be expressed as

$$\frac{\mu}{\tau_L}\frac{\partial G(X,\mu)}{\partial X} + \gamma\frac{\partial}{\partial \mu}[(1-\mu^2)G(X,\mu)] + G(X,\mu) = (1-\omega)n^2\Theta^4(X) + \frac{\omega}{2}\int_{-1}^{1} G(X,\mu')\Phi(\mu',\mu)d\mu' \tag{8}$$

with the boundary conditions

$$G(X_W,\mu) = \varepsilon_W n_W^2\Theta_W^4 + 2(1-\varepsilon_W)\int_{-1}^{0} G(X_W,\mu')|\mu'|d\mu', \quad \mu > 0 \tag{9a}$$

$$G(X_E,\mu) = \varepsilon_E n_E^2\Theta_E^4 + 2(1-\varepsilon_E)\int_{0}^{1} G(X_E,\mu')|\mu'|d\mu', \quad \mu < 0 \tag{9b}$$

and

$$\frac{\partial\Theta(X,\zeta)}{\partial\zeta}=[a\Theta(X,\zeta)-a+1]\frac{1}{\tau_L^2}\frac{\partial^2\Theta(X,\zeta)}{\partial X^2}-\frac{(1-\omega)}{N_{cr}}\left[n^2\Theta^4(X,\zeta)-\frac{1}{2}\int_{-1}^{1}G(X,\mu')d\mu'\right] \tag{10}$$

with the initial and boundary conditions

$$\Theta(X,0)=\Theta_0 \tag{11}$$

$$\Theta(X_W,t)=\Theta_W \tag{12a}$$

$$\Theta(X_E,t)=\Theta_E \tag{12b}$$

3 Discretization of Governing Equation and Boundary Conditions Import

3.1 Formulations of Radiative Transfer Equation. The discretized form of dimensionless RTE is obtained by evaluating Eq. (8) at each discrete direction and replacing the integral by numerical quadrature

$$\frac{\mu^m}{\tau_L}\frac{\partial G^m(X)}{\partial X}+\gamma\left\{\frac{\partial}{\partial\mu}[(1-\mu^2)G(X)]\right\}_{\mu=\mu^m}+G^m(X)=(1-\omega)n^2\Theta^4(X)+\frac{\omega}{2}\sum_{m'=1}^{M}G^{m'}(x)\Phi^{m',m}w^{m'} \tag{13}$$

The discrete ordinate representations of the boundary condition, Eq. (9), is given by

$$G_W^m=\varepsilon_W n_W^2\Theta_W^4+2(1-\varepsilon_W)\sum_{\mu^{m'}<0}G_W^{m'}|\mu^{m'}|w^{m'},\quad \mu^m>0 \tag{14a}$$

$$G_E^m=\varepsilon_E n_E^2\Theta_E^4+2(1-\varepsilon_E)\sum_{\mu^{m'}>0}G_E^{m'}|\mu^{m'}|w^{m'},\quad \mu^m<0 \tag{14b}$$

The angular derivative term in Eq. (13) is discretized by central difference scheme [35], namely,

$$\left\{\frac{\partial}{\partial\mu}[(1-\mu^2)G(X)]\right\}_{\mu=\mu^m}\approx\frac{\alpha^{m+1/2}G^{m+1/2}-\alpha^{m-1/2}G^{m-1/2}}{w^m} \tag{15}$$

where $G^{m+1/2}$ and $G^{m-1/2}$ are angular intensities in the directions of $m+1/2$ and $m-1/2$ and the central difference scheme is adopted to correlate them to the unknown G^m, i.e., $G^m=\frac{1}{2}(G^{m+1/2}+G^{m-1/2})$. The constants $\alpha^{m+1/2}$ and $\alpha^{m-1/2}$ only depend on the difference scheme and can be determined by the following recurrence:

$$\alpha^{m+1/2}-\alpha^{m-1/2}=-2\mu^m w^m$$

$$\alpha^{1/2}=\alpha^{M+1/2}=0 \tag{16}$$

Finally, Eq. (13) can be rewritten as

$$\frac{\mu^m}{\tau_L}\frac{\partial G^m}{\partial X}+\left[\frac{\gamma}{w^m}\max(\alpha^{m+1/2},0)+\frac{\gamma}{w^m}\max(-\alpha^{m-1/2},0)+1\right]G^m=\frac{\gamma}{w^m}\max(-\alpha^{m+1/2},0)G^{m+1}+\frac{\gamma}{w^m}\max(\alpha^{m-1/2},0)G^{m-1}+(1-\omega)n^2\Theta^4+\frac{\omega}{2}\sum_{m'=1}^{M}G^{m'}\Phi^{m',m}w^{m'} \tag{17}$$

The above equation group (Eq. (17)) for $m=1,2,\cdots,M$ will not be iteratively solved based on discrete ordinates method as the conventional way in Ref. [33]. In our work, the spectral collocation method will be used for the spatial discretization. Similar in Ref. [36], the strategy of RTE discretization in this article belongs to the category of so called space-angle decoupling.

First, the mapping of arbitrary interval $X\in[X_W,X_E]$ to standard interval $s\in[-1,1]$ is needed to fit the requirement of Chebyshev polynomial

$$s=\frac{2X-(X_W+X_E)}{X_E-X_W},\quad X=\frac{s(X_E-X_W)+(X_W+X_E)}{2} \tag{18}$$

After mapping, Eq. (17) becomes

$$\left[\frac{\mu^m}{\tau_L}\left(\frac{2}{X_E-X_W}\right)\frac{\partial}{\partial s}+\frac{\gamma}{w^m}\max(\alpha^{m+1/2},0)+\frac{\gamma}{w^m}\max(-\alpha^{m-1/2},0)+1\right]G^m=\frac{\gamma}{w^m}\max(-\alpha^{m+1/2},0)G^{m+1}+\frac{\gamma}{w^m}\max(\alpha^{m-1/2},0)G^{m-1}+(1-\omega)n^2\Theta^4+\frac{\omega}{2}\sum_{m'=1}^{M}G^{m'}\Phi^{m',m}w^{m'} \tag{19}$$

The Chebyshev–Gauss–Lobatto collocation points are used for spatial discretization

$$s_i=-\cos\frac{\pi i}{N},\quad i=0,1,\cdots,N \tag{20}$$

The Chebyshev approximation of dimensionless radiative intensity reads the following matrix equation:

$$G_N^m(s)=\sum_{k=0}^{N}\hat{G}_k^m T_k(s) \tag{21}$$

where the coefficients $\hat{G}_k^m$, $k=0,1,\cdots,N$ are determined by requiring $G_N^m(s)$ to coincide with $G^m(s)$ at the collocation points s_i $i=0,1,\cdots,N$ and the $T_k(s)$ is the first kind Chebyshev polynomial. The polynomial of degree N defined by Eq. (21) can be the Lagrange interpolation polynomial based on the set $\{s_i\}$ such as

$$G_k(s)=\sum_{j=0}^{N}h_j(s)G(s_j) \tag{22}$$

where $h_j(s)$ is a function of the first-order derivative of Chebyshev polynomial and its detail definition and expression can be found in Ref. [17].

By substituting Eq. (22) into Eq. (19), the final discretized form of Eq. (19) reads

$$A^m G^m=F^m \tag{23}$$

where the elemental expressions A^m and F^m are

$$A_{ik}^m = \begin{cases} \dfrac{\mu^m}{\tau_L}\left(\dfrac{2}{X_E - X_W}\right) D_{s,ik}^{(1)} + \dfrac{\gamma_i}{w^m}\max(\alpha^{m+1/2},0) + \dfrac{\gamma_i}{w^m}\max(-\alpha^{m-1/2},0) + 1, & i = k \\ \dfrac{\mu^m}{\tau_L}\left(\dfrac{2}{X_E - X_W}\right) D_{s,ik}^{(1)}, & \text{otherwise} \end{cases} \tag{24a}$$

$$F_i^m = \frac{\gamma_i}{w^m}\max(-\alpha^{m+1/2},0) G_i^{m+1} + \frac{\gamma_i}{w^m}\max(\alpha^{m-1/2},0) G_i^{m-1} + (1 - \omega) n^2 \Theta_i^4 + \frac{\omega}{2}\sum_{m'=1}^{M} G_i^{m'} \Phi^{m',m} w^{m'} \tag{24b}$$

where the matrix $D_s^{(1)}$ is the first-order derivative matrix in s direction corresponding to Chebyshev–Gauss–Lobatto collocation points and its detailed computation can be originally found in Ref. [15,31].

After the boundary conditions Eqs. (14*a*) and (14*b*) import, Eq. (23) becomes

$$\widetilde{A}^m \widetilde{G}^m = \widetilde{F}^m \tag{25}$$

where

$$\widetilde{A}^m = \begin{cases} A^m(1{:}N, 1{:}N), & \mu^m > 0 \\ A^m(0{:}N-1, 0{:}N-1), & \mu^m < 0 \end{cases} \tag{26a}$$

$$\widetilde{G}^m = \begin{cases} G^m(1{:}N), & \mu^m > 0 \\ G^m(0{:}N-1), & \mu^m < 0 \end{cases} \tag{26b}$$

$$\widetilde{F}^m = \begin{cases} F^m(1{:}N) - A^m(1{:}N, 0) G^m(0), & \mu^m > 0 \\ F(0{:}N-1) - A^m(0{:}N-1, N) G^m(N), & \mu^m < 0 \end{cases} \tag{26c}$$

From above equations the physical means of the problem should be clearly understood. For positive direction $\mu^m > 0$, the radiative intensities on the west surface G_W^m corresponding to above vector element $G^m(0)$ are computed by Eq. (14*a*) and should be imported through Eq. (26*c*) but the radiative intensities on east surface G_E^m corresponding to above vector element $G^m(N)$ are unknowns. For this situation, a subsquare matrix $\widetilde{C}^m$ with deletion of its first row and first column times the unknown vector $\widetilde{G}^m$ with its first element cancelled constitute the left hand side of matrix Eq. (25). For negative direction $\mu^m < 0$, the situation is just reverse.

3.2 Formulations of Energy Equation. Using the fully implicit time different scheme for Eq. (10), the temporal discretization of energy equation is as follows:

$$\frac{\Theta^{\zeta+\Delta\zeta} - \Theta^{\zeta}}{\Delta\zeta} = (a\Theta^{\zeta+\Delta\zeta} - a + 1)\frac{1}{\tau_L^2}\frac{\partial^2 \Theta^{\zeta+\Delta\zeta}}{\partial X^2} - \frac{(1-\omega)}{N_{cr}}\left[n^2 (\Theta^{\zeta+\Delta\zeta})^4 - \frac{1}{2}\sum_{m}^{M} G^{m,\zeta+\Delta\zeta} w^m \right] \tag{27}$$

The fully implicit time difference scheme is unconditionally stable. Equation (27) can be arranged as

$$(a\Theta^{n+1} - a + 1)\frac{\Delta\zeta}{\tau_L^2}\frac{\partial^2 \Theta^{n+1}}{\partial X^2} - \frac{\Delta\zeta}{N_{cr}}(1-\omega) n^2 (\Theta^{n+1})^4 - \Theta^{n+1} = -\Theta^n - \frac{1}{2}\frac{\Delta\zeta}{N_{cr}}(1-\omega)\sum_{m}^{M} G^{m,n+1} w^m \tag{28}$$

Now the remaining discretization of energy Eq. (27) is needed only in space domain $[X_W, X_E]$. After the mapping of $[X_W, X_E]$ to $[-1, 1]$, Eq. (28) becomes

$$(a\Theta^{n+1} - a + 1)\left(\frac{2}{X_E - X_W}\right)^2 \frac{\Delta\zeta}{\tau_L^2}\frac{\partial^2 \Theta^{n+1}}{\partial s^2} - \frac{\Delta\zeta}{N_{cr}}(1-\omega) n^2 (\Theta^{n+1})^4 - \Theta^{n+1} = -\Theta^n - \frac{1}{2}\frac{\Delta\zeta}{N_{cr}}(1-\omega)\sum_{m}^{M} G^{m,n+1} w^m \tag{29}$$

Employing the Chebyshev collocation spectral method for Eq. (29) in the same way as it for RTE, we obtain the following matrix equation:

$$P\Theta = V \tag{30}$$

where the elemental expressions for P and V are

$$P_{ik} = \begin{cases} (a\Theta_i^{*,n+1} - a + 1)\left(\dfrac{2}{X_E - X_W}\right)^2 \dfrac{\Delta\zeta}{\tau_L^2} D_{s,ik}^{(2)} - \dfrac{\Delta\zeta}{N_{cr}}(1-\omega) n_i^2 (\Theta_i^{*,n+1})^3 - 1, & i = k \\ (a\Theta_i^{*,n+1} - a + 1)\left(\dfrac{2}{X_E - X_W}\right)^2 \dfrac{\Delta\zeta}{\tau_L^2} D_{s,ik}^{(2)}, & \text{otherwise} \end{cases} \tag{31a}$$

$$V_i = -\Theta_i^n - \frac{1}{2}\frac{\Delta\zeta}{N_{cr}}(1-\omega)\sum_{m}^{M} G_i^{m,n+1} w^m \tag{31b}$$

where the superscript "$*$" of Θ denotes the last iterative value and the matrix $D^{(2)}$ ($D^{(2)} = D^{(1)} \times D^{(1)}$) is the second-order derivative matrix corresponding to Chebyshev–Gauss–Lobatto collocation points.

After the Dirichlet boundary condition (Eq. (12)) import, Eq. (30) becomes

$$\widetilde{P}\widetilde{\Theta} = \widetilde{V} \tag{32}$$

where

$$\widetilde{P} = P(1{:}N-1, 1{:}N-1) \tag{33a}$$

$$\tilde{\Theta} = \Theta(1{:}N-1) \tag{33b}$$

$$\tilde{V} = V(1{:}N-1) - P(1{:}N-1,0)\Theta(0) - P(1{:}N-1,N)\Theta(N) \tag{33c}$$

For the above equation, the temperature on the west surface Θ_W (corresponding to the above vector $\Theta(0)$) and the east surface Θ_E (corresponding to the above vector $\Theta(N)$) are computed by Eq. (12) and imported by Eq. (33*c*).

4 Simultaneous Solution Procedure

The implementation of spectral collocation method for solving transient coupled conduction and radiation heat transfer problem in graded index medium can be executed through the following routine.

Step 1. Choose the resolution (number of collocation points) N and compute the coordinate values of the nodes; initialize the radiative intensity field and the temperature field.
Step 2. Prepare to compute the $D^{(1)}$, $D^{(2)}$, and A matrices once for everything.
Step 3. Loop at each time step $n=1,2,\cdots,N_t$.
Step 4. Calculate the matrix F^m; impose the boundary condition and directly solve the matrix RTE (Eq. (25)) by $\tilde{G}^m = (\tilde{A}^m)^{-1}\tilde{F}^m$ in each direction.
Step 5. Calculate the P and V matrices; impose the boundary condition and directly solve the matrix energy equation (Eq. (32)) by $\tilde{\Theta} = (\tilde{P})^{-1}\tilde{V}$.
Step 6. Terminate the iteration if the relative maximum absolute difference in dimensionless radiative intensities for all nodes and directions or temperature for all nodes is less than the tolerance (10^{-8} for example), otherwise go back to step 4.
Step 7. If it is not finished on time, go back to step 3 or else, do postprocessing.

From the formulations and the above routine, the computation tasks mainly exit in the category of linear algebra. The two most important steps especially for the matrix equations solving are steps 4 and 5, which can be executed directly and efficiently while the other steps are concerned with the assembling of matrices only.

5 Results and Discussion

In the numerical community, the main superiorities of spectral methods over different finite methods, FVM and FEM, are their exponential convergence and high accuracy [15]. In our present work, we consider transient combined radiation and conduction heat transfer in graded index medium. In this case, the initial temperature of the medium is $T_0=1000$ K, the temperatures of boundary walls are imposed as $T_W=1000$ K and $T_E=1000$ K, and the thickness of the slab keeps a constant value of 1 cm. In the next parts of this paper, the dimensionless time step $\Delta\zeta=1.0\times10^{-4}$ is used and steady-state condition is assumed to have been achieved while the maximum absolute difference in dimensionless temperature Θ at any location between two consecutive time levels does not exceed 1.0×1.0^{-8}.

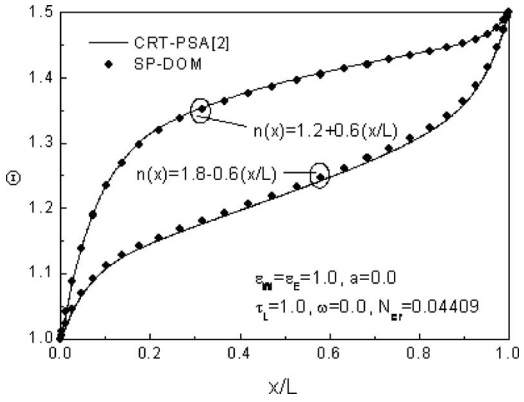

Fig. 2 Comparisons of dimensionless temperature profiles of SP-DOM with those of CRT-PSA for the cases of $n(x)=1.2+0.6(x/L)$ and $n(x)=1.8-0.6(x/L)$

In Fig. 2, for conduction-radiation parameter $N_{cr}=0.04409$, optical thickness $\tau_L=1.0$, scattering albedo $\omega=0.0$, wall emissivities $\varepsilon_W=\varepsilon_E=1.0$, and constant thermal conductivity ($a=0.0$) for graded index $n(x)=1.2+0.6(x/L)$ and $n(x)=1.8-0.6(x/L)$ individually, dimensionless temperature results of SP-DOM are compared with those reported in literature [2]. It is seen that the results of SP-DOM match very well with those of Xia et al. [2] by CRT-PSA.

In Table 1, the effects of the number of collocation points and the number of directions on dimensionless temperature, which reached the steady-state at five locations of $x/X=0.125$, 0.250, 0.500, 0.750, and 0.875, are listed for SP-DOM. These results are shown for optical thickness $\tau_L=1.0$, scattering albedo $\omega=0.0$, wall emissivities $\varepsilon_W=\varepsilon_E=1.0$, constant thermal conductivity ($a=0.0$), conduction-radiation parameter $N_{cr}=0.1$, and constant graded index $n=1.5$. It can be seen that the dimensionless temperature Θ does not obviously change when the number of collocation points is greater than 29. With 29 collocation points, the results of the different order of S_N approximation on Θ at the five locations are also listed in Table 1. No significant differences can be observed

Table 1 Effects of the number of collocation points and the number of directions on steady-state at five locations for $\tau_L=1.0$, $\omega=0.0$, $\varepsilon_W=\varepsilon_E=1.0$, $a=0.0$, $N_{cr}=0.1$, and $n=1.5$

Number of collocation points	Number of directions	x/X 0.125	0.250	0.500	0.750	0.875
Effect of collocation points						
9	S_6	1.1704	1.2439	1.3111	1.3560	1.4087
19	S_6	1.1704	1.2437	1.3111	1.3563	1.4086
29	S_6	1.1704	1.2437	1.3111	1.3563	1.4085
39	S_6	1.1704	1.2437	1.3111	1.3563	1.4085
Effect of the angular discretization order						
29	S_4	1.1693	1.2439	1.3112	1.3558	1.4095
29	S_6	1.1704	1.2437	1.3111	1.3563	1.4085
29	S_8	1.1706	1.2435	1.3110	1.3563	1.4082
29	S_{12}	1.1706	1.2435	1.3110	1.3563	1.4080

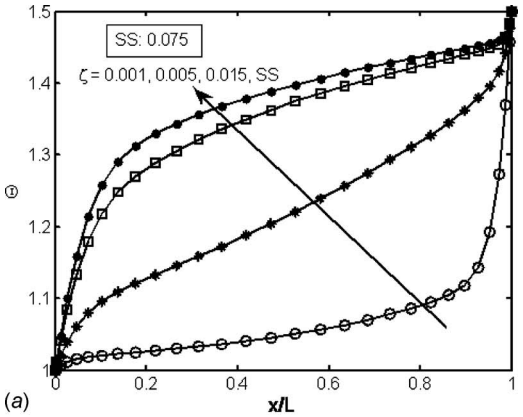

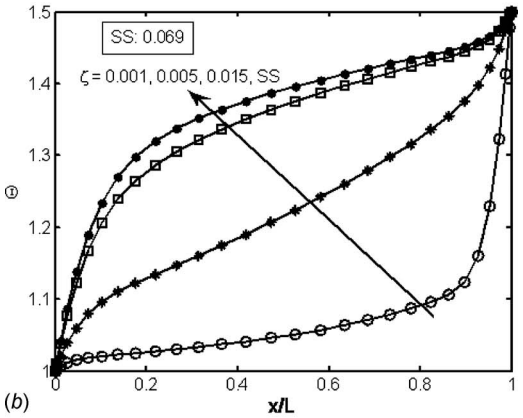

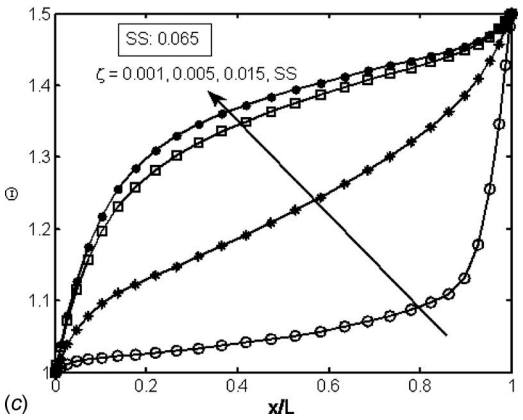

Fig. 3 Effect of variable thermal conductivity on dimensionless temperature profile in linear refractive index medium: (*a*) $a=-2.0$, (*b*) $a=0.0$, and (*c*) $a=2.0$

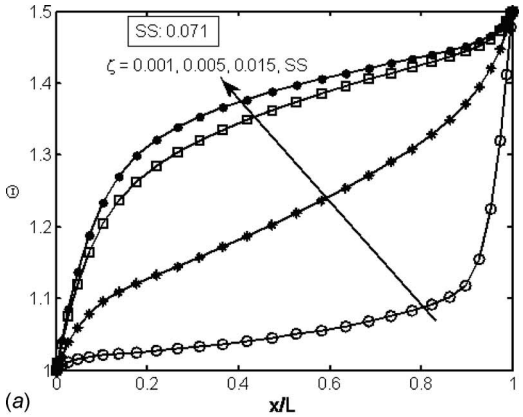

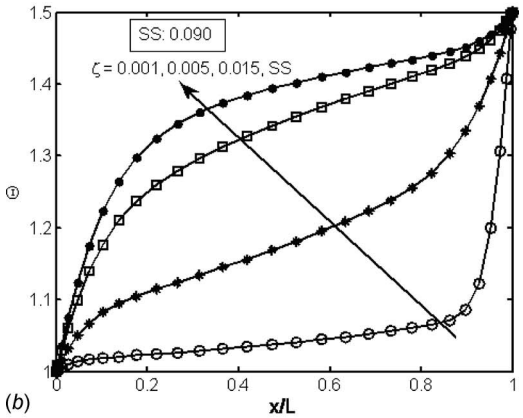

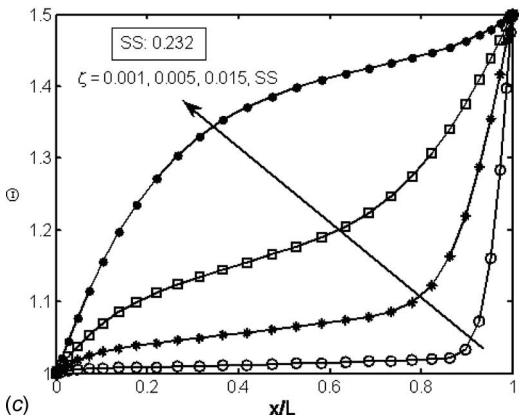

Fig. 4 Effect of scattering albedo on dimensionless temperature profile in graded index medium: (*a*) $\omega=0.1$, (*b*) $\omega=0.5$, and (*c*) $\omega=0.9$

for S_4, S_6, S_8, and S_{12} approximations. Therefore, in the following, we used 29 collocation points for space discretization and S_6 approximation for angular.

In Fig. 3, the effect of variable thermal conductivity with $a=-2.0$, 0.0, and 2.0 on dimensionless temperature profile has been shown in the case of $n(x)=1.2+0.6(x/L)$, $\tau_L=1.0$, $\omega=0.0$, $N_{cr}=0.04409$, and $\varepsilon_W=\varepsilon_E=1.0$. It is seen that at $\zeta=0.001$, the temperature of the medium near the hot boundary increase with the increasing of thermal conductivity while the temperature of the medium near the cold boundary decrease. This trend becomes more obvious with over time. The reason can be explained that for $a=2.0$, the thermal conductivity is proportional to the temperature. For $a=-2.0$, the phenomenon is just the opposite.

Figure 4 shows the effect of scattering albedo on dimensionless temperature profile in graded index medium. The results are shown for $n(x)=1.2+0.6(x/L)$, $\tau_L=1.0$, $a=0.0$, $N_{cr}=0.04409$, and $\varepsilon_W=\varepsilon_E=1.0$. Compared with the small scattering albedo under the case of large scattering, the temperature gradient, which is near the hot boundary becomes larger, and the time to reach steady-state becomes longer.

In Fig. 5, the effect of emissivity of boundary has been shown on dimensionless temperature profile under the case of $n(x)=1.2+0.6(x/L)$, $\tau_L=1.0$, $a=0.0$, $\omega=0.0$, and $N_{cr}=0.04409$. From Fig. 5, we know that the temperature level of the medium increases with the increase in emissivity of the hot boundary while in reverse, the temperature level of the medium decreases with the increasing of emissivity of the cold boundary.

In Fig. 6, for $n(x)=1.2+0.6(x/L)$, $\tau_L=1.0$, $a=0.0$, $\omega=0.0$, and $\varepsilon_W=\varepsilon_E=1.0$, the dimensionless temperature profiles have been shown for three values of the conduction-radiation parameter N_{cr}.

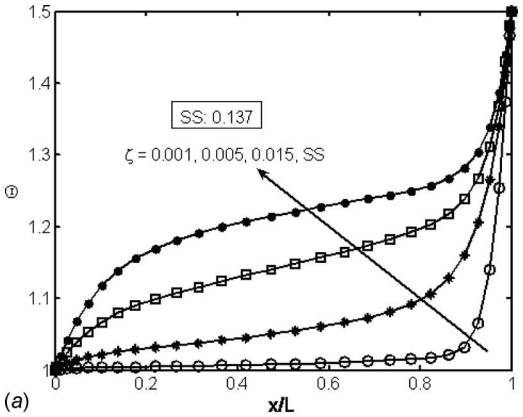

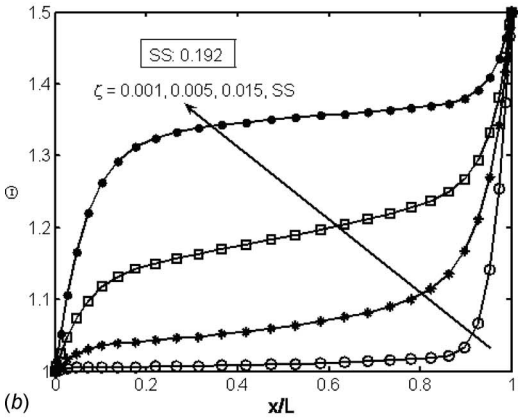

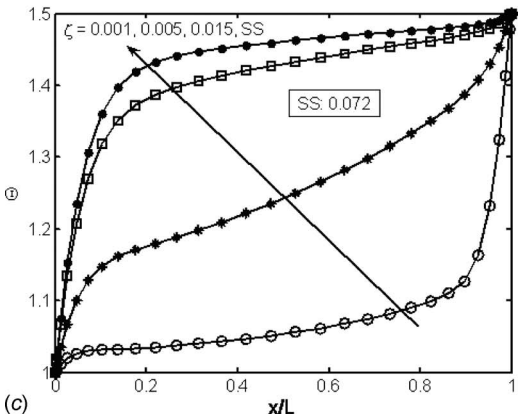

Fig. 5 Effect of emissivity of boundary on dimensionless temperature profile in graded index medium: (*a*) ε_W=1.0, ε_E=0.1; (b) ε_W=0.1, ε_E=0.1; and (*c*) ε_W=0.1, ε_E=1.0

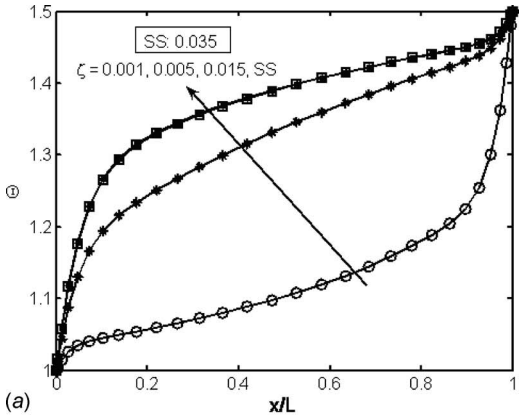

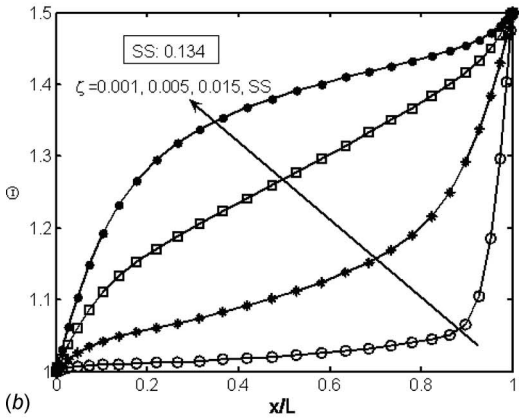

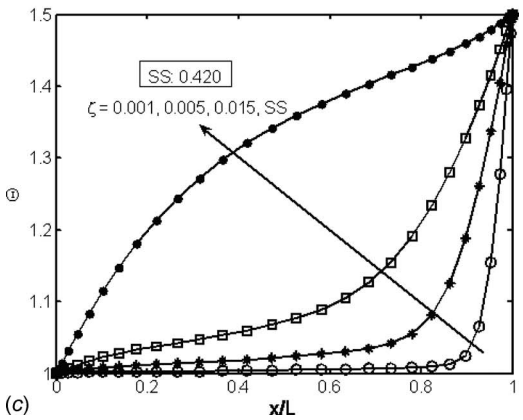

Fig. 6 Effect of conduction-radiation parameter on dimensionless temperature profile in graded index medium: (*a*) N_{cr}=0.02, (*b*) N_{cr}=0.1, and (*c*) N_{cr}=0.5

It is seen from Fig. 6 that with the increase in conduction-radiation parameter N_{cr}, Θ near the hot boundary increases. While near the cold boundary, an opposite trend is observed. The curve of Θ is more linear for higher N_{cr}. For the conduction dominated case (N_{cr}=0.5), the time to reach steady-state becomes longer.

In Fig. 7, for $n(x)=1.2+0.6\sin(\pi x/L)$, a=0.0, ω=0.0, and $\varepsilon_W=\varepsilon_E$=1.0, the dimensionless temperature profiles have been shown for different optical thickness τ_L. As optical thickness increases, the temperature profiles gradually become steep from the west to the east. The reason is clear, for large optical thickness (τ_L=5.0 for example) of the medium and the radiation is strongly attenuated within the medium.

In Fig. 8, keeping other parameters of Fig. 7 is fixed; the effect of graded index on dimensionless temperature profiles in graded index is shown. In the case of $n(x)=1.2+0.6\sin(\pi x/L)$, the temperature near the cold boundary increase. The situation is opposite for the temperature near the hot boundary. Thus, the temperature curves become flat in the middle region. Compare with the case of $n(x)=1.2+0.6\sin(\pi x/L)$, in the case of $n(x)=1.8-0.6\sin(\pi x/L)$ and $n(x)=1.5$, the temperature near the hot boundary increases. Near the cold boundary, an opposite trend is observed. This trend becomes obvious over time. This trend owes it to the fact that the graded index contributes to the nonlinearity. The emitting ability of medium is proportional to the square of graded index.

6 Conclusions

To avoid the complicated computation of curved ray-tracing, the spectral collocation method based on discrete ordinates equation is successfully applied to solve transient combined radiation and conduction heat transfer problems in semitransparent graded

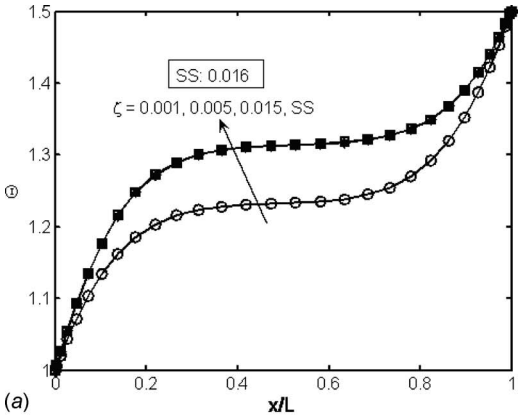

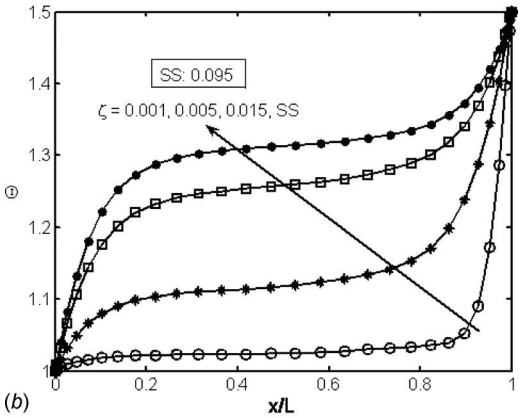

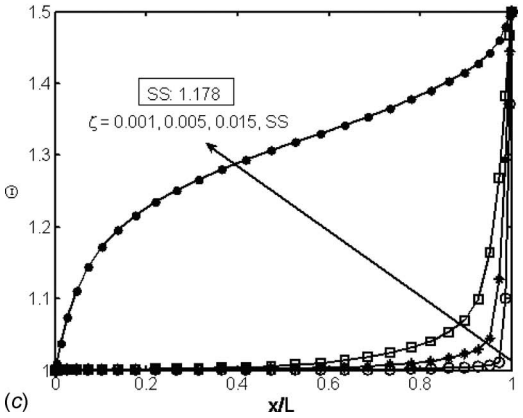

Fig. 7 Effect of optical thickness on dimensionless temperature profile in graded index medium: (*a*) $\tau_L=0.2$, (*b*) $\tau_L=1.0$, and (*c*) $\tau_L=5.0$

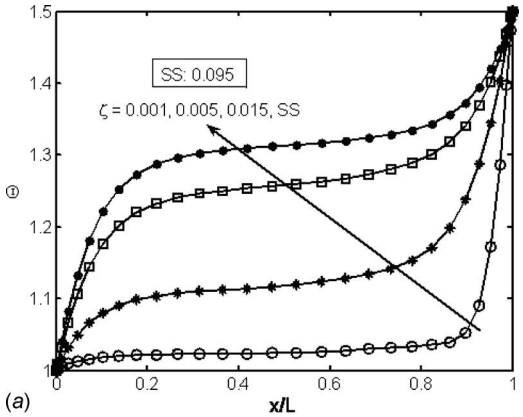

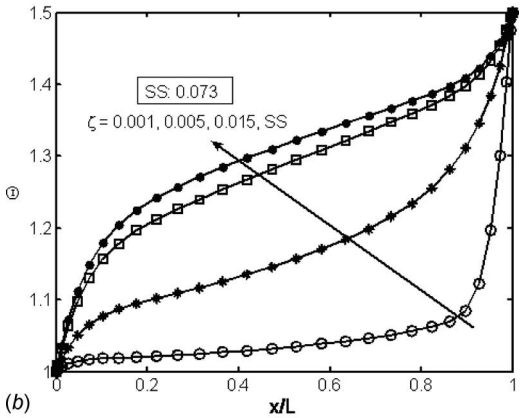

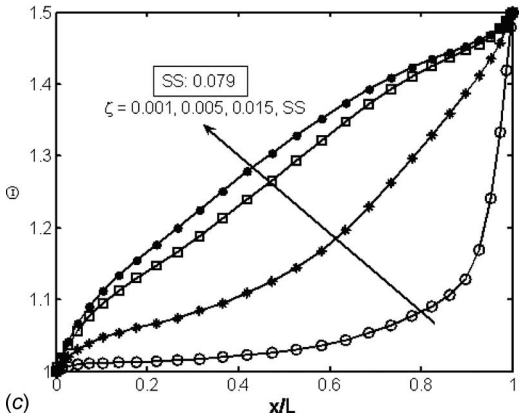

Fig. 8 Effect of graded index on dimensionless temperature profile: (*a*) $n(x)=1.2+0.6\sin(\pi x/L)$, (*b*) $n(x)=1.5$, and (*c*) $n(x)=1.8-0.6\sin(\pi x/L)$

index medium. The angular dependent radiative intensity is discretized by DOM and the spatial dependent radiative intensity and temperature are expressed by Chebyshev polynomial and discretized by spectral collocation method. The results of the SP-DOM are compared with those available data in literatures for variable refractive index. The comparisons indicate that the SP-DOM has a good accuracy and efficiency even using only 29 nodes and six directions of the S_N approximation. Effects of variable thermal conductivity parameter, scattering albedo, emissivity of boundary, conduction-radiation parameter, optical thickness, and refractive index on transient thermal behavior are also studied.

Acknowledgment

This work was supported by the National Fundamental Research Programme of China (under Contract No. 2006CB601203).

Nomenclature

a = dimensionless coefficient of thermal conductivity variation
a' = variable thermal conductivity parameter
A = matrix defined in Eq. (23)
$\tilde{A}$ = matrix defined in Eq. (25)
c_p = specific heat of medium, J Kg^{-1} K^{-1}
$D^{(1)}$ = the first-order derivative matrix
$D^{(2)}$ = the second-order derivative matrix
F = matrix defined in Eq. (23)
$\tilde{F}$ = matrix defined in Eq. (25)
G = dimensionless radiative intensity
$\hat{G}$ = coefficients for spectral approximation in Eq. (21)

h_j = function of the first-order derivative of Chebyshev polynomial
I = radiative intensity, W m^{-2} sr^{-1}
I_b = blackbody radiative intensity, W m^{-2} sr^{-1}
k_a = absorption coefficient, m^{-1}
k_s = scattering coefficient, m^{-1}
L = slab thickness, m
M = the direction number
ρ = density of medium, Kg m^{-3}
σ = Stefan–Boltzmann constant, W m^{-2} K^{-4}
ω = scattering albedo
Φ = scattering phase function
τ_L = optical thickness
n = refractive index
N = total number of solution nodes
N_{cr} = conduction-radiation parameter
P = matrix defined in Eq. (30)
$\tilde{P}$ = matrix defined in Eq. (32)
V = matrix defined in Eq. (30)
$\tilde{V}$ = matrix defined in Eq. (32)
s = standard Gauss–Lobatto points
T = temperature, K
w^m = weight corresponding to the direction m
x = axial coordinate, m
X = dimensionless axial coordinate

Greek Symbols

α = Coefficient defined in Eq. (15)
β = extinction coefficient, m^{-1}
γ = dimensionless derivative of graded index
γ' = derivative of graded index
ε = emissivity
Θ = dimensionless temperature
λ = thermal conductivity, W m^{-1} K^{-1}
μ = direction cosine
ζ = dimensionless time, $\zeta=\alpha\beta^2 t$

Subscripts

i,j,k = solution node index
0 = reference
E,W = east, west

Superscripts

$m,m',m\pm1/2$ = angular direction of radiation
n = time step
$*$ = the last iterative value

References

[1] Abdallah, P. B., and Le Dez, V., 2000, "Radiative Flux Field Inside an Absorbing-Emitting Semi-Transparent Slab With Variable Spatial Refractive Index at Radiative Conductive Coupling," J. Quant. Spectrosc. Radiat. Transf., **67**, pp. 125–137.

[2] Xia, X. L., Huang, Y., and Zhang, X. B., 2002, "Simultaneous Radiation and Conduction Heat Transfer in a Graded Index Semitransparent Slab With Gray Boundaries," Int. J. Heat Mass Transfer, **45**, pp. 2673–2688.

[3] Huang, Y., Xia, X. L., and Tan, H. P., 2004, "Coupled Radiation and Conduction in a Graded Index Layer With Specular Surfaces," J. Thermophys. Heat Transfer, **18**, pp. 281–285.

[4] Huang, Y., 2002, "A Study on the Thermal Radiative Transfer in Gradient Index Semitransparent Medium," Ph.D. thesis, Harbin Institute of Technology, Harbin, People's Republic of China.

[5] Liu, L. H., Tan, J. Y., and Li, B. X., 2006, "Meshless Approach for Coupled Radiative and Conductive Heat Transfer in One-Dimensional Graded Index Medium," J. Quant. Spectrosc. Radiat. Transf., **101**, pp. 237–248.

[6] Liu, L. H., and Tan, H. P., 2004, "Transient Temperature Response in Semitransparent Variable Refractive Index Medium Subjected to a Pulse Irradiation," J. Quant. Spectrosc. Radiat. Transf., **83**, pp. 333–344.

[7] Yi, H. L., Tan, H. P., Luo, J. F., and Dong, S. K., 2005, "Effects of Graded Refractive Index on Steady and Transient Heat Transfer Inside a Scattering Semitransparent Slab," J. Quant. Spectrosc. Radiat. Transf., **96**, pp. 363–381.

[8] Tan, H. P., Yi, H. L., Luo, J. F., and Zhang, H. C., 2006, "Transient Coupled Heat Transfer Inside a Scattering Medium With Graded Refractive Index," J. Thermophys. Heat Transfer, **20**, pp. 583–594.

[9] Yi, H. L., Tan, H. P., Zhang, H. C., and Luo, J. F., 2006, "Ray-Tracing/Nodal-Analyzing Model for Transient Thermal Behavior of a Scattering Medium With a Variable Refractive Index," Numer. Heat Transfer, Part A, **49**, pp. 607–634.

[10] Mishra, S. C., Krishna, N. A., Gupta, N., and Chaitanya, G. R., 2008, "Combined Conduction and Radiation Heat Transfer With Variable Thermal Conductivity and Variable Refractive Index," Int. J. Heat Mass Transfer, **51**, pp. 83–90.

[11] Luo, J. F., Tan, H. P., Ruan, L. M., and Tong, T. W., 2003, "Refractive Index Effects on Heat Transfer in Multilayer Scattering Composite," J. Thermophys. Heat Transfer, **17**, pp. 407–419.

[12] Tan, H. P., Luo, J. F., Ruan, L. M., and Yu, Q. Z., 2003, "Transient Coupled Heat Transfer in a Multi-layer Composite With Opaque Specular Surfaces and Semitransparent Specular Interfaces," Int. J. Therm. Sci., **42**, pp. 209–222.

[13] Yi, H. L., Xie, M., and Tan, H. P., 2008, "Transient Coupled Heat Transfer in an Anisotropic Scattering Composite Slab With Semitransparent Surfaces," Int. J. Heat Mass Transfer, **51**, pp. 5918–5930.

[14] Gottlieb, D., and Orszag, S. A., 1977, *Numerical Analysis of Spectral Methods: Theory and Applications*, SIAM, Philadelphia, PA.

[15] Canuto, C., Hussaini, M. Y., Quarteroni, A., and Zang, T. A., 2006, *Spectral Methods: Fundamentals in Single Domains*, Springer-Verlag, Berlin, Germany.

[16] Canuto, C., Hussaini, M. Y., Quarteroni, A., and Zang, T. A., 1988, *Spectral Methods in Fluid Dynamics*, Springer-Verlag, New York.

[17] Peyret, R., 2002, *Spectral Methods for Incompressible Viscous Flow*, Springer-Verlag, New York.

[18] Belgacem, F. B., and Grundmann, M., 1998, "Approximation of the Wave and Electromagnetic Diffusion Equations by Spectral Methods," SIAM J. Sci. Comput. (USA), **20**, pp. 13–32.

[19] Shan, X. W., Montgomery, D., and Chen, H. D., 1991, "Nonlinear Magnetohydrodynamics by Galerkin-Method Computation," Phys. Rev. A, **44**, pp. 6800–6818.

[20] Shan, X. W., 1994, "Magnetohydrodynamic Stabilization Through Rotation," Phys. Rev. Lett., **73**, pp. 1624–1627.

[21] Zenouzi, M., and Yener, Y., 1992, "Simultaneous Radiation and Natural Convection in Vertical Slots," *Developments in Radiative Heat Transfer*, ASME HTD-Vol. 203, pp. 179–186.

[22] Kuo, D. C., Morales, J. C., and Ball, K. S., 1999, "Combined Natural Convection and Volumetric Radiation in a Horizontal Annulus: Spectral and Finite Volume Predictions," ASME J. Heat Transfer, **121**, pp. 610–615.

[23] de Oliveira, J. V. P., Cardona, A. V., Vilhena, M. T., and Barros, R. C., 2002, "A Semi-Analytical Numerical Method for Time-Dependent Radiative Transfer Problems in Slab Geometry With Coherent Isotropic Scattering," J. Quant. Spectrosc. Radiat. Transf., **73**, pp. 55–62.

[24] Lara, F. E., and Rieutord, M., 2007, "The Dynamics of a Fully Radiative Rapidly Rotating Star Enclosed Within a Spherical Box," Astron. Astrophys., **470**, pp. 1013–1022.

[25] Modest, M. F., and Yang, J., 2008, "Elliptic PDE Formulation and Boundary Conditions of the Spherical Harmonics Method of Arbitrary Order for General Three-Dimensional Geometries," J. Quant. Spectrosc. Radiat. Transf., **109**, pp. 1641–1666.

[26] Zhao, J. M., and Liu, L. H., 2006, "Least-Squares Spectral Element Method for Radiative Heat Transfer in Semitransparent Media," Numer. Heat Transfer, Part B, **50**, pp. 473–489.

[27] Zhao, J. M., and Liu, L. H., 2007, "Solution of Radiative Heat Transfer in Graded Index Media by Least Square Spectral Element Method," Int. J. Heat Mass Transfer, **50**, pp. 2634–2642.

[28] Zhao, J. M., and Liu, L. H., 2007, "Spectral Element Approach for Coupled Radiative and Conductive Heat Transfer in Semitransparent Medium," ASME J. Heat Transfer, **129**, pp. 1417–1424.

[29] Li, B. W., Sun, Y. S., and Yu, Y., 2008, "Iterative and Direct Chebyshev Collocation Spectral Methods for One-Dimensional Radiative Heat Transfer," Int. J. Heat Mass Transfer, **51**, pp. 5887–5894.

[30] Sun, Y. S., and Li, B. W., 2009, "Chebyshev Collocation Spectral Method for One-Dimensional Radiative Heat Transfer in Graded Index Media," Int. J. Therm. Sci., **48**, pp. 691–698.

[31] Li, B. W., Sun, Y. S., and Zhang, D. W., 2009, "Chebyshev Collocation Spectral Methods for Coupled Radiation and Conduction in a Concentric Spherical Participating Medium," ASME J. Heat Transfer, **131**, pp. 062701–9.

[32] Sun, Y. S., and Li, B. W., "Chebyshev Collocation Spectral Approach for Combined Radiation and Conduction Heat Transfer in One-Dimensional Semitransparent Medium With Graded Index," Int. J. Heat Mass Transfer, in press.

[33] Lemonnier, D., and Le Dez, V., 2002, "Discrete Ordinates Solution of Radiative Transfer Across a Slab With Variable Refractive Index," J. Quant. Spectrosc. Radiat. Transf., **73**, pp. 195–204.

[34] Kim, T. K., and Lee, H., 1988, "Effect of Anisotropic Scattering on Radiative Heat Transfer in Two-Dimensional Rectangular Enclosures," Int. J. Heat Mass Transfer, **31**, pp. 1711–1721.

[35] Modest, M. F., 2003, *Radiative Heat Transfer*, 2nd ed., Academic, New York.

[36] Pontaza, J. P., and Reddy, J. N., 2005, "Least-Squares Finite Element Formulations for One-Dimensional Radiative Transfer," J. Quant. Spectrosc. Radiat. Transf., **95**, pp. 387–406.

Thermal Wave Applications in Flow Fields With Steady Velocity Profile

Zhefu Wang
e-mail: zhefu_wang@amat.com

Richard B. Peterson
e-mail: richard.peterson@oregonstate.edu

Department of Mechanical Engineering,
Oregon State University,
204 Rogers Hall,
Corvallis, OR 97331

This study explores the use of a thermal wave approach for flow field measurement applications, such as flow diagnostics near surfaces and in microfluidic systems. The basic mathematical characteristics of the governing equations of heat convection, with periodic heating boundary conditions in steady flow, are discussed and the validity of applying the complex combination method to this problem is illustrated. A scaling analysis of a two-dimensional thermal wave configuration with a linear velocity profile is performed to provide important insights into this type of heat transfer phenomena. A two-dimensional conjugate heat transfer model is developed and solved numerically with a finite difference method to demonstrate an example of imposing a thermal wave onto a flow field. The simulation results show that the temperature signal, especially the phase information, can be used for the measurement of flow properties near the surface, such as the wall shear stress. [DOI: 10.1115/1.3194758]

Keywords: convection, periodic boundary conditions, complex combination, phase shift

1 Introduction

The thermal wave concept is a heat transfer phenomenon describing how temperature fluctuations propagate inside a material domain. Historically, the concept has been exploited to determine thermal properties of thin films in semiconductor devices [1–3]. The study of thermal properties of solid materials using thermal wave concepts can be traced back to Angstrom's method of measuring the thermal diffusivity of metals [4]. In most of the studies, a periodic heating source in the material domain, or a periodic heating flux at the boundaries, generates a temperature oscillation that propagates into the domain. The basic heat conduction equation is solved and the measured temperature signal can then be matched to the solution to determine the thermal properties of the sample. The complex combination method is a powerful mathematical tool to find the sustained part of the solution which is of the most importance in many cases [5].

Flow fields with well-structured velocity profiles are very common in many science and technology applications, and of engineering significance. For example, the universal law of the wall describes the structure of the turbulent boundary layer with finite wall shear stress. Due to the ultimate domination of the viscous force in the flow regime right next to the wall, a linear velocity profile exists in the so-called viscous sublayer [6]. Another example concerns microfluidic technology. The small channel size in microfluidic systems implies a low Reynolds number flow, and in turn the flow behavior can be well-defined. Here we are interested in a class of convection heat transfer problems with a periodic heating flux at the boundary of a steady flow field. Also, the fluid/thermal transport and thermodynamic properties are assumed to be independent of the temperature field in some narrow temperature range. This class of heat transfer phenomena could have extensive engineering applications, such as flow diagnostics near surfaces and in microfluidic systems.

In light of the above discussion, this work introduces the concept of thermal wave into the study of convection heat transfer problems. Discussion about linearity and homogeneity of the basic mathematical formulation of the problem shows the validity of using superposition and the complex combination method. A scaling analysis of a two-dimensional thermal wave configuration with a linear velocity profile is performed to provide important insights about this type of heat transfer phenomenon. A two-dimensional conjugate heat transfer simulation demonstrates the potential of using the thermal wave approach to detect important flow properties, such as the velocity gradient at the wall or the wall shear stress.

2 Equations

Linearity of the governing equations implies that superposition can be used to solve complicated heat transfer problems by separating the original problem into several simple subproblems [5]. The final solution can be synthesized by superimposing those solutions of the subproblems together. This will expedite the process of solving complex engineering problems and help identify the critical information in signal processing and data analysis.

Variation in parameters can be employed to solve heat conduction problems with periodic boundary conditions and source terms [5]. If the governing equations and boundary conditions are linear, the solution can be decoupled into two parts: a sustained part and a transient part. The transient part will approach a steady-state solution as time progresses and have no effect on the sustained part. Although this method can provide a complete solution, the process to obtain the whole solution is complicated. The so-called complex combination method is normally employed to find only the sustained solution if the transient part of the solution is of little engineering interest.

The complex combination method assumes the solution format based on the mathematical properties of the governing equation and the boundary conditions [5]. There are two conditions for using this method: the governing equation and the boundary conditions must be linear and the problem needs to be entirely homogeneous except for the periodic terms. A new problem in complex form is constructed to eliminate the transient term in the differential equation. Superposition is normally employed to ensure the condition of homogeneity by isolating the subproblem with only the periodic boundary condition from the whole problem.

Historically, the above theories and methods have been developed for heat conduction. The convection problems are far more complex due to the nonlinear terms in the energy governing equations, such as the velocity term. However, in some simple flow patterns with constant thermal properties, the mathematical methods outlined above, such as superposition and complex combination could be used to simplify this type of heat convection problem.

With no internal heat generation or viscous dissipation, the general three-dimensional convection heat transfer equation with constant thermal properties can be written as

$$k\left(\frac{\partial^2 T}{\partial x^2}+\frac{\partial^2 T}{\partial y^2}+\frac{\partial^2 T}{\partial z^2}\right)=\rho c_p\left(\frac{\partial T}{\partial t}+u\frac{\partial T}{\partial x}+v\frac{\partial T}{\partial y}+w\frac{\partial T}{\partial z}\right) \quad (1)$$

where k is the thermal conductivity, c_p is the heat capacity, and ρ is the density of the liquid. All the material properties are assumed to be constant throughout this work. The variables $u=u(x,y,z)$,

Contributed by the Heat Transfer Division of ASME for publication in the JOURNAL OF HEAT TRANSFER. Manuscript received May 22, 2008; final manuscript received June 6, 2009; published online March 5, 2010. Review conducted by Pamela M. Norris.

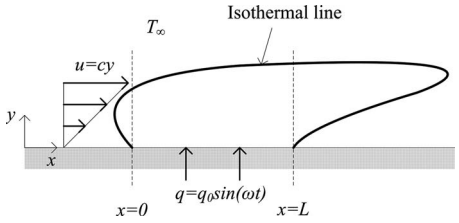

Fig. 1 Schematic of scaling analysis

$v=v(x,y,z)$, and $w=w(x,y,z)$ are the velocity components in the x, y, and z directions, respectively. The velocity components are functions of position only and independent of temperature and time. Therefore, the energy equation is decoupled from the known velocity field.

Since our goal is to explore the possibility of applying the complex combination method to convection, the simplest problem with an essential convection component will be addressed in this work. With the above linear governing equation, we assume that there is only one boundary condition which will be nonhomogeneous, that of a pure sinusoidal function. Based on the above discussion, the complex combination method can be applied and the solution is assumed to have the following form:

$$T(x,y,z,t) = T_{\text{new}}(x,y,z)e^{i\omega t} \tag{2}$$

where ω is the frequency of the periodic boundary condition and i is the complex constant. Upon substituting Eq. (2) into Eq. (1), the differential equation can be written as

$$k\left(\frac{\partial^2 T}{\partial x^2}+\frac{\partial^2 T}{\partial y^2}+\frac{\partial^2 T}{\partial z^2}\right)=\rho c_p\left(i\omega T+u\frac{\partial T}{\partial x}+v\frac{\partial T}{\partial y}+w\frac{\partial T}{\partial z}\right) \tag{3}$$

Note that T_{new} is changed back to T again for simplicity because we will always deal with the complex T in the following development.

Equation (3) is the new governing equation without the transient term and, instead, a complex source term replaces the time derivative of temperature. Compared with Eq. (1), this equation can yield to a numerical solution in a straightforward manner. Several points about this equation deserve our attention. First, the dependent variable—temperature, is a complex number, which contains both magnitude and phase information. Second, this equation is still linear and the solutions at different frequencies can be decoupled from one another. Third, the solution of the above equation will be only the sustained part of the total solution. In real engineering practice, the dynamic response of the system needs to be examined carefully because the temperature signal measured could contain some frequency components generated from the transient terms.

3 Scaling Analysis: An Example

A scaling analysis can reduce the number of variables and parameters of the problem and provide insight into the physics of heat transfer phenomena. To explain the basic principle of this study, a two-dimensional flow field with a linear velocity profile on a flat plate will be considered, as shown in Fig. 1. A periodic heat flux is applied on the wall between two specified x-locations.

The important assumptions of the flow field are (i) the velocity component in the y direction, v, is zero and (ii) the velocity component in the x direction, u, is a linear function of y, or $u=cy$, with c as the velocity gradient and a constant value. The two-dimensional convection heat transfer governing equation of this flow field will be written as

$$k\left(\frac{\partial^2 T}{\partial x^2}+\frac{\partial^2 T}{\partial y^2}\right)=\rho c_p\left(\frac{\partial T}{\partial t}+cy\frac{\partial T}{\partial x}\right) \tag{4}$$

The boundary conditions of this problem can be assumed to be homogeneous by setting the temperature or temperature gradient at the boundaries to zero except that at the heating area. Therefore, the complex combination method converts the governing equation to

$$\alpha\left(\frac{\partial^2 T}{\partial x^2}+\frac{\partial^2 T}{\partial y^2}\right)=i\omega T+cy\frac{\partial T}{\partial x} \tag{5}$$

The first step of the scaling analysis is to normalize the differential equation. The scales of temperature, x length and y length, are marked with a star superscript and the normalized temperature, x length and y length, are designated with a bar as follows:

$$T=T^*\overline{T},\quad x=x^*\overline{x},\quad y=y^*\overline{y}$$

Based on the conventional theory of the thermal wave method [5], the length scale can be chosen as the penetration depth of the thermal wave. This so-called penetration depth is developed in transient heat conduction analysis and is a characteristic length that indicates how far the wave, or the temperature oscillations, travels before decaying to a negligible level.

$$x^*=y^*=\sqrt{\alpha/\omega} \tag{6}$$

The governing equation in the dimensionless form will become

$$\frac{\partial^2\overline{T}}{\partial\overline{x}^2}+\frac{\partial^2\overline{T}}{\partial\overline{y}^2}=i\overline{T}+\frac{c}{\omega}\overline{y}\frac{\partial\overline{T}}{\partial\overline{x}} \tag{7}$$

A new nondimensional number is found in Eq. (7), which is the ratio between the flow velocity gradient and the operating frequency. It is instructive to examine how different values of the nondimensional number c/ω lead to different solutions.

If c/ω approaches zero, the second term on the right side of the equation will vanish. The governing equation is reduced to the pure heat conduction model. In other words, under this situation, the system will not contain any information about the flow velocity gradient c. When c/ω is much larger than unity, the complex term in the equation can be ignored and the governing equation will be approximated as the conventional heat convection model with a constant heat flux on the wall [7]. No phase information about the temperature signal will be present in the solution.

Only when c/ω is of the same order as unity will the system contain the information on both the complex term and the convection term. Therefore, the relationship between the velocity gradient and the temperature signal, especially the phase part, can be established. Another reasonable prediction will be that the temperature signal shall be more sensitive to change in the velocity gradient if the operating frequency is lower.

One important aspect of this heat transfer phenomena is the amplitude of the temperature signal. Scaling analysis about the heating flux boundary condition will be able to provide some insight about the temperature amplitude. For example, the heating flux boundary condition can be written as

$$q=-k\left.\frac{\partial T}{\partial y}\right|_{x,y=0}=q_0\sin(\omega t) \tag{8}$$

By substituting the penetration depth of thermal wave as our length scale into the above boundary condition equation, the scale for temperature is

$$T^*=\frac{q_0}{k}\sqrt{\frac{\alpha}{\omega}} \tag{9}$$

The above formula suggests that the temperature amplitude decreases with the increase in the exciting frequency in a square root relation. This provides a guideline for choosing the operating frequency and the magnitude of the heating flux in engineering design.

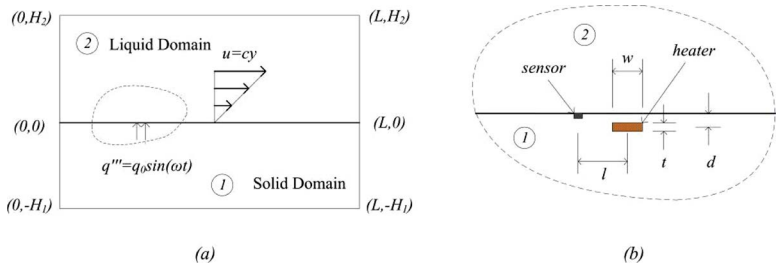

Fig. 2 Schematic of wall shear stress measurement design: (*a*) computation domain and (*b*) sensor design schematic

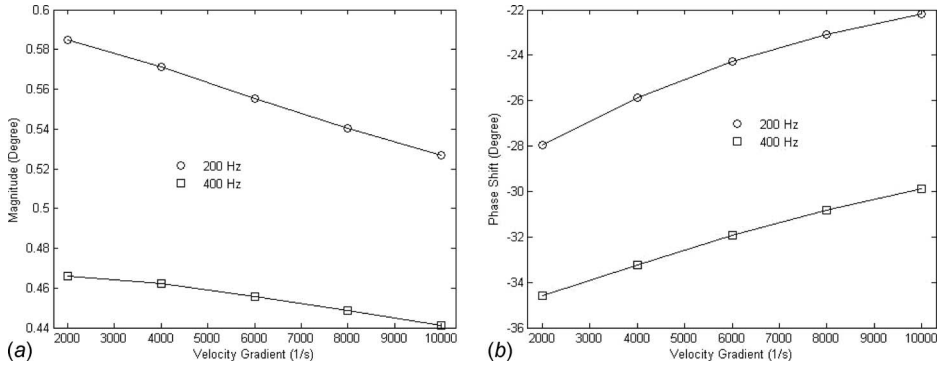

Fig. 3 Temperature magnitude (right) and phase shift (left) versus velocity gradient

4 Simulation Results: An Example

In order to illustrate the potential application of the above theory and gain a basic understanding about this heat transfer problem, a wall shear stress measurement design is proposed and a two-dimensional conjugate heat transfer model is developed and solved numerically. As shown in Fig. 2(*a*), the computational domain is divided into two regions. Region one is a silicon dioxide solid domain. Region two is a water liquid domain with a linear velocity profile. The values of thermal properties are constant and taken from a standard reference [8]. Another assumption is the zero thermal resistance at the solid/liquid interface, which ensures the homogeneity at the interface. A schematic of the sensor design is illustrated in Fig. 2(*b*). The heater is a metal strip, 4 μm wide and 2 μm thick. The distance between the heater and the solid surface, d, is 2 μm, and the distance between the center of the heater and the temperature sensor, l, is 6 μm. With the use of current microfabrication technology, a temperature sensor with thermally negligible size could be easily fabricated. Therefore, a perfect temperature sensor is assumed in this study even though the thermal properties of the sensor material can be very different from that of the substrate. The sizes of the computational domain, L, H_1, and H_2, are set to be large enough so that the temperature signals near the boundaries will decay to zero.

The temperatures at the boundaries are all set to zero. The heating source is applied to the heater under the interface as shown in Fig. 2(*b*) and can be expressed as Eq. (9).

A standard finite difference discretization scheme is employed to solve the above differential equations. The nodes at the solid/liquid interface need special treatment. At the interface, the upper half of the computation cell is assigned to be the liquid domain and the lower half is the solid domain. In the discretized energy conservation equation, the thermal properties in the x direction are the mean values of those of the two materials and no adjustment is required in the y direction. The total nodal numbers in the x and y directions are 200 and 200, respectively.

In this study, two operating frequencies, 200 Hz and 400 Hz, are used and the velocity gradient varies from 2000 l/s to 10000 l/s. The right side of Fig. 3 shows that the magnitude of the temperature signal decreases with the increasing of the velocity gradient. The left side of Fig. 3 shows how the phase shift of the temperature signal varies with the change in the velocity gradient. For both operating frequencies, the phase shift increases with the velocity gradient and demonstrates good sensitivity. At low frequencies, the phase shift shows a stronger dependence on the velocity gradient, as does the magnitude. This trend from the numerical results is consistent with the predictions of the scaling analysis. Not presented in the figures, simulations also indicate that the sensitivity of the phase shift to the velocity gradient increases when the sensor moves away from the heater. However, the temperature magnitude declines rapidly in space and puts a limit on the distance between the heater and the sensor. Another important fact is that the magnitude signal is related to the energy storage mechanism in the heat transfer system and proportional to the heating flux. However, the phase information is independent of the heating flux and provides additional flexibility in the sensor design.

5 Conclusions

This paper examines the heat convection problem with periodic boundary conditions in steady flows and demonstrates how to simplify the governing equations by using complex combination. The scaling analysis of a two-dimensional heat convection configuration with a linear velocity profile provides some important insights about the basic physics of this problem. A wall shear stress measurement design based on the thermal wave concept is proposed and a two-dimensional conjugate heat transfer simulation is conducted. Linearity and locality of this class of heat transfer systems suggest that the experimental validation studies could be very simple, especially with current microfabrication technology. Utilization of this type of thermal signal in small scale stud-

ies should have extensive engineering applications in science and technology, such as flow diagnostics near surfaces and in microfluidic systems.

References

[1] Zhang, X., and Grigoropoulos, C. P., 1995, "Thermal Conductivity and Diffusivity of Free-Standing Silicon Nitride Thin Films," Rev. Sci. Instrum., **66**, pp. 1115–1120.

[2] Chen, G., Tien, C. L., Wu, X., and Smith, J. S., 1994, "Thermal Diffusivity Measurement of GaAs/AlGaAs Thin-Film Structures," ASME J. Heat Transfer, **116**, pp. 325–331.

[3] Indermuehle, S. W., and Peterson, R. B., 1999, "A Phase-Sensitive Technique for the Thermal Characterization of Dielectric Thin Films," ASME J. Heat Transfer, **121**, pp. 528–536.

[4] Angstrom, A. J., 1861, "Neue Methode das Warmeleitungsvermogen der Korper zu. bestimmen," Ann. Phys. Chem., **114**, pp. 513–530.

[5] Myers, G. E., 1998, *Analytical Methods in Conduction Heat Transfer*, 2nd ed., AMCHT, Madison, WI.

[6] Schlichting, H., and Gersten, K., 2000, *Boundary-Layer Theory*, 8th ed., Springer, New York.

[7] Goldstein, S., 1996, *Fluid Mechanics Measurements*, 2nd ed., Hemisphere, New York.

[8] Incropera, F. P., Dewitt, D. P., and Bergman, T. L., 2006, *Fundamental of Heat and Mass Transfer*, 6th ed., Wiley, New York.

Vapor Flow Analysis in Flat Plate Heat Pipes Using Homotopy Perturbation Method

Hamid Reza Seyf
Islamic Azad University,
Karaj Branch,
P.O. Box 31485-313,
Tehran, Karaj 31397, Iran

Mohammad Layeghi
Assistant Professor
University of Tehran,
P.O. Box 31485-77871,
Tehran, Karaj 31587-77871, Iran
e-mail: mlayeghi@ut.ac.ir

In the present study, an analytical solution for 2D vapor flow in flat plate heat pipes is presented. The governing equations are solved analytically using the homotopy perturbation method, and numerically using the finite volume method, based on collocated grids. The analytical results are obtained for nondimensional velocity profiles and axial pressures distribution along the entire length of the heat pipe, and compared with the numerical ones. It is shown that there is a relatively small difference of about 1% in the worst case between the analytical and numerical results. Furthermore, the effects of the Reynolds number and the ratio of condenser to evaporator lengths on the flow variables are discussed. [DOI: 10.1115/1.4000448]

Keywords: flat plate heat pipe, vapor flow, laminar and incompressible, homotopy perturbation method, numerical method

1 Introduction

Flat plate heat pipes (FPHPs) are effective heat transfer devices in many industrial applications such as electronic cooling [1,2]. They also find applications in spacecraft radiator segments [3,4] and in the thermal management in the irradiation facility for boron neutron capture therapy [5–9].

Vafai et al. [5] investigated the liquid and vapor flows, as well as the overall performance of an asymmetrical aluminum-D_2o FPHP, analytically. Zhu and Vafai [7] carried out a 3D analytical study, and for the first time, a 3D numerical study for the steady incompressible vapor and liquid flows in an asymmetrical FPHP. The results show that for a vapor channel with width to height ratio greater than 2.5, the 2D study of vapor flow is a good approximation of the 3D study. In their second paper [8], they developed an analytical model to predict the transient thermal behavior of asymmetrical flat plate and disk shaped heat pipes during the startup process. Wang and Vafai [9] developed two transient 1D analytical models for simulating the transient thermal performance of FPHPs in startup and shutdown operations.

Xuan et al. [10] experimentally and numerically studied the performance of a FPHP with a narrow vapor chamber. Chen et al. [11] developed a simplified and efficient 3D linear model to study the transient response of FPHPs. Sonan et al. [12] presented an analytical approach to determine the transient performance of a FPHP subjected to heating with multiple electronic components.

Experimental investigations on FPHPs were conducted by some researchers. Thomson et al. [3] performed experiments to investigate the application of FPHPs in cooling of high power amplifiers for communication satellites. Koito et al. [13] carried out an experimental and numerical analysis of heat transfer in FPHPs with a single axisymmetric heat source. Boukhanouf et al. [14] experimentally investigated the performance of a FPHP using an IR thermal imaging camera. Other numerical simulations and experimental investigations on FPHPs can be found in Refs. [15–18].

Homotopy perturbation method (HPM) is one of the well-known, novel, and recent methods to solve large variety of linear and nonlinear problems. This method was established in 1999 by He [19–23] and was successfully applied to solve many types of linear and nonlinear problems in science and engineering by many authors [24–27]. A complete review is available in Ref. [20]. HPM is a combination of the perturbation and homotopy method.

In the present work, a closed form solution is obtained for the study of vapor flow in flat plat heat pipes using HPM, and its accuracy and validity has been checked at various Reynolds numbers. The results are compared with numerical ones and have shown very good agreement (less than 1% difference) for all compared cases.

2 Mathematical Modeling and Governing Equations

A FPHP, as shown in Fig. 1, usually consists of two parts: evaporator or heat addition section, and condenser or heat rejection section. In the present analysis, we assume that the values of Q_e and Q_c are constant, however, the evaporator and condenser lengths are variables.

Based on Zhu and Vafai's [7] observations, for the vapor channel with width to height ratio greater than 2.5, 2D analysis is valid. Thus, in this study, it is assumed that the distance between two adjacent vertical wicks is sufficiently large that it can also be assumed that the heat pipe has no vertical wick.

Evaporation and condensation phenomena are also modeled as uniform injection and suction of vapor at the liquid-vapor interface in the evaporator and condenser sections, respectively. The dimensionless governing equations for conservation of mass, x-momentum, and y-momentum are

$$\frac{\partial U}{\partial X}+\frac{\partial V}{\partial Y}=0 \tag{1}$$

$$U\frac{\partial U}{\partial X}+V\frac{\partial U}{\partial Y}=-\frac{\partial P}{\partial X}+\frac{\mathrm{Re}_h}{\mathrm{Re}_l^2}\frac{\partial^2 U}{\partial X^2}+\frac{1}{\mathrm{Re}_h}\frac{\partial^2 U}{\partial Y^2} \tag{2}$$

$$\frac{\mathrm{Re}_h^2}{\mathrm{Re}_l^2}\left(U\frac{\partial V}{\partial X}+V\frac{\partial V}{\partial Y}\right)=-\frac{\partial P}{\partial Y}+\frac{\mathrm{Re}_h^3}{\mathrm{Re}_l^4}\frac{\partial^2 V}{\partial X^2}+\frac{\mathrm{Re}_h}{\mathrm{Re}_l^2}\frac{\partial^2 V}{\partial Y^2} \tag{3}$$

where

$$X=\frac{x}{L} \tag{4a}$$

$$Y=\frac{y}{h} \tag{4b}$$

$$P=\frac{p}{\rho u_l^2} \tag{4c}$$

$$U=\frac{u}{u_l} \tag{4d}$$

$$V=\frac{v}{v_1} \tag{4e}$$

Contributed by the Heat Transfer Division of ASME for publication in the JOURNAL OF HEAT TRANSFER. Manuscript received March 24, 2009; final manuscript received September 23, 2009; published online March 8, 2010. Assoc. Editor: L. C. Chow.

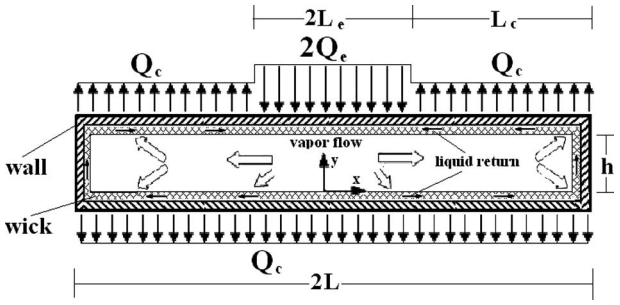

Fig. 1 Schematic of flat plate heat pipe sections and vapor and liquid flows

$$u_l = \frac{L}{h} v_1 \tag{4f}$$

$$\alpha = \frac{v_2}{v_1} = \frac{1}{1+2\beta} \tag{4g}$$

$$\mathrm{Re}_h = \frac{\rho v_1 h}{\mu} \tag{4h}$$

$$\mathrm{Re}_l = \frac{\rho u_1 h}{\mu} \tag{4i}$$

$$\beta = \frac{L_c}{L_e} \tag{4j}$$

v_1 and v_2 are the vapor injection and suction velocities in evaporator and condenser sections, which are related to each other by applying the conservation of mass in the entire length of the heat pipe

$$v_1 = \frac{Q_e}{\rho L_e h_{fg}}, \quad v_2 = \frac{Q_c}{\rho(2L_c + L_e)h_{fg}}, \quad \frac{v_2}{v_1} = \frac{L_e}{(2L_c + L_e)} \tag{5}$$

α and β are the suction to injection velocities ratio and the condenser to evaporator lengths ratio, respectively. The boundary conditions for Eqs. (1)–(3) are

$$U(0,y) = \frac{\partial V}{\partial x}(0,y) = 0 \tag{6a}$$

$$U(1,y) = V(1,y) = 0 \tag{6b}$$

$$U(x,0) = U(x,1) = 0 \tag{6c}$$

$$V(x,0) = -\alpha \tag{6d}$$

$$V(x,1) = \begin{cases} -1 & 0 \le X \le \dfrac{1}{1+\beta} \\ \alpha & \dfrac{1}{1+\beta} < X \le 1 \end{cases} \tag{6e}$$

3 Method of Solution

The governing equations are transformed to a nonlinear ODE by using an appropriate change of variable based on the conservation of mass equation. A homotopy perturbation method is used to solve the nonlinear ODE for the evaporator and nearly similar equations for the condenser sections along with their associated boundary conditions [22].

Furthermore, the governing equations of vapor flow with corresponding boundary conditions are solved numerically using the finite volume method based on a collocated grid system. The discretized equations are solved using SIMPLE algorithm [28], and the QUICK scheme is employed to discretize the convections term and the central difference scheme for diffusion terms. The systems of discretized equations are solved using the algebraic multigrid method [29].

4 Results and Discussion

Figure 2(*a*) shows dimensionless velocity profiles at the evaporator section for different condenser to evaporator lengths ratios. It can be seen that the maximum velocity at a given location in the evaporator section increases by increasing condenser to evaporator lengths ratios. This is due to the fact that for a given and constant input heat flux, smaller evaporator length causes higher injection velocity at the evaporator section. Figure 2(*b*) shows dimensionless velocity profiles at the evaporator section for different Reynolds numbers. It can be seen that the velocity profile changes smoothly by increasing the Reynolds number from 1 to 9. The velocity maxima in the evaporator part of the heat pipe have been shifted toward the bottom wick, which causes the shear stress at the bottom wall to increase and the top wall to decrease.

Figure 3(*a*) shows the dimensionless pressure distributions along the FPHP at Reynolds numbers 1 to 9 for $\beta=2$. It can be seen that dimensionless pressure drop decreases by increasing the Reynolds number. Figure 3(*b*) shows the dimensionless pressure distributions along the FPHP at Reynolds numbers 1 to 9 for $\beta=4.5$. It can be seen that dimensionless pressure drop decreases by increasing the Reynolds number less than the case $\beta=2$ in Fig. 3(*a*).

A comparison between calculated dimensionless velocity profiles for different orders and numerical ones show that the analytical results obtained from the HPM for fourth and sixth order solutions are very close together and to the numerical one. There-

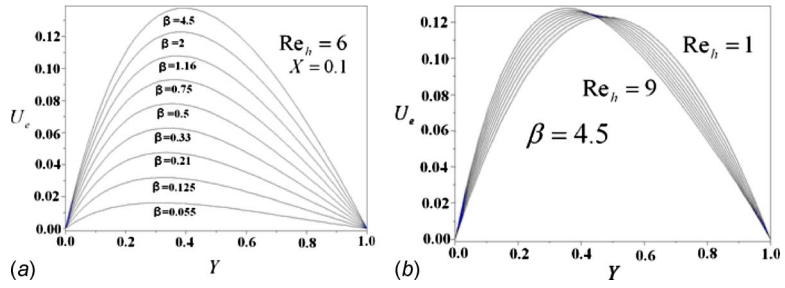

Fig. 2 (*a*) The effect of evaporator to condenser lengths ratio on the dimensionless velocity profiles at the evaporator section at $X=0.1$. (*b*) The effect of Reynolds number on the dimensionless velocity profiles at the evaporator section at $X=0.09090$.

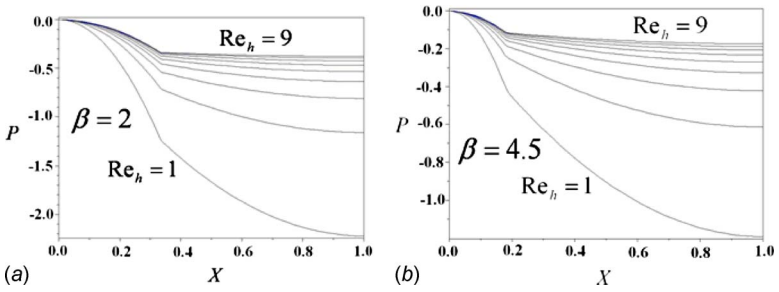

Fig. 3 (*a*). Dimensionless pressure distributions along the FPHP at Reynolds numbers 1 to 9 for β=2. (*b*) Dimensionless pressure distribution along the FPHP at Reynolds numbers 1 to 9 for β=4.5.

fore, the sixth order solution provides acceptable accuracy and it was used to obtain analytical velocity profiles and pressure distributions throughout this paper.

5 Conclusion

Two-dimensional vapor flow in FPHPs has been studied analytically using the HPM and compared with the numerical results of a finite volume code at low Reynolds numbers (less than 10). It has been shown that there is a very good agreement between the analytical and numerical results. It has been shown that with the increase in the Reynolds number, the pressure drop at FPHP decreases, and the velocity maxima in the evaporator part of heat pipe are shifted toward the bottom wick. As well as, for Reynolds numbers less than 10, the pressure in the condenser section decreases.

Nomenclature

h = heat pipe height
h_{fg} = heat of vaporization
Q_c = heat rejection at the condenser section
Q_e = heat addition at the evaporator section
L = heat pipe length
L_e = evaporator length
L_c = condenser length
p = vapor pressure
P = dimensionless vapor pressure
Re = Reynolds number
u = vapor velocity component in the x direction
U = dimensionless vapor velocity component in x direction
v = vapor velocity component in the y direction
V = dimensionless vapor velocity component in the y direction
x = horizontal coordinate
X = dimensionless horizontal coordinate
y = vertical coordinate
Y = dimensionless vertical coordinate

Greek Symbols

α = suction to injection velocities ratio
β = condenser to evaporator lengths ratio
μ = vapor viscosity
ρ = vapor density

Subscripts

c = condenser
e = evaporator
ini = initial guess

References

[1] Basiulis, A., Tanzer, H., and McCabe, S., 1986, "Thermal Management of High Power PWB's Through the Use of Heat Pipe Substrates," *Proceedings of the Sixth Annual International Electronics Packaging Conference*, San Diego, CA, Vol. 6, p. 501.

[2] Rightley, M. J., Tigges, C. P., Givler, R. C., Robino, C. V., Mulhall, J. J., and Smith, P. M., 2003, "Innovative Wick Design for Multi-Source Flat Plate Heat Pipes," Microelectron. J., **34**, pp. 187–194.

[3] Thomson, M., Ruel, C., and Donato, M., 1989, "Characterization of a Flat Plate Heat Pipe for Electronic Cooling in a Space Environment," *Proceedings of the 1989 National Heat Transfer Conference, Heat Transfer in Electronics HTD*, Vol. 111, pp. 59–65.

[4] Ooijen, H., and Hoogendoorn, C. J., 1979, "Vapor Flow Calculations in a Flat-Plate Heat Pipe," AIAA J., **17**, pp. 1251–1259.

[5] Vafai, K., Zhu, N., and Wang, W., 1992, "Analysis of Flow and Heat Transfer Characteristics of an Asymmetrical Flat Plate Heat pipe," Int. J. Heat Mass Transfer, **35**, pp. 2087–2099.

[6] Vafal, K., Zhu, N., and Wang, W., 1995, "Analysis of Asymmetrical Disk-Shaped and Flat-Plate Heat Pipes," ASME J. Heat Transfer, **117**, pp. 209–218.

[7] Zhu, N., and Vafai, K., 1998, "Vapor and Liquid Flow in an Asymmetrical Flat Plate Heat Pipe: A Three Dimensional Analytical and Numerical Investigation," Int. J. Heat Mass Transfer, **41**, pp. 159–174.

[8] Zhu, N., and Vafai, K., 1998, "Analytical Modeling of the Startup Characteristics of Asymmetrical Flat Plate and Disk-Shaped Heat Pipes," Int. J. Heat Mass Transfer, **41**, pp. 2619–2637.

[9] Wang, Y., and Vafai, K., 2000, "Transient Characterization of Flat Plate Heat Pipes During Startup and Shutdown operations," Int. J. Heat Mass Transfer, **43**, pp. 2641–2655.

[10] Xuan, Y., Hong, Y., and Li, Q., 2004, "Investigation on Transient Behaviors of Flat Plate Heat Pipes," Exp. Therm. Fluid Sci., **28**, pp. 249–255.

[11] Chen, Y. S., Chien, K. H., Wang, C. C., Hung, T. C., and Pei, B. S., 2006, "A Simplified Transient Three-Dimensional Model for Estimating the Thermal Performance of the Vapor Chambers," Appl. Therm. Eng., **26**, pp. 2087–2094.

[12] Sonan, R., Harmand, S., Pellé, J., Leger, D., and Fakès, M., 2008, "Transient Thermal and Hydrodynamics Model of Flat Heat Pipe for the Cooling of Electronics Components," Int. J. Heat Mass Transfer, **51**, pp. 6006–6017.

[13] Koito, Y., Imura, H., Mochizuki, M., Saito, Y., and Torii, S., 2006, "Numerical Analysis and Experimental Verification on Thermal Fluid Phenomena in Vapor Chamber," Appl. Therm. Eng., **26**, pp. 1669–1676.

[14] Boukhanouf, R., Haddad, A., North, M. T., and Buffone, C., 2006, "Experimental Investigation of a Flat Plate Heat Pipe Performance Using IR Thermal Imaging Camera," Appl. Therm. Eng., **26**, pp. 2148–2156.

[15] Chien, L., and Chang, C. C., 2002, "Experimental Study of Evaporator Resistance on Porous Surface in Flat Heat Pipes," *Proceedings of the Inter Society Conference on Thermal Phenomena IEEE*, pp. 1052–1057.

[16] Simura, T., Sho, H., and Nakamura, Y., 2002, "The Aluminum Flat Heat Pipe Using Cyclopentane as Working Fluid," *Proceedings of the Inter Society Conference on Thermal Phenomena IEEE*, pp. 224–229.

[17] Chesser, J. B., Peterson, G. P., and Lee, S., 2000, "A Simplified Method for Determining the Capillary Limitation of Flat Heat Pipes in Electronics Cooling," *Proceedings of the NHTC '00, Thirty-Fourth National Heat Transfer Conference.*

[18] Um, J. Y., Chow, L. C., and Baker, K., 1994, *An Experimental Investigation of Flat Heat Pipe*, *Fundamentals of Heat Pipes*, ASME HTD, New York, Vol. 278, pp. 21–26.

[19] He, J. H., 1998, "Approximate Analytical Solution for Seepage Flow With Fractional Derivative in Porous Media," Comput. Methods Appl. Mech. Eng., **167**, pp. 57–68.

[20] He, J. H., 1999, "Homotopy Perturbation Technique," Comput. Methods Appl. Mech. Eng., **178**(3–4), pp. 257–262.

[21] He, J. H., 2000, "A Coupling Method of Homotopy Technique and Perturbation Technique for Nonlinear Problems," Int. J. Non-Linear Mech., **35**, pp. 37–43.

[22] He, J. H., 2006, "Homotopy Perturbation Method for Solving Boundary Value Problems," Phys. Lett. A, **350**(1–2), pp. 87–88.

[23] He, J. H., 2006, "Some Asymptotic Methods for Strongly Nonlinear Equations," Int. J. Mod. Phys. B, **20**(10), pp. 1141–1199.

[24] Ariel, P. D., 2007, "The Three-Dimensional Flow Past a Stretching Sheet and

the Homotopy Perturbation Method," Comput. Math. Appl., **54**, pp. 920–925.
[25] Ganji, D. D., and Sadighi, A., 2006, "Application of He's Homotopy Perturbation Method to Nonlinear Coupled Systems of Reaction Diffusion Equations," Int. J. Nonlinear Sci. Numer. Simul., **7**(4), pp. 411–418.
[26] Ganji, D. D., 2006, "The Application of He's Homotopy Perturbation Method to Nonlinear Equations Arising in Heat Transfer," Phys. Lett. A, **355**, pp. 337–341.
[27] Siddiqui, A. M., Mahmood, R., and Ghor, Q. K., 2006, "Thin Film Flow of a Third Grade Fluid on a Moving Belt by He's Homotopy Perturbation Method," Int. J. Nonlinear Sci. Numer. Simul., **7**(1), pp. 7–14.
[28] Patankar, S. V., 1980, *Numerical Heat Transfer and Fluid Flow*, Hemisphere, New York.
[29] Ferziger, J. H. and Peric, M., 1999, *Computational Methods for Fluid Dynamics*, 2nd ed., Springer, New York.

Transient Conduction in a Hollow Cylinder With Variable Thermal Conductivity

M. Kandula
ASRC Aerospace,
NASA Kennedy Space Center,
FL 32899
e-mail: max.kandula-1@nasa.gov

A closed form approximate solution has been obtained for the transient temperature distribution in a hollow cylinder with a linear variation in thermal conductivity with temperature. The boundary conditions considered are convective heating (Newton's law) at the exposed inner surface and adiabatic outer surface. The solution is obtained using the method of optimal linearization, with the initial solution given by the integral method. The nonlinear analytical solution is shown to compare well with the finite difference solution. [DOI: 10.1115/1.4000471]

Keywords: transient heat conduction, hollow cylinder, variable thermal conductivity, optimal linearization

1 Introduction

The thermal design of heat sink rocket nozzles requires the transient temperature distribution in the finite cylindrical wall subjected to heating by Newton's law at the exposed surface and negligible heat loss from the outer. Similar situations arise in many other heating and cooling applications. Because of the high temperature range involved and considerable variation in thermal conductivity with temperature for the commonly employed materials, the customary assumption of constant average property can lead to significant inaccuracies in the desired wall thickness. It is, therefore, essential that the variation in thermal conductivity is taken into account in the thermal analysis.

The earliest heat conduction solution involving variable conductivity is that of Yang [1] for the case of a semi-infinite slab subjected to a constant surface temperature, which considers successive approximation (iteration) following Boltzmann (similarity) transformation [2]. Many approximate analytical solutions for the transient conduction with variable thermal conductivity have been reported for the relatively simple geometry of a finite slab. For example, a simple closed form approximate solution for a transient conduction in a finite slab with a linear variation in conductivity with temperature has been reported by the author [3], published under a different name (K. Mastanaiah; see Acknowledgment). The solution has been obtained using the method of optimal linearization [4] with the initial solution for the constant conductivity case determined by Goodman's integral method [5] with a parabolic profile for the temperatures. Lin [6] obtained a solution for the finite slab with temperature-dependent thermal conductivity by using the orthogonal collocation method, with the spatial derivatives in the energy equation approximated by an orthogonal polynomial. As indicated by Meyer [7], the equivalent slab treatment would not be valid for the thickness to radius ratio exceeding 0.2, which is the case in the vicinity of the throat region of a rocket nozzle, and will always give conservative estimate for temperatures in the cylindrical structure.

Contributed by the Heat Transfer Division of ASME for publication in the JOURNAL OF HEAT TRANSFER. Manuscript received June 29, 2009; final manuscript received September 2, 2009; published online March 9, 2010. Assoc. Editor: O. A. Ezekoye.

Nonlinear heat conduction with temperature-dependent thermal conductivity continues to be of interest. Mishra and Pavan Kumar [8] treated hyperbolic conduction (non-Fourier effect) and radiation in a planar participating medium with temperature-dependent thermal conductivity and pulse type internal heat source by using the lattice Boltzmann method in conjunction with the finite volume procedure for radiative calculations. Transient heat transfer in a partially cooled cylindrical rod (with temperature-dependent thermal conductivity) was numerically (finite differences) investigated by Agbezuge [9] for application to the cooling of spent nuclear fuel rods with uniform internal heat generation.

With regard to the hollow cylinder, Lin and Chen [10] treated a composite hollow cylinder with variable thermal conductivity through the application of Laplace transforms in conjunction with the finite difference or finite element method, with linearization by means of Taylor series. Chen and Ozisik [11] considered the problem of a hollow cylinder by means of a variational method in conjunction with the finite difference discretization. It is the intent of this note to present a simple closed form approximate solution for the transient temperature distribution in a finite hollow cylinder with a linear variation in thermal conductivity with temperature. This article is based primarily on the author's work [12].

2 Analysis

A schematic of the hollow cylinder configuration is displayed in Fig. 1. Since the region considered is finite, the proposed solution will be treated in two time domains [2]: early-time domain (when the penetration depth or the so-called thermal layer is less than the cylinder wall thickness) and large-time domain (when the penetration depth equals or exceeds the wall thickness). Note that the penetration depth loses its significance when it exceeds the wall thickness [2].

2.1 Semi-infinite Domain ($t \le t_\delta$). This is the early-time domain in which the outer surface remains at the initial temperature. With the usual assumptions (one-dimensional heat flow, constant thermophysical properties other than conductivity, and so on), and following nondimensionalization and transformation $R=\ln(r/r_1)$, the equations to be solved are:

$$\frac{\partial\theta}{\partial t} = e^{-2R}\frac{\partial}{\partial R}\left[K(\theta)\frac{\partial\theta}{\partial R}\right], \quad 0 < R < s, t > 0 \tag{1a}$$

$$\frac{\partial\theta}{\partial R} = B_1[\theta(R,t) - 1], \quad R = 0 \tag{1b}$$

$$\theta(\delta,t) = 0 \tag{1c}$$

$$\theta(R,0) = 0 \tag{1d}$$

The above transformation reduces Eqs. (1*a*)–(1*d*) to an equivalent slab form, thus affording simplification. This logarithmic transformation for cylindrical regions is considered by Lardner and Pohle [13].

We now seek to find the solution of Eqs. (1*a*)–(1*d*) by using the method of optimal linearization first introduced by West [14] for nonlinear problems, and later applied to heat transfer problems in Ref. [4]. The initial solution $\theta=\psi$ for the constant conductivity case is obtained with the aid of the integral method with a parabolic profile assumed for temperatures. The details are, however, not presented here, and for the basic principle of optimal linearization the method in Ref. [4] may be consulted. Briefly the method involves the following key steps. Consider the equation

$$\frac{\partial\theta}{\partial t} = e^{-2R}\lambda\frac{\partial^2\theta}{\partial R^2}, \quad 0 < R < s, t > 0 \tag{2a}$$

where λ is an adjustable parameter, so that Eq. (2*a*) approximates Eq. (1*a*) in an optimal sense. This parameter λ_{opt} is obtained from

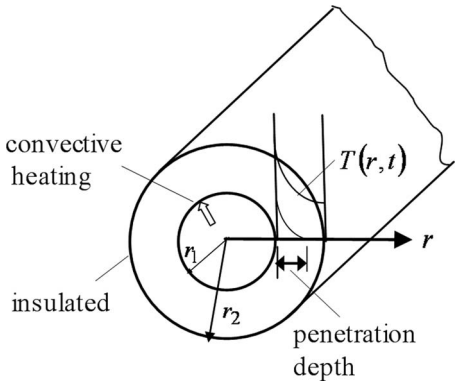

Fig. 1 Schematic of the hollow cylinder configuration

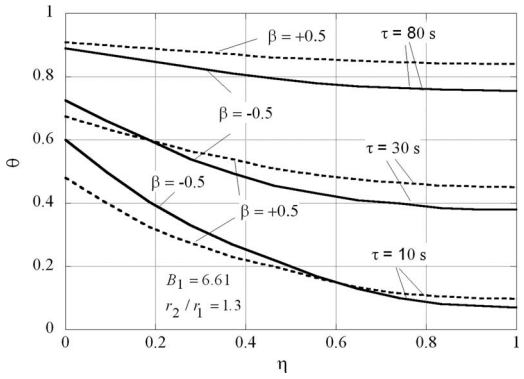

Fig. 2 Temperature distribution in a hollow cylinder with variable thermal conductivity

$$\partial I(\lambda)/\partial\lambda = 0 \tag{2b}$$

where

$$I(\lambda) = \int_0^t \int_0^R \varepsilon^2\left(\lambda, \theta, \frac{\partial\theta}{\partial R}, \frac{\partial^2\theta}{\partial R^2}\right) dR dt \tag{2c}$$

The quantity ε refers to the difference between Eqs. (2*a*) and (1*a*), and is expressed by

$$\varepsilon = e^{2R}\left\{\lambda\frac{\partial^2\theta}{\partial R^2} - \frac{\partial}{\partial R}\left[K(\theta)\frac{\partial\theta}{\partial R}\right]\right\} = e^{2R}\left[\lambda\frac{\partial^2\theta}{\partial R^2} - \frac{dK(\theta)}{d\theta}\left(\frac{\partial\theta}{\partial R}\right)^2 - K(\theta)\frac{\partial^2\theta}{\partial R^2}\right] \tag{2d}$$

The final solution for the nonlinear case is expressed as

$$\theta(R,t) = \left[\frac{B_2}{\delta(2+B_2\delta)}\right](\delta - R)^2, \quad 0 < R < \delta \tag{3a}$$

where δ is given by the implicit relations

$$3t\lambda_{\text{opt}} = \int_0^\delta \frac{x^2(4+B_2x)}{(2+B_2x)(1-e^{-2x})}dx \tag{3b}$$

$$B_2 = B_1/\lambda_{\text{opt}} \tag{3c}$$

$$\lambda_{\text{opt}} = 1 + \frac{3\beta}{8}\int_0^t \frac{a_0^3}{\delta^6}(1 - e^{-4\delta} - 4\delta + 8\delta^2)dt \Big/ \int_0^t \frac{a_0^2}{\delta^4}(1 - e^{-4\delta})dt \tag{3d}$$

$$a_0 = B_1\delta/(2+B_1\delta) \tag{3e}$$

Also

$$t_\delta = \frac{1}{3\lambda_{\text{opt}}}\left[\int_0^s \frac{x^2(4+B_2x)}{(2+B_2x)(1-e^{-2x})}dx\right] \tag{3f}$$

where t_δ corresponds to the time when the penetration depth $\delta = s$.

The quantity δ has to be determined from Eqs. (3*b*)–(3*e*), involving numerical integrations. This requires an iterative process, where for any given time we start with an assumed value of δ. Iteration is continued until the convergence in δ is achieved.

2.2 Finite Domain ($t > t_\delta$). This time domain is of importance in many practical situations. Here the boundary condition at the outer surface will be

$$\frac{\partial\theta}{\partial R}(R,t) = 0, \quad R = s \tag{4}$$

instead of Eq. (1*c*), which applies for the case of the early-time domain. The initial solution of the constant property case is again determined by the integral method, and optimal linearization is once again carried out. The resulting solution for the nonlinear problem is expressed by

$$\theta(R,t) = 1 - [2/(2+B_2s)](1 + B_2R - B_2R^2/2s)\exp[\{-B_1/\phi_2(s)\}(t - t_\delta)] \tag{5}$$

$$B_2 = B_1/\lambda_{\text{opt}} \tag{6}$$

$$\lambda_{\text{opt}} = 1 + \beta + \frac{\beta}{8s(2+B_1s)(1-e^{-4s})}[(8B_1s^2 + 16s - 3B_1)e^{-4s} + 16s^2B_1 - 12sB_1 + 3B_1 - 16s]\frac{(E^3-1)}{(E^2-1)} \tag{7}$$

$$E = \exp[-B_1(t - t_\delta)/\phi_1(s)] \tag{8}$$

$$\phi_1(s) = \tfrac{1}{8}[e^{2s}(4 + 2B_1s - B_1/s) - 4 + 2B_1 + B_1/s] \tag{9}$$

and

$$\phi_2(s) = \tfrac{1}{8}[e^{2s}(4 + 2B_2s - B_2/s) - 4 + 2B_2 + B_2/s] \tag{10}$$

3 Results and Discussion

Figure 2 displays the temperature distributions in a finite hollow cylinder with $B_1 = 6.61$ and $r_2/r_1 = 1.3$ ($r_1 = 0.18$ m) at $\tau = 10$ s, 30 s, and 80 s with the parameter $\beta = +0.5$ and -0.5. For convenience, the temperature distributions are presented as functions of the variable η defined by

$$\eta = (r - r_1)/(r_2 - r_1) \tag{11}$$

The dimensional value of t_δ (which corresponds to the time for which the physical penetration depth of 0.054 m equal to the thickness of the cylinder) is 8.1 s for $\beta = -0.5$ and 4.8 s for $\beta = +0.5$. At $\tau = 30$ s, the value of λ_{opt} is 0.75 for $\beta = -0.5$ and 1.25 for $\beta = +0.5$ (note that λ_{opt} is a dimensionless quantity with a value of 1.0 at $\beta = 0$). It is interesting to observe that the intersection point of the two curves moves toward the left with increasing τ. For sufficiently large τ, temperatures for $\beta = +0.5$ are higher than those for $\beta = -0.5$ throughout the section. This latter trend is well known for the special case of $B_1 \to \infty$ corresponding to a constant wall temperature [2,15]. The general behavior of the results is similar to that observed for the case of a finite slab [2].

As there is no exact solution available for this problem, the present solution (optimal linearization method or OLN) is com-

Table 1 Comparison of optimal linearization solution with finite difference solution at $\tau = 30$ s ($B_1 = 6.61$, $r_2/r_1 = 1.3$)

r (m)	$\beta = -0.5$		Error (%)	$\beta = +0.5$		Error (%)
	OLN	FDS		OLN	FDS	
0.18	0.725	0.726	−0.2	0.670	0.683	−1.9
0.1897	0.598	0.594	+0.8	0.593	0.605	−1.9
0.1999	0.500	0.490	+2.1	0.534	0.536	−0.4
0.2107	0.429	0.414	+3.8	0.492	0.481	+2.2
0.2220	0.387	0.367	+5.5	0.466	0.445	+4.8
0.2340	0.373	0.351	+6.2	0.458	0.433	+5.7

pared with a finite difference solution (FDS) in Table 1. In the numerical FDS, which uses two-time level Crank–Nicholson implicit procedure, Taylor's forward projection method is employed to take into account the nonlinearities for achieving an unconditional stability [16]. One hundred space intervals and a time interval of 0.1 s are taken to ensure convergence of the solution. Table 1 reveals that at $\tau = 30$ s, the two solutions are in fairly good agreement with each other. The maximum error is found to be about 6%. The error decreases, however, with increasing time, as the system tends to reach a steady state as $t \to \infty$.

The temperature dependence of thermal conductivity of materials can be carried out on the basis of this analysis in conjunction with measured surface temperatures.

4 Conclusions

A closed form approximate solution has been obtained for the transient temperature distribution in a hollow cylinder with a linear variation in thermal conductivity with temperature. The resulting solution agrees closely with the finite difference numerical solution.

Acknowledgment

The author was with the Indian Space Research Organization (ISRO) from 1971 to 1977. Papers by the author from 1973 to 1982 were published under the name K. Mastanaiah.

Nomenclature

B_1 = Biot number, hr_1/k_0 (dimensionless)
c_p = specific heat, J/kg K
h = heat transfer coefficient, W/m^2 K
k = thermal conductivity, W/m K
k_0 = reference thermal conductivity, W/m K
$k(\theta)$ = $k_0(1+\beta\theta)$
$K(\theta)$ = $k(\theta)/k_0$
r = radial coordinate, m
r_1, r_2 = inner and outer radius of a cylinder, respectively, m
R = transformed variable, $\ln(r/r_1)$
s = $\ln(r_2/r_1)$
T = temperature, K
T_g = effective gas temperature, K
t = dimensionless time (Fourier number), $\alpha_0\tau/r_1^2$
t_δ = time corresponding to penetration depth s, dimensionless

Greek Symbols

α_0 = reference thermal diffusivity, m^2/s; $k_0/(\rho c_p)$
β = coefficient of thermal conductivity variation
δ = penetration depth, dimensionless
η = $(r-r_1)/(r_2-r_1)$
λ = adjustable parameter
ρ = density, kg/m^3
τ = time, s
ψ = initial constant property solution
θ = dimensionless temperature, $(T-T_0)/(T_g-T_0)$

Subscripts

0 = initial value (uniform)
1, 2 = inner and outer radii, respectively

References

[1] Yang, K. T., 1958, "Transient Conduction in a Semi-infinite Solid With Variable Thermal Conductivity," ASME J. Appl. Mech., **89**, pp. 146–147.
[2] Ozisik, M. N., 1989, *Boundary Value Problems of Heat Conduction*, Dover, New York.
[3] Mastanaiah, K., and Muthunayagam, A. E., 1975, "Transient Conduction in a Finite Slab With Variable Thermal Conductivity," AIAA J., **13**(7), pp. 954–956.
[4] Vujanovic, B., 1973, "Application of Optimal Linearization Method to the Heat Transfer Problem," Int. J. Heat Mass Transfer, **16**, pp. 1111–1117.
[5] Goodman, T. R., 1961, "The Heat Balance Integral—Further Considerations and Refinements," ASME J. Heat Transfer, **83**, pp. 83–86.
[6] Lin, S. H., 1978, "Transient Heat Conduction With Temperature-Dependent Thermal Conductivity by the Orthogonal Collocation Method," Lett. Heat Mass Transfer, **5**, pp. 29–39.
[7] Meyer, E., 1952, "Heat Flow in Composite Slabs," J. Am. Rocket Soc., **22**, pp. 150–158.
[8] Mishra, S. C., and Pavan Kumar, T. B., 2009, "Analysis of a Hyperbolic Heat Conduction-Radiation Problem With Temperature Dependent Thermal Conductivity," ASME J. Heat Transfer, **131**, p. 111302.
[9] Agbezuge, L., 2009, "Transient Heat Transfer in a Partially Cooled Cylindrical Rod," ASME J. Heat Transfer, **131**, p. 074504.
[10] Lin, J.-Y., and Chen, H.-T., 1992, "Radial Axisymmetric Transient Conduction in Composite Hollow Cylinders With Variable Thermal Conductivity," Eng. Anal. Boundary Elem., **10**, pp. 27–33.
[11] Chen, C. J., and Ozisik, M. N., 1994, "Optimal Convective Heating in a Hollow Cylinder With Temperature Dependent Thermal Conductivity," Appl. Sci. Res., **52**, pp. 67–79.
[12] Mastanaiah, K., 1975, "Transient Heat Conduction in a Hollow Cylinder With Variable Thermal Conductivity," *Proceedings of the Third National Heat and Mass Transfer Conference*, Indian Institute of Technology, Bombay, Dec. 11–13, Paper No. HMT-02-75.
[13] Lardner, T. J., and Pohle, F. B., 1961, "Application of Heat Balance Integral to the Problems of Cylindrical Geometry," ASME J. Appl. Mech., **92**, pp. 310–312.
[14] West, J. C., 1960, *Analytical Techniques for Nonlinear Control Systems*, English Universities, London.
[15] Eckert, E. R. G., and Drake, R. M., 1987, *Analysis of Heat and Mass Transfer*, Hemisphere, New York, p. 191.
[16] Mastanaiah, K., 1976, "On the Numerical Solution of Phase Change Problems in Transient Nonlinear Heat Conduction," Int. J. Numer. Methods Eng., **10**, pp. 833–844.

Oscillatory Streaming Flow Based Mini/Microheat Pipe Technology

Z. Zhang

C. Liu

A. Fadl

D. M. L. Meyer

Department of Mechanical Engineering,
University of Rhode Island,
Kingston, RI 02881

M. Krafczyk
Department of Mechanical Engineering,
University of Rhode Island,
Kingston, RI 02881;
Department of Architecture, Civil Engineering, and Environmental Sciences,
Institute for Computational Modeling in Civil Engineering,
TU Braunschweig,
Braunschweig 38023, Germany

H. Sun
Department of Mechanical Engineering,
University of Rhode Island,
Kingston, RI 02881;
Department of Mechanical Engineering,
University of Massachusetts,
Lowell One University Avenue, Lowell, MA 01854

The sustained drive for faster and smaller micro-electronic devices has led to a considerable increase in power density. The ability to effectively pump and enhance heat transfer in mini-/microchannels is of immense technological importance. Using oscillatory flow to enhance the convective heat transfer coefficients in micro-/minichannels is one of many new concepts and methodologies that have been proposed. In this paper, a novel and simple concept is presented on oscillating streaming flow based mini/microheat pipe or heat spreader technology. Phenomena of the flow streaming can be found in zero-mean velocity oscillating flows in many channel geometries. Although there is no net mass flow (zero-mean velocity) passing through the channel, discrepancy in the velocity profiles between the forward and backward flows causes fluid particles near the walls to drift toward one end while particles near the centerline drift to the other end. This unique characteristic of flow streaming could be used for various applications. Some of the advantages include enhanced heat/mass transfer, pumpless fluid propulsion, multichannel fluid distribution, easy system integration, and cost-effective operation. Preliminary work has been conducted on scaling analysis, computer simulations, and visualization experiments of fluid streaming, propulsion, and multichannel distribution by flow oscillation in mini-tapered channels and channel networks. Results show that streaming flow has the potential to be used as a cost-effective and reliable heat pipe and/or as a heat spreader technique when fluid thermal conductivity is low. [DOI: 10.1115/1.4000443]

Keywords: heat pipe, flow streaming, oscillation flow, bifurcation, microchannel

1 Introduction

A considerable number of studies on heat transfer in oscillating/pulsating macrochannel flows have been published [1–10, and many others] in the last few decades, although the results were inconclusive. Both enhancement and reduction in heat transfer rates have been found in experiments. Results varied with oscillating parameters, boundary conditions, fluid type, and geometries. There is limited study on oscillation flow heat transfer (OFHT) in microsystems until the last few years [1,11]. A new microheat spreader (MHS) concept for efficient transport of large concentrated heat using oscillation flows was introduced [12]. The potential advantages of the MHS include its ability to control the maximum surface temperature and the easy integration into the microchip components as an onboard cooling system. Most recently, Suzuki [13] reported the OFHT experiments in minichannels with inner diameters ranging from 0.3 mm to 0.8 mm. It was concluded that the effective conductivity of the oscillation heat transfer device was about 25 times higher than that of copper, which made this technique attractive for next-generation electronic cooling.

In spite of the differing in the degree of enhancement, a common finding is that the changes in the heat transfer rate due to flow oscillation are more pronounced in the entrance and exit regions [6,12,14,15]. In this paper, a novel and simple streaming-based microchannel cooling technology is proposed using oscillatory flows.

Many papers on steady streaming in macrochannel oscillatory flows have been published in the past few decades [15–29]. Various geometries and flow arrangements were covered in the literature, including streaming flow induced by a torsionally oscillated disk, streaming adjacent to a cylinder oscillating along its diameter, streaming in oscillating flow along a curved tube, pressure-driven oscillatory flow within a tapered tube, oscillatory flow through bifurcations, and streaming in the channel entrance region.

These previous studies greatly advance the knowledge of flow streaming during flow oscillation. However, still many issues have not been studied nor are well-understood. There is a great need for the fundamental understanding of flow streaming dynamics and for the full exploration of its potential applications, both in macro- and microscales. Many important research questions, including practical applications of flow streaming in heat and mass transport, have not been addressed. This is particularly true for streaming flow in micro-/minichannels; very few studies have been reported to-date in the literature. In this study, the feasibility of applying flow streaming in heat pipe or heat spreader technologies is investigated.

2 Research Methods

2.1 Mechanisms of Flow Streaming. The phenomena of flow streaming are found in zero-mean velocity oscillating flows in a wide range of channel geometries. Although there is no mass flow (zero-mean velocity) passing through the channel, the discrepancy in the velocity profiles between the forward and backward flows causes fluid particles near the walls to drift toward one end while fluid particles near the centerline drift to the other end. It is hypothesized that the unique characteristics of flow streaming

Contributed by the Heat Transfer Division of ASME for publication in the JOURNAL OF HEAT TRANSFER. Manuscript received January 12, 2009; final manuscript received August 20, 2009; published online March 5, 2010. Assoc. Editor: S. J. Kim.

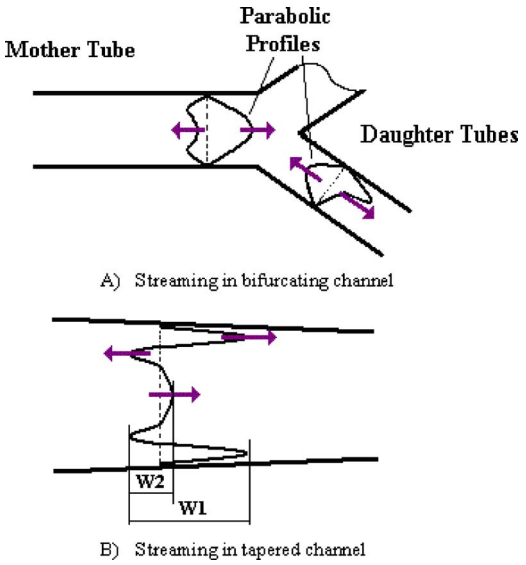

Fig. 1 Mechanisms of flow streaming in a bifurcation channel

could be used to achieve the convective cooling needed in heat pipe and heat spreader technologies.

Figure 1 illustrates mechanisms of flow streaming in two common geometries. Figure 1(*a*) shows a qualitative picture of the axial velocity profiles of fluid in a macrochannel bifurcation tube based on the work of Haselton and Scherer [23]. During the inflow (to the right), the parabolic velocity profile in the mother tube was split in half at the location of U_c when entering the daughter tubes, resulting in a nonsymmetrical profile with the maximum velocity skewed to the inner wall of the daughter tubes. During the backflow (to the left), two fully-developed, parabolic flow profiles in the daughter tubes merge at the center of the bifurcation and result in an (epsilon) ε-shaped symmetrical profile in the mother tube with a zero velocity at the center. A discrepancy in the velocity profiles between inflow and backflow causes fluid elements near the walls to drift toward the mother tube (negative drift) while fluid near the centerline drifts toward the daughter tubes (positive drift).

Figure 1(*b*) shows the sketch of a fluid streak deformation profile in a tapered macrochannel based on the work of Grotberg [26] due to a discrepancy between oscillating divergent (from narrow end to wide end) and convergent flows (from wide end to narrow end) in a tapered channel. One of the successful applications of flow streaming is the high-frequency-ventilation (HFV) technique used in emergency rooms of hospitals. HFV operates with tidal volume much smaller than the anatomic dead space (or with a very small oscillation amplitude) of the lungs at a higher rate of breathing. The successive bifurcation networks coupled with the tapered lung airways geometry promote two-way O_2/CO_2 fluid streaming within the entire human lungs.

2.2 Dimensional Analysis. There are six major independent variables that characterize a flow streaming process, i.e., oscillation amplitude A, oscillation frequency f, fluid kinematic viscosity ν, mother channel height (planar channel) or diameter (circular channel) h, a fluid streaming parameter (can be either the streaming displacement S or the average streaming velocity V), and one or more geometry variables. This additional geometry variable could be the length of the mother or daughter channels L, the daughter channel height h_1, the aspect ratio of the channel length to height L/h, the bifurcation angle, or the slope of the tapered channel, and others. There is a wide range of selections and variations among these geometry variables. They are not the focus of this study. It is assumed that the fluid is in a single phase, and surface tension and other surface forces can be neglected.

There are several methods of reducing a number of dimensional variables into a smaller number of dimensionless groups [15]. The Buckingham Pi Theorem was used in this study [30]. The streaming displacement S was used as the major streaming flow parameter. The fluid viscosity ν and mother channel height h were used as the repeating variables in forming the Pi groups, since both ν and h were used in the conventional Pi groups, such as flow Reynolds number and Womersley number. The Womersley number Wo is a nondimensional oscillation frequency defined as $h(2\pi f/\nu)^{1/2}$.

Based on the above discussion, the six flow streaming variables were combined to yield four chosen nondimensional groups; nondimensional streaming displacement $\overline{S}$ = function (oscillation flow Reynolds number Re, Womersley number Wo, and a nondimensional geometry parameter), where Re is based on the mean oscillation velocity, defined as $2Afh/\nu$. The geometry parameter represents the effects of channel configuration on flow streaming. This is a complex topic and is not the focus of this study.

2.3 Scaling Analysis. Using scaling analysis, the magnitude of the streaming velocity in a tapered channel can be estimated. Based on mass conservation principles for incompressible oscillating flows in a planar tapered channel, it can be shown that the instantaneous volume flow rate at any axial location of the channel must be a constant

$$hu = C \tag{1}$$

where h and u are the channel height and mean velocity, respectively. Equation (1) can be written in the differential form

$$du/dx = -(u/h)(dh/dx) \tag{2}$$

or

$$\Delta u/\Delta x = -\mathrm{Re}(\upsilon/h^2)\Phi \tag{3}$$

where x is the coordinate along the channel axis, Φ is the slope of the channel dh/dx, and υ is the fluid kinematic viscosity. Streaming flow is induced by oscillating the convergent (accelerating) and divergent (decelerating) flows. The strength of flow streaming per oscillation cycle V' with a finite oscillation amplitude L may be approximated as the mean velocity difference between the divergent and convergent flows within a distance of L

$$V' \sim \Delta u \sim \mathrm{Re}\, L(\upsilon/h^2)\Phi \sim O(1/h) \tag{4}$$

Multiplying Eq. (4) with the oscillation frequency f, the streaming velocity V in terms of meters per second is obtained. The above scaling analysis shows that the relative streaming velocity in a microtapered channel will be higher than that in the macrochannels when the flow rate is a constant. It is noted that the velocity profile differences between the developed and developing flows give rise to flow streaming, which is directly correlated with the size of the surface area within the zone of the developing flows. As the channel diameter decreases, the ratio of surface area to volume changes increases, and the relative strength of streaming flow will increase. For a typical water experiment of Re=10, L =10 mm, $\upsilon = 1\times10^{-6}$ m^2/s, h=1 mm, Φ=0.005, and f=10 Hz, $U_{\max}$ is estimated to be 5 mm/s.

It is noted that for a circular tapered channel, Eq. (1) becomes $h^2u = C$ and the cross-sectional area decreases faster as the channel diameter decreases. Consequently, the value of maximum streaming velocity is twice the value for a planar tapered channel.

However, there is a limit on how small the channel size can be. The power consumptions (or the pressure drop) versus the channel diameter will increase faster than that of the flow streaming.

Flow streaming in a bifurcating structure is more complicated than that in a straight tapered channel. In addition to the aforementioned parameters, it also depends on the diameter ratio of mother to daughter tubes as well as bifurcation angles. To simplify

the analysis, one may assume that the inflow has a perfect parabolic velocity profile, and the backflow has a perfect uniform velocity profile in the mother tube with zero-mean velocity. The maximum streaming velocity V should occur at the center with the order of mean flow velocity U. For a 30 deg bifurcation water experiment with Reynolds number Re=10, $\upsilon=1\times10^{-6}$ m^2/s, $h=1$ mm, and $f=10$ Hz, V is estimated to be 10 mm/s.

The convective heat Q_{st} carried by flow streaming across a channel length L can be estimated as follows:

$$Q_{st} \sim \dot{m}C\Delta T \sim \rho A_c VC\Delta T \tag{5}$$

when the effects of axial thermal diffusion in streaming flow are neglected, where ρ is the density of fluid, C is the specific heat, V is the streaming velocity, and ΔT is the temperature difference across the channel longitudinal direction. While the heat conduction along the longitudinal direction of channel Q_c with length L, cross-sectional area A_c, and thermal conductivity K can be calculated as

$$Q_c \sim KA_c\Delta T/L \tag{6}$$

Therefore, the ratio of heat transfer enhancement, or the ratio of streaming convection over pure heat conduction can be written as

$$Q_{st}/Q_c = \rho CVL/K \tag{7}$$

It is noted that $V_t/A_c=A$, where V_t is the tidal volume of oscillation, A_c is the channel cross-sectional area, and A is the oscillation amplitude. Assuming the streaming velocity is an order of magnitude smaller than the mean oscillation velocity for typical microchannel applications, as suggested in the scaling analysis, i.e., $V=0.1U$, where $U=2Af$, the ratio of convective streaming heat transfer to conduction heat transfer Q_{st}/Q is then

$$Q_{st}/Q_c \sim 0.1\rho CfAL/K \tag{8}$$

The above equation (Eq. (8)) shows that the ratio of streaming convection to conduction is directly proportional to the thermal properties of the fluids, oscillation amplitude, oscillation frequency, and heat transfer distance and inversely proportional to the material conductivity. In the above estimation, if the liquid water is used as the working medium and copper is used for the heat conduction material, oscillation frequency is 10 Hz, oscillation amplitude is 0.004 mm, and channel length is 100 mm, the estimated ratio of the heat transfer rate for streaming convection to copper heat conduction is about eight.

2.4 Computer Simulations. Zhang et al. [31,32] conducted computer simulations of flow streaming in bifurcation channels. In this study, computer simulations were conducted of streaming and heat flows in multigeneration mini-/microbifurcation as well as tapered channels using the commercial computational fluid dynamics (CFD) software FLUENT V.6.2 (ANSYS, Inc., Canons, PA). Computer simulation is a necessary tool to display the dynamic distribution patterns of fluid streak lines in microchannels and in particular, to theoretically eliminate mass diffusion in the fluid. These simulated streaming flow patterns are essential in understanding the physics of flow streaming, but not yet possible to obtain experimentally based on current experimental techniques.

The configuration of the bifurcation network model used in the computer simulation is shown in Fig. 2, which is the same model used in our previous work [31]. The symmetrical bifurcation channel network consisted of four generations and 15 channels. All channels had the length of 1 mm except the length of 1.5 mm for the mother channel. The height of the mother tube was 1 mm and it decreased by one-half after each bifurcation. As a result, mean oscillation velocities of the fluid in all channels were maintained at the same value, thus providing a meaningful and fair comparison of results. The bifurcating angle was 60 deg for all bifurcations.

The fluid was modeled as an incompressible, Newtonian fluid. Two-dimensional flows were simulated for the sake of simplicity.

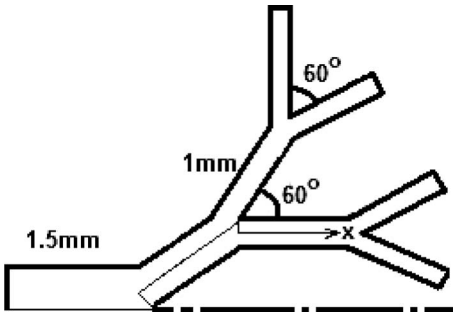

Fig. 2 Bifurcation channel networks used in the computer simulation

Fluid motion was governed by the Navier–Stokes (N–S) equations and the continuity equation. The second-order implicit, semi-implicit method for pressure-linked equations, consistent (SIMPLEC) numerical scheme was used. The flows were considered to be strictly laminar. The convective heat transfer equation was numerically solved simultaneously with the N–S equations. The fluid conductivity K was set to zero, so that the effect of thermal diffusivity would be theoretically eliminated and the resultant temperature distribution patterns were purely created by fluid streaming. The initial temperature of the fluid inside the channel network was zero. At $t>0$, fluids, with constant properties but a high temperature, entered the mother channel. A time-dependent parabolic velocity profile, in which the center velocity U_c is defined as $U_c=U_{max}\sin(2\pi ft)$, was applied at the inlet of the mother tube. Zero-gradient velocity and temperature boundary conditions were applied at the outlet of eight daughter channels. Zero heat flux boundary conditions were applied on all wall surfaces. Since thermal diffusions between fluids were artificially eliminated in the computer simulations, the unsteady temperature patterns mimic the patterns of fluid streak lines, displaying the vivid pictures of flow streaming.

Total friction loss was used as the bench mark for grid converging tests since wall shear stress was susceptible to the mesh size used in the simulations [32]. It was the numerical integration of wall shear stress over the entire channel networks' surfaces and over an oscillation cycle. As a compromise between computational accuracy and the CPU time, mesh size $80(H)\times200(L)$ and time steps of 32 per oscillation cycle were used in all simulations. The residual tolerances for continuity and velocities were 10×10^{-3} and the mass transport equation was 10×10^{-6}. The numerical scheme was also validated by analytical solution of oscillation flow in a straight pipe. The effects of the boundary conditions on the oscillation flow streaming were negligible when oscillation frequencies $f<15$ [31].

2.5 Experimental Studies. Photographic streaming flow visualization experiments were conducted in a minichannel bifurcation network. The purpose of the experiments was to qualitatively confirm and visualize the flow streaming and its transport characteristics within a micro-/miniscale of networks of channels. The experimental setup and channel network configurations are shown in Fig. 3. Flow was generated by an in-house made syringe oscillator, which was in turn driven by an electromagnetic device. An electrical signal generator with variable voltage and frequency output controlled the electromagnetic device. Open minichannel networks, with square cross-sectional channel geometries of 0.8×0.8 mm^2 (1/32 in. (width)$\times$1/32 in. (depth)) were milled into an $80\times80\times5$ mm^3 transparent Plexiglas panel. The network had three channel generations. Each mother channel was branched to four daughter channels. There was one channel in generation I, four channels in generation II, and 16 channels in Generation III. The lengths of the channels were 40 mm, 20 mm, and 10 mm for

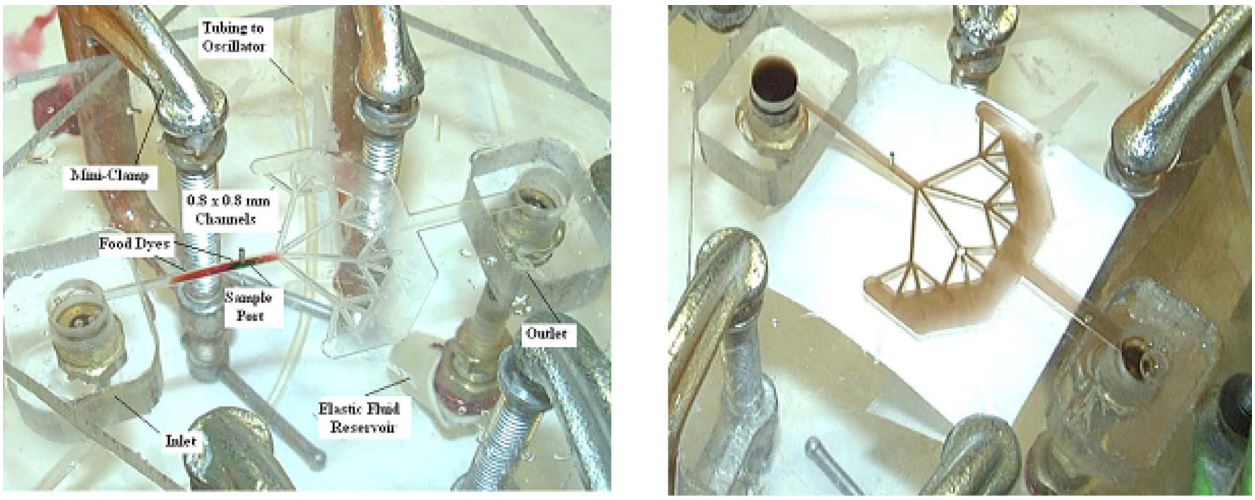

(*a*) (*b*)

Fig. 3 The experimental setup and channel network configurations: (*a*) color patterns before the flow streaming (*T* = 6 s); (*b*) fluid mixing, propulsion, and multichannel distribution by oscillation flow streaming (*T* = 14 s)

generations I, II, and III, respectively. Branching angles were 22.5 deg for all channels.

Minitube fittings were glued to the Plexiglas panel at the bottom, forming the fluid entrance and exit. A clear PVC tubing of 0.8 mm in inner diameter connected the oscillator with the tube fitting at the inlet. It is noted that flow streaming is a phenomenon of bidirectional flow in a single tube, hence there is no need for a looped tubing arrangement, as required in conventional pumping. A small water balloon was connected to the outlet (from the bottom) and served as an elastic water reservoir to accommodate oscillating fluid pressure and volumes. The second Plexiglas panel was then clipped from the top of the first Plexiglas panel by four miniclamps to form the closed fluid passages. A sample input port with a diameter of 0.4 mm was constructed by drilling through the top Plexiglas panel and connecting to the mother channels at the midsection. The sample port was sealed during the experiments. To facilitate the viewing of streaming patterns, food dyes (red and green) (McCormick and Co. Inc., Hunt Valley, MD, relative density = 1) were used. The experiment started with the water filling. Air bubbles trapped in the channels were removed before the start of the experiments. Then one drop of red dye was injected and followed by one drop of green dye through the sample port using PS-26 needles.

Preliminary experiments on flow streaming phenomenon were also conducted in micro bifurcation channels. The bifurcation channels have dimensions of 200(width) $\times$ 200 μm^2 (depth) with a rectangular cross-sectional geometry. The experimental system consists of a microfluidic chip embedded with bifurcating channels, tubing fittings and connections, a fluid reservoir, a fluorescence microscopic, a computer for image storage and display, and an oscillating syringe. Oscillatory flow of variable frequency and amplitude is generated by entrance pressure oscillations. The variable pressure is created by an oscillating syringe, which is in turn driven by a mechanical device fabricated in-house and powered by a variable-speed dc motor. To facilitate the viewing of streaming patterns, fluorescence particles of 0.7 μm in diameter were injected into the channel and microscope pictures were taken before and after the flow oscillations.

3 Results and Discussion

Figure 3(*a*) shows the photography of the food dye distribution before the flow oscillation. The mass diffusion process of the dyes was used to mimic the process of the thermal diffusion based on the similarity of heat and mass transfer. The food dye here may represent a bolus of hot fluid particles located near the injection port inside the microchannel. The objective of the experiment was to move this packet of hot fluid particles away from the injection port by convective streaming flows. The picture was taken about 6 s after the injections of food colorings. A drop of red dye was first injected. Next, a drop of green dye was injected and the injection of green dye pushed the injected red dye away from the sample port, as shown in Fig. 3(*b*). It is observed that initially, the diffusion front of both dyes moved noticeably, then gradually slowed down and became stationary when the distance was approximately several channel diameters away from the injection port. It demonstrates the limited mass transport (thermal transport) capability by a pure diffusion process.

Flow mixing and oscillation ($f = 4$ Hz, $A = 3.2$ mm) were started after the sample injection. Although oscillating tide volume was only about 10% of the mother tube volume, food colorings were propelled quickly into branching networks. Figure 3(*b*) shows the pattern of food dye distribution at $T = 8$ s after the start of oscillation. The red and green dyes, initially located around the sample port, were completely mixed and then distributed almost uniformly into the entire generation II and III channels as well as back flow to the entrance, demonstrating the two-way fluid propulsion, multichannel distribution, and highly efficient mixing.

The same experiment was also carried out at frequency = 2 Hz with the same oscillation amplitude. It was found that the rates of fluid mixing and fluid propulsion were slower compared with the higher frequency experiment. It took approximately twice as much time (17 s after the flow oscillation) for food dyes to arrive at the end of the generation III channels.

Quantitative experimental results on flow streaming were scarce in the literature. The current experimental system was not capable of producing detailed and accurate experimental measurements as well. However, the above experiment did successfully demonstrate the potential of streaming-based heat pipe/spreader technology. This was a multifunctional process including fluid mixing, propulsion, and multichannel distribution in minichannel networks.

Microscopic images of instantaneous particle concentration profiles in a microchannel during the test experiments are shown in Fig. 4. Figure 4(*a*) shows a bright field image of fluorescent particles being injected at a bifurcation junction using a needle. Transient ε-shaped fluorescent particle distribution patterns in the mother tube, a dark field image after 5 cycles of oscillation, is shown in Fig. 4(*b*). Although the oscillation tides are limited to

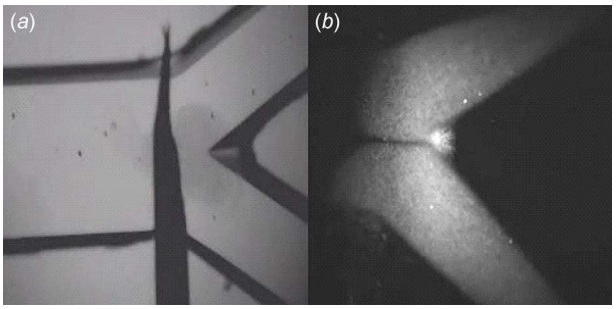

Fig. 4 Images of transient particle transport patterns in microbifurcation under flow streaming

one diameter in length, particles quickly spread out of the tidal volume range, demonstrating the phenomena of flow streaming in microbifurcation under oscillating flows.

Computer simulations of water temperature distribution with the sole effect of flow streaming in a straight tapered channel were conducted, as shown in Fig. 5. From the left, cold fluid enters the channel initially occupied by hot fluid. The objective of the simulations was to demonstrate the convective transport of cold fluid from left to right under streaming oscillation flows. The conductivity of the water K was set to zero so the effects of thermal conductivity were mostly eliminated (except numerical diffusion). The boundary conditions were similar to ones used in bifurcation flow simulations as discussed before.

The average height of the channel was 0.6 mm with heights at the inlet and outlet of 1 mm and 0.2 mm, respectively. The channel length was 5 mm, and therefore, the slope of the tapered channel was 0.16. Oscillation frequency $f=10$ Hz and peak oscillation velocity at the channel center $U_c=0.01$ m/s (peak oscillation amplitude $A=0.32$ mm or $A=0.6$ mm of the average channel height) were simulated. Figures 5(*a*) and 5(*b*) display the temperature profiles at the end of the first cycle ($t=0.1$ s) and the 20th cycle ($t=2$ s), respectively. Results again show that although the oscillation amplitude A is much smaller than the channel length (or was only a fraction of the channel height) and heat conductivity of the fluid was zero, the tide of the cold water quickly moves to the right side of the channel due to the action of flow streaming, demonstrating the feasibility of oscillating flow heat pipe technology. Streaming flow accelerated at the narrow end of the channel due to the acceleration of the main oscillation flow. On the contrary, in the case of zero-mean velocity oscillation flows in a straight channel with zero fluid heat conductivity, heat transport in the axial direction will not go beyond the range of flow oscillation. It was noted that the speed of streaming flow across the channel length shown by computer simulation had a very good agreement with the result predicted by Eq. (4) of the scaling analysis.

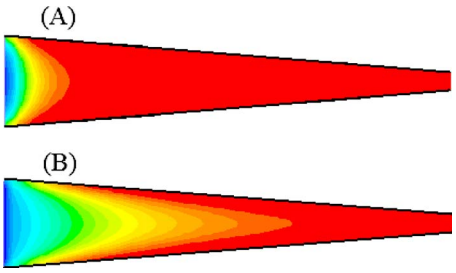

Fig. 5 Oscillating streaming flow induced temperature profile in a tapered channel. From the left, cold fluid enters the channel initially occupied by hot fluid ($Re_{max}=0.7$, $f=10$ Hz, $K=0$): (*a*) $T=0.1$ s (end of the first cycle); (*b*) $T=2.0$ s (end of the 20th cycle)

Theoretically, flow streaming displacement was defined as the front position of the fluid streak line during the oscillation flows. Practically, however, the streaming front was blurred and diluted. There were no steep changes in the temperature/concentration gradient as well as no distinct boundary between the tidal and reserve flows. Also, discussions on the practical definitions of the streaming front and how to measure it were rare in the literature. It was noted in the current dynamics computer simulation that the value of 20% ΔT (the temperature difference between the inlet and outlet) contour was always clearly marked on the color bar and easy to trace by direct observation. For lack of precedent as well as for simplicity, the streaming front definition employed by the current study is the position of the 20% of ΔT contour representing the front of the streaming flow. It is true that such a choice seems arbitrary. A better definition of the streaming front is open for discussion.

Since thermal diffusivity of the fluid was set to zero in the simulations, the resultant streaming patterns were supposedly free of diffusion. This was difficult to do experimentally. Meanwhile, it was also noted that there was always a finite amount of numerical diffusion in the simulations due to inherent errors of the numerical method. The errors induced by the numerical diffusion were indeed negligible. As discussed later in this paper, the diffusion coefficient (or Prandlt number) had little effect on the streaming velocity for a wide range of Prandlt numbers.

Figure 6 illustrated the effects of flow oscillation amplitude on the streaming front displacement in the bifurcation network shown in Fig. 2. Oscillation frequency $f=6$ Hz and amplitude $A=1.06$ mm, 2.12 mm, and 3.18 mm was employed. In Fig. 6(*a*),

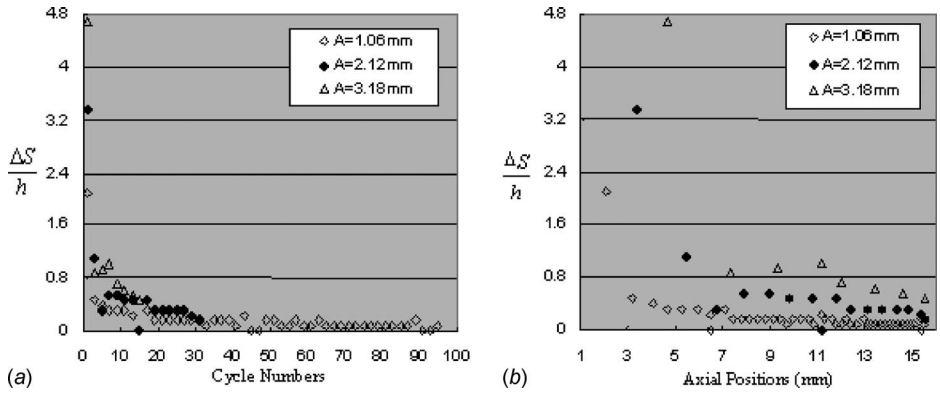

Fig. 6 Effects of oscillation amplitude on relative streaming displacement. Oscillation frequency $f=6$ Hz was simulated; displacement as a function of (*a*) oscillation cycle number and (*b*) axial position

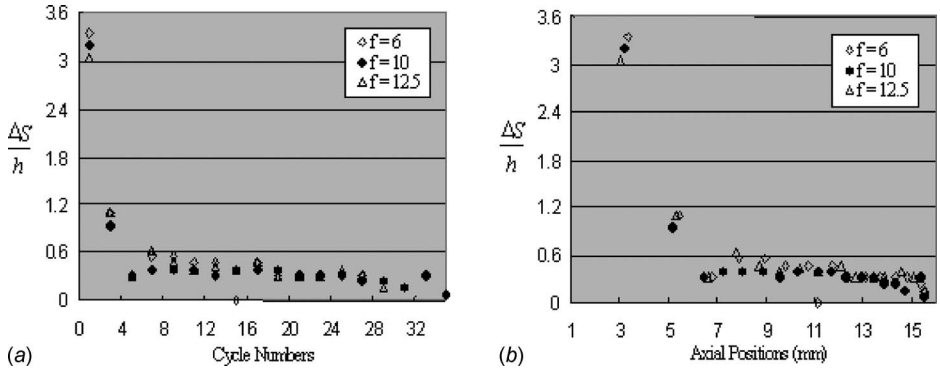

Fig. 7 Effects of oscillation frequency on relative streaming displacement. Oscillation amplitude $A=1$ mm was simulated; displacement as a function of (*a*) oscillation cycle number and (*b*) axial position

the dimensionless relative streaming displacement ($\Delta S/h$) as a function of the number of elapsed oscillation cycle was presented using nondimensional oscillation amplitudes as references. Results show that the peak value of streaming clearly occurred within the first several cycles for all oscillation amplitudes. The strength of the flow streaming then decreased quickly while the tides of the streaming hot fluid current was repeatedly approaching and bypassing the bifurcation junction at a low speed. This result agrees well with the experimental observation of Haselton and Scherer [23]. Their experiments were conducted in a single large Y-shape channel using beads as the streaming flow indicator. Figure 6(*a*) shows that the oscillation amplitude had dominant effects on the streaming velocity. For example, although the oscillation amplitude increased 50% (increase from $A=2.12$ mm to 3.18 mm), the streaming velocity increased by more than 100%. It took 15, 32, and 95 oscillation cycles for streaming to reach the end of the bifurcation channel generation III with oscillation amplitudes $A=3.18$ mm, 2.12 mm, and 1.06 mm, respectively.

In Fig. 6(*b*), the relative magnitude of streaming displacement as a function of channel location was presented with nondimensional oscillation amplitudes as references. Results show a consistent decline of streaming magnitude at locations away from the channel entrance for all oscillation amplitudes.

Flow streaming was a phenomenon confined in the region of the developing flow. In an infinitely long straight tube, which would be approximated in tube regions far away from the entrance and bifurcation, pure oscillation flow would not produce streaming. As the streaming flow front approached the bifurcation, it picked up strength again, as shown in Fig. 6(*b*), axial location right after 6 mm and 12 mm, are the junctions between channel generations I and II, and II and III. For oscillating flow in the bifurcation networks, the location of bifurcations effectively served as a pumping station to keep streaming flow moving.

Figure 7 illustrates the effects of flow oscillation frequency on streaming front displacement in the same bifurcation network. Oscillation amplitude $A=1$ mm and frequency $f=6$ Hz, 10 Hz, and 12.5 Hz, were employed. In Fig. 7(*a*), the dimensionless relative streaming displacement ($\Delta S/h$) as a function of the number of elapsed oscillation cycles is presented using nondimensional oscillation frequency as a reference. In Fig. 7(*b*), the relative magnitude of streaming displacement is presented as a function of channel location. Figure 8 results show a similar trend as one observed in Fig. 6 that there is a consistent decline of streaming magnitude away from the channel entrance for all oscillation parameters, and flow streaming gained strength at the bifurcations. There was no significant difference of streaming displacement as a function of oscillation cycle number between different oscillation frequencies, because the majority of data points overlapped. Since the value of streaming displacement per second (streaming velocity) can be calculated by multiplying the displacement per cycle by frequency, this indicates that streaming velocity is directly proportional to the oscillation frequency.

Changing both the oscillation amplitude and frequency will change the oscillation flow intensity, and therefore changes the characteristics of streaming flows. However, oscillation amplitude had greater effects than the frequency, as in the comparison of results between Figs. 6 and 7. This may be attributed to the fact that higher oscillation amplitude (also oscillation volume) will push the fluid directly closer to the location of the channel bifurcation (e.g., source of streaming), bypass or reduce the exposure of fluid in the zone of low streaming (e.g., zone of straight pipe), and therefore, effectively enhance the average streaming velocity.

Results in Figs. 6 and 7 show that peak values of streaming clearly occur within the first several cycles for all oscillation amplitudes. Figures 6 and 7 also show that at some locations (near the bifurcations) and cycle numbers, the streaming displacement is close to zero, or the streaming flow is stationary. After a few more oscillations, streaming flows started to move again and accelerate. Direct dynamics observation from computer simulations show that flows are still continuously streaming at those points, but with noticeable changes in the streaming velocity profiles. Although the measured streaming displacements were identical (zero net displacement), which was based on the tip positions (usually located at the channel centerline) of the streaming profile, there was a bulk motion of streaming current to the right hand side with the shape of streaming profiles developing from a pointed shape to a blunted shape and sometimes a symmetrical wave shape (off the centerline).

Next, overall convective heat transport was considered by oscillation flow streaming with the effects of fluid thermal conductivity in the aforementioned bifurcation networks. Figure 8 shows the effects of Prandtl number ($\mathrm{Pr}=\nu/\alpha$) or the thermal diffusivity on effective (overall) streaming velocity. With a nonzero thermal diffusivity, thermal transport mechanisms included both streaming advection and thermal diffusion. The effective streaming flow Reynolds number Re_{st}, which is a nondimensional streaming velocity defined as Vr/ν, as a function of Prandtl number, is presented. The streaming velocity is defined as the rate of this 20% of ΔT contour traveling down the channel network at each generation. Oscillation amplitude $A=0.3$ mm and frequency $f=10$ Hz were used in the simulations while the Prandtl number varied from 0.07 to 700. Figure 8 shows that there are no significant changes in streaming velocities (streaming flow Reynolds number) for the entire range of Prandtl numbers greater than one, and this was true for all three channel generations. In other words, Fig. 8 shows that the thermal transport by convective flow streaming is the dominant transport mechanism if the thermal diffusivity of the fluid is less than the kinematic viscosity of the fluid.

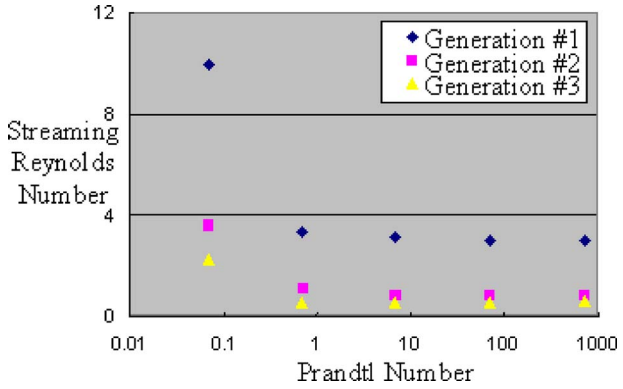

Fig. 8 Effects of the Prandtl number on the convective heat transport process under flow streaming

Due to a similarity between the mass and heat transfer problem, the above conclusion may be extended to other applications involving mass transport. For example, streaming flow can be used as a convective mass transfer means when the Schmidt number ($\mathrm{Sc}=\nu/D$) is greater than one, or as an effective means to transport particles entrained in fluids (such as cells, bacteria, and other fluid suspensions) when the particle diffusivities in fluids are less than the fluid kinematic viscosity.

3.1 Discussions on Applications. The proposed streaming flow based micro-/miniheat pipe technique has both limitations and advantages. The major disadvantage is its low efficiency in transport of fluids. Compared with the main current of the oscillating channel flow, flow streaming is always a second-order flow. Oscillatory flow increases friction losses. Clearly, this inefficiency could limit its applications where direct pumping can be easily applied. However, it has a great potential in micro-/minichannels, where various cost-effective and reliable micropumps are still under development. Also, an additional device which generates oscillating flow may be required, which could be a disadvantage in practical applications.

The oscillation flow in micro-/minichannels can be generated by piezoelectric (PZT) diaphragms. PZT diaphragms can easily produce the needed high pressure head in micro-/minichannels. Streaming flow based microfluidics-driven PZT diaphragms provide many potential advantages. It will be valveless (no check valves needed), low cost (under $1/piece for a dime-size PZT under mass production conditions, and no need for looped piping), reliable (no moving parts except the motion of the PZT), regular battery compatible, and easy system integration. It is also noted that flow streaming can also be generated by thermal oscillations, which is another interesting research topic.

4 Conclusions

Visualization experiments of fluid mixing, propulsion, and multichannel heat/mass distribution by streaming were conducted in mini- and microchannel networks. Computer simulations in tapered channels and bifurcation channel networks demonstrated the feasibility of streaming flow based heat pipe technology. Oscillation streaming flow can be used as a cost-effective and reliable convective transport means when the thermal/mass diffusivity is less than the fluid kinematic viscosity. More work is needed to further study and understand the flow streaming phenomenon and its practical applications.

Acknowledgment

Research described in this article was supported by the National Science Foundation Grant No. 0530203.

Nomenclature

A = oscillation amplitude (m)
A_c = channel cross-sectional area (m^2)
D = mass diffusivity (m^2/s)
f = oscillation frequency (Hz)
h = height or diameter of the channels (m)
h_1 = height or diameter of the daughter channels (m)
K = fluid thermal conductivity (W/m K)
L = length of the mother or daughter channels (m)
Pr = Prandtl number ($\mathrm{Pr}=\nu/\alpha$)
Q_{st} = zero thermal conductivity convection heat transfer due to streaming (W)
Re = flow oscillation Reynolds number, $2Afh/\nu$
S = streaming flow displacement (m)
$\overline{S}$ = nondimensional streaming flow displacement
T = oscillation period (s)
t = time (s)
u = mean flow velocity (m/s)
U_c = flow velocity at the center (m/s)
$U_{\max}$ = maximum flow velocity (m/s)
V' = strength of fluid streaming (m/s per cycle)
V = fluid streaming velocity (m/s)
V_t = tidal volume per oscillation (m^3)
Wo = Womersley number or nondimensional oscillation frequency, $h(2\pi f/\nu)^{1/2}$
α = fluid thermal diffusivity (m^2/s)
ΔT = temperature difference along channel in the axial direction (K)
ρ = fluid density (kg/m^3)
Φ = slope of the tapered channel, dh/dx
ν = fluid kinematic viscosity (m^2/s)

References

[1] Nishio, S., 2004, "Single-Phase Laminar-Flow Heat Transfer and Two-Phase Oscillating-Flow Heat Transport in Microchannels," Heat Transfer Eng., **25**(3), pp. 31–43.
[2] Hargrave, G. K., Kilham, J. K., and William, A., 1986, "Operating Characteristics and Convective Heat Transfer of a Natural-Gas-Fired Pulsating Combustor," J. Inst. Energy, **59**, pp. 63–69.
[3] Tatsuo, N., Atsushi, T., and Yuji, K., 1987, "Flow and Mass Transfer Characteristics in Wavy Channels for Oscillatory Flow," Int. J. Heat Mass Transfer, **30**(5), pp. 1007–1015.
[4] Georgiadis, J. G., 1988, "Heat Transfer in Pulsatile Flow Through a Straight Distensible Tube," HTD (Am. Soc. Mech. Eng.), **101**, pp. 71–76.
[5] Peattie, R. A., 1989, "Heat Transfer in Laminar, Oscillatory Flow in Cylindrical and Conical Tubes," Int. J. Heat Mass Transfer, **32**(5), pp. 923–934.
[6] Kim, S. Y., Kang, B. H., and Hyun, J. M., 1993, "Heat Transfer in the Thermally Developing Region of a Pulsating Channel Flow," Int. J. Heat Mass Transfer, **36**, pp. 2647–2656.
[7] Datta, N., Dalal, D. C., and Mishra, S. K., 1993, "Unsteady Heat Transfer to Pulsatile Flow of a Dusty Viscous Incompressible Fluid in a Channel," Int. J. Heat Mass Transfer, **36**(7), pp. 1783–1788.
[8] Valueva, E. P., Popov, V. N., and Romanova, S. Yu., 1993, "Heat Transfer Under Laminar Pulsating Flow in a Round Tube," Teploenergetika (Moscow, Russ. Fed.), **8**, pp. 47–54.
[9] Inaba, T., and Kubo, T., 1993, "Enhanced Heat Transfer through Oscillatory Flow," Trans. Jpn. Soc. Mech. Eng., Ser. B, **59**(563), pp. 165–170.
[10] Chung, J. H., and Hyun, J. M., 1994, "Heat Transfer From a Fully-Developed Pulsating Flow in a Curved Pipe," Int. J. Heat Mass Transfer, **37**(1), pp. 43–52.
[11] Park, J. H., and Baek, S. W., 2004, "Investigation of Influence of Thermal Accommodation on Oscillating Micro-Flow," Int. J. Heat Mass Transfer, **47**, pp. 1313–1323.
[12] Sert, C., and Beskok, A., 2002, "Oscillatory Flow Forced Convection in Micro Heat Spreaders," Numer. Heat Transfer, **42**, pp. 685–705.
[13] Suzuki, O., 2003, "Design and Manufacturing Challenges of Liquid Heat Sink for Next Generation Liquid Cooling," *Proceedings of the JSME Project Meeting on Design and Manufacturing of High Performance Heat Sinks for Microelectronic Equipment*, Happo-En, Tokyo, Japan, Oct. 14–17.
[14] Zhao, T., and Cheng, P., 1995, "A Numerical Solution of Laminar Forced Convection in a Heated Pipe Subjected to a Reciprocating Flow," Int. J. Heat Mass Transfer, **38**(16), pp. 3011–3022.
[15] Li, P., and Yang, K. T., 2000, "Mechanisms for the Heat Transfer Enhancement in Zero-Mean Oscillatory Flows in Short Channels," Int. J. Heat Mass Trans-

fer, **43**(19), pp. 3551–3566.
[16] Nyborg, W. L., 1953, "Acoustic Streaming Due to Attenuated Plane," J. of American Society of Acoustics, **25**, pp. 68–75.
[17] Rosenblat, S., 1959, "Torsional Oscillation of a Plane in Viscous Fluids," J. Fluid Mech., **6**, pp. 206–220.
[18] Rosenblat, S., 1960, "Flow Between Torsional Oscillating Disks," J. Fluid Mech., **8**, pp. 388–399.
[19] Riley, N., 1965, "Oscillating Viscous Flows," Mathematika, **12**, pp. 161–170.
[20] Riley, N., 1967, "Oscillating Viscous Flows, Review and Extension," J. Inst. Math. Appl., **3**, pp. 419–434.
[21] Jones, A. F., and Rosenblat, S., 1969, "The Flow Induced by Torsional Oscillations of Infinite Planes," J. Fluid Mech., **37**, pp. 337–347.
[22] Lyne, W. H., 1971, "Unsteady Flow Viscous Flow in a Curved Tube," J. Fluid Mech., **45**, pp. 13–31.
[23] Haselton, F. R., and Scherer, P. W., 1982, "Flow Visualization of Steady Streaming in Oscillatory Flow Though a Bifurcation Tube," J. Fluid Mech., **123**, pp. 315–333.
[24] Simon, B., Weinmann, G., and Mitzner, W., 1982, "Significance of Mean Airway Pressure During High Frequency Ventilation," Physiologist, **25**, pp. 282–293.
[25] Tarbell, J. M., Ultman, J. S., and Durlofsky, L., 1982, "Oscillatory Convection Dispersion in a Branching Tube Network," ASME J. Biomech. Eng., **104**, pp. 338–342.
[26] Grotberg, J., 1984, "Volume Cycled Oscillatory Flow in a Taped Channel," J. Fluid Mech., **141**, pp. 249–264.
[27] Gaver, D., and Grotberg, J., 1986, "An Experimental Investigation of Oscillating Flow in a Taped Channel," J. Fluid Mech., **172**, pp. 47–61.
[28] Briant, J. K., and Lippman, M., 1992, "Particle Transport Through a Hollow Canine Airway Cast by High-Frequency Oscillatory Ventilation," Exp. Lung Res., **18**, pp. 385–407.
[29] Goldberg, I., Zhang, Z., and Tran, M., 1999, "Steady Streaming of Fluid in the Entrance Region of a Tube During Oscillatory Flow," Phys. Fluids, **11**(10), pp. 2957–2962.
[30] White, F., 2003, *Fluid Mechanics*, 5th ed., McGraw-Hill, New York.
[31] Zhang, Z., Fadl, A., Liu, C., and Meyer, D., 2008, "A Streaming Flow Based Lab-on-Chip Platform Technology," *Proceedings of the the First ASME Micro/Nanoscale Heat Transfer International Conference (MNHT08)*, Taiwan, Jan. 6–9.
[32] Zhang, Z., Fadl, A., Liu, C., Meyer, D. M. L., and Krafczyk, M., 2009, "Fluid Streaming in Micro/Minibifurcating Networks," ASME J. Fluids Eng., **131**(8), p. 084501.